# Exploring out-of-equilibrium quantum simulation in a many-atom strontium cavity QED platform

by

## Dylan J. Young

B.S., Yale University, 2018

M.S., University of Colorado, Boulder, 2021

A thesis submitted to the
Faculty of the Graduate School of the
University of Colorado in partial fulfillment
of the requirements for the degree of
Doctor of Philosophy
Department of Physics
2025

James K. Thompson, Chair Ana Maria Rey Jun Ye Murray Holland

**Committee Members:** 

Andrés Montoya-Castillo

Young, Dylan J. (Ph.D., Physics)

Exploring out-of-equilibrium quantum simulation in a many-atom strontium cavity QED platform
Thesis directed by Prof. James K. Thompson

In my thesis work, I have explored novel ways to experimentally simulate nonequilibrium quantum models in a cavity quantum electrodynamics (cavity QED) platform consisting of many atoms collectively coupled to an optical cavity. Quantum simulation is a burgeoning field, both in atomic physics and beyond, with the potential to answer many open questions about complex quantum systems. In particular, many of these systems are expected to exhibit nontrivial dynamical phases of matter not observable in thermodynamic equilibrium, which are challenging to observe in nature but could be realized with a controllable quantum simulator. To this end, cavity QED offers the ability to natively engineer infinite-range nonlocal interactions, a feature present in many quantum magnetism and quantum optics models. This makes the platform well-suited to study these models and explore their behavior out of equilibrium.

A key breakthrough in my thesis work was developing a simulator to study dynamics in the BCS model of superconductivity using an ensemble of thermal spins interacting through the cavity. Although this model has been predicted to exhibit three distinct phases of dynamics after quenching the system out of equilibrium, an observation of these phases in real superconducting or superfluid platforms has remained out of reach. Thanks to the ability to engineer cavity-mediated atom-atom interactions and control single-particle energy shifts in our system, I successfully utilized an Anderson pseudospin mapping to experimentally observe all three predicted dynamical phases for the first time in any platform. By expanding the scope of this mapping in straightforward ways, I was able to explore even richer dynamics and performed a study identifying and contrasting two distinct many body energy gaps in the system. My work opens the door towards engineering even richer and more complex quantum models, such as superconductors with nontrivial topology and synthetic lattices experiencing coherent correlation spreading across their sites.

## **Dedication**

To my grandmother, who humored me—and to my grandfather, who had humor.

#### Acknowledgements

I started out my physics career as a theorist, with wonderful and valuable experiences with Professors Sohrab Ismail-Beigi and Liang Jiang who taught me the importance of thinking carefully—but not letting rigor get in the way of progress. Because of my background, however, I had a sharp learning curve when starting as an experimentalist at JILA. The fact that I know anything at all about how to run experiments is thanks to a series of fantastic mentors. In particular, I'm grateful to my advisor James Thompson for his evident love of teaching, as well as for mostly holding back his shock when I told him I didn't know what an op-amp was. His ability to recast almost any atomic physics system as harmonic oscillators and Bloch spheres has profoundly shaped the way I think about physics and about learning in general. At times, Ana Maria Rey almost felt like a second PI, given how often we had theory discussions with her and her group. I have gained so many insights about physics from her, so thank you. Additionally, Juan Muniz and Julia Cline helped me a great deal in the first few years of my Ph.D, even when they had plenty of their own tasks to deal with. Graham Greve and Baochen Wu on the rubidium project were also a big part of making me feel welcome as a younger student.

Time moves on, and soon I became the oldest graduate student on the strontium side of the lab despite still not knowing anything. During that time, everyone in the Thompson Lab has left memorable impressions that distracted from the monotony of breaking things and slowly learning how to fix them. Vera Schäfer always had something interesting to talk about over socially-distanced pandemic-era lunches outside. Chengyi Luo is a brilliant researcher and good friend who had many interesting physics discussions with me. Zhijing Niu shared the dubious distinction with me of being the lead grad student on a project during her second year in lab, and we have figured out a lot together. Eric Song was an irre-

placeable lab partner, memory aide, and source of tea. He has also been a valuable second pair of eyes and always calls me out when I do something without a good reason. I'd also like to thank the "next generation" of the Thompson Lab: Braden Larsen, Hagan Hensley, Chitose Maruko, Cameron Wagner, Seth Chew, and Leah Huzjak, as well as postdocs Eliot Bohr and Joyce Kwan, for bringing life (and memes) to the group after a lot of the culture died off during COVID.

To repeat a trite statement, COVID was a strange time for us all. I'm grateful to have had a robust support network of people to keep me relatively sane. First, to my college friends who have partaken in the noble tradition of Bird Day: hampter. Second, to my D&D party: maybe we'll finally achieve bounty at level 20. To Jeronimo: thank you for Teleparties, introducing me to Huel, and for not laughing at my attempt to ride a OneWheel. To everyone in the Grand Canonical Ensemble: give 'em all what they came here for (music). I'd like to shout out Tyler McMaken in particular for being the driving impetus behind the group's formation. Thank you for giving me a space to practice one of my favorite hobbies.

Will Eckner has been here with me since the beginning, and we have really been through the ringer together. After seven years of physics, movies, games, and ketchup, it will be sad not to live with him anymore. Maybe this is something we can agree on for once? Hannah Yang was here for the middle, although it felt like we had been friends for much longer—her pure verve for life will never not make me smile. We've had so many good memories, from puzzles and jam sessions to road trips and world travels, and I hope to have many more. Jon Huster showed up late, but he latched on quick and pinned me down in the vice grip of friendship. Even though he has bad taste in carbs, he has good taste in vibes. Thank you for your relentless positivity, and maybe even for about 33% of the food.

Finally, I'd like to thank my family. To my sisters, for not rubbing in the fact that I am the only unmarried sibling. To my dad, for always finding interesting physics articles on the web, and for keeping me up to date with everyone. And to my mom, for always being there, even on weeks when I was too busy to say hi. I love you all.

## Contents

## Chapter

1	Intr	roduction	1
	1.1	General motivation	1
	1.2	2 Overview of results	
		1.2.1 Precision measurement of the natural linewidth of an ultranarrow atomic transition	7
		1.2.2 Observing dynamical phases in the Lipkin-Meshkov-Glick model	8
		1.2.3 Observing dynamical phases in the BCS model of superconductivity	10
		1.2.4 Emulating rf spectroscopy of fermionic superfluids using multilevel atoms	12
	1.3	Outline of thesis work	13
2	Coll	lective cavity QED with atoms	14
	2.1	Historical context	14
	2.2	The "bare" optical cavity	15
		2.2.1 Input-output relations	15
		2.2.2 The cavity transfer function	18
		2.2.3 Example: the PDH error signal	21
		2.2.4 Cavity finesse	23
	2.3	The atomic ensemble	24
		2.3.1 Bloch sphere representation of spin states	24
		2.3.2 The collective Bloch sphere	27

				vii
		2.3.3	The Holstein-Primakoff approximation/transformation	29
	2.4	Placir	ng atoms in the cavity	30
		2.4.1	The Jaynes-Cummings model	30
		2.4.2	Extending to many atoms: the Tavis-Cummings model	32
		2.4.3	Optical Bloch equations	35
		2.4.4	Regimes of atom-cavity coupling	36
	2.5	Adiab	atic elimination of the cavity mode	40
		2.5.1	Mean-field adiabatic elimination	41
		2.5.2	Effective Hamiltonian description	43
		2.5.3	Cavity-mediated spin-exchange interactions	46
		2.5.4	Comparing spin-exchange and superradiance regimes in past experiments	49
3	Exp	erimer	atal apparatus	53
	-		structure of strontium	53
	3.2		trontium oven	59
		3.2.1	The strontium volcano	59
		3.2.2	Refilling the oven	61
	3.3	Blue	cooling system	65
		3.3.1	The source and science chambers	65
		3.3.2	Laser breakout	69
		3.3.3	Hollow cathode lamp	72
		3.3.4	461 nm spectroscopy lock	74
		3.3.5	Repumping lasers	77
	3.4	Narro	w-line cooling system	79
		3.4.1	The SWAP MOT	80
		3.4.2	The 689 nm laser system	82
	3.5	The so	c <mark>ience cavity</mark>	85

			viii
		3.5.1 Cavity parameters	85
		3.5.2 813 nm optical lattice	88
		3.5.3 Lattice-induced inhomogeneous broadening	92
		3.5.4 Scalar, vector, and tensor lattice shifts	93
		3.5.5 A magic angle lattice	97
	3.6	The reference cavity	99
	3.7	Homebuilt interference filter ECDLs	103
		3.7.1 Laser linewidth measurements	107
4	Cav	ity-QED measurements of the $^{87}$ Sr millihertz optical clock transition and determination of it	S
	natı	ural linewidth	112
	4.1	Introduction	112
	4.2	Initial experimental setup	115
	4.3	Expected phase shifts for QND probes	117
	4.4	Probing dispersive shifts on the clock transition	121
	4.5	Probing dispersive shifts on the 7.5 kHz transition	125
	4.6	Measuring the ratio of dispersive shifts	127
	4.7	Inferring the clock transition linewidth	129
	4.8	Systematics analysis	131
		4.8.1 Corrections on the phase shift $\Delta \varphi_1$	131
		4.8.2 Corrections on the phase shift $\Delta \varphi_0$	136
		4.8.3 Corrections on the ratio $\left(\Delta\varphi_0/\Delta\varphi_1\right)$	138
		4.8.4 Summary - Full systematic correction	147
	4.9	Statistical estimators of the zero-power, zero-loss phase shift ratio	147
	4.10	Constraining $N$ dependent effects on $\Delta \varphi_0/\Delta \varphi_1$ measurements	150
	4.11	Conclusion	151

5	Expl	loring dynamical phase transitions with cold atoms in an optical cavity	152
	5.1	Introduction	152
	5.2	What is a dynamical phase transition?	153
	5.3	Implementing the Lipkin-Meshkov-Glick model	154
	5.4	Dynamical phase diagram	155
	5.5	The experimental sequence	158
	5.6	Dynamical phases in the absence of a longitudinal field	161
	5.7	Scanning the longitudinal field with fixed transverse field	163
	5.8	Dependence of the dynamical phases on initial conditions	165
	5.9	Details of numerical modeling	167
	5.10	Mapping between the LMG model and macroscopic self-trapping	170
	5.11	Conclusion	171
6	Obs	erving Dynamical Phases of BCS Superconductors in a Cavity QED Simulator	172
	6.1	Introduction	172
	6.2	A primer on BCS theory	174
	6.3	Predicted dynamical phases	177
	6.4	Cavity QED implementation overview	177
	6.5	Phase I to phase II	179
	6.6	Signatures of Higgs oscillations	181
	6.7	Phase II to phase III	184
	6.8	Scan across three dynamical phases	187
	6.9	Details of the experimental setup	188
		6.9.1 Phase I to phase II cut	189
		6.9.2 Cuts through phase III	191
		0.3.2 Cuts through phase in	
		6.9.3 Readout	

	6.10	Details of numerical modeling	197
		6.10.1 Inhomogeneous atom-light coupling	197
		6.10.2 Residual single-particle and collective emission	200
		6.10.3 Exciting motional sidebands	201
	6.11	Conclusion	202
	6.12	2 Additional information: comparison with systems featuring phase synchronization	202
	6.13	3 Additional information: understanding the phase II to phase III frequency dip	205
	6.14	Additional information: intensity distributions for Gaussian beams on Gaussian atomic	
		clouds	207
		6.14.1 1D system, centered	207
		6.14.2 2D system, centered	208
		6.14.3 Displacing the Gaussian beam from center	210
7	Tim	ne-resolved spectral gap spectroscopy in a quantum simulator of fermionic superfluidity insid	e
•		ie reserved spectral gap spectroscopy in a quantum simulator or reminerine supermatarity mora	•
•		optical cavity	212
•	an o		212
•	an o	optical cavity	<b>212</b> 212
•	an o	Optical cavity  Introduction	<ul><li>212</li><li>212</li><li>214</li></ul>
•	an o	Introduction	<ul><li>212</li><li>212</li><li>214</li><li>217</li></ul>
	an o 7.1 7.2 7.3 7.4	Introduction	<ul><li>212</li><li>212</li><li>214</li><li>217</li><li>219</li></ul>
•	an o 7.1 7.2 7.3 7.4	Introduction	<ul><li>212</li><li>214</li><li>217</li><li>219</li><li>222</li></ul>
	an o 7.1 7.2 7.3 7.4	Introduction	212 214 217 219 222 222
	an o 7.1 7.2 7.3 7.4	Introduction	212 214 217 219 222 222 223
•	an o 7.1 7.2 7.3 7.4	Introduction  Mapping RF spectroscopy onto a three-level ensemble  Experimental setup  Time dynamics of the BCS gap subject to dark state coupling  Understanding the spectral gap  7.5.1 The spectral gap prevents the rotation of atomic orbitals  7.5.2 The spectral gap creates a detuning between coupled harmonic oscillators	212 214 217 219 222 222 223 224
	an of 7.1 7.2 7.3 7.4 7.5	Introduction	212 214 217 219 222 223 224 227
	an of 7.1 7.2 7.3 7.4 7.5	Introduction	212 214 217 219 222 223 224 227 229

		7.8.2	The cavity probe setup	236
		7.8.3	Experimental results	239
	7.9	Concl	usion	241
8	Con	clusio	and outlook	243
	8.1	Conn	ections with other recent Thompson Lab experiments	243
		8.1.1	Driven dissipative phases of the cooperative resonance fluorescence model	243
		8.1.2	Cavity-mediated momentum exchange interactions	245
		8.1.3	Many-body gap protection against Doppler dephasing	246
	8.2	Futur	e experiments	248
		8.2.1	Photon-mediated correlated hopping on a synthetic ladder of states	248
		8.2.2	Simulating $p + ip$ superconductors	250

## **Tables**

## Table

2.1	Regimes of atom-cavity coupling	37
3.1	Hyperfine splittings and Zeeman sensitivites for select states in <sup>87</sup> Sr	58
3.2	Science cavity parameters for relevant wavelengths/transitions in strontium	86
3.3	Typical parameters for the 1D 813 nm optical lattice	88
3.4	Table of polarizabilities for narrow-linewidth strontium transitions at 813 nm	96
3.5	Reference cavity parameters for relevant wavelengths/transitions in strontium	100
	Summary of cavity and atomic parameters	118
	sociated uncertainties	130
4.3	Correction factors $F_C$ for the measurement of $\Delta \varphi_1$ measurement	131
4.4	Correction factors $F_C$ for the measurement of $\Delta \varphi_0$ measurement	136
4.5	Correction factors $F_C$ for the measurement of the ratio $\Delta \varphi_0/\Delta \varphi_1$	139
4.6	Fits for several estimators for the ratio $\left(\Delta \varphi_0/\Delta \varphi_1\right)$	150
6.1	Parameters for inhomogeneity generation	193

## Figures

## Figure

1.1	Basic form of the all-to-all cavity-mediated atom-atom interaction	6
1.2	Cooper pair formation in BCS superconductors	10
2.1	A generic two-mirror cavity with input and output fields	16
2.2	Steady-state transmitted and reflected fields for a symmetric cavity	20
2.3	Graphical intuition for the PDH error signal	22
2.4	Bloch sphere visualizations of spin states	26
2.5	Dressed state resonances in the Jaynes-Cummings and Tavis-Cummings models	33
2.6	Bloch sphere representation of the adiabatically eliminated cavity field	42
2.7	Simplified description of the Reiter-Sørensen effective Hamiltonian formulation	44
2.8	Parameter regimes for atom-cavity coupling in past experiments	50
2.9	Absolute frequency scales for the effective atom-atom interaction and collective dissipa-	
	tion after adiabatic elimination	50
3.1	Level diagram for low-lying states in <sup>88</sup> Sr	55
3.2	Images of the strontium oven "volcano" before and after the oven refill	60
3.3	Detailed images of the AOSense strontium oven and refill procedure	63
3.4	The source and science chambers	66
3.5	461 nm laser system breakout	70
3.6	Images of a new and a dead hollow cathode lamp	72

6.6	Scan across three dynamical phases	188
6.7	Experimental configuration	189
6.8	Modeling imperfections in $E_{\mathrm{W}}$ and $\delta_{\mathrm{s}}$	192
6.9	BCS dynamical quench experimental sequence	196
6.10	Numerical simulation of the dynamical phase diagram including inhomogeneous atom-	
	light coupling	198
6.11	Introducing various experimental imperfections into numerical simulations	200
6.12	Frequency dip as a signature of the phase II to phase III transition	205
7.1	Simulating RF spectroscopy with an ensemble of three-level systems	216
7.2	Oscillations in the pairing gap $\Delta_{BCS}$ from excited state coupling $\ \ldots \ \ldots \ \ldots \ \ldots$	220
7.3	Rotating dipole interpretation of the spectral gap	222
7.4	Visualizing spin-exchange gap protection with nonzero inversion	226
7.5	Probing the spectral gap $\Delta_{SG}$	228
7.6	Analysis of the weighted ground state population $N_g'$	231
7.7	Simultaneously measuring $\langle \hat{J}^- \rangle$ and $\langle \hat{J}^z \rangle$	237
7.8	Directly measuring excited state population transfer with the cavity probe	240

#### Chapter 1

#### Introduction

#### 1.1 General motivation

Over the past 200 years, fundamental physics has vastly increased our understanding of how the universe works at its most basic level, culminating in triumphs such as general relativity and the Standard Model. Although these theories are known not to be complete, they have remarkable predictive power over all but the most extreme parameter regimes, both quantitatively (such as calculating the degree of gravitational lensing [1] or the value of the fine-structure constant [2]) and qualitatively (such as predicting the existence of gravitational waves [3] or the Higgs boson [4]).

However, attempting to use the full machinery of general relativity or the Standard Model to calculate the dynamics of a human-scale system would be unnecessary and impractical. Understanding why a ball rolls down a hill does not require knowledge of curved spacetime or the strong force binding its constituent quarks together, and considering these effects would distract from the simpler picture of an object accelerating under a constant downwards force. Using approximate simple models such as this to better understand mechanisms in a complex system is, in many ways, a foundational tenet of physics and science as a whole. That said, the use of such models must be justified. Part of the challenge inherent to physics is determining under what regimes certain models hold predictive power (and to what extent), as well as when counfounding technical details necessitate a more heavyweight description of the system. This determination requires comparing the predictions of these models with the proper experimental measurements.

Alongside our advances in theoretical physics, the advent of computers has increased our ability to

understand complex systems from first principles through the use of computational methods. This provides an alternative avenue for testing the predictions of simple models of a system when experimental measurements are inaccessible. However, computational methods run into challenges when studying highly correlated quantum systems due to the exponential growth in system complexity with the number of particles. Moreover, these kinds of systems often display interesting emergent phenomena, which we would like to understand but which have no obvious analog in smaller or simpler systems (as Philip Anderson famously said, "more is different" [5]). While physicists can propose mechanisms for emergent behavior using some simple model, without the ability to perform experimental measurements or numerical simulations, these mechanisms cannot be tested.

A classic example of this issue lies with superconductors. These are materials that exhibit near-zero electrical resistance and a repulsion of magnetic field lines from the bulk of the material, and which feature large correlations between electrons in the material that give rise to their strange effects. Key insights into superconductivity were made in the 1950s when physicists Bardeen, Cooper, and Schrieffer proposed a model, now called the BCS model, which provided a simple microscopic mechanism for the phenomenon [6]. Despite its successes, the BCS model cannot account for the behavior of unconventional superconductors, including high- $T_c$  superconductors which have received a lot of interest for their potential use in real-world applications. An approximate simple model, the Fermi-Hubbard model, is believed to be a valid minimal model which may capture the behavior of unconventional superconductors [7]. However, generating predictions from the model in the parameter regime of interest, which exhibits competing interaction orders, low temperatures, and strong interactions, is challenging [8].

Analog quantum simulation, an emerging tool that studies quantum systems with another quantum system, has the potential to help test models which experimental and classical numerical methods cannot. The basic reason this method holds such promise is that, unlike simulation on classical computers, the platforms used in quantum simulation are composed of quantum objects which, through the use of Hamiltonian engineering, can directly simulate the model in question. At the same time, the platforms are designed to be more tunable, programmable, and easily measured than the real experimental systems they attempt to emulate. Analog quantum simulators are similar in spirit to quantum comput-

ers, which can in principle perform the same task. The main difference is that quantum computers must first convert the desired dynamics into discrete digital gates (i.e., "digital" quantum simulation), whereas analog systems rely on directly engineering the desired Hamiltonian in almost a bespoke fashion: for a similarly sized system, the latter is less prone to a buildup in infidelity over time [9]. Motivated by this promise, quantum simulation experiments have developed over a variety of different platforms in atomic physics [10–16], attempting to study a variety of problems [9, 17]. One active area of interest is the aforementioned Fermi-Hubbard model [18–23], with some experiments even beginning to provide insight into regimes which are classically difficult to simulate [24].

Another large class of problems which can be probed with quantum simulators are emergent phenomena in out-of-equilibrium quantum systems. Generically, the number of degrees of freedom in such systems far outstrips their equilibrium counterparts, which already host quite rich physics. This results in a variety of new behaviors, some precluded from existence at equilibrium; at the same time, the added complexity can make these systems even more challenging to predict. Therefore, there are many open questions left to be explored [13, 17, 25]. An incomplete list of active areas of research into nonequilibrium systems includes driven-dissipative phases [26, 27], particularly the physics of self-organization [28–39], optical bistability [40], phase synchronization [41–46][47]<sup>[G]</sup>, many-body localization [48, 49], correlation spreading dynamics [50, 51], discrete time crystals [52], quantum many-body scars [53, 54], and prethermal dynamical phase transitions [55] (see Ch. 5 for a more in-depth discussion of this physics).

Despite the huge interest in quantum simulation, the field has a couple of major limitations. Currently, only a few experiments have demonstrated results beyond what can be classically simulated. A lot of the technical challenges facing current quantum simulators boil down to imperfections in initial state preparation, such as working at a finite temperature [24], or imperfections in engineering the desired dynamics [54]. Improving these metrics is an active goal of many experiments. At the same time, due to the bespoke nature of the interactions, quantum simulators are somewhat limited in the number of models they can study. One potential avenue to mitigate this problem is to continue developing multiple different platforms for quantum simulation, with different interaction types. A benefit of atomic systems

the ability to engineer interactions that scale with distance in many different ways [16], from contact interactions in optical lattices [11],  $1/r^6$  van der Waals interactions with Rydberg atoms [12],  $1/r^3$  dipolar interactions [15], and tunable  $1/r^{\alpha}$  interactions ( $\alpha \ge 1$ ) with trapped ions [10], to infinite-range interactions with optical cavities [14]. Continued research into multiple platforms will therefore strengthen the toolbox of quantum simulation.

In this thesis, I will showcase work developing the "tool" of collective cavity quantum electrodynamics (cavity QED), specifically for studying nonequilibrium physics with quantum simulation. At its most general, a cavity QED system studies light-matter interactions when certain electromagnetic modes are amplified via the presence of reflective mirrors which form a resonator. I will specifically focus on the case where we couple many identical atoms (in our case, strontium atoms) to a single mode of a high-finesse (i.e., highly reflective) optical cavity.

What makes cavity QED an appealing platform for study? First, it boasts impressive measurement capabilities, applicable not only towards precision measurement and quantum sensing but also for readout in quantum simulation experiments. The enhanced light-matter interactions displayed by strongly coupled atom-cavity systems enables the collection of photons scattered off the atoms through the cavity mode with high quantum efficiency, making them an appealing candidate for performing fast mid-circuit measurement of qubits in neutral atom quantum computing platforms [56–59]. By performing these measurements on an ensemble of atoms, it is possible to perform quantum nondemolition (QND) measurements of the ensemble which only partially collapse the many-body wavefunction, leading to entanglement generation in the form of spin squeezing [60–62][63–65]<sup>[G]</sup>. This technique, alongside a similar technique in cavity QED systems for deterministically squeezing an ensemble of atoms [66–68], has led to record levels of entanglement [69][70]<sup>[G]</sup>, with ongoing work towards applications in real quantum sensors such as matterwave interferometers [71]<sup>[G]</sup> and optical atomic clocks [72, 73]. In the context of quantum simulation, these capabilities open up the potential to measure correlations in observables below the standard quantum limit.

 $<sup>^{1}</sup>$  Throughout the thesis, I will use the designator " $^{[G]}$ " to indicate when a paper comes from our group (the group of James K. Thompson).

Another draw for utilizing cavity QED for quantum simulation is the wealth of available models and phenomena observable using all-to-all interactions. For example, a series of experiments studying Bose-Einstein condensates trapped in optical cavities [74] has successfully studied an open system implementation of the Dicke model [32, 33, 75, 76] and the related Dicke-Hubbard model [77] using just globally applied drives in combination with an all-to-all cavity interaction. These systems have also been shown to display self-organization behavior [78] and topological pumping of the atoms in real space [38]. Similar setups have been engineered to realize theoretically predicted driven-dissipative phases and phase transitions, including both discrete [37] and continuous time crystals [79], as well as the cooperative resonance fluorescence model from quantum optics [80] [G] and related observations of bistability and photon blockades [26, 40] (see Ch. 8 for a brief discussion of this result). In related work, driven BECs in a ring resonator have demonstrated exotic states of matter such as supersolids [81], as well as collective forms of scattering [82, 83] which can create interesting quantum phases [84]. Away from a dissipative regime, atom-cavity systems can display effective all-to-all atom-atom interactions which emulate different types of quantum magnetism. These include the Heisenberg model and Ising model [85][86][G], as well as a couple of related models discussed in this thesis including, notably, the BCS model of superconductivity (see Sec. 1.2 for an overview). All-to-all interactions could also be used to probe the Sachdev-Ye model [87] and other models of information scrambling [88], which may provide insight into other fast-scrambling systems like black holes [89]. Cavity QED can even be used to generate higher-order interactions such as three-body and four-body terms [90] [G].

I will note that although single-mode cavity QED natively exhibits all-to-all interactions, clever system engineering can modify this behavior and enable the study of a broader range of models. One recent experiment managed to study fractional quantum Hall physics by engineering a Laughlin state out of transverse cavity modes with nonzero angular momentum [91]. Another utilized a confocal cavity geometry to generate local interactions in a 2D plane transverse to the cavity axis to engineer a spin glass and observe replica symmetry breaking behavior consistent with simple models of such systems [27]. Finally, by combining all-to-all interactions with controllable frequency shifts, a third group has demonstrated the capability to generate arbitrary graph states of interactions between individual trap

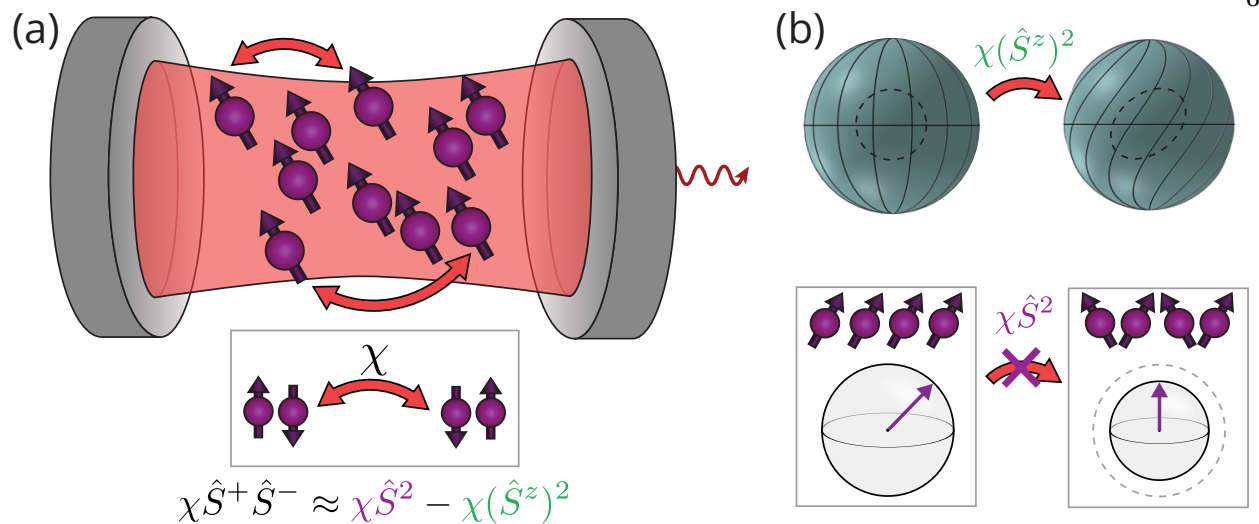


Figure 1.1: Basic form of the all-to-all cavity-mediated atom-atom interaction. (a) Many atoms couple to a single mode of an optical cavity, which we model as spins. Under the right conditions, the cavity mediates an all-to-all "spin-exchange" interaction in which one atom lowers its spin state by emitting a photon into the cavity, and another atom raises its spin state by absorbing the same photon. The interaction takes the form  $\chi \hat{S}^+ \hat{S}^-$ , which can be approximately broken up into two terms:  $\chi \hat{S}^2$  and  $\chi (\hat{S}^z)^2$ . (b) The  $\chi (\hat{S}^z)^2$  term, sometimes called one-axis twisting, induces an inversion-dependent frequency shift on the atoms which looks like twisting on the collective Bloch sphere. This introduces dynamical consequences at the mean-field level (see Ch. 5) and can induce spin squeezing beyond mean-field. The  $\chi \hat{S}^2$  creates a many-body energy gap between manifolds of different total spin angular momentum S. When a term like single-particle dephasing exists that would reduce S, this term acts to gap protect the atomic coherence and prevent dephasing (see Ch. 6). This figure is adapted from [93] [G] (with Matt Norcia as the first author).

sites in an optical cavity [92]. This last example raises an intriguing propsect of combining all-to-all interactions with effects which are not all-to-all (in this case, local detunings), in order to study models with increased complexity. Along this line of thought, combining interaction orders of different systems could be an interesting path forward for simulating an even broader class of problems.

The interaction primarily studied in this thesis is a two-body, all-to-all cavity-mediated interaction which resembles a spin-exchange process (see Fig. 1.1) [94][95]<sup>[G]</sup>. Under the right conditions, discussed in depth in Ch. 2.5.3, the ensemble can undergo a process where one atom emits a photon into the cavity mode, which is reabsorbed by a second atom before it can leak out of the cavity. Treating the atoms as spins, the interaction takes the form  $\chi \hat{S}^+ \hat{S}^-$  using collective spin angular momentum raising and lowering operators  $\hat{S}^{\pm}$ . This can in turn be interpreted as a combination of a one-axis twisting term

 $(\chi(\hat{S}^z)^2)$ , which looks like an inversion-dependent frequency shift on the ensemble, and a many-body gap protection term  $(\chi\hat{S}^2)$ , which acts to preserve coherence within the ensemble. As we will see, just these two ingredients is already sufficient to produce a host of interesting physics.

#### 1.2 Overview of results

ndInIn this section, I will briefly summarize the results which comprise the bulk of this thesis. There are four main experiments to discuss. The first two were led by a former postdoc in the group named Juan Muniz, with me as the second experimental author. I included these two projects in the thesis primarily for the sake of historical completeness; the second experiment in particular sets the stage for later experiments performed by the group. The latter two projects were led by me.

#### 1.2.1 Precision measurement of the natural linewidth of an ultranarrow atomic transition

In this first experiment [96]<sup>[G]</sup> (see Ch. 4), we utilize the collectively enhanced atom-light coupling afforded by cavity QED to probe narrow-linewidth transitions in strontium atoms, including the ultra-narrow linewidth optical "clock" transition, so-named for its use in strontium optical lattice clocks [73, 97–101]. By comparing the response of the clock transition with another, easier to characterize transition in strontium, we are able to measure the linewidth of the clock transition with a lower uncertainty than any previous measurement. Although this project is not directly related to quantum simulation, it showcases the ability of cavity QED platforms to measure collective observables of an atomic ensemble with high precision.

The main challenge in measuring the clock transition linewidth is its anomalously long lifetime. This  $({}^{1}S_{0} - {}^{3}P_{0})$  transition is "doubly forbidden" since it requires a photon to change the total electron spin from a singlet to a triplet configuration, as well as connect two J = 0 angular momentum states, neither of which can normally occur. Only through weak state mixings of the raw hydrogen-like orbitals does the transition decay at all, resuling in a linewidth on the order of 1 mHz and a corresponding lifetime of ~100 s. At such long natural lifetimes, depopulation of the excited clock state may not be limited by spontaneous emission but rather confounding effects such as blackbody radiation induced transitions

[102, 103] and off-resonant scattering from the trapping light [104–106]. The result of such challenges is that, at the time of running this experiment, the uncertainty in the clock transition linewidth was on the order of 30% [104, 107].

In order to circumvent these problems, we infer the natural linewidth not through a measurement of the population decay but rather by probing the dipole matrix element along the optical transition. While the doubly forbidden nature of the transition makes this matrix element quite weak (it is proportional to the square root of the atomic linewidth), placing many atoms into a high-finesse optical cavity allows us to enhance the atom-light interaction to a point where we can probe a resonance feature associated with a millihertz transition, even with a laser whose frequency noise gives it a linewidth several times broader. Moreover, we can do so quite precisely: by sending a weak probe through the optical cavity and detecting the phase shift it receives from this resonance feature using a heterodyne detector, we are able to infer the natural linewidth with an uncertainty of roughly 3%. Key to achieving this level of precision is performing interleaved measurements of the clock transition and a different atomic transition in strontium, which has a still narrow but ultimately more manageable linewidth of 7.5 kHz. By comparing the relative size of the shifts experienced by their respective probes, we gain first-order insensitivity to a slew of systematic effects which would otherwise increase our uncertainty of the measurement. These techniques raise the possibility to directly lock clock lasers to their respective atomic transitions spectroscopically, a prospect that seems far-fetched in free space with current technologies due to the ultranarrow linewidths and weak scattering intrinsic to these transitions.

#### 1.2.2 Observing dynamical phases in the Lipkin-Meshkov-Glick model

In this experiment [108]<sup>[G]</sup> (see Ch. 5), we build off initial work in our group exploring cavity-mediated spin-exchange interactions [95]<sup>[G]</sup> by studying them dynamically. Specifically, we perform quench experiments of the Lipkin-Meshkov-Glick (LMG) model [109, 110], an all-to-all quantum magnetism model which is simple to express but also exhibits nontrivial behavior in the form of two distinct parameter regimes of quench dynamics separated by a so-called dynamical phase transition [55]. We observe this phase transition in our implementation and explore its features, including connections to

the context of macroscopic self-trapping phenomena observed in Josephson junctions [111–114].

Dynamical phase transitions are a class of critical behavior in out-of-equilibrium systems which have experienced a lot of interest over the past decade [115–125]. Unlike many driven-dissipative transitions which describe critical behavior in the steady-state of some open system, dynamical phase transitions as I'm defining them here are prethermal in the sense that the relevant dynamics occurs on a timescale where dissipation can be neglected, effectively treating the system as closed [55]. In these systems, nonlinear or many-body Hamiltonian terms can induce sharp changes in the quench dynamics in the thermodynamic limit  $(N \to \infty)$ . This sharp change can be quantified by defining some time-averaged order parameter which exhibits critical behavior, in analogy to a phase transition in equilibrium thermodynamics. An interesting feature unique to this type of dynamical phase transition occurs before the dynamical phase diagram on initial conditions. Because a dynamical phase transition occurs before the system can reach a steady state, initializing the system in two different ways can lead to two different phases of dynamics even if all other parameters are held fixed. This represents a new degree of freedom which we would like to study and characterize.

To implement the LMG model, we engineer cavity-mediated spin-exchange interactions to produce a one-axis twisting interaction of the form shown in Fig. 1.1(b). We then perform quench experiments by rapidly turning on an applied drive near resonance with an atomic transition, generating the transverse and longitudinal fields present in the model. When probing the dynamics after the quench, we identify two distinct regimes of dynamics depending on the relative strength of the drive compared with the interactions. When the drive is dominant, the atoms undergo Rabi-like oscillation, which we associate with a paramagnetic phase since the time-averaged magnetization is zero. On the other hand, in the interaction-dominated regime, atoms initially in the ground state will not freely oscillate and instead exhibit a persistently negative magnetization, corresponding to a ferromagnetic phase. As we tune the relative strength of the drive and the interactions, we observe a sharp kink in the time-averaged magnetization, indicative of a second-order dynamical phase transition. Additionally, we repeat the experiment for different initial conditions of our atomic ensemble and map out an "initial condition phase diagram," finding that the ultimate dynamical phase depends both in the initial atomic inversion and its phase rel-



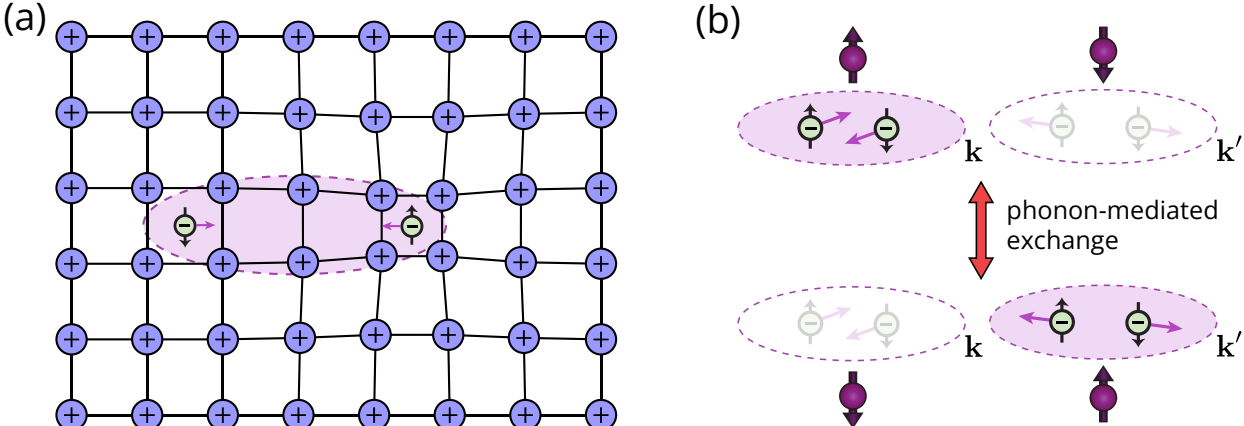


Figure 1.2: Cooper pair formation in BCS superconductors. (a) In BCS superconductors, electrons distort the underlying lattice of positive ions in the metal through Coulomb forces, creating phonons. Through these phonons, they gain an effective attractive interaction. At sufficiently low temperatures, this causes the electrons to condense into Cooper pairs of opposite momentum and spin states. (b) The attractive interaction can be understood as a phonon-mediated exchange process between Cooper pairs of different momentum labels  $\boldsymbol{k}$  (alternatively, the electrons scatter with a negative scattering length). In an s-wave superconductor, this exchange is all-to-all and is analogous to a cavity-mediated spin-exchange interaction.

ative to the applied drive.

#### 1.2.3 Observing dynamical phases in the BCS model of superconductivity

Motivated by the success of the previous work studying the LMG model, in this work [126] <sup>[G]</sup> (see Ch. 6) we continue our exploration of dynamical phases by studying the BCS model of superconductivity [6]. This model, which is famous for providing a first microscopic picture of how superconductivity can arise in some systems, also has been predicted to exhibit three distinct dynamical phases after quenching the Hamiltonian when the system is initially in an equilibrium state [127–137]. Despite attempts in both thin-film superconductors [138–140] and degenerate Fermi gases [141] (and more recently, [142]), only limited signatures of some of these phases have been observed. By engineering the BCS Hamiltonian in our collective cavity QED system, we successfully observe phase transitions across all boundaries of the predicted dynamical phase diagram, and we also provide a first experimental demonstation of "phase III."

Although our physical system, composed of a dilute cloud of thermal atoms in an optical cavity, is quite different from the highly degenerate systems of superconductors and superfluids, we can nonetheless study the BCS model through the use of an abstract mapping between the two systems. This step, known as an Anderson pseudospin mapping [143], simplifies the description of the system by grouping electrons into "Cooper pairs" with opposite momentum and representing each Cooper pair with an abstract pseudospin object, with spin-up and spin-down representing the presence and absence of electrons in the pair, respectively. Under this mapping, an *s*-wave (i.e., isotropic) BCS interaction corresponds to an all-to-all spin-exchange interaction between pseudospins. By making the abstract manifest in our system and assigning Anderson's pseudospin objects to our physical atoms, we can simulate the dynamics of an *s*-wave BCS Hamiltonian. Controllable application of single-particle energy shifts allows us to tune across a two-dimensional dynamical phase diagram, sufficient to observe the three predicted dynamical phases.

Alongside demonstrating the predicted BCS dynamical phases, we refine a physical interpretation of the phase transitions using our hardware-native language of a spin ensemble, providing an approximate simple picture of superfluidity which clarifies some of its features. The phase I to phase II transition in the BCS model reflects a competition between single-particle dephasing and the spin-exchange interaction, which generates a many-body gap protection term  $\chi \hat{S}^2$  (see Fig. 1.1(b)). Therefore, the transition maps directly onto the interaction-protected spin coherence previously observed in cavity QED experiments [85]. So-called "Higgs" oscillations which are characteristic of phase II in this system [137, 142] correspond to detuned oscillations between manifolds of different total spin angular momentum, induced by single-particle dephasing and with the different levels split in frequency by the gap-protection term. Finally, the phase II to phase III transition observed in our experiment reflects a competition between the spin-exchange interaction strength and a single-particle beating between two halves of the ensemble, reflecting states above and below the Fermi energy. These interpretations, made in the context of the *s*-wave BCS model, can be extended to more complex models of superconductivity through similar proposed mappings [144].

#### 1.2.4 Emulating rf spectroscopy of fermionic superfluids using multilevel atoms

The pseudospin BCS Hamiltonian studied in the previous section represents a reduced model of BCS superconductivity, in which we neglect the effect of pair-breaking processes that allow Cooper pairs to be half occupied. In a first attempt to model processes beyond the paradigm of Anderson pseudospins, in this experiment [145]<sup>[G]</sup> (see Ch. 7) we utilize the multilevel structure of our strontium atoms by inducing a coupling outside of the initial two-level system and into a third noninteracting state. In this extended system, we observe two distinct many body gaps and explore their different dependences on the initial atomic state.

Our strategy of driving atoms into auxiliary states is closely analogous to the technique of "radio-frequency (rf) spectroscopy," performed in early experiments of degenerate Fermi gases to verify the formation of Cooper pairs [146–150]. In those works, researchers studied degenerate spin mixtures of fermions in two hyperfine sublevels by applying an rf drive nominally on resonance with a third, noninteracting sublevel and performing spectroscopy. Any nonzero frequency shift (which we call the "spectral gap") observed on the resonance feature would then be a signature of Cooper pairing, since it reflects the energy cost required to break up a pair. This method was successfully used to verify BCS condensation. However, it was not without its issues: technical details led to complications in a quantitative interpretation of the spectral gap [151–153], and there was not a clean probe to distinguish the spectral gap from the typical superconducting energy gap (which we call the "BCS gap") [146, 154, 155].

In contrast, the flexible control of initial conditions and collective readout techniques afforded to us by cavity QED allow us to clarify the distinction between the BCS gap and the spectral gap. In our implementation of the model, the BCS gap corresponds to the quantity  $\chi(\hat{S}^-)$  on the two-level system which defines our Anderson pseudospin, where  $\chi$  is a frequency scale that represents the spin exchange rate between any pair of atoms. Conveniently, we can probe the BCS gap quasi-nondestructively through the cavity since the instantaneous rate of atom-cavity coupling is proportional to  $\langle \hat{S}^- \rangle$ . The spectral gap corresponds to an interaction-induced detuning between one of our states in the two-level system and the third, noninteracting state which scales like  $\chi N_g$ , where  $N_g$  is the number of atoms in the ground

state. By tuning the strength of a dc coupling generated by a magnetic field, we infer this collective detuning. Then, by repeating the experiment for different initial populations of atoms in the ground and excited state of the two-level system, we observe scalings reflective of the  $\hat{S}^-$  and  $N_g$  dependences of the two gap scales. This work showcases the potential promise in utilizing the many degrees of freedom inherent to multilevel atoms to extend vanilla quantum simulation platforms and observe more exotic physics.

#### 1.3 Outline of thesis work

This introduction you have (possibly) just read comprises Ch. 1 of my thesis. In Ch. 2, I provide what is hopefully a pedagogical introduction to the fundamentals of collective cavity QED, including the approximate simple models we use to describe our cavity, atoms, and combined system under various parameter regimes. In Ch. 3, I describe our experimental setup in gory detail, from important atomic and cavity parameters to the technical details and various peculiarities of our laser systems and other technologies. Along the way, I try to provide enough information about the evolution of our setup over time to enable someone to reverse-engineer what our experiment looked like during our various experiments. In Chs. 4–7, I discuss the experiments mentioned in Sec. 1.2 in the order provided. Finally, in Ch. 8 I wrap up my thesis work by highlighting past, present, and future work in our lab related to expanding the scope of cavity QED quantum simulation, as well as discussing potential next steps for the experiment.

#### Chapter 2

#### Collective cavity QED with atoms

#### 2.1 Historical context

A defining theme of the research performed on this project is enhancing atom-light interactions along an optical transition with a well-defined electromagnetic mode. While this regime was initially conceived of and observed using dense ensembles of particles in free space [156–158], it is also straightforward to achieve by placing the atoms inside a high-finesse cavity. Very early work with atom-cavity systems led to the invention of the hydrogen maser [159, 160], which involves hydrogen atoms coherently emitting into a microwave cavity. A couple of decades later, researchers extended this type of physics to beams of Rydberg atoms. Utilizing the sensitivity of atoms in Rydberg states to electric fields, they observed superradiant emission along mm-wave Rydberg transitions, demonstrating strong atom-cavity coupling [161–163]. Work along optical transitions advanced in the following years, and researchers were able to detect cavity-induced frequency shifts on atomic transitions [164] and even observe collective vacuum Rabi splittings [165, 166].

As technologies improved, it soon became possible to control and detect effects of atom-cavity coupling at the single-atom and single-photon level [167–169]. At the same time, interest in collective cavity QED continued. Researchers began trapping increasing numbers of atoms inside high-finesse optical cavities, increasing the collective atom-cavity cooperativity with the eventual goal of pursuing entanglement generation for networking and metrology applications [62, 68, 170, 171]. Another avenue which began to receive interest was trapping Bose-Einstein condensates within optical cavities, with a particular eye toward quantum control and studying interesting dynamical physics [32, 74, 78]. In the

past twenty years, these lines of interest have grown and intermixed, with current cavity QED experiments pushing the boundaries of squeezing [69, 73, 172, 173][70, 71]<sup>[G]</sup>, transduction [174], quantum simulation [27, 37, 77, 91, 175], and more [38].

### 2.2 The "bare" optical cavity

In order to understand how atoms interact with an optical cavity, we first need to describe how the cavity behaves on its own. In our lab, we refer to this system as the **bare cavity**, which essentially means there are no atoms. Even without atoms, these systems can be interesting in their own right, with many different cavity geometries and form factors. For the context of this thesis, we will mainly focus on understanding the bare cavity resonance condition for input and output light.

#### 2.2.1 Input-output relations

Describing how the electric field inside a cavity relates to input and output fields (and vice-versa) is often done using the so-called "input-output formulation" [176, 177]. While this is often treated at the second quantized level in full generality, here I present a simplified description using classical fields which is hopefully somewhat intuitive. For this derivation, we will assume a two-mirror stable resonator with length L as described in Fig. 2.1, but the concepts are easily generalizable to other systems.

Consider an intracavity electric field  $E_c(x,t)$ , assumed to be a complex phasor oscillating with frequency  $\omega$  (such that the real, physical electric field is given by  $E_c^{\text{phys}}(x,t) := \text{Re}\big[E_c(x,t)e^{-i\omega t}\big]$ ). If we assume the field only occupies a single mode of the cavity (valid in the regime where  $E_c$  varies on a timescale much more slowly than the **cavity free spectral range**  $f_{\text{FSR}} = c/2L$ ), we can pull out the spatial dependence in the following way:

$$E_c(x,t) = \mathcal{E}_0 f(x) \alpha(t), \tag{2.1}$$

where  $\mathcal{E}_0$  is a prefactor with units of electric field  $\times \sqrt{\text{volume}}$  ( $\frac{N}{C} \times \sqrt{m^3}$  using SI),  $\alpha(t)$  is a unitless quantity which we will call the **mode amplitude** (since it fully describes the mode occupation), and f(x) is the **mode function** of the cavity mode, satisfying  $\int |f(x)|^2 d^3x = 1$  (see, for example, Steck's *Quantum and* 

 $<sup>^1</sup>$  From here on out, I will use bold notation (i.e.,  $\boldsymbol{E}$  compared to  $\boldsymbol{E}$ ) to denote a vector quantity.

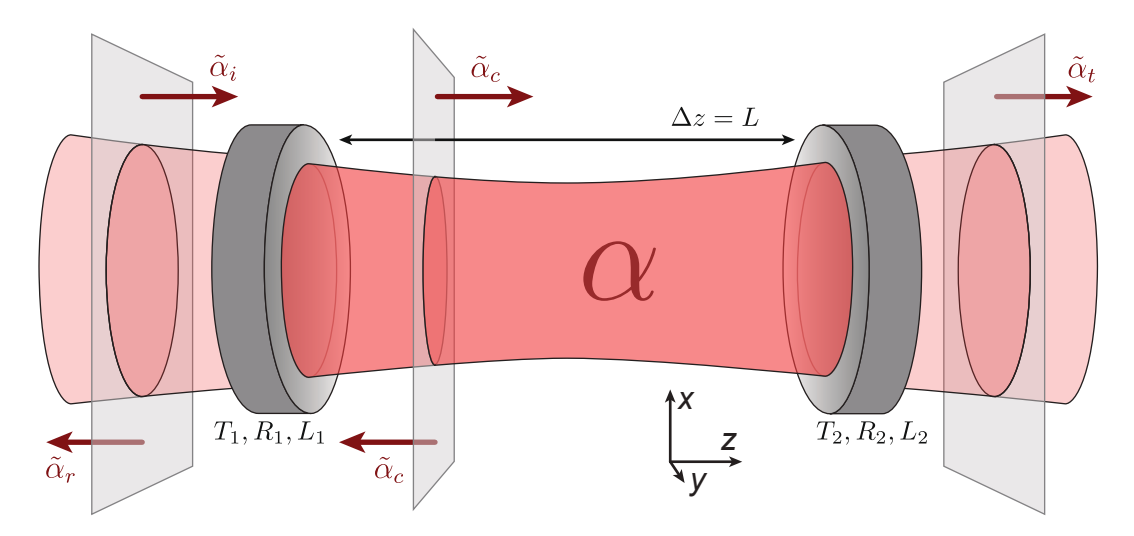


Figure 2.1: A generic two-mirror cavity with length L. Mirror M has transmission, reflection, and loss probabilities given by  $T_M$ ,  $R_M$ , and  $L_M$  respectively. The "tilde" variables  $\tilde{\alpha}_{i,r,c,t}$  denote field fluxes through a fixed phase front with units of  $\sqrt{\text{photons/sec}}$  (see Sec. 2.2.1), representing the input, reflected, intracavity circulating, and transmitted fields respectively. The "non-tilde" variable  $\alpha$  denotes a field amplitude with units of  $\sqrt{\text{photons}}$ , represending the cavity mode occupation. The circulating field amplitude  $\tilde{\alpha}_c$  and the mode amplitude  $\alpha$  represent the same electric field, just with different units.

Atom Optics, Sec. 8.3 [178]). For example, a  $TEM_{00}$  cavity mode in the paraxial approximation and linearly polarized along  $e_x$  (with coordinates as described in Fig. 2.1) has a mode function given by [179]

$$f(r,z) = \frac{1}{\sqrt{V_m}} \frac{w_0}{w(z)} e^{-\frac{r^2}{w(z)^2}} \cos\left(k(z + \frac{r^2}{2R(z)}) - \phi_G(z)\right) e_x, \tag{2.2}$$

where w(z), R(z), and  $\phi_G(z)$  are the Gaussian beam waist, radius of curvature, and Gouy phase at position z respectively;  $w_0$  is the beam waist at the focus (assumed to be at z=0);  $k=\omega/c$ ; and  $V_m:=(\frac{1}{2}\pi w_0^2)(\frac{1}{2}L)=\frac{1}{4}\pi w_0^2L$  is the **mode volume** [180], defined as the volume of the mode if it had a constant energy density equal to the maximum value, holding the total energy fixed.

The total energy contained in the mode is:

$$U(t) = \frac{1}{2} \int \left( \epsilon_0 \left| E_c^{\text{phys}}(\boldsymbol{x}) \right|^2 + \frac{1}{\mu_0} \left| B_c^{\text{phys}}(\boldsymbol{x}) \right|^2 \right) d^3 \boldsymbol{x} = \frac{1}{2} \epsilon_0 \int |E_c(\boldsymbol{x})|^2 d^3 \boldsymbol{x}$$

$$= \frac{1}{2} \epsilon_0 \mathcal{E}_0^2 |\alpha(t)|^2,$$
(2.3)

where  $B_c^{\rm phys}$  is the physical magnetic field, which oscillates 90° out of phase with the physical electric field at a frequency  $\omega$  to give a constant total energy given by the above equation. We know that for a field with  $M_c$  intracavity photons, the total energy should be  $\hbar\omega M_c$  (ignore vacuum energy since we're

working classically). It follows that if we set  $\mathcal{E}_0 := \sqrt{\frac{2\hbar\omega}{\epsilon_0}}$ , then the mode amplitude  $\alpha(t)$  has a nice physical interpretation of  $\sqrt{\text{photons}}$ , since  $|\alpha(t)|^2 = M_c$ . This convention also converts well to a second quantized picture, where  $\alpha$  becomes a coherent state amplitude.

While the mode amplitude describes the occupation of the cavity mode, we want the input and output fields to describe the *rate of change* of this occupation. That means we should determine how electromagnetic waves transfer power, which can be calculated using the time-averaged Poynting vector  $S = \frac{1}{\mu_0} \langle E^{\text{phys}} \times B^{\text{phys}} \rangle_t = \frac{1}{2} \epsilon_0 c^2 \operatorname{Re} [E \times B^*]$  [181]. The intracavity electric field can be split into left-going and right-going components:  $E_c = E_c^{(\rightarrow)} + E_c^{(\rightarrow)}$ , defined by the direction of the wavevector k:

$$E_c^{(\rightleftarrows)} \propto e^{\pm ik(z + \frac{r^2}{2R(z)}) \mp i\phi_G(z)}$$
 (2.4)

In the paraxial approximation, the magnetic field is  $\boldsymbol{B}_c = \frac{\hat{\boldsymbol{k}}}{c} \times (\boldsymbol{E}_c^{(\rightarrow)} - \boldsymbol{E}_c^{(\leftarrow)})$ . This implies:

$$S_{c} = S_{c}^{(\rightarrow)} - S_{c}^{(\leftarrow)} = \frac{1}{2} \epsilon_{0} c \left( |E_{c}^{(\rightarrow)}|^{2} - |E_{c}^{(\leftarrow)}|^{2} \right) \hat{k}, \tag{2.5}$$

where  $S_c^{(\leftrightarrow)} \coloneqq \frac{1}{2} \epsilon_0 c |E_c^{(\leftrightarrow)}|^2 \hat{k}$  represent rightward and leftward power transfer and are manifestly decoupled.

Motivated by this, we will define the **circulating field amplitude**  $\tilde{\alpha}_c(t)$  to satisfy:

$$\frac{1}{2}\epsilon_0 \mathcal{E}_0^2 |\tilde{\alpha}_c(t)|^2 := \iint_A \mathbf{S}_c^{(\to)} \cdot d\mathbf{A} = P_A^{(\to)},\tag{2.6}$$

the rightward power transfer through a phase front A (due to energy conservation, the power is the same through any phase front in the cavity, in both directions). Evaluating the integral allows us to relate  $\tilde{\alpha}_c(t)$  to  $\alpha(t)$ :

$$\tilde{\alpha}_c(t) = \sqrt{\frac{c}{2L}}\alpha(t) = \sqrt{f_{\text{FSR}}}\alpha(t).$$
 (2.7)

The interpretation of this statement is that the total energy in the mode (represented by  $|\alpha(t)|^2$ ) passes through any given phase front every round trip time  $\tau_{\rm RT} = 1/f_{\rm FSR}$ , resulting in a circulating power flow represented by  $|\tilde{\alpha}_c(t)|^2$ . Note that  $\tilde{\alpha}_c(t)$  has the funny units of  $\sqrt{\rm photons/sec}$ .

Now that we have established this machinery, discussing input-output relations in the cavity is straightforward. An output field through mirror M can be described using a field amplitude  $\tilde{\alpha}_{M,o}$ . If

mirror M has a transmission coefficient  $t_M$  (transmission probability  $T_M = t_M^2$ ), then we can relate the output field to  $\alpha$  by:

$$\tilde{\alpha}_{M,o}(t) = t_M \tilde{\alpha}_c(t) = \sqrt{\kappa_M} \,\alpha(t),\tag{2.8}$$

where  $\kappa_M := T_M f_{\rm FSR}$  is the rate at which photons incident on mirror M are transmitted. A similar relation holds for an input field  $\tilde{\alpha}_{M,i}(t)$ : every  $\tau_{\rm RT} = 1/f_{\rm FSR}$ , the circulating field  $\tilde{\alpha}_c$  gains  $t_M \tilde{\alpha}_{M,i}$  in amplitude from the input field. Therefore, the mode amplitude  $\alpha(t)$  responds like:

$$\frac{d\alpha}{dt}\Big|_{\text{input}} = \frac{1}{\sqrt{f_{\text{FSR}}}} \frac{d\tilde{\alpha}_c}{dt}\Big|_{\text{input}} \approx \sqrt{f_{\text{FSR}}} \ t_M \tilde{\alpha}_{M,i}(t)$$

$$= \sqrt{\kappa_M} \ \tilde{\alpha}_{M,i}(t). \tag{2.9}$$

Equations (2.8) and (2.9) describe instantaneous relations between the cavity mode and external fields and hold generally. They do not take the system dynamics into account, however, and thus do not provide a full description of  $\alpha(t)$  on their own.

#### 2.2.2 The cavity transfer function

In the case of the bare cavity, it is straightforward to solve the system dynamics. To start, let's define  $R_M$ ,  $T_M$ , and  $L_M$  to be reflection, transmission, and loss probabilities at mirror M, with  $r_M := \sqrt{R_M}$ ,  $t_M := \sqrt{T_M}$  describing the field coefficients (assumed to be real and positive). The total loss probability in one round trip is  $\Lambda := 1 - \prod_M R_M$ , which satisfies  $\Lambda \approx \sum_M T_M + L_M$  in a low-loss limit. We define the **cavity linewidth**  $\kappa$  to be the rate at which photons in the cavity are lost. This is given by  $\kappa = f_{\rm FSR}\Lambda = \frac{c}{2L}\Lambda$  for a two-mirror cavity.

We will consider the simple case as shown in Fig. 2.1: a constant input tone  $\tilde{\alpha}_i$  through mirror 1 with an optical frequency  $\omega$  and wavevector  $k = \omega/c$ . In steady state, the intracavity circulating field  $\tilde{\alpha}_c$ , reflected field  $\tilde{\alpha}_r$ , and transmitted field  $\tilde{\alpha}_t$  will also oscillate at  $\omega$ . We can solve for the intracavity field as a function of  $\tilde{\alpha}_i$  by noting that the field should not change after one round trip:

$$\tilde{\alpha}_{c} = t_{1}\tilde{\alpha}_{i} + r_{1}r_{2}e^{2ikL}\tilde{\alpha}_{c}$$

$$\Rightarrow \tilde{\alpha}_{c} = \frac{t_{1}}{1 - r_{1}r_{2}e^{2ikL}}\tilde{\alpha}_{i},$$
(2.10)

where the first term represents the injected field during the round trip, and the second term represents the circulating field after traveling a distance of 2L and bouncing off both mirrors. Note that here, we implicitly define the phase of  $\tilde{\alpha}_c$  to be equal to the phase of the input light at mirror 1. Therefore, at different positions along the beam propagation the circulating field will accrue a spatial phase factor  $e^{ik\Delta z}$ .

Assuming a high-finesse limit, the total loss probability satisfies  $\Lambda \ll 1$  such that  $r_1 r_2 = \sqrt{R_1 R_2} = \sqrt{1 - \Lambda} \approx 1 - \frac{\Lambda}{2}$ . This implies

$$\tilde{\alpha}_c = \frac{t_1}{\left(1 - e^{2ikL}\right) + \frac{\Lambda}{2}e^{2ikL}}\tilde{\alpha}_i. \tag{2.11}$$

Since  $t_1$ ,  $\Lambda \ll 1$ ,  $\tilde{\alpha}_c$  is only non-negligible when the term  $|1-e^{2ikL}| \lesssim \frac{\Lambda}{2}$ . Therefore we can also assume  $|1-e^{2ikL}| \ll 1$ , implying  $1-e^{2ikL} \approx -2i(k-k_c)L = -i(\omega-\omega_c)/f_{\rm FSR}$  where  $\omega_c$  is the closest cavity resonance frequency, and  $k_c = \omega_c/c$  is its wavevector. To leading order, then,

$$\tilde{\alpha}_{c} = \frac{t_{1}}{\frac{\Lambda}{2} - i\left(\frac{\omega - \omega_{c}}{f_{\text{FSR}}}\right)} \tilde{\alpha}_{i} = \frac{2t_{1}/\Lambda}{1 - i\left(\frac{\omega - \omega_{c}}{\kappa/2}\right)} \tilde{\alpha}_{i}, \tag{2.12}$$

implying that the steady-state mode amplitude  $\alpha(\omega)$  is

$$\alpha(\omega) = \sqrt{\frac{1}{f_{\text{FSR}}}} \frac{2t_1/\Lambda}{1 - i\left(\frac{\omega - \omega_c}{\kappa/2}\right)} \tilde{\alpha}_i(\omega) = \frac{\sqrt{\kappa_1}}{\kappa/2} \frac{1}{1 - i\left(\frac{\omega - \omega_c}{\kappa/2}\right)} \tilde{\alpha}_i(\omega). \tag{2.13}$$

We can also calculate the transmission through the cavity using the relationship  $\tilde{\alpha}_t = \sqrt{\kappa_2} e^{ikL} \tilde{\alpha}_c$  (the global phase factor  $e^{ikL}$  is unimportant and describes the free-space beam propagation from z=0 to z=L):

$$\tilde{\alpha}_t(\omega) = \frac{\sqrt{\kappa_1 \kappa_2}}{\kappa/2} \frac{e^{ikL}}{1 - i\left(\frac{\omega - \omega_c}{\kappa/2}\right)} \tilde{\alpha}_i(\omega). \tag{2.14}$$

Finally, the reflected field can be calculated by summing the initial reflection of the input field  $\tilde{\alpha}_i$  with the light transmitted through mirror 1 from the intracavity field:

$$\tilde{\alpha}_{r}(\omega) = r_{1}\tilde{\alpha}_{i}(\omega) - t_{1}r_{2}e^{2ikL}\tilde{\alpha}_{c}(\omega) = \left(r_{1} - r_{2}\frac{\kappa_{1}}{\kappa/2} \frac{e^{2ikL}}{1 - i\left(\frac{\omega - \omega_{c}}{\kappa/2}\right)}\right)\tilde{\alpha}_{i}(\omega)$$

$$\approx \left(1 - \frac{\kappa_{1}}{\kappa/2} \frac{1}{1 - i\left(\frac{\omega - \omega_{c}}{\kappa/2}\right)}\right)\tilde{\alpha}_{i}(\omega)$$
(2.15)

in the high-finesse limit. The relative minus sign between the two terms represents the fact that the reflected input light experiences no phase shift on reflection since the interface is a high- to low- index of

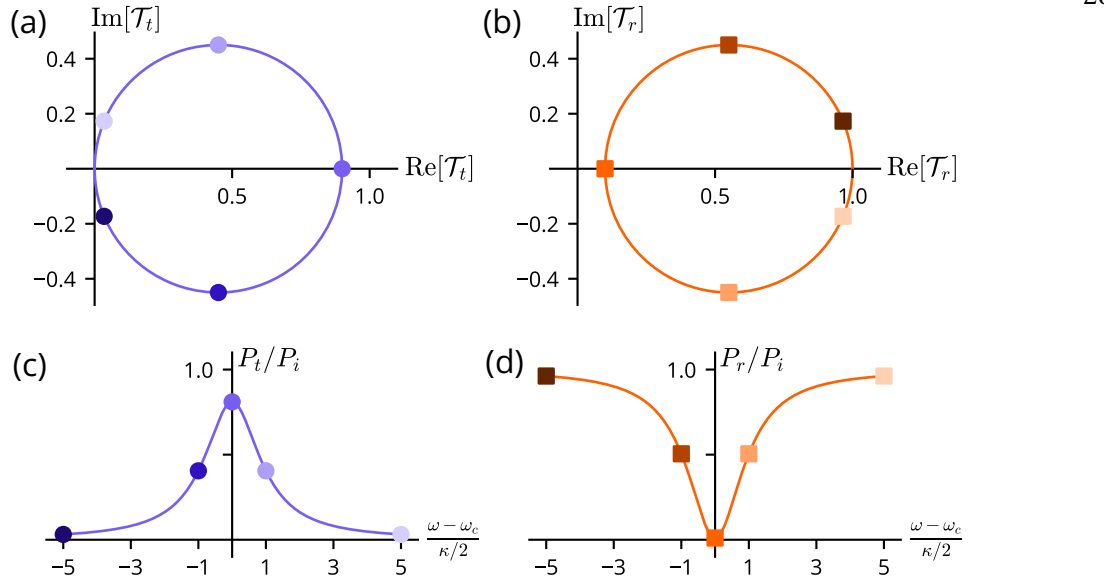


Figure 2.2: Normalized phasor plots describing the steady-state (a) transmitted and (b) reflected transfer functions for a symmetric cavity (with  $\frac{T}{T+L} = 0.9$ ) for different input frequencies  $\omega$ . For each plot, five particular frequencies are selected representing a normalized detuning from cavity resonance given by  $\frac{\omega - \omega_c}{\kappa/2} \in \{-5, -1, 0, 1, 5\}$ , depicted as markers shaded from dark (negative detuning) to light (positive detuning). Panels (c) and (d) show the normalized transmitted and reflected power respectively, plotted against the normalized detuning and including markers analogous to those in panels (a) and (b). This figure is adapted from [182] [G].

refraction boundary, and the transmitted intracavity light experiences a net  $\pi$  phase shift from bouncing off a low- to high- index of refraction boundary an odd number of times inside the cavity.

Equations (2.14) and (2.15) are often referred to as cavity transfer functions since they predict how input fields transfer to reflected and transmitted fields. They are related to the concepts of susceptibilities and Green's functions often seen in other subfields. In our experiment, we work with a (nominally) symmetric cavity, such that  $T_1 = T_2 =: T$ ,  $R_1 = R_2 =: R$ , and  $L_1 = L_2 =: L$ . In this case, we can simplify the expressions further:

$$\mathcal{T}_{t}(\omega) = \frac{T}{T+L} \frac{1}{1-i\left(\frac{\omega-\omega_{c}}{\kappa/2}\right)}$$

$$\mathcal{T}_{r}(\omega) = 1 - \frac{T}{T+L} \frac{1}{1-i\left(\frac{\omega-\omega_{c}}{\kappa/2}\right)},$$
(2.16)

$$\mathcal{T}_{r}(\omega) = 1 - \frac{T}{T + L} \frac{1}{1 - i\left(\frac{\omega - \omega_{c}}{r/2}\right)},\tag{2.17}$$

where  $\mathcal{T}_{t,r}$  are the transmission and reflection transfer functions respectively.

Fig. 2.2 shows what these transmitted and reflected fields look like for a cavity with low losses

 $(\frac{T}{T+L} = 0.9)$ . Interestingly, the phasors always trace out a circle on the complex plane as one scans the probe detuning from cavity resonance [182]<sup>[G]</sup>. This understanding can provide useful intuition any time we care about the phase of a laser interacting with a cavity.

Later in this chapter (in Sec. 2.4.3), we will derive mean-field equations of motion for the combined atom-cavity system called optical Bloch equations. By adding a constant frequency input drive to these equations according to input-output theory as in Eq. (2.9) and solving for the steady state, you can derive a transfer function for the extended atom-cavity system as well. For an example of this, refer to Ch. 4.3.

#### 2.2.3 Example: the PDH error signal

**Pound-Drever-Hall ("PDH") frequency stabilization** [183] is a commonly used technique which stabilizes a laser to the resonance of an optical reference cavity. The experiment I worked on utilizes half a dozen of these locks, as outlined in Ch. 3. While this locking technique has a fancy-sounding name, it essentially can be thought of as frequency-modulation (FM) spectrocsopy of the cavity resonance. The setup is as follows: a laser is frequency modulated at some frequency  $\omega_m$  and directed at the cavity. The reflected light is then captured on a photodiode and demodulated at  $\omega_m$ . The appropriate quadrature of demodulation features a nice error signal which can then be used in a feedback loop. A nice tutorial on the PDH error signal, with a full mathematical description, can be found in [184]. Here, I will give some brief intuition for the error signal that is light on equations and uses intuition from the previous section.

For modulation frequencies slow relative to the cavity linewidth  $(\omega_m \ll \kappa)$ , the reflected power has time to equilibrate to the steady-state value shown in Fig. 2.2(d) for each instantaneous value of  $\omega$ . Therefore, as the laser frequency oscillates according to  $\omega(t) = \omega_0 + \Delta\omega\cos(\omega_m t)$  (for some center frequency  $\omega_0$  and deviation  $\Delta\omega$ ), the power incident on the photodiode will oscillate back and forth on the Lorentzian curve describing the resonance profile. As shown in Fig. 2.3(a), demodulating this oscillation generates a signal that encodes the local slope of the Lorentzian, so long as  $\Delta\omega$  is not too large. This produces a dispersive-like lineshape.

<sup>&</sup>lt;sup>2</sup> In fact, this type of phasor response holds even more generally for any system which can be modeled as a damped single-pole resonance (i.e., with a Lorentzian lineshape) in a linear-response regime, such as a weakly-excited atomic transition.



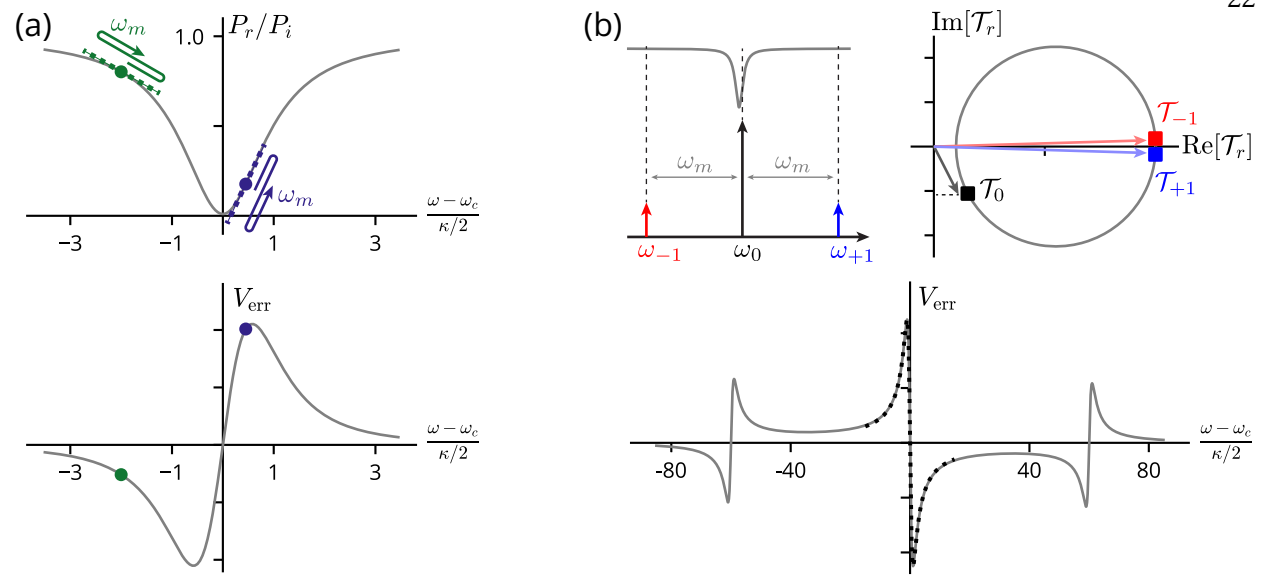


Figure 2.3: Graphical intuition for the PDH error signal. (a) For  $\omega_m \ll \kappa$ , frequency modulation of the laser induces oscillations in the reflected power with a magnitude that depends on the slope of the Lorentzian response profile (top). Demodulation with the proper quadrature therefore produces an error signal proportional to the derivative of a Lorentzian (bottom). (b) For  $\omega_m \gg \kappa$ , frequency modulation produces well-resolved sidebands which beat with the carrier, akin to a heterodyne measurement. When the carrier is close to cavity resonance, only the carrier experiences a nontrivial phasor response  $\mathcal{T}_0$  (top), and the sidebands essentially act as an unperturbed phase reference for the carrier. Demodulation along the proper quadrature therefore approximates an error signal proportional to  $\mathrm{Im}[\mathcal{T}_0]$  (bottom, black dashed). The full PDH error signal (bottom, gray, with  $\omega_m = 60 \times \kappa/2$ ) contains additional features at  $\omega - \omega_c \approx \pm \omega_m$ , which can be explained with a similar argument but with one of the sidebands close to resonance instead of the carrier, leading to a relative sign flip and half the amplitude.

The situation is a bit different when  $\omega_m \gg \kappa$ , which is the regime most often used in our lab. Here, frequency modulation is better thought of as producing FM sidebands at  $\pm \omega_m$  relative to the so-called "carrier" tone at the original frequency  $\omega$ . For any given  $\omega$ , at most one of these three tones is close to resonance with the cavity. When the carrier is close to resonance, the sidebands are not affected by the cavity and essentially act as a phase reference. The carrier, on the other hand, experiences a phasor response which traces out the typical circle in the complex plane, denoted as  $\mathcal{T}_0$  in Fig. 2.3(b). Demodulation along the imaginary or "Q" quadrature results in a dispersive error signal proportional to  $Im[\mathcal{T}_0]$ . Each sideband also produces a similar response when it is close to cavity resonance, leading to

 $<sup>^3</sup>$  If one were to attempt PDH with amplitude ("AM") modulation instead of frequency modulation, the beats between the carrier and each of the  $\pm 1$  sidebands would destructively interfere in this quadrature, leading to no error signal.

a distinctive error signal with features at  $\omega_c$  and  $\omega_c \pm \omega_m$  as shown in Fig. 2.3(b).

### 2.2.4 Cavity finesse

A useful concept for describing the loss properties of a cavity is the **cavity finesse**  $\mathcal{F}$ . It is defined as the ratio of the free spectral range and the full-width half-maximum (FWHM) of a cavity resonance profile. In the low-loss limit ( $\Lambda \ll 1$ ), we can express the finesse as:

$$\mathcal{F} = \frac{f_{\text{FSR}}}{\Delta f_{\text{FWHM}}} = \frac{2\pi f_{\text{FSR}}}{\kappa} \stackrel{\Lambda \ll 1}{\approx} \frac{2\pi}{\Lambda}.$$
 (2.18)

The finesse tends to show up in expressions regarding the fundamentals of cavity systems, such as in the definition of cooperativity as discussed in Sec. 2.4.4. It is proportional to the average number of round trips  $\langle n_{\rm rm} \rangle = 1/\Lambda$  that a photon makes in the cavity before being lost. Relatedly, the finesse is also proportional to the power enhancement between resonant input light and intracavity light. For a symmetric, lossless cavity:

$$P_{c} = \left(\frac{t_{1}}{\Lambda/2}\right)^{2} P_{i}$$

$$\rightarrow \frac{1}{\Lambda/2} P_{i} = \frac{\mathcal{F}}{\pi} P_{i}.$$
(2.19)

For a lossy cavity, the proportionality factor simply changes by  $\frac{T}{T+L}$  to accommodate for additional losses not through transmission.

The finesse is related to a different, commonly-used quantity known as the **quality** (**or Q**) **factor** Q, which is defined as the ratio of the resonance frequency (rather than the free spectral range) to the FWHM cavity linewidth. Assuming we are operating on the nth longitudinal mode of the cavity, the two quantities are related by the simple relation  $Q = n\mathcal{F}$ . The Q factor has a nice physical interpretation as  $(2\pi \text{ times})$  the number of oscillation periods of the cavity field in a single 1/e power decay time of the cavity.

Depending on the physics community, one of these two parameters tends to be preferred. There may be a couple of system-dependent reasons for using one over the other. First, the finesse and the quality factor coincide when working with the fundamental harmonic. If you use multiple longitudinal

modes in an experiment, Q will change while  $\mathcal{F}$  remains the same (up to frequency-dependent transmission and loss properties), which would make  $\mathcal{F}$  a more natural parameter. Conversely, if you only ever work with the fundamental mode, there is no reason to distinguish between the Q factor and finesse. Second, in our derivations above we assume that the losses come only from the mirrors. Under these assumptions,  $\mathcal{F}$  is held constant when changing the cavity length (while holding the resonance frequency fixed by changing longitudinal modes), but Q changes since the cavity linewidth is length-dependent. However, in some systems (such as in nanophotonics), the predominant loss source in a cavity may be the bulk. In this case, increasing the cavity length also increases the losses, and Q will be held fixed while  $\mathcal{F}$  drops. For us, since we work with a cavity mode in vacuum (negligible bulk losses) and work with longitudinal modes at multiple different optical frequencies, the finesse is our preferred quantity.

#### 2.3 The atomic ensemble

Besides the optical cavity, our main system of interest is a cloud of many strontium atoms. Atoms are complicated systems, even more so when they are allowed to interact with each other. For the scope of this chapter, we will start with the simplest possible picture: an ensemble of N identical two-level systems (often referred to as "spins," in reference to a spin-1/2 system spanned by the states  $|\uparrow\rangle$  and  $|\downarrow\rangle$ ).

### 2.3.1 Bloch sphere representation of spin states

We can visualize all possible pure states of a spin on a **Bloch sphere**. For an arbitrary pure state written in the form:

$$|\theta,\phi\rangle = \cos\left(\frac{\theta}{2}\right)|\uparrow\rangle + e^{i\phi}\sin\left(\frac{\theta}{2}\right)|\downarrow\rangle,$$
 (2.20)

we can map this state onto the point  $(\theta, \phi)$  on the surface of the Bloch sphere, as shown in Fig. 2.4(a).

<sup>&</sup>lt;sup>4</sup> *Note*: in the quantum information community, it is common to see  $|0\rangle$  on the north pole. However, when dealing with spin systems, you really want to put  $|\downarrow\rangle$  on the south pole (even if you might be tempted to set  $|\downarrow\rangle = |0\rangle$ ), since you want the spin to literally be pointing down. If you do swap  $|\downarrow\rangle$  and  $|\uparrow\rangle$  on the Bloch sphere, you must also do so for the definition of spin operators (such that in writing these operators,  $|\downarrow\rangle$  corresponds to the first row/column as opposed to the last). Notably, this changes the definition of  $\hat{S}^y$ , which now takes  $|\downarrow\rangle$  to  $i|\uparrow\rangle$ , as opposed to my convention here which takes it to  $-i|\uparrow\rangle$ . (If you do not perform this operator redefinition, all rotations on the Bloch sphere will be *clockwise* instead of counter-clockwise, which is equally confusing.)

Why is the Bloch sphere picture nice? One big reason is that time evolution for non-interacting systems usually corresponds to rotations on the sphere. Suppose you create a spin state  $|\psi_0\rangle \propto |\uparrow\rangle + |\downarrow\rangle$  along a two-level system with a difference frequency  $\omega_{\uparrow} - \omega_{\downarrow} = \delta$ . This corresponds to a Hamiltonian  $\hat{H} = \delta \hat{S}^z$ , where  $\hat{S}^z = \frac{1}{2}(|\uparrow\rangle\langle\uparrow| - |\downarrow\rangle\langle\downarrow|)$ . Then after time  $\delta t = \phi$ , the system will have evolved to the state

$$\left|\psi(t)\right\rangle = e^{-i\hat{H}t} \left|\psi_{0}\right\rangle = e^{-i\phi\hat{S}^{z}} \left|\psi_{0}\right\rangle \propto \left|\uparrow\right\rangle + e^{i\phi} \left|\downarrow\right\rangle, \tag{2.21}$$

which is the original state  $|\psi_0\rangle$  rotated by an angle  $\phi$  along the equator of the Bloch sphere. In general, consider the three spin operators (acting on the spin-1/2 sector and represented using Pauli spin matrices):

$$\hat{S}^{x} = \frac{1}{2} \begin{pmatrix} 0 & 1 \\ 1 & 0 \end{pmatrix}, \qquad \hat{S}^{y} = \frac{1}{2} \begin{pmatrix} 0 & -i \\ i & 0 \end{pmatrix}, \qquad \hat{S}^{z} = \frac{1}{2} \begin{pmatrix} 1 & 0 \\ 0 & -1 \end{pmatrix}, \tag{2.22}$$

where the first row/column is defined to act on  $|\uparrow\rangle$ , and the second row/column acts on  $|\downarrow\rangle$ . Then any Hamiltonian proportional to a linear combination of these spin operators can be expressed in the form  $\hat{H} = \Omega \, \hat{S}^n$  for some frequency  $\Omega$  and a spin operator

$$\hat{S}^{n} := \hat{S} \cdot n = \hat{S}^{x} n_{x} + \hat{S}^{y} n_{y} + \hat{S}^{z} n_{z} \tag{2.23}$$

for some unit vector  $e_n = (n_x, n_y, n_z)$ . Time evolution under this Hamiltonian can be easily visualized as a rotation (counter-clockwise, following the right-hand rule) on the Bloch sphere about the axis pointing along n with angular frequency  $\Omega$ .

The fact that the north and south pole correspond to spin-up and spin-down states suggests that a spin's Bloch sphere representation is connected to the physical direction of its spin. In fact, if you consider the point  $v = (\theta, \phi)$  as a unit vector on a sphere, then a pure state  $|\theta, \phi\rangle$  corresponds exactly to a spin pointing along v! This can be seen in a couple different ways:

(1) The expectations of the Pauli spin operators  $\hat{S}^x$ ,  $\hat{S}^y$ , and  $\hat{S}^z$  correspond to the Cartesian coordinates of v:

$$\langle \hat{S}^{x} \rangle = \sin\left(\frac{\theta}{2}\right) \cos\left(\frac{\theta}{2}\right) \left(e^{i\phi} + e^{-i\phi}\right) = \sin\theta \cos\phi$$

$$\langle \hat{S}^{y} \rangle = \sin\left(\frac{\theta}{2}\right) \cos\left(\frac{\theta}{2}\right) \left(-ie^{i\phi} + ie^{-i\phi}\right) = \sin\theta \sin\phi$$

$$\langle \hat{S}^{z} \rangle = \cos^{2}\left(\frac{\theta}{2}\right) - \sin^{2}\left(\frac{\theta}{2}\right) = \cos\theta.$$
(2.24)

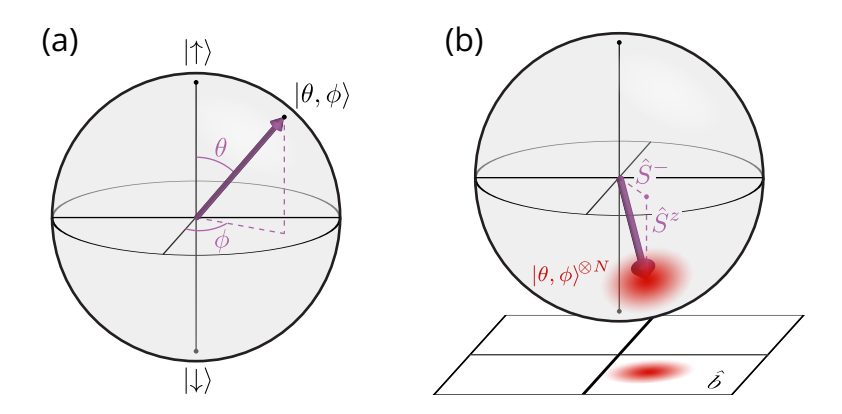


Figure 2.4: Bloch sphere visualizations of spin states. (a) For a single spin-1/2 state, a point with spherical coordinates  $(\theta,\phi)$  on the surface of the Bloch sphere corresponds to state  $|\theta,\phi\rangle$  as defined in Eq. (2.20). (b) An ensemble of spins can be represented with a collective Bloch vector (purple), with its quantum noise represented as a quasiprobability distribution on the collective Bloch sphere (red). Depicted here is a coherent spin state  $|\theta,\phi\rangle^{\otimes N}$  as defined in Eq. (2.27). Sufficiently weakly excited ensembles (Bloch vectors close to the south pole) can be approximated as an excitation of an effective bosonic mode  $\hat{b}$  (bottom plane), as described in Sec. 2.3.3.

(2)  $|\theta,\phi\rangle$  is an eigenstate of  $\hat{S}^v$  with eigenvalue 1/2:

$$\hat{S}^{v} = \frac{1}{2} \begin{pmatrix} \cos \theta & \sin \theta e^{-i\phi} \\ \sin \theta e^{i\phi} & -\cos \theta \end{pmatrix}, \tag{2.25}$$

$$\begin{split} \hat{S}^{v} \left| \theta, \phi \right\rangle &= \frac{1}{2} \left[ \left( \cos \theta \cos \left( \frac{\theta}{2} \right) + \sin \theta \sin \left( \frac{\theta}{2} \right) \right) \left| \uparrow \right\rangle + \left( \sin \theta \cos \left( \frac{\theta}{2} \right) - \cos \theta \sin \left( \frac{\theta}{2} \right) \right) e^{i \phi} \left| \uparrow \right\rangle \right] \\ &= \frac{1}{2} \left[ \cos \left( \frac{\theta}{2} \right) \left| \uparrow \right\rangle + e^{i \phi} \sin \left( \frac{\theta}{2} \right) \left| \downarrow \right\rangle \right] = \frac{1}{2} \left| \theta, \phi \right\rangle. \end{split} \tag{2.26}$$

In general, you can define this vector v for any two-level system, even one that is not literally a spin-1/2 system. We call this vector the **Bloch vector**. Intuitively, the Bloch vector is quite powerful because it allows us to visualize any two-level system as a literal spin. Tying into the discussion earlier in this section, most single-particle Hamiltonians map onto fictitious magnetic fields in this picture, and the time dynamics of the Bloch vector can be visualized as Larmor precession. For example, the earlier example of  $\hat{H} = \delta \hat{S}^z$  looks like a magnetic field pointing along  $\hat{z}$ , and the Bloch vector simply rotates counter-clockwise about the  $\hat{z}$ -axis with an angular frequency  $\delta$ .

# 2.3.2 The collective Bloch sphere

The **collective Bloch sphere** is a natural extension of the spin-1/2 Bloch sphere. In a nutshell, for an ensemble of N spin-1/2 particles, a state vector on (or within) the collective Bloch sphere represents the total (mean-field) spin of the ensemble. More precisely, the point  $\mathbf{v} = (v_x, v_y, v_z)$  within the Bloch sphere represents a spin ensemble where  $\langle \hat{S}^x \rangle = v_x$ ,  $\langle \hat{S}^y \rangle = v_y$ , and  $\langle \hat{S}^z \rangle = v_z$ . Usually, we refer to this point as the **(collective) Bloch vector**, which encodes the mean-field properties of the spin system.  $\mathbf{v}$  can be any point within a sphere of radius N/2, centered on the origin.

Unlike with the single-spin case, the collective Bloch vector does not fully describe the N-spin wavefunction, since the dimension of the Hilbert space  $(2^N)$  is now exponentially large. Still, we can represent much of the important properties of any given state (such as its noise properties) by plotting a quasiprobability distribution<sup>5</sup> on the collective Bloch sphere, alongside the mean-field Bloch vector as shown in Fig. 2.4(b). For many applications (including most in this thesis), we can restrict ourselves to thinking only about the **coherent spin states** (or **CSSs** for short), which we will see are close analogs to coherent states of a harmonic oscillator. We can define the states as follows:

$$|\theta,\phi\rangle^{\otimes N} = e^{-i\theta(\hat{\mathbf{S}}\cdot\mathbf{n}'(\phi))}|\downarrow\rangle^{\otimes N}.$$
 (2.27)

Here,  $n'(\phi) := (-\sin\phi, \cos\phi, 0)$  is the unit vector which rotates a Bloch vector from the south pole along an azimuthal angle  $\phi$ . By definition, these states are single-particle rotations of the ground state  $|\downarrow\rangle^{\otimes N}$ , and so they inherit the minimal noise properties of this state. They are also maximally coherent states, meaning they are eigenstates of the  $\hat{S}^2$  operator with eigenvalue S(S+1) = N(N+2)/4. This can be seen by the fact that  $\hat{S}^2$  commutes with  $\hat{S} \cdot n'(\phi)$  for all  $\phi$ . Consistent with this fact, the Bloch vector representing this state has length S = N/2, which can be seen from calculating the expectations of the operators shown in Fig. 2.4(b):

$$\langle \hat{S}^{-} \rangle = \sum_{i} \langle \hat{S}_{i}^{-} \rangle = \frac{N}{2} e^{-i\phi} \sin \theta \tag{2.28}$$

$$\langle \hat{S}^z \rangle = \sum_i \langle \hat{S}_i^z \rangle = \frac{N}{2} \cos \theta. \tag{2.29}$$

Usually the Husimi Q-function, at least its analog using coherent spin states on the Bloch sphere. The function is defined by  $Q_{|\psi\rangle}(\theta,\phi) := \frac{1}{\pi} |\langle \theta, \phi |^{\otimes N} |\psi\rangle|^2$  [66].

Note that the coherent spin states  $|\theta,\phi\rangle^{\otimes N}$  are not eigenstates of  $\hat{S}^-$ . They are also not eigenstates of any spin-projection operator such as  $\hat{S}^z$  except for along the axis  $v=(\theta,\phi)$  of the CSS. They should be contrasted with eigenstates of a fixed operator such as  $\hat{S}^z$  (of the form  $|S,S^z\rangle$ ), known as **Dicke states** which have well-defined  $S^z$  but perfectly ill-defined azimuthal phase. The two states  $\left|\frac{N}{2},\frac{N}{2}\right\rangle = |\uparrow\rangle^{\otimes N}$  and  $\left|\frac{N}{2},-\frac{N}{2}\right\rangle = |\downarrow\rangle^{\otimes N}$  are the *only* Dicke states that are also CSSs.

As mentioned above, the quantum noise of these states is the minimum allowed by the Heisenberg uncertainty principle, and in fact is evenly distributed between quadratures (just like with coherent states of light), as shown in Fig. 2.4(b). We can see this by analyzing the state  $|\downarrow\rangle^{\otimes N}$ , since all coherent spin states share the same noise properties. Although  $\hat{S}^x$  and  $\hat{S}^y$  have an expectation of 0 for this state, their variance is nonzero. It can be shown that

$$std(\hat{S}^{x}) = \sqrt{\langle (\hat{S}^{x})^{2} \rangle} = \sqrt{\sum_{i} \langle (\hat{S}_{i}^{x})^{2} \rangle} = \frac{\sqrt{N}}{2},$$

$$std(\hat{S}^{y}) = \sqrt{\langle (\hat{S}^{y})^{2} \rangle} = \sqrt{\sum_{i} \langle (\hat{S}_{i}^{y})^{2} \rangle} = \frac{\sqrt{N}}{2},$$
(2.30)

since the cross-terms in  $(\hat{S}^x)^2$  have a vanishing expectation. Note that these results for the standard deviation are just like that of a harmonic oscillator coherent state but with an extra factor of  $\sqrt{N}$ .

For a coherent spin state on the equator, the same noise distribution holds, but now the two orthogonal quadratures are "spin inversion" (i.e.,  $\hat{S}^z$ ) and phase on the Bloch sphere. Since the Bloch vector has length N/2, an uncertainty in the phase quadrature of  $\sqrt{N}/2$  implies a phase resolution of  $1/\sqrt{N}$ . This is known as the **standard quantum limit** (**SQL** for short), since it is a quantum-limit noise floor for phase estimation for "typical" or "classical" states. In principle, it is possible to use different states to attain lower noise along a particular quadrature. For example, the Dicke states mentioned earlier provide a Heisenberg-limited estimate of inversion, with a relative uncertainty of 1/N (but are maximally bad in the other direction since their phase is undefined). For phase estimation, the so-called **GHZ state**  $|\uparrow\rangle^{\otimes N} + |\downarrow\rangle^{\otimes N}$  can reach an uncertainty of 1/N radians (but is maximally bad in the other direction, since it is a superposition of states with maximum and minimum inversion).

# 2.3.3 The Holstein-Primakoff approximation/transformation

Consider an ensemble of N two-level systems ("atoms") with an energy difference  $\hbar\omega_0$ . In the absence of any interactions or other terms, this system has a Hamiltonian which looks like  $\hat{H} = \hbar\omega_0\hat{n}_e$ , where  $\hat{n}_e$  counts the number of atoms in the excited state  $|e\rangle$ . Naively, this looks quite similar to the Hamiltonian of a simple harmonic oscillator, which looks like  $\hat{H}_{SHO} = \hbar\omega_0\hat{b}^{\dagger}\hat{b} = \hbar\omega_0\hat{n}$ . The main difference between these two pictures is that our atomic system can support a finite number of excitations (up to N), whereas the harmonic oscillator can have an infinite number. Still, it doesn't seem like a huge stretch to imagine that, in some limit, we could map the quanta of excitations from  $|g\rangle$  to  $|e\rangle$  in our atomic system onto the quanta of a harmonic oscillator. In particular, when  $n_e \ll N$ , we might imagine that the system "cannot tell" that the number of excitations is finite. This is the essence of the **Holstein-Primakoff approximation**, which approximates the atomic system as a simple harmonic oscillator in a weak-excitation limit.

The Holstein-Primakoff approximation is actually a limit of an exact mapping (the Holstein-Primakoff transformation) between the two systems, of the form:

$$|g\rangle^{\otimes N} \leftrightarrow |0\rangle;$$

$$\hat{S}^{-} \leftrightarrow \sqrt{N}\sqrt{1 - \frac{\hat{b}^{\dagger}\hat{b}}{N}} \hat{b};$$

$$\hat{S}^{z} \leftrightarrow \hat{b}^{\dagger}\hat{b} - \frac{N}{2}.$$
(2.31)

Note that this mapping only considers spin states with maximum total spin angular momentum, i.e.,  $\langle \hat{S}^2 \rangle = S(S+1)$ . In other words, this transformation maps the harmonic oscillator phase space from n=0 to n=N onto the surface of the Bloch sphere, such that the spin eigenstate  $|S,m\rangle = \left|N_g = S - m, N_e = S + m\right\rangle$  maps onto the harmonic oscillator state  $|N_e\rangle$ . To check that this mapping is valid, we check boundary conditions and commutation relations:

$$[\hat{S}^+, \hat{S}^-] = 2\hat{b}^\dagger \hat{b} - N = 2\hat{S}^z; \tag{2.32}$$

$$\hat{S}^{-}|k\rangle = \sqrt{(N-k+1)k}|k-1\rangle = \sqrt{(N_g+1)N_e}|k-1\rangle = \sqrt{S(S+1) - m(m-1)}|k-1\rangle;$$
 (2.33)

$$\hat{S}^{z}|k\rangle = \left(k - \frac{N}{2}\right)|k\rangle = \left(\frac{N_{e} - N_{g}}{2}\right)|k\rangle = m|k\rangle. \tag{2.34}$$

In the regime where  $\langle \hat{b}^{\dagger} \hat{b} \rangle \ll N$ , the mapping simplifies drastically to  $\hat{S}^{-} \approx \hat{b} \sqrt{N}$  (with  $\hat{S}^{z} \approx -\frac{N}{2}$  a constant). It follows that in this limit, excitations really do look like harmonic oscillator states since the spin raising operator is essentially a rescaled bosonic creation operator. Further, coherent spin states map directly onto coherent states. This approximation can be seen geometrically in Fig. 2.4(b): close to the south pole of the Bloch sphere, we can ignore the curvature of the sphere and project the sphere onto a plane (representing the phase space of a harmonic oscillator). Outside the weak excitation limit, the mapping still holds but begins to notice the sphere's curvature, such that CSSs are distorted and no longer map onto coherent states.

### 2.4 Placing atoms in the cavity

The "bare cavity" is fundamentally a linear system, since it ultimately represents a specialized class of boundary conditions for electrodynamics and thus is solved using Maxwell's equations. Atomic systems, on the other hand, are highly nonlinear, particularly when modeled as two-level systems which can only absorb one photon each. All sorts of interesting physics arise when we couple these two systems together, which we will introduce in this section.

### 2.4.1 The Jaynes-Cummings model

We can start by considering a single two-level system ("atom") coupled to a single cavity mode through an electric dipole interaction (ignoring dissipation for now). The Hamiltonian of such a system looks like

$$\hat{H} = \hbar \omega_c \hat{a}^{\dagger} \hat{a} + \frac{\hbar \omega_a}{2} \hat{\sigma}^z - \hat{d} \cdot \hat{E}, \qquad (2.35)$$

where  $\hat{a}$  is the cavity mode annihilation operator,  $\hat{\sigma}^z \coloneqq |e\rangle\langle e| - |g\rangle\langle g|$  is the Pauli Z operator,  $\omega_c$  and  $\omega_a$  are the cavity and atomic resonance frequencies respectively,  $\hat{d}$  is the electric dipole operator, and  $\hat{E}$  is the electric field operator.

The dipole operator acts on the atomic sector and can thus be represented by  $\hat{d} = \mathcal{D}_{eg}\hat{\sigma}^+ + \mathcal{D}_{eg}^*\hat{\sigma}^-$ , where  $\hat{\sigma}^\pm$  are the atomic raising and lowering operators, and  $\mathcal{D}_{eg} \coloneqq \langle e|\hat{d}|g\rangle$  is the **dipole matrix element** 

(vector) coupling the ground and excited states.<sup>6</sup> Without loss of generality, we will assume the dipole matrix element is real. The electric field operator mirrors the expression for the classical field in Eq. (2.1):  $\hat{E} = \mathcal{E}_0 f(x) \frac{\hat{a} + \hat{a}^\dagger}{2}, \text{ where } \mathcal{E}_0 = \sqrt{\frac{2\hbar\omega_c}{\epsilon_0}} \text{ is a prefactor with units of electric field } \times \sqrt{\text{volume}}, \text{ and } f(x) \text{ is the cavity mode function satisfying } f(x) = \frac{1}{\sqrt{V_m}} \varepsilon \text{ at an antinode (where } V_m \text{ is the mode volume, and } \varepsilon \text{ is the electric field polarization)}. Therefore, if we define a coupling frequency <math>g$  by:<sup>7</sup>

$$g := -\left(\mathcal{D}_{eg} \cdot \varepsilon\right) \sqrt{\frac{\omega_c}{2\hbar\epsilon_0 V_m}},\tag{2.36}$$

then the Hamiltonian becomes

$$\hat{H}/\hbar = \omega_c \hat{a}^{\dagger} \hat{a} + \frac{\omega_a}{2} \hat{\sigma}^z + g \left( \hat{a} + \hat{a}^{\dagger} \right) \left( \hat{\sigma}^- + \hat{\sigma}^+ \right). \tag{2.37}$$

This is called **the quantum Rabi model**, first studied semiclassically by Rabi in the context of a rotating classical magnetic field acting on quantum spins [185, 186].

In atomic physics systems, the cavity and atomic resonance frequencies tend to be optical frequencies (100s of THz), much larger than typical values for g (up to 10s of MHz). In this regime, the counter-rotating terms which create or annihilate two quanta of energy ( $\hat{a}^{\dagger}\hat{\sigma}^{+}$  and  $\hat{a}\hat{\sigma}^{-}$ ) are far off resonance, and we can make a rotating-wave approximation to remove those terms. The resulting Hamiltonian is a foundational model in quantum optics known as **the Jaynes-Cummings model** [187]:

$$\hat{H}_{\text{JC}}/\hbar = \omega_c \hat{a}^{\dagger} \hat{a} + \frac{\omega_a}{2} \hat{\sigma}^z + g \left( \hat{a} \hat{\sigma}^+ + \hat{a}^{\dagger} \hat{\sigma}^- \right). \tag{2.38}$$

We can simplify this further by going into the rotating frame of the atoms. Practically, this means that we work in an interaction frame with  $\hat{H}_0 = \omega_a \hat{a}^\dagger \hat{a} + \frac{\omega_a}{2} \hat{\sigma}^z$ , resulting in the interaction Hamiltonian:

$$\hat{H}_{\text{JC,I}}/\hbar = \Delta_{ca}\hat{a}^{\dagger}\hat{a} + g\left(\hat{a}\hat{\sigma}^{+} + \hat{a}^{\dagger}\hat{\sigma}^{-}\right),\tag{2.39}$$

where  $\Delta_{ca} := \omega_c - \omega_a$  is the atom-cavity detuning.

The Jaynes-Cummings model is readily solvable by working in the basis of  $|g, M\rangle$  and  $|e, M\rangle$  states (where M is a quantum number representing the number of photons in the cavity mode) and noting

<sup>&</sup>lt;sup>6</sup> Recall that  $\hat{d} \propto \hat{x}$ . Due to odd-even symmetry in position space, the diagonal elements  $\mathcal{D}_{gg}$  and  $\mathcal{D}_{ee}$  vanish.

<sup>&</sup>lt;sup>7</sup> It is common practice to define g assuming the electric field polarization is aligned to the dipole matrix element of the atomic transition, such that  $\mathcal{D}_{eg} \cdot \varepsilon = |\mathcal{D}_{eg}|$  is independent of the electric field polarization. Applying an electric field with some other polarization then modifies the Hamiltonian in Eq. (2.37) by some geometric prefactor.

that each state only couples to at most one other, as shown in Fig. 2.5(a). The ground state  $|g,0\rangle$  remains unperturbed, and each pair of states  $|g,M\rangle$ ,  $|e,M-1\rangle$  forms a two-level system with a subsystem Hamiltonian with the form

$$\begin{pmatrix} 0 & g\sqrt{M} \\ g\sqrt{M} & \Delta_{ca} \end{pmatrix}. \tag{2.40}$$

Fig. 2.5(b) shows the eigenenergies for the first excitation manifold (M=1) as a function of the atom-cavity detuning  $\Delta_{ca}$ . On resonance  $(\Delta_{ca}=0)$ , the unperturbed states  $|e,0\rangle$  and  $|g,1\rangle$  hybridize to form states of the form  $|\pm\rangle \propto |e,0\rangle \pm |g,1\rangle$  with the excitation evenly split between atom-like and cavity-like character. Sometimes, such eigenstates are referred to as polaritons, referencing similar concepts in solid-state physics [188, 189], but I will not use that language here. The energy splitting from this hybridization is called the **vacuum Rabi splitting** [190, 191] and is a signature of strong atom-light coupling. For large detunings  $(\Delta_{ca} \gg g\sqrt{M})$ , the eigenstates are mostly atom-like and cavity-like with dressing from the other, leading to a small "dispersive" energy shift. This shift is spiritually similar to the concept of an AC Stark shift, which is a shift on an atomic state induced by a detuned classical field. In this case, we consider the shifts on both the atom and the cavity field mode.

#### 2.4.2 Extending to many atoms: the Tavis-Cummings model

While the case of a single atom coupled to cavity is interesting in its own right, our experiment is primarily concerned with the case of many atoms. If we consider N two-level systems with a homogeneous coupling strength g, the quantum Rabi model from Eq. (2.37) becomes the more general **Dicke** model [156, 192], given by

$$\hat{H}/\hbar = \omega_c \hat{a}^{\dagger} \hat{a} + \omega_a \hat{S}^z + g \left( \hat{a} + \hat{a}^{\dagger} \right) \left( \hat{S}^- + \hat{S}^+ \right), \tag{2.41}$$

where here we define collective angular momentum operators  $\hat{S}^z \coloneqq \frac{1}{2} \sum_{i=1}^N \hat{\sigma}_i^z$  and  $\hat{S}^\pm \coloneqq \sum_{i=1}^N \hat{\sigma}_i^\pm$ . In the limit where  $N \to \infty$  with the atom-light coupling g renormalized by  $1/\sqrt{N}$  to hold the mean-field interaction strength constant, this model exhibits a second-order phase transition in its ground state, sometimes called the "Dicke" or "superradiant" phase transition<sup>8</sup> [32, 75, 192].

<sup>&</sup>lt;sup>8</sup> *Not* to be confused with the superradiant phase observed in Sec. 8.1.1 in an entirely different model. In general, the qualifiers "Dicke" and "superradiant" have become pretty muddy and ambiguous in the community, so you should make sure to clearly define what you mean when using these terms.

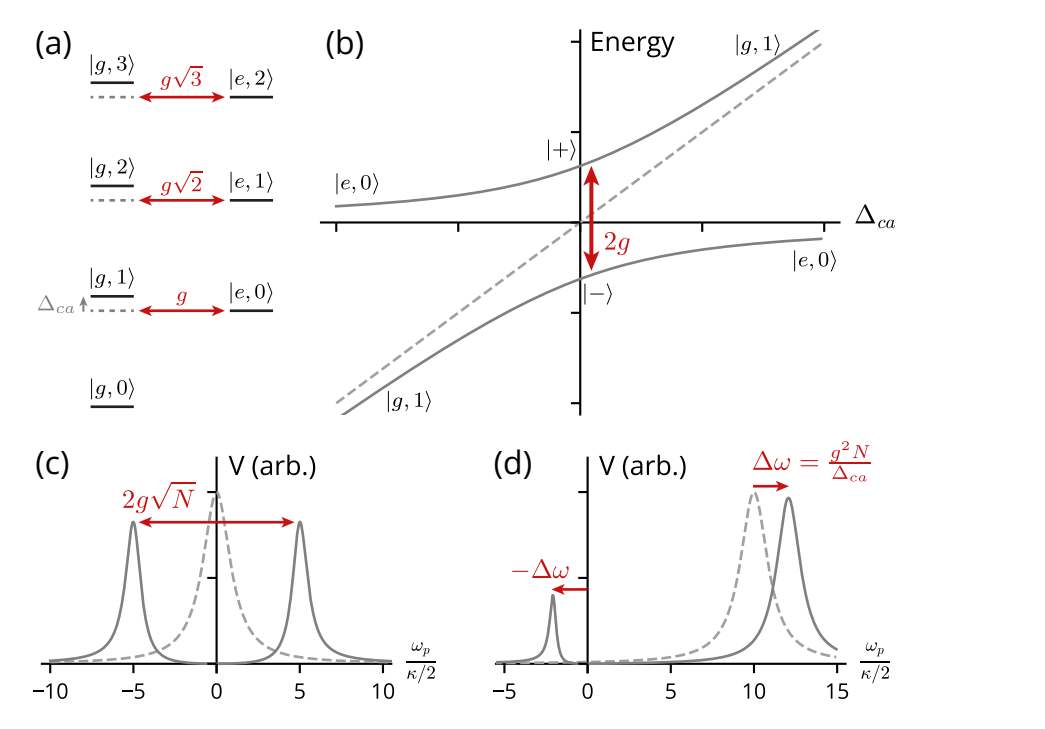


Figure 2.5: Dressed state resonances in the Jaynes-Cummings and Tavis-Cummings models. (a) Ladder of states for a two-level system coupled to a cavity mode, with coupling strengths imposed by the Jaynes-Cummings model in red. (b) Eigenenergies for the first excitation manifold  $(|g,1\rangle,|e,0\rangle)$  as a function of the atom-cavity detuning  $\Delta_{ca}$ . The atom-light coupling produces a classic avoided crossing between the two states, leading to a hybridization of atom-like and photon-like excitations near  $\Delta_{ca}=0$ . (c) An ensemble of N atoms resonantly coupled to a cavity mode produces a mode splitting of size  $2g\sqrt{N}$  in the single excitation manifold, known as a vacuum Rabi splitting (VRS), which can be measured by scanning a probe with frequency  $\omega_p$  through the cavity to look for resonant transmission. Shown here is an example VRS profile (gray) with  $\frac{g\sqrt{N}}{\kappa/2}=5$  and atomic linewidth  $\gamma\ll\kappa$ . The dashed curve represents the unsplit cavity resonance. (d) In a limit where the cavity is detuned by  $\Delta_{ca}\gg\kappa/2$ , the vacuum Rabi splitting manifests as a weak dressing of the atom-like and photon-like excitations, leading to a repulsive shift  $\Delta\omega=\frac{g^2N}{\Delta_{ca}}$  (gray solid curve) relative to the noninteracting resonances (dashed curve). Here, we plot the case where  $\frac{\Delta_{ca}}{\kappa/2}=10$ .

Again, for a typical atom-cavity system, we can perform a rotating-wave approximation to ignore the off-resonnat pair-creation and pair-annihilation process. The many-atom limit of the Jaynes-Cummings model is known as the Tavis-Cummings model [193], and it takes the form

$$\hat{H}_{TC}/\hbar = \Delta_{ca}\hat{a}^{\dagger}\hat{a} + g\left(\hat{a}\hat{S}^{+} + \hat{a}^{\dagger}\hat{S}^{-}\right) \tag{2.42}$$

in the interaction picture. At the mean-field level, the Tavis-Cummings model behaves much the same as the Jaynes-Cummings model but with an enhancement of the interaction frequency from  $g \to g\sqrt{N}$ .

There are a few ways to understand this scaling. One relatively simple way is to recall the Holstein-Primakoff approximation from Sec. 2.3.3. In the weak excitation limit (where the excited state population  $N_e$  always satisfies  $N_e \ll N$ ), we can treat the atomic ensemble as a harmonic oscillator with the substitution  $\hat{S}^- \to \hat{b}\sqrt{N}$ , leading to the following Hamiltonian describing two coupled harmonic oscillators:

$$\hat{H}_{TC}/\hbar \approx \Delta_{ca}\hat{a}^{\dagger}\hat{a} + g\sqrt{N}\left(\hat{a}\hat{b}^{\dagger} + \hat{a}^{\dagger}\hat{b}\right). \tag{2.43}$$

In this picture, when  $\Delta_{ca} = 0$  then a weak excitation (such as a photon in the cavity) will resonantly oscillate back and forth between a cavity and atom excitation with an oscillation frequency  $g\sqrt{N}$ , demonstrating the collectively enhanced coupling in the system.

The collective enhancement of atom-light coupling leads to atom number dependent frequency shifts of the atom-cavity resonance spectrum, as shown in Fig. 2.5(c-d). When the cavity is on resonance with the atomic transition, this manifests as a vacuum Rabi splitting with a full width equal to  $2g\sqrt{N}$ . The larger splitting afforded by the  $\sqrt{N}$  factor historically enabled early studies of the strong atom-cavity coupling regime on optical transitions [165]. In more recent times, it has also allowed measurement of the atom number N below a fractional precision of  $1/\sqrt{N}$ , set by the standard quantum limit as described in Sec. 2.3.2, leading to spin squeezing [63, 182] [G]. Far from atom-cavity resonance  $(\Delta_{ca} \gg g\sqrt{N})$ , the dispersive shifts of the atom-like and cavity-like modes increase in kind to  $\frac{g^2N}{\Delta_{ca}}$ . Even more so than the resonant case, this regime has attracted much interest for engineering spin squeezing through a measurement of N via the size of the dispersive shift [60-62], as well as through deterministic atom number dependent Hamiltonians such as one-axis twisting [66-68, 94, 194-197]. Both such techniques have been demonstrated to generate spin squeezing to the level of ~18 dB of metrological gain over the standard quantum limit [69][70]<sup>[G]</sup>. There are a host of other proposals for utilizing cavity QED for generating squeezing, such as through engineering two-mode squeezing [198] or two-axis countertwisting [199][86]<sup>[G]</sup>, as well as for performing various quantum nondemolition measurements, such as tracking the atomic state or position using lattice fields [200, 201] or tracking the atomic phase through applied probes [202]. Many resources exist for learning about spin squeezing in cavity QED systems and its various iterations; Zilong Chen's thesis from our group is one good example [203] [G].

# 2.4.3 Optical Bloch equations

The previous sections only consider the unitary time evolution of the atom-cavity system. In real systems, we have to deal with dissipation, both through the cavity (set by the FWHM cavity resonance linewidth  $\kappa$ , equivalent to the reciprocal of the 1/e decay time for photons in the cavity) and into free space (set by the FWHM atomic resonance linewidth  $\gamma$ , equivalent to the spontaneous emission rate). For many situations, studying the mean-field equations of motion for the cavity field and single-atom observables is sufficient to understand the physics. In a slight abuse of notation, our lab likes to call this set of equations the optical Bloch equations for the system.

To derive the optical Bloch equations, we start by considering the time evolution of the system's density matrix  $\hat{\rho}$ , which we assume to be governed by the following **Lindblad master equation**:

$$d_t \hat{\rho} = -i[\hat{H}, \hat{\rho}] + \kappa \mathcal{L}[\hat{a}](\hat{\rho}) + \gamma \sum_i \mathcal{L}[\hat{\sigma}_i^-](\hat{\rho}), \qquad (2.44)$$

where  $d_t$  is a shorthand for a time derivative, index i refers to atom  $i \in \{1, ..., N\}$ , and  $\mathcal{L}[\hat{\Omega}](\hat{\rho}) \coloneqq \hat{\Omega}\hat{\rho}\hat{\Omega}^{\dagger} - \frac{1}{2}\{\hat{\Omega}^{\dagger}\hat{\Omega},\hat{\rho}\} = \hat{\Omega}\hat{\rho}\hat{\Omega}^{\dagger} - \frac{1}{2}\{\hat{\Omega}^{\dagger}\hat{\Omega}\hat{\rho} + \hat{\rho}\hat{\Omega}^{\dagger}\hat{\Omega}\}$  is a Lindblad-type superoperator on  $\hat{\rho}$  which describes the effects of dissipation through a weak coupling to a Markovian bath with a jump operator  $\hat{\Omega}$  [207]. In other words, it describes how the density matrix evolves, under the assumptions that coupling to the bath can be modeled as a stochastic process in which the system randomly experiences a jump  $\hat{\Omega}$  with a probability that is uncorrelated with all past moments. We can intuitively understand this form as being composed of two terms: the "jump" term  $\hat{\Omega}\hat{\rho}\hat{\Omega}^{\dagger}$ , in which the operator  $\hat{\Omega}$  is applied, and the "no-jump" term  $\frac{1}{2}\{\hat{\Omega}^{\dagger}\hat{\Omega},\hat{\rho}\}$ , in which the measured lack of a jump leads to a re-weighting of proabilities in the density matrix due to an update of Bayesian priors about the system. Such a breakdown is explicitly used in the **Monte Carlo wave function (MCWF)** method for numerically simulating open quantum systems [208].

From knowledge of the time evolution, it's straightforward to obtain equations of motion for observable expectations (which we will refer to as "mean-field" quantities). In this thesis, I'll adopt the

<sup>&</sup>lt;sup>9</sup> The term "optical Bloch equations" is commonly used in the quantum optics community to refer to the semiclassical equations of motion for a single atom that is subject to a classical electromagnetic field [177, 204]. The name comes from the strong connection between this system and a spin in an external magnetic field, which are described by "Bloch equations" first studied by Bloch in 1946 [205]. With equations for the electromagnetic field included, the equations are sometimes called the "Maxwell-Bloch equations" [206]. The equations described in this section are similar but are a bit more general in scope.

notation where the lack of an "operator hat" represents a mean-field quantity:  $\emptyset \coloneqq \langle \hat{\mathbb{O}} \rangle$  for some operator  $\hat{\mathbb{O}}$ . With this notation, we can utilize the cyclic property of the trace to obtain:

$$\begin{split} \mathbf{d}_{t} & \hat{\mathbf{G}} = \mathbf{d}_{t} \operatorname{Tr} \left[ \hat{\mathbf{G}} \hat{\rho} \right] = \operatorname{Tr} \left[ \hat{\mathbf{G}} \, \mathbf{d}_{t} \hat{\rho} \right] \\ & = \operatorname{Tr} \left[ \left( i [\hat{H}, \hat{\mathbf{G}}] + \kappa \tilde{\mathcal{L}} [\hat{a}] (\hat{\mathbf{G}}) + \gamma \sum_{i} \tilde{\mathcal{L}} [\hat{\sigma}_{i}^{-}] (\hat{\mathbf{G}}) \right) \hat{\rho} \right] \\ & = i \left\langle [\hat{H}, \hat{\mathbf{G}}] \right\rangle + \kappa \left\langle \tilde{\mathcal{L}} [\hat{a}] (\hat{\mathbf{G}}) \right\rangle + \gamma \sum_{i} \left\langle \tilde{\mathcal{L}} [\hat{\sigma}_{i}^{-}] (\hat{\mathbf{G}}) \right\rangle, \end{split} \tag{2.45}$$

where  $\tilde{\mathcal{L}}[\hat{\Omega}](\hat{\mathbb{G}}) := \hat{\Omega}^{\dagger}\hat{\mathbb{G}}\hat{\Omega} - \frac{1}{2}\{\hat{\Omega}^{\dagger}\hat{\Omega},\hat{\mathbb{G}}\}$ . We want to study the time evolution of the Tavis-Cummings Hamiltonian on the cavity field and atomic observables, which we can track with the mean-field quantities a,  $\sigma_i^-$ , and  $\sigma_i^z$ . Combining Eq. (2.45) with Eq. (2.42) for these observables gives:

$$d_{t}a = -ig\sum_{i}\sigma_{i}^{-} - \left(\frac{\kappa}{2} + i\Delta_{ca}\right)a$$

$$d_{t}\sigma_{i}^{-} = ig\left\langle \hat{a}\hat{\sigma}_{i}^{z}\right\rangle - \frac{\gamma}{2}\sigma_{i}^{-}$$

$$d_{t}\sigma_{i}^{z} = 2ig\left(\left\langle \hat{a}^{\dagger}\hat{\sigma}_{i}^{-}\right\rangle - \left\langle \hat{a}\hat{\sigma}_{i}^{+}\right\rangle\right) - \gamma(1 + \sigma_{i}^{z}).$$

$$(2.46)$$

If we further simplify by assuming these operators are uncorrelated, such that the remaining expectations can be simplified like  $\left\langle \hat{a}\hat{\sigma}_{i}^{z}\right\rangle \approx a\sigma_{i}^{z}$ , then we end up with a complete set of equations that fully determines the mean-field behavior of the system. Further simplifying the notation by using collective angular momentum observables  $S^{-}=\sum_{i}\sigma_{i}^{-}$  and  $S^{z}=\frac{1}{2}\sum_{i}\sigma_{i}^{z}$  results in our typical expression for the optical Bloch equations:

$$d_t a = -igS^- - \left(\frac{\kappa}{2} + i\Delta_{ca}\right) a$$

$$d_t S^- = 2igaS^z - \frac{\gamma}{2}S^-$$

$$d_t S^z = -2g\operatorname{Im}[a^*S^-] - \gamma\left(\frac{N}{2} + S^z\right).$$
(2.47)

#### 2.4.4 Regimes of atom-cavity coupling

As can be seen in Eq. (2.47), multiple frequency scales ( $\kappa$ ,  $\gamma$ , g,  $\Delta_{ca}$ ) contribute to the physics of this system. Depending on the relative sizes of these processes, the qualitative nature of the dynamics can change quite a bit. In this section, we will briefly go through the different regimes of atom-cavity

	$NC \ll 1$	$NC\gg 1$	
$\kappa \ll \gamma$ ("good-cavity")	No lasing threshold	$g\sqrt{N}\ll\gamma$	$g\sqrt{N}\gg\gamma$
		Traditional lasing $(\gamma \gg g\sqrt{N} \gg NC\kappa \gg \kappa)$	"resolved VRS" regime $(g\sqrt{N} \gg \gamma \gg \kappa)$
$\kappa \gg \gamma$ ("bad-cavity")	Below threshold for superradiance	$g\sqrt{N}\!\ll\!\kappa$	$g\sqrt{N}\gg \kappa$
		Superradiance $(\kappa \gg g\sqrt{N} \gg NC\gamma \gg \gamma)$	Coherent dynamics/ "resolved VRS" regime $(g\sqrt{N} \gg \kappa \gg \gamma)$

Table 2.1: Regimes of atom-cavity coupling. The three conditions here (bad- vs. good-cavity, large or small collective cooperativity, and resolved or unresolved VRS) are necessary and sufficient to generate a hierarchy of scales for the four parameters  $\kappa$ ,  $\gamma$ ,  $g\sqrt{N}$ , and  $NC\gamma$  (or  $NC\kappa$  for the good-cavity case).

coupling, summarized in Table 2.1. For the time being, we will assume the cavity is on resonance with the atomic transition ( $\Delta_{ca} = 0$ ); refer to Sec. 2.5.3 for the effects of a nonzero detuning.

First, we can directly compare the size of coherent interactions and dissipation. As described in Sec. 2.4.2, excitations in the system will oscillate between the cavity (as a photon) and the atoms (placing an atom in the excited state) at a rate set by  $g\sqrt{N}$  in the weak-excitation limit. We can see this quantitatively by making the Holstein-Primakoff approximation  $S^- \to b\sqrt{N}$ ,  $S^z \to -\frac{N}{2}$  for some effective bosonic mode b describing the atomic ensemble (see Sec. 2.3.3) to simplify the optical Bloch equations:

$$\begin{aligned} \mathbf{d}_{t}a &= -ig\sqrt{N}b - \frac{\kappa}{2}a\\ \mathbf{d}_{t}b &= -ig\sqrt{N}a - \frac{\gamma}{2}b, \end{aligned} \tag{2.48}$$

which looks exactly like damped oscillations between a and b. Solving for the dynamics of this system, we find that the system attains critical damping when  $2g\sqrt{N} = \frac{\kappa + \gamma}{2}$ . Spectroscopically, this has the interpretation that the vacuum Rabi splitting is equal to the effective linewidth of the VRS peaks, and therefore the splitting is on the edge of being resolvable.

The critical point demarcates two distinct coupling regimes: first, the underdamped regime (where  $g\sqrt{N}\gg\kappa+\gamma$ ) is dominated by coherent oscillations. Sometimes, we call this the "resolved VRS regime." Second, the overdamped regime (where  $g\sqrt{N}\ll\kappa+\gamma$ ) is dominated by dissipation. Spectroscopically, this means the coupling  $g\sqrt{N}$  is not strong enough to split out the hybrid atom-cavity resonances be-

yond their natural linewidths. In the time domain, it implies that if we excite the atoms, that excitation will decay (either through the cavity or into free space) faster than coherent oscillations can build up. This is the regime of many conventional laser systems like solid-state diodes, whose gain media are typically quite broad (large effective  $\gamma$ ).

The overdamped regime is also required for conventional **superradiance** [211, 212]. First studied by Dicke in 1954 [156], superradiance is a phenomenon in which identical emitters (such as atoms) collectively emit into a common electromagnetic mode. The in-phase nature of the collective emission causes constructive interference in the emitted electric field, resulting in an *N*-fold enhancement in the emitted power over incoherent spontaneous emission, as well as in the emission rate. In recent years, superradiance along narrow-linewidth optical atomic transitions has received much interest due to the potential in building an ultranarrow **superradiant laser**, which could be used as a sort of active optical atomic clock. This interest has led to multiple theoretical proposals [213–220] and a great deal of progress towards an experimental realization of a (continuous-wave) superradiant laser in our group [93, 221–225] [G] and elsewhere [226–229]. [11]

How do we distinguish superradiance from traditional lasing? Essentially, the difference lies in where dissipation primarily occurs. Traditional lasers operate in the **good-cavity limit** where  $\kappa \ll \gamma$ . As such, the atoms (or whatever composes the gain medium) undergo many cycles of decay and repumping in the time it takes for the average photon to leak out of the cavity. In this limit, the laser frequency (and its phase coherence) are almost entirely determined by the cavity. Superradiance, on the other hand, occurs in the **bad-cavity limit** where  $\kappa \gg \gamma$ . In this limit, photons emitted into the cavity by the atoms will almost immediately leak out of the cavity, such that it is possible to observe a coherent superradiant laser pulse with less than one photon in the cavity on average [221]<sup>[G]</sup>. Such an experiment is possible because the phase coherence is stored in the atomic ensemble, rather than the cavity. This property is what enables many of the desirable features of a superradiant laser, such as its potentially narrow

<sup>&</sup>lt;sup>10</sup> While it is possible for lasing to occur in the underdamped regime, particularly with small mode volume systems like nanocavities, it is uncommon and nontrivial to achieve [209, 210].

<sup>&</sup>lt;sup>11</sup> Hidetoshi Katori's group in Tokyo has demonstrated a continuous source of <sup>88</sup>Sr atoms [230], which has the potential to explore continuous-wave superradiance as well.

linewidth and its robustness against cavity frequency noise. For a more detailed discussion of these features, our lab's progress towards developing superradiant lasers, and more, I recommend reading Matt Norcia's and Julia Cline's theses [224, 231].

While both lasing and superradiance can occur in an overdamped regime where  $\kappa + \gamma \gg g\sqrt{N}$ , they still both require a macroscopic buildup of phase coherence. Intuition tells us that if the dissipation rates are too large compared to the atom-cavity interaction, they should eventually dominate and kill such effects. The threshold between a coherent regime and a dissipation-dominated regime for a single atom is set by the **the** (**single-atom**) **cooperativity** C. The normalization of this quantity is not always consistent [180, 232, 233], but here we will define the cooperativity to be:

$$C := \frac{4g^2}{\kappa \gamma}.\tag{2.49}$$

This normalization relates the square of the single-photon atom-cavity Rabi frequency 2*g* to the product of the atom and cavity linewidths.

While it may look like the cooperativity is dependent on atomic properties, it is a purely geometric quantity equivalent to the Purcell factor [234]:

$$C = \frac{24\mathcal{F}}{\pi k^2 w^2},\tag{2.50}$$

where  $\mathcal{F}$  is the cavity finesse,  $k=2\pi/\lambda$  is the wavevector of the cavity resonance, and w is the cavity waist. [180] is a fantastic resource which derives this form of the cooperativity in a purely classical regime. That work makes it clear that the cooperativity describes the relative likelihood that an atom emits a photon into the cavity mode, rather than into free space, essentially due to the geometry of the system. Increasing the solid angle subtended by the cavity mode (by decreasing the cavity waist) increases this likelihood, as does increasing the reflectivity of the mirrors due to constructive interference effects. Placing N atoms in the cavity further enhances the likelihood of emitting into the cavity for similar reasons of constructive interference. For an atomic ensemble, therefore, this relative likelihood is given by the collective cooperativity NC.

 $<sup>\</sup>overline{}^{12}$  Recall that  $g \propto \sqrt{\gamma} \propto \mathfrak{D}_{eg}$ 

The collective cooperativity determines whether dissipation out of the system is primarily coherent (i.e., collective emission through the cavity) or incoherent (i.e., spontaneous emission). The former occurs in the regime where  $NC \gg 1$ : since all atoms couple to the same cavity mode, emission through the cavity provides no information about which atom emitted the photon. Therefore, phase coherence is preserved. In this regime, either lasing or superradiance can occur without preseeding, given sufficient inversion (and repumping rate for a laser). When  $NC \ll 1$ , most emission out of the system is in the form of spontaneous emission, which is an incoherent process. In this regime, unseeded superradiance cannot occur because the atoms dephase faster than coherence can build up due to collective emission. Lasing also cannot occur, since in this regime the system cannot achieve a positive gain, no matter how strong the gain medium is repumped. 13

# 2.5 Adiabatic elimination of the cavity mode

Sometimes, in order to model dynamics of the atom-cavity system accurately, we need to model all of the terms we introduced in the previous sections. But in many of the regimes listed above, we don't. For example, in the superradiant regime,  $\kappa$  is the dominant frequency scale. This means the cavity mode damps on a time scale much faster than the rest of the dynamics, and you might imagine that we can somehow "ignore" it. **Adiabatic elimination** is a common theoretical tool which formalizes exactly this intuition of "ignoring" some degree of freedom in the system over relevant experimental timescales. In this section, we will briefly discuss how this technique allows us to derive both mean-field dynamics and an effective Hamiltonian description of the simplified problem. We will also apply this technique to the example of eliminating the cavity mode in our atom-cavity system, which is the regime we operate in for nearly all of the work described in this thesis.

<sup>&</sup>lt;sup>13</sup> This can be seen by setting up the optical Bloch equations (Sec. 2.4.3) for an incoherently pumped ensemble of atoms in the Tavis-Cummings model with dissipation, adiabatically eliminating (Sec. 2.5) the atomic coherence  $S^-$  by assuming  $\gamma$  is the largest dissipation scale, solving for the steady state  $S^z$  in a small-signal limit ( $\langle \hat{a} \rangle = a$  small), and then looking for a critical point where the damping rate R in the equation  $\dot{a} = -Ra$  drops to zero to obtain a threshold condition. For sufficiently small NC, no such threshold exists. Unfortunately, I couldn't find a publication detailing this calculation, so this can be an exercise for the reader.

#### 2.5.1 Mean-field adiabatic elimination

To understand the idea of "ignoring" the dynamics of some observable, let's recall the optical Bloch equations for our system from Eq. (2.47):

$$d_t a = -igS^- - \left(\frac{\kappa}{2} + i\Delta_{ca}\right) a$$

$$d_t S^- = 2igaS^z - \frac{\gamma}{2}S^-$$

$$d_t S^z = -2g\operatorname{Im}[a^*S^-] - \gamma\left(\frac{N}{2} + S^z\right).$$
(2.51)

There are two related but separate conditions that lead to adiabatic elimination. First, suppose  $\kappa$  is the dominant frequency scale. If the atoms emit into the cavity mode with rate  $-igS^-$ , this excitation will damp very quickly. On timescales slower than  $1/\kappa$ , the cavity field a will have reached a quasi-steady state  $a_{ss}$  satisfying  $d_t a_{ss} = 0$ , where

$$a_{\rm ss} = \frac{-g}{\Delta_{ca} - i\frac{\kappa}{2}} S^{-}. \tag{2.52}$$

We can then say that the cavity field a adiabatically follows  $S^-$ . Alternatively, suppose  $\Delta_{ca}$  is the largest frequency scale in the system. Then a will oscillate with a period of  $2\pi/\Delta_{ca}$ , averaging out the  $-igS^-$  coupling which changes much more slowly and reducing the size of a on average. Therefore, coarse-graining the time dynamics with sufficiently large time steps ( $\Delta t \gg 2\pi/\Delta_{ca}$ ) will also make a appear to have reached a quasi-steady state, satisfying Eq. (2.52) as well.

It will be useful for later to define the following effective frequencies:

$$\chi := \operatorname{Re}\left[\frac{g^2}{\Delta_{ca} - i\frac{\kappa}{2}}\right] = \frac{g^2 \Delta_{ca}}{\Delta_{ca}^2 + \left(\frac{\kappa}{2}\right)^2}$$

$$\frac{\Gamma}{2} := \operatorname{Im}\left[\frac{g^2}{\Delta_{ca} - i\frac{\kappa}{2}}\right] = \frac{1}{2} \frac{g^2 \kappa}{\Delta_{ca}^2 + \left(\frac{\kappa}{2}\right)^2}.$$
(2.53)

Here,  $\chi$  and  $\Gamma$  represent the quadratues of the quasi-steady state cavity field which are in-phase and out-of-phase with  $S^-$ , respectively, since Eq. (2.52) then reduces to  $a_{ss} = -\left(\frac{2\chi+i\Gamma}{2g}\right)S^-$ , which has a Rabi frequency equal to  $2ga_{ss} = (2\chi+i\Gamma)S^-$ . We can visualize the separate roles of these in-phase and out-of-phase components in Fig. 2.6: the  $\chi$  term causes the Bloch vector to precess azimuthally, preserving the atomic inversion  $S^z$ . As we will see next section, this corresponds to an effective all-to-all interaction between atoms. Meanwhile, the  $\Gamma$  term drives the Bloch vector towards the south pole of the Bloch

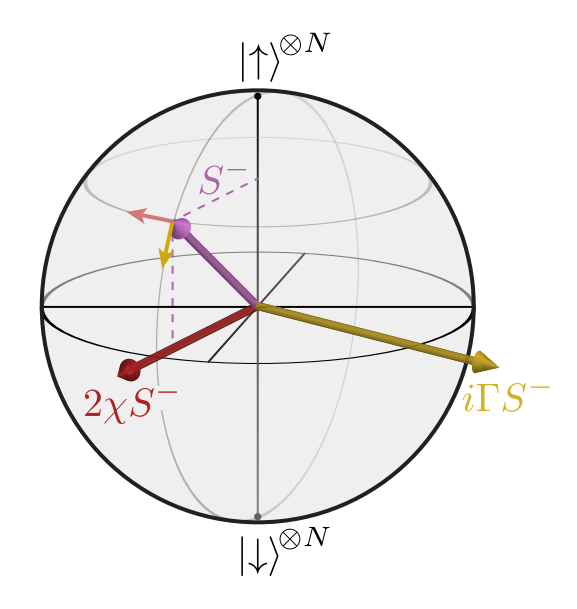


Figure 2.6: Bloch sphere representation of the adiabatically eliminated cavity field. When  $\kappa$  or  $\Delta_{ca}$  is the largest frequency scale, the cavity field amplitude approximately adiabatically follows the atomic coherence  $S^-$  with a constant complex prefactor. The components of the field which are in-phase (red arrow) and out-of-phase (yellow arrow) with the Bloch vector (purple arrow) correspond to  $S^z$ -preserving and dissipative terms, respectfully, with Rabi frequencies equal to  $2\chi |S^-|$  and  $\Gamma |S^-|$ . For further discussion, refer to Fig. 7.4 in Ch. 7.5.3.

sphere. As such, this component of the field represents collective decay through the cavity mode, otherwise known as superradiance. As defined,  $\Gamma$  can be written in terms of the cooperativity C:

$$\Gamma = \frac{4g^2}{\kappa} \frac{1}{1 + \left(\frac{\Delta_{ca}}{\kappa/2}\right)^2} = \frac{C\gamma}{1 + \left(\frac{\Delta_{ca}}{\kappa/2}\right)^2}.$$
 (2.54)

We see that, when the cavity is on resonance ( $\Delta_{ca} = 0$ ), the decay rate through the cavity for a single atom is C times the spontaneous emission rate, consistent with our interpretation of cooperativity as a ratio of decay probabilities as discussed in Sec. 2.4.4. Off resonance, we can think of the effective cooperativity of the system as being reduced by the Lorentzian profile in the above equation, corresponding to a reduced constructive interference of photons bouncing back and forth in the cavity. For N atoms, the emission rate speeds up, which can be seen by the fact that the Rabi drive  $\Omega_{SR} = \Gamma |S^-|$  increases with  $S^-$ . Again, this is because the N atoms can emit in-phase into the cavity mode, increasing the constructive interference and thus increasing the collective cooperativity.

Having calculated the quasi-steady state value  $a_{ss}$ , we can plug the value into the remaining optical

Bloch equations to simplify the equations of motion, thereby "eliminating" the cavity mode. In terms of  $\chi$  and  $\Gamma$ , Eq. (2.51) then becomes:

$$d_t S^- = -\left(\left(\frac{\gamma}{2} + \Gamma S^z\right) + 2i\chi S^z\right) S^-$$

$$d_t S^z = -\Gamma |S^-|^2 - \gamma \left(\frac{N}{2} + S^z\right).$$
(2.55)

Here, the roles of  $\gamma$  and  $\Gamma$  as interaction and dissipation terms is evident.

#### 2.5.2 Effective Hamiltonian description

We have alluded to the fact that the  $\chi$  term corresponds to atom-atom interactions. This can be seen at a mean-field level by noting that  $a_{ss} \propto S^-$ , so the Hamiltonian term  $\hat{a}\hat{S}^+ + \hat{a}^\dagger\hat{S}^-$  should look something like  $\hat{S}^+\hat{S}^-$ . We can formalize this idea essentially by using perturbation theory on the large frequency scale  $\Delta_{ca}$  or  $\kappa$  to generate an effective Hamiltonian (and effective dissipation terms as well). In this section, I will explain and summarize the effective operator formalism used by Reiter and Sørensen [235], which accomplishes exactly that. In the next section, we will apply the formalism to adiabatic elimination of the cavity (so skip this section if you don't care about the derivation).

To start, we can build intuition from reviewing time-independent perturbation theory in quantum mechanics. The typical setup for this involves an unperturbed Hamiltonian  $\hat{H}_0$  with eigenstates  $|n^{(0)}\rangle$  and eigenenergies  $E_n^{(0)}$ . Perturbing the Hamiltonian with some interaction  $\hat{V}$ , parametrized by some "sufficiently small" scale  $\lambda$ , allows us to write expand the new solution perturbatively in  $\lambda$ :

$$(\hat{H}_0 + \lambda \hat{V}) |n\rangle = E_n |n\rangle$$

$$|n\rangle = |n^{(0)}\rangle + \lambda |n^{(1)}\rangle + \lambda^2 |n^{(2)}\rangle + \dots$$

$$E_n = E_n^{(0)} + \lambda E_n^{(1)} + \lambda^2 E_n^{(2)} + \dots$$

$$(2.56)$$

If we consider perturbations which act purely as couplings, meaning diagonal terms such as  $\langle n^{(0)} | \hat{V} | n^{(0)} \rangle$  are zero, then the first-order energy corrections vanish:  $E_n^{(1)} = 0$ . The leading-order perturbations are

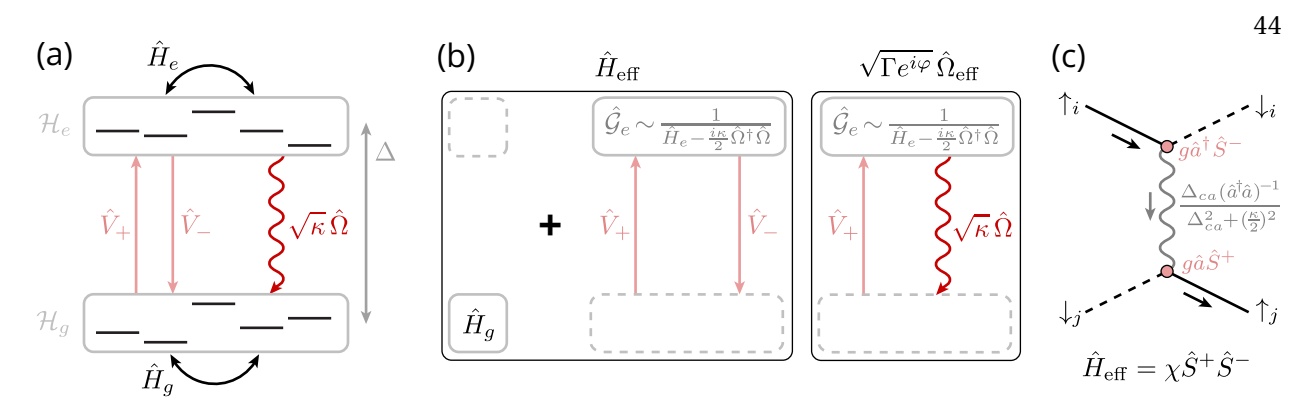


Figure 2.7: Simplified description of the Reiter-Sørensen effective Hamiltonian formulation. (a) The Hilbert space is broken up into two subspaces (gray boxes): a ground subspace  $\mathcal{H}_g$  where most of the physics occurs, and an excited subspace  $\mathcal{H}_e$  (higher lying in frequency by  $\Delta$ ), each governed by noninteracting Hamiltonians  $\hat{H}_g$ ,  $\hat{H}_e$ . The system is subject to dissipation through a jump operator  $\hat{\Omega}$  going from  $\mathcal{H}_e$  to  $\mathcal{H}_g$  with rate  $\kappa$ . A weak perturbation  $\hat{V} = \hat{V}_+ + \hat{V}_-$  is introduced to couple the two subspaces. Elimination of  $\mathcal{H}_e$  is possible when  $|\hat{V}| \ll \max(\kappa, \Delta)$ . (b) Left: an effective Hamiltonian  $\hat{H}_{\text{eff}}$  can be defined on  $\mathcal{H}_g$  using a technique akin to perturbation theory in  $|\hat{V}|/|\hat{H}_e|$ . The leading-order perturbation is a second order process where the system is raised from ground to excited subspace via  $\hat{V}_+$  and later lowered via  $\hat{V}_-$ . The Hamiltonian evolution in the excited space is governed by the equivalent of a propagator  $\hat{\mathcal{G}}_e$ , with units of inverse energy, defined explicitly in the main text. Right: Elimination of the excited subspace also introduces an effective jump operator  $\hat{\Omega}_{eff}$  occurring at rate  $\Gamma$ . Its leading order process involves raising the system with  $\hat{V}_+$ , propagating in the excited state with  $\hat{\mathcal{G}}_e$ , and then jumping down to the ground state via the original jump operator  $\hat{\Omega}$ . (c) Eliminating excitations in the cavity mode produces an effective "spin-exchange" Hamiltonian where one atom emits a photon into the cavity, which then gets reabsorbed by another atom before it can emit out of the cavity mode. This takes the form  $\chi \hat{S}^+ \hat{S}^-$  and is all-to-all, since every atom in the cavity can participate.

then given by:

$$|n\rangle = |n^{(0)}\rangle - \lambda \sum_{k \neq n} \frac{V_{kn}}{E_{kn}^{(0)}} |k^{(0)}\rangle + O(\lambda^{2})$$

$$E_{n} = E_{n}^{(0)} - \lambda^{2} \sum_{k \neq n} \frac{V_{nk} V_{kn}}{E_{kn}^{(0)}} + O(\lambda^{3}),$$
(2.57)

where  $V_{kn} = \langle k^{(0)} | \hat{V} | n^{(0)} \rangle$  is the interaction rate, and  $E_{kn}^{(0)} = E_k^{(0)} - E_n^{(0)}$  is the energy difference between the states. From the form of these corrections, we can reasonably conclude that perturbation theory will converge if the interaction energy coupling two states is much smaller than the energy difference between them; i.e.,  $|V_{kn}| \ll E_{kn}^{(0)}$ .

The intuition for generating an effective "perturbed" Hamiltonian is effectively the same, and the formalism parallels the argument for perturbing the eigenstate energies (just with operators instead of

numbers). Let us split the system's Hilbert space into ground and excited subspaces  $\mathcal{H}_g$  and  $\mathcal{H}_e$ , respectively, split by a some rough scale  $\Delta \sim |\hat{H}_e| - |\hat{H}_g|$  for uncoupled Hamiltonians  $\hat{H}_g$  and  $\hat{H}_e$  (shown in Fig. 2.7(a)). We can introduce a weak perturbation  $\hat{V} = \hat{V}_+ + \hat{V}_-$ , composed of operators  $\hat{V}_\pm$  which raise and lower the system between the ground and excited subspaces. Ignoring the possibility of dissipation for now, we can adiabatically eliminate  $\mathcal{H}_e$  when  $|\hat{V}| \ll \Delta$ . For simplicity, we also assume the ground state energies are close to 0; i.e.,  $|\hat{H}_g| \ll |\hat{H}_e|$ .

Under these conditions, we can define an effective ground state Hamiltonian satisfying the following form [235]:

$$\hat{H}_{\text{eff, no diss.}} = \hat{H}_g - \hat{V}_- \hat{H}_e^{-1} \hat{V}_+,$$
 (2.58)

closely mirroring the perturbation theory for calculating eigenstate energies in Eq. (2.57). This perturbation can be visualized diagrammatically as shown in Fig. 2.7(b): at second order, the system raises into the excited subspace and then drops back down again with  $\hat{V}_{\pm}$  operators. We can describe the time spent in the excited state with the operator  $\hat{\mathcal{G}}_{e,\text{no diss.}} = \hat{H}_e^{-1}$ , which is analogous to a propagator in QFT [236]. 15

When considering the effects of dissipation, we have to include additional processes within and coming out of the excited subspace  $\mathcal{H}_e$ . As discussed in Sec. 2.4.3, we model the dynamics of a jump operator  $\hat{\Omega}$  applied randomly with 1/e time  $\kappa$  with a Lindbladian superoperator. For convenience, we can absorb the rate  $\kappa$  into a dimensionful jump operator  $\hat{L} := \sqrt{\kappa} \hat{\Omega}$ , so the superoperator takes the form  $\kappa \mathcal{L}[\hat{\Omega}](\hat{\rho}) = \hat{L}\hat{\rho}\hat{L}^{\dagger} - \frac{1}{2}\{\hat{L}^{\dagger}\hat{L},\hat{\rho}\}$ . The second term corresponds to no-jump dynamics of the system, which can be incorporated into  $\hat{H}_e$  to form a non-Hermitian Hamiltonian of the form  $\hat{H}_{\rm NH} = \hat{H}_e - \frac{i}{2}\hat{L}^{\dagger}\hat{L}$ . This modifies the excited state propagator to take the form  $\hat{\mathcal{G}}_e = \hat{H}_{\rm NH}^{-1}$ , and the full effective Hamiltonian looks

<sup>&</sup>lt;sup>14</sup> If the ground manifold energies are not close to zero, you must first rewrite the system to satisfy this requirement before the formalism works. For example, when working with a single-particle drive through the cavity, using this formalism requires defining a bosonic mode operator with the drive field subtracted out (i.e.,  $\hat{a} = \alpha + \delta \hat{a}$  where  $\hat{a}$  is the full cavity mode amplitude,  $\alpha$  is some classical field generated by the drive, and  $\delta \hat{a}$  is the remaining quantum operator).

<sup>&</sup>lt;sup>15</sup> In our case of calculating effective cavity-mediated interactions, the analogy is much less abstract. It's called cavity QED for a reason: we are essentially working with an interaction vertex which couples to a photon field (albeit with a very sharp frequency-dependent coupling), analogous to the QED vertex but with an atom instead of an electron. More on this in the next section.

<sup>&</sup>lt;sup>16</sup> While we only consider a single jump operator for simplicity, the formalism can handle multiple dissipation processes just fine. The effective operators simply add together their effects.

like

$$\hat{H}_{\text{eff}} = \hat{H}_g - \frac{1}{2}\hat{V}_-(\hat{\mathcal{G}}_e + \hat{\mathcal{G}}_e^{\dagger})\hat{V}_+, \tag{2.59}$$

where we now must include a conjugate term to recover Hermiticity.

The first term of the Lindbladian form represents a discontinuous jump from  $\mathcal{H}_e$  into  $\mathcal{H}_g$  with probability  $\kappa$ . As shown in Fig. 2.7(b), this adds a new second-order process in the perturbation theory involving a coherent raising of the system via  $\hat{V}_+$ , followed by propagation through  $\mathcal{H}_e$  with  $\hat{\mathcal{G}}_e$ , and finally an application of the jump operator, weighted by the rate  $\kappa$ :  $\hat{L} = \sqrt{\kappa} \hat{\Omega}$ . Since this process involves a jump, it can be modeled by an effective Lindbladian within the ground subspace, with a dimensionful jump operator taking the form

$$\hat{L}_{\text{eff}} = \sqrt{\Gamma e^{i\varphi}} \,\hat{\Omega}_{\text{eff}} = \hat{L}\hat{\mathcal{G}}_e \hat{V}_+,\tag{2.60}$$

where  $\Gamma$  is the rate of the effective jump operator, and  $\varphi$  is an unimportant complex phase defined to let  $\Gamma$  be real. The full effective ground subspace dynamics then looks like:

$$d_t \hat{\rho}_g = -i[\hat{H}_{\text{eff}}, \hat{\rho}_g] + \Gamma \mathcal{L}[\hat{\Omega}_{\text{eff}}](\hat{\rho}_g). \tag{2.61}$$

# 2.5.3 Cavity-mediated spin-exchange interactions

Let's now apply this formalism to our case of adiabatically eliminating the cavity. We define  $\mathcal{H}_g$  to be the subspace of states where the cavity is empty, and  $\mathcal{H}_e$  to be the space where there is at least one photon in the cavity. Starting with the Tavis-Cummings Hamiltonian from Eq. (2.42), the subspace Hamiltonians and coupling terms take the following form:

$$\hat{H}_g = 0;$$
  $\hat{H}_e = \Delta_{ca} \hat{a}^{\dagger} \hat{a};$   $\hat{V}_+ = g \hat{a}^{\dagger} \hat{S}^-;$   $\hat{V}_- = g \hat{a} \hat{S}^+.$  (2.62)

There are two different forms of dissipation in the system: spontaneous emission from the atoms, associated with jump operators  $\hat{\sigma}_i^-$  which lower individual atoms incoherently at a rate  $\gamma$ , and emission out of the cavity, given by a the jump operator  $\hat{a}$  occurring at a rate  $\kappa$ . Since spontaneous emission does not couple the ground and excited subspaces considered here (it doesn't change the cavity population), it doesn't change during adiabatic elimination. We do have to include emission out of the cavity, however.

Our excited state propagator is therefore given by

$$\hat{\mathcal{G}}_e = \frac{(\hat{a}^\dagger \hat{a})^{-1}}{\Delta_{ca} - \frac{i\kappa}{2}},\tag{2.63}$$

leading to the following effective Hamiltonian and Lindblad operators, which hold in the ground subspace  $\mathcal{H}_g$  (defined by  $\langle \hat{a}^{\dagger} \hat{a} \rangle = 0$ ):

$$\hat{H}_{\text{eff}} = -\frac{1}{2} \left( g \hat{a} \hat{S}^{\dagger} \right) \left( \frac{(\hat{a}^{\dagger} \hat{a})^{-1}}{\Delta_{ca} - \frac{i\kappa}{2}} + \frac{(\hat{a}^{\dagger} \hat{a})^{-1}}{\Delta_{ca} + \frac{i\kappa}{2}} \right) \left( g \hat{a}^{\dagger} \hat{S}^{-} \right) = -\chi \hat{S}^{\dagger} \hat{S}^{-}$$

$$\hat{L}_{\text{eff}} = \left( \sqrt{\kappa} \hat{a}^{\dagger} \right) \left( \frac{(\hat{a}^{\dagger} \hat{a})^{-1}}{\Delta_{ca} - \frac{i\kappa}{2}} \right) \left( g \hat{a}^{\dagger} \hat{S}^{-} \right) = \sqrt{\Gamma e^{i\varphi}} \hat{S}^{-},$$
(2.64)

where  $\chi$ ,  $\Gamma$  are defined as before in Eq. (2.53), and  $\varphi$  represents an unimportant complex phase.

 $\hat{L}_{\rm eff}$  corresponds to superradiance: it is an effective dissipation process by which atoms emit with an enhanced rate  $\Gamma |S^-|^2$  through the cavity mode, consistent with the mean-field description in Sec. 2.5. Unlike spontaneous emission, the jump operator  $\hat{S}^-$  does not provide information about which atom emitted the photon, making this a collective process and leading to the coherent Bloch vector dynamics shown Fig. 2.6.

The effective Hamiltonian term,  $-\chi \hat{S}^+ \hat{S}^-$ , is an all-to-all spin exchange process. We can think of the process diagrammatically as in Fig. 2.7(c): one atom in the excited ("spin-up") state emits a photon into the cavity mode, lowering its state. Before the photon can dissipate, another atom in the ground ("spin-down") state absorbs the photon, raising its state. I have depicted the process like a Feynman diagram to emphasize the connection between the two fields. The "vertices" here are not QED vertices; instead, they represent the Tavis-Cummings atom-light interaction. The exchanged photon is "virtual" in the same sense as internal lines in Feynman diagrams represent virtual particles: the photon is off resonance (i.e., "off shell") from the resonance frequency of the cavity mode represented by  $\hat{a}$ , since  $\Delta_{ca} \neq 0$ . This does *not* mean that the photon does not exist; in fact, in Ch. 6 and Ch. 7, we detect these photons on a photodector. What terms like "virtual" and "off shell" really mean is that the photon can only exist in the cavity on a timescale set by the detuning from resonance: in this case, a time of  $\Delta_{ca}^{-1}$  in

the limit of large  $\Delta_{ca}$ . <sup>17</sup>

There are a couple different effects of spin-exchange interactions on the system. To understand these effects, it helps to rewrite the interaction term into an equivalent form:

$$\hat{S}^{+}\hat{S}^{-} = \hat{S}^{2} - (\hat{S}^{z})^{2} + \hat{S}^{z} \approx \hat{S}^{2} - (\hat{S}^{z})^{2}, \tag{2.65}$$

where we can ignore the single-particle  $\hat{S}^z$  term when N is sufficiently large. The second term, sometimes referred to as a **one-axis twisting** term, generates an  $\hat{S}^z$ -dependent frequency shift at the meanfield level. Beyond mean-field, such a process is commonly utilized to generate squeezing in atomic ensembles [62, 66, 67, 69, 194][71, 237]<sup>[G]</sup>, and multiple squeezing protocols have been proposed utilizing cavity-mediated exchange interactions along both spin [94, 196, 238] and momentum degrees of freedom [195, 202, 239–241]. In this thesis, we will discuss how we have studied this term out-of-equilibrium and how it generates a dynamical phase transition (see Ch. 5). The first term,  $\hat{S}^2$ , doesn't modify the dynamics within the maximally symmetric manifold of states (i.e., on the surface of the collective Bloch sphere with S = N/2). However, if there are processes which reduce the total Bloch vector length such as single-particle dephasing, the  $\hat{S}^2$  term supplies a many-body energy gap between different S manifolds which suppresses the Bloch vector shortening. This gap protection has prevoiusly been explored spectroscopically in our group [95]<sup>[G]</sup> and dynamically elsewhere [85]. In this thesis, we use it to protect spin coherence against dephasing, in the context of simulating dynamical phases in the BCS and related models (see Ch. 6 and Ch. 7).

Before moving on, I will also briefly mention a related effective Hamiltonian, which our lab sometimes calls the **QND Hamiltonian**:

$$\hat{H}_{\text{QND}}/\hbar = \left(\Delta_{ca} - 2\chi \hat{S}^z\right) \hat{a}^{\dagger} \hat{a}. \tag{2.66}$$

This effective Hamiltonian essentially describes how the cavity resonance frequency is modified by an atomic ensemble with inversion  $\hat{S}^z$  along an atomic transition closely detuned from the cavity mode. In

<sup>&</sup>lt;sup>17</sup> I would be so bold as to claim that this intuition should hold throughout QFT: all so-called "virtual" particles represented by internal lines in Feynman diagrams actually exist, just with small field amplitudes which die off as one over the deviation from the on-shell energy of the particle. Think of the virtual fields as the particle off-resonantly exciting the harmonic oscillator of the field in question. If someone were to attempt to measure these virtual particles, they would detect a nonzero number with a very small (but nonzero) probability, since particle number is proportional to field squared and is thus quadratically small. If a heterodyne-type measurement of these fields were possible, the probability of detecting something nonzero would go up.

our lab, we often call this a "dispersive shift" of the cavity resonance, and it is commonly used to either perform  $\hat{S}^z$  measurements for squeezing, or to induce one-axis twisting by injecting an  $\hat{S}^z$ -dependent number of photons into the cavity, also to generate squeezing. How do we justify the existence of this extra term, which does not show up in our adiabatic elimination at all? When eliminating the cavity, we assume that the cavity is far off resonance from anything in the system, either internal like the atoms or external like a drive. However, utilizing the QND Hamiltonian requires sending a macroscopic number of photons into the cavity, usually by sending in a probe close to cavity resonance. This breaks the required condition for adiabatic elimination. With proper care, however, it is possible to take advantage of spin-exchange interactions and a QND probe simultaneously. We manage to do exactly this in Ch. 7, and I explain how it works in Sec. 7.8.1.

### 2.5.4 Comparing spin-exchange and superradiance regimes in past experiments

Our atom-cavity system has been tuned to multiple different parameter regimes along two different narrow-linewidth transitions in strontium (the 7.5 kHz linewidth  ${}^{3}P_{1} - {}^{1}S_{0}$  transition and the mHz linewidth  ${}^{3}P_{0} - {}^{1}S_{0}$  transition). Depending on the goals of the experiment, tuning between different regimes optimizes for superradiance, spin-exchange interactions, or coherent atom-cavity interactions. I thought it would be helpful to place all our past experiments onto a single parameter plot, shown in Fig. 2.8, as a way of identifying the relationship between various effects we have observed.

To read this figure, first find the experiment in question, displayed as either a point or line on the plot (the legend lists a shorthand for the name of the associated paper, with a citation in the caption). The coordinates of the experiment represent the ratios  $\frac{|\Delta_{ca}|}{\kappa/2}$  (for the x coordinate) and  $\frac{g\sqrt{N}}{\kappa/2}$  (for the y coordinate) on a log-log plot to capture the breadth of parameter regimes explored. The lefthand side of the plot represents "close to zero" detuning to represent experiments performed on resonance. The plot is split into three regions, corresponding to regimes where  $g\sqrt{N}$ ,  $\frac{\kappa}{2}$ , and  $\Delta_{ca}$  respectively are the largest

<sup>&</sup>lt;sup>18</sup> While it might sound mysterious, the effect is essentially due to the atomic ensemble acting like a dielectric medium in the cavity, introducing a phase shift in the round-trip propagation of cavity photons which therefore shifts the resonance condition. It just so happens that the index of refraction is (a) inversion-dependent, which essentially describes the ensemble becoming transparent as the transition saturates; and (b) sharply frequency-dependent around the atomic resonance (corresponding to the dispersive shape of  $\chi$  as a function of atom-cavity detuning).

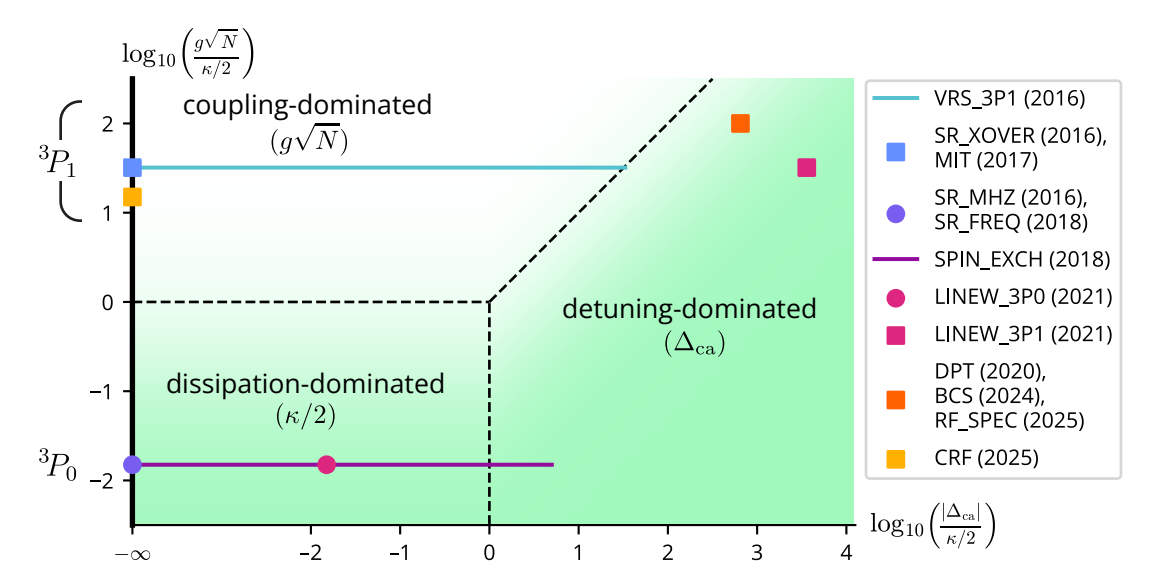


Figure 2.8: Parameter regimes for atom-cavity coupling in past experiments. The vertical axis compares the collectively enhanced coupling strength  $g\sqrt{N}$  compared to the HWHM cavity linewidth  $\kappa/2$ . The horizontal axis compares the atom-cavity detuning  $\Delta_{ca}$  to the cavity linewidth. Green regions denote parameter regimes where adiabatic elimination of the cavity is a valid approximation. Circles represent experiments performed along the  $^3P_0$  transition, and squares represent those along the  $^3P_1$  transition. Curves represent a scan over different parameter values. Citations for past experiments: VRS\_3P1 (2016) [242] [G], SR\_XOVER (2016) [222] [G], MIT (2017) [243] [G], SR\_MHZ (2016) [223] [G], SR\_FREQ (2018) [93] [G], SPIN\_EXCH (2018) [95] [G], LINEW\_3P0/LINEW\_3P1 (2021) [96] [G], DPT (2020) [108] [G], BCS (2024) [126] [G], RF\_SPEC (2025) [145] [G], CRF (2025) [80] [G].

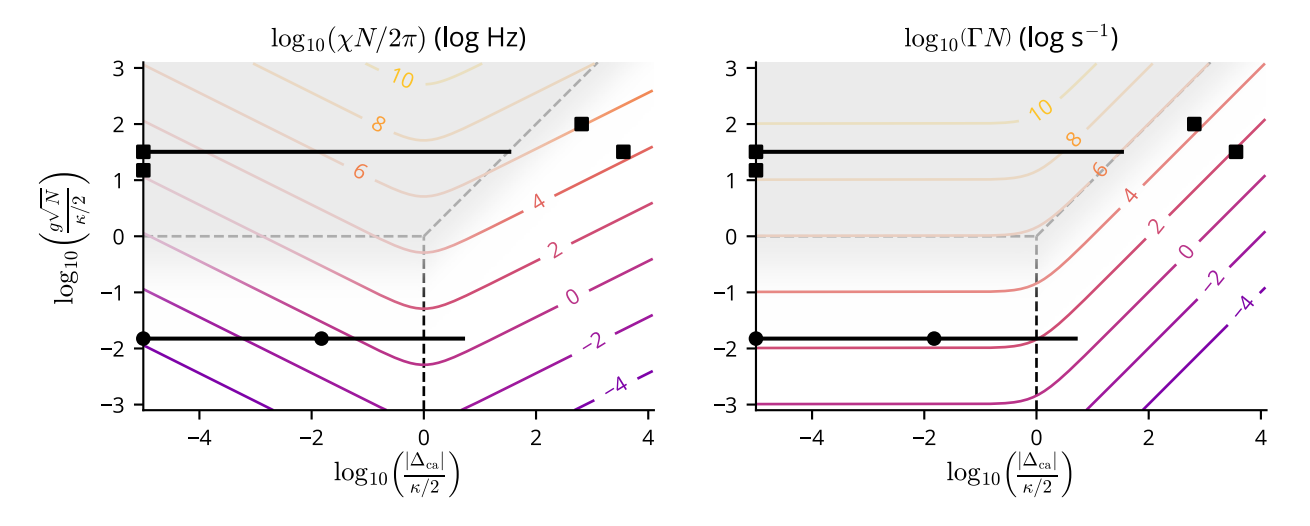


Figure 2.9: Absolute frequency scales for the effective spin-exchange interaction  $(\chi N)$  and collective dissipation  $(\Gamma N)$  after adiabatic elimination of the cavity mode, plotted for an assumed cavity FWHM linewidth of  $\kappa/2\pi=150$  kHz (approximately the linewidth along both  $^3P_1$  and  $^3P_0$  transitions in our experiment). A countour with integer k corresponds to a frequency of  $10^k$  Hz (for  $\chi N$ , to estimate the period frequency) or s<sup>-1</sup> (for  $\Gamma N$ , to denote a 1/e decay probability per atom). The shaded gray region corresponds to parameter regimes where adiabatic elimination is not allowed. The black points and solid curves correspond to past experiments, matching the labels in Fig. 2.8.

frequency scales in the system. Only in the latter two regions (shaded green) is adiabatic elimination of the cavity a valid approximation.

Looking at the distribution of points on this plot, it looks like we have explored all three regions on the plot fairly extensively. Experiments in the coupling-dominated regime tend to feature well-resolved vacuum Rabi splittings and fast superradiance (in an underdamped regime). Conversely, experiments in the dissipation-dominated regime focus mostly on overdamped superradiance. Exceptions include the 2018 spin-exchange paper which explores the effect of spin-exchange processes, albeit in the presence of superradiance in the background which occurs faster, as well as the 2021 linewidth measurement paper which probed the the weak atom-cavity coupling in a weakly excited limit (see Ch. 4). Finally, experiments in the detuning-dominated regime focus either on the dynamics of spin-exchange interactions or on dispersive shifts of the cavity from a QND-like Hamiltonian. It's worth noting that all the experiments performed along the  ${}^3P_1 - {}^1S_0$  transition are on the top half of the plot, and those performed on the  ${}^3P_0 - {}^1S_0$  transition are on the bottom. This is due to the differences in linewidths between the two transitions (a difference of  ${}^-6 \times 10^6$ ), which sets a ratio of the single-atom couplings:  $g_{3P1}/g_{3P0} = \sqrt{\gamma_{3P1}/\gamma_{3P0}} \approx 2.4 \times 10^3$ . While nominally, tuning the number of atoms can change the vertical position on the plot, the collective coupling only scales like  $\sqrt{N}$  and thus limits the vertical extent for each transition to 1 (maybe 2) orders of magnitude.

It can also be informative to plot the absolute size of the spin-exchange interactions (parameterized by  $\chi N$ ) and the collective emission rate (parameterized by  $\Gamma N$ ). This is shown in Fig. 2.9, using a similar log-log plot as the previous figure, for a cavity with a FWHM linewidth of  $\kappa/2\pi=150$  kHz which matches our science cavity along both transitions. The size of each frequency scale is shown using contours of constant value, calculated using Eq. (2.53): each contour with label k represents a frequency of  $10^k$  Hz (for  $\chi N$ ) or  $s^{-1}$  (for  $\Gamma N$ ). The difference in units between the two represents the fact that  $\chi N$  represents a Hamiltonian process with some oscillation period, whereas  $\Gamma N$  represents a dissipation rate which is most easily described by the average number of events per unit time. From this plot, we can see that operating with a large spin-exchange interaction requires operating along the  $^3P_1-^1S_0$  transition for our cavity, with as many atoms as possible to push the parameter regime far to the upper right of the

plot. Pushing into the detuning-dominated regime along the  $^3P_0-^1S_0$  transition leads to sub-Hz interaction rates, which is prohibitively slow. A hidden scale in this consideration is the ratio of spin-exchange interactions to the natural linewidth of the transition, which determines the number of coherent oscillations achievable before all the atoms spontaneously decay to the ground state. The maximum size of the spin-exchange interactions while still operating in a detuning-dominated regime scales like  $g\sqrt{N} \propto \sqrt{\gamma}$ . Therefore, in order to achieve the largest separation of scales between  $\chi N$  and  $\gamma$ , you should work with lots of atoms along a narrow linewidth transition. In principle, working with a narrower cavity linewidth  $\kappa$  could allow one to reap these benefits along the  $^3P_0-^1S_0$  transition by speeding up the maximum attainable spin-exchange dynamics (recall that g is independent of cavity linewidth).

# Chapter 3

# **Experimental apparatus**

This chapter is all about the tools we use to make our experiment function. Many of these tools were originally built by Matt Norcia, as detailed in his thesis [231]. However, while the fundamental apparatus has remained the same, many details of the setup, particularly with respect to the laser systems, have changed over time. When relevant, I have tried to record the evolution of these systems over time, which will hopefully provide some context for the current state of the experiment.

### 3.1 Level structure of strontium

Before diving into lab-specific systems, let us first discuss the tool nature has given us to work with: the strontium atom. There are several theses that cover the atomic properties of strontium in exquisite detail, such as [244, 245]. I will mainly focus on transition frequencies and decay rates, since our experiment is not as dependent on other atomic properties such as the scattering rate. While writing this section, some peers in Munich released a handy Steck-style reference sheet for <sup>88</sup>Sr on the arXiv [246], which I highly recommend using.

Strontium is the 38<sup>th</sup> element in the periodic table and has four stable isotopes: <sup>84</sup>Sr, <sup>86</sup>Sr, <sup>87</sup>Sr, and <sup>88</sup>Sr. Of these, <sup>88</sup>Sr is the most common, with a natural abundance of 82.6%. It is notable for having a ground state *s*-wave scattering length of almost 0 which makes it a poor choice for studying interacting degenerate gases [245]; however, our experiment often cares about trapping a large number of atoms without regard for the strength of contact interactions, so we use this isotope frequently in our experiments. <sup>87</sup>Sr, with an abundance of 7%, is special because it is the only fermionic isotope of Sr. All bosonic

isotopes of even-proton elements have zero nuclear spin, essentially due to the Pauli exclusion principle applied to protons and neutrons. As a result, only  $^{87}$ Sr has a nonzero nuclear spin, which at I = 9/2 results in 10 total nuclear spin sublevels. The large degeneracy can be interesting from a quantum simulation perspective, as we will briefly discuss in Ch. 8. The presence of a nuclear spin also opens up the so-called strontium "clock" transition, discussed later, and as such is commonly used in optical atomic clocks.

Strontium is an alkaline earth metal in the second column of the periodic table, which means it has two electrons in its valence shell. The total spin of these two electrons can combine to form a singlet or a triplet configuration, adding richness to the level structure compared to an alkali atom. Fig. 3.1 shows the low-lying electronic states for <sup>88</sup>Sr, with the wavelengths and decay rates of certain important transitions labeled. The other bosonic isotopes (<sup>84</sup>Sr and <sup>86</sup>Sr) have essentially the same structure but with isotope shifts less than 1 GHz in size. <sup>87</sup>Sr carries the additional complication of hyperfine structure, which I will briefly discuss later.

The ground state of strontium is the state  $5s^2$   $^1S_0$ , which has both electrons occupying the lowest open s orbital with opposite spin, consistent with the Pauli exclusion principle. From this state, the only dipole-allowed transition within optical frequencies is the transition to the 5s5p  $^1P_1$  state, in which one electron is excited to the n=5 p-orbital but maintaining the spin singlet configuration. In  $^{88}$ Sr, this transition has a (blue) wavelength of 461.861980(3) nm [247] and a lifetime of 5.23(3) ns (based off several measurements mentioned in [248]), corresponding to a linewidth of  $\gamma/2\pi = 30.4$  MHz. The  $^1S_0 - ^1P_1$  transition is commonly used to Doppler cool strontium using a so-called "blue MOT." However, it is not perfectly cycling: with some small branching ratio, an atom in the  $^1P_1$  decays into the 5s5d  $^1D_2$  state. Historically, there has been a tension in estimates of this branching ratio, with some calculations predicting 1:20,000 and some predicting 1:50,000 [249]. However, recent measurements of tweezer losses combined with careful calculations suggest that the 1:20,000 value is more accurate [250]. The  $^1D_2$  state has a lifetime of 300  $\mu$ s [251], after which it predominantly decays into the  $^3P_1$ ,  $^3P_2$  states with a 2:1 relative decay probability.

The  ${}^{3}P$  manifold consists of three 5s5p fine-structure states:  ${}^{3}P_{0}$ ,  ${}^{3}P_{1}$ , and  ${}^{3}P_{2}$ , corresponding

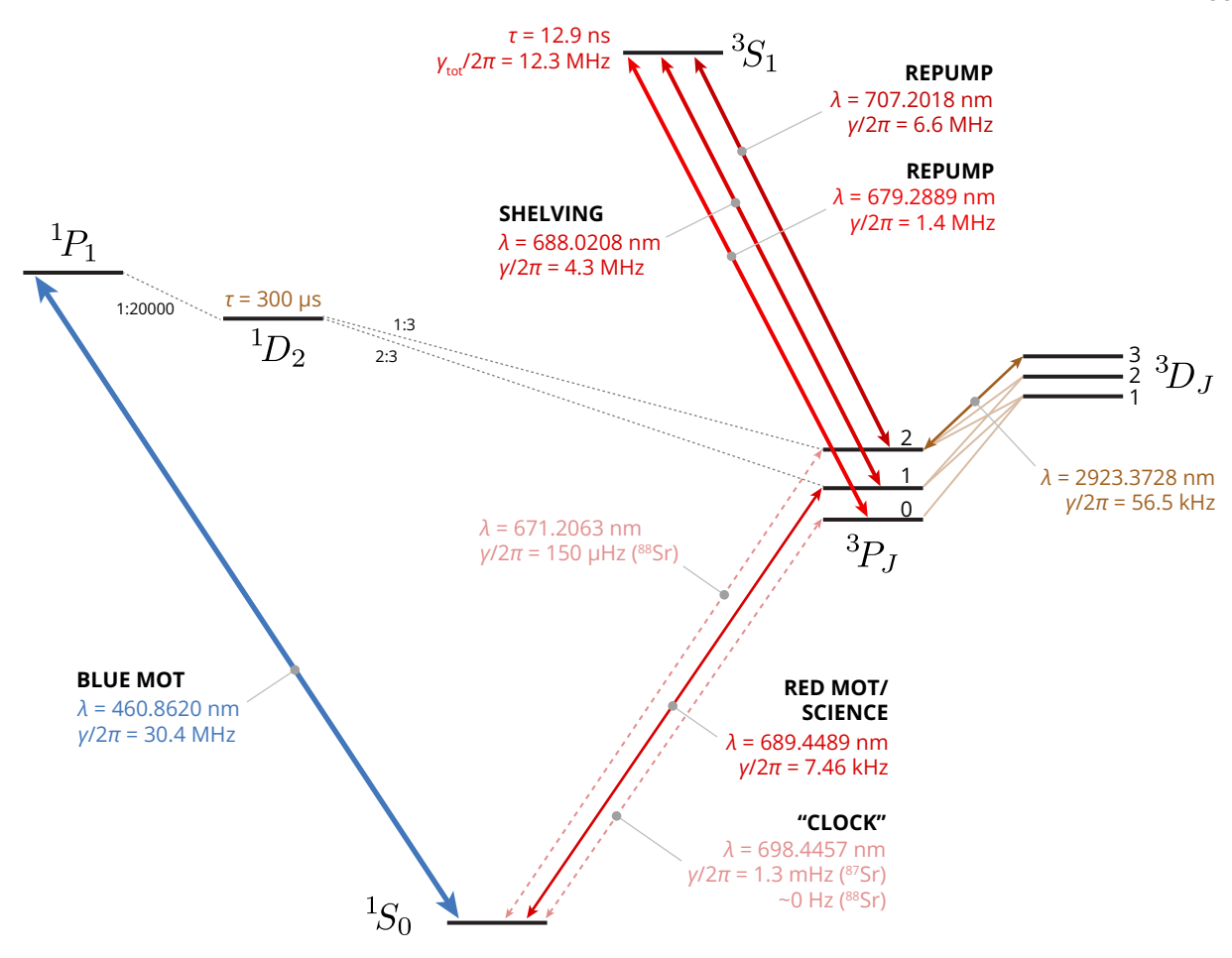


Figure 3.1: Level diagram for low-lying states in <sup>88</sup>Sr. Wavelengths and decay rates of important transitions are listed (the wavelengths for other strontium isotopes may differ due to hyperfine splittings and isotope shifts). The transitions used in this thesis are labeled with their primary functions in black.

to angular momentum addition of the p orbital electron (L=1) with the total electron spin (S=1). These three states connect to the ground state  $^1S_0$  with transition wavelengths 698.4457096... nm [99], 689.4488968... nm [252], and 671.2063331... nm [253] respectively. None of these transitions are formally allowed by electric dipole selection rules, since they involve a spin flip from S=0 to S=1. However, the true eigenstates of the atom actually involve a small amount of admixture between  $^1P_1$  and  $^3P_1$ . This is due to an additional spin-orbit coupling process only present in multi-electron atoms, between the spin of one electron and the orbit of the other [107, 254]. As a result of this coupling, the  $^3P_1$  state gains a small decay probability, with a lifetime of 21.326  $\mu$ s and corresponding linewidth of  $\gamma/2\pi=7.46$  kHz

[101]. This transition is commonly used to perform narrow-linewidth Doppler cooling using a so-called "red MOT," discussed in the context for our experiment in Sec. 3.4.

The other two  $^3P$  states are "doubly forbidden" from connecting to the ground state, since they not only have the wrong spin state but also represent disallowed changes in angular momentum (J must go to J or  $J\pm 1$ , and J=0 to J=0 is forbidden). The  $^1S_0-^3P_2$  transition nonetheless has a nonzero (albeit very small) linewidth in  $^{88}$ Sr since it can be driven by a magnetic quadrupole transition. Current estimates of this linewidth place it under 1 mHz, with a recent calculation claiming  $\gamma/2\pi=147(8)$   $\mu$ Hz corroborated by a significantly less precise experimental measurement [255]. We do not use this transition currently in our experiment, but it could be an option in the future if we wanted to use an extremely narrow-linewidth transition for some reason. On the other hand, the  $^3P_0$  state is not allowed by any higher-order electromagnetic selection rule in  $^{88}$ Sr. Nonetheless, it is possible to drive this transition by turning on a large magnetic field, which off-resonantly couples the  $^3P$  states [256, 257]. In  $^{87}$ Sr, the nonzero nuclear spin performs a similar admixture with no applied field necessary, endowing the  $^3P_0$  state with a natural linewidth which we have measured to be  $\gamma/2\pi=1.3$  mHz [96] (see Ch. 4). This narrow linewidth makes the  $^1S_0-^3P_0$  transition an amazingly precise frequency reference, making it a popular choice for state-of-the-art optical atomic clocks [101].

As mentioned earlier, atoms in  $^1P_1$  occasionally decay into the  $^3P$  manifold, which contains two metastable states. To ensure continuous operation of a blue MOT stage, we can repump the atoms by exciting them to the higher-lying 5s6s  $^3S_1$  state, a dipole-allowed transition. This state has a lifetime of total lifetime of 12.9 ns [258, 259], and due to differing branching ratios the  $^3P_J - ^3S_1$  transitions have different decay rates corresponding to linewidths of  $\gamma/2\pi \in \{1.4, 4.3, 6.6\}$  MHz for  $J \in \{0, 1, 2\}$  respectively. If an atom lands in  $^3P_1$ , then it will decay back to the ground state, successfully closing the blue MOT cycle. As such, the standard repumping scheme involves connecting  $^3P_0$  and  $^3P_2$  to  $^3S_1$  with 679.2889 nm [260] and 707.2018 nm [253] respectively. The remaining transition connecting to  $^3P_1$  is at 688.0208 nm [260], which we sometimes address when we want to shelve atoms from  $^3P_1$  into the metastable states (essentially, the opposite of repumping).

The 5s4d <sup>3</sup>D manifold sits just above the <sup>3</sup>P manifold, separated by mid-IR frequencies. Of partic-

ular interest to our group is the  ${}^3P_2 - {}^3D_3$  transition, which has a wavelength of 2923.37283...  $\mu$ m [261]. This is a cycling transition with a metastable lower state and therefore is a good alternative candidate for a cooling transition. And, since its wavelength is so long, the linewidth is substantially narrower. The  ${}^3D_3$  state has a predicted natural decay linewidth of 56.5(6) kHz [262, 263], in the realm of narrow-linewidth transitions. The strontium ring cavity experiment has recently purchased a 2.9  $\mu$ m laser from Precilasers (part no. FL-SF-2923-0.6-CW). Although we have not implemented it yet, the plan is to explore addressing this transition with an "IR MOT" instead of our current red MOT. For completeness, the  ${}^3D_2$  state has a predicted linewidth of linewidth 66.2(7) kHz [262, 263]. The  ${}^3D_1$  state has had its decay lifetime precisely measured by researchers on Jun Ye's strontium optical lattice clock experiment in order to characterize blackbody shifts on the  ${}^3P_0$  "clock" state, with a measured lifetime of 2.156(5.2)  $\mu$ s and an associated linewidth of  $\gamma/2\pi = 73.8$ (2) kHz [101]. Additionally, the  ${}^3P_2 - {}^3D_2$  transition has a wavelength of 3011.843(2) nm [264], and the  ${}^3P_0 - {}^3D_1$  transition has an estimated wavelength of 2603 nm [101]. These frequencies should be sufficient to determine the transition for any possible  ${}^3P - {}^3D$  transition.

In <sup>87</sup>Sr, the presence of a nuclear spin of I = 9/2 induces hyperfine splittings in all states with  $J \neq 0$ . Table 3.1 shows the hyperfine splittings for many of the states shown in Fig. 3.1, which range from the 10s of MHz up to GHz-level splittings. I should note that, in addition to the hyperfine splittings, <sup>87</sup>Sr also experiences an isotope shift in its transition frequencies relative to <sup>88</sup>Sr, which basically represents changes in the binding energies for the different electronic states depending on the composition of the nucleus. For an incomplete list of isotope shifts, you can refer to Simon Stellmer's thesis [244]; Annie Park's thesis also shows a convenient visualization of the isotope shifts combined with the <sup>87</sup>Sr hyperfine splittings, assuming the ground state stays at the same energy [269].

Finally, the hyperfine levels of <sup>87</sup>Sr have different magnetic field sensitivities due to a modification in their Landé g-factor, relative to their fine-structure state. Table 3.1 also provides the modified g-factors, defined by the weak-field Zeeman effect Hamiltonian  $\hat{H}/\hbar = \mu_B g m_F B$  (where  $\mu_B$  is the Bohr magneton typically expressed in units of MHz/G,  $m_F$  is the hyperfine sublevel quantum number, and B

<sup>&</sup>lt;sup>1</sup> Note that, all else held equal, the natural linewidth of an atomic transition scales like  $\lambda^{-3}$ .

State	Hyperfine level		Hyperfine splitting		Landé $g$ -factor	Field sensitivity	
$5s^2  {}^1S_0$	<sup>88</sup> Sr	-	-	-	0	0	kHz/G
	<sup>87</sup> Sr	F = 9/2	-	-	$-1.3177 \times 10^{-4}$ [265]	-0.18443	kHz/G
$5s5p$ $^{1}P_{1}$	<sup>88</sup> Sr	-	-	-	1	1399.6	kHz/G
	<sup>87</sup> Sr	F = 7/2	+37	MHz	$-0.2224 \approx -\frac{2}{9}$	-311.3	kHz/G
		F = 11/2	-6	MHz	$0.1817 \approx \frac{2}{11}$	254.3	kHz/G
		F = 9/2	-23	MHz	$0.0403 \approx \frac{4}{99}$	56.4	kHz/G
$5s5p^3P_0$	<sup>88</sup> Sr	-	-	-	0	0	kHz/G
	<sup>87</sup> Sr	F = 9/2	-	-	$-2.08 \times 10^{-4} [107, 266]$	-0.291	kHz/G
$5s5p^3P_1$	<sup>88</sup> Sr	-	-	-	$1.5012 \approx \frac{3}{2}$	2101.1	kHz/G
	<sup>87</sup> Sr	F = 7/2	+1414.12	MHz	$-0.3338 \approx -\frac{1}{3}$	-467.2	kHz/G
		F = 9/2	+283.86	MHz	$0.0605 \approx \frac{2}{33}$	84.7	kHz/G
		F = 11/2	-1179.29	MHz	$0.2728 \approx \frac{3}{11}$	381.8	kHz/G
5s5p <sup>3</sup> P <sub>2</sub>	<sup>88</sup> Sr	-	-	-	$1.5012 \approx \frac{3}{2}$	2101.1	kHz/G
	<sup>87</sup> Sr	F = 5/2	+2371.28	MHz	$-0.8580 \approx -\frac{6}{7}$	-1200.9	kHz/G
		F = 7/2	+1597.14	MHz	$-0.1431 \approx -\frac{1}{7}$	-200.3	kHz/G
		F = 9/2	+618.55	MHz	$0.1818 \approx \frac{2}{11}$	254.5	kHz/G
		F = 11/2	-551.55	MHz	$0.3568 \approx \frac{51}{143}$	499.4	kHz/G
		F = 13/2	-1898.05	MHz	$0.4618 \approx \frac{6}{13}$	646.3	kHz/G
5 <i>s</i> 6 <i>s</i> <sup>3</sup> <i>S</i> <sub>1</sub>	<sup>88</sup> Sr	-	-	-	2.0023 ≈ 2	2802.5	kHz/G
	<sup>87</sup> Sr	F = 7/2	+2981	MHz	$-0.4451 \approx -\frac{4}{9}$	-623.0	kHz/G
		F = 9/2	+542	MHz	$0.0808 \approx \frac{8}{99}$	113.1	kHz/G
		F = 11/2	-2439	MHz	$0.3640 \approx \frac{4}{11}$	509.5	kHz/G

Table 3.1: Hyperfine splittings and Zeeman sensitivites for select states in  $^{87}$ Sr. The splittings are quoted in reference to a hypothetical I=0 state, as calculated in [244, 267]. Full detunings of various hyperfine levels from the  $^{88}$ Sr transition frequencies must also take isotope shifts into account [244]. Unless otherwise labeled, Landé g-factors are calculated using the angular momentum quantum numbers S, L, J, I, and F, an electron spin g-factor of 2.0023, and a nuclear g-factor for  $^{87}$ Sr of -0.24284 [268]. Fractional approximations assume no nuclear g-factor and an electron spin g-factor of 2. The field sensitivity is equivalent to  $\mu_B g$ , where  $\mu_B = 1.3996$  MHz/G is the Bohr magneton, and it describes the frequency shift per  $m_F$  in response to a magnetic field in the weak-field Zeeman regime.

is the magnetic field strength, typically expressed in Gauss), and first-order Zeeman sensitivities (defined as  $\mu_B g$ ) for the hyperfine levels. Most of these values are calculated using the typical formula for the Landé g-factor as a function of angular momentum quantum numbers. However, the values for  ${}^1S_0$  and  ${}^3P_0$  are taken from experimental measurements. Both of these states have no first-order Zeeman sensitivity in  ${}^{88}$ Sr due to their J=0 character but gain small g-factors in  ${}^{87}$ Sr at the  $10^{-4}$  level due to the presence of a nuclear magnetic moment. At this scale, other processes such as state mixing also affect the magnetic sensitivities; this makes it prudent to have empirical measurements, since characterizing this transition is important for optical atomic clocks using strontium.

### 3.2 The strontium oven

In order to do anything with strontium, we need a source of individual atoms. Strontium is a solid at room temperature and has a fairly low vapor pressure, so to generate an atomic beam we heat up a strontium sample inside an oven purchased from AOSense (part of a larger source chamber, part no. AOS-SrBEAM S/N 0011, as described in Sec. 3.3.1), at temperatures that historically have varied between 440°C and 520°C. We purchased this oven all the way back in 2013, making it one of AOSense's first strontium ovens. Unlike many subsequenct ovens purchased by other groups in JILA that died from various malfunctions, our oven has survived to the present day mostly<sup>2</sup> unscathed. There have been complications along the way, however, which would be useful to document here.

#### 3.2.1 The strontium volcano

The AOSense oven generates an atomic beam by heating up a sample of strontium and allowing them to escape from the oven through long, thin capillaries which I estimate by eye to be roughly 2 cm long and with a ~300  $\mu$ m inner diameter (give or take 100  $\mu$ m). The geometry of the capillaries restricts which atoms can escape, which mostly only lets through atoms which pass straight through the holes. The resulting atomic beam is mostly collimated, but there is also a diffuse background from atoms which bounce off the capillary walls and then scatter at oblique angles. These atoms will stick to

<sup>&</sup>lt;sup>2</sup> for some definition of "mostly."

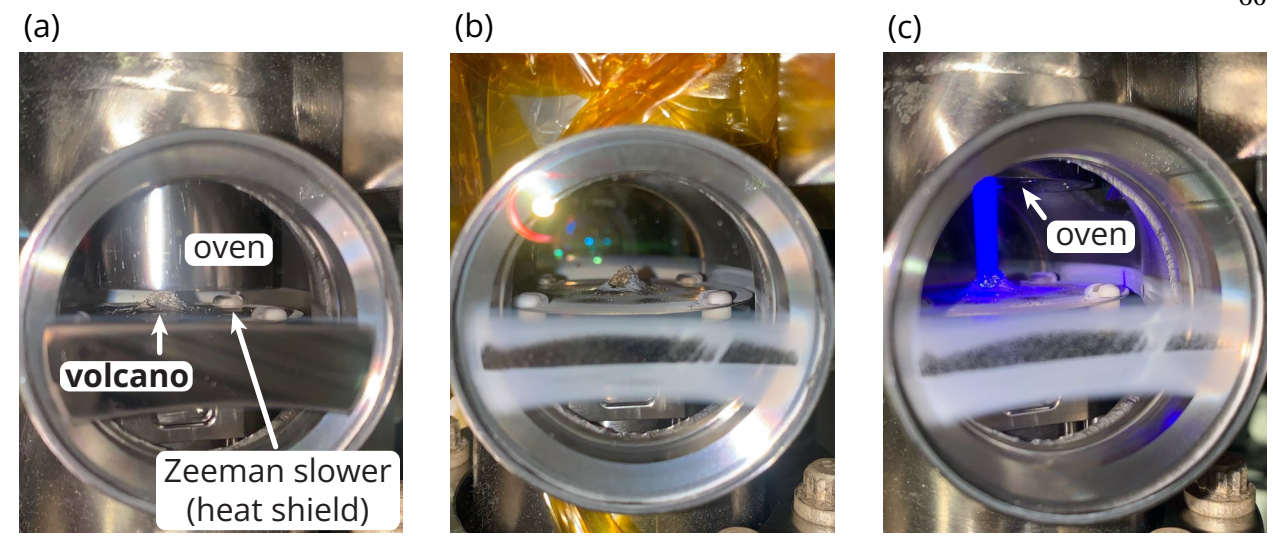


Figure 3.2: Images of the strontium oven "volcano" before and after the oven refill. (a) Before the refill, the volcano had grown to almost touch the oven (as it did in 2018). (b) The full extent of the volcano can be seen after removing the oven. The white dusting on the volcano and viewport is strontium that oxidized due to a vacuum mishap during the removal. (c) After refilling the oven with strontium, we positioned it farther back by placing a 1" spacer flange between the oven and its mounting flange, in order to prevent volcano-induced shorts. The blue "eruption" is fluorescence from strontium in a functional Zeeman slower stage, slightly oversaturated on the camera.

the first cold surface they come across, including a viewport in the strontium source chamber as can be seen in Fig. 3.2(a). A large fraction of these atoms scatter at relatively small angles away from the atomic beam and therefore stick onto the next cooling stage in the source chamber, which is the Zeeman slower module. Over time, these atoms build up and form a volcano shape on the heat shield of the Zeeman slower.

The reason the strontium volcano is a problem lies in the geometry of the source chamber. The AOSense oven and source chamber were originally designed to be as low-power and compact as possible, as part of a DARPA grant aimed at advancing compact atomic sensors. As such, the oven is designed to sit very close to the Zeeman slower stage. While this helps increase the atom flux into the Zeeman slower, it also does not leave a lot of room for the volcano, which continues to grow until it ultimately makes contact with the outer oven heat shield. At this point, the oven experiences a thermal short and can no longer heat the strontium to sufficiently high temperatures to get a high-flux atomic beam, and the entire source becomes useless. We first encountered this problem in the summer of 2018, just before I

joined the group. At that time, then-postdoc Juan Muniz and then-graduate student Julia Cline fixed the issue by removing the oven and scraping away at the volcano until it was shorter.<sup>3</sup> This bought us a few more years. However, in 2024 when Eric and I refilled the oven with new strontium (see the next section for details), we decided to enact a more permanent solution by adding a 1" spacer flange on the oven mounting flange. This had the effect of increasing the gap between the oven and the Zeeman slower, as shown in Fig. 3.2(c). Hopefully, this will prevent the volcano from touching the oven again, no matter how voraciously it absorbs strontium atoms. Still, just to be safe, I scraped away more of the volcano during the replacement procedure.<sup>4</sup>

# 3.2.2 Refilling the oven

Besides the volcano, the main issues we've had with the oven have essentially been symptoms of old age: we simply started running out of strontium. Over the years, we have periodically measured the flux of strontium exiting the oven by sending a weak 461 nm probe across the mouth of the oven and measuring the absorption of the probe. Based on historical measurements, our oven has seen a reduction in flux at a constant temperature by 50-70% every 2 years between 2014 and 2020. This has posed a recurring challenge for running experiments with a large number of atoms, which includes almost all of our recent experiments. To compensate for the loss in flux, we have improved our loading and trapping efficiency by optimizing MOT alignments, frequencies, and powers. Even with this, we were forced to work with ever-increasing oven temperatures (up from 480°C to 500°C and even sometimes 520°C right before the replacement) and longer loading times (leading to cycle times of 3-6 seconds).

The most straightforward way to fix this problem was to add more strontium to the oven, which is what Eric and I finally did in 2024. I had thought about performing this operation as early as 2020 but didn't for several reasons: we were trying to limit the number of people in lab simultaneously due to COVID-19, I was setting up to perform the experiments in Ch. 6 and Ch. 7, and, most importantly, we

<sup>&</sup>lt;sup>3</sup> On my first day in the Thompson Lab, I got to watch Juan and Julia perform surgery on the volcano. I guess there is poetic justice to the fact that I had to do the same near the end of my Ph.D.

<sup>&</sup>lt;sup>4</sup> This procedure essentially involved sticking a long-handle flathead screwdriver into the source chamber through the oven flange, which is an extremely awkward task similar to a game of Operation but requiring more force. Strontium is not the hardest metal, but it is quite difficult to scrape because it tends to deform rather than chip. Words I would use to describe the texture are "sticky" and "gummy." If you've ever machined copper before, it's a little like that.

weren't sure that we could do it ourselves without breaking the oven. In a conversation with an AOSense engineer, we were told that the oven construction is "pretty fragile," and that AOSense breaks 1 in 10 of their own ovens when loading strontium, and so they would not provide instructions for disassembly. This was not encouraging. However, as the alternative was to pay \$15,000 for them to replace the strontium instead, we decided to hold off. Later, in 2021 the (much newer) AOSense oven in the strontium ring cavity experiment broke. Luckily, we had a spare oven available for their experiment to use, so their project was not delayed too much. But this failure was actually an opportunity in disguise: then-postdoc Vera Schäfer and I were able to dissect the oven and learn how it was put together. Pictures of the interior of this oven can be seen in Fig. 3.3(c),(e), which turned out to be identical to ours except for the addition of an extra heat shield on the newer (dead) oven. During this dissection, we learned that refilling the strontium is actually quite simple in principle: remove the heat shields from the oven, unscrew the cap to the strontium chamber (which also holds the capillaries), and reload. This gave us confidence that we could complete the task ourselves with at least as high a success probability as the 90% rate of a professional AOSense engineer.

Finally, in 2024 Eric and I bit the bullet and attempted the oven refill. The timing was right: we had just finished taking data for the current round of experiments and would soon need to switch to <sup>87</sup>Sr for the next round. Since <sup>87</sup>Sr has a lower natural abundance, we would struggle to trap a substantial number of atoms with the poor excuse for an oven flux we had by that time. The plan was to remove the oven and place it in a portable transfer chamber under argon, move the chamber to Dan Dessau's lab in Duane, and perform the replacement under argon in a glove box there with the help of then-graduate student Hope Whitelock. Then, we would transfer the oven back onto the source chamber and hope for the best.<sup>6</sup>

The procedure had an inauspicious start: when removing the oven, we accidentally let some oxygen into the source chamber, oxidizing some of the strontium in that chamber (the white residue in

<sup>&</sup>lt;sup>5</sup> There was an electrical short in the oven due to strontium leaking into the back of the oven around the heating leads. A (different) representative at AOSense said it was "inconceivable" that strontium could have made its way back there, but apparently they lacked vision.

<sup>&</sup>lt;sup>6</sup> I should note that we had a few backup plans in case we accidentally destroyed the oven in the process. We weren't *that* arrogant. The careful planning was fortunately unnecessary because the oven replacement worked on our first try.

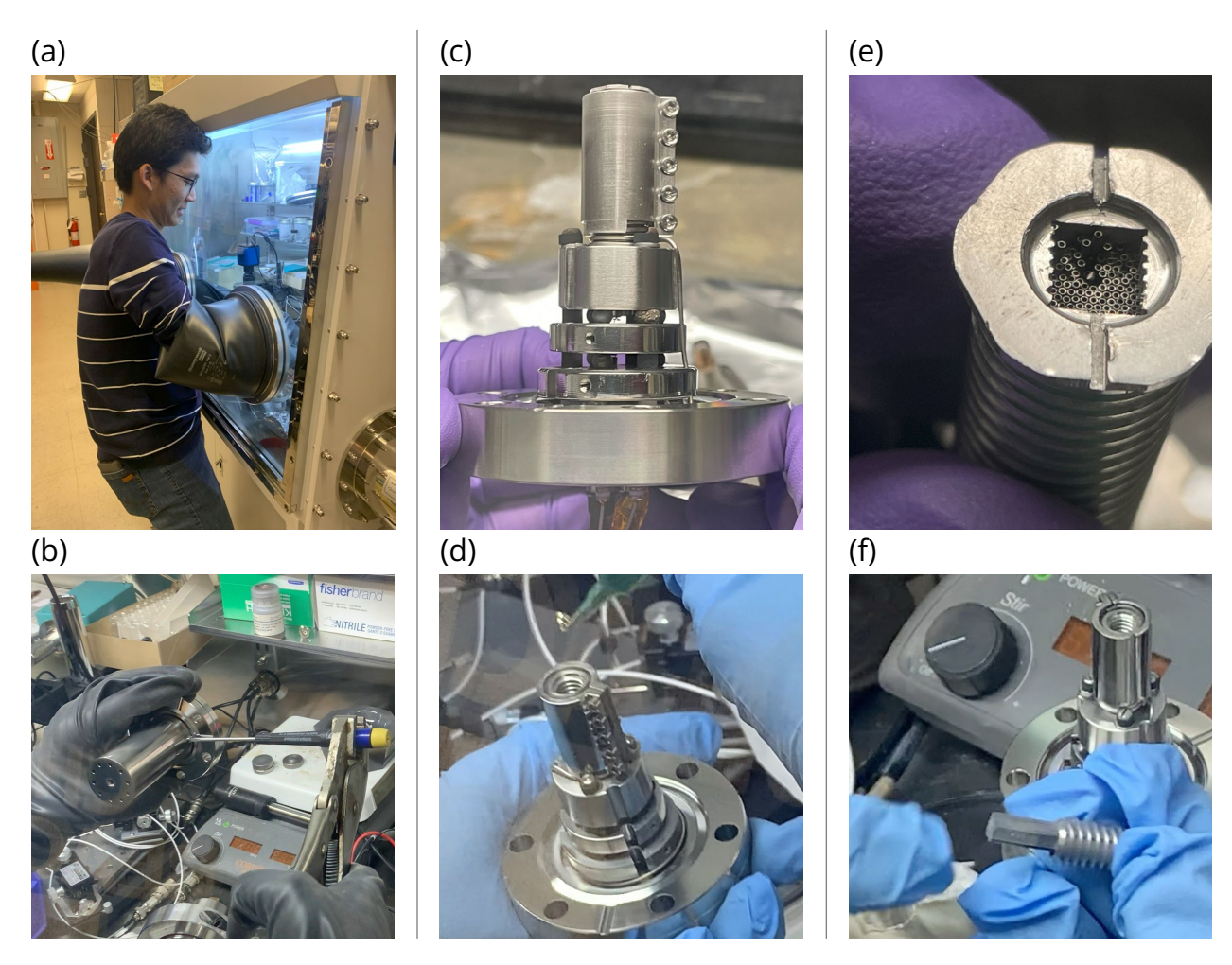


Figure 3.3: Detailed images of the AOSense strontium oven and refill procedure. (a) Eric operated an argon-filled glove box in Dan Dessau's lab under the supervision of Hope Whitelock, ensuring a low-oxygen environment. (b) Our strontium oven has two heat shields (unlike later versions with three), which are attached with screws. The screws can sometimes get stuck however, necessitating the use of force. (c) Beneath the heat shields lies a tiered design, consisting of additional heat shields (bottom) between the strontium chamber (top) and the oven flange. The strontium chamber is surrounded by a coil of wire, which is in turn surrounded by a metal clamp, presumably to ensure efficient heating. This image is from a 2021 disassembly of a three heat shield oven for the strontium ring cavity experiment, but the design is functionally identical to ours ignoring the heat shields. (d) The strontium chamber has an unscrewable cap, giving access to the interior of the chamber. We loaded the oven with chunks of strontium from a sealed glass tube, totaling ~0.5-1 g in mass. (e) The cap of the strontium chamber has ~120 capillaries compression-fitted together into a roughly square shape. It is possible for them to fall out. This image is from the 2021 ring cavity disassembly. (f) While refilling the oven, our capillaries fell out of the cap but mostly stuck together thanks to the compression fit. We stuck the capillaries back in, losing ~6 capillaries in the process.

Fig. 3.2(b)-(c)). Luckily, we had gated off the connection between the source and science chambers (see Sec. 3.3.1), so the oxidation was limited to the source chamber. The fault can be traced back to a somewhat sketchy argon feed-through scheme, where we first pumped the system down with a turbo pump, opened a valve to the source chamber, and then sent argon through a glove taped to the vent exhaust port on our pump station simultaneously with turning off the pump. I believe that the glove attachment became slightly loose, letting some oxygen in. We managed to learn from our mistakes when replacing the refilled oven, avoiding a second oxidation incident. Additionally, we have since purchased a proper valve attachment to the pump station vent hole, allowing for a less error-prone flow line. However, after talking with James, I would not recommend repeating our approach for venting the source chamber with argon. When turning off its roughing pump stage, the pump station experiences backflow and can fill with atmosphere, providing an additional potential inflow mechanism for oxygen. Instead, he recommended we *displace* the air before the source chamber valve by continuously flowing argon through a cross, avoiding the use of a pump station altogether.

The oven refill procedure in the glove box in Duane was ultimately successful, with a few stressful moments. First, some of the screws attaching the heat shields to the oven body had gotten stuck, possibly from repeated thermal cycling. Hope Whitelock helped us solve this problem by holding the screwdriver in a pair of pliers (see Fig. 3.3(b)), allowing her to apply a large torque on the screws and ultimately remove them. Actually adding strontium to the chamber was relatively straightforward, but we had to ensure that we added strontium chunks which actually fit in the chamber. By our rough estimate, we installed between 0.5-1 g of strontium into the chamber. The real challenge in this procedure is protecting the oven capillaries, shown in Fig. 3.3(e)-(f). These capillaries are likely compression-fitted into their intended position inside the cap, which means friction is the only force holding them in place. When we first removed the oven cap, the capillaries were sticking almost all the way out of the cap. During the procedure, they actually fell out completely. Fortunately, the capillaries mostly stuck together into their square-like shape, possibly due to fraction from the initial compression fitting. As such, Eric was able to literally pick up the bundle of capillaries and stick it back into the cap, losing only ~6 capillaries in the process. The final proof of success was that, after reinstalling the oven, we were able to trap

atoms in a MOT again. In fact, the oven flux was substantially higher than anything observed previously during my Ph.D., allowing us to work at 440°C and observe as many or more atoms than we could see pre-refill at 500°C.

# 3.3 Blue cooling system

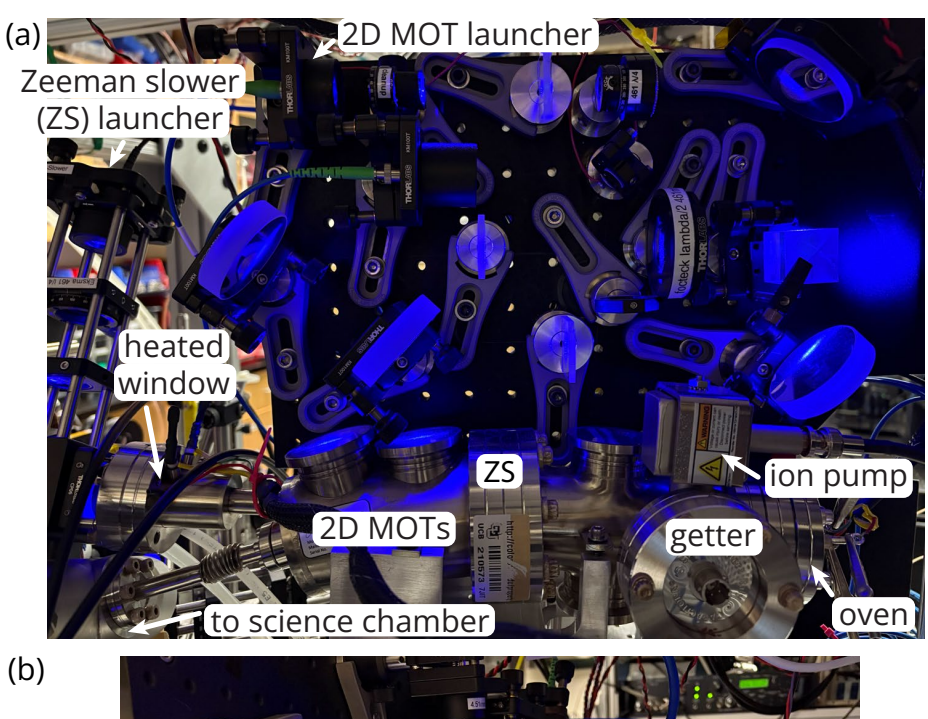
The first step of cooling and trapping our strontium atoms is a series of cooling stages addressing the dipole-allowed  ${}^{1}P_{1} - {}^{1}S_{0}$  transition using 461 nm (blue) light. This light serves multiple stages: the Zeeman slower, the 2D MOTs, and the 3D MOT. In order to operate all three cooling stages, we need a combined total of at least 100 mW of blue light out of multiple optical fibers. Our resulting laser system and breakout is somewhat complicated, and it has also changed quite a bit over the seven years of my time in the lab. In this section, I'll describe what how it operated near the end of my Ph.D. work, circa 2024.

### 3.3.1 The source and science chambers

In addition to the oven, AOSense provided us with a full source chamber which includes a Zeeman slower and in-vacuum optics and magnetic fields for two stages of 2D MOT, pictured in Fig. 3.4(a). The source chamber is kept under ultrahigh vacuum at the  $10^{-10}$  torr level, with the help of a 3 L/s ion pump and two getters. The main getter is from SAES and has a pump speed of 50 L/s (part no. CapaciTorr D 50), located next to the oven. There is also a smaller 5 L/s getter also made by SAES (part no. St 172 HI/9.5-7.5/250C, according to an AOSense representative), located on the bottom of the source chamber near the 2D MOTs. However, after our last vacuum break we have not reactivated this getter, so it's currently doing nothing. This was following the advice from an AOSense representative, who told us they don't believe this smaller getter has a significant impact on vacuum levels.

<sup>&</sup>lt;sup>7</sup> At one point, the 461 nm laser for the ring cavity experiment was locked to our laser; later, our laser was locked to theirs. Eventually, we fully separated the two laser systems.

<sup>&</sup>lt;sup>8</sup> Non-evaporable getters (NEGs) are essentially chunks of porous material that passively capture certain gases through sorption. However, they can become saturated and no longer provide pumping power. You should assume this happens every time you break vacuum. To fix this, we "activate" the getter (i.e., purge it of the gases it's trapping) by running a certain amount of current through the NEG for a certain amount of time, with specific values recorded in our lab notes. This should occur while a turbo pump is attached to the system and running, so that all the purged gases are removed from the system.



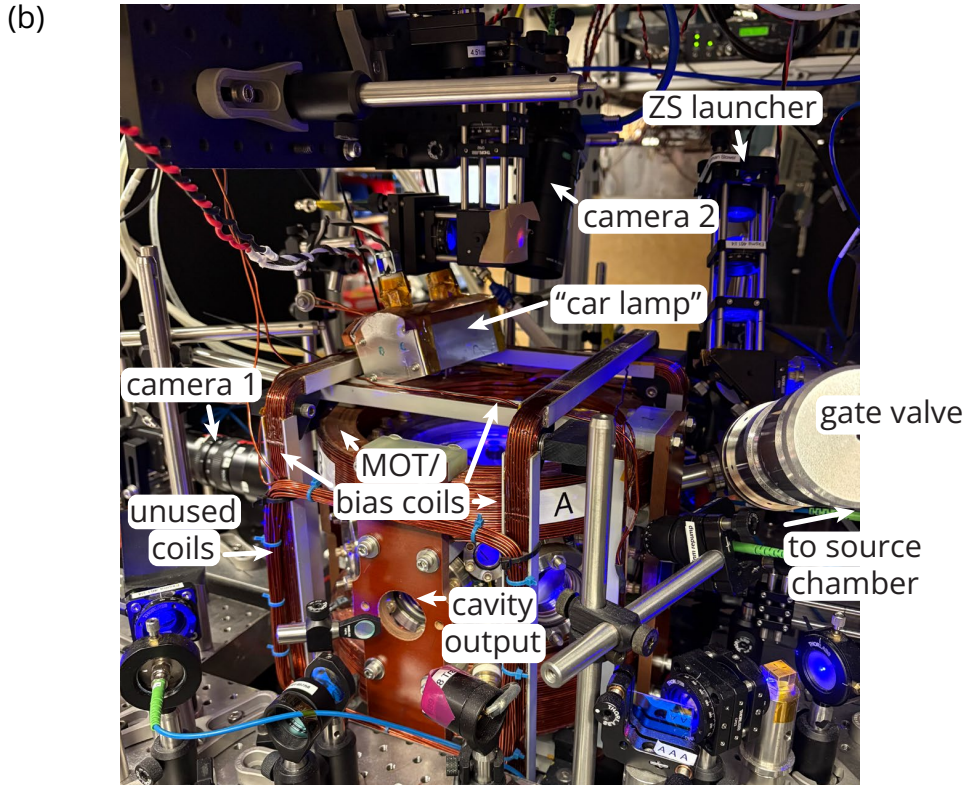


Figure 3.4: (a) The source chamber, containing the strontium oven (right), a Zeeman slower (with light launched from the left), and in-vacuum 2D MOT optics (with light launched from the vertical breadboard). (b) The science chamber. Blue and red MOT optics are sent vertically and through horizontal ports "A" and "B", with repumps sent thorugh the side. Water-cooled MOT coils surround the chamber, oriented vertically. Additional uncooled coils form three-axis bias fields, with the z coils wrapped around the MOT coils. Our science cavity is inside (see Sec. 3.5). Two cameras are mounted for fluorescence imaging. The "car lamp" is occasionally used to heat the science cavity spacer (see Ch. 4.2).

The Zeeman slower consists of a 461 nm beam with ~50 mW of power, launched into the source chamber from the left in the figure and traveling to the right, counter-propagating with the atomic beam. By scattering many photons from this beam, the atoms slow down from their initial r.m.s. velocity of ~250-270 m/s down to something closer to ~5-10 m/s. A velocity change this large causes the  ${}^{1}P_{1}$  –  ${}^{1}S_{0}$  transition to undergo Doppler shifts of over 400 MHz, much larger than the 32 MHz linewidth of the transition. In order to resonantly scatter enough photons, the Zeeman slower uses a magnetic field gradient (here, constructed by AOSense using in-vacuum permanent magnets) to counteract the Doppler shifts with Zeeman shifts. Compared to some other Zeeman slowers, our slower is quite short, which is a testament to AOSense's compact design. To make the Zeeman slower function, we send in circularly polarized light that is roughly -430 MHz red-detuned from the unperturbed atomic transition but close to resonance with the Doppler-shifted transition frequency of atoms coming out of the oven.

The 2D MOT stages require a total of two circularly polarized beams, one sent into each of the two viewports on the top left of the source chamber. Inside the chamber are mirrors oriented in a V-shape, such that the input beam bounces twice before exiting the chamber in a retroreflected manner. Combined with a 2D quadrupole field, this creates the 2D MOT. The vertically-mounted optics board in Fig. 3.4(a) allows us to send these two beams into the viewports with the proper shape, angle, and power (totaling around 40 mW). As can be seen in the figure, the two viewports are at angle. The purpose of this angle is to deflect the atoms captured in the 2D MOT and send them through a bellows, shown on the bottom left. Atoms not trapped in the 2D MOT continue in a straight line towards the Zeeman slower window. To prevent strontium from sticking to this window and making it opaque, we heat the window to 250°C. At this temperature, the strontium bounces off the window and sticks on whatever other colder surface it collides with next.

The bellows sends the atoms through an all-metal gate valve, not pictured in the top figure but visible on the right of Fig. 3.4(b). This valve allows us to isolate the source chamber when performing oven work. Past the valve is our science chamber, which is an 8" spherical octagon from Kimball physics (part no. MCF800-ExtOct-G2C8A16), with windows AR coated for all our visible and near IR wavelenghts. The reason for our chamber's large size is to provide lots of optical access and hold our science cavity

(described later in Sec. 3.5). This chamber must also be kept under ultrahigh vacuum at the  $10^{-10}$  torr level, but since the volume is larger than the source chamber it needs substantially more pumping power. To that end, we have a 75 L/s TiTan ion pump from Gamma Vacuum (part no. 75S-CV-62-SC-N-N) which rests underneath the science chamber on the lower level of our optical table. There is also a titanium sublimation pump installed in case we need to improve the vacuum, although I have never used it, and Matt claims he did not notice a major difference after using it [231]<sup>[G]</sup>.

Surrounding our science chamber are several magnetic field coils. The largest coils are hollow-core copper wires mounted in a near anti-Helmholtz configuration, oriented vertically. Running current through these coils creates a magnetic quadrupole field for our MOT stages. I will refer the reader to Matt Norcia's thesis for a detailed discussion of the design principles and implementation, both of the coils and of the MOSFET-based circuit that drives them and stabilizes the current [231]. Practically speaking, we run up to 80 A of current through the coils at 15 V, which generates roughly a 17 G/cm magnetic field gradient in the horizontal directions and a 33 G/cm gradient in the vertical direction. This amount of power generates a fair bit of heat, so to keep the MOT coils from melting we send processed chilled water through the wires (which are hollow-core). Additionally, there are three pairs of bias field coils oriented along the three principal axes of the chamber, also driven by a MOSFET-based circuit. These coils do not need to be water cooled. As of March 2025, they can receive up to 10 A of current, generating between 27 G and 30 G of field at the position of the atoms depending on the coil. If we need to create larger bias fields in the future, the driver circuit could potentially be upgraded.

With these coils, we can generate the necessary fields to trap atoms in a 3D blue MOT centered at a position of our choosing. To form this MOT, we couple  $\sim$ 50 mW of light into a 1x3 fiber splitter. This light is distributed into three MOT arms, corresponding to one vertical beam and two horizontal beams. Once the beams are the proper size (with a waist of a couple cm) and polarization (roughly circular), the beams are sent into the science chamber through viewports labeled 'A,' 'B,' and 'Z' (with 'A' shown in Fig. 3.4(b)). After passing through the chamber, they are reflected back in with the opposite polarization (but the same helicity since the k-vector is swapped relative to a fixed quantization axis), completing the six-beam geometry of a standard MOT. We actually use a few different stages of blue MOT to trap

and cool our atoms, which differ in the laser frequency and power used. In the first "trapping" MOT stage, we use as much power as we can, with a detuning of around -30 MHz from the atomic transition (approximately  $-\gamma$  where  $\gamma/2\pi=32$  MHz is the linewidth of the  $^1P_1$ -SingletSZero transition). This is farther detuned than an ideal MOT configuration (with laser beams detuned by  $-\gamma/2$  to gain maximum frequency sensitivity in the scattering rate). My hypothesis is that the larger detuning allows us to capture more atoms initially entering the science chamber. In later stages, we lower the MOT power and move the laser frequency closer to the more standard  $-\gamma/2$  detuning.

#### 3.3.2 Laser breakout

Generating all the light required for the Zeeman slower, 2D MOT, and 3D MOT stages requires a fairly involved 461 nm laser system and breakout. The system starts with two distinct Toptica DL Pro ECDLs (external cavity diode lasers), each of which can output up to 50 mW of single-mode laser light as shown in Fig. 3.5(a). One of these lasers (ECDL 2) is stabilized via a spectroscopy lock using a hollow cathode lamp, as described in Sec. 3.3.3. The other laser (ECDL 1) is locked to ECDL 2 through a beat note board, shown in the inset. In the past, this was a frequency lock which used a delay line after the photodiode to generate an error signal related to free spectral range of the delay line. This lock had a lot of issues with stability and was sensitive to ground loops and/or RF pickup from nearby sources. Eventually, we switched over to a phase lock using a JILA-made evaluation board clone (JILA part no. TJ007A1) for a phase-frequency detector chip from Analog Devices (part no. HMC440QS16G). This lock has proved more robust, although we sometimes observe in-lock broadening of the beat note on a readout spectrum analyzer.<sup>9</sup>

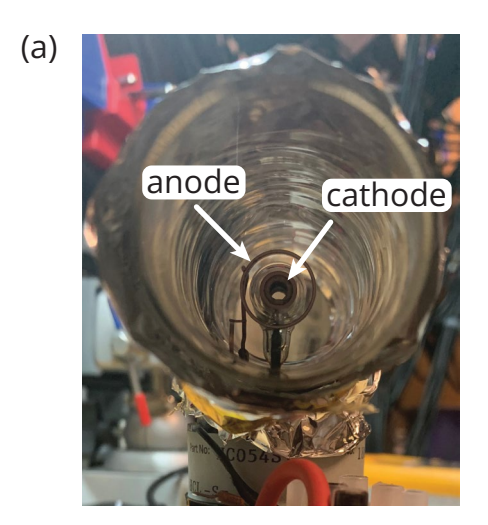
Since the DL Pros don't output enough power to operate all of our cooling stages, we use them to seed higher power diodes through **injection locks**. An injection lock works by sending ~mW of power into a single-mode diode, mode-matched with the diode's output light. Usually, this seed light is sent through the rejected port of an optical isolator, as shown in Fig. 3.5(b). Within certain current ranges, the

<sup>&</sup>lt;sup>9</sup> We have not pinned down the source of this broadening. Sometimes, we notice an improvement when we connect or disconnect the PZT out port from the loop filter interface box to the Toptica controller, which may suggest a ground loop issue. However, it doesn't seem to affect our MOT quality too much, possibly because the broadening is still smaller than the  $^1P_1$  linewidth of  $\gamma/2\pi = 32$  MHz.

Figure 3.5: 461 nm laser system breakout. Detunings are relative to <sup>88</sup>Sr and valid for cooling on <sup>88</sup>Sr. (a) Two Toptica DL Pros are phase locked to each other and stabilized to a spectroscopy source. (b) To obtain more power, we seed a 500 mW injection lock diode with ECDL light and partition the output.

diode frequency will be "pulled" to match the seed. When I joined the lab, we used three injection lock diodes: one AR coated diode from Sacher (part no. SAL-0455-030) for the 3D MOT stage, and two non-AR coated diodes from Nichia (part no. NDB4216E) for the Zeeman slower and 2D MOT stages [231]<sup>[G]</sup>, each of which can output up to around 100 mW. In practice, this setup was a bit of a pain to work with because the Nichia diodes often dropped out of their injection locks. This unreliability led Matt to use the Sacher diode for the 3D MOT stage, but it was on the expensive side (around \$7600 in 2015).

Around 2020, we discovered a new non-AR coated diode from Nichia (part no. NDB4916) that can output up to 500 mW. After buying one and testing it out, I rebuilt our 461 nm breakout from scratch to power all three cooling stages from just one injection lock diode, as shown in Fig. 3.5(b). We controlled the injection lock using the same Thorlabs current and temperature controllers used by the previous, unreliable injection lock stages (part nos. LDC205C, TED200C). However, instead of using a Thorlabs diode mount, we used a homebuilt mount, also shown in the figure. 11 The current injection lock diode receives around 6 mW of seed power, more than the older stages. However, it also seems to be more reliable, and in practice the injection lock can stay locked for many hours (unless someone is working on the same optical table). We are also able to match or exceed the amount of power used previously. Since none of our blue cooling stages are currently saturated, we have reason to believe that more power translates to more atoms trapped in our MOT. Based off this assumption, the younger members in lab have recently (c. 2025) purchased more injection lock diodes to significantly increase the amount of power sent to each stage. This is likely to improve loading times and overall atom number, but it does carry the risk of reducing the stability of the 461 nm chain, since any of the injection locks dropping will then break the experiment. If it becomes a problem, one potential solution could be to set up an active feedback loop to prevent the injection locks from dropping [270].



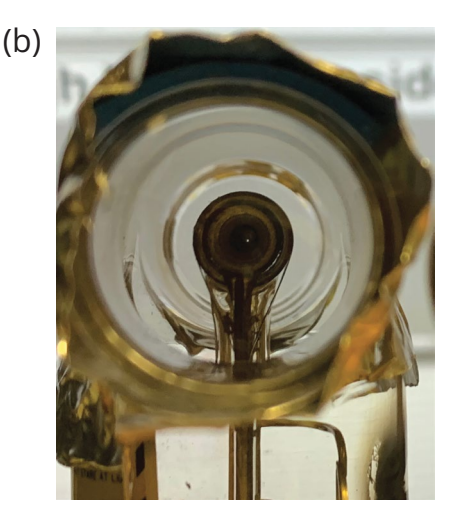


Figure 3.6: (a) A new optogalvanic hollow cathode lamp (HCL) as viewed through one end. A large voltage ionizes the interior buffer gas, causing electrons to flow toward the anode and buffer gas ions towards the cathode. The ions then collide with strontium atoms in the cathode, expelling them into the hollow central region. The plasma emits UV radiation, so we have wrapped foil around the sides of lamp to minimize exposure. (b) A dead HCL. Buildup of (presumably) strontium has closed up the central hole, preventing laser light from passing through the lamp.

## 3.3.3 Hollow cathode lamp

To stabilize our 461 nm pathways, we lock to a spectroscopy signal generated using strontium atoms in a so-called (optogalvanic) hollow cathode lamp (here, "HCL"). As can be seen in Fig. 3.6(a), a hollow cathode lamp is essentially a glass cell filled with a relatively low pressure of an inert buffer gas, containing both an anode and a hollow cylindrical cathode which do not physically touch. The cathode contains an element of choice (strontium, in our case). When you apply a sufficiently strong ignition voltage, the buffer gas ionizes to form a plasma arc between the anode and cathode. The ions in the plasma bombard the cathode, kicking up (strontium) atoms into the donut hole of the cathode. By shining a laser beam through the donut hole, you can therefore probe for spectroscopic signals. HCLs represent a good alternative to vapor cells for elements like strontium that have low vapor pressures at room temperature and otherwise need to be heated substantially to generate a large optical depth.

Our present lamp is sourced from an Australian company called Spectrolamps (part no. HC054ST)

<sup>&</sup>lt;sup>10</sup> The drop rate depended strongly on the specific diode used. The Zeeman slower injection lock often stayed locked for multiple hours (not all day, however), but the 2D MOT injection lock dropped as often as every 30 minutes.

<sup>&</sup>lt;sup>11</sup> The housing for the mount was designed to look like Birdo from the Mario games. Yes, this is vital information to pass down.

and has a 4 Torr neon buffer gas. In the past, we have purchased them from Hamamatsu, but they appear to have discontinued selling "optogalvanic" HCLs, i.e., "see-through" lamps that allow you to send a laser beam through the cathode. Currently, we also use a power supply purchased from Spectrolamps (part no. HCLPS1) that can send up to 30 mA of current to the lamp in steady state at 400  $V_{dc}$ . You can also use a custom power supply as long as it can supply a sufficient voltage. It might also be important to transiently generate a larger voltage upon switching on the supply in order to ionize the buffer gas, but we have not tested this claim. Previously when we worked with a custom supply, a short-time voltage of 650 V with a decay time constant of 66  $\mu$ s was sufficient to ignite.

When Matt first built our experiment, he managed to generate spectroscopic signals for both the 461 nm ( ${}^{1}P_{1}$  –  ${}^{1}S_{0}$ ) and 707 nm ( ${}^{3}S_{1}$  –  ${}^{3}P_{2}$ ) transitions using a hollow cathode lamp [271] [G]. However, in recent years we have switched back to only locking our 461 nm system to the lamp. The main reason for this 12 was to protect the lifetime of the HCL. In order to see an error signal on the  ${}^3S_1 - {}^3P_2$  transition, there needs to be a sufficient number of atoms in the metastable  ${}^{3}P_{2}$  excited state. The energetic bombardment of buffer gas ions onto the cathode naturally excites a small fraction of the strontium atoms into the correct state, but the optical depth is way smaller than for the ground state. Therefore, to see a sizable error signal, we had to run a pretty large current through the lamp (20 mA). This actually substantially reduced the signal-to-noise of our 461 nm error signal, since the optical depth along the  ${}^{1}P_{1} - {}^{1}S_{0}$ transition was so high that the spectroscopy probe beam was almost completely attenuated after passing through the lamp. Moreover, it caused our lamp to die roughly every 18 months, which was not ideal. 13 The most common failure mechanism for our HCLs run in this mode can be seen in Fig. 3.6(b): somehow, the donut hole shrinks in size due to buildup of what is presumably strontium, to the point where our spectroscopy beams can no longer pass through the lamp. For the second half of my Ph.D., we drastically lowered the current sent to the HCL to  $\lesssim$  3 mA, which should improve the lifetime quite a bit. The other consequence of this change is that our error signal for 461 nm spectroscopy is now substantially

<sup>&</sup>lt;sup>12</sup> Besides the error signal becoming finicky, that is.

<sup>&</sup>lt;sup>13</sup> Even when functional, the error signal would actually shrink over the course of several hours after turning on the lamp, by an amount which would noticeably change the laser frequency due to a nonzero in-lock DC voltage. Close to death, the lock would drop multiple times a day.

larger, compared to both background noise and unintentional DC offsets.

## 3.3.4 461 nm spectroscopy lock

We originally locked our 461 nm laser to the strontium atoms in the hollow cathode lamp using a technique called polarization rotation spectroscopy [272][271]<sup>[G]</sup>. In a nutshell, this was a Doppler-free spectroscopy technique which used a counterpropagating, circularly polarized pump to excite the atoms, causing them to exhibit circular birefringence when the pump is close to resonance (see the bottom cartoon in Fig. 3.7(a)). Then, a linearly polarized probe passing through the ensemble would experience polarization rotation with an angle which depended on the precise resonance condition. While this technique was simple and effective, there were certain downsides. For example, the basic version of polarization rotation spectroscopy is a modulation-free technique and therefore sensitive to DC drifts. To avoid this issue, we strobed the system by "chopping" an AOM on and off with a 99 kHz square wave [271]<sup>[G]</sup>, essentially amplitude-modulating the signal. This limited the bandwidth of the lock to much less than 99 kHz, but it essentially worked. A bigger problem was that the error signal was sensitive to drifts in polarization over time, which would cause the error signal to look asymmetric and change the zero point of the lock. This form of DC drift could not be easily corrected with a chop technique.

At some point, we decided to try out a different method known as modulation transfer spectroscopy (here, MTS) [273–275], which our colleagues on the cold rubidium experiment had tested out and seen promising results from. MTS differs from polarization rotation spectroscopy in a couple of ways, illustrated in Fig. 3.7(a). First, it requires frequency modulating the laser at some frequency  $\omega_m$ , which can be substantially larger than the old 99 kHz AOM chop and therefore does not, in principle, limit the bandwidth of the lock. Second, the error signal is generated not from the probe polarization but by the phase relation between the probe carrier and sidebands, making MTS less sensitive to polarization drifts. From these two metrics, one could reasonably consider modulation transfer spectroscopy to be a form of frequency modulation (FM) spectroscopy, similar to how we used to lock our 707 nm laser [271]<sup>[G]</sup> or to a PDH lock (see Sec. 2.2.3). The key feature of MTS that distinguishes it from other related methods is that the probe is not directly frequency modulated. Rather, a counterpropagating pump with

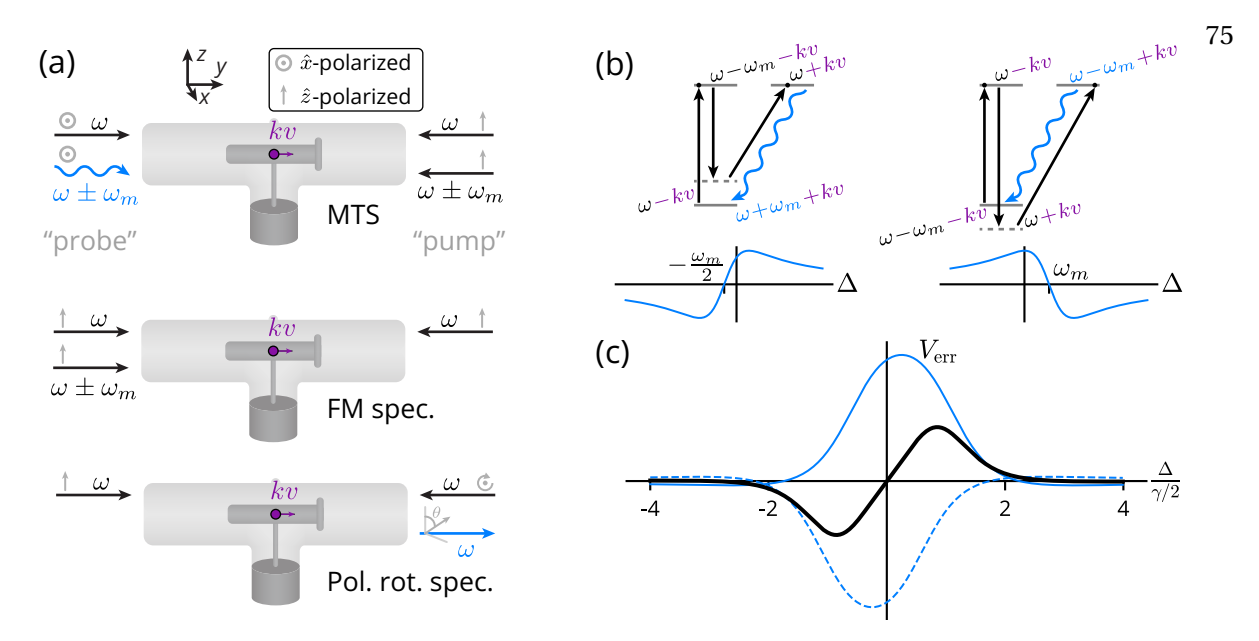


Figure 3.7: (a) Top: modulation transfer spectroscopy (MTS) setup. Two counter-propagating "pump" (frequency modulated at  $\omega_m$ ) and "probe" (initially unmodulated) beams with opposite polarization pass through the hollow cathode lamp. The atoms induce a four-wave mixing (4WM) process that generates sidebands  $\omega \pm \omega_m$  on the probe (blue arrow). The bottom two cartoons highlight the differences between the MTS setup and that of two other Doppler-free techniques: FM spectroscopy (modulation on the probe instead of the pump, same polarization) and polarization rotation spectroscopy (no modulation, circularly polarized pump induces rotation in the probe polarization). (b) Two 4WM resonances involving the  $\omega$  and  $\omega - \omega_m$  pump tones along a J=0 to J=1 transition (with the m=-1 excited state suppressed for simplicity). Each resonance constrains the carrier frequency  $\omega$  and the velocity class of atoms involved (Doppler shift kv). The bottom plots show the contribution of each resonance to the probe electric field, demodulated at  $\omega_m$ , as a function of the detuning from atomic resonance  $\Delta:=\omega-\omega_a$ . (c) The full MTS error signal (black, calculated) is a combination of signals from four 4WM resonances: the two processes from (b) (total field shown as a solid blue curve), and two mirror processes using the  $\omega$  and  $\omega+\omega_m$  pump tones (dashed blue curve). The plot shows the case where  $\omega_m=1\times\gamma/2$ , which is close to experimental parameters.

opposite polarization is modulated, which transfers modulation sidebands to the probe via a four-wave mixing (4WM) process only under specific atomic resonance conditions. It has been argued [276] that the lack of modulation sidebands on the probe far from atomic resonance makes the error signal robust against residual amplitude modulation (RAM) of the probe, which is also known to generate a drifting DC offset. Empirically, it seems like the error signal is quite robust, so we have stuck with it ever since.

The error signal generated from modulation transfer spectroscopy is deceptively complex [277]. Here, I will attempt to convey a basic understanding, accompanied by Fig. 3.7. The basic four-wave

mixing process involves absorbing and emitting tones from the pump separated in frequency by  $\omega_m$ , absorbing an unmodulated probe tone with opposite polarization, and then finally emitting a new probe tone with a frequency offset of  $\omega_m$ . Depending on the velocity v of the atom interacting with the beams, the pump and probe beams will experience opposite Doppler shifts  $\Delta\omega_D=\pm kv$  in the rest frame of that atom. Therefore, for a broad range of laser frequencies  $\omega$  within the Doppler-broadened lineshape of the atomic ensemble inside the hollow cathode lamp, there exists some velocity class of atoms which will bring the emitted probe tone onto resonance with the atomic transition (i.e., the three-photon resonance of the three input tones). By tuning the carrier frequency  $\omega$ , it is possible to also attain a "one-photon" resonance in which the absorbed pump photon is also resonant with the atomic transition, greatly enhancing the 4WM process. Further, these simultaneous constraints determine both  $\omega$  and the velocity class kv of participating atoms and therefore create a Doppler-free signal.

Complicating this picture is the fact that, depending on which pump tone is absorbed, the resonance condition will change. In total, there are four distinct 4WM processes: absorbing a pump photon at  $\omega$  and emitting at  $\omega \pm \omega_m$ , and vice-versa. Fig. 3.7(b) depicts the two processes involving the  $\omega$  and  $\omega - \omega_m$ , for a J=0 to J=1 transition (like the 461 nm transition in strontium). Each of the two resonances in this "doublet" (occuring at  $\Delta := \omega - \omega_0 \in \{-\frac{\omega_m}{2}, \omega_m\}$ ) generates a dispersive lineshape when demodulated in the proper quadrature, with opposite sign since they generate probe sidebands with opposite detunings from carrier. In the regime we operate, where  $\omega_m/2\pi=30$  MHz is smaller than the pressure-broadened linewidth of the atoms in the hollow cathode lamp, these individual processes are not fully resolvable. Adding together the signals from all four 4WM processes therefore generates a single error signal shown in Fig. 3.7(c) with a zero crossing at  $\Delta=0$ . This is the signal we use to lock our laser.

 $<sup>^{14}</sup>$  We can roughly estimate the pressure broadening in the lamp by looking at the MTS error signal, which contains signals from both  $^{88}$ Sr and  $^{86}$ Sr. We know the transition in these isotopes is split by roughly 125 MHz (see, for example, [245]), and by modeling the functional form of the MTS error signal [273] we can estimate the effective pressure-broadened linewidth to be  $110 \pm 30$  MHz.

## 3.3.5 Repumping lasers

The  ${}^{1}P_{1}$  –  ${}^{1}S_{0}$  transition is not a closed transition, as shown in Fig. 3.1. In particular, there is roughly a 1 in 20,000 chance for an atom to decay from the excited 5s5p  ${}^{1}P_{1}$  state into the 5s4d  ${}^{1}D_{2}$  state, rather than the ground  $5s^{2}$   ${}^{1}S_{0}$  state. From there, the atom decays into the  ${}^{3}P_{2}$  and  ${}^{3}P_{1}$  states, the former of which is metastable. Since the atoms spend a relatively short amount of time in our Zeeman slower and 2D MOT stages (on the order of 10 ms given the expected initial and final atomic velocities), we can cool a decent fraction of atoms in these stages with only 461 nm light without them being shelved into dark metastable states. This is not the case for the 3D MOT, since we often rely on loading our MOT for multiple seconds in order to trap sufficient atoms for our experiments. As such, repumping the atoms out of the metastable  ${}^{3}P$  states is absolutely crucial for us.

To repump the atoms, we use two lasers: a 707 nm laser, which addresses the  ${}^3S_1 - {}^3P_2$  transition, and a 679 nm laser, which drives the  ${}^3S_1 - {}^3P_0$  transition. Both of these are home-built diffraction grating ECDLs [231]<sup>[G]</sup>. Together, these lasers induce shelved atoms to repeatedly excite into the  ${}^3S_1$  state and decay back down into the  ${}^3P$  manifold. Roughly 1/3 of the time, an atom will decay into the  ${}^3P_1$  state, which decays to the ground state with a 1/e time of 21  $\mu$ s. Thus, the average atom cycles through three photons during repumping. We shine both lasers at the position of the 3D MOT, on resonance with their respective transitions, and observe a substantial improvement of both the MOT population and lifetime. When working with  ${}^{88}$ Sr, repumping is relatively straightforward since the lack of nuclear spin means there is no hyperfine structure. Empirically, we have found that around 1 mW of 679 nm light and 5 mW of 707 nm light is enough to maximize the number of atoms in a continuously loaded blue MOT. For

 $<sup>^{15}</sup>$  There will be some shelved atoms, however. For an atom at 440°C, it takes ~25,000 photons for the Zeeman slower to fully slow an atom. This is comparable to 20,000, which roughly equals the 1/e shelving probability for a 1 in 20,000 shelving rate. If the 2D MOT beams are detuned by  $\gamma/2$  and have an intensity of  $0.1I_{\rm sat}$ , then they scatter 20,000 photons in ~4 ms. The fact that the shelving probability seems to be less than 1 but also not negligible may not be a coincidence if AOSense designed their source with this in mind, but I have not asked them about it.

 $<sup>^{16}</sup>$  It's worth noting that this amount of power is likely more than one saturation intensity: if we assume the repumping beams have a waist of 3 mm, and that the atomic dipoles are randomly oriented relative to the laser beam, then the beams have an intensity roughly equal to  $I = 4I_{\rm sat} - 5I_{\rm sat}$ . This makes sense if you believe the scattering rate out of the metastable states to be the bottleneck for our MOT atom number, since  $R_{\rm sc} \propto \frac{I}{I + I_{\rm sat}}$  increases by less than 5% per additional  $I_{\rm sat}$  at these intensities (compared to a 33% increase per  $I_{\rm sat}$  at  $I = I_{\rm sat}$ ).

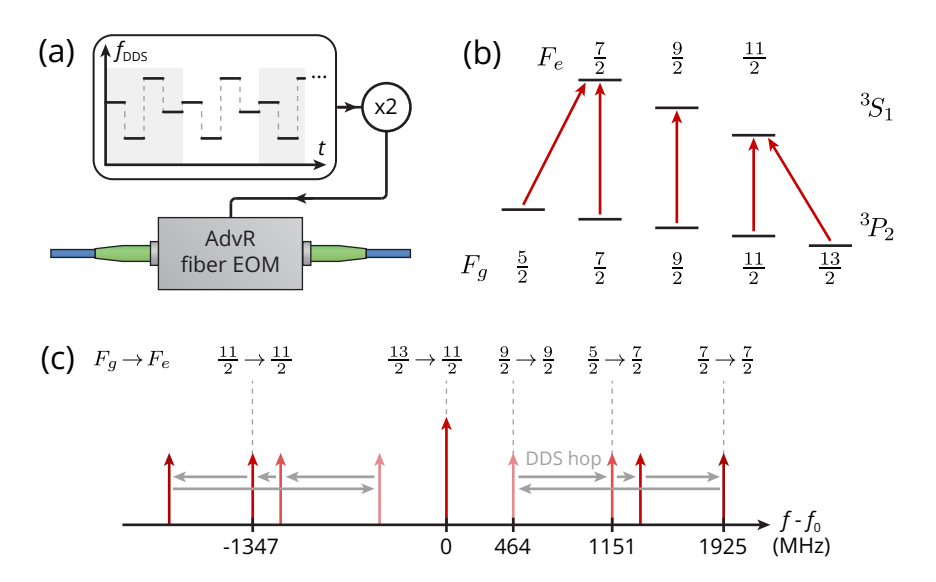


Figure 3.8: 707 nm repumping scheme for  $^{87}$ Sr. (a) To repump on multiple hyperfine states in  $^3P_2$ , we send 707 nm light through an AdvR fiber phase modulator. We use a DDS (and a frequency doubler for dynamic range) combined with an Arduino controller to periodically hop between multiple RF tones, each tone hitting a different hyperfine transition, to save on power. (b) Diagram of the hyperfine structure along the  $^3S_1 - ^3P_2$  transition. We address a total of five hyperfine transitions: one for each metastable state in  $^3P_2$ . (c) Frequency landscape of the frequency modulated 707 nm light. We lock the carrier frequency on resonance with the  $(F_g, F_e) = (\frac{13}{2}, \frac{11}{2})$  transition (here denoted by  $f_0$ ) and use a total of four RF tones to address the four other transitions.

since J = 0, but the  ${}^{3}P_{2}$  state splits into five hyperfine states, all of which are metastable. Therefore, we need at least five different 707 nm laser tones: one for each hyperfine state.

We accomplish this by using a DDS board (part no. AD9959) to drive a fiber-coupled electro-optic modulator (fiber phase modulator, or fiber EOM) and generate FM sidebands on the 707 nm light. This fiber EOM is sourced from AdvR (part no. WPM-K0707-P78P78AL0) and uses a potassium titanyl phosphate (KTP) crystal and can handle tens of mW of input power, unlike some other crystals used for phase modulating red wavelengths. We send in around 17 mW of power into the fiber EOM, limited by the ECDL, which generates 4.5 mW out of a fiber onto the atomic chamber. Attempting to drive five different transitions at once using multiple RF tones would severely limit the amount of power available for each transition, so instead we use an Arduino microcontroller to periodically hop between different profiles saved in the DDS evaluation software every 10  $\mu$ s, as shown in Fig. 3.8(a). These RF tones are then frequency-doubled to increase the dynamic range of output frequencies beyond the clock rate of

the DDS.

While this apparatus existed before my time in the lab, the previous RF setup [231]<sup>[G]</sup> was empirically derived and difficult in practice to replicate, particularly given the low oven fluxes we were working with at the time. Ultimately, we determined which RF tones to use from scratch, shown in Fig. 3.8(b-c). We addressed a total of 5 hyperfine transitions using 4 distinct RF tones, down from the 7 tones used in the previous generation [231]<sup>[G]</sup>, allowing us to address each transition more often. This was accomplished by locking the carrier tone to be on resonance with the  $F_g = \frac{13}{2}$  to  $F_e = \frac{11}{2}$  transition. This transition seemed to successfully repump the most atoms, possibly due to a large fraction of atoms getting trapped in the  $F_g = \frac{13}{2}$  metastable state and the favorable branching ratio on this transition. By assigning it to the carrier, we ensured the transition would see repumping across all DDS hops. Then, we chose four additional transitions that have relatively large branching ratios and empirically led to the best repumping. Of these, the most effective seemed to be the  $F_g = \frac{11}{2}$  to  $F_e = \frac{11}{2}$  tone. This is likely because, when combined with the carrier, the tone forms an almost-closed system since the  $F_e = \frac{11}{2}$  excited state only decays to the  $F_g = \frac{9}{2}$  state 5% of the time that it decays into  $^3P_2$ , leading to efficient depumping within a single 10  $\mu$ s DDS hop.

While not used during the blue MOT stage, we also have a 688 nm laser (also a home-built diffraction grating ECDL) that addresses the  ${}^3S_1 - {}^3P_1$  transition, which shelves atoms out of the  ${}^3P_1$  state and into the metastable  ${}^3P$  states. We occasionally use this laser when running experiments on the narrow-linewidth  ${}^3P_1 - {}^1S_0$  transition in order to quickly freeze dynamics and perform (relatively slow) readout on the excited and ground state populations (see Ch. 5.5 for an example of this in practice). All three repumping/shelving lasers are locked with a PDH lock to a stable reference cavity, as described in Sec. 3.6.

# 3.4 Narrow-line cooling system

The blue cooling stages in the previous section are all Doppler cooling methods, which involve selectively driving atoms by velocity class in order to narrow the velocity distribution (and thus the temperature). The minimum temperature attainable with these types of schemes is determined by a dynamic equilibrium between cooling forces and random atomic recoil; as argued in [278], this tempera-

ture scales with the atomic transition linewidth  $\gamma$ :  $T_D := \hbar \gamma/2k_B$ , where  $k_B$  is the Boltzmann constant, and  $T_D$  is the **Doppler limit**. For typical dipole-allowed optical transitions used for laser cooling with linewidths in the 5-50 MHz range (the  $^1P_1$ – $^1S_0$  transition in Sr has a linewidth of  $\gamma/2\pi \approx 32$  MHz), this sets a Doppler cooling limit around 100  $\mu$ K–1 mK. For alkali (group I) atoms, cooling beyond this point usually calls for sub-Doppler cooling techniques such as polarization gradient cooling [279, 280] or gray molasses cooling [281, 282]. However, alkaline earth atoms typically utilize a narrow-linewidth transition connected to the ground state which allows for Doppler cooling down to significantly lower temperature. For strontium, this transition (with a wavelength of 689 nm, connecting  $^3P_1$ – $^1S_0$ ) has a linewidth of  $\gamma/2\pi = 7.5$  kHz corresponding to a Doppler limit of 180 nK. $^{18}$  Therefore, by adding a second stage of MOT along this narrow-linewidth transition (which we call the **red MOT**), we can attain substantially lower temperatures.

#### 3.4.1 The SWAP MOT

While MOTs on a narrow-linewidth transition work the same as on Doppler-allowed transitions in principle, practically the longer timescales introduce new challenges that must be addressed. In particular, the Doppler broadening out of the initial MOT stage is often substantially broader than the atomic transition linewidth. To give concrete values for our experiment, atoms in our blue MOT start with a temperature around 1 mK, leading to an r.m.s Doppler shift of 450 kHz, compared to a linewidth of 7.5 kHz on the  ${}^3P_1 - {}^1S_0$  transition in Sr. This is a problem because optimal MOT operation calls for laser beams which are red-detuned by  $\gamma/2$ , which is not feasible if the atomic transition is inhomogeneously broadened past this level. As a result, only a small fraction of the atoms will be effectively cooled by a traditional fixed-frequency MOT. To get around this problem, initial experiments demonstrating narrow-line MOTs [289–291] used "broadband" cooling light, either by introducing many different RF tones or by sweeping

 $<sup>^{17}</sup>$  Li and K are an exception since their small hyperfine splitting traditional sub-Doppler cooling techniques challenging. One solution is to use a higher-lying narrow-linewidth transition [283, 284], which requires UV and blue lasers and have Doppler limits around 4 and 29  $\mu$ K for Li and K, respectively. The invention of the Λ-enhanced gray molasses introduced a highly effective and fast alternative, which is now commonly used [285–287].

<sup>&</sup>lt;sup>18</sup> This is actually less than the **recoil limit** for strontium, defined as the temperature  $T_r$  corresponding to a kinetic energy equal to the recoil energy imparted on the atom by a single photon:  $E_{\text{kin}} = E_{\text{rec}} := \frac{\hbar^2 k^2}{2m}$ . Doppler cooling is also limited by the recoil limit [288], which for strontium sets a minimum temperature of  $T_r = 460$  nK.

the frequency in a periodic ramp. This successfully cooled a substantial fraction of the atoms down to a lower temperature. Then, application of a single-frequency MOT could cool the atoms down close to the recoil limit.

In contrast, our experiment uses a technique (accidentally discovered by Matt)<sup>19</sup> which we call sawtooth-wave adiabatic passage (SWAP) cooling [292, 293] [G]. Implementing SWAP cooling in practice is easy: we sweep the frequency of our 689 nm laser, but instead of a symmetric sweep (typically a triangle wave), we sweep with an asymmetric sawtooth wave which ramps upwards in optical frequency. This process relies on the principle of adiabatic transfer: if a laser frequency sweeps across resonance with the atomic transition sufficiently slowly, the atom will be adiabatically transferred from the ground state to the excited state. The basic intuition for how SWAP cooling works in 1D is as follows: an atom with velocity v sees both a co-propagating beam, which is blue-shifted by  $\Delta \omega = k v$ , and a counter-propagating beam, which is red-shifted by  $\Delta \omega = -k v$ . An increasing sweep in optical frequency means the counterpropagating beam will cross into resonance first, causing the atom to deterministically absorb a photon and lose  $\hbar k$  of momentum. Later, when the co-propagating beam crosses onto resonance, the atom is still in the excited state (assuming it has not undergone spontaneous emission), so the beam adiabatically transfers the atom back to the ground state. This causes the atom to deterministically emit a photon forwards and lose another  $\hbar k$  of momentum, for a total slowing of  $2\hbar k$  per sweep. A full understanding of SWAP cooling is significantly more complicated, particularly in a MOT setting. Discussion of these intricacites has led to a series of theory papers from Murray Holland's group in collaboration with our group [294] [G] [295, 296] [297] [G] to model the process. These papers also tease out subtle details, such as the crucial role of spontaneous emission in a process which is often explained using unitary dynamics. I will not go into detail here but would instead highly recommend reading Ch. 10 of Matt Norcia's thesis [231]<sup>[G]</sup>, which introduces the topic quite well.

Using a SWAP MOT over a symmetric ramp MOT has several advantages. Empirically in our experiment, the SWAP MOT captures a larger fraction of atoms out of our blue MOT, and this capture fraction

<sup>19</sup> A quote from the JILA outreach article *A Little Less Spontaneous* by Catherine Klauss, 2018: "Basically, I pressed a button on the function generator,' said Norcia."

is more robust to changes in the atomic transition frequency, especially in  $^{87}$ Sr [231]  $^{[G]}$ . This robustness makes it easy to cool atoms into our optical lattice (described in Sec. 3.5.2), which is quite deep and thus induces large AC Stark shifts on this transition. The SWAP MOT generates larger acceleration forces than would be possible with pure Doppler cooling, leading to faster cooling. Finally, the SWAP MOT does not need so-called "stirring beams," often used in traditional narrow-line cooling of  $^{87}$ Sr to rapidly mix the ground  $m_F$  states and prevent atom loss [298].

In our experiment, we typically use two different stages of SWAP MOT with different sizes of frequency sweep. The first stage, with a peak-to-peak sweep of 9 MHz, is designed to recapture atoms out of the blue MOT and cool them down from 1 mK to 10s of  $\mu$ K. The second stage sweeps over a much smaller range with a peak-to-peak deviation of 1.4 MHz. This stage cools the atoms further to somewhere between  $10-20~\mu$ K, and it simultaneously loads the atoms into the 813 nm optical lattice described in Sec. 3.5.2. I'll note that these two objectives may be in slight tension with one another. Empirically, I have found that by tuning the center frequency of this second-stage SWAP MOT, I can decrease the atom temperature to below 5  $\mu$ K, and the MOT becomes substantially denser and more spherical in shape. However, we cannot trap as many atoms in the optical lattice. For our actual second-stage SWAP settings, the MOT flattens into a large pancake shape, which I suspect is better mode-matched to the cavity. My personal explanation for this is that we have tuned the SWAP to be below the atomic resonance, so the center of the magnetic quadrupole field does not provide good cooling power. As a result, the atoms fall below the zero of the quadrupole field due to gravity until they see a large enough magnetic field to shift the transitions onto atomic resonance, creating a flattening effect. Horizontally, the atoms spread out in all directions away from the quadrupole zero, leading to the pancake shape.

## 3.4.2 The 689 nm laser system

The laser system used to generate our red MOT light, as well as any science beams for addressing the atoms along the  ${}^{3}P_{1} - {}^{1}S_{0}$  transition, is outlined in Fig. 3.9. We start with 15 mW of light from a

<sup>&</sup>lt;sup>20</sup> It also cools with fewer total scattered photons, which makes it an appealing candidate for systems with non-closed narrow-linewidth transitions, such as YO molecules [295].

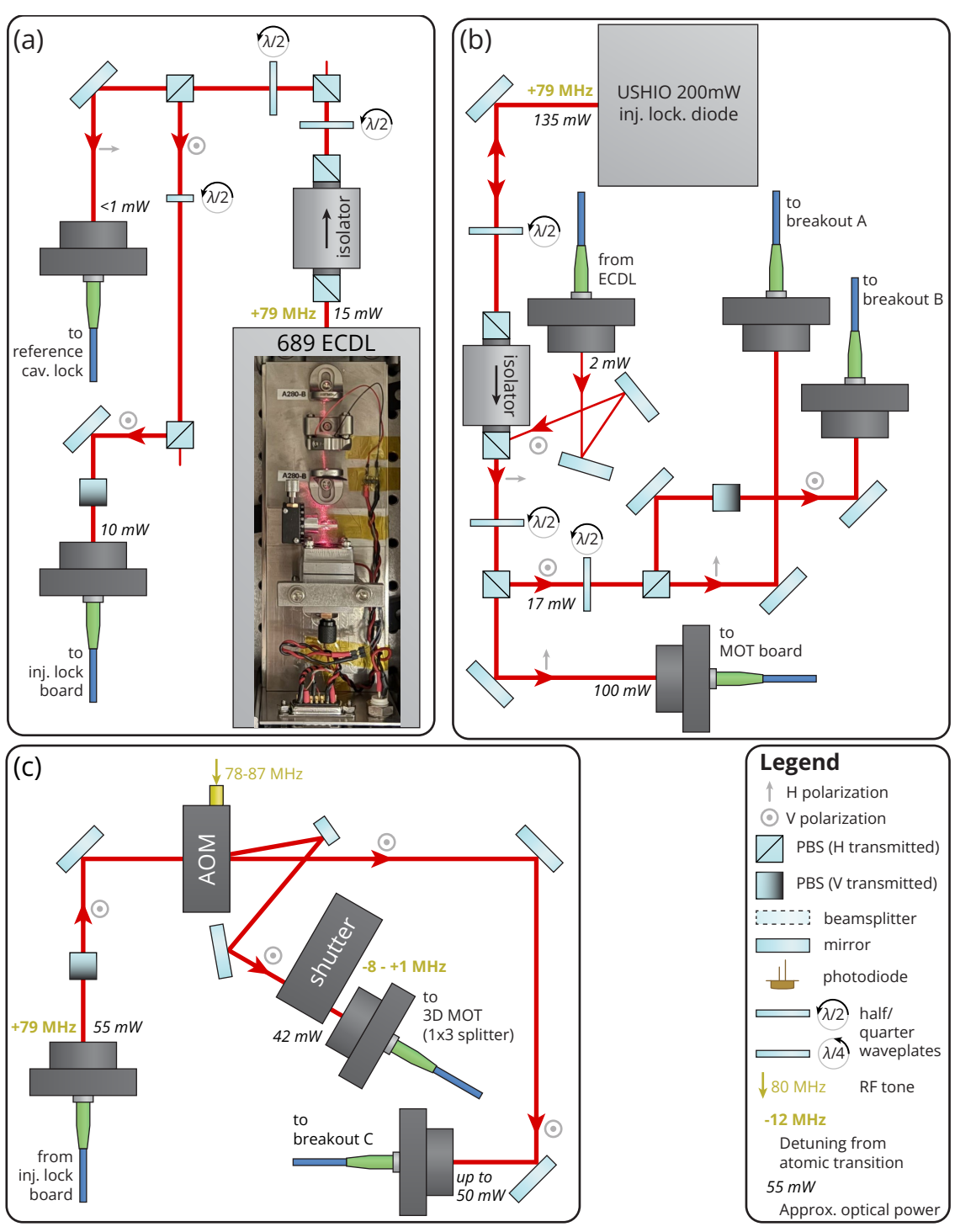


Figure 3.9: 689 nm laser system breakout. (a) We use a home-built interference filter ECDL (see Sec. 3.7) to generate light and stabilize it to our reference cavity (see Sec. 3.6). (b) To generate enough power for our MOT and science beams, we seed a single-mode diode from USHIO which generates up to 200 mW of light, which is partitioned between the MOT and other flexibly allocated pathways. (c) The MOT light goes through an AOM which is driven by a sawtooth-wave RF tone for the SWAP MOT. The frequency of the SWAP MOT is centered below the atomic transition frequency but sweeps onto and then above resonance.

homebuilt interference filter ECDL (IF-ECDL), described in detail in Sec. 3.7. Before we built this laser in 2024, this was a commercial IF-ECDL purchased from AOSense (part no. AOS-ECDL-689), which was more compact but more expensive. As we will discuss later, our homebuilt laser has lower phase noise than the commercial version, which should improve the signal-to-noise ratio when probing the atoms with this laser or making heterodyne measurements.

Just as with the blue laser system in Sec. 3.3, the 689 nm ECDL on its own does not output enough power for all of our needs, so we need a gain stage. The form of this stage has undergone several changes during my time in the lab. At the end of Matt's Ph.D. in 2017, this stage took the form of an Eagleyard tapered amplifier (part no. EYP-TPA-0690). However, tapered amplifiers do not work very well at red wavelengths compared to IR, and the performance of this chip quickly degraded to provide a net gain (after fiber coupling) of less than 2. By the time I joined the lab, we had installed an additional injection lock stage with a 30 mW diode from Thorlabs (part no. HL6738MG) to send more initial power into the tapered amplifier. In 2020, I gave the tapered amplifier to Julia for use in the strontium ring cavity experiment and instead upgraded the injection lock to use a 50 mW diode from Thorlabs (part no. HL6750MG). This was more than enough to compensate for the barely functional tapered amplifier.

Around this time, the ring cavity experiment was accumulating an impressive collection of 689 nm injection lock diodes due to their many red cooling and slowing beams. This was becoming a bit of a hassle for them; fortunately, in 2022 we became aware of a higher-powered 210 mW single-mode diode made by USHIO (distributed by RPMC, part no. HL69001DG). This enabled both experiments to work with significantly more 689 nm power. The only caveat to this diode is its limited quoted lifetime of 10,000 hours. To stretch out the lifetime of this object, we turn the diode off at night and over the weekend. Currently, our gain stage is as shown in Fig. 3.9(b). We don't currently use all of the rated 200 mW power since there currently isn't a need for more power, but that could change in the future. Some of this power is sent to the SWAP MOT (see also Fig. 3.9(c)), and the rest is sent to various other breakout stages labeled 'A', 'B', and 'C' in the figure. These pathways can be flexibly allocated to various beams used in the experimental pulse sequence, which are not the same between different experiments.

# 3.5 The science cavity

During the final SWAP MOT stage, we cool the atoms into an 813 nm optical lattice, formed by sending 813 nm light through a high-finesse optical cavity which we call the **science cavity**. This effectively couples the atoms to the cavity mode (with caveats that we will touch on soon), initializing our many-atom cavity QED platform which allows us to perform all the experiments in this thesis. In this section, I will present relevant details about our science cavity and the optical lattice used to trap the atoms.

## 3.5.1 Cavity parameters

Our science cavity was constructed by Matt Norcia in 2014 [231][G], and we have not modified it since. At a high level, it is a symmetric two-mirror cavity, shorter than confocal (with a nominal mirror radius of R = 5 cm and a nominal length of L = 4 cm). The mirrors have coatings supplied by Advanced Thin Films which provide a high finesse near 689 nm and 698 nm (on the order of 25000) and a moderately high finesse near the lattice wavelength of 813 nm (around 2500). The mirrors are mounted on a macor cavity spacer, with piezoelectric transducer (PZT) tubes on each side which allow the cavity length to be changed. The tubes are cut to 0.25 inches each from a larger tube purchased from Piezomechanik (part no. PiT 10x36x1). <sup>21</sup> The piezos are designed to operate up to a positive voltage of 1000 V and down to a negative voltage of -200 V. The total combined throw of the two piezo tubes over its full voltage range is about 6.8  $\mu$ m, given the length of the tubes, with a positive voltage causing contraction (shortening). However, currently our voltage driver only goes between 0 and 150 V, resulting in a more limited throw of 850 nm. Still, this is sufficient to tune the cavity length over more than two free spectral ranges at our laser frequencies.<sup>22</sup> The spacer, PZT tubes, and mirror are mounted together through the use of a macor "hat," in order to recess the mirrors inside the spacer and prevent strontium from coating the mirrors. To see the geometry of the setup and the mirror mounting, I'd recommend looking at Matt's thesis [231][G]. I also show a cartoon depiction of the mounting scheme next section in Fig. 3.11, since it is relevant to

 $<sup>^{21}</sup>$  I don't think Piezomechanik sells the tubes we bought for our science cavity anymore. I saved a spec sheet for the tube in question onto the lab OneDrive.

<sup>&</sup>lt;sup>22</sup> Further tuning requires creativity, as discussed in Ch. 4.

Description	Symbol	<b>689 nm</b> [ <sup>3</sup> P <sub>1</sub> ]	<b>698 nm</b> $[^3P_0]$	813 nm	Units
Free spectral range	$\omega_{ m FSR}/2\pi$	3.71459(2) <sup>(PRR)</sup>	3.71461(3) <sup>(PRR)</sup>	3.715(1) <sup>(v)</sup>	GHz
Cavity length	L	4.03534(2)(^)	4.03532(3) <sup>(^)</sup>	4.035(1) (est.)	cm
FWHM linewidth	$\kappa/2\pi$	153.0(4) <sup>(PRR)</sup>	140.9(3)(PRR)	1584 <sup>(v)</sup>	kHz
Cavity finesse	${\mathcal F}$	24280(60)(^)	26360(60)(^)	2345.5 <sup>(V)</sup>	-
Mirror total loss	$T_m + L_m$	129.4(3) <sup>(^)</sup>	119.2(3) <sup>(^)</sup>	1339.4 <sup>(v)</sup>	ppm
Mirror transmission	$T_m$	106.52(*)(!)	95.297 <sup>(*)(!)</sup>	1339.4 <sup>(*)</sup>	ppm
Mirror loss	$L_m$	22.9(3)(^)	23.9(3)(^)	small?	ppm
Mode waist	$w_0$	73.37(7) <sup>(PRR)</sup>	73.85(7) <sup>(PRR)</sup>	79.7(1) <sup>(PRR)</sup>	$\mu$ m
Rayleigh length	$z_R$	2.453(5)(^)	2.453(5)(^)	2.453(6)(^)	cm
Peak cooperativity	$C_0$	0.415(1)(^)	0.456(1)(^)	-	-
Atomic linewidth	$\gamma/2\pi$	7.463(12) kHz <sup>(YE)</sup>	1.35(3) mHz <sup>(PRR)</sup>	-	-
Peak J.C. coupling	$g_0/2\pi$	10.88(2) kHz <sup>(^)</sup>	4.66(5) Hz <sup>(^)</sup>	-	

Table 3.2: Science cavity parameters for relevant wavelengths/transitions in strontium. The top section contains parameters which do not depend on atomic transitions. The bottom section of the table contains atom-cavity coupling parameters along the associated atomic transitions for 689 nm and 698 nm, assuming a Clebsch-Gordan coefficient of 1.

how we stabilize the length of the science cavity.

Table 3.2 details our current best understanding of various cavity parameters. Many of these values, particularly at the 689 nm and 698 nm wavelengths, were calculated around 2019 by then-postdoc Juan Muniz in order to determine the linewidth of the  ${}^{3}P_{0}-{}^{1}S_{0}$  transition, as detailed in Ch. 4 and in [96] [G]. Other values are derived from those measurements: for example, the cavity finesse is calculated from the free spectral range and the cavity linewidth using Eq. (2.18), the loss per mirror is calculated from the finesse using the same equation, the cooperativity is calculated from the finesse and the waist using Eq. (2.50), and the Jaynes-Cummings atom-cavity coupling  $g_{0}$  is calculated from the cooperativity

<sup>(</sup>PRR) Linewidth measurement paper in *Phys. Rev. Res.* (2021) [96]

<sup>(</sup>YE) Sr I clock evaluation paper in *Phys. Rev. Lett.* (2024) [101]

<sup>(\*)</sup> From Advanced Thin Films coating spec sheet

<sup>(!) 689</sup> nm and 698 nm transmission values are assumed to be mistakenly swapped on the spec sheet

<sup>(</sup>A) Derived from above quantities

<sup>(</sup>V) Derived from below quantities

and the atomic and cavity linewidths using Eq. (2.49).

To distinguish between transmission and loss probabilities in the cavity mirrors, we currently rely on data from the Advanced Thin Films spec sheet. Unfortunately, there's a bit of ambiguity associated with these numbers. The spec sheet actually claims that the transmission rates  $T_m$  for 689 nm and 698 nm are swapped relative to what is reported in Table 3.2. If this is true, it would imply that the power loss probabilities  $L_m$  for the two wavelengths are different by a factor of three. For this reason, Matt posited that the values should be switched to what we currently report. The current best piece of independent data we have to dispute or corroborate this claim is a measurement I performed in 2021, where I optimized the 689 nm cavity coupling and then measured the transmission as a fraction of the input light. Assuming no losses outside the cavity, a perfectly symmetric cavity, and perfect cavity coupling, then this fraction should be  $P_t/P_i = \left(\frac{T_m}{T_m + L_m}\right)^2$  as derived last chapter in Eq. (2.16). With additional losses, this puts a lower bound on  $T_m$ . Having measured a fraction of 0.54, this suggests that  $T_m \gtrsim 95$  ppm, which does not entirely rule out the possibility that the spec sheet was correct. A good future test of this would be to repeat this transmission measurement with 698 nm light, since if the spec sheet is correct the fractional transmission of this wavelength should be substantially higher at 0.80. If the transmission is similar to that of 689 nm light, that would be strong evidence that the reported values in Table 3.2 are correct.

Additionally, we have substantially fewer measurements of cavity parameters at 813 nm. Juan measured the waist of the cavity mode, but for everything else we currently rely on the Advanced Thin Films spec sheet providing the transmission probability. I have performed quick and dirty measurements of the cavity linewidth at 813 nm by fitting the shape of the PDH error signal lock to the science cavity (see Sec. 3.6 for the locking chain) given knowledge of the PDH sideband frequency, which suggests that the cavity linewidth is larger than the value reported in Table 3.2 at  $\kappa/2\pi = 2.1$  MHz. However, it would be cleaner to perform a ringdown experiment (say, by sending in a tone one FSR away and then rapidly turning it off to measure the exponential decay time). Nominally, you might expect that the cavity length should be the same as for 689 nm and 698 nm. However, as the different wavelengths may have different penetration depths in the cavity mirrors, this is not exactly the case. We see some amount of evidence for this up to potentially the 10  $\mu$ m level, as discussed in Sec. 3.6. As a result, the free spectral range at

Description	Symbol	Typical value	Units
Transmitted power	$P_t$	8.3 <sup>(meas.)</sup>	mW
Axial trap frequency	$\omega_{\rm ax}/2\pi$	165(10) <sup>(meas.)</sup>	kHz
Radial trap frequency	$\omega_{ m rad}/2\pi$	0.41(2) <sup>(^)</sup>	kHz
	$U_0$	580(70)(^)	$E_{ m rec}$
Trap depth (for ${}^1S_0$ )	$\omega_{ m depth}/2\pi$	2.0(2)(^)	MHz
	$T_{ m depth}$	95(12) <sup>(^)</sup>	$\mu$ K
Lamb-Dicke parameter (for 689 nm/698 nm)	η	0.170(5)(^)	-
Axial temperature	$T_{\mathrm{ax}}$	18(3) <sup>(meas.)</sup>	μΚ
Mean axial quantum num.	$\overline{n}_{\mathrm{ax}}$	1.8(4) <sup>(^)</sup>	-
Effective Lamb-Dicke param. (for 689 nm/698 nm)	$\eta_{ ext{eff}}$	0.37(4)(^)	-
Radial temperature	$T_{\rm rad}$	17(3) <sup>(meas.)</sup>	μK
Mean radial quantum num.	$\overline{n}_{\mathrm{rad}}$	860(160) <sup>(^)</sup>	_
Radial r.m.s. extent	$\sigma_{ m rad}$	15.5(1.7) <sup>(^)</sup>	μm

Table 3.3: Typical parameters for the 1D optical lattice. Values in the top half describe properties of the lattice as pertains to atoms in the ground state at zero temperature. Values in the bottom half depend on the temperature of the atomic ensemble.

 $^{(meas.)}$  Measured value, given  $P_t = 8.3 \text{ mW}$ 

813 nm could be different by as much as 1 MHz and would benefit from being independently measured.

Finally, it is entirely possible for some of these parameters, like the cavity finesse, to degrade over time. A possible mechanism for this is strontium coating the cavity mirrors, which may increase losses. For future experiments which rely on precision measurements of cavity parameters, I'd recommend repeating Juan's measurements.

### 3.5.2 813 nm optical lattice

To create an optical lattice, we send in several mW of 813 nm light through the cavity and stabilize the 813 laser frequency to the cavity resonance through a PDH lock off the science cavity (the full locking chain is described in Sec. 3.6). Properties of the optical lattice depend on exactly how much power we

<sup>(^)</sup> Derived from above quantities

send through the cavity, as more optical power results in deeper trap depths. Table 3.3 shows values for typical optical lattice depths used in the experiment. As the table shows, there are several important parameters which describe the optical lattice. Here, I'll briefly describe what each of the parameters represents.

Let us assume that we trap the atoms near the waist of an optical lattice beam. Then the lattice generates a potential landscape of the form

$$U(r,z) = -U_0 e^{-2r^2/w_0^2} \cos^2\left(\frac{2\pi z}{\lambda}\right)$$
 (3.1)

for a lattice beam of wavelength  $\lambda$  and waist  $w_0$ . Here,  $U_0$  is the maximum depth of the potential well, known as the trap depth, and it is often expressed in units of frequency, temperature, and  $E_{\text{rec}}$  (the recoil energy of a lattice photon).<sup>23</sup> Expanding around (r, z) = (0, 0), we approximate a harmonic trap:

$$U(r,z) \approx -U_0 \left( 1 - \frac{2r^2}{w^2} \right) \left( 1 - \left( \frac{2\pi z}{\lambda} \right)^2 \right)$$

$$\approx -U_0 + \frac{2U_0}{w^2} r^2 + \frac{4\pi^2 U_0}{\lambda^2} z^2$$

$$= -U_0 + \frac{1}{2} m\omega_{\text{rad}}^2 r^2 + \frac{1}{2} m\omega_{\text{ax}}^2 z^2,$$
(3.2)

where m is the atomic mass and  $\omega_r$ ,  $\omega_z$  are the radial and axial trap frequencies. Finally, we back out explicit formulas for the radial and axial trap frequencies:

$$\omega_{\rm rad} = \frac{2}{w_0} \sqrt{\frac{U_0}{m}} \tag{3.3}$$

$$\omega_{\rm ax} = \frac{2\pi}{\lambda} \sqrt{\frac{2U_0}{m}}.$$
 (3.4)

It follows that, for atoms near the bottom of the potential well, the trap looks like a 3D harmonic trap with a level spacing of  $\omega_{ax}$  along the axial direction and  $\omega_{rad}$  along the radial direction.

In terms of supplying measured values, one of the easier quantities to measure is the axial trap frequency  $\omega_{ax}$ . I measured this by utilizing a phenomenon known as **parametric heating**, which is a process by which periodic modulation of the trap potential at twice the trap frequency leads to a coherent buildup of motional excitation (and generally leading to atoms falling out of the trap). This process can

The recoil energy is the amount of kinetic energy gained by an atom upon absorption of a lattice photon. It is given by the form  $E_{\text{rec}} = \frac{\hbar^2 k^2}{2m}$ , where m is the mass of the atom, and k is the wavevector of the lattice light.

be intuitively understood by comparing the atoms to a kid<sup>24</sup> on a swing. Without any modulation, the kid will swing back and forth periodically with fixed amplitude (until friction causes damping). However, if someone pushes on the swing whenever it is at its maximum point, the kid will swing higher and higher until the swing inverts, and the kid falls off. For this measurement, I amplitude modulated the trap depth for different modulation frequencies and found the point of maximum loss from parametric heating, allowing me to infer  $\omega_{\rm ax}/2\pi=165(10)$  kHz.

When placing atoms in the optical lattice, the temperature of the ensemble determines which quantum states the atoms occupy. For sufficiently hot atoms (i.e., when  $k_B T \gg \hbar \omega$  for a trap frequency  $\omega$ ), the ensemble effectively displays a classical Boltzmann distribution, which in a harmonic potential implies a Gaussian distribution. In the radial direction, this is certainly true for our system, so the 2D transverse position distribution is given by:

$$P_{\rm rad}(\mathbf{r}) = \left(\frac{1}{\sqrt{2\pi\sigma_{\rm rad}^2}}\right)^2 e^{-\frac{|\mathbf{r}|^2}{2\sigma_{\rm rad}^2}},\tag{3.5}$$

where r = (x, y) is a 2D position vector pointing transverse to the lattice k-vector, and  $\sigma_{rad}$  is the r.m.s. radial extent of the distribution along either axis. By the equipartition theorem, we can relate  $\sigma_{rad}$  to other quantities by using the form of the harmonic potential:

$$\frac{1}{2}m\omega_{\rm rad}^2\sigma_{\rm rad}^2 = \frac{1}{2}kT$$

$$\Rightarrow \sigma_{\rm rad} = \frac{1}{\omega_{\rm rad}}\sqrt{\frac{kT}{m}} = \frac{w_0}{2}\sqrt{\frac{T}{T_{\rm depth}}}.$$
(3.6)

Along the axial direction, it's less clear if a classical approximation is valid since  $k_B T_{\rm ax}/\hbar\omega_{\rm ax} = 2.2$ . Instead, we can consider the mean occupation number  $\overline{n}$ . For a given temperature  $\beta = (k_B T)^{-1}$ , the equilibrium occupation number in a trap with frequency  $\omega$  is given by:

$$\overline{n} = \frac{\sum_{n} n e^{-\beta \hbar \omega n}}{\sum_{n} e^{-\beta \hbar \omega n}} = \frac{1}{e^{\beta \hbar \omega} - 1}.$$
(3.7)

This suggests that in the axial direction  $\overline{n}_{ax}\approx 1.8$ , which is pretty close to but a bit smaller than the classical approximation of  $1/\beta\hbar\omega_{ax}=2.2$ . This means that, even in the axial direction, there is still substantial atomic motion.

<sup>&</sup>lt;sup>24</sup> or adult.

Despite this, in many experiments we ignore the effects of atomic motion to first order. The reason this is a reasonable approximation is due to the fact that we work in the **Lamb-Dicke regime**. At a high level, this regime allows us to approximately decouple motional and internal (electronic) degrees of freedom along the cavity axis, because the trap is "sufficiently deep." The general argument is as follows: a laser drive in the form of a plane electromagnetic wave has a position-dependent phase factor that looks like  $e^{ik_dz}$ , where  $k_d$  is the wavevector of the driving light, and z is the position along the cavity axis. Let us assume that z=0 at the center of one of the lattice sites. Then we can rewrite the position as the operator  $\hat{z}=z_0(\hat{a}_{\rm ax}+\hat{a}_{\rm ax}^\dagger)$  for a motional ground state position spread  $x_0$  and an axial trap lowering operator  $\hat{a}_{\rm ax}$ . Let us define the **Lamb-Dicke parameter**  $\eta:=k_dz_0$ , which also happens to be equal to  $\sqrt{\omega_{\rm rec}/\omega_{\rm ax}}$ , where  $\omega_{\rm rec}=E_{\rm rec}/\hbar=\frac{\hbar k_d^2}{2m}$  is the recoil frequency of the drive. Then the ability for the drive to excite motional transitions is proportional to:

$$\langle n' | \hat{E}_{\text{drive}} | n \rangle \propto \langle n' | e^{i\eta(\hat{a}_{ax} + \hat{a}_{ax}^{\dagger})} | n \rangle$$

$$\approx \langle n' | \left( 1 + \eta(\hat{a}_{ax} + \hat{a}_{ax}^{\dagger}) \right) | n \rangle + O(\eta^{2}), \tag{3.8}$$

where we have expanded perturbatively in  $\eta$ . In the limit where  $\eta \ll 1$  (the Lamb-Dicke regime), therefore, we can see that the probability of undergoing first-order sideband transitions  $(n \to n \pm 1)$  is suppressed by a factor of  $\eta^2 \left( |\langle n-1| \hat{a}_{\rm ax} |n\rangle|^2 + |\langle n+1| \hat{a}_{\rm ax}^\dagger |n\rangle|^2 \right) = \eta^2 (2n+1)$  compared to the carrier  $(n \to n)$ . For ground state atoms, this suppression is simply  $\eta^2$ . For a thermal cloud of atoms with an average occupation of  $\overline{n}_{\rm ax}$ , we can define an effective Lamb-Dicke paramter  $\eta_{\rm eff} \coloneqq \eta \sqrt{2\overline{n}_{\rm ax} + 1}$ , such that  $\eta_{\rm eff}^2 \ll 1$  provides the equivalent suppression condition for the Lamb-Dicke regime.

In our cavity system, our drives take the form of a standing wave since they are sent through the cavity, rather than a unidirectional plane wave. Moreover, our drive lasers (usually 689 nm or 698 nm) are incommensurate with our trapping laser (813 nm), meaning that different trap sites experience different spatial phases of this standing wave. This modifies the traditional Lamb-Dicke picture in an interesting way. Let us consider two atoms: one which sits at an antinode (AN) of the drive field, experiencing maximum intensity, and another which sits at a node (N), experiencing minimum intensity. These two

atoms experience different sideband couplings:

$$\langle n' | \hat{E}_{\text{drive}} | n \rangle_{\text{AN}} \propto \langle n' | \cos \left( \eta (\hat{a}_{\text{ax}} + \hat{a}_{\text{ax}}^{\dagger}) \right) | n \rangle \approx \langle n' | n \rangle$$
 (3.9)

$$\langle n' | \hat{E}_{\text{drive}} | n \rangle_{\text{N}} \propto \langle n' | \sin \left( \eta (\hat{a}_{\text{ax}} + \hat{a}_{\text{ax}}^{\dagger}) \right) | n \rangle \approx \eta \langle n' | (\hat{a}_{\text{ax}} + \hat{a}_{\text{ax}}^{\dagger}) | n \rangle.$$
 (3.10)

From these equations, we see that maximum or "peak" couplers are very unlikely to undergo first-order sideband transitions (but could still, in principle, undergo second-order transitions). Conversely, minimum or "weak" couplers can undergo sideband transitions at a Lamb-Dicke-suppressed rate, but they are unlikely to undergo carrier transitions.

Finally, for drives with Rabi frequencies weaker than the axial sideband frequency ( $\Omega_d \ll \omega_{\rm ax}$ ), you can operate in a resolved sideband regime. In this regime, you can park the drive laser on resonance with the carrier transition but off resonance from the sideband transitions, which provides an additional suppression factor of  $\left(\frac{\Omega_d}{\omega_{\rm ax}}\right)^2$  in driving sideband transitions. This condition is usually met when driving along the clock transition but is much harder to achieve on the  $^3P_1-^1S_0$  transition, since  $\Omega_d=2g_0\sqrt{M_c}$  where  $M_c$  is the number of intracavity photons, and  $g_0$  scales with the square root of the transition linewidth. Also note that, if the drive is only on for a very short period of time (less than  $1/\omega_{\rm ax}$ ), the drive is Fourier-broadened in frequency space and thus doesn't benefit from this additional condition.

## 3.5.3 Lattice-induced inhomogeneous broadening

The trap depth in the previous section describes the negative AC Stark shift experienced by atoms in the ground state. For other states, generically speaking these shifts will be different, leading to a differential transition frequency between ground and excited states that depends on the local intensity of the trap light. For a given two-level system, it is often possible to work with a **magic wavelength** trapping potential, which has equal AC Stark shifts in both states and thus doesn't shift the transition frequency. This is the underlying reason for our choice of an 813 nm optical lattice: as has been measured quite precisely [299], the magic wavelength for the  ${}^3P_0 - {}^1S_0$  clock transition in strontium is at 813.427 nm. When working along the clock transition, therefore, we don't have to worry as much about differential light shifts.

On the other hand, dealing with light shifts on the narrow-linewidth  ${}^3P_1 - {}^1S_0$  transition can be quite a bit more complex. To start, our optical lattice is not at a magic wavelength for any of the  ${}^3P_1$  states. As discussed in Table 3.3, our atomic ensemble experiences a radial spread due to its finite temperature, which means that the atoms experience inhomogeneous broadening in the  ${}^3P_1$  transition frequency. As we will derive in Ch. 6.14, if we assume that the atoms only have a substantial spread transverse to the cavity (i.e., a 2D thermal distribution), then the fractional variation in trap depth  $\mathfrak{u} = U/U_0$  satisfies the following probability distribution:<sup>25</sup>

$$P(\mathfrak{u}) = \left(\frac{T_{\text{depth}}}{T}\right) \mathfrak{u}^{(T_{\text{depth}}/T)-1}; \qquad \mathfrak{u} \in [0,1].$$
(3.11)

With the temperature quoted in Table 3.3, this implies that the distribution sees a mean trap depth of  $0.85(3)U_0$  and a standard deviation of  $0.13(2)U_0$ . As a result, the atomic ensemble will see inhomogeneous broadening which is 13% of the maximum differential AC Stark shift.

### 3.5.4 Scalar, vector, and tensor lattice shifts

Different Zeeman sublevels in  ${}^3P_1$  (and hyperfine sublevels for  ${}^{87}$ Sr) will also generically experience different AC Stark shifts induced by the lattice. The differences can be understood with a geometric argument: keep in mind that angular momentum states  $|j,m\rangle$  form a basis for all possible states with angular momentum j. An electric field with fixed polarization will couple to some orientations of angular momentum state more than others, so it is only natural that a detuned electric field will shift the states differently.

Exactly how the AC Stark shifts differ can be neatly described using a spherical tensor decomposition, and Dan Steck's *Quantum Optics* [178] provides all the relevant derivations and formulas in Sec. 7.7. Here, we will not dive too deeply into the equations and instead focus on interpretation. To start, suppose we have an electric field oscillating at a frequency  $\omega$ , described by  $\mathbf{E}^{\text{phys}}(t) := \text{Re}[\mathbf{E}e^{-i\omega t}]$  as in Ch. 2.2.1,

<sup>&</sup>lt;sup>25</sup> This distribution works for any elliptical Gaussian lattice beam, so long as the atoms sample the lattice potential in a way that satisfies a classical Boltzmann distribution. For a circular Gaussian beam, that implies a cylindrically symmetric atomic distribution. For an elliptical beam, it implies an elliptical atomic distribution with an ellipticity matching the lattice beam. You can think of the elliptical case as a "stretching" of the circular case along one direction: the atomic distribution and lattice potential stretch in the same way, so the fractional intensity distribution remains unchanged.

where E is a complex phasor. Classically, this field can induce a dipole moment in an atom which we will call  $d := \overline{\alpha}(\omega)E$ , where  $\overline{\alpha}(\omega)$  is the (electric dipole) polarizability tensor. As defined,  $\overline{\alpha}$  could be complex if the dipole moment responds to the field with some phase delay, and the real physical dipole moment given by  $d^{\text{phys}}(t) := \text{Re}[de^{-i\omega t}]$  oscillates out of phase with  $E^{\text{phys}}$ . The fact that  $\overline{\alpha}$  is a tensor allows for the possibility that the induced dipole does not point in the same direction of the electric field. From now on, we will use Einstein summation notation to denote vector and tensor indices, such that  $d_{\mu} = \alpha_{\mu\nu}(\omega)E_{\nu}$ . An induced dipole interacts with the external electric field with a potential that looks like  $V = -\frac{1}{2}d_{\nu}^{\text{phys}}E_{\nu}^{\text{phys}}$ , where the factor of  $\frac{1}{2}$  comes from the fact that the dipole is induced. In terms of the polarizability tensor, this interaction evaluates to:

$$V \approx -\frac{1}{2} \left( \frac{d_{\nu}^* E_{\nu} + d_{\nu} E_{\nu}^*}{4} \right) = -\frac{1}{8} \left( \alpha_{\mu\nu}^* + \alpha_{\mu\nu} \right) E_{\mu} E_{\nu}^*$$

$$= -\frac{1}{4} \operatorname{Re}[\alpha_{\mu\nu}] E_{\mu} E_{\nu}^*, \tag{3.12}$$

after ignoring counterrotating terms which oscillate at  $2\omega$ .<sup>26</sup> We see that the energy shift experienced by the atom depends entirely on the nature of the polarizability tensor  $\alpha_{\mu\nu}$ .

This intuition generalizes well to quantum mechanics. Suppose an atom in state  $|i\rangle$  is subject to a classical electric field oscillating at  $\omega$ . Then we can write the system Hamiltonian as

$$\hat{H} = \hbar \sum_{k} \omega_{ki} |k\rangle\langle k| - \hat{d}_{\mu} \left( \frac{E_{\mu} e^{-i\omega t} + E_{\mu}^{*} e^{i\omega t}}{2} \right), \tag{3.13}$$

where  $\hat{d}_{\mu}$  is an operator describing the electric dipole projection along coordinate  $\mu$ , and  $\omega_{ki} = \omega_k - \omega_i$  is the transition frequency between  $|i\rangle$  and some other atomic state  $|k\rangle$ . As described in Dan Steck's *Quantum Optics*, Sec. 14.3.1 [178], we can calculate the energy shift on  $|i\rangle$  using time-dependent perturbation theory with the dipole interaction as the perturbation,<sup>27</sup> resulting in the following second-order energy shift:

$$U_{i}^{(2)} = -\frac{1}{4} \left( \sum_{k \neq i} \frac{2\omega_{ki} \mathcal{D}_{ik,\mu} \mathcal{D}_{ki,\nu}}{\hbar(\omega_{ki}^{2} - \omega^{2})} \right) E_{\mu} E_{\nu}^{*}, \tag{3.14}$$

<sup>&</sup>lt;sup>26</sup> If looking at Steck's formulas, note that there is a factor of 4 difference in the expression for the potential; however, the definition for the polarizability is consistent. Ultimately, the factor of 4 comes from Steck's convention for describing the electric field: instead of the physical field representing the real part of a single complex phasor, he uses a sum of two counterrotating phasors:  $E^{\text{phys}} = E^{(+)} + E^{(-)}$ , where  $E^{(+)} = \frac{E}{2}e^{-i\omega t}$  with E defined with my notation. Therefore, by Steck's convention,  $V = -\text{Re}[\alpha_{\mu\nu}][E^{(+)}]_{\mu}[E^{(-)}]_{\nu}$ .

<sup>&</sup>lt;sup>27</sup> The perturbation theory calculation is essentially equivalent to performing time-independent perturbation theory twice, once on each of the  $\pm \omega$  terms in the perturbation, by moving into a rotating frame, followed by summing together the energy shifts.

where  $\mathcal{D}_{ki,v} = \langle k | \hat{d}_v | i \rangle$  is the v component of the dipole matrix element coupling  $|i\rangle$  to  $|k\rangle$ . In analogy to the classical description discussed earlier, we assign the term in parentheses to (the real part of) the polarizability tensor  $\alpha_{uv}(\omega;i)$  for state  $|i\rangle$ .

Knowledge of the polarizability tensor is powerful because it allows us to calculate AC Stark shifts for arbitrary electric fields. However, a challenge is that each state  $|i\rangle$  has a different tensor. This may seem daunting, particularly in <sup>87</sup>Sr where the different hyperfine structure manifolds have on the order of 10 states each. On the other hand, we know that the states  $|F, m_F\rangle$  transform into each other under rotations in physical space, which means that, from a coordinate-free perspective, we should really be able to describe the full F manifold with a single polarizability tensor  $\overline{\alpha}_F(\omega)$ . Moreover, by studying how tensors transform under rotation, we should be able to express the polarizability  $\alpha_{\mu\nu}(\omega; m_F)$  in a full coordinate representation for any  $m_F$ . The formal machinery by which we define these relations involves decomposing the tensor into its irreducible components under rotation (see, for example, [300]). To recap, any rank-2 tensor can be written as a sum of three components: a **scalar** component, which is isotropic and does not change under rotation, a **vector** component, which transforms like an axial vector (pseudovector), and a "**tensor**" component, which transforms like a (traceless, symmetric) quadrupole tensor.<sup>28</sup> For a state  $|F, m_F\rangle$  given a choice of quantization axis  $Q_\mu$ , the full polarizability tensor can then be written like [178, 301]:

$$\alpha_{\mu\nu}(\omega; m_F) = \alpha^{(S)}(\omega)\delta_{\mu\nu} + \alpha^{(V)}(\omega) \left(i\epsilon_{\mu\nu\sigma}Q_{\sigma}\right) \left(\frac{m_F}{F}\right) + \alpha^{(T)}(\omega) \left(\frac{3Q_{\mu}Q_{\nu} - \delta_{\mu\nu}}{2}\right) \left(\frac{3m_F^2 - F(F+1)}{F(2F-1)}\right), \tag{3.15}$$

where  $\epsilon_{\mu\nu\sigma}$  is the Levi-Civita symbol which essentially represents a cross product, and  $\alpha^{(S,V,T)}(\omega)$  are numbers which we call the **scalar, vector, and tensor polarizabilities** respectively. Note that  $\alpha^{(S,V,T)}(\omega)$  do not depend on  $m_F$ , implying that these three numbers are sufficient to calculate AC Stark shifts for any hyperfine sublevel and any field polarization. It even turns out that, when the driving field is much farther detuned than any hyperfine splitting, you can even relate polarizabilities for different hyperfine

Formally, this partitioning of the tensor reflects the decomposition of the space of rank-2 tensors into irreducible representations of SO(3):  $V^{(1)} \otimes V^{(1)} = V^{(0)} \oplus V^{(1)} \oplus V^{(2)}$ , where  $V^{(k)}$  represents the space of rank-k spherical tensors. They are called as such because they transform under rotations in the same way as the set of degree-k spherical harmonics.

State	$\alpha^{(S)}$ (813 nm)	$lpha^{(V)}$ (813 nm)	$lpha^{(T)}$ (813 nm)	Units
<sup>88</sup> Sr <sup>1</sup> S <sub>0</sub>	280(14) [302]	0	0	a.u.
$^{87}$ Sr $^{1}S_{0}$	280(14) [302]	$4.8(2) \times 10^{-5} [302]$	$1.57(8) \times 10^{-5} [302]$	a.u.
$^{87}$ Sr $^{3}P_{0}$	289(14) [302]	$1.91(10) \times 10^{-1} [302]$	$3.65(18) \times 10^{-4} [302]$	a.u.
$^{88}$ Sr $^{3}P_{1}$	290(40)(meas.)	-128(6) [303]	59(7) <sup>(meas.)</sup>	a.u.
$^{87}$ Sr $^{3}P_{1}$ , $F = 7/2$	290(40)(^)	100(5)(^)	27(3)(^)	a.u.
$^{87}$ Sr $^{3}P_{1}$ , $F = 9/2$	290(40)(^)	-23.3(1.2) <sup>(^)</sup>	-85(11) <sup>(^)</sup>	a.u.
$^{87}$ Sr $^{3}P_{1}$ , $F = 11/2$	290(40)(^)	-128(6) <sup>(^)</sup>	59(7) <sup>(^)</sup>	a.u.

Table 3.4: Table of polarizabilities for narrow-linewidth strontium transitions at 813 nm. All units are in "a.u.," or "atomic units," defined such that 1 a.u. =  $4\pi\epsilon_0 a_0^3$  where  $\epsilon_0$  is the vacuum permittivity, and  $a_0$  is the Bohr radius. Ground and clock state polarizabilities are taken from [302], with an assumed 5% uncertainty since the scalar polarizabilities for these two states should be the same at the magic wavelength condition (reflecting uncertainty in the oscillator strengths). Vector polarizabilities for the  $^3P_1$  transition are calculated using the table of oscillator strengths in [303], also with an assumed 5% uncertainty. Scalar and tensor for the  $^3P_1$  polarizabilities are derived from measurements of AC Stark shifts in our experiment, with precision limited by the quoted uncertainties of the absolute trap depth in Table 3.3. Finally, polarizabilities for the hyperfine states in  $^{87}$ Sr are calculated from the values in  $^{88}$ Sr using Eqs. (7.472) and (7.484) from Steck's *Quantum Optics* [178], assuming that the differences arise purely from hyperfine structure and not from isotope shifts between 87 and 88.

states in the same fine-structure manifold, as Steck shows for the tensor polarizability in Sec. 7.4.2.4 of *Quantum Optics* [178].<sup>29</sup>

Calculating the polarizabilities precisely can be a daunting task because it in principle requires knowledge of the dipole matrix elements for every possible atomic transition. Table 3.4 compiles my current best knowledge of polarizabilities on the ground and narrow-linewidth excited states in strontium. Many of these values come from theoretical calculations by other groups [302, 303], which should be trusted to the few percent level due to imperfect knowledge of oscillator strengths in strontium. I have empirically measured the scalar and tensor polarizabilities of  ${}^{3}P_{1}$  in our experiment by measuring AC Stark shifts of different  $m_{J}$  sublevels in  ${}^{88}$ Sr and then inferring the underlying polarizability tensor. Although measuring the AC Stark shifts themselves has fairly high (few percent) precision, ultimately the

<sup>&</sup>lt;sup>29</sup> Note that the version of Steck I used has a sign error in its expression for the large-detuning vector polarizability in Eq. (7.484), which I have fixed when calculating vector polarizabilities in Table 3.4. The sign in Eq. (7.472) is correct. I emailed Steck about it, so maybe in your version the sign will be fixed?

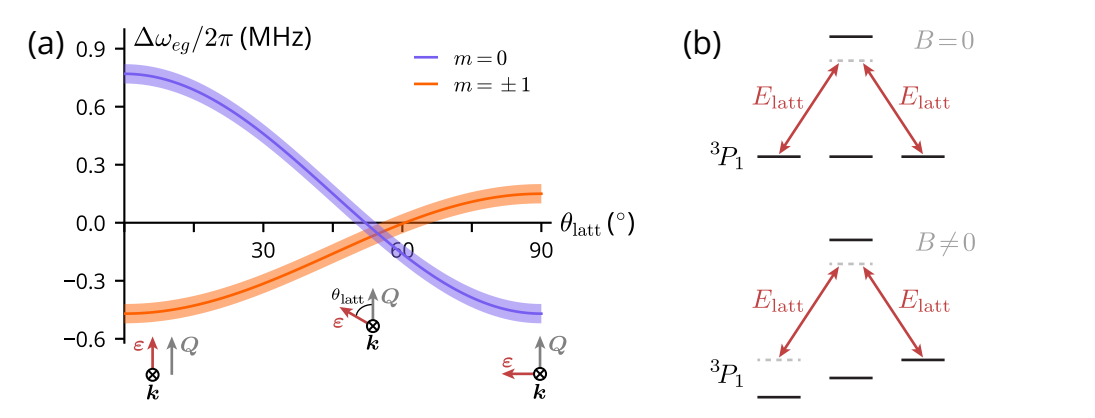


Figure 3.10: The magic angle condition for  ${}^3P_1 - {}^1S_0$  with 813 nm light. (a) The differential shift  $\Delta\omega_{eg}$  between excited and ground states along the  ${}^3P_1 - {}^1S_0$  transition for different angles  $\theta_{\text{latt}}$  between the 813 nm lattice polarization and the quantization axis, measured for a trap depth of  $U_0/\hbar = 2\pi \times 2.0(2)$  MHz in the ground state. Uncertainty bands reflect the uncertainty in the differential shift measured at  $\theta_{\text{latt}} = 0^{\circ}$ . A magic angle condition is attained when  $\Delta\omega_{\text{eg}} = 0$ , which is not guaranteed to occur at the same angle for all  $m_F$  levels. (b) A lattice polarization not parallel to the quantization axis can induce Raman transitions which lead to unwanted dynamics between sublevels, reflecting a limitation of the polarizability formalism. This dynamics can be suppressed by creating a sufficient energy separation between sublevels which overwhelms the Raman process, for instance by applying a large bias field.

quoted uncertainties come from imperfect knowledge of the ground state trap depth, which we used in deriving the polarizabilities.

## 3.5.5 A magic angle lattice

As we discussed in the previous section, the frequency shift an atomic state experiences from an AC electric field can depend on the field polarization. In some cases, it is possible to tune the polarization of the light in order to attain a so-called **magic angle** condition, analogous to a magic wavelength, in which the total AC Stark shift for some excited state sublevel  $|F_e, m_{F_e}\rangle$  is equal to the shift on the ground state. This is useful because it nulls out the lattice-induced inhomogeneous broadening mentioned in Sec. 3.5.3. In our experiment, we often perform this trick on the  ${}^3P_1 - {}^1S_0$  transition (see Ch. 5 and 6), so I will describe the technique and its limitations.

To start, let us fix a quantization axis Q and k-vector of the lattice light, where we will restrict to the condition that  $k \perp Q$  for simplicity. We'll also assume that the light has a linear polarization  $\varepsilon$  with an angle  $\theta$  from the quantization axis, such that  $Q \cdot \varepsilon = Q_{\mu} \varepsilon_{\mu} = \cos \theta$ . Then, using Eq. (3.14) and Eq. (3.15),

the total AC Stark shift is given by:

$$\Delta U = -\frac{1}{4} \left( \alpha^{(S)}(\omega) + \alpha^{(T)}(\omega) \left( \frac{3\cos^2 \theta - 1}{2} \right) \left( \frac{3m_F^2 - F(F+1)}{F(2F-1)} \right) \right) |E|^2. \tag{3.16}$$

Notice that the vector shift is 0, which is always true for linearly polarized light. Fig. 3.10(a) shows the differential AC Stark shift between excited and ground states along the  ${}^3P_1 - {}^1S_0$  transition with our 813 nm lattice, measured with the trap depth quoted in Table 3.3. We see that, for a lattice angle of  $\theta_{\text{latt}} = 51(3)^{\circ}$ , we predict a magic angle condition along the m = 0 transition, consistent with the values we use in later chapters.

However, there is a caveat to the magic angle condition. As illustrated in Fig. 3.10(b), a lattice whose polarization is not parallel to the quantization axis can induce Raman transitions between sublevels within a fine (or hyperfine) manifold. This is a problem if you are trying to induce frequency shifts on a two-level system in the atom and don't want population to leak into auxiliary states. Why weren't we warned about this possibility from the polarizability calculations? Essentially, it's because we were calculating AC Stark shifts on the initial state without considering the possibility of resonant couplings, one-photon or two-photon. We can account for these effects by first writing down the lattice shifts with the lattice polarization parallel to the quantization axis and then rotating the coordinate system (thereby rotating the quantization axis). As an example, let us consider the  $^3P_1$  state in  $^{88}$ Sr. When the lattice polarization is aligned with the quantization axis, we can write down an effective diagonal Hamiltonian describing the AC Stark shifts:

$$\hat{H}(\theta = 0^{\circ}) = \begin{pmatrix} U^{(S)} + U^{(T)} & 0 & 0 \\ 0 & U^{(S)} - 2U^{(T)} & 0 \\ 0 & 0 & U^{(S)} + U^{(T)} \end{pmatrix} \qquad |m = 1\rangle |m = 0\rangle \qquad (3.17)$$

where  $U^{(S,T)} := -\frac{1}{4}\alpha^{(S,T)}|E|^2$  are the scalar and tensor light shifts.

To rotate the quantization axis by  $\theta$ , we simply change our basis by mapping  $|\psi\rangle \to \hat{R}_n(-\theta)|\psi\rangle = e^{i(\hat{J}\cdot n)\theta}|\psi\rangle$ , such that the components of our wavefunction now correspond to  $m_F$  states in the rotated basis. The Hamiltonian then transforms like  $\hat{H} \to \hat{R}_n(-\theta)\hat{H}\hat{R}_n(\theta)$ . As an example, let us consider a

rotation by  $90^{\circ}$  about an axis orthogonal to Q:

$$\hat{H}(\theta = 90^{\circ}) = \begin{pmatrix} U^{(S)} - \frac{U^{(T)}}{2} & 0 & -\frac{3U^{(T)}}{2} \\ 0 & U^{(S)} + U^{(T)} & 0 \\ -\frac{3U^{(T)}}{2} & 0 & U^{(S)} - \frac{U^{(T)}}{2} \end{pmatrix} \qquad |m = 1\rangle$$

$$(3.18)$$

We see that, as illustrated in Fig. 3.10(b), a lattice polarization orthogonal to the quantization axis induces Raman couplings between the  $m = \pm 1$  states. The diagonal elements of this matrix correspond to the lattice shifts predicted by our polarizability calculations, but the off-diagonal terms are not considered. Fortunately, in some cases it is possible to mitigate this issue. If you apply a large bias field along the preferred quantization axis direction, it creates large detunings between the different  $m_F$  sublevels, pushing any Raman couplings off resonance. Intuitively, this bias field "enforces" the quantization axis by making its basis of  $m_F$  states the right eigenstates for the system. However, if you are running an experiment where the states need to be degenerate, this strategy is not viable, and the only way to avoid these couplings altogether is to use a polarization parallel to the desired quantization axis.

# 3.6 The reference cavity

Up to this point, I have described several laser systems designed to address specific atomic transitions, as well as our science cavity which needs to be on or close to resonance with those transitions. Ensuring these objects stay at their intended frequencies requires a frequency reference, but so far I have only described how we stabilize our 461 nm laser (through a modulation transfer spectroscopy lock; see Sec. 3.3.4). The remaining lasers are all locked to a stable reference cavity, which I will now describe.

Our reference cavity (sometimes we shorten this to "rCav" to distinguish it from our science cavity, or "sCav") was purchased from Stable Laser Systems (part no. SLS-6010-1-4bore) in 2015. The cavity consists of a 10 cm long ULE (ultralow-expansion glass) spacer with 10 mm diameter bore holes drilled through it and mirrors attached to either end of the bores to form optical cavities. As the part number suggests, there are four such bores in the cavity, allowing us to lock multiple lasers along different optical pathways.<sup>30</sup> The cavity is plano-concave, with a 50 cm radius of curvature for the concave mirror,

<sup>&</sup>lt;sup>30</sup> While this is convenient, we could likely work just as well with a single-bore cavity using a combination of beamsplitters, dichroics, and polarization control to send many laser beams into the same cavity. I have also heard that the single-bore design is more stable, but I don't have any data for this.

Description	Symbol	<b>689 nm</b> [ <sup>3</sup> P <sub>1</sub> ]	<b>698 nm</b> [ <sup>3</sup> P <sub>0</sub> ]	813 nm	Units
Free spectral range	$\omega_{ m FSR}/2\pi$	1.4960(5) <sup>(meas.)</sup>	1.50 <sup>(v)</sup>	1.4961(2) <sup>(meas.)</sup>	GHz
Cavity length	L	10.020(3)(^)	10 <sup>(spec.)</sup>	10.0191(13)(^)	cm
FWHM linewidth	$\kappa/2\pi$	113.2 <sup>(^V)</sup>	79.3 <sup>(^V)</sup>	55.39 <sup>(^V)</sup>	kHz
Cavity finesse	${\mathcal F}$	13200 <sup>(V)</sup>	18900 <sup>(V)</sup>	27000 <sup>(v)</sup>	-
Mirror transmission	$T_m$	238(*)	166 <sup>(*)</sup>	116 <sup>(*)</sup>	ppm
Mode waist	$w_0$	210 <sup>(∨)</sup>	211 <sup>(v)</sup>	228 <sup>(v)</sup>	$\mu\mathrm{m}$
Rayleigh length	$z_R$	20 <sup>(spec.)</sup>	20 <sup>(spec.)</sup>	20 <sup>(spec.)</sup>	cm

Table 3.5: Reference cavity parameters for relevant wavelengths/transitions in strontium. Mirror losses are assumed to be negligible, but we could test this by directly measuring the cavity linewidth.

resulting in a reasonable ~200  $\mu$ m waist located at the flat mirror. Generally, we send light in through the concave mirror, so a beam which couples optimally to the cavity mode should be slighty converging towards a focus on the back of the cavity. Table 3.5 lists our knowledge of the reference cavity parameters.

What makes our "stable" reference cavity stable? First, ULE has a small coefficient of thermal expansion at room temperature; moreover, there is usually a "zero-crossing" temperature where the coefficient crosses through zero and length changes are quadratically suppressed. On top of this, the cavity is kept under a  $\sim 10^{-8}$  torr vacuum with an ion pump and temperature controlled to further suppress any thermal drifts in the cavity resonance. The cylindrical ULE spacer sits on top of Viton balls to isolate against mechanical perturbations, within an Invar "cradle" which registers the cavity's position and prevents it from rolling. As a result, we generally trust the cavity to be both mechanically and thermally stable. The main limitation in the stability of the reference cavity is an observed long-term drift in the cavity resonances, at the rate of a few kHz per day. We believe this to be due to slow relaxation processes

<sup>(</sup>meas.) Measured in lab

<sup>(</sup>spec.) Derived from the quoted mirror specs

<sup>(\*)</sup> From Advanced Thin Films coating spec sheet

<sup>(</sup>A) Derived from above quantities

<sup>(</sup>V) Derived from below quantities

<sup>&</sup>lt;sup>31</sup> However, the spacer could potentially slide forwards or backwards in this cradle. In 2024, when we moved the reference cavity to its current position on the optical table in the middle of X1B21, we made great pains to ensure that the cradle would remain level and not allow the spacer to slide.

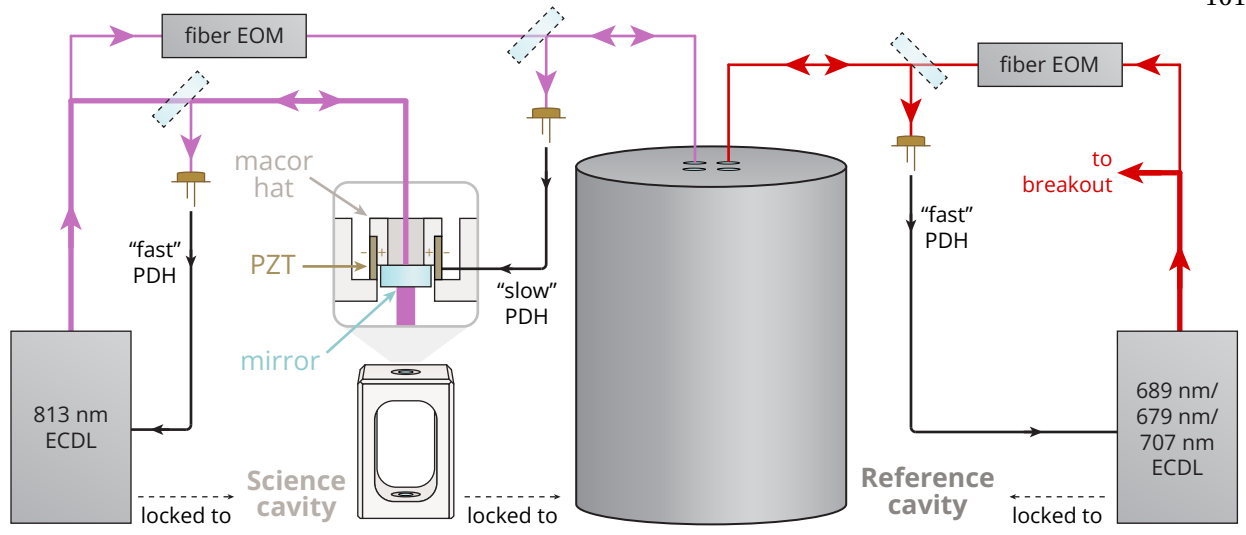


Figure 3.11: Locking pathways to the science cavity and the reference cavity. The red lasers (689 nm, 679 nm, and 707 nm, with the capability to lock 688 nm as well) are stabilized to the reference cavity (rCav) through a PDH lock. Since these lasers need to shine at specific frequencies tied to atomic transitions, the locking light is sent through a fiber EOM to generate an FM sideband at the nearest rCav resonance. The 813 nm laser is locked directly to the science cavity (sCav) with a high-bandwidth PDH lock in order to have a stable optical lattice. The sCav resonances are prone to drift due to thermal or mechanical fluctuations, and they need to be stabilized relative to the atomic transitions in strontium to perform cavity QED experiments. To accomplish this, we send 813 nm light through a fiber EOM to generate an FM sideband at the nearest rCav resonance and generate a PDH error signal. This signal then actuates the sCav piezos, feeding back on the cavity length and thus stabilizing the sCav to the rCav. Since the piezos have resonances at 9 kHz, the bandwidth of this lock is low at the ~100 Hz scale.

in the ULE spacer (since it is a glass and not a crystal). This is not a big deal on the day-to-day timescale, but keep in mind that over the course of a year, any lasers locked to the reference cavity could drift by as much as 1 MHz. This matters for the 689 nm laser in particular, which drives a narrow-linewidth transition and so could drift off resonance if working with low Rabi frequencies. To compensate for this drift, we have historically tuned an EOM frequency in the locking chain (see Fig. 3.11).<sup>32</sup>

Locking our red lasers to the reference cavity is fairly straightforward, as shown on the right side of Fig. 3.11: we generate a PDH error signal in reflection off the cavity (see Ch. 2.2.3 for a refresher on PDH locks) and use it to actuate the laser current, thereby stabilizing the frequency. The bandwidths of these locks tend to lie between 100 kHz and 1 MHz, limited mostly by path length delays between the

<sup>&</sup>lt;sup>32</sup> This is also a good way to check the current drift rate of the reference cavity, which we have observed to be slower than originally reported by Matt. Perhaps the drift is slowing over time as internal stresses in the glass settle?

lasers and the reference cavity. For 679 nm and 707 nm, we don't care so much about having a tight lock since these lasers address MHz-linewidth transitions, and the lasers currently sit quite far away from the reference cavity (for a round trip path length around ~25 m). We care more about the 689 nm laser since it addresses a narrow-linewidth transition, and so this laser sits next to the reference cavity (for a round trip path length closer to ~5 m). Since these lasers need to address well-defined frequencies corresponding to their respective atomic transitions, we pass the locking light through a fiber EOM. By sending the proper modulation frequency into the fiber EOM, we can stabilize the ECDL frequency with an RF sideband on resonance with the reference cavity and the carrier frequency close to the atomic transition.

We also stabilize the science cavity (sCav) to the reference cavity (rCav) as well, but since the sCav does not generate laser light, we need a more complicated locking chain compared to the red laser stabilization setups. To accomplish this, we use the 813 nm laser as a bus to send information about the sCav resonance to the rCav, as shown on the left side of Fig. 3.11. First, we lock the 813 nm laser to the sCav in the same way that we lock our red lasers to the rCav: using a moderately high-bandwidth PDH lock. Independent of locking the sCav resonance, this is necessary for us to stabilize the power of our 813 nm optical lattice, which strongly depends on the laser being on resonance with the cavity mode. In a separate pathway, we pass 813 nm light through a fiber EOM to generate FM sidebands at some tunable modulation frequency. By generating a PDH error signal off one of the sidebands and using this signal to actuate the piezo tubes on the sCav, we can stabilize the sCav length. We observe mechanical resonances in the piezo-hat-mirror assemblies (see Fig. 3.11) at around 9 kHz, limiting the bandwidth of this "slow" lock to the ~100s of Hz range.

The tunable modulation frequency sent to the fiber EOM allows us to move the sCav resonances to the desired detuning condition from our atomic transitions. Although in principle, our locking scheme should exactly stabilize the sCav length, empirically we notice that resonances near 689 nm (and presumably 698 nm as well) appear to drift slowly even while in lock. This is despite the fact that the in-lock error signal for the sCav-to-rCav lock does not appear to substantially move away from zero. I have talked with Leon Lu from Dan Stamper-Kurn's cavity microscope experiment (E6), and he also notices this issue in their cavity (locked at 1560 nm, with drifts observed at 780 nm). Their leading theory is that

their 1560 nm and 780 nm lasers experience different penetration depths in their sCav mirrors, and so the length stabilized by their 1560 nm laser is not the same length experienced by their 780 nm laser. When the sCav experiences thermal drifts, the 780 nm cavity length can therefore change (albeit at a suppressed rate), shifting the resonances.

Is this theory plausible? Empirically, I have observed shifts in the 689 nm cavity resonances at the 100 kHz level in our experiment over the course of a couple of hours, which I estimate can correspond to a 1°C temperature change arising after turning on the MOT coils and water cooling stages. Assuming the cavity mirrors have a thermal expansion coefficient of  $10^{-6}$  °C<sup>-1</sup> (fractional length change), this requires the difference in cavity length between our 689 nm and 813 nm of around  $\Delta L \approx 10~\mu\text{m}$ . Mirror coatings for many ultrahigh reflectivity mirrors rely on dielectric stacks of alternating low- and high-index materials, with 20-50 layers each of quarter-wave [304, 305] or near-quarter-wave [306, 307] thickness. If we assume our cavity mirrors are similar, then the light could see as much as 15  $\mu$ m of effective cavity length inside the mirror coatings. Based off this, the theory of different pentration depths as a mechanism for the observed resonance drift is on the edge of plausible.<sup>33</sup> We could test this by measuring the free spectral range of our science cavity at 813 nm and 689 nm at the same time: a difference of 1 MHz would be sufficient to explain the drifts.<sup>34</sup>

#### 3.7 Homebuilt interference filter ECDLs

Many of the lasers in our experiment were built by members of the lab, rather than purchased from a company. The primary motivation for doing so is to cheaply construct lasers with low phase noise. Although we could splurge ~\$100,000 on a narrow-linewidth fiber laser from PreciLasers or an equivalent company, an affordable alternative is the **external cavity diode laser (ECDL)**, which consists of a single-mode laser diode placed inside a weak optical cavity. Since these lasers are fairly simple, our goal was to learn how to construct them ourselves and optimize them for narrow-linewidth operation.

<sup>&</sup>lt;sup>33</sup> The reference cavity does not see a significant different in FSR between 689 nm and 813 nm, as shown in Table 3.5. However, this could be because the rCav has similar reflectivities for these two wavelengths, and the sCav does not. It seems reasonable to guess that different reflectivities could have different penetration depths.

<sup>&</sup>lt;sup>34</sup> We don't see this for the reference cavity, but you could argue that the order or magnitude different finesse values for 689 nm and 813 nm in the science cavity is responsible for the different penetration depths into the cavity mirrors, and the reference cavity does not share this difference in finesse.

In some cases, we have succeeded tremendously, but there is still a lot we don't know about why certain lasers seem to be narrower than others. In this section, I'll discuss the history of our lab's ECDL design and our current knowledge about the resulting lasers.

In particular, we have focused on interference filter ECDLs (IF-ECDLs), first developed in 2006 [308] and explained in detail in this review paper [309]. The essential features of such a design are twofold: first, inside the cavity is an interference filter, which is essentially a narrow-line bandpass filter where the passband is tunable based on the light's angle of incidence. This object provides a sharp frequency-selective edge in the composite gain medium of the ECDL, which helps ensure single-mode operation. Importantly, rotating the interference filter to change the laser frequency does not substantially change the alignment of the laser path. By comparison, an alternative ECDL design using a diffraction grating in the "Littrow" configuration [310, 311] experiences a change in alignment when rotating the diffraction grating, although a clever design can mitigate these effects [312]. Second, in an IF-ECDL, the light is focused with a lens onto a partial retroreflector, which provides optical feedback onto the diode. The retroreflector also acts as an output coupler, since it is partially transmissive. This focusing and direct retroflection is often called a "cateye configuration," making an analogy to the way light reflects inside a cat's eyes to improve their night vision (which is what makes their eyes glow at night). A benefit of these features are built-in mechanical robustness. Because the output coupler is positioned at a focus, which has a large angular spread, alignment is robust against small angular displacements of the output coupler. Additionally, rotating the interference filter leads to only a small positional displacement compared to the (typically) large beam size at the filter, so tuning the laser wavelength does not misalign the cavity. This is not the case in diffraction grating ECDLs, whose alignment is typically sensitive to tuning the grating angle and therefore often see large spikes in their frequency noise spectrum around mechanical resonances [309].

Fig. 3.12(a) shows a CAD model of our lab's design (made by then-postdoc Vera Schäfer for a 689 nm IF-ECDL on the ring cavity experiment). First, we place a single-mode (ideally AR coated) diode into a homebuilt diode mount, which is temperature-controlled using a thermistor glued onto the side of the mount (the central hole) and a Peltier cooler (between the mount and the laser base). The light

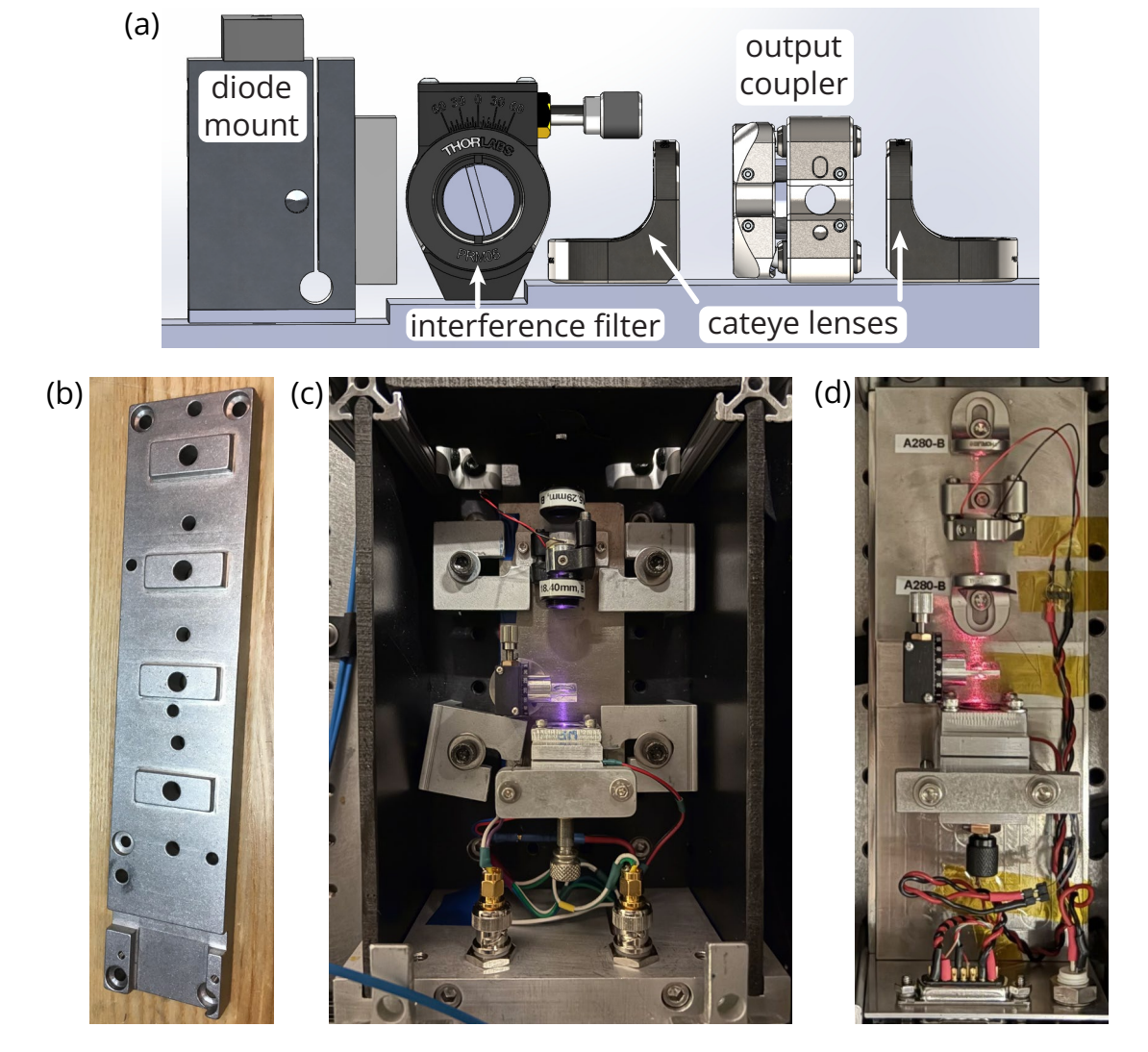


Figure 3.12: Interference filter ECDL (IF-ECDL) design and implementation. (a) CAD model of the strontium ring cavity experiment 689 nm IF-ECDL, courtesy of Vera Schäfer, showcasing the generic design. A laser diode (ideally AR coated) is placed in a temperature-controlled mount with an aspheric lens for collimation. The light passes through an interference filter, i.e., a narrow-line bandpass filter, which is tuned to the proper angle to provide sharp frequency selectivity near the desired wavelength. A pair of lenses focus the light down to a small spot and then re-collimate outside the ECDL. At the focus, we place our output couplter: a cateye retroreflector which partially transmits and partially reflects the light directly back towards the diode. (b) The laser base for my first IF-ECDL, now part of the ring cavity experiment's 813 nm laser. The multiple holes allowed us to compare the laser's performance with different cavity lengths. (c) Image of our 813 nm IF-ECDL, constructed by me in 2019. This laser has a titanium base which is not actively temperature controlled since its coefficient of thermal expansion is three times smaller than aluminum. The lavender scatter on the laser base is 813 nm light, which can be imaged on my smartphone (iPhone 16) because the phone's CMOS sensors are sensitive to NIR. (d) Image of our 689 nm IF-ECDL, constructed by Eric Song in 2024. This laser base is made of Invar, which is even less prone to thermal expansion and also is not actively temperature controlled.

is collimated using an asphere (front plate of the diode mount). Then, it passes through an interference filter, mounted on a Thorlabs precision rotation mount (part no. PRM05) which provides a fine control knob for the filter angle. Our output coupler is a partially reflective beamsplitter plate, often with 30% reflectivity, and an AR-coated back face which ideally should be wedged to minimize unwanted optical feedback from this surface. The output coupler is mounted on a three-axis kinematic mount, allowing us to align the output coupler to the diode, along with a piezo to lock the ECDL frequency to some external frequency reference. Surrounding the output coupler is a pair of aspheres, usually with a focal length between 10-20 mm, in fixed mounts. All of these elements sit on a monolithic laser base, which may or may not be temperature controlled.

This design originated from then-undergraduate Ben Johnston in Adam Kaufman's group, who built an IF-ECDL in 2018 designed to operate at 698 nm. The first laser we wanted to build in our lab was an 813 nm laser for the strontium ring cavity experiment, which was assigned to me in 2018. I copied many of the elements of Ben's design but replaced his diode mount with a design commonly used in our lab. This design, created by Matt and later adapted by Julia, provides a knob for controlling the diode collimation and also places a thermistor very close to the diode, enabling a temperature control loop with minimal delay times. Additionally, Ben's laser had a cavity length close to 5 cm. I wanted to test longer cavity lengths, under intuition from the Schawlow-Townes linewidth that longer cavities could provide narrow linewidths. Fig. 3.12(b) shows the base I machined for this laser, which was made of aluminum and designed to be temperature-controlled separate from the diode mount. The base allowed us to test four different cavity lengths: 4.9 cm, 8.3 cm, 11.6 cm, and 15.0 cm. From our tests, I found that longer cavity lengths indeed decreased the free-running laser linewidth, but the mode-hop-free tuning range also decreased. We decided to compromise and work at the 8 cm cavity length, which was copied by all subsequent lasers in our lab.

Since these tests, we have built several IF-ECDLs across both strontium experiments. For the standing-wave cavity experiment, we currently have two lasers: an 813 nm IF-ECDL built by me in 2019

<sup>&</sup>lt;sup>35</sup> The measured mode-hop-free tuning ranges were (from shortest to longest) 12.2 GHz, 5.0 GHz, 1.8 GHz, and 1.3 GHz, measured with an optimized feedforward ratio between the ECDL current and piezo voltage.

(Fig. 3.12(c)), and a 689 nm IF-ECDL built by Eric in 2024 (Fig. 3.12(d)). The two designs are functionally similar, with some minor differences including the specific diodes and optics used. The 813 nm laser uses an Eagleyard AR-coated diode (part no. EYP-RWE-0840-06010-1500-SOT02-0000, serial no. AC-03921) and a 3 mm thick Iridian bandpass filter (part no. MI000002) with a 3.1 nm bandpass, centered at 813 nm for an angle of incidence (AOI) of 15°. The output coupler is a 30% reflectivity plate from Thorlabs (part no. BSS05), which is 3 mm thick and has a 30 arcminute wedge on the back face. Finally, the base is machined out of titanium and is not temperature controlled. Titanium has a thermal expansion coefficient of  $8.6 \times 10^{-6}$  °C<sup>-1</sup>, about three times smaller than aluminum, partially justifying the lack of temperature control. The 689 nm laser uses an AR-coated diode from Sacher (part no. SAL-0690-025, serial no. 6738-217) and a 1 mm thick Iridian bandpass filter (part no. GX000007) with a 0.3 nm bandpass, centered at 685 nm for AOI of 15°. The output coupler is a 30% reflectivity plate from Thorlabs (part no. BSS11R), which is also a 30% reflectivity plate from Thorlabs. Finally, the base is machined out of Invar and is not temperature controlled. Invar has a much lower thermal expansion coefficient of  $1.2 \times 10^{-6}$  °C<sup>-1</sup>, so we don't expect the base length to change too much from thermal drifts.

## 3.7.1 Laser linewidth measurements

Seeing as part of our goal in building these homebrew lasers was to minimize the laser frequency noise, we have on multiple occasions attempted to measure the frequency noise of these objects. Unfortunately, these measurements have historically been very inconsistent. Part of the issue is that frequency noise is not straightforward to measure. A naive attempt might be to look at the power spectral density (PSD) of the laser light through, say, a heterodyne measurement. However, the resulting spectrum represents a convolution of the two lasers, so unless one is substantially lower-noise than the other then the signal can be difficult to interpret.

Our first attempt was back in 2019 when characterizing the 813 nm IF-ECDL made for the ring cavity experiment. The method at the time was to lock the laser to our science cavity with a low bandwidth and measure the PSD of the in-lock error signal, which I will call  $S_V(f)$ . The error signal acts as a frequency-to-voltage ("f-to-V") converter, so combined with a calibration of the error signal slope, the

resulting spectrum is directly proportional to the frequency noise PSD, or  $S_f(f)$ . At the time, we were primarily interested in the frequency noise with an offset from carrier around 400 kHz because this was where we expected parameteric heating to occur in the ring cavity. We measured the frequency noise in this band to be dominated by white frequency noise, contributing to a Lorentzian linewidth of around 130 Hz. This linewidth was substantially lower than expected, to the point of suspicion; however, empirically we found that forming an optical lattice with this laser led to science cavity lattice lifetimes 16 times longer than our Littrow-configuration 813 nm laser (then in use on our experiment), when subtracting out the background vacuum lifetime. This was clear evidence that, even if we didn't trust the absolute value of our Lorentzian linewidth measurement, the newly-built IF-ECDL was substantially lower noise than our diffraction grating laser.

Another method to estimate the Lorentzian linewidth of a laser is to beat it with a second laser, ideally a copy of itself. As explained earlier, beating two lasers together and measuring the result on a heterodyne detector provides a measurement in frequency space which is the convolution of the two individial lasers' lineshapes:  $S_{E_{tot}}(f) \sim S_{E_1}(f) * S_{E_2}(f)$ . If one of the lasers is much narrow than the other, then its lineshape effectively looks like a  $\delta$ -function, and the convolution returns the original lineshape of the noisier laser. Otherwise, both lasers contribute to the total lineshape. In the special case of two Lorentzian lineshapes, the combined lineshape will also be a Lorentzian with a FWHM linewidth equal to the sum of the component lineshapes. This allows us to place an upper bound on the Lorentzian linewith of each individual laser.<sup>37</sup> In 2021, Zhijing Niu (a current graduate student on the ring cavity experiment) and I set up a beat note between the two 813 nm IF-ECDLs that I made. From the analysis, we measured a composite lineshape with an estimated Lorentzian linewidth of 1.8 kHz. Assuming each laser has the same noise properties, that would imply a 900 Hz Lorentzian linewidth for each laser. This was seven times larger than my previous measurement, which was a bit disheartening.

 $<sup>^{36}</sup>$  In the specific case of white frequency noise, i.e.,  $S_f(f) = h_0$  is contant, the laser lineshape will be a Lorentzian with a full-width at half-maximum (FWHM) linewidth equal to  $\Delta f_{\rm FWHM} = \pi h_0$  [313]. Note that the laser lineshape represents the PSD of the electric field, sometimes referred to as  $S_E(f)$ , which is *not* equivalent to the frequency noise  $S_f(f)$  (although the two are related).

<sup>&</sup>lt;sup>37</sup> Real lasers are not perfect Lorentzians since they usually have more than just white frequency noise. However, usually a laser's frequency noise will approach a white noise floor for sufficiently large detunings from the carrier frequency, so we should still be able to estimate the Lorentzian linewidth by looking at these large frequency noise sidebands.

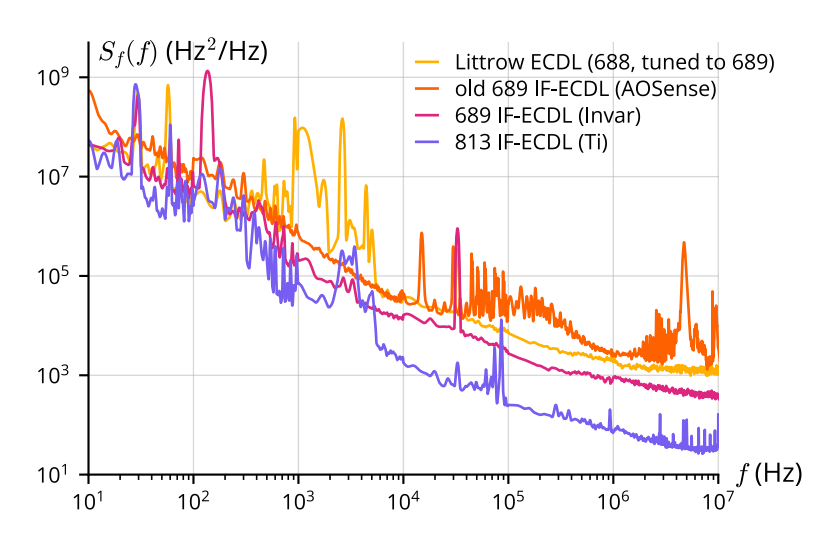


Figure 3.13: Frequency noise power spectral density measurements of 689 nm and 813 nm ECDLs, in units of  $Hz^2/Hz$ . All measurements are taken with the OEWaves phase noise analyzer and smoothed with a Hann window (21 point width).

More recently in 2023, we gained access to an optical phase noise analyzer from OEwaves (part no. OE4000), purchased by the Kaufman and Ye groups. We believe that this device performs delay-line interferometry on the input light, which essentially involves beating the laser against itself but with a large path length delay between the two arms of the interferometer. Independently, a graduate student from Dan Blumenthal's group at UCSB named Andrei Isichenko visited our lab to discuss and test a new laser technology<sup>38</sup> with the rubidium matterwave interferometry experiment. As part of his test equipment, he brought a home-built delay-line interferometer which we believe essentially performs the same measurement as the OEwaves device. He was gracious enough to measure the frequency noise of our 813 nm IF-ECDL and our old 689 nm ECDL (before building the new IF-ECDL in 2024, we had an IF-ECDL from AOSense which had a cavity length of ~4 cm). His agreements agreed with the measurements from OEwaves, which suggests that the results are at least reproducible and somewhat more trustworthy.

Fig. 3.13 shows a comparison of the frequency noise spectra for four lasers: a home-built diffraction grating ECDL in the Littrow configuration, normally used for 688 nm light but tuned to 689 nm for the measurement; the old AOSense IF-ECDL at 689 nm; the new homebuilt 689 nm IF-ECDL; and the homebuilt 813 nm IF-ECDL. All of the lasers were measured in a free-running mode, not frequency-

<sup>&</sup>lt;sup>38</sup> Two technologies, actually: a "self-injection lock" laser and a "stimulated Brillouin scattering" laser.

stabilized to anything. There are several interesting takeaways from this data. First, the AOSense 689 nm laser actually has worse high-frequency noise (say, above 100 kHz) than the Littrow laser, with a large spike between 4.5-5 MHz. I have personally observed this spike manifested as noise sidebands on the old 689 nm laser lineshape, for example when sweeping the laser across our science cavity and looking at the frequency-dependent transmission. The new 689 nm IF-ECDL has lower high-frequency noise by a factor of at least 3 compared to the AOSense laser, and by a factor of 2 compared to the Littrow laser. The 813 nm IF-ECDL has an order of magnitude less frequency noise than all of the other lasers, despite the strong similarities in its design. We don't know why this might be, other than some quirk of the diodes we use.<sup>39</sup>

Additionally, we generically expect that at sufficiently large offsets from carrier, the frequency noise asymptotes to a horizontal line, representing the background white frequency noise. This can be seen in the Littrow ECDL above about 1 MHz. If the frequency noise approaches  $S_f(f) \rightarrow h_0$  for some constant  $h_0$  with units of  $Hz^2/Hz$ , then we can back out a Lorentzian (or "instantaneous") linewidth of  $\Delta f_{\rm FWHM} = \pi h_0$ . For the Littrow laser, this implies a Lorentzian linewidth of less than 5 kHz, which is lower than expected. Interestingly, neither of the two homebuilt IF-ECDLs seem to settle to a constant value until, maybe, around 10 MHz. If we use the 10 MHz freuqency noise value as the white frequency noise background, it implies Lorentzian linewidths of 1.3 kHz and 100 Hz for the 689 nm and 813 nm lasers respectively, consistent with my 2019 measurmeent of the 813 nm linewidth but significantly lower than what we thought was feasible.

I should note, however, that the Lorentzian linewidth is not always the relevant measure of frequency noise for our applications. For the 813 nm laser, we want low phase noise at twice the lattice trap frequency to avoid parametric heating (see Sec. 3.5.2). For our typical trap frequencies, this process occurs at around 330 kHz offset from carrier, which experiences a factor of four more frequency noise (out of lock) than at 10 MHz. For the 689 nm laser, we care about noise in a broader bandwidth. For example,

<sup>&</sup>lt;sup>39</sup> One idea that could be interesting to test is varying the output power of each diode. The Eagleyard 840 nm diode is rated to output up to 100 mW of power, and the Sacher 690 nm diode only outputs up to 25 mW (15 mW in practice). The Schawlow-Townes linewidth scales inversely with power, so perhaps the 813 nm laser would have a larger linewidth if we turned down the power?

when sweeping this laser across our science cavity to perform a vacuum Rabi splitting measurement, we typically sweep across the cavity resonance in ~100  $\mu$ s. Frequency noise slower than a 10 kHz offset from carrier can change the position of this laser from shot to shot, which necessitates a high-bandwidth servo loop to reduce the frequency noise in this band. Alternatively, when performing heterodyne measurements with the 689 nm laser to look at MHz-scale dynamics as in Ch. 6, frequency noise up to a MHz offset from carrier determines our signal-to-noise ratio. In general, the Lorentzian linewidth is a good starting place. For a characterization of the phase noise on top of the white frequency noise background, analysis tools like the  $\beta$ -separation line [314] and the  $\chi$ -separation line [315] can be helpful in describing the effective laser linewidth and the effects of a servo on noise reduction. However, for a precise statistical understanding about the role of noise on a measurement, you should always consider the specifics of your experimental setup.

## Chapter 4

# Cavity-QED measurements of the <sup>87</sup>Sr millihertz optical clock transition and determination of its natural linewidth

#### 4.1 Introduction

Ultranarrow-linewidth optical transitions have emerged as the new standard for precision optical metrology, providing fast phase evolution, long coherence times, and intrinsic insensitivity to key environmental perturbations that have allowed remarkable fractional accuracy at the  $10^{-19} - 10^{-18}$  level [98, 101, 299, 316–322]. They have a wide range of potential applications for fundamental physics, such as gravitational wave detection using matter-wave interferometry or dark-matter searches [323–330], quantum many-body physics [331–334][95, 108]<sup>[G]</sup>, novel cavity QED applications for superradiant lasing [95, 223]<sup>[G]</sup>, and spin squeezing on an optical clock transition [72, 73].

The value of the fundamental intrinsic linewidth for these ultranarrow clock transitions is important for understanding the ultimate limits on quantum coherence offered by various atomic transitions and species. However, a precise determination of these linewidths is, in general, challenging when the natural lifetime of the excited state surpasses 100 s, which can occur in several atomic species [103, 335-341]. This is because various competing processes can preclude the observation of the natural excited state lifetime, such as black-body radiation-induced decay [102, 103] or scattering due to optical lattice light used to trap the atoms [104-106], preventing the application of standard population decay techniques to determine their lifetimes. For example, as of 2021, state-of-the-art optical lattice clocks have only demonstrated coherence up to  $\sim 10 \text{ s}$  [98, 105, 106] which is limited mostly by Raman scattering of the lattice light off an excited state [106] (since 2022, working at extremely shallow lattices in Wannier-

Stark clocks has extended this coherence time to 30 s [101, 125, 299]). In fact, most of the systems where these long excited state lifetimes have been precisely measured consist of atoms trapped without optical potentials, such as magnetic or ion traps [103, 335–341], and in some non destructive detection has been performed [342].

A particular transition of interest is the  ${}^1S_0 - {}^3P_0$  transition in  ${}^{87}$ Sr. As of 2021, the two reported values for the  ${}^3P_0$  excited state lifetime are  $\tau = 330(140)$  s from Ref. [104] obtained from population decay measurements from excited metastable states, and  $\tau = 145(40)$  s from Ref. [107] obtained from effective atomic models and measurements of differential Landé g-factors between ground and excited clock states, while ab-initio calculations estimate a lifetime between 110-130 s [343, 344]. With the implementation of new potential landscapes for operating with reduced lattice-induced scattering [106, 346, 347] that can suppress these effects, and with reference optical cavities whose coherence times start to approach the minute time scale [348–350], the full enhancement of these ultranarrow optical transitions can be achieved.

In this chapter, we present a series of cavity-enhanced spectroscopic measurements directly on the  $^{87}$ Sr clock transition which allow us to directly determine the natural lifetime of the excited clock state  $^3P_0$  ( $|e_0\rangle$ ). Our technique consists of precisely and simultaneously measuring the *ratio* of single-photon Rabi frequencies along two optical transitions—the millihertz transition ( $^1S_0 = |g\rangle \rightarrow ^3P_0 = |e_0\rangle$ ) and the 7.5 kHz transition ( $^1S_0 \rightarrow ^3P_1 = |e_1\rangle$ )—using a common atomic ensemble inside an optical resonator. These single-photon Rabi frequencies, denoted by  $2g_{0,1}$  for light-matter coupling strengths along the millihertz and 7.5 kHz transitions respectively, depend on the electric dipole moment of the atoms along with well-known and independently characterized geometric factors [180], such as the cavity's mode waist (w) and length (L). The natural linewidth  $\gamma_0$  can then be linked to the known natural linewidth  $\gamma_1$  from the measured coupling strength ratio as:

$$\frac{\gamma_0}{\gamma_1} = \left(\frac{L_0}{L_1}\right) \left(\frac{w_0}{w_1}\right)^2 \left(\frac{\omega_{A0}}{\omega_{A1}}\right)^2 \left(\frac{g_0}{g_1}\right)^2,\tag{4.1}$$

<sup>&</sup>lt;sup>1</sup> Since the result described in this chapter, a new measurement of the linewidth was released with a higher precision by estimating the dipole matrix element from measurements of the Rabi frequency [345]. This result conflicts with our measurement in this chapter and should be addressed.

where  $\omega_A$  is the (well-known) atomic transition frequency. Note that, for this manuscript, we generically use subscripts 0 and 1 to denote quantities for the clock transition (with wavelength  $\lambda_0=698.44$  nm) and the 7.5 kHz transition (with wavelength  $\lambda_1=689.45$  nm) respectively. The idea of using phase shifts induced on probe light by ultranarrow transitions has previously been proposed for laser frequency stabilization [351–353] in the saturated and resonant configuration, which is intrinsically destructive. By contrast, here we use weak dispersive probes which do not substantially excite the atoms. Calculating a ratio of shifts as opposed to just the millihertz transition Rabi frequency allows for the cancellation of many common noise and systematic effects such as atom number fluctuations, inhomogeneous atom-cavity coupling, cavity and laser frequency noise, and finite ensemble size effects.

Using this approach, we determine the natural linewidth of the clock transition to be  $\gamma_0/2\pi=1.35(3)$  mHz, with a corresponding excited state lifetime of  $\tau=118(3)$  s. The 30  $\mu$ Hz resolution implies that we could detect states with lifetimes just below 2 hours. With straightforward future improvements, we could detect states with lifetimes up to 15 hours using measurement trials that last only a few hundred milliseconds, eliminating the need for long storage times in optical potentials.

While the techniques presented here have been performed before on kHz and MHz linewidth transitions [72, 172, 354–358] [242]  $^{[G]}$ , this work represents a first direct quantum non-demolition detection of a millihertz linewidth optical transition. Our observation provides a direct spectroscopic signal to which a laser could in principle be frequency stabilized [351], analgous to efforts along the  $^1S_0$ – $^3P_1$  transition in strontium [228, 352, 359, 360] [243]  $^{[G]}$ , a transition which is broader by seven orders of magnitude. Our technique contributes towards the aim of creating a new type of atomic clock built with optical cavities that is complementary to traditional discretely-sampled atomic clocks based on Ramsey and Rabi spectroscopy, and it offers enhanced measurement bandwidth and similar sensitivities as are predicted in superradiant lasers [213, 214, 361][93] $^{[G]}$ . The increased bandwidth could help reduce the challenging requirements on local oscillators and would enhance the bandwidth for searches for dark matter or other new fields [329], for example. The nondestructive readout of atomic populations will also reduce the problem of Dick noise aliasing in traditional atomic clocks that rely on destructive read out.

# 4.2 Initial experimental setup

Our system, also described in [93, 223]<sup>[G]</sup>, consists of an ensemble of up to  $10^5$  <sup>87</sup>Sr atoms cooled using SWAP cooling on the 7.5 kHz  $^1S_0$  –  $^3P_1$  transition [292, 293]<sup>[G]</sup> and subsequently trapped within a high finesse optical cavity using a  $\lambda_{\text{trap}}$  = 813 nm, near-magic wavelength intracavity optical lattice [98, 362] which is less than ~2 GHz from the magic wavelength (i.e., half a free spectral range of the cavity). From here on out, we will refer to the atomic transition frequencies as  $\omega_{A0/A1}$  and to the relevant cavity resonance frequencies as  $\omega_{C0/C1}$ , with detunings  $\delta_{C0/C1}$  from the atomic transition.

As shown in Fig. 4.1(b), we tune the cavity length such that one of its longitudinal (TEM<sub>00</sub>) modes is resonant with the  ${}^{1}S_{0} - {}^{3}P_{0}$  clock transition. Simultaneously, we would like the  ${}^{1}S_{0} - {}^{3}P_{0}$  transition to be within a few hundred MHz from resonance with a different longitudinal mode, which is not guaranteed since our cavity free spectral range is ~3.7 GHz. In order to set the proper cavity detuning while keeping the cavity on resonance with the clock transition, we heat up our ceramic cavity spacer with a set of lights<sup>2</sup> by about 10 K from room temperature. This shifted the 698 nm cavity resonance by 8 free spectral ranges, with each free spectral range adjusting the detuning near 689 nm by around 48 MHz. Ultimately, we set the cavity-atom detuning from the F = 9/2  ${}^{3}P_{1}$  manifold to be  $\delta_{C1}/2\pi = 277.5(8)$  MHz.

At these settings, we measure several cavity parameters, tabulated in Table 4.1 (among other quantities which we will discuss later in the chapter). We observe a free spectral range (FSR) of  $\Delta_{\rm FSR,0}=2\pi\times3.71461(3)$  GHz for the clock transition and  $\Delta_{\rm FSR,1}=2\pi\times3.71459(2)$  GHz for the 7.5 kHz transition. The cavity waist at the clock transition  $^3P_0$  wavelength is determined to be  $w_0=73.85(7)~\mu{\rm m}$ . For the broader transition  $^3P_1$  transition's wavelength, the waist is  $w_1=73.37(7)~\mu{\rm m}$ . These values are predicted by the Gaussian beam propagation theory using the known wavelengths, mirror radius of curvature, and cavity free spectal range. The waist sizes have been independently verified to agree at the 0.1% level by measuring the spacing between the TEM<sub>00</sub> mode and the TEM<sub>1,0/0,1</sub> modes relative to the measured free spectral range of the cavity [364].

The atoms are loaded at the cavity center (in between the two mirrors), as confirmed by taking

<sup>&</sup>lt;sup>2</sup> Affectionately called the "car lamp" due to the bulbs we installed.



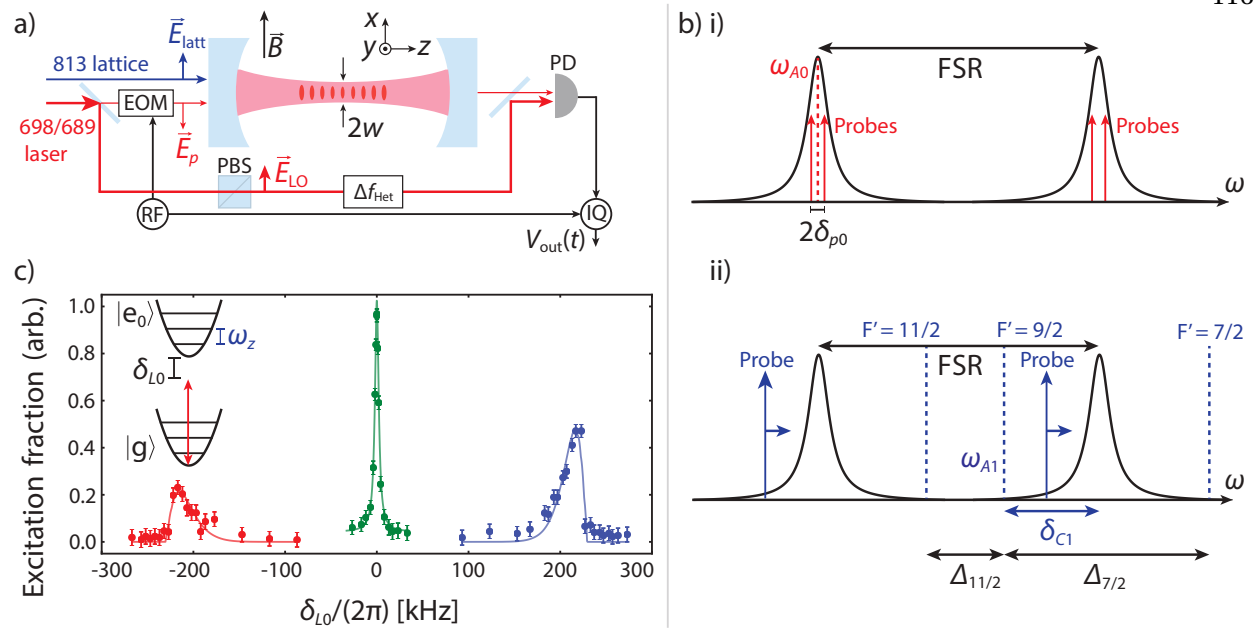


Figure 4.1: Probe setup for measuring dispersive shifts on narrow-linewidth transitions in strontium. (a) Experimental set up. An 813 nm optical lattice confines atoms with an axial temperature of  $14(1)~\mu K$ . A 689/698 nm laser addresses the atomic transitions between the ground  $^1S_0$  state and the  $^3P_1$  and  $^3P_0$  states, respectively. The different laser probe tones are generated by a fiber phase modulator (fiber EOM) and RF function generators. From the same laser, we produce a (much higher power) optical local oscillator. The local oscillator is frequency shifted by  $\Delta f_{\rm Het}$ , polarization filtered along  $\hat{x}$  with a polarization beam splitter (PBS), and forms a heterodyne beat with the transmitted probes, detected on a photodiode. The photocurrent is demodulated by the RF frequency for each tone in parallel, resulting in multiple band-limited voltage signals  $V_{\rm out}(t)$ . (b) The probe tones used to address the clock transition are shown in (i), and the tones and hyperfine levels for the excited  $^3P_1$  manifold are shown in (ii). The cavity resonance most closely resonant with the  $^3P_1$  manifold has a frequency defined by the detuning  $\delta_{C1}$  relative to the F=9/2 manifold. Frequencies are not to scale. (c) Vibrational spectroscopy on the clock transition. We scan a strong 698 nm probe across resonance with the transition with a variable detuning  $\delta_{L0}:=\omega_{L0}-\omega_{A0}$  and record the excitation fraction. We follow the procedure in Ref. [363] to fit the occupation number, temperature, and trap frequency.

fluorescence images of the loaded atoms. The Rayleigh length of the modes ( $\sim 2.453(5)$  cm) is typically much longer than the longitudinal extent of the cold atomic cloud ( $\sigma_{long}=0.30(5)$  mm). Finally, we determine the cavity linewidth using cavity ringdown measurements. For these measurements, we probed the cavity on resonance with light polarized along  $\hat{x}$  (see Fig. 4.1(a) for a definition of the coordinate system). After quickly turning off the probe light with the EOM, we observed the photocurrent on a fast DC coupled photodiode directly positioned after the cavity. We determine a linewidth of  $\kappa_0/2\pi=140.9(3)$  kHz at the clock transition and  $\kappa_1/2\pi=153.0(4)$  kHz at the 689 nm transition, after tak-

ing statistics over several trials. At this linewidth, both the clock transition and the 7.5 kHz transition fall into the so-called bad cavity regime, since  $\kappa \gg \gamma$ .

To determine the mean occupation number and trap frequency of the lattice, as well as the temperature of the atoms, we perform axial sideband spectroscopy using a cavity probe near resonance with the clock transition, following the approach of Ref. [363]. The fraction of atoms excited by this probe as we scan its frequency is shown in Fig. 4.1(c). We consistently measure the axial trap frequency to be  $\omega_z/2\pi = 230(1)$  kHz, the temperature to be T = 14(1)  $\mu$ K, and the mean occupation number to be  $\overline{n}_z = 0.9(1)$ . The Lamb-Dicke parameter computed for the  $^3P_0$  transition is  $\eta_0 = 0.1425(6)$ , and  $\eta_1 = 0.1443(6)$  for the  $^3P_1$  transition.

To measure the linewidth of the clock transition, we define a quantization along  $\hat{x}$ , established by a static magnetic field  $B = B_0 \hat{x}$  with  $B_0 \sim 100$  mG. Then, we optically pump the atoms into a 50/50 spin mixture of the  $^1S_0$  hyperfine sublevels  $m_F = \pm 9/2$ , with less than 5% of atoms remaining in the other 8  $m_F$  sublevels. After initializing the atoms in the stretched  $m_F = \pm 9/2$  states, we send weak probes far off resonance from the atomic transitions through the cavity (as shown in Fig. 4.1(a)). The probe tones are generated with a fiber phase modulator and can be switched on and off using acousto-optic modulators located before the phase modulators. Both probes are polarized along the quantization direction  $\hat{z}$ , established by a static magnetic field B. The different probe tones are driven by different RF sources, indicated by a generic RF generator in Fig. 4.1(a). The different cavity modes probed for each transition are shown in Fig. 4.1(b), which also indicates the relative frequency difference of the hyperfine states of the  $^3P_1$  excited state. Further details for the individual transitions are provided in the following sections.

# 4.3 Expected phase shifts for QND probes

The two narrow-linewidth probes receive a phase shift arising from an interference between the incident and scattered fields in the forward direction. In particular, we perform consecutive measurements of the dispersive cavity resonance frequency shift  $\Delta\omega_1$  (or equivalently the multi-pass phase shift  $\Delta\varphi_1$ ) on the 7.5 kHz transition, as well as the dispersive phase shift  $\Delta\varphi_0$  on the millihertz transition. These phase shifts depend directly on the light-matter coupling strength and therefore scale as  $\Delta\varphi_0/\Delta\varphi_1$ 

Description	Symbol	Value	Unit
Probe wavelength 0 - <sup>3</sup> P <sub>0</sub> probe [259]	$\lambda_0$	698.4457	nm
Probe wavelength 1 - ${}^{3}P_{1}$ probe [259]	$\lambda_1$	689.4485	nm
Trap wavelength	$\lambda_{trap}$	813.4257(2)	nm
Cavity FWHM 0 for probe polarized along $\hat{x}$	$\kappa_0/2\pi$	140.9(3)	kHz
Cavity FWHM 1 for probe polarized along $\hat{x}$	$\kappa_1/2\pi$	153.0(4)	kHz
Mode waist 0	$\mathbf{w}_0$	73.85(7)	$\mu\mathrm{m}$
Mode waist 1	$\mathbf{w}_1$	73.37(7)	$\mu\mathrm{m}$
Lattice waist	W <sub>trap</sub>	79.7(1)	$\mu\mathrm{m}$
Rayleigh Range 0,1	$z_R$	2.453(5)	cm
Free Spectral Range 0	$\Delta_{\mathrm{FSR,0}}/2\pi$	3.71461(3)	GHz
Free Spectral Range 1	$\Delta_{\mathrm{FSR},1}/2\pi$	3.71459(2)	GHz
Cavity Length 0	$L_0$	4.03532(3)	cm
Cavity Length 1	$L_1$	4.03534(2)	cm
Axial trap frequency on axis	$\omega_z/2\pi$	230(1)	kHz
Radial trap frequency	$\omega_r/2\pi$	528(2)	Hz
Axial temperature	$T_z$	14(1)	$\mu \mathrm{K}$
Radial temperature	$T_r$	12(2)	$\mu \mathrm{K}$
RMS thermal radius	$\sigma_r$	14(1)	$\mu\mathrm{m}$
RMS longitudinal cloud radius	$\sigma_{long}$	0.30(5)	mm
Axial vibrational quanta	$ar{n}_z$	0.9(1)	
Axial Lamb-Dicke parameter 0	$\eta_0$	0.1425(6)	
Axial Lamb-Dicke parameter 1	$\eta_1$	0.1443(6)	
Cavity detuning 0	$\delta_{C0}/2\pi$	0(10)	kHz
Cavity detuning 1	$\delta_{C1}/2\pi$	277.5(8)	MHz
Birefringent cavity mode full splitting 0	$\delta_{b0}/2\pi$	23(3)	kHz
Birefringent cavity mode full splitting 1	$\delta_{b1}/2\pi$	24(3)	kHz
Birefringent cavity mode polar angle on Poincaré sphere (Jones vector)	$\theta_b$	30(2)	deg
Birefringent cavity mode azimuthal angle on Poincaré sphere (Jones vector)	$arphi_b$	±14(4)	deg
$^{3}P_{1}$ linewidth [365]	$\gamma_1/2\pi$	7.48(1)	kHz
$^{3}P_{1} F' = 11/2$ detuning from 9/2 [259]	$\Delta_{11/2}/2\pi$	-1463.15(6)	MHz
$^{3}P_{1} F' = 7/2$ detuning from 9/2 [259]	$\Delta_{7/2}/2\pi$	1130.26(6)	MHz

Table 4.1: Summary of cavity and atomic parameters.

 $\propto (g_0/g_1)^2$ , thereby allowing us to infer the ratio  $\gamma_0/\gamma_1$  as described in Eq. (4.1) [187, 232]. In free space, the sizes of  $\Delta\omega_0$  and  $\Delta\omega_1$  would be miniscule due to the weak oscillator strengths of the narrow-linewidth transitions, as well as the fact that the atoms will emit into a large solid angle which reduces the quantum efficiency in the direction of the probe. The optical cavity greatly magnifies the phase shifts because it allows the probes to pass through the atoms multiple times, and because it causes the atoms to preferentially emit into the cavity mode [180]. An optical resonator also introduces systematic effects that we take into account later in this manuscript.

What is the expected form of these phase shifts? We can derive them in the weak probe limit using the optical Bloch equations, as detailed in Ch. 2.4.3. To redefine the system here, we consider N two-level atoms, described by the usual Pauli operators  $\hat{\sigma}^i_j$ , with i=x,y,z and j=1,...,N, equally coupled to a single cavity mode with annihilation operator  $\hat{a}$ . In this case the Jaynes-Cummings Hamiltonian [187, 232] in the atomic frame is:

$$H = \hbar \delta_c \hat{a}^{\dagger} \hat{a} + \hbar g (\hat{a} \hat{J}^+ + \hat{a}^{\dagger} \hat{J}^-), \tag{4.2}$$

where  $\hat{J}^{\pm} = \sum_{i=1}^{N} \hat{\sigma}_{i}^{\pm}$  are the collective raising and lowering operators for the atoms,  $\delta_{c} = \omega_{c} - \omega_{a}$  is the cavity detuning from the atomic transition  $(\omega_{a})$ , and 2g is the single photon Rabi frequency. We can further define  $\hat{J}^{z} = \frac{1}{2} \sum_{i=1}^{N} \hat{\sigma}_{i}^{z}$ , in order to have a closed angular momentum algebra.

If we add a cavity drive  $a_i(t)$  with constant amplitude and a frequency  $\omega_p$ , where  $a_i$  has units of  $\sqrt{\text{photons/s}}$ , we can use the input-output formalism from quantum optics [176][182]<sup>[G]</sup> to write the Heisenberg-Langevin equations of motion for the cavity and atomic mean operators ( $\hat{\mathbb{G}} = \langle \hat{\mathbb{G}} \rangle$ ) in the rotating frame of the atoms as follows:

$$\begin{split} \dot{a} &= -\left(i\delta_c + \frac{\kappa}{2}\right)a - igJ^- + \sqrt{\kappa_m}a_i(t); \\ \dot{J}^- &= i2gJ^z a - \gamma_\perp J^-; \\ \dot{J}^z &= -ig\left(aJ^+ - a^*J^-\right) - \gamma\left(\frac{N}{2} + J^z\right). \end{split}$$

Here, we have included the spontaneous emission rate  $\gamma$ , a transverse dephasing term  $\gamma_{\perp}$ , and cavity losses characterized by the cavity decay linewidth  $\kappa$ . We additionally define  $\sqrt{\kappa_m}$  as the rate at which photons are transmitted through one of the mirrors (such that without mirror losses,  $\kappa = 2\kappa_m$ ). In the

rotating frame, the incident cavity field is  $a_i(t) = a_{i0}e^{-i\delta_p t}$ , with  $\delta_p = \omega_p - \omega_a$  defined to be the drive detuning from the optical transition. The above equations agree with our derivation in Ch. 2.4.3 (Eq. (2.47)) but are slightly more general, since they include an input drive and allow the ensemble to experience inhomogeneous broadening (i.e.,  $\gamma_\perp > \gamma/2$ ).

At long times, the system attains a steady state with all optical frequency observables responding to the input drive by oscillating with a detuning  $\delta_p$ :  $J^- = \tilde{J}^- e^{-i\delta_p t}$ , and  $a = \tilde{a}e^{-i\delta_p t}$ . Working in the weak probe approximation, such that all the atoms remain in the ground state, we can solve the steady-state optical Bloch equations, which give a steady-state collective atomic coherence  $\tilde{J}^-$  satisfying:

$$\tilde{J}^{-} = \frac{igN\tilde{a}}{(i\delta_{p} - \gamma_{\perp})}.$$
(4.3)

. We can also solve for the steady-state cavity field amplitude  $\tilde{a}$ . We express this in terms of the transmitted field  $\tilde{a}_t = \sqrt{\kappa_m} \tilde{a}$ , which satisfies  $\tilde{a}_t = T(\delta_p) a_{i0}$  for a transfer function  $T(\delta_p)$  given by:

$$T(\delta_p) = \frac{1}{1 - i\left(\frac{\delta_p - \delta_c}{\kappa/2}\right) + \frac{NC\gamma/2}{\gamma_\perp - i\delta_p}},\tag{4.4}$$

where  $C=(2g)^2/(\gamma\kappa)$  is the single-atom cooperativity. The form of this transfer function is quite similar to that of the bare cavity derived in Ch. 2.2.2 (specifically, Eq. (2.16)), with an additional resonance absorption feature corresponding to the atomic transition frequency that scales in amplitude with  $NC\gamma/2$ . This term is responsible for the vacuum Rabi splitting in a strong coupling limit. In this chapter, we will also explore the weak coupling limit where  $NC\gamma \ll \kappa$ , in which this feature looks like an undepleted absorption dip inside the cavity resonance.

The phase  $\delta \varphi_t(\delta_p)$  acquired by the transmitted field (defined by  $\tilde{a}_t = |T(\delta_p)| e^{i\delta \varphi_t(\delta_p)} a_{i0}$ ) satisfies

$$\tan(\delta\varphi_t(\delta_p)) = \frac{-2\left(\delta_p g^2 N + (\delta_c - \delta_p)(\delta_p^2 + \gamma_\perp^2)\right)}{\gamma_\perp 2g^2 N + \kappa(\gamma_\perp^2 + \delta_p^2)}.$$
 (4.5)

Depending on which transition we probe (to  ${}^{3}P_{0}$  or to  ${}^{3}P_{1}$ ), the various frequency scales in this general expression will satisfy a different hierarchy which simplifies the expression considerably. We will see what these simplified forms look like in the following sections.

## 4.4 Probing dispersive shifts on the clock transition

The millihertz optical transition falls into a less common regime relative to typical ensemble cavity experiments: even in a regime where  $NC_0\gg 1$ , the collective vacuum Rabi splitting in unresolved, since  $NC_0\gamma_0\ll\kappa_0$  [95]<sup>[G]</sup>. Instead, the atom-cavity coupling results in an absorption feature with a characteristic width of order  $NC_0\gamma_0$ , which can be mapped out with a sufficiently weak probe as shown in simulations in Fig. 4.2(a). As we detail below, our probe tones are detuned by approximately  $|\delta_p|/2\pi\approx 1$  kHz from the atomic transition, which is simultaneously far-detuned from the absorption resonance in order to prevent strongly exciting the ensemble, while also being on resonance with the cavity. Remarkably, due to the ultranarrow linewidth of the clock transition, our probe is also in the resolved motional sideband limit (meaning  $\delta_p\ll\omega_z$ , where  $\omega_z$  is the axial trapping frequency), despite operating in a dispersive regime. This scenario does not have precedent in the atomic quantum non-demolition (QND) measurement community.

Under this set of circumstances, the system obeys the following hierarchy of scales:

$$g_0 \sqrt{N} \sim \delta_p \ll \kappa$$

$$\gamma_{0\perp} \ll \delta_p \tag{4.6}$$

$$|\delta_{C0} - \delta_p| \sim \delta_p,$$

which allows us to approximate the probe phase shift in Eq. (4.5) to the following:

$$\tan(\delta\varphi_{t}(\delta_{p})) \approx -\frac{g_{0}^{2}N}{\delta_{p}(\kappa/2)} - \frac{\delta_{C0} - \delta_{p}}{\kappa/2} 
= -\frac{NC_{0}\gamma}{2\delta_{p}} - \frac{\delta_{C0} - \delta_{p}}{\kappa/2}.$$
(4.7)

The first term on the right hand side of Eq. 4.7 is the atomic like phase shift, and the other term is a cavity-like phase shift, independent of the atoms. For our measurements, we are interested in the first term as it encodes the collective interactions  $(g_0^2N)$ . The last term represents a background and must be subtracted through an independent measurement, which will be explained later. The farther detuned the probe is from the atomic transition, the larger this background will be  $(\propto \delta_{C0} - \delta_p)$  relative to our atomic signal  $(\propto 1/\delta_p)$ . For scale, at our chosen detuning of 1 kHz, the phase shift from the atomic resonance is  $\sim 15$  mrad, compared to a cavity-induced shift of  $\sim 40$  mrad.

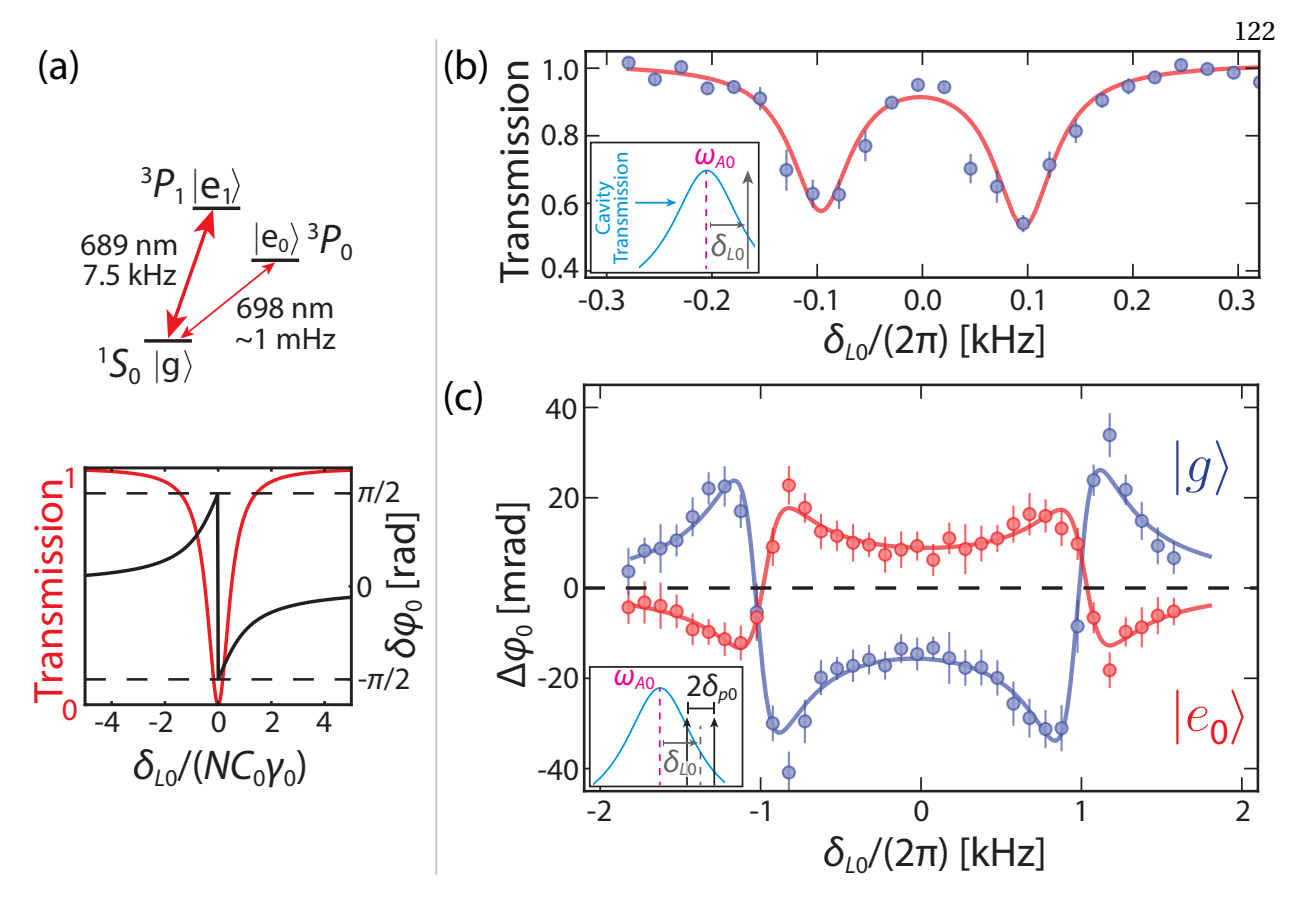


Figure 4.2: Probing a cavity-enhanced absorption feature along a millihertz linewidth transition. (a) Top: a simplified energy level diagram for relevant states in  $^{87}$ Sr. Bottom: Simulated transmssion and phase shift  $\delta\varphi_0$  as a function of the probe detuning  $\delta_{L0}$  for  $\delta_{C0}=0$ , in units of  $NC_0\gamma_0$ , for the clock transition (subindex 0). At a given detuning, the phase shift produced by the atomic ensemble is proportional to  $\gamma_0$ . On this scale, the cavity is always on resonance since  $\kappa\gg NC_0\gamma_0$ . (b) Transmitted power for a single tone versus its detuning  $\delta_{L0}$  from the narrow clock transition frequency  $\omega_{A0}$  (see inset). The two dips correspond to atoms in the ground  $m_F=\pm 9/2$  states in the presence of a 200 mG magnetic field that creates a 200 Hz nuclear Zeeman splitting in the optical transition frequency. (c) Atomic induced phase shift  $\Delta\varphi_0$  on the clock transition as the central frequency detuning,  $\delta_{L0}$ , of the probes from the clock transition frequency,  $\omega_{A0}$ , is scanned (see inset). The probes are detuned  $2\delta_{p0}/2\pi=2$  kHz from each other. Blue (red) markers are for atoms initially in  $|g\rangle$  ( $|e_0\rangle$ ). Solid lines are empirical fits that take into account the finite excitation fraction. Either the transmitted probe amplitudes or phases could serve in the future as frequency references for laser frequency stabilization to an ultranarrow optical transition.

To verify this physics, we investigate the cavity transmission characteristics in the presence of atoms for the ultranarrow transition in Fig. 4.2(b)-(c). The atomic clock transition is addressed with light from a stabilized state-of-the-art sub-10 mHz linewidth laser [348–350]. The power transmission of a near-resonant probe, detuned by  $\delta_{L0}$  from the atomic transition, exhibits two distinct absorption dips (Fig. 4.2(b)), associated with the  $m_F = \pm 9/2$  ground states in the presence of a magnetic field [107].

We attribute the absence of full absorption in this example data to an overly large probe power causing atoms to transition to the excited state  ${}^{3}P_{0}$ . The imbalance in the depth of the absorption features is attributed to imbalance on the relative  $m_{F} = \pm 9/2$  populations. As a remark, these observed spectroscopic signals are quite narrow, with a characteristic width of around 100 Hz, and could be utilized in the future for stabilization of a laser to the atomic transition frequency, providing an atomic clock with complementary properties to traditional atomic clocks.

Uncertainty in the atomic transition frequency and laser frequency noise can both lead to uncertainty in our probe frequency. To gain partial immunity to this, we probe the cavity with two symmetrically detuned tones at  $\delta_{L0} \pm \delta_{p0}$ , where typically  $\delta_{p0}/2\pi = 1$  kHz, as shown in Fig. 4.1(b). Each probe tone receives a phase shift equal to  $\delta\varphi_0(\delta_{L0} \pm \delta_{p0})$ , and the *difference* between these two phases is quadratically insensitive to small deviations of  $\delta_{L0}$  away from 0. Simultaneously, we probe a consecutive TEM<sub>00</sub> cavity mode with an identical pair of tones, which receive phase shifts of the form  $\delta\varphi_0(\Delta_{\rm FSR,0} + \delta_{L0} \pm \delta_{p0})$ . The phase shift from this additional pair represents the cavity-induced phase shift term in Eq. (4.7), allowing us to remove its contribution and extract only the phase shift from the atomic resonance. The full phase shift we calculate is the pair-wise difference:

$$\Delta \varphi_0 := \left[ \delta \varphi_0 \left( \delta_{L0} + \delta_{p0} \right) - \delta \varphi_0 \left( \delta_{L0} - \delta_{p0} \right) \right] - \left[ \delta \varphi_0 \left( \Delta_{\text{FSR},0} + \delta_{L0} + \delta_{p0} \right) - \delta \varphi_0 \left( \Delta_{\text{FSR},0} + \delta_{L0} - \delta_{p0} \right) \right]. \tag{4.8}$$

For the rest of the chapter,  $\Delta \varphi_0$  refers to this quantity. Expanding perturbatively in small ratios (and keeping only the largest higher order terms), this phase shift should equal

$$\Delta \varphi_0 = -\frac{NC\gamma}{\delta_{p0}} \left( 1 - 4 \frac{\delta_{C0}^2}{\kappa^2} + 4 \frac{\delta_{p0}^2}{\kappa^2} + \frac{(NC\gamma)^2}{12\delta_{p0}^2} - \frac{NC\gamma}{\kappa} \right). \tag{4.9}$$

The higher order terms in Eq. (4.9) will be considered later in the chapter as systematic corrections. Finally, the above expression was derived assuming homogeneous atom-light coupling and a Clebsch-Gordan coefficient of 1 along the transition addressed by our probes. In reality, the overall size of the phase shift is modified by these effects. Since our drives are  $\pi$ -polarized and drive a  $F = 9/2 \rightarrow F' = 9/2$  transition, the phase shift must include a factor of  $|c_{C0}|^2 = \frac{9}{11}$ , where  $c_{C0}$  is the Clebsch-Gordan coefficient. Inhomogeneous atom-light coupling effectively reduces the number of atoms by a factor of

two:  $N \rightarrow N/2$ . However, as we will compute a ratio of phase shifts which both are subject to this effect, this correction will cancel.

To implement this four probe measurement, we turn on the probe beams for 20 ms to 40 ms, with substantially more power sent in the two probe tones one free spectral range away from the atomic transition to reduce their photon shot noise contributions to the final noise floor (since they will not actually scatter any atoms, we are not concerned about sending in too much power). The initial time dynamics exhibits transient ringing, of duration  $NC\gamma$ , associated with the homogeneous solution of the optical Bloch equations, which in our system lasts about 2 ms. We want the steady state dynamics, so in postprocessing we remove the first interval of width  $T_H \approx 5$  ms. We beat the resulting signals against a local oscillator, linearly polarized along  $\hat{x}$  in Fig. 4.1(a). The two pairs of probe tones are separately IQ demodulated to a base band of 20 kHz using the same RF sources used to drive the phase modulator. The demodulated IQ voltage signals  $V_{\rm IQ}(t)$  are digitally sampled into the computer and then fitted to extract the difference in the phases for a single pair. For example, the near-resonant pair of tones that probe the clock transition are demodulated to  $20\pm1$  kHz, for  $\delta_{p0}/2\pi=1$  kHz. Then, we extract the four phase shifts and compute  $\Delta \varphi_0$  as defined above.

Fig. 4.2(c) displays the experimentally measured phase shift  $\Delta \varphi_0$  as a function of  $\delta_{L0}$  (which for the actual measurement is nominally 0) for atoms initially in  $|g\rangle$  (blue data) or  $kete_0$  (i.e., the clock state; red data). The sharp resonances near  $\delta_{L0}=\pm\delta_{p0}$  occur when one of the tones is near resonant with the atoms. For this magnetic field ( $\sim 100$  mG) and probe power, the Zeeman level resonances are not resolved. This data confirms that, when  $|\delta_{L0}|\ll\delta_{p0}$ ,  $\Delta\varphi_0$  is only quadratically sensitive  $\delta_{L0}$ . Furthermore, we measure  $\Delta\varphi_0$  after having adiabatically transferred the atoms to  $|e_0\rangle$  [93, 223] [G], and remove the remaining atoms in  $|g\rangle$  using the strong  ${}^1S_0-{}^1P_1$  transition at 461 nm (red markers). We clearly observe  $\Delta\varphi_0$  switching sign along with the atomic inversion  $(N\to -N)$ , as well as a reduction of the signal, in agreement with the measured adiabatic transfer efficiency. The two sets are shifted from one another in frequency by less than 100 Hz, which represents the typical uncertainty to determine  $\delta_{L0}=0$ . The sign flip provides corroborating evidence to our claim that the phase shift is proportional to the atomic response to the probe field. It also illustrates that the observed phase shifts can be used to provide a

differential readout of atomic populations in the ground and excited states for nondestructive readout of traditional Ramsey and Rabi spectroscopy or entanglement generation. The high frequency resolution also means that dual simultaneous probing of two transitions at once can provide rejection of magnetic field noise.

### 4.5 Probing dispersive shifts on the 7.5 kHz transition

Our strategy to measuring the clock transition linewidth  $\gamma_0$  is measuring the ratio of the single photon Rabi frequencies  $g_0/g_1$  between the  ${}^1S_0-{}^3P_0$  clock transition and the 7.5 kHz  ${}^1S_0-{}^3P_1$  transition. This is accomplished by comparing the phase shift  $\Delta\varphi_0$  from the clock transition probing scheme with a comparable measurement on the 7.5 kHz transition. Our system typically satisfies  $NC_1\gamma_1\gg\kappa_1$ , with  $C_1=(2g_1)^2/\kappa_1\gamma_1$  denoting the single atom cooperativity parameter that characterizes the cavity-enhanced interactions on this transition  $[232][182]^{[G]}$ . This gives a resolved collective vacuum Rabi splitting when the cavity is on resonance with the atomic transition (i.e.,  $\delta_{C1}=0$ ). For this experiment, we instead operate in the dispersive limit ( $\delta_{C1}\gg\sqrt{N}g_1$ ), and the vacuum Rabi splitting manifests as a dispersive shift  $\delta\omega_1=Ng_1^2/\delta_{C1}$  [182] due to the presence of N atoms in the ground state. This frequency shift corresponds to an equivalent multi-pass phase shift  $\delta\varphi_1=\delta\omega_1/(\kappa_1/2)=NC_1\gamma_1/2\delta_{C1}$ . This regime has been explored in many different QND platforms [61, 62, 69, 366][63, 64, 70]^{[G]}.

We set the cavity length such that the closest mode to the excited  ${}^3P_1$  F'=9/2 state is detuned by  $\delta_{C1}/2\pi=277.5(8)$  MHz. The cavity phase shift  $\delta \varphi_1$  is computed by measuring the cavity frequency shift  $\delta \omega_1$  of the TEM<sub>00</sub> mode detuned by  $\delta_{C1}$  from  $\omega_{A1}$ . To probe  $\delta \omega_1$ , we scan the frequency of a weak  $\pi$ -polarized probe across the cavity resonance. As before, in order to gain further insensitivity with respect to cavity and laser frequency noise, we simultaneously probe a consecutive longitudinal TEM<sub>00</sub> mode of the cavity at frequency  $\delta_{C1} - \Delta_{\rm FSR,1}$  (see Fig. 4.1(b)), and compute the difference:

$$\Delta \varphi_1 := \delta \varphi_1(\delta_{C1}) - \delta \varphi_1(\delta_{C1} - \Delta_{\text{ESR},1}). \tag{4.10}$$

From now on we will refer to  $\Delta \varphi_1$  as this measured quantity, representing the multi-pass phase shift of the dispersive probe along the  ${}^1S_0 - {}^3P_1$  transition.

Although naively, the value of  $\Delta \varphi_1$  is given by the dispersive shift along a two-level system, the phase shift actually has multiple contributions due to the hyperfine structure in  $^3P_1$ , which effectively creates three atomic resonances within ~2.5 GHz. Since our atoms are initialized in the  $m_F = \pm 9/2$  states and are probed with  $\pi$ -polarized light, the probes do not couple to the F' = 7/2 excited state manifold, so the general form for the phase shift is given by:

$$\Delta \varphi_1 = \frac{g_1^2 N}{\kappa_1 / 2} \left[ \left( \frac{c_{N1}^2}{\delta_{C1}} + \frac{c_{N2}^2}{\delta_{C1} - \Delta_{11/2}} \right) - \left( \frac{c_{N1}^2}{\delta_{C1} - \Delta_{FSR,1}} + \frac{c_{N2}^2}{\delta_{C1} - \Delta_{11/2} - \Delta_{FSR,1}} \right) \right], \tag{4.11}$$

where  $c_{N1}$  and  $c_{N2}$  are the Clebsch-Gordan coefficient for  $\pi$ -polarized light probing the stretched states on the  $F=9/2 \rightarrow F'=9/2$  and  $F=9/2 \rightarrow F'=11/2$  transitions, respectively  $(c_{N1}=\sqrt{\frac{9}{11}},c_{N2}=\sqrt{\frac{2}{11}})$ ,  $\Delta_{11/2}/2\pi=-1463.15(6)$  MHz is detuning of F'=11/2 with respect to the F'=9/2 manifold [259], and  $\Delta_{FSR,1}/2\pi$  is the cavity free spectral range at 689 nm. The first term in the sum contributes an order of magnitude more phase shift than any of the others due to a combination of the larger detunings and smaller Clebsch-Gordan coefficients on the other terms. Therefore, while the full form in Eq. (4.5) will be used to calculate the precise value of the clock transition linewidth, to leading order we can approximate the phase shift by:

$$\Delta \varphi_1 \approx \frac{g_1^2 N}{\kappa_1 / 2} \frac{c_{N1}^2}{\delta_{C1}}.\tag{4.12}$$

Practically speaking, the frequency shifts  $\delta\omega_1$  of the two longitudinal cavity modes are probed by simultaneously sweeping the two probe tones across the cavity resonance with a linear frequency ramp. As in Sec. 4.4, the transmission of these probes through the cavity is measured with a heterodyne detector and subsequently IQ demodulated. The IQ data is fitted to extract the resonance frequencies up to a common offset, and an estimate of the differential frequency shift between the two cavity modes  $\Delta\omega_1$  is then computed.

## 4.6 Measuring the ratio of dispersive shifts

Using the forms of Eq. (4.8) and Eq. (4.5), to leading order we can infer the ratio of single-photon Rabi frequencies  $g_0/g_1$  from the ratio of dispersive shifts according to:

$$\left(\frac{g_0}{g_1}\right)^2 \approx -\frac{1}{2} \left(\frac{\Delta \varphi_0}{\Delta \varphi_1}\right) \left(\frac{\kappa_0}{\kappa_1}\right) \left(\frac{\delta_{p0}}{\delta_{C1}}\right), \tag{4.13}$$

allowing us to calculate  $\gamma_0$  from the known  $\gamma_1$  via Eq. (4.1).

However, certain unavoidable aspects of the experimental setup lead to systematics that require a careful measurement sequence to suppress. The above ratio assumes that no atoms are excited into the excited state, but at a finite probe power this is not the case. To alleviate this, we measure  $\Delta \varphi_0/\Delta \varphi_1$  over a range of optical powers. Then, we extrapolate to P=0 to approach the zero-power limit where no atomic excitations are created. Additionally, our lattice exhibits nonnegligible atom loss during the measurement sequence (with a lifetime of ~500 ms at the time of measurement). To gain insensitivity to atom loss, our experimental scheme relies on non-destructive interleaved measurements of  $\Delta \varphi_0$  and  $\Delta \varphi_1$  during a single shot such that the inhomogeneity of the atom-cavity coupling [62][63]<sup>[G]</sup> and fluctuations in the atom number N are common to both measurements and cancel in the final computed ratio. The measurement sequence, shown in the inset of Fig. 4.3(b), consists of three short (~ 2 ms)  $\Delta \varphi_1$  measurements with two longer (~ 25 ms)  $\Delta \varphi_0$  measurements. From these five measurements we build a suitable estimator for the ratio  $\Delta \varphi_0/\Delta \varphi_1$  and extract the ratio  $(g_0/g_1)^2$ , which is described in detail in Sec. 4.9.

Experimental results are shown in Fig. 4.3(b). Probe optical powers  $P_0$  and  $P_1$  for the 698 nm and 689 nm probes, respectively, are reduced to interpolate to the zero-power value for  $\Delta \varphi_0/\Delta \varphi_1$ . Three different measurement sets (markers) are shown for consistency and repeatability, each fitted with a quadratic polynomial on  $P_0$  (solid lines) with reduced  $\chi^2_v$  near 1 for all sets. For these data sets, we have verified that the  $P_1$  was already sufficiently low to avoid creating excitations in  $|e_1\rangle$ . Each of these sets were taken on different days and with independent cavity alignments to the clock transition. A simultaneous fit to the three sets is shown as a solid black line. Using different estimators and fit methods (Sec. 4.9), we consistently measure a zero-power crossing ratio  $(\Delta \varphi_0/\Delta \varphi_1)_{\rm exp} = -8.95(9) \times 10^{-2}$ .

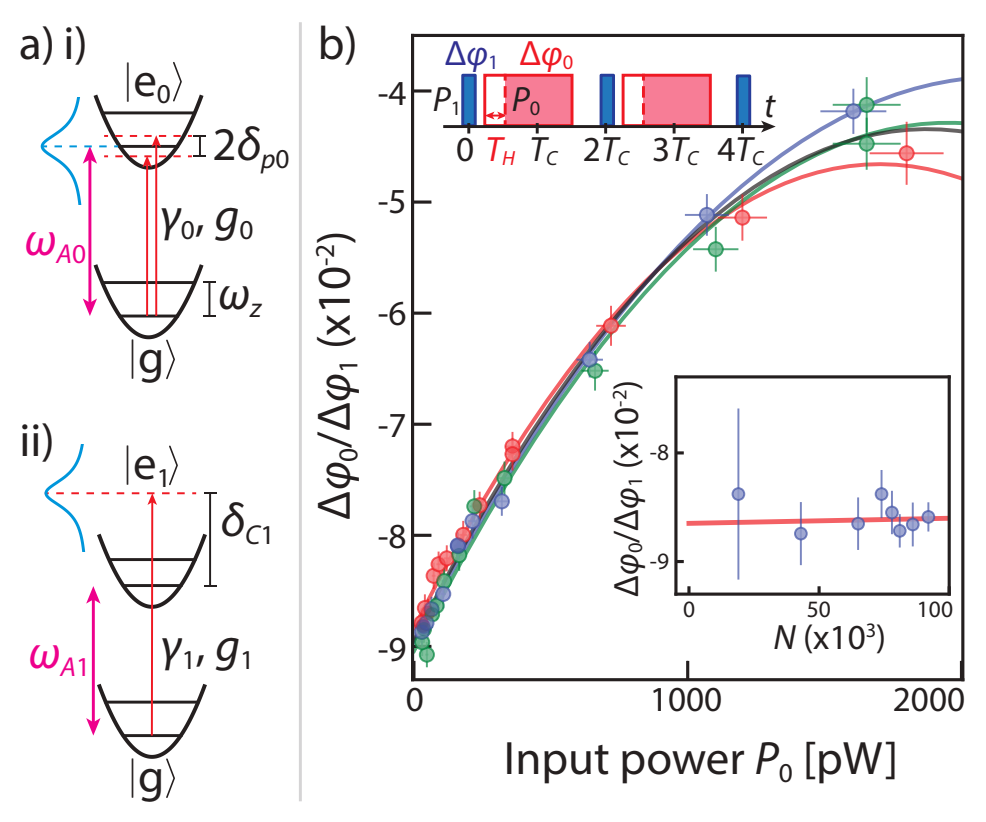


Figure 4.3: Extracting the ratio of phase shifts  $\Delta \varphi_0/\Delta \varphi_1$  in a zero-power limit. (a) (i) For the phase shift measurement  $\Delta \varphi_0$ , the two probe tones are detuned by only 1 kHz from the atomic transition, much smaller than the spacing between the axial motional levels  $\omega_z/2\pi=230$  kHz. In this resolved-sideband regime, the probe tones experience a differential phase shift primarily from the carrier transition that does not change the motional quantum number. Due to finite axial confinement, the carrier transition strength is reduced by 6%, the largest correction factor that must be applied to our measurement. (ii) In contrast, for the phase shift measurement  $\Delta \varphi_1$  the probe tones are far detuned and the probe experiences a phase shift due to interacting with all motional sideband transitions. (b) Ratio  $\Delta \varphi_0/\Delta \varphi_1$ measurement, from the interleaved pulses sequence (top inset) as  $P_0$  is changed. Different colors correspond to different measurement sets (markers), over different days, and their color matching solid lines are quadratic polynomial fits on  $P_0$  according to our model discussed in Sec. 4.9. Statistical errors (1 $\sigma$ ) are indicated by the errorbars. The top inset shows the measurement sequence, which alternates three 2 ms  $\Delta \varphi_1$  measurements between two 25 ms  $\Delta \varphi_0$  measurements (the first  $T_H$  = 5 ms are removed for the extraction of  $\Delta \phi_0$ ). The solid black line is a global fit to the three measurements. The bottom inset shows  $\Delta \varphi_0/\Delta \varphi_1$  (markers) and its weighted linear fit (solid line), for a fixed set  $(P_0, P_1)$ , as the atom number N is changed.

We note that the spread of the zero-power values for different sets is consistent with the effect of the estimated uncertainty on our ability to tune  $\delta_{C0}$  to zero for each data set. The bottom inset in Fig. 4.3(b) shows  $\Delta \varphi_0/\Delta \varphi_1$  for different atom numbers N and fixed powers  $P_0$  and  $P_1$ , with the red line indicating a linear weighted fit. The variation of the measured values suggests that we can constrain any unknown first order variation with N or  $N^{-1}$  to the 2% level within our final uncertainty, limited by signal to noise. Since there is not an underlying model for why such a scaling would exist (beyond offsets in  $\Delta \varphi_0$  and  $\Delta \varphi_1$  accounted for separately), no adjustment to the quoted uncertainty is applied.

# 4.7 Inferring the clock transition linewidth

To precisely determine the excited clock state linewidth from the measured  $(\Delta \varphi_0/\Delta \varphi_1)_{\rm exp}$ , several systematic effects need to be accounted for. A detailed description is given in Sec. 4.8, but here we focus on the most important corrections (displayed in Table 4.2). The largest systematic correction that must be applied arises from the fact that the phase shift measurements  $\Delta \varphi_0$  are made in a resolved sideband regime in which the probe detunings  $\delta_{p0}/2\pi = \pm 1$  kHz are much less than the axial trapping frequency  $\omega_z/2\pi = 230(1)$  kHz, as shown in Fig. 4.3(a). To be in a dispersive regime requires  $\delta_{p0} \gg NC_0\gamma_0$ ; for most fully allowed optical transitions, this typically implies  $\delta_{p0} \gg \omega_z$  when  $NC_0 \gg 1$ . However, here  $\gamma_0$  being so small allows us to operate in the dispersive regime, probing the carrier transition, even when  $\delta_{p0} \ll \omega_z$ . For our atomic sample, the correction to the measured  $\Delta \varphi_0/\Delta \varphi_1$  is 1.062(4), where we also take into account the inhomogeneous coupling between probes and atoms across the optical lattice.

The cavity also possesses intrinsic birefringence which modifies both phase shifts and therefore changes  $\Delta \varphi_0/\Delta \varphi_1$ . Rather than a single polarization-independent cavity resonance, birefringence creates two normal modes split by frequencies  $\delta_{b0}$  and  $\delta_{b1}$  at  $\lambda_0$  and  $\lambda_1$  respectively. If  $\theta_b$  is the opening angle between the probe beam polarization  $(\hat{x})$  and the birefringent eigenmode axis on the Poincaré sphere, the correction on each phase shift scales as  $(\delta_{bi}/(\kappa_i/2)\sin\theta_b)^2$  for  $i\in\{0,1\}$ . Including relevant measurement details, such as the hyperfine structure of the relevant states, imperfect state preparation in the ground state hyperfine manifold, uncertainty in the polarization alignment of the local oscillator polarization relative to the probe's polarization, and possible differential linewidths for both birefringent

Effect	Target	Correction
Finite axial confinement	$\Delta \varphi_0/\Delta \varphi_1$	1.062(4)
Cavity birefringence	$\Delta arphi_0/\Delta arphi_1$	1.012(5)
Atomic resonance uncertainty	$\Delta arphi_0$	0.994(6)
Cavity resonance offset	$\Delta arphi_0$	1.008(6)

Table 4.2: Largest identified corrections to the clock transition linewidth measurement and their associated uncertainties.

normal modes, we determine a correction factor on the phase shift ratio of 1.012(5).

Furthermore, the atomic phase shift measurement  $\Delta \varphi_0$  is quadratically sensitive to uncertainty in the detuning  $\delta_{L0}/2\pi = 0 \pm 100$  Hz (as shown in Fig. 4.2(c)). Corrections on the measured value of  $\Delta \varphi_0$  from this effect scale as  $(1 - \left(\delta_{L0}/\delta_{p0}\right)^2)$ . Similarly,  $\Delta \varphi_0$  depends quadratically on the cavity resonance condition, i.e., how close  $\delta_{C0}$  is to 0. This correction scales as  $(1 + (\delta_{C0}/(\kappa_0/2))^2)$ , where typically  $|\delta_{C0}|/2\pi \lesssim 10$  kHz.

Considering all of the other systematic effects studied in Sec. 4.8, the total size of the correction factor to  $(\Delta \varphi_0/\Delta \varphi_1)_{\rm exp}$  is  $F_C=1.074(16)$ . The corrected ratio is then  $\Delta \varphi_0/\Delta \varphi_1=-9.61(17)\times 10^{-2}$ . In order to use the measured value for  $\Delta \varphi_{0,1}$  to determine  $(g_0/g_1)^2$  as in Eq. 4.13, we need to take into account the hyperfine structure in the  ${}^3P_1$  state manifold, meaning we must use the full expression for  $\Delta \varphi_1$  as in Eq. (4.5). From this, we extract  $(g_0/g_1)^2=1.83(3)\times 10^{-7}$ . Finally, using Eq. 4.1 we determine  $\gamma_0/\gamma_1=1.81(3)\times 10^{-7}$ , where the waist (w) and length (L) for each mode are independently characterized [364]. Using the value of  $\gamma_1/2\pi=7.48(1)$  kHz measured in Ref. [365], we finally find  $\gamma_0/2\pi=1.35(3)$  mHz for the clock excited state natural linewidth. This value implies an excited state lifetime of  $\tau_0=118(3)$  s, in agreement with Ref. [107] but in disagreement with Ref. [104]. Ab-initio atomic structure calculations place the atomic linewidth at 1.4(5) mHz in Ref. [344], and 1.2 mHz in Ref. [343]. We also note that the value used for  $\gamma_1$  reported in Ref. [365] is consistent with previous less precise determinations, with relative uncertainties at the 2% level, from decay and photoassociation measurements [367, 368].

Effect	$1-F_C$	Uncertainty on $F_{C}$
Polarization uncertainty	$2 \times 10^{-4}$	$6 \times 10^{-5}$
Differential lattice shift	$-2.3 \times 10^{-3}$	$8 \times 10^{-4}$
Saturation during probe	$-2 \times 10^{-4}$	$2 \times 10^{-4}$
Probe optical pumping and losses	$-4 \times 10^{-4}$	$4 \times 10^{-4}$
Zeeman shift	$2 \times 10^{-8}$	$1 \times 10^{-9}$
Higher order corrections	$-2.5 \times 10^{-4}$	$1 \times 10^{-4}$

Table 4.3: Correction factors  $F_C$  for the measurement of  $\Delta \varphi_1$ .

### 4.8 Systematics analysis

This measurement approach for determining natural lifetimes of long-lived states is new, and it is important to think broadly about potential systematic corrections that must be applied, as well as the uncertainties on these corrections. In this section, we will discuss nearly 20 different systematic corrections. Most of these are small enough to be ignored, but we include them for completeness and for the sake of future applications of the technique, in which details of the experimental system might make these effects larger.

We roughly break up the systematics discussion into three categories: those that affect individually the cavity phase shift measurement  $\Delta \varphi_1$  on the 7.5 kHz transition, those that affect the phase shift measurement  $\Delta \varphi_0$  on the clock transition, and those that affect the measured ratio  $(\Delta \varphi_0/\Delta \varphi_1)$ . We define the correction factors  $F_C$  as the ratio of the ideal quantity  $Q^i$  and the actually measured quantity  $Q^m$  such that the ideal quantity can be recovered from the measured quantity as  $Q^i = F_C Q^m$ .

### **4.8.1** Corrections on the phase shift $\Delta \varphi_1$

In this section we discuss effects that affect the measured cavity frequency shift  $\Delta \varphi_1$  for the two consecutive TEM<sub>00</sub> modes on the 7.5 kHz transition at 689 nm. The magnitude of the correction factors  $F_C$  are shown in Table 4.3

### **4.8.1.1** Polarization uncertainty in the ${}^{3}P_{1}$ probe

The polarization uncertainty effect refers to the fact that the probe light's polarization might not have been perfectly  $\pi$ -polarized. To optimize the probe polarization's orientation relative to the magnetic field, we performed a measurement of  $\Delta \varphi_1$  at a (variable) value of the transverse magnetic field  $B_t$  first, and within 4 ms we measure it again at another magnetic field  $B_t^{\rm ref}$  that we believe to be close to the value that cancels the transverse components. Magnetic fields along  $\hat{x}$ ,  $\hat{y}$ ,  $\hat{z}$  are generated by three respective sets of Helmholtz coils driven by a stabilized current source, which allow us to rapidly perform small changes in the y and z components of  $B_t$  in order to perform this measurement (with coordinates defined in Fig. 4.1(a)). In this way, we have the ability to compute the ratio in each experimental repetition, which gives us further insensitivity with respect to other quantities that fluctuate shot-to-shot, like atom number.

The ratio of the two measurements,  $\Delta \varphi_1(B_t)/\Delta \varphi_1(B_t^{\rm ref})$ , is maximized when the y and z components are nulled, as our model shows. An example of this measurement is shown in Fig. 4.4(a). If the reference field  $B_t^{\rm ref}$  was not properly chosen, we can change it accordingly and evaluate the ratio again, until we consistently find the right value for  $B_t^{\rm ref}$ , where we would like to operate the experiment. Typically, we observed day to day shifts of 3 mG as we repeat this procedure before any of the measurements to establish the linewidth ratio. The associated correction factor  $F_C$  takes into account the effect of a small magnetic field fluctuations of magnitude 3 mG on typical data sets as shown in Fig. 4.4(a). Based on our model, we find that we can realize a probe with 98% pure  $\pi$  polarization. The fitted quadratic dependence of the phase shift magnitude along with this 3 mG uncertainty is used to estimate the correction factor for this effect.

### **4.8.1.2** Differential lattice shift in the ${}^{3}P_{1}$ probe

The differential lattice shift is due to the fact that the lattice is not quite magic for the  ${}^3P_1$  states. However, the expected differential AC Stark shifts, around 0.7(2) MHz for our trap depth, are very small compared to the cavity detuning from the atomic transition  $\delta_{C1}$ . Experimentally, we determine  $\Delta \varphi_1$  to change by less than 1% for trap depths changing by 50%. The uncertainty is estimated based on a combination of trap depth, resonance frequency and cavity detuning uncertainties.

# **4.8.1.3** Saturation and optical pumping due to the ${}^3P_1$ probe

While probing the cavity phase shift  $\Delta \varphi_1$ , the probe itself can excite atoms, especially if the probe power is large. To characterize this effect, we measure the change in  $\Delta \varphi_1$  as a function of the probe power. In each experimental repetition, we perform three consecutive measurements as depicted in Fig. 4.4(b): first at a (variable) power  $P_1^H$ , then at a (low) reference power  $P_1^L$ , then again at the same (variable) power  $P_1^H$ . This allow us to be insensitive to, for instance, shot to shot variations in atom number, while allowing us to characterize the effect of a high power probe on each measurement.

In each experimental shot, we obtain three cavity phase shifts for each of the previous powers that we denote as  $\Delta\varphi_1^1$ ,  $\Delta\varphi_1^2$ , and  $\Delta\varphi_1^3$ , respectively. We model the effect of any possible probe power related effect during the probe, in the low power limit, as a modification in the measured phase shift as  $\Delta\varphi_1(P) = \Delta\varphi_1(P=0)(1-2(P/P_0))$ , where P is the probe optical power,  $P_0$  is some parameter that works as an effective saturation power in this model (the beam area is fixed by the cavity), and  $\Delta\varphi_1(P=0)$  is the zero-power phase shift that is the interest of our measurement. In order to characterize this behaviour, we change  $P_1^H$  and measured the effect on  $\Delta\varphi_1$  using the ratio  $s_S = ((\Delta\varphi_1^1 + \Delta\varphi_1^3)/2 - \Delta\varphi_1^2)/(\Delta\varphi_1^2)$ ; for low excitation fractions, this is linear in the input power  $P_1^H$  and scales as  $s_S = (P_0 - 2P_1^H)/(P_0 - 2P_1^L)$ . For a given probe power P, the correction factor would be  $F_C = 1/(1-2(P/P_0))$ . As we measure  $P_1^L$  and  $s_S$ , we can determine  $P_0$  in our model to estimate the correction.

The measurement is shown in Fig. 4.4(b), where we fit a linear function (red line) to the input probe power  $P_1^H$ . This allows us to establish that the excitation fraction is not significant (< 0.0001) for cavity probe input powers below 1 nW. The value quoted for the associated correction factor, takes into account the maximum power used for the data presented in 4.3(b), which was around 1 nW and was decreased together with the clock transition probe power to extract the ratio  $\Delta \varphi_0/\Delta \varphi_1$ . The uncertainty is taken to cover the full range of power used in the  $\Delta \varphi_0/\Delta \varphi_1$  measurement in Sec. 4.6. We assign a value  $F_C = 1.0002(2)$  for the correction factor.

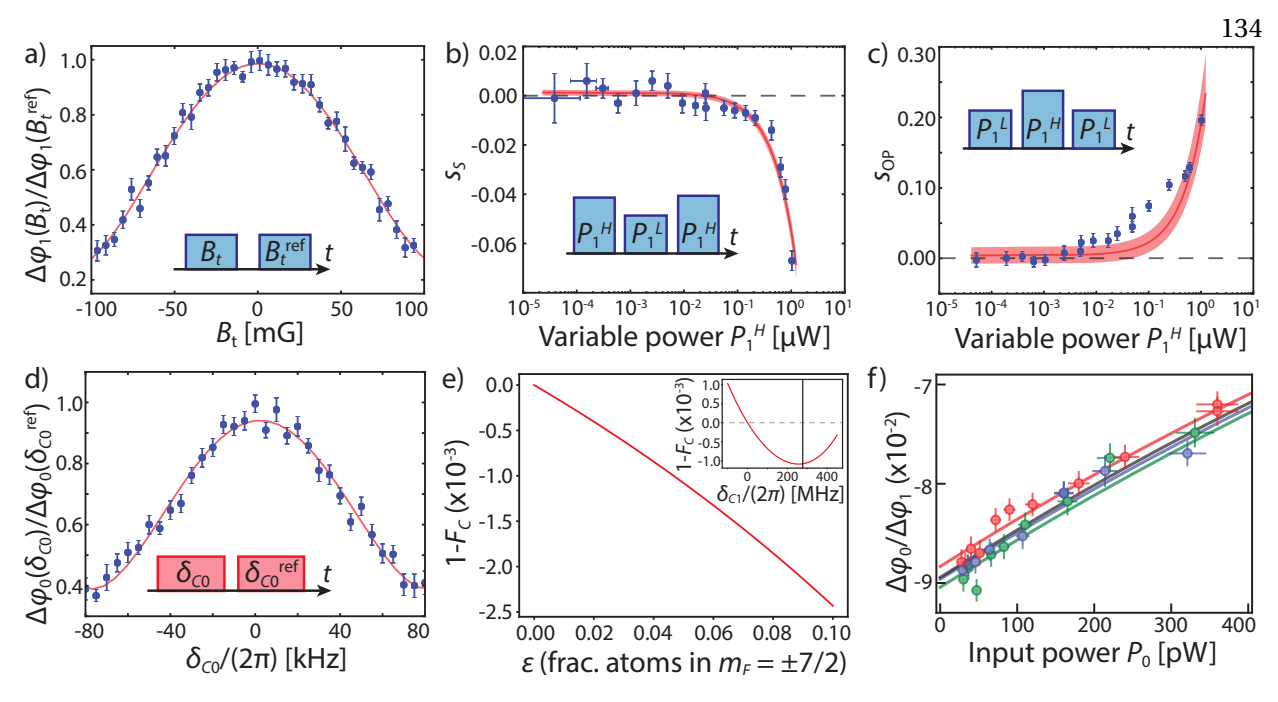


Figure 4.4: Assorted measurements for the systematics analysis of the clock transition linewidth measurement. (a) Polarization alignment using cavity phase shift measurements while changing one of the transverse magnetic field components. In a single shot, we compute the ratio between two measurements at a variable transverse field,  $B_t$ , and a reference transverse field  $B_t^{\rm ref}$ . Typical day-to-day fluctuations are around 3 mG. (b) Saturation effects on the 689 nm transition probe. We use interleaved  $\Delta \varphi_1$  measurements at different powers to determine the relative reduction on  $\Delta \varphi_1$  as the probe power increases. (c) Power induced reduction on the 689 nm transition phase shift. We use interleaved  $\Delta \varphi_1$  measurements at different powers to determine the relative reduction on  $\Delta \varphi_1$  as the probe power increases. (d) Influence of the cavity detuning  $\delta_{C0}$  on the atom-like phase shift  $\Delta \varphi_0$  on the clock transition. We tune the cavity at two different cavity detunings, one fixed  $(\delta_{C0,\rm ref})$ , and one variable  $\delta_{C0}$ , and in a single show we compute the ratio  $\Delta \varphi_0(\delta_{C0})/\Delta \varphi_0(\delta_{C0,\rm ref})$  that maximizes when  $\delta_{C0} = \delta_{C0,\rm ref} = 0$ . (e) Optical pumping correction factor  $F_C$ , where we take the fractional population on the  $\pm 7/2$  states to be  $\varepsilon$ , on the  $\pm 5/2$  states is  $\varepsilon^2$ , on the  $\pm 3/2$  states is  $\varepsilon^3$ , and on the  $\pm 1/2$  states is  $\varepsilon^4$ . Inset shows the dependence of the correction factor for  $\varepsilon = 0.05$  versus the cavity detuning  $\delta_{C1}$  to the  $\delta_{C0}$  manifold. (f) Zoom in for low powers for Fig. 4.3(b). Results and fits shown for estimator  $E_3$  as described in this text.

Furthermore, the probe itself can cause more permanent effects. For instance, it can cause atom loss or optically pump atoms to different magnetic sub-levels, modifying  $\Delta \varphi_1$  and eventually  $\Delta \varphi_0$  on interleaved measurement sequences. To characterize this effect, we again use three consecutive measurements to obtain  $\Delta \varphi_1^1$ ,  $\Delta \varphi_1^2$ , and  $\Delta \varphi_1^3$ : first at a (low) reference power  $P_1^L$ , then at a (variable) power  $P_1^H$ , then again at a (low) reference power  $P_1^L$ . This scheme allow us to, in a single shot, characterize the change that occurs after applying a relative high power probe.

The values for  $\mathbb{P}^L_1$  used here fall into the low power region from the the previous analysis, such that

for simplicity we will consider they do not have a significant effect. However, we will consider the second high power probe has a more permanent effect. For example, we consider the case that during, and after, the second pulse with power  $P_1^H$  the measured phase shift is modified by an effective value  $(1-(P_1^H/P_{OP}))$  from its zero power value. Again, this  $P_{OP}$  tries to capture any effect such as redistribution in the ground state hyperfine state manifold or atom loss as consequence of a higher probe power.

To characterize this effect and estimate the necessary correction, we consider the parameter  $s_{OP} = 1 - (\Delta \varphi_1^3)/(\Delta \varphi_1^1)$ , that measures the differential phase shift after applying a higher probe power in between the two pulses. In particular, our model predicts a behaviour of the form  $s_{OP} = (P_1^H/P_{OP})$ . We show the result of these measurements in Fig. 4.4(c), where we varied the optical power of the second probe  $P_1^H$ . For the final optical power used in the phase shifts ratio measurement presented in the text, we use maximum probe powers in the 689 nm transition on the order of 1 nW. From this characterization, we assign a correction factor  $F_C = 1.0004(4)$ , to cover the full range of variation for the used powers.

## **4.8.1.4 Zeeman shifts in the** ${}^{3}P_{1}$ **probe**

The Zeeman shift on the different ground and excited states changes the effective atom-cavity detuning by a few hundred kHz, which is much smaller than the cavity detuning  $\delta_{C1}$ . The typical magnetic field that we use is 95 mG, as calibrated using the splitting between the peaks in the superradiant pulses [93]<sup>[G]</sup> and corroborated by the splitting measured in Fig. 2(a), for example. Taking this effect into account we expect a very small correction to the ratio of phase shifts.

### **4.8.1.5** Higher order corrections on the $\Delta \varphi_1$ measurement

Higher order corrections on the cavity frequency shift manifest in  $\delta\omega_1$  as  $\delta\omega_1=Ng_1^2/\delta_{C1}(1-2Ng_1^2/\delta_{C1}^2)$  [182]<sup>[G]</sup>. We note that this correction is N-dependent. For typical experimental parameters we have  $2Ng_1^2/\delta_{C1}^2\lesssim 1\times 10^{-3}$ . We calculate the correction factor  $F_C$  based on an independent atom number calibration using florescence imaging, while its uncertainty is estimated assuming extreme 50% fluctuations in typical N.

Effect	$1-F_C$	Uncertainty on $F_{C}$
Polarization uncertainty	$-3 \times 10^{-4}$	$3 \times 10^{-4}$
Atomic resonance uncertainty	$6 \times 10^{-3}$	$6 \times 10^{-3}$
Cavity resonance drift	$-8 \times 10^{-3}$	$6 \times 10^{-3}$
Zeeman shift	$2.3\times10^{-3}$	$5 \times 10^{-4}$
Higher order corrections	$4 \times 10^{-4}$	$2 \times 10^{-4}$

Table 4.4: Correction factors  $F_C$  for the measurement of  $\Delta \varphi_0$ .

### **4.8.2** Corrections on the phase shift $\Delta \varphi_0$

In this section we discuss effects that affect the measured atomic-like phase shift  $\Delta \varphi_0$  on the millihertz transition at 698 nm. The magnitude of the correction factors  $F_C$  are shown in Table 4.4.

## **4.8.2.1** Polarization uncertainty in the ${}^{3}P_{0}$ probe

The polarization uncertainty correction takes into account any possible misalignment between the probe polarization and the applied magnetic field that defines the quantization axis. Based on the measurements for  $\Delta\omega_1$  presented before, we model in a very similar way what the effect would have been for the atomic phase measurement  $\Delta\varphi_0$  with a typical 3 mG uncertainty on the transverse magnetic fields.

## **4.8.2.2** Atomic resonance uncertainty in the ${}^{3}P_{0}$ probe

The clock transition is addressed with light from a state-of-the-art laser, used in the <sup>87</sup>Sr optical lattice clock experiments at JILA [98, 322, 350]. To determine the atomic resonance, we perform Rabi spectroscopy, measuring the excitation fraction versus the probe light's frequency. The probe frequency is changed by changing the in-fiber EOM driving frequency. For sufficiently low power, we are able to determine the central frequency with less than 10 Hz uncertainty, but the full-width at half maximum of the spectroscopic feature is typically between 50 Hz and 100 Hz, similar to the data shown in Fig. 2(b). The frequency might be shifted from the natural <sup>87</sup>Sr frequency due to various atomic frequency shifts,

such as DC Stark shifts, Doppler shifts, collective shifts, and differential AC Stark shifts from a lattice imperfectly tuned to the clock states magic wavelength. However, we have already fully characterized all these possible cock transition frequency shifts to be well below 100 Hz in Ref. [93]<sup>[G]</sup>.

Because we are using two symmetric tones to address the atomic transition, the associated correction factor  $F_C$  to the measured phase shift scales as  $(1-\left(\delta_{L0}/\delta_{p0}\right)^2)$  with  $\delta_{L0}$  the detuning from the tones central frequency to the atomic transition, as defined earlier. Note that this effects increases the absolute value of the measured phase shift  $\Delta \varphi_0$ , as can be seen in Fig. 2(b). Assuming that  $|\delta_{L0}|/2\pi < 100$  Hz but is equally likely to take on any value in this range, we calculate a correction factor centered on the rms average of  $F_C(\delta_{L0})$  over possible values of  $\delta_{L0}$ , accompanied by an uncertainty large enough to cover the full range.

### **4.8.2.3** Cavity resonance uncertainty in the ${}^{3}P_{0}$ probe

By probing and subtracting the phase shifts for two consecutive  $\text{TEM}_{00}$  modes, one on resonance with the atomic clock transition, we guarantee that any instantaneous cavity length fluctuation will be instantaneously removed from our measurement. However, if the initial cavity detuning from the clock transition,  $\delta_{C0}$ , is non-zero, the phase shift will be modified by a factor  $(1 + (\delta_{C0}/(\kappa_0/2))^2)$ , as noted in Eq. 4.9. Typically, we can align the initial cavity length and minimize cavity drifts such that  $|\delta_{C0}|/2\pi \le 10$  kHz during each of the measurement in 4.3(b). We had verified analytically and experimentally what would be the effect of a cavity resonance drift, with good agreement. For example, Fig. 4.4(d) shows the relative change in  $\Delta \varphi_0$  as  $\delta_{C0}$  is intentionally changed. For this measurement, we are able to change the cavity detuning by changing the drive voltage on the PZTs after the atoms are already loaded in the lattice, as shown in the inset. We first measure  $\Delta \varphi_0$  for a variable detuning  $\delta_{C0}$  and then change the cavity length to a reference detuning  $\delta_{C0}^{\text{ref}}$ , which allow us to remove unwanted effects, such as atom number drifts, from our measurements as we did when we analyze the impact of transverse components of the magnetic field on the phase measurements. Based on these results, and a precise determination of the cavity FSR, we estimate a correction of less than 1% if we average over cavity detunings below a maximum 10 kHz drift. In fact the drifts in the zero-power value for  $\Delta \varphi_0/\Delta \varphi_1$  reported in 4.3(b) are consistent with

cavity frequency misalignment within our 10 kHz uncertainty.

### **4.8.2.4** Zeeman shift in the ${}^{3}P_{0}$ probe

The small magnetic field present to define the quantization axis generates a Zeeman splitting between the two ground states, of typical magnitude 100 Hz, smaller than the probes splitting  $2\delta_{p0}/2\pi = 2$  kHz. We can accurately calibrate the magnetic field by observing the splitting between superradiant pulses, as in Ref. [93]<sup>[G]</sup>. By using two symmetric tones to address the clock transition, the phase shift will be only second order sensitive to the Zeeman splitting. We calculate this value and assign and uncertainty based on a 5% uncertainty on the determination of the magnetic field along the quantization axis.

#### **4.8.2.5** Higher order corrections on the $\Delta \varphi_0$ measurement

Higher order corrections on the four-tones phase shift method are derived in Eq. (4.9). The second correction factor  $((2\delta_c/\kappa)^2)$  is the cavity resonance drift considered above. The other higher order terms, remnant from the small angle approximation, contribute at the level of  $10^{-4}$  for typical atom numbers, obtained through an independent calibration of our fluorescence imaging. Its uncertainty is estimated assuming extreme 50% fluctuations in typical N.

### **4.8.3** Corrections on the ratio $(\Delta \varphi_0/\Delta \varphi_1)$

In this section we discuss effects that modify both the measured atomic-like phase shift  $\Delta \varphi_0$  on the millihertz transition at 698 nm and the cavity phase shift  $\Delta \varphi_1$  on the 7.5 kHz transition at 689 nm. The magnitude of the correction factors  $F_C$  are shown in the following table.

#### **4.8.3.1** Offsets in $\Delta \phi_{0,1}$

The effect of non cancelled offsets in our measurements is to alter the measured values of  $\Delta\phi_0$  and  $\Delta\phi_1$ . In particular, because the desired phase shifts are collective, while the offset are not, it can cause an N-dependent correction to the ratio  $\Delta\phi_0/\Delta\phi_1$ .

Effect	$1-F_C$	Uncertainty on $F_{C}$
Offsets in $\Delta \phi_{0,1}$	0	$1 \times 10^{-2}$
Axial inhomogeneous probe coupling	0	$2 \times 10^{-3}$
Differential radial average	$7 \times 10^{-5}$	$1\times10^{-5}$
Finite axial confinement/ resolved carrier correction	$-6.2 \times 10^{-2}$	$4 \times 10^{-3}$
Ground state $m_F$ distribution	$-1 \times 10^{-3}$	$1 \times 10^{-3}$
Lifetime in the lattice	$-2 \times 10^{-3}$	$2 \times 10^{-3}$
Cavity birefringence	$-1.2 \times 10^{-2}$	$5 \times 10^{-3}$

Table 4.5: Correction factors  $F_C$  for the measurement of the ratio  $\Delta \varphi_0/\Delta \varphi_1$ .

Assuming single atom phase shifts  $\Delta\phi^a_{0,1}$  and offsets  $\Delta\phi^{\rm off}_{0,1}$  on each measurement, we can express the desired ratio as

$$\frac{\Delta\phi_0}{\Delta\phi_1} = \frac{N\Delta\phi_0^a + \Delta\phi_0^{\text{off}}}{N\Delta\phi_1^a + \Delta\phi_0^{\text{off}}}.$$
(4.14)

For the three different sets shown in 4.3(b) we measured low power sets with no atoms in the cavity, and verified that  $\Delta\phi_{0,1}^{\rm off}=0$  within error bars. To be specific, we typically measure  $\Delta\phi_{0}^{\rm off}=0$ (0.25) mrad and  $\Delta\phi_{1}^{\rm off}=0$ (4) mrad, while the low power phase shifts for  $N=80\times10^3$  atoms are approximately  $\Delta\phi_{0}=40$  mrad and  $\Delta\phi_{1}=400$  mrad. Therefore, the offsets do not alter the measured ratios at the 1% level, limited by the uncertainty in our determinations of the offsets.

We consider in this case the correction factor to be  $F_C = (\Delta \phi_0^a/\Delta \phi_1^a)/(\Delta \phi_0/\Delta \phi_1)$  that for small offsets  $(\Delta \phi_{0,1}^{\text{off}} \ll N\Delta \phi_{0,1}^a)$  is approximately  $F_C = 1 + \left((\Delta \phi_1^{\text{off}}/\Delta \phi_1^a) - (\Delta \phi_0^{\text{off}}/\Delta \phi_0^a)\right)/N$ . For the values just quoted and summing in quadrature the uncertainties for each phase shift, we have  $F_C = 1.00(1)$ , which represents the largest single uncertainty contribution to the final  $F_C$ . It is worth noticing that the uncertainty in the phase shifts measurements can potentially be improved by, for example, increasing the probe detunings and their power, and improving the final quantum efficiency of the detection system.

#### 4.8.3.2 Axial inhomogeneous probe coupling

The optical lattice at  $\lambda_{\rm trap}=813$  nm, the probe at  $\lambda_1=689$  nm and the probe at  $\lambda_0=698$  nm all form standing waves in the cavity that are all incommensurate with each other. Focusing on just the two probes, the couplings vary approximately as  $g_{0/1}^2=g_{m,0/1}^2\cos^2\left(2\pi z/\lambda_{0,1}+\psi_{0/1}\right)$  where z is the location along the cavity axis, z=0 is at the center of the cavity, and the spatial phase of the standing waves are  $\psi_{0/1}=0$  or  $\pi/2$ , depending the relative parity of the modes. The maximum coupling at an antinode is  $g_{0/1,m}^2$ .

As one moves along the cavity axis, the standing wave of the two probes continuously transform every 13  $\mu$ m from being aligned (having antinode aligned to antinode) to anti-aligned (having anitnodes aligned to nodes.) As a result, the probes do not interact with exactly the same set of atoms. However the atoms are loaded into lattice sites spanning approximately 0.6 mm along the cavity axis (rms diameter) so that one expects the reduction in the coupling due to spatial averaging to be nearly identical and thus cancel in the ratio of the measured couplings. Assuming atoms are only located every  $\lambda_{\rm trap}/2$ , and are spread uniformly along 0.6 mm, the ratio of averaged couplings is modified by  $< 2 \times 10^{-3}$ . If a more reasonable Gaussian envelope with standard deviation 0.3 mm (rms radius) is used to describe the loading of the lattice sites, the ratio of averaged couplings is changed by many orders of magnitude less. Here, we conservatively apply a correction  $F_C = 1$  with an uncertainty on  $F_C$  of  $2 \times 10^{-3}$ .

#### 4.8.3.3 Radial inhomogeneous probe coupling

The measured phase shifts are also modified when averaging over the radial positions of the atoms due to the finite difference in the probe mode waist sizes  $w_0$  and  $w_1$  characterizing the  $1/e^2$  in intensity radius of the Gaussian TEM<sub>00</sub> probe modes (see Table 4.1). The ratio of waists scales as  $w_1/w_0 = \lambda_1/\lambda_0 \approx 1-1.29 \times 10^{-2}$ . For an atom at a distance r away from the cavity axis, the ratio of the couplings  $g_0^2/g_1^2$  is modified by the factor f compared to its on-axis value

$$f = e^{-2\left(\frac{r}{\bar{w}}\right)^2 \left(\frac{w_1^2 - w_0^2}{\bar{w}^2}\right)},\tag{4.15}$$

where  $\bar{\mathbf{w}} = \sqrt{\mathbf{w_0 w_1}}$  is the geometric mean of the waists. For scale, at the rms thermal radius of the atomic cloud  $\sigma_r = 14~\mu\text{m}$ , the correction factor is f = 1.0007. After averaging over the atomic radial distribution, the averaged coupling  $g_0^2$  and  $g_1^2$  are both reduced by about 4% but the ratio  $g_0^2/g_1^2$  is changed by less than  $10^{-4}$ . We expect that the rms thermal radius is common to both measurements because we do interleaved nondestructive probes and because we interpolate to zero probe power so that any potential mechanical forces on the atoms is also interpolated to zero.

#### 4.8.3.4 Finite axial confinement and resolved carrier correction

The largest systematic correction that must be applied arises from the finite localization of the atoms along the axial direction. The atoms are trapped in the Lamb-Dicke regime along the cavity axis with spacing dictated by the lattice wavelength (813 nm). The probe tones almost exclusively interact with the well-resolved motional carrier transition since  $\delta_{p0} \ll \omega_z$ . Lastly, because of the finite localization of the atomic wave-function (i.e. finite Lamb-Dicke parameter) the effective strength of the carrier transition (i.e. the effective  $g_0^2$  is reduced by an estimated 6.2(4)% for which we apply a correction).

In order to evaluate the apparent modification to  $g_0^2$  from this effect, we estimate the probability distribution P(n) of finding an atom in the  $n^{th}$  axial vibrational level. The estimate is made using sideband spectroscopy measurements as shown in Fig. 4.1(c), following Ref. [363]. Based on this probability distribution, we calculate the average correction to  $g_0^2$ . We model the light-matter coupling as  $g_0^2(\phi,\hat{z}) = g_{0,m}^2\cos^2(k_p\hat{z}+\phi)$ , where  $k_p$  is the probe wave-vector,  $\hat{z}$  is the harmonic oscillator position operator,  $g_{0,m}$  is the value of  $g_0$  at a probe anti-node, and  $\phi$  is a uniformly distributed phase between 0 and  $2\pi$  that accounts for the inhomogeneous coupling of the trap atoms to the probe. This is justified as the probe and the axial atomic distribution are incommensurate and the beating length is much shorter than the cloud extent.

Furthermore, the radial spreading of the cloud means that each atom will have a slightly different axial trap frequency. To leading order, an atom at distance r from the center will have an axial frequency  $\omega_z(r) = \omega_{z,0}(1 - (r/w_{\rm trap})^2)$ , where  $\omega_{z,0}$  is the maximum axial frequency  $(\omega_{z,0}/2\pi = 230(1) \text{ kHz})$  and  $w_{\rm trap}$  is the trap waist  $(w_{\rm trap} = 79.7 \ \mu\text{m})$ . As both directions are decoupled, we have that the average axial

frequency over the atomic ensemble is  $\langle \omega_z \rangle = \omega_{z,0} (1 - (\langle r^2 \rangle / w_{\rm trap}^2))$ . For a Gaussian radial density distribution profile, we have  $\langle r^2 \rangle = 2\sigma_r^2 = 2k_B T_r / (m\omega_r^2)$ , with  $T_r$  the radial temperature determined from the motional sideband fit,  $k_B$  is the Boltzmann constant,  $\omega_r$  the radial trap frequency, and  $\sigma_r$  the rms thermal radius of the cloud along its radial direction.

We calculate the average value  $\langle g_0^2 \rangle$  over this distribution for this effective axial trap frequency  $\langle \omega_z \rangle$ , that is the value that enters in our measurement result for  $\Delta \varphi_0$ , as

$$\langle g_0^2 \rangle = \sum_{n=0}^{n=Nz} \frac{1}{2\pi} \int_0^{2\pi} P(n) \langle n | g_{0,m}^2 \cos^2(k_p \hat{z} + \phi) | n \rangle d\phi, \tag{4.16}$$

where  $N_z$  is the maximum harmonic level on the trap  $(N_z \sim 17)$  [363] and  $|n\rangle$  are the eigenstates of the unperturbed harmonic potential along the z-direction. We follow a similar procedure for the 689 nm probe, but taking into account that we are probing every transition, i.e. we sum over all possible initial and final states correcting the relative detuning between each harmonic oscillator state. Based on the reconstructed probability distribution P(n), we obtain a correction factor  $F_C = 1.062(4)$ , dominated by the uncertainty on the fitted temperature on the axial and radial coordinates. This is the biggest correction we apply to the measured ratio  $(\Delta \varphi_0/\Delta \varphi_1)$ .

We emphasize that for the  ${}^3P_1$  probe, where the probe detuning is much bigger than the trap frequency ( $\delta_{C1} \gg \omega_z$ ), the vibrational degrees of freedom do not play a significant role. However, the average over the phase  $\varphi$  in Eq. 4.16 gives a 1/2 reduction on  $g_1^2$ , that is also present in the  $g_0^2$  term, making this a common mode effect whose impact is highly suppressed. Imperfect cancellation of this factor is taken into account on the previous section *Axial inhomogeneous probe coupling*.

#### **4.8.3.5** Ground state $m_F$ distribution

The initial distribution among the different magnetic  $m_F$  sub-levels in the ground states is extremely important. For example, if there are atoms in any other  $m_F$  state other than  $\pm 9/2$ , both  $\Delta \varphi_0$  and  $\Delta \varphi_1$  (or the measured  $\Delta \omega_1$ ) will be affected. Measuring the frequency splitting between the superradiant pulses on the clock transition [93]<sup>[G]</sup>, confirmed that the initial optical pumping efficiency is at least 95% to the  $\pm 9/2$  states. In order to estimate the correction to the dispersive phase shift ratio, we assume

a conservative bound of 5% of the atoms in a wrong state. We model the measured ratio  $(\Delta \varphi_0/\Delta \varphi_1)$  when 5% of the atoms are allowed to be in any of the other  $m_F$  levels as a function of the detuning  $\delta_{C1}$ . Because the position of the different hyperfine levels on the  $^3P_1$  state relative to the cavity modes (hyperfine splitting is comparable to cavity free spectral range - see Fig. 4.1(b)), and the fact that each transition has a different set of Clebsch-Gordan coefficients, the correction factor is highly sensitive to the cavity detuning  $\delta_{C1}$ . A detail explanation follows below.

We consider a realization of the atomic distribution among the ground hyperfine state levels  $P_G$  that contains the list of probabilities of finding an atom in each ground state  $m_F$ . Ideally, all the atoms are in the stretched states, such that  $P_G = \{1/2, 0, ..., 0, 1/2\}$ , for the set  $m_F = \{-9/2, -7/2, ..., 7/2, 9/2\}$ . For the phase shift on  ${}^1S_0 \rightarrow {}^3P_0$  transition at 698 nm,  $\Delta \varphi_0$ , the new phase shift for an arbitrary distribution  $P_G$  on the  $m_F$  manifold is

$$\Delta \varphi_{0,\{m_F\}} = \sum_{m_F = -9/2}^{m_F = 9/2} P_G(m_F) \frac{4N(c_{\pi}^0(m_F))^2 g_0^2}{\kappa_0 \delta_{p0}},\tag{4.17}$$

where  $c_{\pi}^{0}(m_{F})$  is the Clebsch-Gordan coefficient for  $\pi$ -polarized light probing the  $m_{F}$  hyperfine ground state on the  ${}^{1}S_{0} \rightarrow {}^{3}P_{0}$  transition, populated with probability  $P_{G}(m_{F})$ .

For the phase shift at the  ${}^1S_0 \rightarrow {}^3P_1$  transition at 689 nm,  $\Delta \varphi_1$ , the equivalent modification is

$$\Delta \varphi_{1,\{m_F\}} = \sum_{k=\{0,1\}} \sum_{m_F=-9/2}^{m_F=9/2} P_G(m_F) \frac{2\pi N g_1^2}{\kappa_1} (-1)^k \times \left( \frac{(c_{\pi,9/2}^0(m_F))^2}{\delta_{C1} - k \times \Delta_{\text{FSR},1}} + \frac{(c_{\pi,11/2/2}^0(m_F))^2}{\delta_{C1} - \Delta_{11/2} - k \times \Delta_{\text{FSR},1}} + \frac{(c_{\pi,7/2}^0(m_F))^2}{\delta_{C1} - \Delta_{7/2} - k \times \Delta_{\text{FSR},1}} \right),$$

$$(4.18)$$

where  $c_{\pi,9/2}^0(m_F)$ ,  $c_{\pi,9/2}^0(m_F)$  and  $c_{\pi,9/2}^0(m_F)$  are the Clebsch-Gordan coefficients for the  $\pi$ -polarized transition on the F=9/2,11/2,7/2 hyperfine manifolds for each  $m_F$  state, populated with probability  $P_G(m_F)$ . Note that the sum subtracts the shifts on the two cavity modes (k index), as shown in Fig. 4.1(b), and the signs on  $\Delta_{9/2}$  and  $\Delta_{7/2}$  are taken to be consistent with the cavity detuning definition ( $\delta_{C1}$ ).

Corrections on the measured ratio are shown in Fig. 4.4(e) for the case where the fractional population on the  $\pm 7/2$  states is  $\varepsilon$ , on the  $\pm 5/2$  states is  $\varepsilon^2$ , on the  $\pm 3/2$  states is  $\varepsilon^3$ , and on the  $\pm 1/2$  states is  $\varepsilon^4$ . We determine the value of  $F_C$  as the one for  $\varepsilon = 0.05$ , and its uncertainty the one associated to the spread in order to cover up to  $\varepsilon = 0.1$ , giving  $F_C = 1.001(1)$ . We point out again the dependence on the

cavity detuning to the  ${}^3P_1$  manifold,  $\delta_{C1}$ , on the correction factor  $F_C$  on Fig. 4.4(e) inset for  $\varepsilon$  = 0.05. For the value we choose to operate ( $\delta_{C1}/2\pi$  = 277.5(8) MHz) we are near the maximum correction factor, but we gain in insensitivity with respect to the cavity detuning.

### 4.8.3.6 Finite lifetime on the optical lattice

Any of our measurement sequences that involve a few consecutive measurements per experimental trial are susceptible to atom loss from the trap. In particular, the lifetime in the lattice is  $\tau_{\text{latt}} \sim 500 \text{ ms}$  (limited by parametric heating), while typical measurements on the clock transition last  $T_m \sim 20 \text{ ms}$  typically. By combining 5 of these measurements, as in 4.3(b), we can use the different outcomes and partially cancel the effect of the trap lifetime, by retaining a correction  $1 + \alpha (T_m/\tau_{\text{latt}})^2$ , where  $\alpha$  can vary from 0 to 1 according to the way we combine the measurement outcomes (see next sections). The magnitude and uncertainty on the correction contemplates a uniform spread of  $\alpha$ .

#### 4.8.3.7 Cavity birefringence

In an ideal atom-cavity system, light polarized along the atoms' quantization axis will only interact with  $\pi$  transitions. However, the presence of cavity birefringence featuring normal modes misaligned with this axis leads to a coupling between  $\pi$ -polarized light and atomic transitions normally driven by circularly polarized light that is quadratic in the birefringent energy splitting. This effect introduces corrections to both phase shift measurements which do not cancel in their ratio, leading to a systematic on the ratio measurement. Calculating these corrections requires modifying the cavity transfer function shown in Eq. (4.4).

In the presence of cavity birefringence, a single longitudinal mode splits into two resonances characterized by polarization eigenmodes  $\hat{a}_{\pm}$ , such that

$$\hat{H}_{cav} = (\omega_c - \frac{\delta_b}{2})\hat{a}_-^{\dagger}\hat{a}_- + (\omega_c + \frac{\delta_b}{2})\hat{a}_+^{\dagger}\hat{a}_+$$
 (4.19)

for birefringent splitting  $\delta_b$ . Since the probe beam polarization and quantization axis are aligned to a common vertical direction ( $\hat{x}$  as in Fig. 4.1(a)), it makes sense to express these eigenmodes in this basis

as well. This is accomplished using two parameters  $\theta_b$ ,  $\varphi_b$ :

$$\hat{a}_{-} = \left[\cos(\theta_b/2)\right] \hat{v} + \left[-\sin(\theta_b/2)e^{-i\varphi_b}\right] \hat{h}$$

$$\hat{a}_{+} = \left[\sin(\theta_b/2)e^{i\varphi_b}\right] \hat{v} + \left[\cos(\theta_b/2)\right] \hat{h},$$
(4.20)

such that light along  $\hat{h}$  ( $\hat{y}$  as in Fig. 4.1(a)) and  $\hat{v}$  polarizations interact with  $\sigma$  and  $\pi$  transitions respectively. The above expressions are essentially Jones vector representations of the eigenmodes; correspondingly,  $\theta_b$  and  $\varphi_b$  can be thought of as spherical coordinates for the eigenmodes on the Poincaré sphere with poles defined by h and v polarizations.

As long as the atoms occupy stretched states ( $m_F = \pm 9/2$ ), there is only one  $\sigma$  transition. Therefore one can unambiguously define collective spin operators along the two transitions, denoted by  $J_{\pi/\sigma}^{\pm} = \sum_{i=1}^{N} \sigma_{i,\pi/\sigma}^{\pm}$  and  $J_{\pi/\sigma}^{z} = \frac{1}{2} \sum_{i=1}^{N} \sigma_{i,\pi/\sigma}^{z}$  for single particle operators  $\sigma_{i,\pi/\sigma}^{*}$ . We go into the rotating frame of the atoms, assuming the two transitions are degenerate in frequency, to construct the following Hamiltonian:

$$\hat{H} = \left[ \left( \delta_c - \frac{\delta_b}{2} \cos \theta_b \right) \hat{v}^{\dagger} \hat{v} + \left( \delta_c + \frac{\delta_b}{2} \cos \theta_b \right) \hat{h}^{\dagger} \hat{h} + \frac{\delta_b}{2} \sin \theta_b \left( \hat{h}^{\dagger} \hat{v} e^{i\varphi_b} + \hat{h} \hat{v}^{\dagger} e^{-i\varphi_b} \right) \right] + \left[ g_{\pi} \left( \hat{v} \hat{J}_{\pi}^{+} + \hat{v}^{\dagger} \hat{J}_{\pi}^{-} \right) + g_{\sigma} \left( \hat{h} \hat{J}_{\sigma}^{+} + \hat{h}^{\dagger} \hat{J}_{\sigma}^{-} \right) \right]. \tag{4.21}$$

Analogously to the derivation at the start of this document, one can derive Optical Bloch equations to analyze mean-field behavior  $(O = \langle \hat{O} \rangle)$ . Assuming a vertically polarized cavity drive  $v_i(t)$  at detuning  $\delta_p$  from atomic resonance, these equations are given by

$$\dot{v} = -i\left[\left(\delta_{c} - \frac{\delta_{b}}{2}\cos\theta_{b}\right)v + \left(\frac{\delta_{b}}{2}\sin\theta_{b}e^{-i\varphi_{b}}\right)h\right] - ig_{\pi}J_{\pi}^{-} - \frac{\kappa}{2}v + \sqrt{\kappa_{m}}v_{i}(t)$$

$$\dot{h} = -i\left[\left(\delta_{c} + \frac{\delta_{b}}{2}\cos\theta_{b}\right)h + \left(\frac{\delta_{b}}{2}\sin\theta_{b}e^{i\varphi_{b}}\right)v\right] - ig_{\sigma}J_{\sigma}^{-} - \frac{\kappa}{2}h$$

$$\dot{J}_{\pi}^{-} = 2ig_{\pi}vJ_{\pi}^{z} - \gamma_{\pi}^{\perp}J_{\pi}^{-} \qquad \dot{J}_{\sigma}^{-} = 2ig_{\sigma}hJ_{\sigma}^{z} - \gamma_{\sigma}^{\perp}J_{\sigma}^{-}$$

$$\dot{J}_{\pi}^{z} = ig_{\pi}\left(v^{\dagger}J_{\pi}^{-} - vJ_{\pi}^{+}\right) - \gamma_{\pi}N_{\pi} \qquad \dot{J}_{\sigma}^{z} = ig_{\sigma}\left(h^{\dagger}J_{\sigma}^{-} - hJ_{\sigma}^{+}\right) - \gamma_{\sigma}N_{\sigma},$$

$$(4.22)$$

where  $N_{\pi/\sigma}$  represents the number of atoms excited along the  $\pi/\sigma$  transition. In the weak probe limit, both of these go to 0 as there are no excited atoms available to decay.

From these equations, one can determine how the input probe  $v_i(t) = \tilde{v}_i e^{-i\delta_p t}$  changes in transmission through the atom-cavity system. In general for a birefringent cavity, the transmitted light's polarization may be different from the probe due to different resonance conditions for the two normal

polarization modes. In our experiment, we beat the transmitted light with a vertically polarized local oscillator to measure the light in heterodyne, so the signal of interest is the vertical component of any transmitted light. We are therefore interested in the transfer function  $T_v(\delta_p)$ , defined by  $\tilde{v}_t = T_v(\delta_p)\tilde{v}_i$ . It turns out that  $T_v$  can be expressed in terms of the following transfer functions, which decouple the horizontal and vertical excitations:

$$T_{\pi}(\delta_{p}) = \frac{1}{1 - i(\frac{\delta_{p} - \delta_{c} + \delta_{b}/2 \cos \theta_{b}}{\kappa/2}) + \frac{NC_{\pi}\gamma_{\pi}/2}{\gamma_{\pi}^{\perp} - i\delta_{p}}}$$

$$T_{\sigma}(\delta_{p}) = \frac{1}{1 - i(\frac{\delta_{p} - \delta_{c} - \delta_{b}/2 \cos \theta_{b}}{\kappa/2}) + \frac{NC_{\sigma}\gamma_{\sigma}/2}{\gamma_{\sigma}^{\perp} - i\delta_{p}}}.$$

$$(4.23)$$

Then the full transfer function is given by

$$T_{\nu}(\delta_{p}) = \frac{T_{\pi}(\delta_{p})}{1 + (\frac{\delta_{b}}{\kappa} \sin \theta_{b})^{2} T_{\sigma}(\delta_{p}) T_{\pi}(\delta_{p})}.$$
(4.24)

Note that the transfer function does not depend on the azimuthal angle  $\varphi_b$ ; this holds as long as the transmitted light is only measured along  $\nu$ . For small birefringent splitting,  $F_{\nu}$  can be calculated perturbatively by expanding in powers of  $(\frac{\delta_b}{\kappa}\sin\theta_b)^2$ . It follows that leading order corrections to the cavity shifts will be quadratic in  $\delta_b$ .

Using a simple polarimetry setup consisting of PBSs, waveplates, and photodiodes, we were able to measure  $\delta_{b0}/\kappa_0 = +0.16(2)$ ,  $\delta_{b1}/\kappa_1 = +0.16(2)$ , and  $\theta_b = 30(2)^\circ$ . This implies  $(\frac{\delta_b}{\kappa}\sin\theta_b)^2 = 0.006(2)$  along both transitions, justifying a perturbative treatment. From this, we can calculate the modified shifts and derive a correction factor for the shift ratio  $\Delta\varphi_0/\Delta\varphi_1$ , which turns out to be  $F_C = 1.012(3)$ . This value accounts for all differential shift measurements, as well as the full hyperfine landscape.

Considering the effect of cavity birefringence opens up new potential sources of uncertainty. First, one might imagine that an imperfect optical pumping scheme might conspire with the cavity's birefringence to produce larger corrections than previously discussed. In fact, numerical calculations show the two effects are largely decoupled and can be treated separately. Second, if the local oscillator is misaligned from vertical polarization by some small angle  $\alpha$ , all phase shifts will receive a linear correction proportional to  $\alpha \frac{\delta_b}{\kappa} \sin \theta_b$ . However, the experiment's differential probe design leads to partial cancellation of these shifts. Assuming  $\alpha$  is uncertain by 5°, the additional uncertainty on  $F_C$  is at most

0.003. Finally, if the two birefringent normal modes exhibit slightly different linewidths, the optical Bloch equations change accordingly and lead to further phase shift modifications. Data used to determine  $\delta_b$  allows us to constrain any linewidth difference to  $\delta\kappa\lesssim 0.05\kappa$ , which limits the correction on  $F_C$  to  $\lesssim 0.001$ . Incorporating these additional sources of uncertainty into the birefringence correction factor gives  $F_C=1.012(5)$ .

This experiment was performed before the discovery of cavity birefringence in our system. In principle, for future experiments one could mitigate the effect of this systematic by aligning all beam polarizations and the atoms' quantization axis along the birefringent eigenmode axis. If the eigenmodes are linearly polarized, the probe beam will only excite one of the two modes, completely removing any birefringent coupling. Otherwise, any ellipticity the eigenmodes possess will limit the ability to suppress the coupling with a linearly polarized probe beam, which is necessary for this experiment. In our system, the effect of birefringence could be suppressed by approximately ~ 17 by such an alignment.

#### 4.8.4 Summary - Full systematic correction

Taking all this effects into account we infer a correction factor  $F_C = 1.074(16)$  on the measured ratio  $(\Delta \varphi_0/\Delta \varphi_1)$ . Its value is determined by multiplying the systematic corrections detailed in Tables 4.3, 4.4, and 4.5, while its uncertainty is properly summed in quadrature. The uncertainty on  $F_C$  is dominated, mostly, by technical issues, such as the uncertainty in the clock atomic frequency, the cavity alignment with the atomic resonance, and alignment of the probe polarization with respect to the cavity eigenmode axis considering birefringence, which can be further improved. Furthermore, its uncertainty is also dominated by technical aspects such as signal to noise in our data and its influence on determining the phase shifts offsets, as well as uncertainty in the atomic transition frequency and cavity alignment on the clock transition.

### 4.9 Statistical estimators of the zero-power, zero-loss phase shift ratio

In this section, we will discuss the details of the low power measurement presented in 4.3(b). Absent systematic corrections, it remains to determine the zero-probe-power value for the ratio  $(\Delta \varphi_0/\Delta \varphi_1)$ ,

that we will name  $(\Delta \varphi_0/\Delta \varphi_1)_{P=0}$ .

We measured the ratio of the atomic phase shift to cavity frequency shift while simultaneously decreasing both 698 and 689 probe powers,  $P_0$  and  $P_1$  respectively, and taking longer sets to accumulate similar statistics for lower optical power measurements, as expected from the photon-shot noise scaling. The ratio is expected to strongly depend on both powers, although the maximum 689 nm optical power was already low enough to be a significant effect, according to the results shown in panels b and c in Fig. 4.4. We measure  $\Delta \varphi_0$  and  $\Delta \varphi_1$  in an interleave form, to gain insensitivity with respect to lattice lifetime. We realize five measurements every  $T_c = 25$  ms, as shown in 4.3(b), interleaving three  $\Delta \varphi_1$  short measurements ( $\sim 2$  ms) with two longer  $\Delta \varphi_0$  measurements ( $\sim 25$  ms). Upon further detailed inspection, the ratio of the average of two  $\Delta \varphi_0$ 's and the average of the three  $\Delta \varphi_1$ 's measurements will have the same linear sensitivity to atom loss, therefore a ratio of the two quantities will be quadratically sensitive to  $T_c/\tau_{\rm latt}$ .

The 698 nm clock transition probe could excite atoms to  $|e_0\rangle$ , and those atoms will not be counted by the following dispersive 689 nm probe. We assume, in the weak probe power limit, that each clock transition probe excites a fraction  $\beta_0$  of atoms into  $|e_0\rangle$  every  $T_c/2$  interval while they are being probed. Reversely, if there are atoms in the excited state, a fraction  $\beta_0$  is transferred to  $|g\rangle$ . For the 689 nm probe, we assume an excitation fraction  $\beta_1$ , but also that any atom in the excited state is reset to the ground state before the following  $\Delta \varphi_0$  measurement, as the spontaneous emission decay time is only 21  $\mu$ s. Furthermore, losses from the lattice are treated as an exponential loss decay with time constant  $\tau_{\text{latt}}$ , which was experimentally verified repeatedly.

We use the measurement outcomes of the different  $\Delta \varphi_0$  and  $\Delta \varphi_1$  measurements to construct different estimators for the zero-power ratio  $(\Delta \varphi_0/\Delta \varphi_1)_{P=0}$ . Examples of these estimators, to name a few,

are

$$E_{1} = \frac{3}{2} \left( \frac{\Delta \varphi_{0}^{1} + \Delta \varphi_{0}^{2}}{\Delta \varphi_{1}^{1} + \Delta \varphi_{1}^{2} + \Delta \varphi_{1}^{3}} \right)$$

$$E_{2} = 2 \left( \frac{\Delta \varphi_{0}^{1} + \Delta \varphi_{0}^{2}}{\Delta \varphi_{1}^{1} + 2\Delta \varphi_{1}^{2} + \Delta \varphi_{1}^{3}} \right)$$

$$E_{3} = 4 \left( \frac{\Delta \varphi_{0}^{1} + \Delta \varphi_{0}^{2}}{\Delta \varphi_{1}^{1} + 6\Delta \varphi_{1}^{1} + \Delta \varphi_{1}^{3}} \right),$$
(4.25)

where the super-index orders each of the five measurements, i.e.  $\Delta \varphi_1^2$  is the second  $\Delta \varphi_1$  measurement.

For low optical power  $\beta_0$  ( $\beta_1$ ) is proportional to the probe optical power  $P_0$  ( $P_1$ ) on the clock transition (7.5 kHz transition) and satisfies  $\beta_0$  ( $\beta_1$ )  $\ll$  1). In this case we can compute how populating the  $|e_0\rangle$  and  $|e_1\rangle$  states during the measurement sequence affects the estimators, for example,

$$E_{1} = \left(\frac{\Delta\varphi_{0}}{\Delta\varphi_{1}}\right)_{P=0} \left(1 - \beta_{0} + 2\beta_{1} - \frac{5}{6} \left(T_{c}/\tau_{\text{latt}}\right)^{2} + O\left(\beta_{0}, \beta_{1}, T_{c}/\tau_{\text{latt}}\right)\right)$$

$$E_{2} = \left(\frac{\Delta\varphi_{0}}{\Delta\varphi_{1}}\right)_{P=0} \left(1 - \beta_{0} + 2\beta_{1} - \frac{1}{2} \left(T_{c}/\tau_{\text{latt}}\right)^{2} + O\left(\beta_{0}, \beta_{1}, T_{c}/\tau_{\text{latt}}\right)\right)$$

$$E_{3} = \left(\frac{\Delta\varphi_{0}}{\Delta\varphi_{1}}\right)_{P=0} \left(1 - \beta_{0} + 2\beta_{1} + O\left(\beta_{0}, \beta_{1}, T_{c}/\tau_{\text{latt}}\right)\right),$$
(4.26)

where  $O\left(\beta_0, \beta_1, T_c/\tau_{\text{latt}}\right)$  refers to higher order terms in combinations of  $\beta_0, \beta_1$ , and  $T_c/\tau_{\text{latt}}$ , and  $\left(\frac{\Delta \varphi_0}{\Delta \varphi_1}\right)_{P=0}$  is the zero-power ratio that we want to determine.

In 4.3(b) we show the result for the so-called  $E_3$  estimator above and show quadratic polynomial fits in the optical power  $P_0$  for the clock transition ( $\beta_0 \propto P_0$ ). In Table 4.6 we show the fitted  $\left(\frac{\Delta \varphi_0}{\Delta \varphi_1}\right)_{P=0}$  for different estimators and fit methods, as a way to show a consistent method-independent value. The data is not corrected by any systematic. We also point out that we did not take  $\beta_1$  or  $P_1$  into consideration for either of these fits, as doing so does not significantly modify the other fitted parameters, because the maximum value that  $P_1$  takes on all the 4.3(b) measurements is already low enough to cause significant population in  $|e_1\rangle$ .

The results are consistent with a zero power crossing  $\left(\frac{\Delta \varphi_0}{\Delta \varphi_1}\right)_{P=0} = -8.95(9) \times 10^{-2}$ . We finally note that for single measurement instances as represented by the red, green and blue data sets, independently of the estimators we compute, the data is spread consistently with a 10 kHz uncertainty on the alignment of the cavity resonance frequency to the clock atomic transition ( $\delta_{C0}$ ), as described previously. A zoom

Estimator	Fit method/origin	$\left(\frac{\Delta \varphi_0}{\Delta \varphi_1}\right)_{P=0} \times 10^{-2}$	$\frac{150}{\chi_v^2}$
Estimator $E_1$	Quadratic on $P_0$ . Mean value for crossing.	-8.92(6)	
Estimator $E_2$	Quadratic on $P_0$ . Mean value for crossing.	-8.92(6)	
Estimator $E_3$	Quadratic on $P_0$ . Mean value for crossing.	-8.95(6)	
Estimator $E_3$	Linear on $P_0$ ( $P_0 \le 400$ pW). Mean value for crossing.	-8.95(6)	
Estimator $E_3$ (removing 7 ms data)	Quadratic on $P_0$ . Mean value for crossing.	-8.95(6)	
Estimator $E_3$ (only for red set)	Quadratic on $P_0$ .	-8.86(6)	0.7
Estimator $E_3$ (only for green set)	Quadratic on $P_0$ .	-9.02(7)	1.2
Estimator $E_3$ (only for blue set)	Quadratic on $P_0$ .	-8.95(4)	0.6
Estimator $E_3$	Quadratic on $P_0$ . Using a global fit to the three sets.	-8.95(4)	1.1

Table 4.6: Fits for several estimators for the ratio  $(\Delta \varphi_0/\Delta \varphi_1)$ .

in of the data presented in 4.3(b) is shown in Fig. 4.4(f). Fits are for the estimator  $E_3$  for each set, and the black solid line is a global fit for all the data sets.

### **4.10** Constraining N dependent effects on $\Delta \varphi_0 / \Delta \varphi_1$ measurements.

As discussed on a few of the systematic corrections presented previously, sometimes we can find atom number dependent corrections that do not completely cancel when measuring the ratio  $\Delta \varphi_0/\Delta \varphi_1$ . For example, when discussing the independent phase shifts offsets or higher order corrections.

In order to check the influence of these effects, and lacking an underlying model to believe they would impact our measurement, we decided to perform  $\Delta \varphi_0/\Delta \varphi_1$  measurements for different atom number N. These measurements are presented as an inset in 4.3(b).

For that set, our phase shifts measurements present some non-zero phase shifts offsets that were properly measured. The most simplistic model, as introduced in Eq. 4.14, serves us as a proxy to further investigate any unknown variations with N and 1/N on the ratio measurements. All in all, by considering different variations of these fits, taking into account the N=0 point and the offsets we measured, we find agreement at the 2% level with the weighed average of the measured phase shift ratio (the value that we

would assign for the ratio if no *N* dependent effect were present). This uncertainty is dominated by the signal to noise ratio on the current data set.

Therefore, we constrain any unknown N dependent effect on the ratio at the 2% level, which is at the level of our final uncertainty on the phase shift ratio and linewidth ratio. We consider this experiment as a sanity check, but we do not use this independent constraint to modify our final uncertainty.

#### 4.11 Conclusion

In conclusion, we show that cavity enhanced dispersive measurements can be used to realize spectroscopic measurements directly on ultranarrow optical transitions. We report state-dependent phase shifts on the <sup>87</sup>Sr clock transition, that are notably nondestructive, allowing for continuous tracking of the transition frequency and potentially allowing laser stabilization to these transitions. With further improvements on our detection setup, this scheme could be used as an atom counting tool directly on the clock transition, in contrast to other systems [354–358][242]<sup>[G]</sup>. This tool would be particularly useful for new optical lattice clocks built with optical cavities. Moreover, our setup represents a potential path for laser stabilization to ultranarrow lines such as in a continuous superradiant laser.

Finally, we report a lifetime resolution of 30  $\mu$ Hz, which implies we could determine excited state lifetimes of up to 90 minutes in comparable integration time ~100 ms. With reasonable improvements in our setup, we could expect to determine up to 15 hour lifetimes, i.e., by reducing  $\delta_{p0}$  to increase the signal, if no systematic effects are taken into account. For instance, it could be used to directly measure the magnetic-field-dependent linewidth of bosonic isotopes in Sr [105, 256], determine the Sr  $^3P_2$  excited state lifetime or even longer lived states such as the predicted ~10  $\mu$ Hz nuclear transition on  $^{229}$ Th being pursued as a next generation clock [369–372], or obtain data on exotic systems of interest for atomic structure calculations, such as highly charged ions [342, 373, 374], in cases where suitable transitions can be found.

#### Chapter 5

### Exploring dynamical phase transitions with cold atoms in an optical cavity

#### 5.1 Introduction

Arrays of ultracold alkaline-earth atoms with narrow linewidth optical transitions are the basis of some of the most precise atomic clocks [317] and are also used for quantum simulation [375] and quantum information processing [376]. As we saw in Ch. 4, placing these atoms inside an optical cavity opens up new avenues for performing precision measurement. Similarly, collective cavity QED on long-lived transitions provides a means of investigating collective (many-body) quantum physics in controlled environments. Such ensembles of atoms in cavities have been proposed for studying collective quantum spin models, where the atomic internal levels mimic a spin degree of freedom and interact through long-range interactions tunable by changing the cavity parameters [68, 377, 378][95]<sup>[G]</sup>. Non-classical steady-state phases arising from the interplay between atom-light interactions and dissipation of light from the cavity have previously been investigated [32–36, 76, 379]. These systems also offer the opportunity to study so-called "dynamical phases" of matter that are precluded from existence at equilibrium but can be stabilized by driving a system out of equilibrium [48, 115, 380–382], as demonstrated by recent experiments [120, 121, 383–386]. These phases can also display universal behaviors akin to standard equilibrium phase transitions [379, 387, 388].

The work described in this chapter (which can be found at [108]<sup>[G]</sup>) represents an advance towards the goal of simulating quantum magnetism in an optical cavity. In particular, we use an ensemble of about a million <sup>88</sup>Sr atoms in an optical cavity to simulate a collective Lipkin-Meshkov-Glick model [109, 110], an iconic model in quantum magnetism, and report the observation of distinct dynamical phases

of matter in this system. Our system allows us to probe the dependence of dynamical phase transitions on system size, initial state and other parameters. These observations can be linked to similar dynamical phases in related systems, including the Josephson effect in superfluid helium [389], or coupled atomic [112] and solid-state polariton [114] condensates. The system itself offers potential for generation of metrologically useful entangled states in optical transitions, which could permit quantum enhancement in state-of-the-art atomic clocks [98, 317].

More broadly speaking, this work represents the first of a series of experiments from our group exploring nonequilibrium phases of dynamics and their associated phase transitions, resulting in work described in Ch. 6, Ch. 7, and part of Ch. 8. We will return to this work in future chapters to compare and contrast the different models studied.

#### 5.2 What is a dynamical phase transition?

The concept of a phase of matter, along with the notion of transitions between such phases, has conventionally been used to describe behavior of a system in thermodynamic equilibrium. For some definition of an order parameter characterizing the thermodynamic ground state, phase transitions occur when the order parameter discontinuously jumps (a first-order phase transition) or exhibits a nonanalytic critical point (a second-order phase transition) as a function of some parameter of the system such as temperature or an applied external field. Equilibrium physics already encompasses a vast breadth of physical systems with rich behavior and many unanswered questions. Considering out-of-equilibrium systems expands the number of possible systems significantly and have received much interest in recent years.

We can expand the notion of phase transitions to encompass nonequilibrium systems as well. Generically, a "nonequilibrium phase transition" is characterized by the existence of a critical point for some broader definition of an order parameter, which now no longer has to describe the thermodynamic ground state but can be some generalized observable that separates nonequilibrium "phases" with distinct properties. Such systems have been described in many different contexts. In driven open systems, nonequilibrium phases are signaled by different steady states that depend on system parameters such

as pump or loss rates [34–36, 390–392], independent of initial conditions. For the scope of this thesis, I will refer to these transitions as **dissipative** or **driven-dissipative transitions**.

Here, we focus on a different class of systems: those featuring nonequilibrium phase transitions in a closed system. In these cases, which we will call **dynamical phase transitions (DPTs)**, the nonequilibrium quantum phases are dynamical in nature, rather than reflecting only a steady state. Above and below some critical point, we should observe qualitatively distinct behaviors with a sharp transition between the two regimes [115–119] using a time average of an order parameter such as magnetization. DPTs are typically initiated by quenching control parameters and depend on the initial state of the system. Examples of these transitions have been observed experimentally in arrays of trapped ions [120] and cold gases [121], as well as previously in the context of macroscopic self-trapping [111–114]. Here we demonstrate a DPT in a system of cold atoms with global interactions mediated by an optical cavity.

### 5.3 Implementing the Lipkin-Meshkov-Glick model

A feature of our cavity simulator (see Fig. 6.1(a)), compared with many aforementioned experiments, is the use of a large ensemble of  $N \approx 10^5$ - $10^6$  cold atoms. We use two long-lived electronic levels in these atoms,  $|\downarrow\rangle$  ( ${}^1S_0$ ,  $m_J=0$ ) and  $|\uparrow\rangle$  ( ${}^3P_1$ ,  $m_J=0$ ) states, with a transition wavelength of 689 nm between the two, to mimic a spin-1/2 system ( $|\downarrow\rangle$  and  $|\uparrow\rangle$ , respectively). Our atoms are trapped in an 813 nm one-dimensional optical lattice, similar to previous works from our group [93, 95, 223, 242]<sup>[G]</sup>, and described in more detail in Sec. 5.5. We operate in a regime where the atoms couple to a single common transverse electromagnetic (TEM<sub>00</sub>) mode of the optical cavity with resonance frequency  $\omega_c$  detuned from the optical atomic transition  $\omega_a$  by  $\Delta = \omega_c - \omega_a$ . Here,  $|\Delta|$  is much larger than the cavity linewidth  $\kappa/2\pi=153.0(4)$  kHz, the atomic transition linewidth  $\gamma/2\pi=7.5$  kHz, and also the vacuum Rabi splitting  $2g\sqrt{N}$  induced by the atoms, with g represents half the single-photon Rabi frequency  $2g/2\pi=21.8$  kHz. In this limit, the cavity mediates a global spin-exchange interaction, which is microscopically described by a flip-flop process in which the emission of a photon from atom i in state  $|\uparrow\rangle$  into the cavity mode

<sup>&</sup>lt;sup>1</sup> The usage of the term "dynamical phase transition" is not always consistent across the literature. Sometimes, you will see people use the term to refer to what we call dissipative phase transitions. If you use the term, make sure to clarify what you many

is subsequently absorbed by atom j in state  $|\downarrow\rangle$ , as depicted in 6.1(a)(iii). As explained in Ch. 2.5.3, the interaction rate scales as  $\chi N$ , where  $\chi = -\frac{g^2}{\Delta}$  in the large-detuning limit. In contrast to previous work in our group studying spin-exchange physics  $[95]^{[G]}$ , superradiant emission does not play an active role due to the large detuning. Finally, the interaction dynamics are faster than spontaneous emission, i.e.,  $|\chi|N\gg\gamma$ , and the system obeys the hierarchy  $|\Delta|\gg g\sqrt{N}\gg\kappa$ ,  $\gamma$ . This parameter regime allows us to explore the closed-system dynamics associated with our predicted dynamical phases on a timescale shorter than  $1/\gamma$ .

Under these circumstances, the system can be described by the well-known Lipkin-Meshkov-Glick (LMG) model [109, 110], which has been studied in various contexts including quantum magnetism. The LMG model obeys the following Hamiltonian:

$$\hat{H}/\hbar = \chi \hat{J}^{+} \hat{J}^{-} + \Omega \hat{J}_{x} - \delta \hat{J}_{z}. \tag{5.1}$$

Here,  $\Omega$  represents a transverse field, physically represented in our system by a global drive along the  ${}^1S_0 - {}^3P_1$  transition. The detuning  $\delta := \omega_p - \omega_a$  of this drive (at frequency  $\omega_p$ ) from the atomic transition (at frequency  $\omega_a$ ) represents a longitudinal field (see 6.1(a)(ii) for a depiction). We have also introduced the collective spin operators  $\hat{J}_\alpha := \sum_j \hat{\sigma}_j^\alpha/2$ , where  $\hat{\sigma}_j^\alpha$  is a Pauli operator for the jth atom with  $\alpha = x, y, z$  and  $\hat{J}^{\pm} = \hat{J}_x \pm i \hat{J}_y$ . The summation runs over the individual atoms  $j \in [1, ..., N]$  in the cavity. The model is realized in the limit in which the cavity field couples identically to all atoms trapped in the optical lattice (see Sec. 5.9 for modifications due to inhomogeneity in this coupling).

#### 5.4 Dynamical phase diagram

On varying the ratios between  $\Omega$ ,  $\delta$  and  $\chi$ , two distinct dynamical phases emerge, for which the time-averaged collective magnetization (along  $\hat{z}$ ) of the atomic ensemble  $\overline{\langle \hat{J}_z \rangle} \coloneqq \lim_{T \to \infty} \frac{1}{T} \int_0^T \langle \hat{J}_z(t) \rangle dt$  serves as an order parameter. When all spins are initially prepared in the  $|\downarrow\rangle$  state with  $\delta=0$ , the system features a sharp second-order transition [393] between a dynamical ferromagnetic phase with  $\overline{\langle \hat{J}_z \rangle} \neq 0$  and a dynamical paramagnetic phase with  $\overline{\langle \hat{J}_z \rangle} = 0$ . This transition is indicated by the solid green line (V1) on the phase diagram shown in Fig. 6.1(b), as well as its projection on the  $\overline{\langle \hat{J}_z \rangle}$  vs.  $\Omega$  plane in the

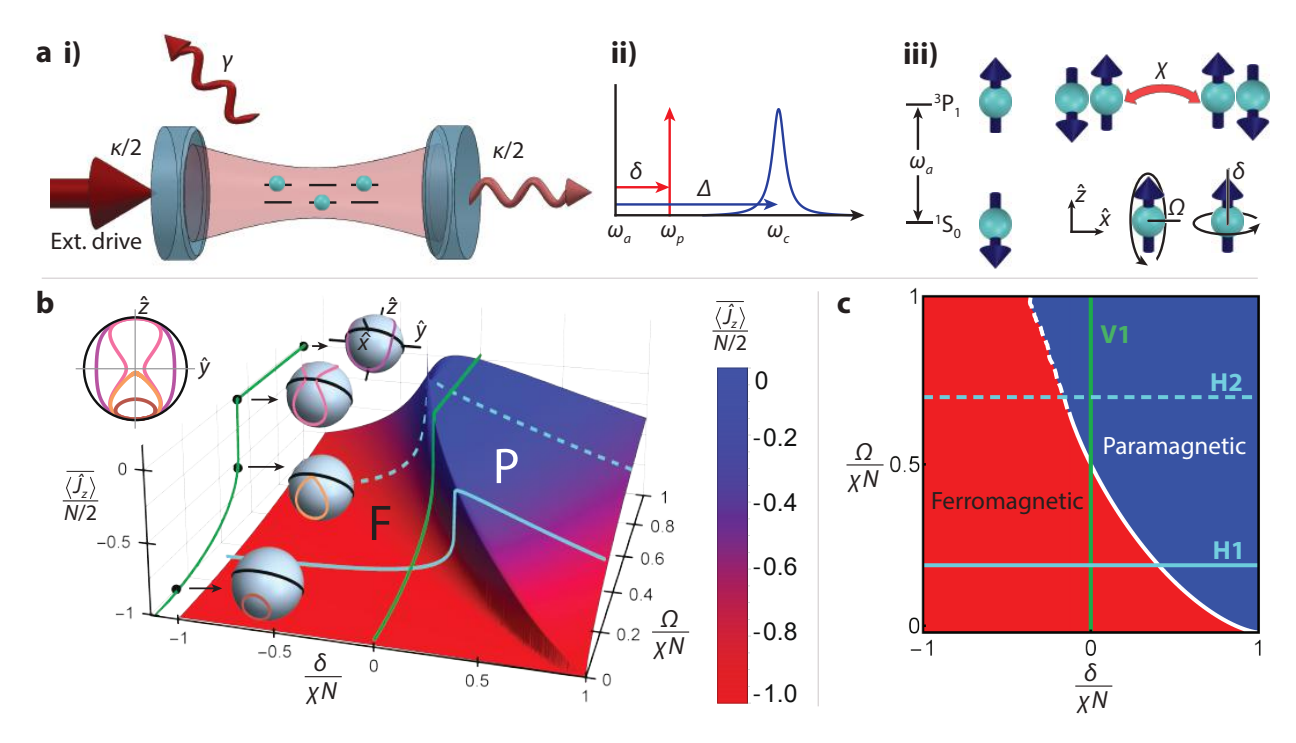


Figure 5.1: System overview and dynamical phase diagram of the Lipkin-Meshkov-Glick model. (a) (i) An ensemble of <sup>88</sup>Sr atoms is trapped in a 1D optical lattice supported by an optical cavity. The atoms are coupled to a single cavity mode with a single-photon Rabi frequency 2g and a resonance frequency  $\omega_c$ detuned by  $\Delta = \omega_c - \omega_a$  from the optical atomic transition  ${}^1S_0$ ,  $m_I = 0$  ( $|\downarrow\rangle$ ) to  ${}^3P_1$ ,  $m_I = 0$  ( $|\uparrow\rangle$ ) (with frequency  $\omega_a$  and linewidth  $\gamma$ ). Light leaks out of the cavity at a total rate  $\kappa$ . The cavity is driven externally by a laser with frequency  $\omega_p$  that, if on resonance with an empty cavity, would establish a coherent state inside the cavity with average intracavity photon number  $|2\Omega_p/\kappa|^2$ . As shown in (ii) and (iii), for the fardetuned cavity system in consideration, the external drive generates a transverse field that drives Rabi flopping at frequency  $\Omega = -2g\Omega_p/\Delta$ . The external drive detuning  $\delta = \omega_p - \omega_a$  establishes a longitudinal field. The detuned cavity field generates an effective spin exchange interaction of strength  $\chi = -g^2/\Delta$ as shown in (iii). (b) The collective Lipkin-Meshkov-Glick (LMG) model with transverse and longitudinal fields features a second-order dynamical phase transition (DPT) between paramagnetic (P, blue) and ferromagnetic phases (F, red). The DPT is characterized by the long-time average of the collective magnetization  $\langle \hat{J}_z \rangle$ , and its dynamics can be characterized by trajectories of the classical Bloch vector on the pseudospin Bloch sphere (see projection and associated sphere insets). For  $\delta = 0$ , in the paramagnetic phase the trajectories circumnavigate the Bloch sphere, whereas in the ferromagnetic phase the trajectories are trapped below the equator. (c) The two-dimensional map shows the DPT indicated by a sharp change in  $\langle \hat{J}_z \rangle$  (white solid line) for  $\delta/\chi N \ge -1/8$ . The white dashed line  $(\delta/\chi N < -1/8)$  signals a smooth crossover between the two phases (see Methods). Curves for  $\delta = 0$  (green solid line, V1),  $\Omega/\chi N = 0.2$ (blue solid line, H1), and for  $\Omega/\gamma N = 0.7$  (blue dashed line, H2) are shown on both diagrams and experimentally investigated in Figs. 5.3(b), 5.4(a), and 5.4(b) respectively. The dependence of the transition point on both  $\delta/\chi N$  and  $\Omega/\chi N$  is investigated in Fig. 5.6(b).

same panel and in Fig. 6.1(c).

In the ferromagnetic phase (red region in Fig. 6.1(b), (c)), the instantaneous magnetization  $\langle \hat{J}_z \rangle$  oscillates about a non-zero time-averaged value, and the collective pseudospin Bloch vector given by  $\langle \hat{J} \rangle \coloneqq (\langle \hat{J}_x \rangle, \langle \hat{J}_y \rangle, \langle \hat{J}_z \rangle)$  remains trapped below the equator of the Bloch sphere throughout the dynamics. This phase is dominated by the interactions which can be understood in a mean-field approximation as  $\chi \hat{J}^+ \hat{J}^- \approx \chi (\hat{J} \cdot \hat{J} - \hat{J}_z^2) \approx \chi (N/2)^2 - 2\chi \langle \hat{J}_z \rangle \hat{J}_z$ . The term  $\hat{J} \cdot \hat{J}$  is a constant when restricted to the fully symmetric spin manifold, which is the case of interest here. The second term describes a self-induced precession of the collective Bloch vector about the  $\hat{z}$ -axis, which effectively tilts the axis of rotation of the comparatively weak transverse field, such that the trajectory of the Bloch vector deforms into an orbit that remains below the equatorial plane. Conversely, the paramagnetic phase (blue region in Fig. 6.1(b), (c)) is dominated by Rabi flopping driven by the transverse field  $\Omega \hat{J}_x$ . This term causes large oscillations of the instantaneous  $\langle \hat{J}_z \rangle$ , and, for  $\delta = 0$ , the collective Bloch vector breaks through the equatorial plane and rotates about the entire Bloch sphere.

For  $\delta=0$ , the transition between the paramagnetic and ferromagnetic phases occurs at a critical drive  $\Omega_c=\chi N/2$ , as shown in Fig. 6.1(b), (c). The sharp transition in the dynamical behavior of the system is traced back to the change in direction of the self-generated precession proportional to  $\chi\langle\hat{J}_z\rangle\hat{J}_z$  as the Bloch vector crosses the equatorial plane at  $\langle\hat{J}_z\rangle=0$ , generating an abrupt shift to large-amplitude oscillations for  $\Omega>\Omega_c$ . Typical dynamics of the collective Bloch vector in the ferromagnetic and paramagnetic phases are shown as insets in Fig. 6.1(b). The solid green (V1), solid blue (H1) and dashed blue (H2) lines in Fig. 6.1(b) and (c) indicate analogous trajectories in the phase diagram which will be explored experimentally later in Figs. 5.3(b), 5.4(a), and 5.4(b) respectively.

More generally, as a function of the parameters  $\Omega$  and  $\delta/\chi N \ge -1/8$ , we observe a nonanalyticity of the order parameter  $\overline{\langle \hat{J}_z \rangle}$  (indicated by a solid white line in Fig. 6.1(c)), which marks a second-order transition between the two dynamical phases. However, the transition line is interrupted at a critical point  $[\delta/\chi N = -1/8]$ . Beyond this, there is a smooth crossover regime (indicated by a white dashed line in Fig. 6.1(c)) in which the system is ruled mainly by single-particle physics (set by  $\delta$  and  $\Omega$ ) and has an intermediate behavior between that of a ferromagnet and a paramagnet. The phase boundary for

 $\delta/\chi N > -1/8$  (assuming homogeneous atom-light coupling) can be analytically solved, with a derivation provided in the Supplementary Information of [108]<sup>[G]</sup>. The boundary describes the dependence of the critical Rabi frequency  $\Omega_c$  on the longitudinal field  $\delta$  and is given by:

$$\frac{\Omega_c(\delta)}{\chi N} = \frac{1}{2} \left[ 2 \left( 1 - \frac{\delta}{\chi N} \right) \left( 1 + \frac{2\delta}{\chi N} \right) - \frac{3}{2} \left( \frac{8\delta}{\chi N} + 1 \right) + \frac{1}{2} \left( 1 + \frac{8\delta}{\chi N} \right)^{3/2} \right]^{1/2}.$$
 (5.2)

#### 5.5 The experimental sequence

To simulate quench dynamics of the LMG model, we start by laser cooling the atoms to 14  $\mu$ K and trapping in the optical lattice supported by a symmetric, high-finesse optical cavity with a linewidth of  $\kappa/2\pi=153.0(4)$  kHz near the  $^1S_0-^3P_1$  atomic transition frequency. The lattice has a typical axial trap oscillation frequency of  $\omega_{\rm trap}/2\pi=200$  kHz, placing the system in the Lamb-Dicke regime and thus decoupling the spin dynamics of the atoms from their motional state to leading order (see Fig. 3.5.2 for a description of this regime). This lattice is nominally near magic with respect to the ultranarrow millihertz  $^1S_0-^3P_0$  clock transition at 698 nm but not along the  $^1S_0-^3P_1$  transition. However, we can attain a "magic angle" lattice (see Ch. 3.5.5) by setting the angle between the linear polarization of the lattice and the quantization axis, in order to reduce potential dephasing due to the transverse spreading of the atoms in a non-magic trap. To define the quantization axis, we apply a strong magnetic field perpendicular to the cavity axis. We estimate that residual inhomogeneous broadening due to the lattice is less than 2 kHz, much smaller than relevant frequency scales in the system.

Fig. 5.2(a) illustrates the various beams applied to our atom-cavity system for this experiment. To measure the number of atoms trapped in the lattice, we perform fluorescence imaging on the dipole-allowed  ${}^1S_0 - {}^1P_1$  transition at 461 nm, calibrating the fluorescence count to an atom number by comparing the results with a vacuum Rabi splitting measurement along the  ${}^1S_0 - {}^3P_1$  transition, as detailed in Ref. [242]<sup>[G]</sup>. We also use this measurement to determine the atom-cavity resonance condition (i.e.,  $\Delta = 0$ ). When simulating quench dynamics, we then tune the cavity to  $\Delta/2\pi = \pm 50$  MHz, depending on the dataset. We adjust the cavity length using piezoelectric transducers (PZTs) which mount our cavity mirrors onto a spacer, and we stabilize the length to a stable reference cavity to ensure consistency from

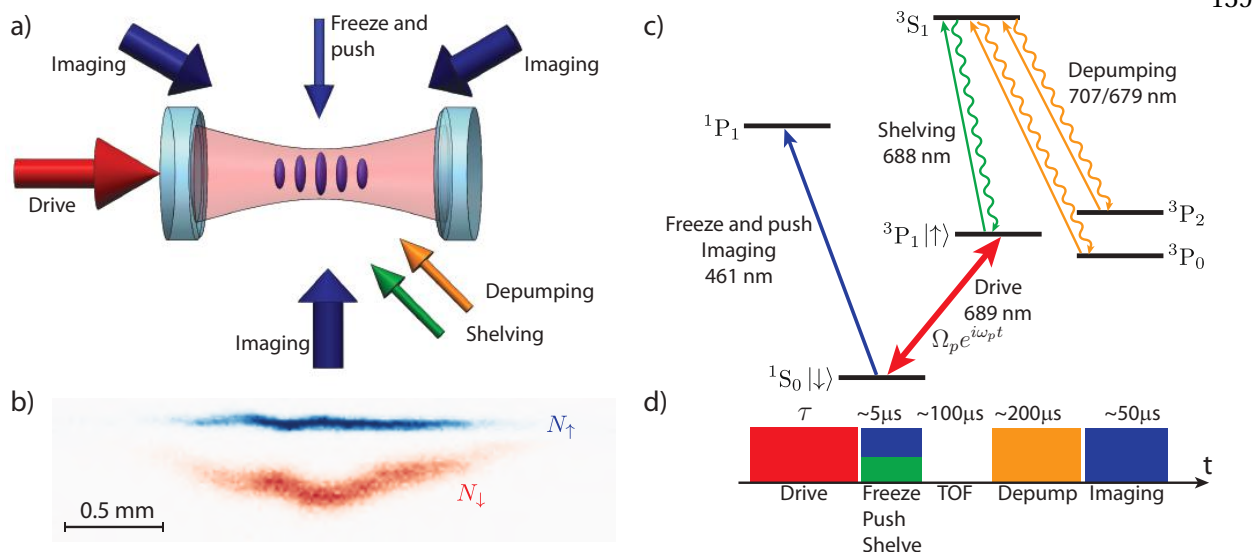


Figure 5.2: Details of the experimental sequence. (a) An optical cavity is driven by a 689 nm coherent field that establishes an intra-cavity field  $\Omega_p e^{i\omega_p t}$ , which is near resonance with the  ${}^1S_0 - {}^3P_1$  transition in  ${}^{88}$ Sr. Inside the cavity, an ensemble of atoms is confined in a one-dimensional optical lattice at 813 nm. Different lasers are applied for shelving excited state atoms into long-lived metastable excited states, for freezing the system dynamics, for applying a radiation pressure force that pushes ground states in a direction transverse to the cavity axis, for optically pumping atoms from long lived metastable excited states back to the ground state, and for fluorescence imaging of atoms in the ground state. (b) A typical fluorescence image captured on a CCD showing the state-resolved imaging technique. One sees that the  $N_e$  excited state atoms that were shelved into  ${}^3P_0$  and  ${}^3P_2$  while the freeze/push beam was applied remain near the trapping region. The  $N_g$  ground state atoms are pushed away from the trapping region. Based on their spatial location, the atoms assigned to be in the excited (ground) state are shown in false color blue (orange). (c) We show the relevant energy levels for  ${}^{88}$ Sr, the laser wavelengths, and their functions. (d) Experimental timing sequence and typical timescales are shown.

#### shot to shot.

We realize the transverse fields  $\Omega$  and  $\delta$  by injecting laser light at frequency  $\omega_p$  into the optical cavity through one mirror, creating a coherent driving field  $\Omega_p e^{i\omega_p t}$  inside the cavity. Here,  $\Omega_p$  represents the rate at which the cavity would be populated with photons if the drive and cavity were on resonance (which they are not). It is related to the input power P by the expression  $\Omega_p = \sqrt{\kappa_m P/(2\hbar\omega_p)}$ , where  $\kappa_m = \kappa T_m/(T_m + T_L)$  for single-mirror transmission and loss coefficients  $T_m = 105$  ppm and  $T_L = 23$  ppm, respectively. In the rotating frame at  $\omega_p$ , the laser light's detuning from atomic resonance  $\delta = \omega_p - \omega_a$  provides the longitudinal field  $\delta \hat{J}_z$  in Eq. 5.1. Moreover, the applied laser rapidly builds up a classical field within the cavity on a timescale of approximately  $1/\Delta$ , which couples  $|\downarrow\rangle$  to  $|\uparrow\rangle$ . This realizes the trans-

verse field  $\Omega \hat{J}_x$  in Eq. 5.1, where  $\Omega = -2g\Omega_p/\Delta$ . The external drive is polarized along the magnetic field direction to isolate the two-level pseudospin system defined by  $|\downarrow\rangle = |{}^1S_0, m_J = 0\rangle$  and  $|\uparrow\rangle = |{}^3P_1, m_J = 0\rangle$ . We adopt the convention that the transverse field is oriented along  $\hat{x}$  in the pseudospin coordinate system such that by jumping the phase of the laser light, we are able to create transverse fields oriented along any direction in the pseudospin xy-plane.

The atoms begin in the ground state  $|\downarrow\rangle$ . For experiments in 5.5, we initialize the atomic ensemble to orient the Bloch vector along a tunable orientation; for all other results the atoms remain in the ground state at initial times. Then, we perform a pulse sequence summarized in Fig. 5.2(d). We first quench the system by rapidly turning on our external drive in approximately 10 ns using an in-fiber electro-optical modulator (EOM), which modulates a laser carrier far from atomic or cavity resonance to produce our desired drive tone. All other EOM sidebands are sufficiently far from resonance to not affect the physics.

The observation of the DPT requires that we be able to take a snapshot of the magnetization  $\langle \hat{J}_z \rangle$  after some period of dynamical evolution. To achieve this, we have developed a technique to quickly freeze the dynamics and then apply state-dependent spatial displacements of the cloud such that the populations in the ground and excited states  $N_1$  and  $N_1$  are imaged onto two different regions of a CCD, shown in Fig. 5.2(b). After the drive is applied for some time  $\tau$ , we turn off the coherent drive by extinguishing the applied EOM sideband. In order to effectively count atoms in both excited and ground state immediately after the drive, and freeze any dynamics that could be caused by spontaneous emission or the transient decay of the cavity field, we shine a strongly focused 461 nm beam along the  $\hat{z}$  axis and apply a strong 688 nm shelving beam. The 461 nm beam immediately stops the dynamics as it dephases the atoms, overwhelming the single particle rotation and any collective interactions. In addition, the 461 nm beam exerts a radiation pressure force that gives a momentum kick to the ground state atoms, causing them to move away from the trapping region. Simultaneously, the shelving beam optically pumps excited state atoms to the metastable  $^3P_0$  and  $^3P_2$  states (see the level diagram in Fig. 5.2(c)). We apply the shelving pulse for 5  $\mu$ s. For scale, we observe that more than 90% of the atoms have been shelved after  $2\mu$ s.

To finish our state dependent detection, we allow for a short time of flight (~100  $\mu$ s) so that the

momentum kick applied to the ground state atoms is translated into a few 100  $\mu$ m displacement in space. We then optically pump the shelved atoms back to  ${}^3P_1$  using 679 nm and 707 nm light applied for 200  $\mu$ s. The atoms then decay to the ground state via single-atom decay with a 1/e decay lifetime of 21  $\mu$ s. We then perform fluorescence imaging for 50  $\mu$ s to observe the number of atoms in the two spatially resolved clouds, producing a CCD image like the one in Fig. 5.2(b). This allows us to measure both the total atom number  $N = N_{\downarrow} + N_{\uparrow}$  and the magnetization  $\langle \hat{J}_z \rangle = \frac{N_{\uparrow} - N_{\downarrow}}{2N}$  in a single shot. The efficiency of this process is above 98%, limited mostly by the efficiency of the shelving process.

### 5.6 Dynamical phases in the absence of a longitudinal field

First, we explore cut V1 on the dynamical phase diagram in Fig. 5.1(c) by placing the atomic drive on resonance ( $\delta = 0$ ), thereby setting the longitudinal field to zero. Then, we perform the quench experiment for different sizes of the tranverse field  $\Omega$  and measure the magnetization. Representative time traces are presented in Fig. 5.3(a). For drives deep in the ferromagnetic phase (Fig. 5.3(a)(i)), we observe small-amplitude oscillations that are in excellent agreement with our theoretical model based on a mean-field description of the system. Close to the experimental critical point (Fig. 5.3(a)(ii-iii)), the dynamics become more complicated due to the interplay between interactions, drive and single-particle decoherence from undesirable atomic motion in the optical lattice. Deep in the paramagnetic phase (Fig. 5.3(a)(iv)), we observe dynamics of the magnetization consistent with single-particle Rabi flopping with frequency  $\Omega$  and in good agreement with our simulation. Damping of the oscillations occurs predominantly because of inhomogeneity in the coupling of the spins to the common cavity mode, shot-toshot fluctuations in  $\Omega/\chi N$  (attributed mostly to atom number fluctuations at about the 5% (root mean square, r.m.s.) level) and atomic motion in the lattice. Spontaneous emission and decoherence related to leakage of photons from the cavity are negligible. We include these effects in our theoretical model (Fig. 5.3(a), red solid line), and fluctuations in  $\Omega/\chi N$  are indicated by the red shaded regions. Typically, we notice that the experimentally calibrated parameters overestimate the value of  $\Omega/\chi N$  by about 10% compared with the numerical simulations. We attribute this systematic disagreement to drifts on the calibration parameters and details not captured by the theory model.

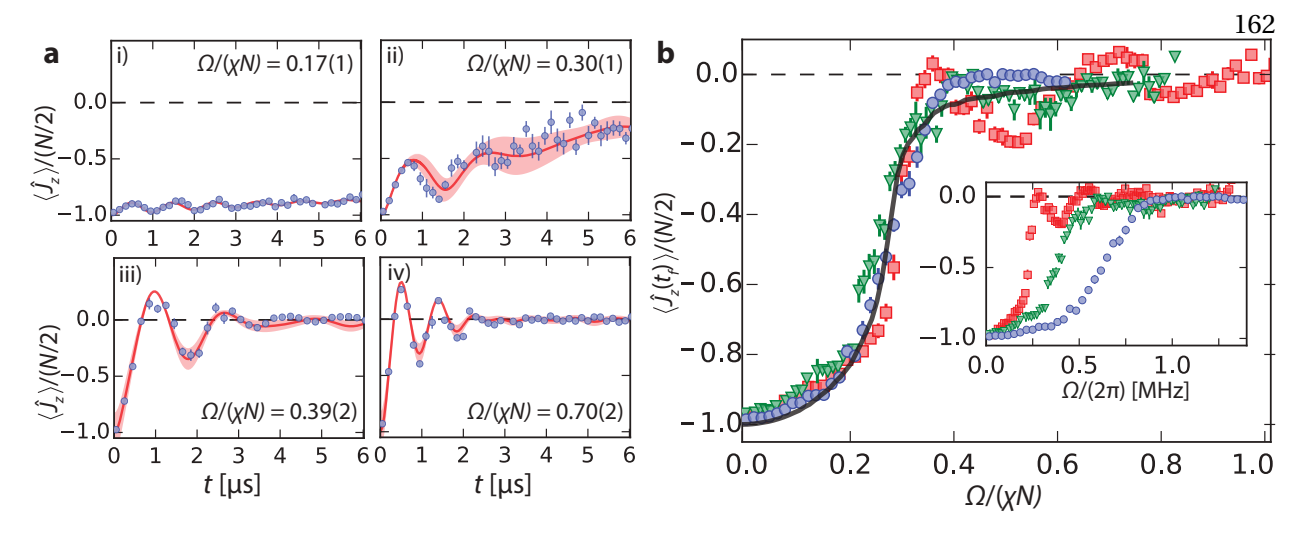


Figure 5.3: Characteristic evolution of dynamical phases and scaling of the DPT with atom number. (a) Time traces of the mean magnetization  $\langle \hat{J}_z \rangle$  after a quench with all spins initially in  $|\downarrow\rangle$  and no longitudinal field ( $\delta=0$ ), for four different post-quench transverse field strengths  $\Omega$  representing both the ferromagnetic ((i) and (ii)) and paramagnetic ((iii) and (iv)) phases. Traces are taken with  $N=950\times 10^3$  atoms and a cavity-atom detuning of  $\Delta/2\pi=+50$  MHz. The experimental data (blue) is compared to numerical simulations (red lines) based on a mean-field description including relevant experimental details (see Sec. 5.9). The shaded red region corresponds to an uncertainty band in the numerical simulations accounting for shot-to-shot fluctuations in  $\Omega/\chi N$ . Each point is the average of 12 experimental shots. (b) The magnetization  $\langle \hat{J}_z(t_f) \rangle$  for different numbers of atoms  $N=(935, 620, 320)\times 10^3$  (blue, green and red, respectively) after  $t_f=4$   $\mu s$  of evolution, plotted against the normalized drive strength  $\Omega/\chi N$ . This measurement maps to the green solid line (V1) in Fig. 6.1(b) and (c). The drive strength is normalized on a shot-to-shot basis from the fluorescence measurement of the total atom number. The solid black line indicates the simulated average (0 to 6  $\mu s$ ) as a function of the normalized drive including dephasing sources. The inset shows the magnetization versus non-normalized transverse field strength  $\Omega$  for the same datasets. All error bars in experimental data are statistical (1 $\sigma$ ).

We characterize the behavior of the DPT with system size by measuring  $\langle \hat{J}_z(t_f) \rangle$  at time  $t_f = 4~\mu s$  for different atom numbers N. Measuring  $\langle \hat{J}_z \rangle$  at a fixed time serves as a proxy of the long-term time-averaged magnetization, as considerable damping is caused by the previously mentioned effects. In the inset of Fig. 5.3(b), we observe a transition in the magnetization at different values of the transverse field  $\Omega$ , depending on the atom number N. The dependence of the transition as a function of system size is demonstrated by rescaling the corresponding drive to the normalized value  $\Omega/\chi N$ , analogous to the green curve in Fig. 5.1(b), (c). As displayed in the main panel of Fig. 5.3(b), the normalized traces collapse onto one another, showcasing the collective scaling of the cavity-mediated interactions. In particular, we observe a second-order dynamical phase transition between the ferromagnetic and paramagnetic

phases at a critical drive strength of  $\Omega_c^{\rm exp}=0.35(3)\chi N$ . While this is different from the predicted critical point of from the ideal LMG model, which is at  $\Omega_c/\chi N=1/2$ , this can primarily be explained by inhomogeneous atom-light coupling, and full numerical simulations of our system (explained in Sec. 5.9) show reasonable agreement (solid black line). The fact that the transition is not perfectly sharp as predicted in the ideal model (Fig. 5.1(b)) can be explained by residual single-particle decoherence of the atoms. Nevertheless, a clear transition can be observed, as shown by comparing to the theoretical calculation.

### 5.7 Scanning the longitudinal field with fixed transverse field

The DPT can also be probed using our ability to controllably introduce a longitudinal field proportional to  $\delta \hat{J}_z$  by detuning the injected light from the atomic transition, as shown in Fig. 5.1(b). In Fig. 5.4, we map out the response of the system to the drive detuning  $\delta$  by measuring the order parameter  $\langle \hat{J}_z(t_f) \rangle$  at  $t_f = 4~\mu s$  for two fixed values of the drive strength  $\Omega$  above and below the  $(\delta = 0)$  critical point  $\Omega_c^{\rm exp}$ , as well as for two opposite cavity detunings  $\Delta/2\pi = \pm 50~{\rm MHz}$ .

First, we consider a weak drive strength below the critical point  $(\Omega=0.070(3)\chi N<\Omega_c^{\rm exp})$ , representing the blue solid line H1 shown in Fig. 6.1(b), (c). When scanning the drive detuning  $\delta$ , we observe a sharp transition in the order parameter  $\langle \hat{J}_z \rangle$ , separating the ferromagnetic and the paramagnetic dynamical phases (plotted in Fig. 6.4(a)), for both a positive and negative cavity-atom detuning  $\Delta/2\pi=\pm50$  MHz. The phase transition corresponds to the "inside edges" of the resonant features, which occur symmetrically for each  $\Delta$  at  $\delta_c/|\chi N|=\mp0.27(2)$ . The critical value of  $\delta_c$  and the gradual decrease in  $\langle \hat{J}_z \rangle$  for large detuning show good agreement with a mean-field calculation. The symmetric response of the magnetization for  $\Delta \leftrightarrow -\Delta$  demonstrates the dependence of the interaction strength on the detuning sign:  $\chi N \leftrightarrow -\chi N$ .

We also consider a drive strength above the critical point; namely,  $\Omega=0.44(1)\chi N>\Omega_c^{\rm exp}$ , representing the blue dashed line H2 shown in Fig. 6.1(b), (c). For this parameter cut, shown in Fig. 6.4(b), we observe a smoother crossover between the paramagnetic and ferromagnetic phases about the detuning  $\delta_c/|\chi N|=\pm 0.04(3)$  in agreement with the mean-field calculation. Tuning  $\delta<\delta_c$  (for positive cavity-atom detuning  $\Delta$ , and vice-versa for negative  $\Delta$ ) reduces the influence of the collective interactions and

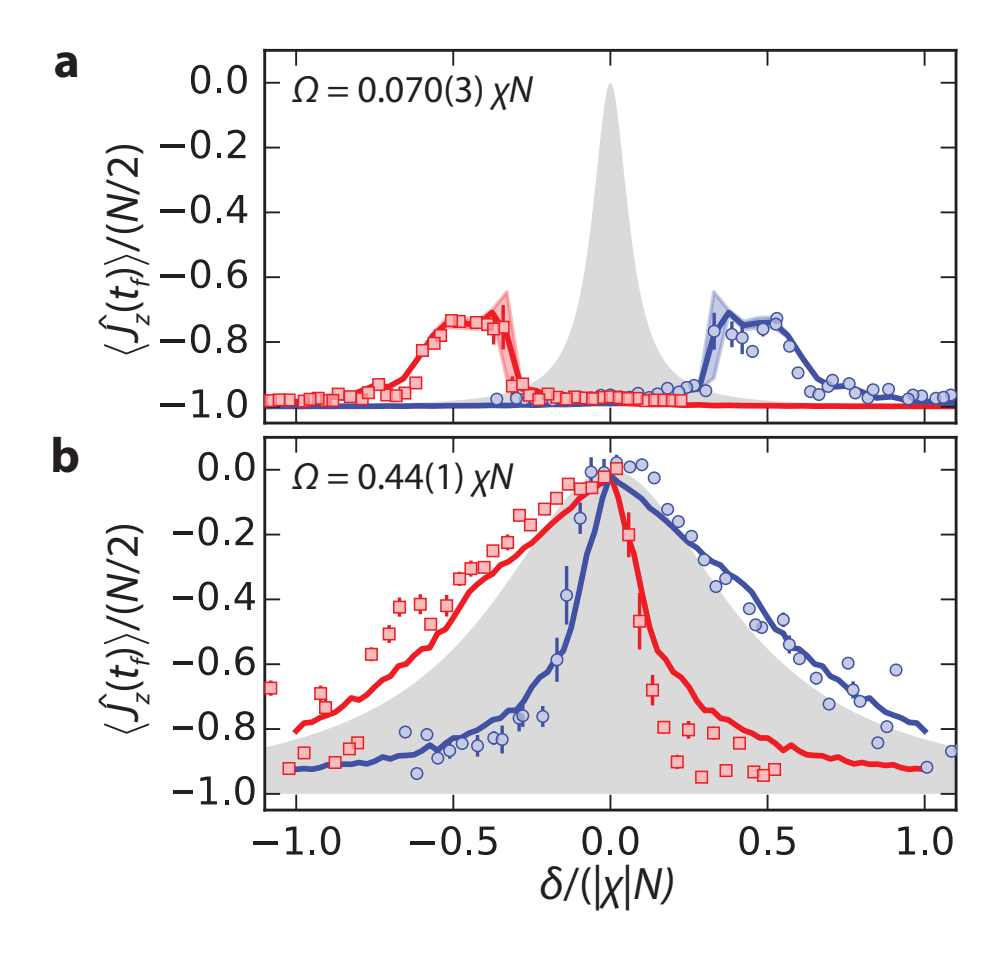


Figure 5.4: Exploring the DPT by scanning the longitudinal field for two different transverse field values at fixed  $\chi N$ . The atomic magnetization  $\langle \hat{J}_z(t_f) \rangle$  at  $t_f = 4~\mu s$  is measured as a function of the normalized drive detuning  $\delta/(|\chi|N)$  for cavity detunings  $\Delta/2\pi = \pm 50~\mathrm{MHz}$  (red,  $+50~\mathrm{MHz}$ ; blue,  $-50~\mathrm{MHz}$ ) for two different drive strengths: (a)  $\Omega = 0.070(3)\chi N$  and (b)  $\Omega = 0.44(1)\chi N$ . The inner edges of the resonant features in panel (a) indicate a sharp transition from ferromagnetic to paramagnetic phases as  $|\delta|$  is increased. In contrast, the corresponding crossover in panel (b) is smoothed. Numerical simulations are shown as blue and red solid lines with corresponding shaded regions. The gray shaded area indicates the non-interacting limit of Rabi-flopping. Measurements in (a) and (b) map, respectively, to cuts represented by the blue lines H1 and H2 in Fig. 6.1(b), (c). All error bars in experimental data are statistical  $(1\sigma)$ .

the magnetization resembles the prediction of single-particle detuned Rabi flopping.

In both cases, the response of the system to  $\delta$  can be understood by interpreting the single-particle shift and interaction in Eq. (5.1) as a nonlinear detuning proportional to  $(2\chi\langle\hat{J}_z\rangle+\delta)\hat{J}_z$ , which competes with the coherent drive. Depending on the sign of the interaction and the instantaneous magnetization, the single-particle term  $\delta$  can either cancel or enhance the contribution of the interactions relative to the

coherent drive, tuning the system between the ferromagnetic and paramagnetic dynamical phases. The predominant role of the interactions in the dynamics, especially below the critical point, can be observed by contrasting with the purely single-particle model of detuned Rabi oscillations. This is represented by the gray shaded areas, which plot the r.m.s. amplitude of such Rabi oscillations, taking the following functional form:

$$\langle \hat{J}_z \rangle_{\chi=0}^{\text{rms}} = -\frac{1}{2} \frac{\Omega^2}{(\delta^2 + \Omega^2)} - \frac{1}{2}.$$
 (5.3)

Both above and below the critical Rabi frequency  $\Omega_c^{\rm exp}$ , interactions modify the magnetization response of the system. However, only below  $\Omega_c^{\rm exp}$  does this modification correspond to distinct dynamical phases.

### 5.8 Dependence of the dynamical phases on initial conditions

The single-particle control achievable in our experimental platform allows us to explore the DPT as a function of the initial state, as shown in Fig. 5.5. Specifically, we are able to demonstrate that the critical point of the transition is state-dependent, by preparing the collective pseudospin in different positions on the Bloch sphere. For example, we can prepare the system with  $\Omega < \Omega_c^{\rm exp}$  such that the some initial states near the south pole remain trapped below the equator, representing a ferromagnetic phase. For different initial states prepared further towards the equator, the same transverse field can induce large oscillations around the Bloch sphere which are characteristic of the paramagnetic phase.

Probing the dynamical response to different initial conditions allows us to establish a connection between the DPT in our effective spin model and the phenomena of macroscopic self-trapping and Josephson tunneling observed in coupled atomic condensates [112] and solid state polariton condensates [114]. Fig. 6.6(a) schematically shows a double-well atomic condensate, where the initial magnetization of the collective state on the Bloch sphere is analogous to the initial population imbalance between the wells, while the azimuthal angle maps to the relative phase difference of the condensates. Similarly, the ferromagnetic and paramagnetic phases can be related to the self-trapped and tunneling phases respectively [111].

To generate states with different initial conditions, we first prepare each spin in  $|\downarrow\rangle$  and then rotate

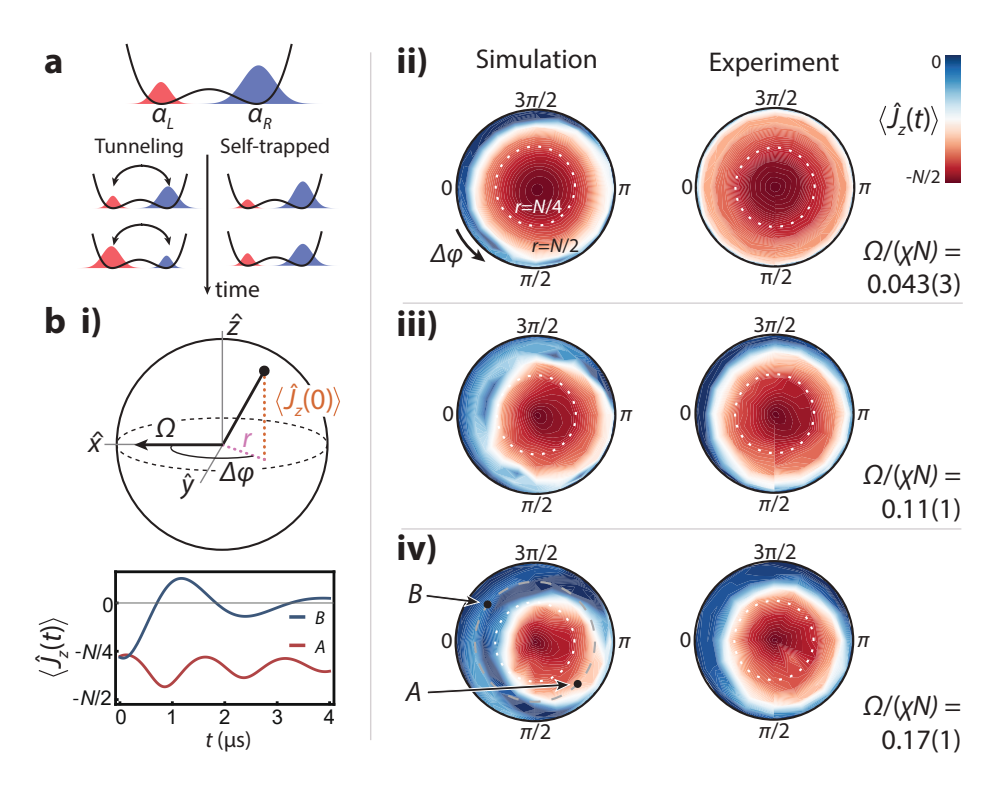


Figure 5.5: Dependence of dynamical phases on initial conditions. (a) The initial state on the Bloch sphere and subsequent dynamics of the spin model can be mapped to that of atomic condensates in a double-well potential, described by coherent complex amplitudes in the left and right wells,  $\alpha_L$  and  $\alpha_R$ , respectively. A population imbalance between the wells maps onto the magnetization  $(J_z \sim |\alpha_L|^2 - |\alpha_R|^2)$ , and the relative phase of the condensate wavefunctions maps onto the azimuthal angle of the spin state  $(\Delta\phi)$ . As time evolves, the population imbalance either oscillates as atoms tunnel back and forth between the wells (the tunneling phase) or remains approximately constant (the self-trapped phase). (b) (i) The initially prepared spin state can be parameterized in terms of the projection onto the equatorial, given by  $r = \sqrt{(N/2)^2 - \langle \hat{J}_z(0) \rangle^2}$ , and the relative azimuthal phase  $\Delta\phi$  between the initial collective Bloch vector and the coherent drive. (ii)-(iv) Color map of  $\langle J_z(t_f) \rangle$  after an evolution time of  $t_f = 4~\mu s$ , plotted using a polar projection of the Bloch sphere with coordinates defined by the initial condition as in panel (i) (initial conditions are always below the equator; they are shown above the equator in the figure to simplify visualization). Left (right) panels show simulated (experimental) results for  $\langle J_z(t_f) \rangle$  at  $t_f = 4~\mu s$  of evolution for different normalized drives  $\Omega/\chi N$ . The adjacent plot of  $\langle \hat{J}_z(t) \rangle$  (bottom of (i)) indicates typical dynamics in the red and blue regions.

them on the Bloch sphere with a strong drive, i.e.,  $\Omega_{\rm init}\gg\Omega_c$ , to initialize a certain drive angle. At this point, which we call t=0, the system has acquired a tunable initial magnetization  $\langle \hat{J}_z(0) \rangle$ . We then simultaneously shift the phase of the driving field by  $\Delta \phi - \pi/2$  and its amplitude to the desired transverse field strength  $\Omega$ , which completes the quench. The phase and amplitude jumps are accomplished by changing the phase and amplitude of the rf tone driving the electro-optic modulator used to control

the drive. We are then able to initialize the collective pseudospin Bloch vector at different positions on the Bloch sphere, such that  $\langle \hat{J}_z(0) \rangle$  and  $\Delta \phi$  define the polar and the azimuthal angles, respectively, as indicated in Fig. 6.6(b)(i). As the phase of the driving field naturally defines the  $\hat{x}$  and  $\hat{y}$  axes for the spin degree of freedom, our protocol can equivalently be viewed as preparing the collective Bloch vector at analogous positions on the pseudospin Bloch sphere.

In the rightmost panels (Fig. 6.6(b)(ii-iv)), we plot the measured magnetization after a time evolution of 4  $\mu$ s using a polar projection of the Bloch sphere for different drive strengths  $\Omega$ , over a 2D scan of the initially prepared state J(0) via the initial magnetization and azimuthal phase. As we increase the drive strength between panels, the set of initial conditions that lead to the ferromagnetic phase shrinks (red region) while also becoming increasingly asymmetric about the south pole. Both of these features are in qualitative agreement with our theoretical calculations (also shown in Fig. 6.6(b)(ii-iv)), which take into account coupling inhomogeneities, dephasing and shot-to-shot fluctuations on  $\Omega/\chi N$ . Quantitative differences arise predominantly due neglecting axial motion of the atoms in the theoretical model.

# 5.9 Details of numerical modeling

The dynamics of the experimental system is modeled by a master equation for the density operator  $\hat{\rho}$  of the complete atom-light system, given by:

$$\frac{d\hat{\rho}}{dt} = -\frac{i}{\hbar} \left[ \hat{H}_{\text{tot}}, \hat{\rho} \right] + \mathcal{L}_c[\hat{\rho}] + \mathcal{L}_e[\hat{\rho}] + \mathcal{L}_s[\hat{\rho}]. \tag{5.4}$$

Here, the Hamiltonian  $\hat{H}_{tot} = \hat{H}_A + \hat{H}_L + \hat{H}_{AL}$  is split into three contributions characterizing the atoms, pumping of the cavity field with the external drive, and the atom-light interaction respectively:

$$\hat{H}_{A} = \frac{\omega_a}{2} \sum_{i} \hat{\sigma}_i^z, \tag{5.5}$$

$$\hat{H}_{L} = \omega_{c} \hat{a}^{\dagger} \hat{a} + \Omega_{p} \left( \hat{a} e^{i\omega_{p}t} + \hat{a}^{\dagger} e^{-i\omega_{p}t} \right), \tag{5.6}$$

$$\hat{H}_{AL} = \sum_{i} g_i \left( \hat{a} \hat{\sigma}_i^+ + \hat{a}^\dagger \hat{\sigma}_i^- \right), \tag{5.7}$$

where  $\hat{a}$  ( $\hat{a}^{\dagger}$ ) is the annihilation (creation) operator of the cavity mode. To reiterate,  $\omega_a$  is the frequency of the atomic transition,  $\omega_c$  the frequency of the relevant cavity mode,  $\Omega_p$  the effective amplitude of the

injected field and  $\omega_p$  the corresponding frequency. The spatial dependence of the coupling is characterized by  $g_j = g\cos(kj)$  and  $k = \pi \lambda_L/\lambda_c$ , where 2g is the single-photon Rabi frequency at an anti-node of the cavity mode. This form arises because the magic wavelength of the 1D optical lattice  $\lambda_L = 813$  nm is incommensurate with the wavelength  $\lambda_c = 689$  nm of the cavity mode the atomic transition is coupled to. For simplicity, we take the summation to run over  $i \in [1, 2, ..., N]$  total lattice sites, such that each site is assumed to be occupied by only a single atom. In reality, there are  $\sim 10^3$  relevant lattice sites, each occupied by  $\sim 10^2$ - $10^3$  atoms. However, as we assume contact interactions are not relevant and the atom-light coupling is consistent across the entire atomic sample, this simplification is reasonable.

Decoherence due to the leakage of photons from the cavity at rate  $\kappa$  is described by the Lindblad term

$$\mathcal{L}_{c}[\hat{\rho}] = \frac{\kappa}{2} \left( 2\hat{a}\hat{\rho}\hat{a}^{\dagger} - \hat{a}^{\dagger}\hat{a}\hat{\rho} - \hat{\rho}\hat{a}^{\dagger}\hat{a} \right), \tag{5.8}$$

while spontaneous emission on the atomic transition at rate  $\gamma$  and single-particle homogeneous broadening of the ensemble at rate  $\gamma_{el}$  are described by

$$\mathcal{L}_{s}[\hat{\rho}] = \frac{\gamma}{2} \sum_{i} 2\hat{\sigma}_{i}^{-} \hat{\rho} \hat{\sigma}_{i}^{+} - \hat{\sigma}_{i}^{+} \hat{\sigma}_{i}^{-} \hat{\rho} - \hat{\rho} \hat{\sigma}_{i}^{+} \hat{\sigma}_{i}^{-}, \tag{5.9}$$

$$\mathcal{L}_{el}[\hat{\rho}] = \frac{\gamma_{el}}{2} \sum_{i} \hat{\sigma}_{i}^{z} \hat{\rho} \hat{\sigma}_{i}^{z} - \hat{\rho}. \tag{5.10}$$

The latter is attributed to a range of effects, including undesirable motion of the atoms in the optical lattice, and is discussed in more detail in the SI.

The simulations presented in Fig. 5.3, Fig. 5.4, and Fig. 5.5 are the result of the numerical solution of Eq. (5.4) within the mean-field approximation (with the exception of the lower panels of Fig. 6.2(a) which include additional effects due to axial motion that are discussed in the SI). Specifically, we solve equations of motion for  $\sigma_i := (\langle \hat{\sigma}_i^x \rangle, \langle \hat{\sigma}_i^y \rangle, \langle \hat{\sigma}_i^z \rangle)$  and  $\langle \hat{a} \rangle$ , and factorize higher-order moments of the operators, i.e.,  $\langle \hat{\sigma}_i^x \hat{\sigma}_i^y \rangle := \langle \hat{\sigma}_i^x \rangle \langle \hat{\sigma}_i^y \rangle$ .

The effective spin model which describes the nonlinear atomic dynamics throughout this work is obtained from the atom-light model (Eq. (5.4)) by separate adiabatic elimination of the injected field and intracavity fluctuations, and the full calculation is detailed in the Supplementary Information of [108]<sup>[G]</sup>.

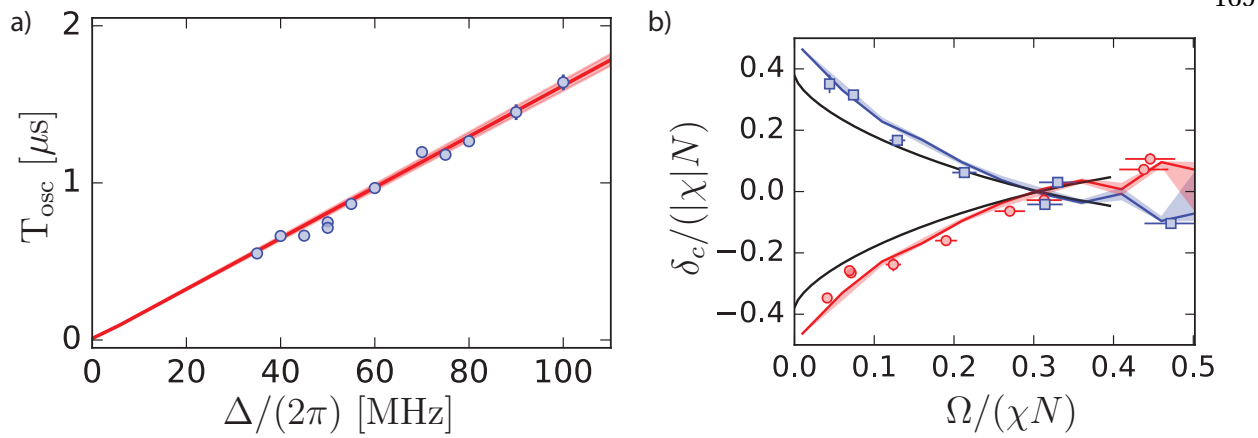


Figure 5.6: Probing many-body dynamics and mapping the phase boundary in the presence of inhomogeneous atom-light coupling. (a) The oscillation period as function of the cavity-atom detuning  $\Delta$  for  $2\Omega_p/(gN)=0.104(4)$ ,  $\delta=0$ , and with the atoms starting in  $|\downarrow\rangle$ . Blue markers are experimental values, and the solid red line represents mean-field predictions, with the shaded red area representing an uncertainty band in the prediction corresponding to typical experimental fluctuations on  $2\Omega_p/(Ng)$ . The period is extracted from sinusoidal fits to the data as in Fig. 5.3(a), after removing a linear term caused by the single-particle dephasing effects. The mean-field value takes the analytic form  $T_{\rm osc}=2\pi/(\chi N)$ , rescaled properly to account for inhomogeneous atom-light coupling. Measurements are taken in the dispersive atom-cavity coupling limit, i.e.,  $|\Delta|\gg g\sqrt{N}$ . (b) The critical detuning  $\delta_c$  as function of the drive  $\Delta$  for  $\Delta/2\pi=\pm50$  MHz (blue and red markers respectively). We also plot the theoretical prediction for the phase boundary (Eq. (5.2)) with rescaled parameters, as well as numerical simulations (solid lines) which include uncertainty bands based on typical fluctuations in  $\Omega/\chi N$ . All error bars are statistical ( $1\sigma$ ).

Here, we merely present the resulting Hamiltonian for the atoms:

$$\hat{H} = \hbar \sum_{i,j} \chi_{ij} \hat{\sigma}_i^+ \hat{\sigma}_j^- + \hbar \sum_i \frac{\Omega_i}{2} \hat{\sigma}_i^x - \frac{\hbar \delta}{2} \sum_i \sigma_i^z, \tag{5.11}$$

where  $\chi_{ij} = -g_i g_j / \Delta$ ,  $\Omega_i = -2g_i \Omega_p / \Delta$  with  $\delta = \omega_p - \omega_a$  and  $\Delta = \omega_c - \omega_a$ . Moreover, we have assumed  $|\Delta| \gg \kappa, g\sqrt{N}, \sqrt{g\Omega_p}, \delta$ . In the limit  $k = 2n\pi$  for  $n \in \mathbb{Z}$ , i.e. uniform atom-light coupling  $g_j \to g$ , then we recover the collective XY model of Eq. (5.1).

Although in the experimental platform the atom-light coupling  $g_j$  is spatially varying due to the incommensurate cavity and lattice wavelengths, the qualitative physics we explore is still consistent with the framework of the collective XY model. Specifically, while the simulations of Fig. 5.3, Fig. 5.4, and Fig. 5.5 take the proper form of  $g_j$  into account, we observe that features of the detailed inhomogeneous model such as the critical point and dynamical time-scales are consistent with the collective model upon

a rescaling of the atom-light coupling.

For weak drives deep in the paramagnetic phase, the collective model replicates the quantitative predictions of the inhomogeneous model upon replacement of the atom-light coupling with the r.m.s. average:  $g \to g/\sqrt{2}$ ,  $\chi \to \chi/2$ , and  $\Omega \to \Omega/\sqrt{2}$ . We check the validity of this approximation by analyzing the quench dynamics deep in the ferromagnetic phase, which exhibits weak oscillations predicted to have a period proportional to  $1/\chi N$ . In Fig. 5.6(a), we extract this period from the experimental data as a function of cavity detuning  $\Delta$ , which is equivalent to varying the interaction strength  $\chi \propto 1/\Delta$ . We confirm that the fitted slope agrees with the  $\chi \to \chi/2$  correction for inhomogeneous atom-light coupling.

As the drive is increased closer towards the phase transition, the proper rescaling required for a quantitative comparison changes. Specifically, comparing to the critical point  $\Omega_c^{\text{theory}}/\chi N$  obtained from a numerical calculation of the inhomogeneous model in the absence of decoherence, we find that the corresponding collective model requires a rescaling of  $g\to 0.62g$ , implying  $\chi\to 0.38\chi$ , and  $\Omega\to 0.62\Omega$ , in order to match the critical value  $\Omega_c^{\text{theory}}/\chi N\approx 0.31$ . The reduction of this value below the true collective critical drive  $\Omega_c/\chi N=1/2$  is consistent with experimental observations ( $\Omega_c^{\text{exp}}/\chi N=0.35(3)$ ). In Fig. 5.6(b), we verify that the theoretically predicted phase boundary (black), represented by the critical detuning  $\delta_c$ , agrees with experimental data (red, blue) under this rescaling over a range of different transverse field strengths  $\Omega$ . The experimental data and analytical predictions qualitatively agree over the entire phase diagram, justifying the rescaling.

### 5.10 Mapping between the LMG model and macroscopic self-trapping

The connection between the collective spin model in Eq. (5.1) and the phenomena of macroscopic self-trapping and Josephson oscillations observed in atomic and solid-state polariton condensates can be formalized using an appropriate mapping between the spin and bosonic models.

For the condensate examples, a simple description of self-trapping and Josephson oscillations can be obtained by a two-well model in the single-mode approximation [394] with a Hamiltonian given by

$$\hat{H} = \frac{U}{2} \left[ \hat{n}_R (\hat{n}_R - 1) + \hat{n}_L (\hat{n}_L - 1) \right] + \mathcal{J} \left( \hat{a}_R^{\dagger} \hat{a}_L + \hat{a}_L^{\dagger} \hat{a}_R \right) + \frac{\epsilon}{2} \left( \hat{n}_L - \hat{n}_R \right), \tag{5.12}$$

where  $\hat{a}_{R(L)}$  is the bosonic annihilation operator of the right (left) well, and  $\hat{n}_{R(L)} = \hat{a}_{R(L)}^{\dagger} \hat{a}_{R(L)}$ . Contact interactions between the constituent atoms of the condensate are characterized by U,  $\mathcal{J}$  defines the tunnelling between the two wells, and  $\epsilon$  is some controllable energy difference.

Given that the total particle number  $\hat{n}_R + \hat{n}_L$  is conserved, and introducing the Schwinger boson mapping  $\hat{J}_z = (1/2)(\hat{n}_L - \hat{n}_R)$ ,  $\hat{J}^+ = \hat{a}_R^{\dagger}\hat{a}_L$ , with  $\hat{J}^- = \hat{a}_L^{\dagger}\hat{a}_R$ , we can recover from Eq. (5.12) the following effective spin Hamiltonian:

$$\hat{H} = U\hat{J}_z^2 + 2\mathcal{J}\hat{J}_x + \epsilon\hat{J}_z + \frac{U}{4}N(N-2). \tag{5.13}$$

Note that the total number of particles  $N=(\hat{n}_L+\hat{n}_R)$  commutes with the Hamiltonian and is therefore a conserved quantity. Finally, given that  $\hat{J}^2$  is also a conserved quantity of this Hamiltonian, and that  $\hat{J}_z^2:=\hat{J}^2-\hat{J}^+\hat{J}^-+\hat{J}_z$ , we find that Eq. (5.13) is identical to the collective XY model with transverse and longitudinal fields upon recognizing:  $\chi=-U$ ,  $\Omega=2\mathcal{J}$  and  $\delta=U+\epsilon$ .

## 5.11 Conclusion

The demonstration of the cooperation and competition between coherent drive and infinite-range interactions in an optical transition opens a path to the quantum simulation of richer spin models and out-of-equilibrium physics. For example, more complex spin-spin couplings can be engineered by using the available Zeeman sublevels of the  $^3P_1$  state with two different cavity polarizations [377]. Moreover, in the presence of additional inhomogeneous terms, our system can explore dynamical phases predicted to exist in Bardeen-Cooper-Schrieffer superconductors [127, 137], and by modulation of the transverse field our platform should be able to realize the archetypal model of a kicked top [89], relevant for explorations of quantum chaos and scrambling dynamics [395]. Lastly, our investigation of non-equilibrium dynamics using the  $^{88}$ Sr ( $^{1}S_0 - ^{3}P_1$ ) optical transition can lead to insight into how to generate entangled states for quantum sensing with the long-lived  $^{87}$ Sr ( $^{1}S_0 - ^{3}P_0$ ) optical transition used in state-of-the-art atomic clocks [98].

### Chapter 6

## Observing Dynamical Phases of BCS Superconductors in a Cavity QED Simulator

#### 6.1 Introduction

Superconductivity, and its more general counterpart superfluidity, describe a rich set of phenomena that span a remarkable breadth of energy scales, from the large and hot at the core of neutron stars (MK temperatures) [396, 397] to the human scale of traditional and high- $T_c$  superconductors (1-100 K temperatures) [398], all the way down to the ultracold regime of degenerate gases of fermionic atoms (nK temperatures) [399]. A large part of our modern understanding of superconductivity stems from what we call the **BCS theory** [6], originally proposed by physicists Bardeen, Cooper, and Schrieffer in 1957. While this theory is now quite well understood, how this model behaves when quenched out of equilibrium has been less thoroughly studied.

Of particular interest to us are the prethermal dynamical phases [55] predicted to emerge from quenches of BCS superconductors and superfluids [127–137, 400, 401], creatively named phases I, II, and III. Observing such phases experimentally has proved difficult: while there has been great progress in pump-probe experiments of superconductors to induce the necessary fast quenches using THz technology, and signs of phases I and II have been observed, the intense pump pulses couple nonlinearly to the Cooper pairs in the superconductor and complicate a clean observation of the dynamical phases [138–140]. For these reasons, the realization of fermionic superfluids in ultracold atomic gases [155] has generated great excitement in potentially exploring this physics [129–132, 134, 135, 137]. However, until recently observations have been limited to spectroscopic signatures rather than the full time dynamics [141]. In the past few years, a quintessential feature of phase II known as Higgs oscillations has been

observed in the quench dynamics of such a system [142]. Still, in neither system has a systematic scan of the dynamical phase diagram been performed to our knowledge, and phase III in particular has not been observed.

Quantum simulation offers a path towards better understanding a broad range of phenomena, from high-temperature superconductivity and correlated quantum magnetism in condensed matter physics [402] to quarks and gluons in nuclei and matter under extreme conditions [403], as well as the black hole information paradox in gravitational physics [404]. In this spirit, discussions with our group led by theorists in Ana Maria Rey's group led to a 2021 proposal to observe the three predicted dynamics in a cavity QED platform, using internal electronic states to encode effective Cooper pairs and cavity-mediated atom-atom interactions to represent the BCS interaction [405]<sup>[G]</sup> [406].

In this chapter, I summarize the theoretical proposal and walk through the subsequent experimental results as described in [126]<sup>[G]</sup>. At a high level, we probe all three dynamical phases (phases I, II, and III) predicted to exist in BCS superconductors by utilizing the high degree of control and flexibility in state initialization, interaction control, and non-destructive measurements available when coupling long-lived atoms to an optical cavity. Behaviors intrinsic to phase I (normal phase) and phase II (finite steady-state superconductivity) had previously been observed in spin systems realized in optical cavities [85][95]<sup>[G]</sup> and in two-level atoms interacting via collisions [121, 407–409]. We build on this work by clarifying the connection between these dynamical phases from the BCS model and the physics of many-body gap protection in spin systems. Our results also provide the first demonstration of phase III (a self-generated Floquet phase featuring persistent oscillations of the order parameter), which is predicted to dynamically emerge in superconductors via quenches from weak to strong interactions [130, 137]. In our system, we instead engineer this phase using flexible control of the single-particle dispersion [405]<sup>[G]</sup>[401], dynamically resembling the low-energy condition of a BCS superconductor. For all experiments, we perform real-time tracking of the superconducting order parameter, enabling fast readout of the dynamics.

## 6.2 A primer on BCS theory

At a high level, the innovation of BCS theory was realizing that electrons in a metal interact with the underlying lattice of positively charged ions via Coulomb forces, giving rise to an effective attractive interaction between electrons.<sup>1</sup> It can be useful to think of this process diagrammatically in momentum space: two electrons with initial momenta  $\hbar k_1$  and  $\hbar k_2$  exchange a phonon with momentum  $\hbar k_p$ , leading to new outgoing momenta  $\hbar k_1' = \hbar (k_1 - k_p)$ ,  $\hbar k_2' = \hbar (k_2 + k_p)$ . This leads to an interaction term of the form

$$\hat{c}_{\boldsymbol{k}_{1}^{\prime},\sigma_{1}}^{\dagger}\hat{c}_{\boldsymbol{k}_{2}^{\prime},\sigma_{2}}^{\dagger}\hat{c}_{\boldsymbol{k}_{2},\sigma_{2}}\hat{c}_{\boldsymbol{k}_{1},\sigma_{1}},\tag{6.1}$$

where  $\hat{c}$  are fermionic annihilation operators, and  $\sigma_i \in \{\uparrow,\downarrow\}$  is the spin state of electron i. This changes the nature of the ground state, which attains the lowest possible energy by maximizing the number of state configurations  $(k_1,k_2)$  which phase-coherently undergo phonon exchanges, due to the attractive nature of the exchanges. As argued by Bardeen, Cooper, and Schrieffer [6], the way to maximize such exchange processes is for the electrons to pair up in so-called **Cooper pairs**, with opposite spin and momenta. If we only consider such pairings, we get the following effective BCS Hamiltonian:

$$\hat{H}_{BCS} = \sum_{k,\sigma} \frac{\varepsilon_{k}}{2} \hat{c}_{k,\sigma}^{\dagger} \hat{c}_{k,\sigma} - \hbar \sum_{k,k'} \chi_{k,k'} \hat{c}_{k',\uparrow}^{\dagger} \hat{c}_{-k',\downarrow}^{\dagger} \hat{c}_{-k,\downarrow} \hat{c}_{k,\uparrow}, \tag{6.2}$$

where the first term describes the single-particle electron dispersion relation (with energy  $\varepsilon_k/2$  at momentum  $\hbar k^3$ ), and  $\chi_{k,k'}$  is a potentially momentum-dependent interaction scale in frequency units. Often, people will consider the momentum dependence of this interaction in the language of partial waves. For our purposes, we will assume it has an *s*-wave character, and specifically that the interaction is uniformly all-to-all such that all terms of the summation have a single frequency scale  $\chi$  [405]<sup>[G]</sup>[130].

In a zero temperature, low energy limit (such as the ground state), we can assume from the form of the Hamiltonian that the wavefunction does not include terms in which any Cooper pairs  $|k,\uparrow\rangle |-k,\downarrow\rangle$  are

<sup>&</sup>lt;sup>1</sup> More abstractly, any attractive interaction between electrons would lead to BCS superconductivity, regardless of the microscopic origin. However, in their original paper Bardeen, Cooper, and Schrieffer focused on the electron-phonon interaction [6].

<sup>&</sup>lt;sup>2</sup> It is possible for Cooper pairing to occur with nonzero net momentum, particularly in the presence of an external field [410, 411]. The interaction term including only zero net momentum is sometimes referred to as the **reduced BCS Hamiltonian** [143][405]<sup>[G]</sup>.

<sup>&</sup>lt;sup>3</sup> The factor of  $\frac{1}{2}$  in this definition is there for reasons related to the mapping onto our system. Essentially,  $\varepsilon_k$  as defined here is the single-particle energy associated with a Cooper pair, which has twice the energy of a single electron.

broken, since such "pair-broken" terms disrupt the attractive interaction. This allows us to shift our view from individual electrons to Cooper pairs by means of a simplifying description known as an **Anderson pseudospin mapping** [143], illustrated in Fig. 6.1(a) (with electron spin suppressed). This description maps the presence and absence of a Cooper pair with momentum label k to a spin-up and spin-down at k, respectively. Formally, this is done through a definition of operators  $\hat{s}^-$ ,  $\hat{s}^z$ :

$$\hat{s}_{k}^{-} := \hat{c}_{-k,\downarrow} \hat{c}_{k,\uparrow}; \qquad 2\hat{s}_{k}^{z} + 1 := \hat{c}_{k,\uparrow}^{\dagger} \hat{c}_{k,\uparrow} + \hat{c}_{-k,\downarrow}^{\dagger} \hat{c}_{-k,\downarrow}, \tag{6.3}$$

which satisfy the proper commutation relations for spin- $\frac{1}{2}$  operators in the usual way [405]<sup>[G]</sup>. Using this new picture, we can recast the BCS Hamiltonian as describing a spin ensemble:

$$\hat{H}_{BCS} = \sum_{k} \varepsilon_{k} \hat{s}_{k}^{z} - \hbar \chi \sum_{k,k'} \hat{s}_{k'}^{+} \hat{s}_{k}^{-}$$

$$= \sum_{k} \varepsilon_{k} \hat{s}_{k}^{z} - \hbar \chi \hat{S}^{+} \hat{S}^{-},$$

$$(6.4)$$

where  $\hat{S}^- := \sum_k \hat{s}_k^-$  is the collective spin lowering operators on Cooper pair states, which we will call  $\uparrow_c$ ,  $\downarrow_c$  to differentiate from electron spin  $\uparrow$ ,  $\downarrow$ . We see that the BCS interaction looks functionally equivalent to an all-to-all spin-exchange interaction, which is exactly what we will use in our system to simulate the model. Equation (6.4) is sometimes called the Richardson-Gaudin spin model [412, 413].

The ground state of the system is depicted in Fig. 6.1(b) using an Anderson pseudospin picture. Near the Fermi energy, electrons settle into superposition states of a presence and absence of a Cooper pair, like:  $|\uparrow_c\rangle_k + |\downarrow_c\rangle_k$ . Importantly, the superpositions are phase-coherent between different momenta k, represented in Fig. 6.1(b) by the fact that the spins point along the same azimuthal angle on the collective Bloch sphere. This phase coherence is what enhances the exchange interaction and lowers the total energy of the many-body state. If we set the Fermi energy to be  $\varepsilon_F = 0$  without loss of generality, then the ground state has mean-field expectations given by [130]:

$$\langle \hat{s}_{\mathbf{k}}^{-} \rangle_{gs} = \frac{1}{2} \frac{2\Delta_{BCS}}{\sqrt{4\Delta_{BCS}^{2} + \varepsilon_{\mathbf{k}}^{2}}}; \qquad \langle \hat{s}_{\mathbf{k}}^{z} \rangle_{gs} = -\frac{1}{2} \frac{\varepsilon_{\mathbf{k}}}{\sqrt{4\Delta_{BCS}^{2} + \varepsilon_{\mathbf{k}}^{2}}}. \tag{6.5}$$

Here,  $\Delta_{BCS}$ , which we call the **BCS gap**, is self-consistently defined by  $\Delta_{BCS} := \hbar \chi \langle \sum_{k} \hat{c}_{k,\uparrow} \hat{c}_{-k,\downarrow} \rangle = \hbar \chi \langle \hat{S}^{-} \rangle$ , and it has the physical interpretation as (half) the energy required to break up one Cooper pair superpo-

<sup>&</sup>lt;sup>4</sup> The single-particle energy of the system has also been shifted by a constant offset.

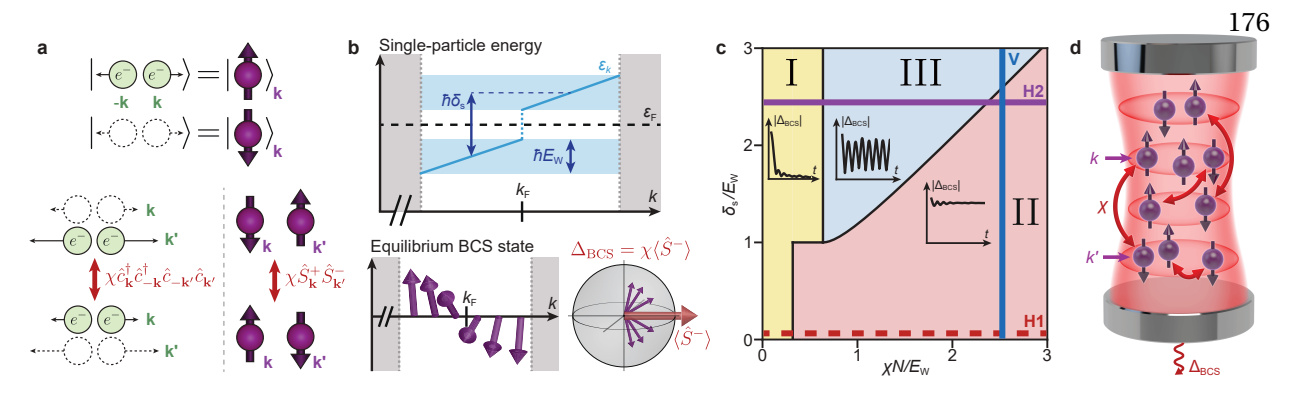


Figure 6.1: Engineering BCS dynamical phases. (a) The Anderson pseudospin mapping encodes the presence and absence of a Cooper pair as the up and down states of a spin-1/2 system, respectively. Under this mapping, the attractive interaction  $\chi \hat{c}_{k}^{\dagger} \hat{c}_{-k'}^{\dagger} \hat{c}_{-k'} \hat{c}_{k'}$  between electrons is equivalent to an allto-all exchange interaction  $\chi \hat{S}^+_k \hat{S}^-_{k'}$  between pseudospins. (b) Model parameters. The top plot shows the effective dispersion relation near the Fermi surface engineered in our system as a function of parameters  $\delta_{\rm s}$  and  $E_{\rm W}$ , controlled using AC Stark shifts. The bottom plot visualizes the ground state of a BCS superconductor using Anderson pseudospins. Near the Fermi momentum, the pseudospins develop a phasecoherent superposition at a scale set by a nonzero BCS pairing gap  $\Delta_{BCS}$ . This gap is self-consistently defined from the spin coherence as shown on the Bloch sphere. (c) Dynamical phase diagram. The three dynamical phases can be realized by varying parameters  $\chi N$ ,  $\delta_s$ , and  $E_W$ . Representative dynamics of the BCS order parameter  $|\Delta_{BCS}|$  for each phase are shown as insets. We explore cut H1 (dashed line) in Fig. 6.2 using a single ensemble of atoms and cuts V and H2 (solid lines) in Figs. 6.4 and 6.6 using two separately controlled sub-ensembles. (d) Cavity QED implementation of the BCS interaction. Coupling many strontium atoms to a detuned optical cavity generates infinite-range spin-exchange interactions mediated by a virtual exchange of cavity photons. This interaction also causes a field proportional to  $\Delta_{BCS}$  to leak out of the cavity, providing a real-time probe of the dynamics.

sition state. Traditionally, this gap is considered as a thermodynamic order parameter, i.e., a quantity that characterizes the system in equilibrium. Above the critical temperature for a superconductor  $(T > T_c)$ ,  $\Delta_{BCS} = 0$ , implying that the system exhibits normal metal behavior since it is not thermodynamically favorable for electrons to condense into Cooper pairs. Below the critical temperatue  $(T < T_c)$ ,  $\Delta_{BCS} > 0$  rises in a second order phase transition, and the system is in a superconducting phase. As we will see in the next section, however, the BCS gap can be extended to describe the superconducting nature of systems out of equilibrium just as well.

## 6.3 Predicted dynamical phases

In the mid 2000s, motivated in part by the recent successful formation of degenerate Fermi gases in cold atom platforms [399, 414, 415] and the ability in those systems to tune interaction strengths across a Feshbach resonance, a series of theory papers were released from multiple theorists [127, 129–132, 416] which studied the behavior of BCS superconductors and superfluids as the interaction strength is rapidly changed. Among these various studies, Barankov and Levitov seem to be the first to recognize that the parameter space of possible quenches exhibits critical points that demarcate three dynamical phases [130]. The three phases, depicted in Fig. 6.1(c), represent distinct regimes of dynamical behavior that arise after a sudden perturbation of a control parameter in a closed many-body system. They are described using a time-averaged or steady-state order parameter that demonstrates non-analytic behavior at the boundary between phases. In particular, the BCS model is predicted to exhibit second-order dynamical phase transitions in quantities derived from the time dynamics of the BCS gap  $\Delta_{\text{BCS}}$ .

Phase I is characterized by a steady state with a vanishing order parameter  $|\Delta_{BCS}(t)| \to 0$  at long times. Phase II exhibits a steady state with a constant nonzero order parameter  $\Delta_{\infty} := \lim_{t \to \infty} |\Delta_{BCS}(t)| > 0$ . Finally, phase III features oscillations in  $|\Delta_{BCS}(t)|$  that persist to long times, realizing a Floquet superfluid despite not being periodically driven [134–137]. The long-time behavior of these dynamical phases admits a simpler description in terms of the Lax-reduced Hamiltonian (used by our theorist colleagues), which is an effective Hamiltonian taking the same form of Eq. (6.4) but with rescaled parameters and a reduced number of spins [55, 137]. Under this formulation, phases I, II, and III emerge when the Lax-reduced Hamiltonian describes effective zero-spin, one-spin, and two-spin systems respectively.

# 6.4 Cavity QED implementation overview

While the BCS interaction in Eq. (6.4) looks formally identical to the cavity-mediated spin-exchange interactions utilized in Ch. 5, its indices still refer to the momentum states k in a superconductor. To use our system to simulate a superconductor, we make a simple but subtle replacement of the electron mo-

mentum k with the lattice site or positional label k for an atom in our optical cavity,<sup>5</sup> giving the following (now explicitly) spin-spin Hamiltonian:<sup>6</sup>

$$\hat{H} = \sum_{k} \varepsilon_k \hat{s}_k^z + \hbar \chi \hat{S}^+ \hat{S}^-. \tag{6.6}$$

Now,  $\chi$  refers to the dispersive part of the effective atom-atom interaction attained from adiabatic elimination of the cavity mode. We have defined the spin operators relative to the inferred spin-1/2 system encoded in the electronic ground state  $|\downarrow_c\rangle=|^1\mathrm{S}_0, m_J=0\rangle$  and the long-lived optical excited state  $|\uparrow_c\rangle=|^3\mathrm{P}_1, m_J=0\rangle$  (mapping to the Anderson pseudospins of Cooper pair states), such that  $\hat{s}_k^-=|\downarrow_c\rangle\langle\uparrow_c|_k$  and  $\hat{s}_k^z=(|\uparrow_c\rangle\langle\uparrow_c|_k-|\downarrow_c\rangle\langle\downarrow_c|_k)/2$  for single atoms with labels  $k\in\{1,...,N\}$ , and we have further defined the collective lowering operator  $\hat{S}^-=\sum_k\hat{s}_k^-$  and raising operator  $\hat{S}^+=(\hat{S}^-)^\dagger$ . Whereas in previous work such as in Ch. 5, we nominally studied the dynamics of spin-exchange interactions in the fully collective manifold, in this work we explicitly break this assumption by engineering a spread in single-particle energies  $\varepsilon_k=\hbar\omega_k$  using applied AC Stark shifts  $\omega_k$  [417, 418]. These shifts compete with the spin-exchange interaction, as we will later see.

How, exactly, should we assign our atom labels k to various momenta k in this mapping? One might imagine that there are combinatorially many ways to do so, but since our interactions are all-to-all the precise mapping of which atom gets which momentum state is unimportant. In fact, the only real control knobs we have to affect the physics are the interaction strength and the overall distribution of single-particle energies ("density of states"), which we will call  $\rho(\omega)$ . The distribution  $\rho(\omega)$  could have arbitrarily many degrees of freedom, but we found that only two such degrees of freedom are necessary to explore the desired dynamical phases. For practical convenience, we introduce experimental control in the form of an overall frequency splitting  $\delta_s$  between two atomic subensembles and an effective frequency width  $E_W$  of each sub-ensemble to engineer a tunable dispersion relation  $\varepsilon_k$  as in Fig. 6.1(b), both engineered using 461 nm light shifts. This choice is inspired by the two-spin system of the Lax-reduced Hamiltonian and will be explored further in Sec. 6.7. Phase I and phase II can also be observed using

<sup>&</sup>lt;sup>5</sup> Recall that our atoms are thermal. While we have hundreds of atoms per optical lattice site, and many of these share the same axial wavefunction, each will have a different radial motional state which gives them distinguishable position labels.

<sup>&</sup>lt;sup>6</sup> This distinction may at first glance seem overly pedantic. Empirically, however, I have found that not spelling this out in talks or poster presentations can sometimes confuse theorists, who fall under the mistaken assumption that our atoms are also indexed by momentum.

a single ensemble of atoms as shown in Fig. 6.2 (and, in fact, we do so). Both experimental setups can nonetheless be described by a common phase diagram as shown in Fig. 6.1(c).

Additionally, we can tune the interaction strength as a third control knob. In principle, we could do this by changing the atom-cavity detuning (recall that  $\chi \approx g^2/\Delta_{ca}$  in the far-detuned cavity limit). In practice, constantly changing the cavity detuning would have been a pain.<sup>7</sup> Instead, we load in different atom numbers N into the cavity from shot to shot of the experiment, which has the effect of rescaling the mean-field interaction strength  $\chi(\hat{S}^-) \propto \chi N$ .

We initialize all the atoms in the  $|\downarrow_c\rangle$  state and then apply a coherent  $\pi/2$  pulse through the cavity in 100 ns such that  $\Omega \gg \chi N$ , where  $\Omega$  is the pulse Rabi frequency, and  $\chi N$  is the characteristic interaction strength for an ensemble of N atoms. This establishes a large BCS order parameter  $\Delta_{BCS}$  on a timescale faster than any other relevant dynamics, mimicking the ground state of a Hamiltonian with an infinite interaction strength  $\chi$  (far right on the horizontal axis of the phase diagram in Fig. 6.1(c)). We then quench the system by rapidly turning on  $\varepsilon_k$ , which sets a finite ratio  $\chi N/E_W$  and a variable  $\delta_s/E_W$ , allowing us to explore the dynamical phase diagram shown in Fig. 6.1(c) which is plotted in terms of dimensionless ratios of our three control knobs. Although our quench of the single-particle energies is not the proposed interaction quench of the original theory papers identifying the dynamical phases [130], the resulting phases can be shown to be connected through a Lax vector analysis.

For a more complete description of the experimental setup, refer to Sec 6.9 near the end of this chapter. For now, though, we will jump into the results.

### 6.5 Phase I to phase II

We probe the phase I to phase II transition by varying the ratio  $\chi N/E_W$  between the interaction strength and the width of the single-particle energy distribution. As shown in Fig. 6.2(a), we shine an off-resonant 461 nm beam onto a single atomic ensemble from the side of the cavity that generates a distribution of AC Stark shifts with a spread  $E_W$ . Careful shaping of the 461 nm beam allows us to realize

<sup>&</sup>lt;sup>7</sup> We didn't have a cavity sweep set up at the time. Also, moving the cavity around would change our effective drive power and require us to dynamically change our cavity probe frequency and RF demodulation as well (see Sec. 7.8.2 for a longer discussion of the cavity probe).

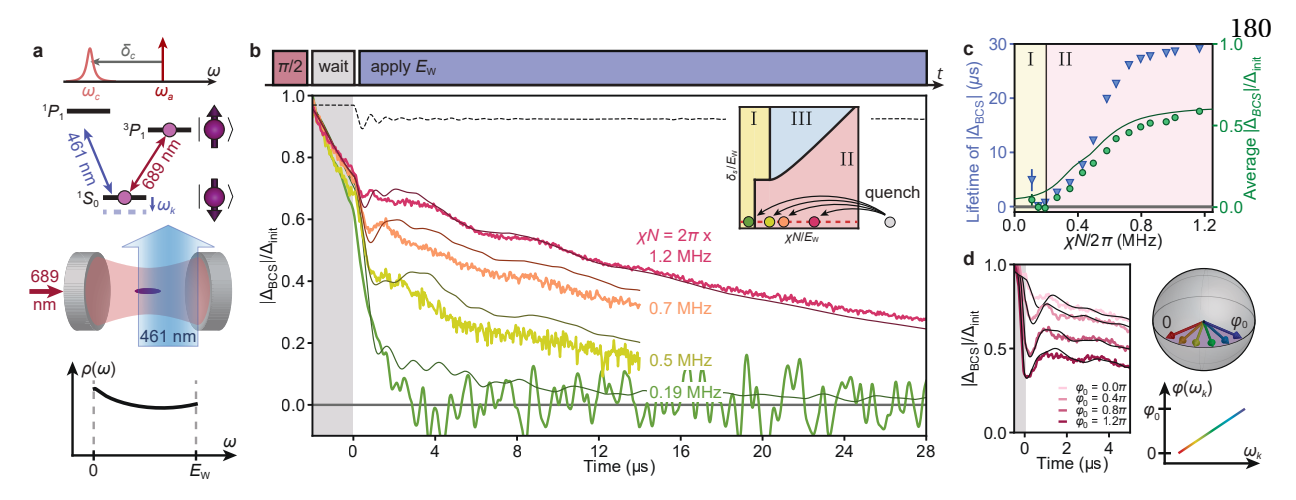


Figure 6.2: Phase I to phase II transition. (a) Tuning the single-particle dispersion. We shine an offresonant 461 nm beam onto the atoms from outside the cavity. This generates a distribution of AC Stark shifts representing a roughly uniform density of states  $\rho(\omega)$  (bottom plot). (b) Probing phase I and phase II. We perform a rapid  $\pi/2$  pulse to prepare a highly coherent initial state, wait for 2  $\mu$ s, quench to a variable  $\chi N/E_W$  with  $\delta_s = 0$ , and then let the system evolve. The inset shows the explored parameter cut and identifies post-quench  $\chi N/E_{\rm W}$  values with colored dots. The main plot shows experimental time traces of  $|\Delta_{BCS}|$  (colored curves) accompanied by numerical simulations (darker lines). Two curves are extended to demonstrate long-time coherence protection, with the  $\chi N/2\pi = 0.19$  MHz trace smoothed for clarity. For  $\chi N/2\pi = 1.2$  MHz, we show an ideal simulation neglecting dissipation and motional effects (dashed line), which exhibits transient Higgs oscillations. Hints of these oscillations are present in experimental data with additional damping. (c) Characterizing the phase transition. Blue triangles show the fitted coherence time of  $|\Delta_{BCS}|$  from  $t = 1 \mu s$  to 30  $\mu s$ . Green circles show the time-averaged  $|\Delta_{BCS}|$  between  $t=3~\mu s$  and 8  $\mu s$ , with the dark green line representing numerical simulations. In all cases, we identify a phase transition at  $\chi N/2\pi = 0.2$  MHz. Error bars in all plots represent the s.e.m. of boostrap resamplings on experimental shots. (d) Varying initial conditions. Before t = 0, we shine a high-intensity 461 nm beam within 300 ns, engineering an initial phase spread  $\varphi(\omega_k) \in [0, \varphi_0]$  depicted on the Bloch sphere. The phase  $\varphi(\omega_k)$  applied to atom k is proportional to the post-quench frequency shift  $\omega_k$ . Traces represent different  $\varphi_0$  and show enhanced oscillations with increasing  $\varphi_0$ .

a roughly flat density of states (see Sec. 6.9.1), resulting in a setup consistent with the  $\delta_s=0$  line in Fig. 6.1(c). After the initial  $\pi/2$  pulse, we wait for 2  $\mu$ s to let transient dynamics settle and then turn on the 461 nm beam to quench on  $E_W/2\pi=0.83$  MHz from an initial value  $E_W^{(0)}/2\pi\ll0.1$  MHz. The beam exhibits a rise time of roughly 50 ns, much faster than the relevant dynamics. To scan across the phase diagram in the inset of Fig. 6.2(b), we vary the interaction strength  $\chi N$  between shots by changing the atom number N.

As shown in Figs. 6.2(b)-(c), we observe two distinct dynamical behaviors corresponding to phases I and II, signalled by the decay rate of  $|\Delta_{BCS}|$ . For experiments with sufficiently small  $\chi N$ , such as  $\chi N/2\pi =$ 

0.19 MHz,  $|\Delta_{BCS}|$  decays with a 1/e coherence time of  $0.9 \pm 0.1~\mu s$ . This coherence time is consistent with single-particle dephasing of  $\langle \hat{S}^- \rangle$  set by the energy spread  $\hbar E_W$  and is nearly constant throughout this regime. We identify the fast decay of  $|\Delta_{BCS}|$  as an experimental signature of phase I. For larger interaction strengths, we observe a rapid increase in coherence time up to a maximum of 29  $\mu s$  when  $\chi N/2\pi = 1.2$  MHz; this constitutes an improvement of more than a factor of 30. We identify this extended coherence time regime as phase II. The residual decay of  $|\Delta_{BCS}|$  in this regime can be attributed to intrinsic dissipative processes including spontaneous emission, off-resonant superradiant emission, and scattering of 461 nm light [95, 223]<sup>[G]</sup>, which set a maximum predicted coherence time of 29  $\mu s$  (see Sec. 6.9.1). All experimental observations (colored traces) are in good agreement with numerical simulations based on experimental conditions (dark lines—see Sec. 6.10).

Due to the separation of timescales in the decay of  $|\Delta_{BCS}|$ , we are able to determine the boundary between phase I and phase II in our experiment by calculating the average  $|\Delta_{BCS}|$  in a time window from 3  $\mu$ s to 8  $\mu$ s as a function of  $\chi N$  (see Fig. 6.2(c)). In this analysis, phase I features a vanishing average  $|\Delta_{BCS}|$ , while phase II sees a nonzero  $|\Delta_{BCS}|$  that increases with  $\chi N$ . The sharp rise of average  $|\Delta_{BCS}|$  around  $\chi N/2\pi = 0.2$  MHz indicates a dynamical phase transition, which agrees with the point predicted by numerical simulations. In a spin-model picture, the BCS pairing gap corresponds to the energy gap between collective angular momentum states, which exists due to the spin-exchange interaction  $\chi \hat{S}^+\hat{S}^-$  [419]. Phase II corresponds to the parameter region where such interactions are sufficiently strong to protect against single-particle dephasing. As a result, the observed transition directly relates to previous experiments exploring coherence protection in other systems [85, 95, 121, 407–409]. In this picture, single-particle dephasing couples the atomic ensemble from some initial angular momentum quantum number S to S-1, and  $|\Delta_{BCS}|$  represents (half) the energy gap between these two states due to the spin-exchange interaction.

## 6.6 Signatures of Higgs oscillations

In BCS superconductors, the excitation of a Higgs mode is predicted to occur in phase II. This mode can be characterized by a collective damped oscillation of the order parameter  $|\Delta_{BCS}|$  with a characterized by a collective damped oscillation of the order parameter  $|\Delta_{BCS}|$ 

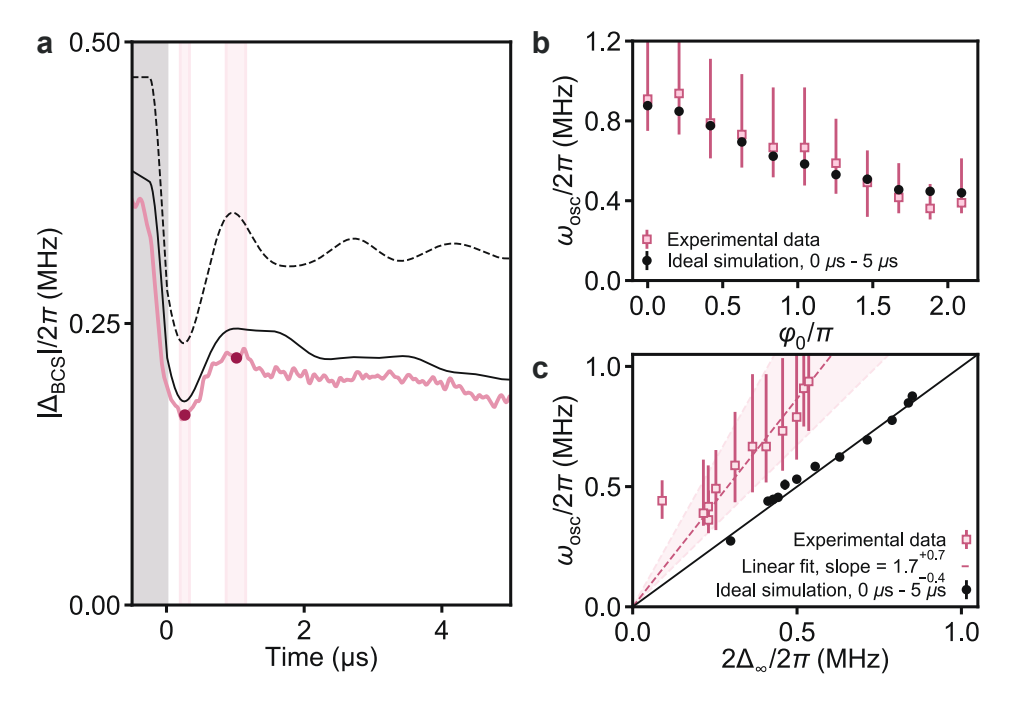


Figure 6.3: Collective scaling in damped phase II oscillations. (a) Time dynamics of  $|\Delta_{BCS}|$  measured after engineering an initial phase spread over  $[0, \varphi_0]$  where  $\varphi_0 = 0.8\pi$  as in Fig. 6.2(d), plotted in absolute frequency units (pink trace). The solid black curve represents a numerical simulation of the full system, whereas the dashed curve represents an ideal simulation neglecting dissipation and motional effects. We obtain a crude estimate of oscillation frequency in the experimental data by fitting a trough and peak to smoothed data (after subtracting slow-moving behavior) within the first couple  $\mu$ s (magenta points), using these points to infer a half period of oscillation, and with uncertainties determined using a 90% amplitude threshold (pink bands). (b) Comparing oscillation frequency estimates of experimental data (pink squares) with those of ideal simulations (black dots) for different  $\varphi_0$ . Theory oscillation frequencies are calculated using a Fourier transform from  $t = 0 \mu s$  to  $t = 5 \mu s$ . Error bars for experimental data are set by the minimum and maximum frequencies implied by uncertainties in the half period shown in (a). The two frequency estimates agree within error bars. (c), Collective scaling of oscillation frequency. For each  $\varphi_0$  measured in the experiment, we plot the oscillation frequency against the long-time BCS gap  $\Delta_{\infty}$ , calculated at  $t=18~\mu s$  for ideal simulations and at  $t=3~\mu s$  for experimental data. The solid black line is defined by  $\omega_{\rm osc} = 2\Delta_{\infty}$ , demonstrating the expected scaling for Higgs oscillations. The dashed pink line represents a linear fit to the experimental data. The pink band shows the uncertainty in the slope assuming correlated error in  $\omega_{\rm osc}$ , such that its bounds are defined by linear fits to the data assuming maximum and minimum values for  $\omega_{\rm osc}$  as defined by the error bars.

acteristic frequency of  $2\Delta_{\infty}$ , the long-time value of  $|\Delta_{BCS}|$  [137]. From an atomic physics perspective, we can equivalently think of this mode as representing the detuned coupling between S and S-1 angular momentum states induced by the single-particle dephasing term, which in a far-detuned limit (when the interactions are much stronger than the dephasing term) should oscillate at a frequency set by the interaction-induced detuning. We observe hints of Higgs oscillations by comparing the experimental

trace of  $|\Delta_{BCS}|$  at  $\chi N/2\pi = 1.2$  MHz (red curve in Fig. 6.2(b)) with the dissipation-free simulation (dashed line in Fig. 6.2(b)) and noticing that the first dip in the experimental trace coincides with the first cycle of Higgs oscillations. The size of this feature can be increased experimentally by engineering an initial phase spread  $\varphi(\omega_k) \in [0, \varphi_0]$  between atoms which is correlated with the post-quench frequency shifts  $\omega_k$  of the atoms, as shown in Fig. 6.2(d). The initial state with a nonzero opening angle  $\varphi_0$  shares qualitative features with the BCS ground state at finite  $\chi$  up to a  $\pi/2$  rotation on the Bloch sphere [405], in contrast to the initial state mimicking the BCS ground state with infinite  $\chi$  in Fig. 6.2(b).

We can check if these oscillations scale properly with the long-time BCS order parameter  $\Delta_{\infty}$  as  $\omega_{\rm osc}=2\Delta_{\infty}$ . We confirm this scaling in theory by measuring the oscillation frequency from t=0  $\mu s$  to t=5  $\mu s$  in idealized numerical simulations ignoring dissipation and motional effects (black dashed line in Fig. 6.3(a). For different values of the phase spread extent  $\varphi_0$ , the system reaches its steady state at a different long-time BCS gap  $\Delta_{\infty}$ . By parametrically plotting the oscillation frequency vs.  $2\Delta_{\infty}$  as a function of  $\varphi_0$  in panel (c), we observe the expected scaling.

Oscillations in  $|\Delta_{BCS}|$  are consistently smaller and decay more quickly in experiment than in theory (See Sec. 6.10.3 for a brief discussion). Nonetheless, we obtain a crude estimate of the experimental oscillation frequency by measuring a half period from the first trough and peak of  $|\Delta_{BCS}(t)|$ , as shown in panel (a). In panel (b), we compare the frequency in experimental data to that of ideal simulations for different  $\varphi_0$  and show that the frequencies agree within error bars. This suggests that the transient dynamics observed in  $|\Delta_{BCS}|$  are related to the Higgs oscillations present in theory.

Although the experimental oscillation frequency agrees with simulations, the steady-state order parameter  $\Delta_{\infty}$  is much smaller, as can be seen in Fig. 6.3(a). As a result, the measured frequencies scale linearly with  $\Delta_{\infty}$  but with a different prefactor. In panel  $\mathbf{c}$ , we fit a linear relation of  $\omega_{\rm osc} = (1.7^{+0.7}_{-0.4}) \times 2\Delta_{\infty}$  to the data, where the slope uncertainty bounds are calculated assuming errors in  $\omega_{\rm osc}$  are perfectly correlated. Most of the reduction in  $\Delta_{\infty}$  can be captured in theory by considering dissipation and motional effects (solid black trace). We see an additional small difference in  $|\Delta_{\rm BCS}|$  between full numerical simulations and experimental data, which we attribute to drifts in experimental alignments and calibration factors over time. This difference is not apparent in Fig. 6.2(d) because we plot  $|\Delta_{\rm BCS}|$  in normalized



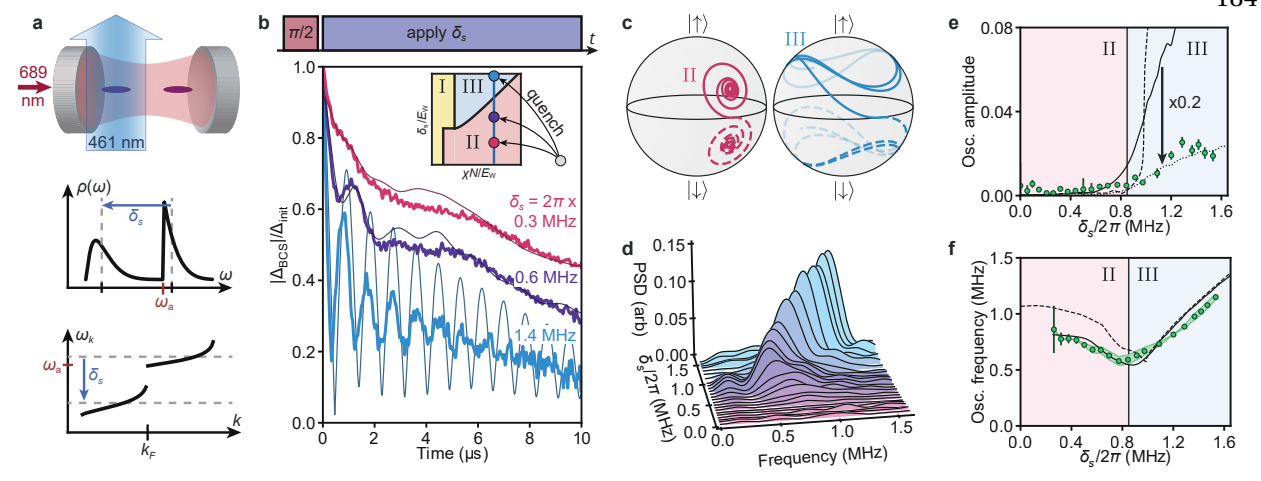


Figure 6.4: Phase II to phase III transition. (a), Engineering a bimodal energy distribution. We prepare two atomic clouds with centers separated by 3 mm and shine an off-resonant 461 nm beam centered on one cloud. This generates a density of states  $\rho(\omega)$  (middle plot), equivalent to a dispersion relation  $\varepsilon_k = \hbar \omega_k$  (bottom plot). (b) Probing phase II and phase III. We prepare the same initial state as in Fig. 6.2(b) with a  $\pi/2$  pulse, quench to a finite  $\delta_s/E_W$ , and then let the system evolve. The inset shows the explored parameter cut and identifies post-quench  $\delta_s/E_W$  values with colored dots. As before, colored traces represent experimental time traces of  $|\Delta_{BCS}|$ , and darker lines represent numerical simulations. (c) Ideal simulations of mean-field trajectories for the two sub-ensembles (solid and dashed curves) in phase II (magenta) and phase III (blue). The trajectories are projected onto the surface of the Bloch sphere for visual clarity. (d) Fourier response of  $|\Delta_{BCS}|^2$  for different  $\delta_s$ , plotted as power spectra of the dynamics from  $t = 0.5 \mu s$  to 4  $\mu s$  after subtracting slow-moving behavior. (e) Average oscillation amplitude between  $t = 3 \mu s$  and  $8 \mu s$ . For the remaining plots, dashed lines represent ideal simulations (ignoring dissipation or motional effects), and solid dark lines correspond to full simulations. The additional dotted line represents numerical simulations rescaled by ×0.2, plotted to show similar trend behavior between experimental data and simulations. We identify a phase transition around  $\delta_s/2\pi = 0.85$  MHz. (f) Oscillation frequency of  $|\Delta_{BCS}|$ , measured using power spectra calculated in (d). We correct for systematics inferred from our data analysis and assume this correction has an uncertainty of 100%, shown by the green band. The phase transition point observed in data in panels (e) and (f) agrees well with simulations.

units.

## 6.7 Phase II to phase III

We probe the phase II to phase III transition using a vertical cut through the dynamical phase diagram. To realize this, we introduce an energy splitting  $\hbar \delta_s$  between two individually addressable clouds of atoms along the cavity axis using AC Stark shifts from our 461 nm beam, as shown in Fig. 6.4(a). In combination with a background energy spread  $\hbar E_W$  associated with lattice shifts (see Sec. 6.9.2), this

produces a bimodal density of states and a dispersion relation similar to the one proposed in Fig. 6.1(b). As before, we begin the experiment with a highly coherent state and with  $\delta_s = 0$ . Then, we quench on a nonzero  $\delta_s$  and let the system evolve. Between shots, we scan  $\delta_s$  while fixing  $\chi N/2\pi = 0.9$  MHz and  $E_W/2\pi \approx 0.34$  MHz to explore the vertical cut.

The resulting dynamics show a marked change in the dynamical evolution of  $|\Delta_{BCS}|$  over the scan as shown in Fig. 6.4(b), which we attribute to a transition between phase II and phase III dynamics. For small  $\delta_s$ , we either see Higgs-like oscillations which are damped after 3  $\mu$ s (the trace where  $\delta_s/2\pi=0.6$  MHz) or, for very small splittings, no oscillations resolvable above the noise floor ( $\delta_s/2\pi=0.3$  MHz). We associate this regime with phase II since it overlaps with the previously observed phase II dynamics in parameter space. For larger  $\delta_s$ , curves instead show large-amplitude oscillations that persist for more than 5  $\mu$ s ( $\delta_s/2\pi=1.4$  MHz). We identify the long-lived oscillations in this parameter regime as an experimental signature of phase III.

Intuitively, we can understand the difference between the two phases by identifying the two subensembles of atoms with two Bloch vectors (see Fig. 6.4(c), and Sec. 6.13 for a more detailed study). In phase II, a finite  $\delta_s$  causes the Bloch vectors to precess in different directions, but the dominant scale  $\chi N$  locks them together to form the solid and dashed magenta orbits. In the presence of a finite  $E_W$ , the orbits decay, but the Bloch vectors maintain phase coherence. On the other hand, in phase III  $\delta_s$  is large enough that the two Bloch vectors accrue an unbounded relative phase, as in the blue orbits. The presence of interactions locks each sub-ensemble separately against a finite  $E_W$ , leading to persistent oscillations. This effective beating of two large spins in a macroscopic array of spin-1/2 particles is truly an interaction-driven effect since the interactions are strong enough to lock the spins within each sub-ensemble but not strong enough to lock both sub-ensembles together.

We can experimentally define a boundary between phase II and phase III using the separation of timescales observed for oscillations in  $|\Delta_{BCS}|$ . Fig. 6.4(e) shows the average oscillation amplitude in a time window from  $t=3~\mu s$  to 8  $\mu s$ . In this analysis, we observe a sharp rise in oscillation amplitude at  $\delta_s/2\pi=0.85~{\rm MHz}\approx \chi N/2\pi$  as we increase  $\delta_s$ , which we identify as a dynamical phase transition. Numerical simulations plotted in Fig. 6.4(e) agree fairly well with data in capturing trend behavior and

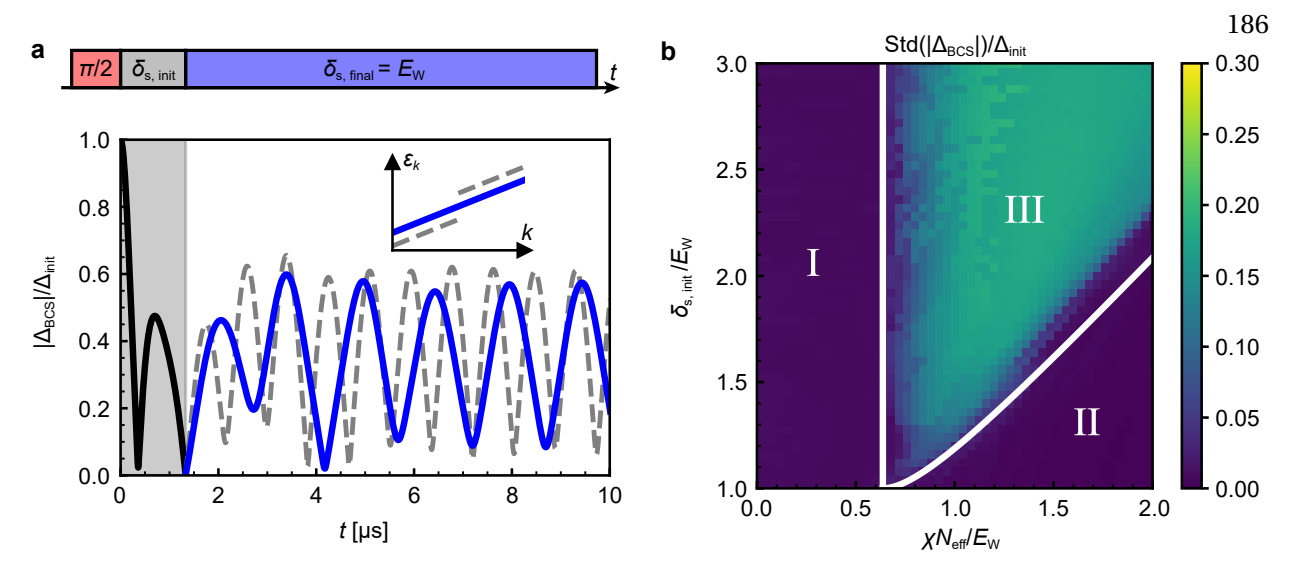


Figure 6.5: Justifying our alternative approach for probing phase III. (a) Simulation of an alternative experimental sequence. As described by the timing sequence at the top, we simulate an experiment that prepares the initial state using a  $\pi/2$  pulse, lets the system evolve under a bimodal distribution of single-particle energy (inset) until  $|\Delta_{BCS}|$  reaches its minimum value, and then quenches the system back to a continuous distribution of single-particle energies (inset). The theoretically predicted time trace of  $|\Delta_{BCS}|$  with  $\chi N/E_W=1.0$  and  $\delta_{s,init}/E_W=1.6$  is shown at the bottom. The blue (gray dashed) line shows phase III dynamics under a continuous (bimodal) distribution. (b) Long-time standard deviation of  $|\Delta_{BCS}(t)|$  after quenching to the continuous distribution shown in (a). The white lines are dynamical phase boundaries for bimodal distributions. Nearly all the choices of parameter for phase III using bimodal distributions can lead to phase III behaviors after quenching to the continuous distribution.

estimating the phase transition point. However, we see a discrepancy in the absolute size of the observed and predicted oscillation amplitudes. We attribute this to an extra dephasing mechanism (likely residual motional effects) in our system or other imperfections in the experimental sequence not captured by the theory model.

We verify the location of the phase II to phase III transition using the short-time oscillation frequency (from  $t=0.5~\mu s$  to 4  $\mu s$ ) as an additional experimental signature. As can be seen in the Fourier responses in Fig. 6.4(d) and quantified in Fig. 6.4(f), the oscillation frequency exhibits a dip vs.  $\delta_s$  at the previously-identified phase boundary. This dip is present in roughly the same location for experiment and theory and is expected to coincide with the phase II to phase III transition (see Sec. 6.13).

Our implementation of phase III in this work is not how it was originally envisioned [130], in which the system starts in the ground state of a weakly superconducting system and is subsequently quenched

to a system with much stronger interactions. Instead, we start with the ground state of a strongly superconducting system and quench on a bimodal distribution of single-particle energies, which is quite a different prescription.

Despite their qualitative differences, these two situations generate similar phase III dynamics and can in fact be dynamically connected to each other with numerical analysis. This is done by the protocol shown in Fig. 6.5(a), which uses a bimodal distribution ( $\delta_{s,init} > E_W$ ) just to generate a state with minimum  $|\Delta_{BCS}|$ . At this point the system's dispersion is restored to be continuous by setting  $\delta_{s,final} = E_W$ . This approach more closely resembles the phase III quench discussed in actual BCS superconductors, where phase III is observed by quenching from a state with weak BCS paring gap  $|\Delta_{BCS}|$  to one with a strong pairing gap [137]. Numerical simulations show that nearly all choices of parameters that lead to phase III using a bimodal distribution also lead to phase III dynamics when quenching to a continuous distribution. The only exception is a small parameter regime close to the boundary between phase III and phase II (see Fig. 6.5(b)).

# 6.8 Scan across three dynamical phases

Finally, we observe all three dynamical phases in a single cut through parameter space, as shown in Fig. 6.6(a). We run the same experimental sequence described in Fig. 6.4, but instead scan  $\chi N$  between shots with  $\delta_s/2\pi=1.1$  MHz and  $E_W/2\pi=0.46$  MHz fixed. This allows us to probe phase I, phase III and then phase II by increasing atom number N. Using order parameters established in Figs. 6.2 and 6.4, we determine boundaries between the three phases. As shown in Fig. 6.6(b), the long-time average of  $|\Delta_{BCS}|$  rises suddenly around  $\chi N/2\pi=0.25$  MHz in both data and simulations. This transition marks the boundary between phase I and phase III. Additionally, at  $\chi N/2\pi=1.0$  MHz we observe a dip in the short-time oscillation frequency of  $|\Delta_{BCS}|$  (Fig. 6.6(c)), marking a transition between phase III and phase II. For this scan, we do not use the long-time oscillation amplitude as an order parameter due to poor signal-to-noise for smaller values of  $\chi N$ .

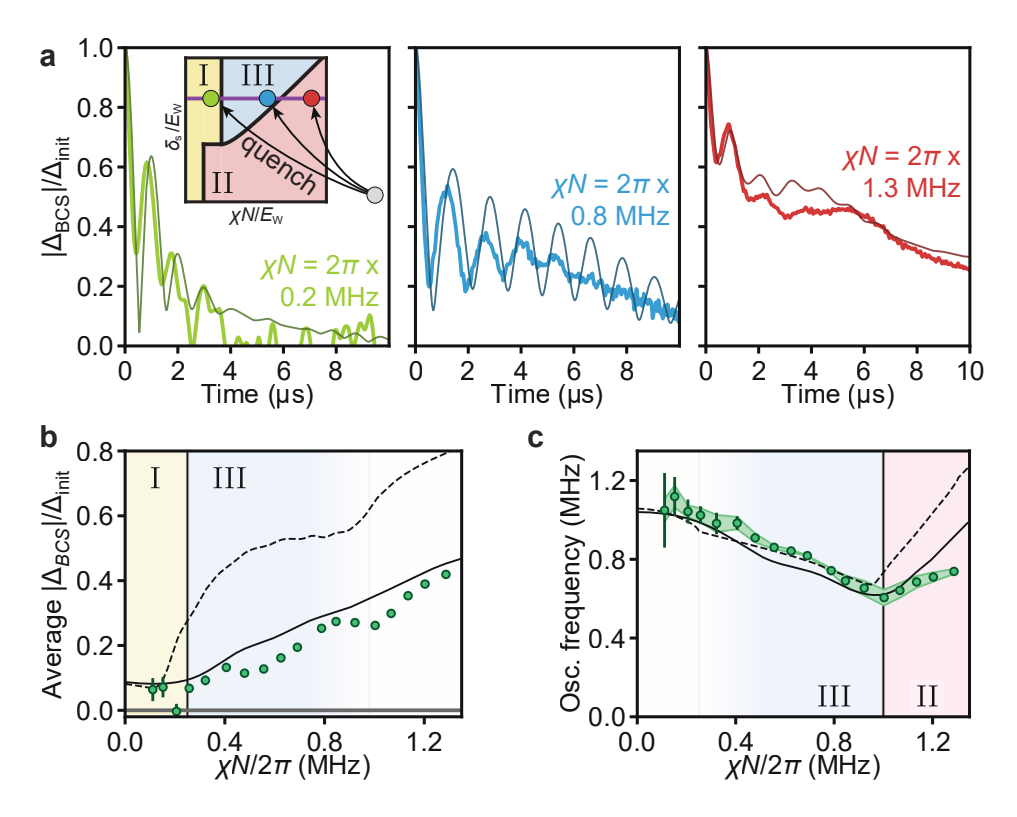


Figure 6.6: Scan across three dynamical phases. (a), Probing phase I, II and III dynamics using time traces of  $|\Delta_{BCS}|$ . Quenches are performed in the same manner as in Fig. 6.4(b), except between shots we hold post-quench values of  $\delta_s$  fixed and vary  $\chi N$  instead. The inset shows the explored cut through the phase diagram and identifies final  $\chi N/E_W$  values with green (phase I), blue (phase III), and red (phase II) dots. The  $\chi N/2\pi = 0.2$  MHz trace is smoothed for clarity. (b) Time average of  $|\Delta_{BCS}|$  in a bin from  $t=3~\mu s$  to 8  $\mu s$  vs. interaction strength. The experimental data shows signatures of a phase I to phase III transition at  $\chi N/2\pi = 0.25$  MHz. (c) Oscillation frequency of  $|\Delta_{BCS}|$  vs. interaction strength in a bin from  $t=0.5~\mu s$  to 4  $\mu s$ . Again, we correct for systematics inferred from our data analysis and assume this correction has an uncertainty of 100%, shown by the green band. This data identifies a phase III to phase II transition at  $\chi N/2\pi = 1.0$  MHz. Experimental data and transitions in both plots are consistent with numerical simulations.

## 6.9 Details of the experimental setup

The experimental setup for this work is quite similar to that of the dynamical phase transition paper described in Ch. 5: we load  $N=10^5-10^6$  <sup>88</sup>Sr atoms from a magneto-optical trap into an 813 nm optical lattice supported by a high-finesse optical cavity with a temperature of roughly 15  $\mu$ K. We measure an axial trapping frequency of  $\omega_x/2\pi=165$  kHz (coordinates defined in Fig. 6.7(a)), giving a Lamb-Dicke parameter of  $\eta=0.17$  for excitation with 689 nm light. At the measured temperature of 15  $\mu$ K,

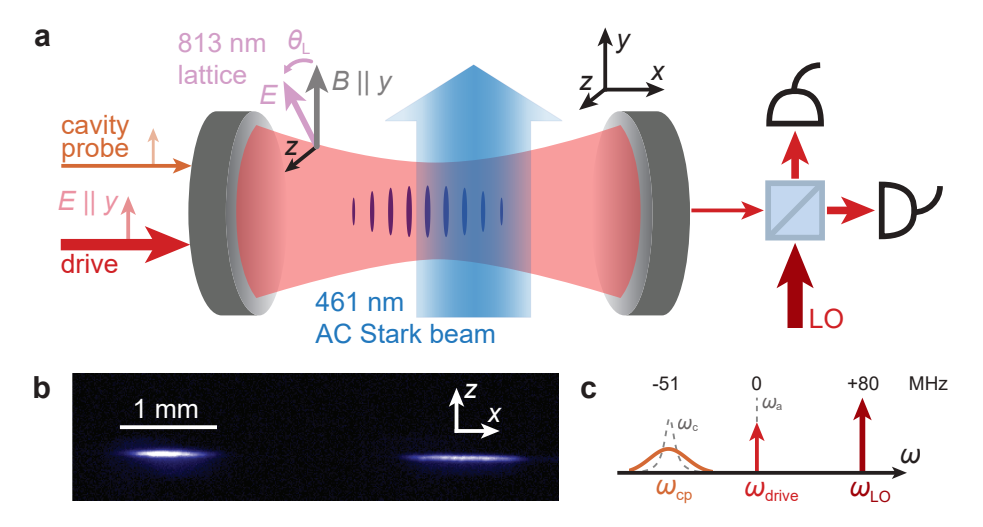


Figure 6.7: Experimental configuration. (a) Detailed diagram of the cavity and all relevant beams. A magnetic field along  $\hat{y}$  sets the quantization axis. The 813 nm optical lattice supported by the cavity has a tunable linear polarization. We drive a  $\pi/2$  pulse with a beam polarized along  $\hat{y}$  through the cavity, and during the experiment we probe the cavity resonance frequency using a second  $\hat{y}$ -polarized beam to measure atom number. A 461 nm beam far-detuned from the  $|{}^1S_0\rangle - |{}^1P_1\rangle$  transition shines on the atoms from the side of the cavity, inducing AC Stark shifts. We probe signals transmitted through the cavity using a balanced heterodyne detector. (b) Fluorescence image of the two atomic clouds used when scanning through phase III in Figs. 6.4 and 6.6. (c) Frequency landscape of 689 nm beams. The atomic drive frequency  $\omega_{\rm drive}$  is resonant with the atomic transition. The cavity probe frequency  $\omega_{\rm cp}$  is nominally centered with the cavity resonance frequency, 51 MHz red-detuned from the atomic transition. The local oscillator used in heterodyne detection has frequency  $\omega_{\rm LO}$  and is 80 MHz blue-detuned from the atomic transition.

 $\eta^2(2\bar{n}+1)=0.11\ll 1$ , placing the atoms in the Lamb-Dicke regime (see Sec. 3.5.2). Using piezoelectric actuators, we stabilize the cavity length to set the closest TEM<sub>00</sub> resonance to be 51 MHz red-detuned from the atomic transition, with a full frequency landscape as displayed in Fig. 6.7(c). This is the same detuning as in Ch. 5, placing us in a regime where cavity-mediated spin-spin interactions dominate.

However, depending on the parameter scan studied, other aspects of the experimental setup change. Generally, we use one of two different setups as described in the following two subsections. The key parameters changed between the two setups are summarized in Table 6.1.

### 6.9.1 Phase I to phase II cut

For exploring the phase I to phase II transition along cut H1 in Fig. 6.1(c), we load the atoms into a single atomic cloud, resulting in a Gaussian distribution transverse to the cavity axis with standard

deviation  $\sigma_y = \sigma_z = 16 \ \mu\text{m}$ . Further, the cloud is extended over thousands of lattice sites, forming a distribution along the cavity axis with a standard deviation  $\sigma_x = 430 \ \mu\text{m}$ . We set a quantization axis along  $\hat{y}$  with a 2.4 G magnetic field and tune the lattice polarization to a "magic angle" relative to this axis, such that the differential lattice shift between ground ( $|^1S_0\rangle$ ) and excited ( $|^3P_1, m_J = 0\rangle$ ) states vanishes (see Sec. 3.5.2) [108]<sup>[G]</sup>. This removes any contribution of the optical lattice on the single-particle energies  $\varepsilon_k$ .

After loading into the lattice, we initialize the atoms with a  $\hat{\gamma}$ -polarized drive through the cavity which is nominally resonant with the atomic transition. Because the drive is far off-resonance from the cavity (which has linewidth  $\kappa/2\pi = 153$  kHz at 689 nm), the induced Rabi frequency is somewhat suppressed. Nonetheless, we find that roughly 5 mW of power before the cavity is sufficient to drive the atoms with a  $\pi/2$  pulse in 100 ns. We allow the atoms to settle for 2  $\mu$ s in order to distinguish the desired physics from transient dynamics observed after state initialization, which we attribute to undesired excitation of sideband transitions. We then shine a 461 nm beam with 17.6 mW of power from the side of the cavity along the  $\hat{y}$  direction, detuned from the  $|{}^1S_0\rangle - |{}^1P_1\rangle$  transition by more than 12.1 GHz, in order to induce AC Stark shifts on the ground state. The beam has waists  $(w_x, w_z) = (1030 \ \mu \text{m}, 75 \ \mu \text{m})$  along the  $\hat{x}$  and  $\hat{z}$  directions at the plane of the atoms, and its center is displaced from the center of the atomic cloud by  $x_0 = 580 \ \mu \text{m}$  along the cavity axis. From these dimensions, we calculate an atomic density of states  $\rho(\omega)$  as a function of frequency shift which is roughly uniform between 0 and a maximum shift  $\hbar \tilde{E}_{W}$  (for the distribution used, refer to the formulas in Sec. 6.14). We estimate that for the power and detuning used in this cut, the 461 nm beam scatters off the atoms with an average rate of  $R_{\rm sc}/2\pi = 1.3$  kHz, roughly a factor of six smaller than  $\gamma/2\pi = 7.5$  kHz, the spontaneous emission rate. Combined with collective emission from the atoms as described in Sec 6.9.3, these dissipation processes set a maximum predicted coherence time in the system of 29  $\mu$ s.

It is worth mentioning that the uniform distribution  $[-\tilde{E}_{\rm W}/2,\tilde{E}_{\rm W}/2]$  can be interpreted in two different ways on the dynamical phase diagram in Fig. 6.1(c). The first is:  $\delta_{\rm S}=0$  and  $E_{\rm W}=\tilde{E}_{\rm W}$ , and the second is:  $\delta_{\rm S}=E_{\rm W}=\tilde{E}_{\rm W}/2$ . In principle, therefore, this cut could map onto a horizontal cut either along the x-axis or along the line  $\delta_{\rm S}/E_{\rm W}=1$  (up to a factor of 2 rescaling on the horizontal axis). Here we prefer the first interpretation  $\delta_{\rm S}=0$  because in this scheme we only have a single control parameter (the

strength of AC Stark shift beam). Additionally, the line  $\delta_s = E_W$  in the dynamical phase diagram has an implication that a small perturbation of  $\delta_s$  can generate a gap in atomic frequency, but such a gap is not physically realizable given the experimental control parameters used in this cut.

## 6.9.2 Cuts through phase III

For the two cuts through phase III described in Figs. 6.4 and 6.6, we load the atoms in two clouds separated by 3 mm, as shown in Fig. 6.7(b). The left cloud has an extent described by standard deviations  $(\sigma_x, \sigma_z) = (200 \ \mu\text{m}, 16 \ \mu\text{m})$ . The right cloud has a similar extent along  $\sigma_z$  but is broader along the cavity axis. We tune the lattice polarization to point along  $\hat{z}$ , which breaks the magic angle condition and introduces a differential trap depth between ground and excited states of 0.47 MHz for atoms experiencing peak lattice intensity. Due to their finite temperature, the atoms experience a spread in lattice intensities which leads to an inhomogeneous trap depth. We estimate the induced distribution of energy shifts by assuming the atoms occupy a 2D Gaussian distribution radially with standard deviation  $\sigma_y = \sigma_z = 16 \ \mu\text{m}$ , compared to the lattice waist  $w_y = w_z = 80 \ \mu\text{m}$ . This produces a peaked distribution equivalent to the narrow peak in Fig. 6.4(a).

In these experiments, we perform a  $\pi/2$  pulse as before and then immediately shine a 461 nm beam centered on the left ("bright") atomic cloud. Unlike in the previous cut, we do not wait for transient dynamics to settle after state initialization, for the sake of simplicity. We do not see major differences between observed and expected behavior when omitting the wait period. The beam has waists  $(w_x, w_z) = (1700 \ \mu\text{m}, 80 \ \mu\text{m})$ . We install a beam block just before the chamber that clips the beam tail that would otherwise hit the right ("dark") atomic cloud. The 3 mm separation between clouds is sufficiently large to ensure the beam does not significantly diffract around the beam block. The beam shifts the mean energy of the bright cloud away from that of the dark cloud, introducing a tunable  $\delta_s$ .

While nominally, we hold  $E_W$  fixed while scanning  $\delta_s$  to explore the phase II to phase III transition, in reality the finite size of the blue beam introduces an additional contribution to  $E_W$  on the bright cloud, as shown in Fig. 6.8(c). As  $\delta_s$  increases, therefore, both the size and shape of the single-particle energy distribution changes. We calculate  $E_W$  in a consistent manner by estimating the standard deviation of

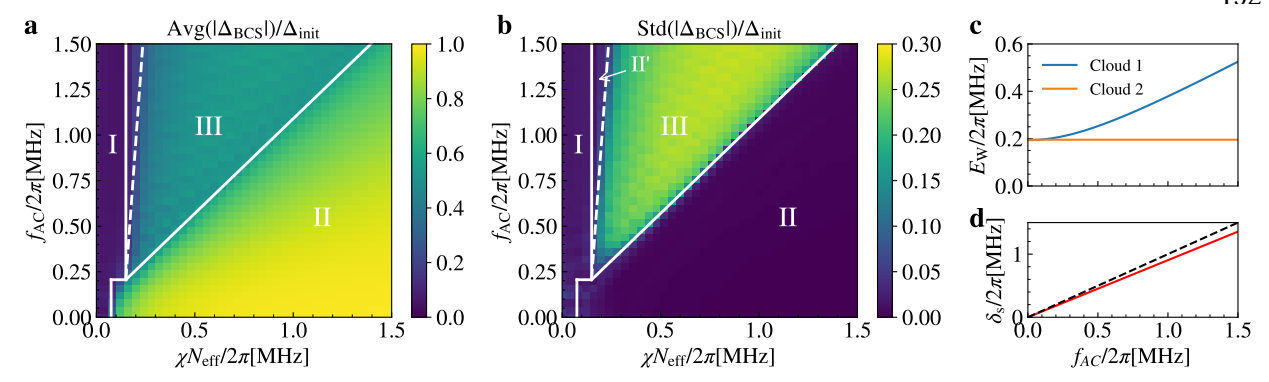


Figure 6.8: Modeling imperfections in  $E_{\rm W}$  and  $\delta_{\rm S}$ . (a) and (b) Dynamical phase diagram for the experiment with two atomic ensembles, in terms of averaged spin-exchange interaction strength  $\chi N_{\rm eff}$  and peak AC Stark shift  $f_{\rm AC}$ . The white lines show the predicted dynamical phase boundaries to guide the eye. The white dashed line marks a small region of phase II' due to the imbalance of  $E_{\rm W}$  for the two atomic ensembles. (c)  $E_{\rm W}$  as a function of peak AC Stark shift  $f_{\rm AC}$ , with AC Stark shift applying to atomic cloud 1. (d)  $\delta_{\rm S}$  as a function of peak AC Stark shift  $f_{\rm AC}$  (red line). The dashed line marks the place where  $\delta_{\rm S} = f_{\rm AC}$ .equency  $\omega_{\rm CP}$  is nominally centered with the cavity resonance frequency, 51 MHz red-detuned from the atomic transition. The local oscillator used in heterodyne detection has frequency  $\omega_{\rm LO}$  and is 80 MHz blue-detuned from the atomic transition.

the bright cloud distribution and matching the result to a uniform distribution with the same standard deviation. When reporting the value of  $E_W$ , we use the value obtained at the phase transition point for the phase II to phase III transition. Additionally, we define  $\delta_s$  to be the mean frequency difference between the two ensembles. At large splittings, the size of  $\delta_s$  also deviates from the peak AC Stark shift, which we call  $f_{AC}$ , as shown in Fig. 6.8(d). This change is relatively small, however.

These imperfections lead to a slight modification in the predicted dynamical phase diagram as depicted in Fig. 6.8(a-b). In particular, the imbalance of  $E_{\rm W}$  for the two atomic ensembles can lead to a small region of phase II' marked by the white dashed line. This occurs because the spin-exchange interaction is able to lock the ensemble with smaller  $E_{\rm W}$ , while the ensemble with larger  $E_{\rm W}$  remains unlocked, which leads to  $|\Delta_{\rm BCS}|$  approaching a small but nonzero constant value. In the experiment, due to other dissipative processes and reduced signal-to-noise ratio for small  $\chi N$ , we do not observe a difference between phase I and phase II'. This leads to a small discrepancy between theory and experiment in describing the phase I to phase II transition point as shown in Fig. 6.6.

Finally, as we increase the 461 nm beam power, the atoms also scatter more blue photons. At the

	Atomic distribution	Generating $E_{ m W}$	Generating $\delta_{ m s}$
Scheme 1 (cut H <sub>1</sub> )	One cloud $\sigma_x = 430 \ \mu \text{m}$ $\sigma_z = 16 \ \mu \text{m}$	$461 \text{ nm beam}$ $(w_x, w_z) = (1030 \ \mu\text{m}, 75 \ \mu\text{m})$ $x_0 = 580 \ \mu\text{m}$ $P = 17.6 \ \text{mW}$ $\delta_{ca}/2\pi = 12.1 \ \text{GHz}$	N/A
Scheme 2 (cuts V, H <sub>2</sub> )	Two clouds $\sigma_x = 203 \ \mu \text{m}$ $\sigma_z = 16 \ \mu \text{m}$ Separation 3 mm	813 nm non-magic lattice $w_0^{({ m cav})}=79.6~\mu{ m m}$ $\Delta\omega_{ m AC}^{({ m peak})}/2\pi=0.47~{ m MHz}$	$461 \text{ nm beam}$ $(w_x, w_z) = (1700 \ \mu\text{m}, 80 \ \mu\text{m})$ $P = 17.3 \ \text{mW}$ $\delta_{ca}/2\pi = 14.0 \ \text{GHz}$

Table 6.1: Parameters for inhomogeneity generation, for each of the two schemes used for different parameter cuts in exploring the BCS dynamical phase diagram.

largest applied AC Stark shift, we estimate that the bright cloud experiences a scattering rate of  $R_{\rm sc}/2\pi =$  3.4 kHz, resulting in lower coherence times for traces with large  $\delta_{\rm s}$ . However, this excess decoherence does not bias our measurements of oscillation amplitude and frequency at times  $t \le 8 \,\mu{\rm s}$ .

#### 6.9.3 Readout

We measure both the pre- and post-quench dynamics of  $|\Delta_{BCS}|$  by monitoring light emitted by the atoms into the cavity as a function of time (see Fig. 6.1(d)). This light arises from a superradiance process which is suppressed when the cavity resonance is detuned from the atomic transition frequency by much more than  $\kappa$ , the cavity power decay linewidth [223, 420, 421]<sup>[G]</sup>. In this limit, the established cavity field adiabatically follows  $\langle \hat{S}^- \rangle$ , which is proportional to  $\Delta_{BCS}$  (see Sec. 2.5 for a discussion on adiabatic elimination). By measuring the leakage of light from the cavity in heterodyne with a local oscillator, we therefore obtain a real-time probe of  $\Delta_{BCS}$ .

Assuming homogeneous atom-light coupling (see Sec. 6.10.1 for modifications due to inhomogeneous coupling), the complex amplitude of the electric field leaking out of the cavity is given by

$$\alpha_{\text{out}}(t) = -\frac{g}{\delta_c} \sqrt{\kappa_m} \langle \hat{S}^-(t) \rangle,$$
 (6.7)

where  $\alpha_{\rm out}$  has units of  $\sqrt{\rm photons/s}$ . Here,  $2g/2\pi=10.9$  kHz is the single-photon Rabi frequency for an atom maximally coupled to the cavity,  $\delta_c/2\pi=(\omega_c-\omega_a)/2\pi=-51$  MHz is the detuning between the

cavity resonance frequency  $\omega_c$  and the atomic transition frequency  $\omega_a$ , and  $\kappa_m/2\pi=41$  kHz is the rate at which photons incident on the cavity mirror are transmitted.  $\alpha_{\rm out}$  is a form of dissipation in the system equivalent to superradiance in a detuned cavity limit. Over the region of parameter space explored in this work, we estimate that the dissipation rate never exceeds  $\gamma_{\rm SR}/2\pi=2.3$  kHz. We measure the detuned superradiant light as it leaks out of the cavity using balanced heterodyne detection, providing us with a real-time probe of  $\langle \hat{S}^- \rangle \propto \Delta_{\rm BCS}$ . In plots of  $|\Delta_{\rm BCS}|$ , we calculate the square magnitude of this quantity and average over 400-1600 shots of the experiment, taken within 2-10 minutes. We then perform background subtraction to remove vacuum noise power from the heterodyne signal. Finally, we take a signed square root of the result to return an estimate of  $|\Delta_{\rm BCS}|$  which averages to zero in the absence of a real signal. This explains why some traces dip below zero despite representing a nonnegative quantity. We also normalize traces to the initial gap size  $\Delta_{\rm init}$  measured right after the  $\pi/2$  pulse.

Additionally, the cavity experiences a (dispersive) shift in its resonance frequency proportional to the number of atoms. We use this fact to measure atom number by sending a pulsed probe tone through the cavity and measuring the frequency shift using the transmitted light. Since this light is spectrally resolved from the light emitted by the atoms, we are able to measure both signals independently on our heterodyne detector. The different optical frequencies involved in the heterodyne beat are compared in Fig. 6.7(c). We separate this signal out from the atomic signal using RF splitters and bandpass filters. We read in both signals using an eight-channel, triggerable analog input card from NI (part no. NI PCI-5105), installed in our data taking computer (named SYNC). It has a sample rate of 60 MS/s for a Nyquist frequency of 30 MHz, which is plenty to resolve the MHz scale time dynamics. It also has an onboard buffer memory of 128 MB, which in practice allows us to take many ms worth of data at the full sample rate before running out of memory.

#### 6.9.4 The experimental sequence

The full experimental sequence has several stages, as outlined in Fig. 6.9. To start, we spend a variable amount of time cooling atoms from our oven source and loading them into the optical lattice. This takes up the majority of the sequence time: the main experimental sequence only lasts a few ms,

compared to somewhere between 1.5 and 6 seconds for the full time. Of this time span, the vast majority is spent loading atoms into the initial blue MOT stage. This is largely due to the low flux of atoms exiting our oven during the operation of this experiment. To give concrete numbers, at an oven temperature of around 500°C, a 3 second sequence time is necessary to generate an interaction strength at the level of  $\chi N/2\pi = 1$  MHz (for an r.m.s. value of  $\chi$ , corresponding to around 860k atoms). We can get more atoms into the lattice by loading for longer times, saturating at around a 6 second sequence length. The largest interaction strength we regularly generate in this experiment is around  $\chi N/2\pi = 1.3$  MHz, achieved with the longest loading times.

After loading atoms into the optical lattice, we align the magnetic bias fields to point along  $\hat{y}$  and let the coils settle for 30 ms. We then start the main portion of the experiment, consisting of multiple experimental shots as well as pre- and post-measurement sequences, each lasting 50  $\mu$ s. At a high level, we interleave 9 pre-measurement sequences with 9 experimental shots. Then, we blow the atoms out of the lattice using 600  $\mu$ s of a resonant 461 nm beam shined from the side of the cavity, followed by 5 post-measurements. For not very important reasons, we actually do not analyze data from the first experimental shot, effectively giving us 8 shots per  $\approx$  3 second loading sequence. This allows us to average down our signal fairly quickly despite working with a relatively slow experimental repetition rate.

The pre-measurement sequence (Fig. 6.9(b)) consists of no applied drive or 461 nm light (used to generate inhomogeneity in the transition frequency). Instead, we measure the cavity resonance frequency using a novel pulsed cavity probe, consisting of a regular train of weak laser pulses (5  $\mu$ s between pulses) centered at the nominal cavity resonance frequency but Fourier-broadened to  $\pm 3.75$  MHz FWHM. This probe is capable of high-bandwidth measurement of the atomic inversion, which is fully outlined in Sec. 7.8.2. For the scope of this experiment, all we really need it for is tracking the number of atoms in the cavity before each experimental shot. We get this information because, as each pulse transmits through the cavity in an undriven ringdown, the frequency of that transmitted light closely

 $<sup>^8</sup>$  Over time, the oven flux slowly got worse (until we refilled it with strontium in May 2024). I took the main data for this experiment between Nov. 2022 and Mar. 2023, so these numbers are valid for that time period. Later, when I took final data for the rf spectroscopy experiment in early 2024, I could not achieve this same performance and had to crank up the oven temperature to around  $515^{\circ}$ C for the largest interaction strengths.

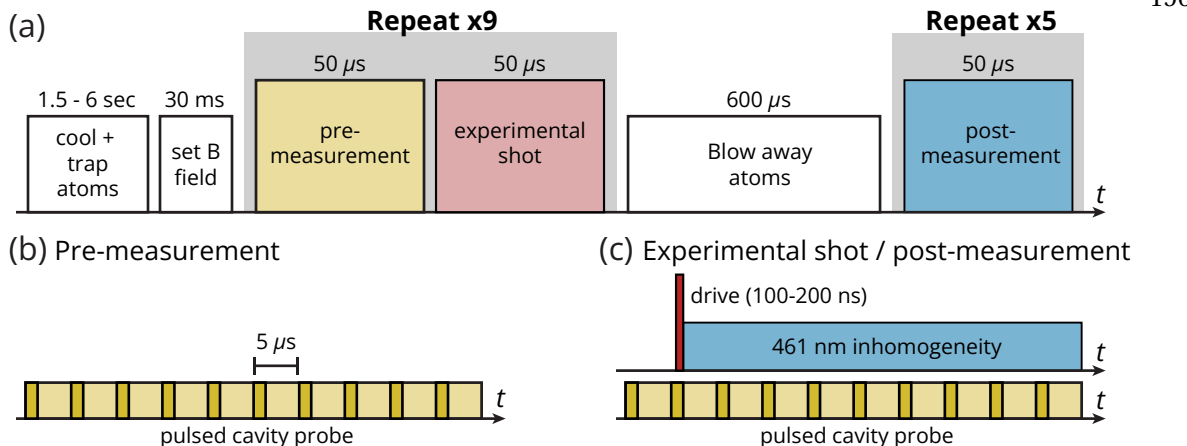


Figure 6.9: BCS dynamical quench experimental sequence. (a) After atom cooling and trapping, we turn on a bias field to set a quantization axis and then start the main experiment. This consists of nine repeated sequences of one pre-measurement and one experimental shot, each lasting 50  $\mu$ s, followed by a 600  $\mu$ s 461 nm pulse to blow away the atoms, and finally by five repeated sequences of a post-measurement. (b) A pre-measurement sequence consists purely of measuring the atom number using the pulsed cavity probe, which essentially consists of a train of short pulses on resonance with the cavity every 5  $\mu$ s with the goal of inferring the instantaneous cavity resonance frequency (see Sec. 7.8.2 for more information on the cavity probe design). (c) Both the experimental shot and post-measurement consist of a short drive to resonantly excite the atoms, followed by a rapid turning on of any 461 nm beams which apply the proper energies  $\varepsilon_k$  to the atoms, accompanied by probing with the cavity probe. The difference between the two subsequences is that the post-measurement does not have any atoms due to the blow-away pulse.

follows the cavity resonance frequency. Since the cavity resonance shifts according to the atom number N (see Ch. 7.8.1), we can infer N. The pre-measurement also plays a second role, which is to add a time delay between experimental shots. At its longest, the lifetime of the atomic coherence is measured to be around 29  $\mu$ s. A 100  $\mu$ s delay gives us 3 1/e times to allow the coherences to decay to no more than 5% of the initial value.

The experimental shots and post-measurements consist of the exact same pulse sequence (Fig. 6.9(c)). First, we initiate the pulsed cavity probe, which in principle allows us to track the evolution of the atomic inversion  $\langle \hat{S}^z \rangle$ . After a few  $\mu$ s, we apply a 689 nm drive resonant with the atomic transition for 100-200 ns, generating a  $\pi/2$  pulse for atoms which maximally couple to the cavity. Immediately following this drive pulse, we shine our 461 nm beams at the atoms to produce the inhomogeneous single-particle

<sup>&</sup>lt;sup>9</sup> Again, we don't actually use this information for this experiment, but it was set up anyway for the experiment in Ch. 7.

energy term. For the remainder of the sequence, we read out the light transmitted through the cavity to infer the dynamics of  $\langle \hat{S}^- \rangle \propto \Delta_{BCS}$ . There are no atoms in the cavity during the post-measurement sequence. The main reasons for performing this step are to calibrate the drive strength (which is easily measured using the amplitude of the transmitted drive light in the absence of an atomic signal) and to calibrate the noise floor of the heterodyne detector (the absence of a signal is a great opportunity to measure the noise). Since the pre-measurement and post-measurement exist in the same measurement record as the experimental shots, we get these measurements for each shot, which is convenient for data analysis particularly when the system drifts.

### 6.10 Details of numerical modeling

While the ideal version of our experiment perfectly implements the Hamiltonian in Eq. (6.6), technical details break this assumption to varying degrees, much to the chagrin of our theorist colleagues. Despite the presence of such imperfections, careful numerical simulations largely performed by Anjun Chu have shown that, for the most part, the physics remains qualitatively unchanged. Here, I briefly go over the highlights and describe how various technical details affect (or do not affect) the numerical predictions.

### 6.10.1 Inhomogeneous atom-light coupling

To simulate an s-wave superconductor, we assume that all of our atoms couple to each other with equal strength. This would be more or less true if all of our atoms saw the same intensity of 689 nm light in the cavity, but in reality the 813 nm trapping lattice is incommensurate with this wavelength. As a result, our atoms effectively experience a uniform distribution in atom-light couplings, parametrized by a phase  $\varphi_k$  representing the 689 nm electric field phase experienced by an atom at position k. Specifically, atom k has a coupling strength  $g_k = g_0 \zeta_k$ , where  $g_0$  is the Jaynes-Cummings coupling strength for an atom experiencing the maximum intensity of 689 nm light, and  $\zeta_k = \cos \varphi_k$  is the position-dependent modification to the coupling.

Recognizing this to be true in our system, we now consider a more accurate effective spin-spin

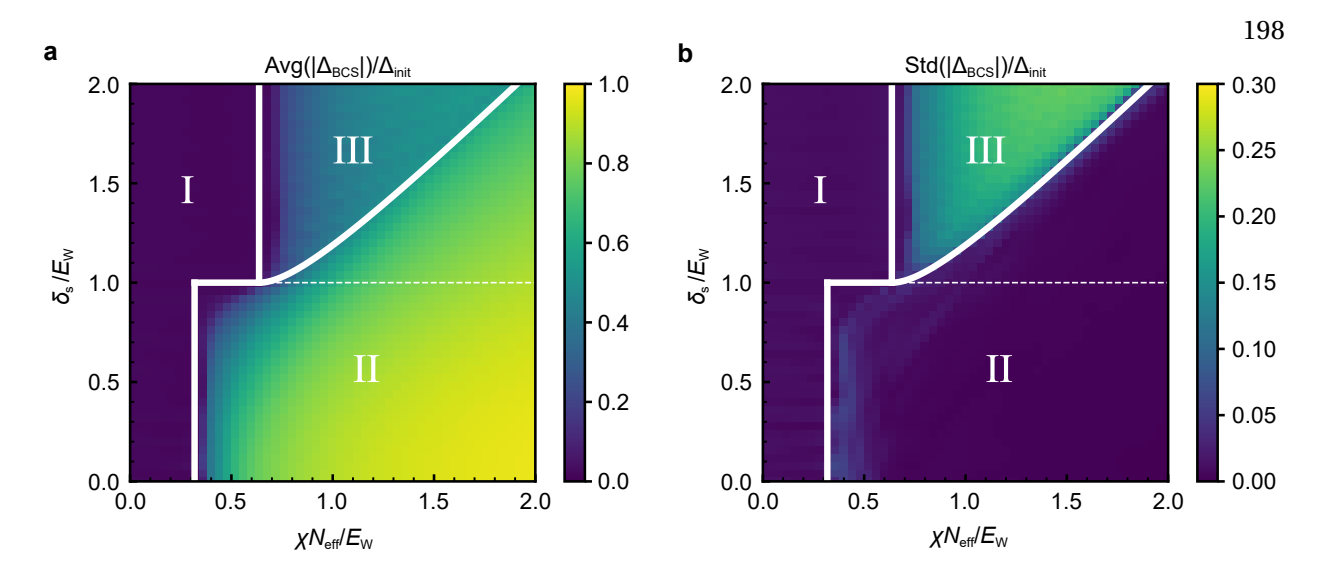


Figure 6.10: Numerical simulation of the dynamical phase diagram including inhomogeneous atom-light coupling. We identify the dynamical phases based on the long-time average (a) and the long-time standard deviation (b) of  $|\Delta_{BCS}(t)|$ , normalized by its initial value  $\Delta_{init} \equiv |\Delta_{BCS}(0)|$ . The white solid lines mark the corresponding dynamical phase boundaries, analytically derived from Eq. (6.6), which agree with the numerical results based on Eq. (6.8). The white dashed lines mark an extra dynamical phase transition that only exists for Eq. (6.6).

Hamiltonian:

$$\hat{H} = \hbar \chi \sum_{jk} \zeta_j \zeta_k \hat{s}_j^+ \hat{s}_k^- + \sum_k \varepsilon_k \hat{s}_k^z, \tag{6.8}$$

similar to Eq. (6.6) but with inhomogeneous atom-light coupling included in the interaction term. In contrast to the homogeneous coupling case, Eq. (6.8) is non-integrable. Nevertheless, as shown in Fig. 6.10, Eq. (6.8) leads to a similar dynamical phase diagram as Eq. (6.6) if we do the following:

- (1) Use a generalized superconducting order parameter  $\Delta_{BCS} = \chi \sum_k \zeta_k \langle \hat{s}_k^- \rangle$ ;
- (2) Interpret the  $\pi/2$ -pulse as a pulse along the cavity axis under the Hamiltonian  $\hat{H}_{\text{drive}} = \hbar \Omega \sum_k \zeta_k \hat{s}_k^y$  that generates the maximum possible  $|\Delta_{\text{BCS}}|$ , which occurs when  $\Omega t = 0.586\pi$ ;
- (3) Replace the atomic number N by an effective atom number  $N_{\rm eff} = N/2$ , such that  $\chi N_{\rm eff}$  represents the averaged interaction strength of Eq. (6.8).

We can still measure the generalized order parameter  $\Delta_{BCS}$  using the field leaking out of the cavity as in the previous section, since with inhomogeneous coupling the transmitted field takes the form

 $\alpha_{\rm out}(t) = -\frac{g}{\delta_c} \sqrt{\kappa_m} \sum_k \zeta_k \langle \hat{s}_k^-(t) \rangle \propto \Delta_{\rm BCS}$ . The dynamical phase diagram in Fig. 6.10 is numerically calculated based on unitary evolution under Eq. (6.8), with  $\chi N$  corresponding to the averaged interaction strength of Eq. (6.8). Since the inhomogeneous Hamiltonian does not admit a Lax vector analysis of the dynamical phases, we instead identify the theoretically predicted dynamical phase based on the long-time average of  $|\Delta_{\rm BCS}|$ , given by

$$\operatorname{Avg}(|\Delta_{\mathrm{BCS}}|) = \lim_{T \to \infty} \frac{1}{T} \int_{0}^{T} |\Delta_{\mathrm{BCS}}(t)| dt, \tag{6.9}$$

as well as the long-time oscillation amplitude of  $|\Delta_{BCS}|$ . Since the oscillations in  $|\Delta_{BCS}|$  might deviate from a sinusoidal form, for theoretical simulations it is easier to use the standard deviation as a measure of the oscillation amplitude:

$$Std(|\Delta_{BCS}|) = \left[\lim_{T \to \infty} \frac{1}{T} \int_{0}^{T} \left(|\Delta_{BCS}(t)| - Avg(|\Delta_{BCS}|)\right)^{2} dt\right]^{1/2}.$$
(6.10)

Using these definitions, the dynamical phases can be characterized in theoretical simulations by:

- Phase I: Avg( $|\Delta_{BCS}|$ ) = 0, Std( $|\Delta_{BCS}|$ ) = 0.
- Phase II:  $Avg(|\Delta_{BCS}|) > 0$ ,  $Std(|\Delta_{BCS}|) = 0$ .
- Phase III: Avg( $|\Delta_{BCS}|$ ) > 0, Std( $|\Delta_{BCS}|$ ) > 0.

In Fig. 6.10, we compare the results of these numerical order parameters (heat map) with the analytical phase boundaries derived from the homogeneously coupled system described by Eq. (6.6) (white solid lines), which were calculated using a Lax vector analysis similar to the one discussed in [405]<sup>[G]</sup>[55]. The two agree quite well, verifying that inhomogeneous coupling does not substantially change the predicted dynamical phases. The only difference is that Eq. (6.6) predicts an extra dynamical phase transition marked by the white dashed line, corresponding to phase IIIa in [405]. This demonstrates that in our system, we only expect to measure phase IIIb as a "true" phase III given the presence of inhomogeneous atom-light coupling.



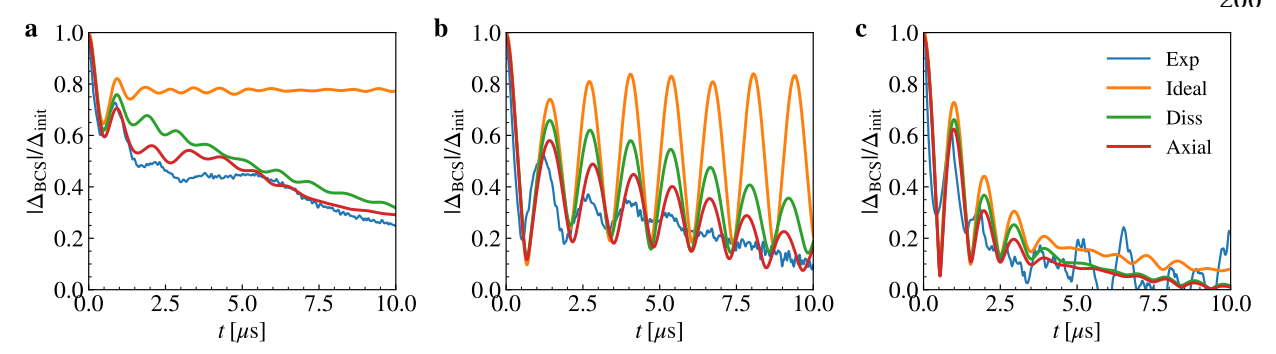


Figure 6.11: Introducing various experimental imperfections into numerical simulations. (a) Example phase II traces with  $\chi N/2\pi = 1.29$  MHz,  $f_{\rm AC}/2\pi = 1.1$  MHz. (b) Example phase III traces with  $\chi N/2\pi = 0.79$  MHz,  $f_{\rm AC}/2\pi = 1.1$  MHz. (c) Example phase I traces with  $\chi N/2\pi = 0.15$  MHz,  $f_{\rm AC}/2\pi = 1.1$  MHz. The blue points are experimental data, the orange lines represent numerical simulations under inhomogeneous atom-light coupling but no dissipation or axial motion (so-called "ideal" simulations), the green lines include dissipative processes on top of the ideal simulations, and the red lines consider both dissipative processes and axial motion effects.

## 6.10.2 Residual single-particle and collective emission

The system we are attempting to simulate is purely Hamiltonian in nature: we start with the ground state of an initial Hamiltonian and quench to a final Hamiltonian, then study the dynamics. In our actual system of strontium atoms coupled to an optical cavity, we also have single-particle spontaneous emission and collective emission, which both affect the system at longer times. This is in conflict with the definitions the three dynamical phases stated earlier in Sec. 6.3, which study the BCS gap at long times.

The solution, as stated in earlier sections analyzing experimental results, is to use properties of  $\Delta_{BCS}$  at intermediate times as a proxy for the long-time values. In fact, we do this both for experimental data and for the numerical simulations, which also include dissipation in the form of Lindbladian terms for single-particle emission and collective decay. Without these terms, numerical simulations deviate significantly from the experimental data as early as 2  $\mu$ s after the quench, particularly in phase II as shown in Fig. 6.11(a).

## 6.10.3 Exciting motional sidebands

Even with the inclusion of dissipation terms in the model, we still see substantial discrepancies between the experimental data and simulations. One such symptom we observe is a faster than expected decay of  $\Delta_{BCS}$  within the first couple of  $\mu$ s, followed by a stabilization of the value. Sometimes the traces also exhibit longer-lasting oscillations with a period of around 5-6  $\mu$ s. Additionally, both the Higgs-like oscillations in phase II and the more persistent oscillations in phase III are consistently smaller in experimental data as compared to numerical simulations. After some debate, we believe the most likely candidate responsible for such discrepancies is dephasing through coupling to different motional states along the cavity axis (often referred to here as "axial motion").

The proposed mechanism is as follows: although our atoms are trapped in the Lamb-Dicke regime (meaning that the spacing between motional levels is much bigger than the effective recoil energy from a 689 nm photon, as discussed in Ch. 3.5.2), a sufficiently large Rabi frequency  $\Omega$  satisfying  $\Omega\eta_{\rm eff}\gtrsim\omega_x$  (where  $\eta_{\rm eff}$  is the effective Lamb-Dicke parameter, and  $\omega_x$  is the trap frequency) can still drive sideband transitions since it cannot spectrally resolve the different motional states. Alternatively, a sufficiently short Rabi pulse will not notice the detuning between motional sidebands due to Fourier broadening and will coherent couple to the sidebands, albeit with a reduced Rabi rate  $\Omega\eta_{\rm eff}$ . Our initial drive in these datasets satisfies both of these conditions: the peak Rabi frequency is around  $\Omega/2\pi=2.5$  MHz (and  $\eta_{\rm eff}=\sqrt{0.11}\approx0.33$ , compared to a trap frequency of  $\omega_x/2\pi=165$  kHz), and the FWHM of the pulse power is around 100 ns, leading to a Fourier broadening of around 9 MHz. Therefore, we expect that some fraction of the atoms will be excited into motional levels. As a rough estimate, we expect the fraction of atoms exited into each of the  $\pm 1$  motional sidebands to be  $\sin\left(\eta_{\rm eff}\frac{\pi}{4}\right)^2\approx0.07$ , since the carrier experiences a  $\pi/2$  pulse. This is not entirely negligible.

Modeling the full motional degree of freedom is apparently difficult, and our theorist collaborator Anjun Chu does not simulate it fully. Instead, he studies the leading order effects by allowing atoms to occupy  $|n\rangle$ ,  $|n\pm1\rangle$  motional states given some starting state  $|n\rangle$ . The results of this simulation, shown as the red traces in Fig. 6.11, are the numerical simulations used to compare to the main experimental

results. They do appear to capture much of the remaining discrepancies, particularly in the phase II trace in panel (a). However, the simulations still overestimate the lifetime of oscillations in both phase II and phase III. It is still not entirely clear whether a full accounting of atomic motion will resolve this discrepancy or not.

#### 6.11 Conclusion

The demonstrated capability to emulate dynamical phases of superconductors in optical cavities opens exciting prospects for quantum simulation. For example, it may be possible to extend this experiment include probing beyond mean-field effects like the spectral form factor [422, 423] and enabling simulation of superfluidity in phenomena relevant to high energy physics [424, 425].

There are also potential avenues for furthering our exploration of BCS physics in our cavity QED system. As a first extension, we will explore rudimentary forms of pair-breaking in the next chapter (Ch. 7), which has strong connections to the technique of rf spectroscopy used in degenerate, fermionic atomic gases to probe for pairing physics. Looking forward, even though so far we have focused our efforts on simulating conventional s-wave superfluids or superconductors, it may also be possible to emulate elusive topologically non-trivial superfluid phases such as chiral p+ip [135] and  $d_{x^2-y^2}+id_{xy}$  superfluids. So far these exotic systems have not been seen in experiments, but research efforts for studying them have steadily grown in doped graphene and other novel materials [426–430], as well as in cuprates using magnetic impurities to mix in different pairing channels [431, 432]. It will be fascinating to see if our cavity simulator can, in the near term, engineer and probe these unconventional phases and even understand competing orders of s, p and d superconductivity in a single system, a long standing open question.

# 6.12 Additional information: comparison with systems featuring phase synchronization

Although physically distinct from this experiment, it is worth discussing a class of related systems studying phase synchronization between superradiantly emitting dipoles, which are predicted to exhibit qualitative features reminiscent of the three BCS dynamical phases discussed in this chapter. In one

theoretical proposal [41], two ensembles of spins are placed in a high-finesse optical cavity with a relative detuning  $\delta$  in their transition frequencies, mirroring the setup in our system. The main difference with our experiment is that the physics is purely dissipative, compared to purely Hamiltonian in our cases—their spins superradiantly emit into the cavity mode with a rate  $N\gamma_c$  (instead of spin-exchange interactions), a process that competes with an incoherent repumping rate w (instead of an applied disorder term in the Hamiltonian). In this modified setup, the Holland and Thompson groups identified three steady-state phases where the two ensembles either exhibit no quantum correlations, spontaneously synchronize their phases, or oscillate independently from each other with a random relative phase [41]. These phases are reminiscent of phases I, II, and III in the BCS model, and they are also sometimes referred to with this nomenclature [42]. Some key features of these dissipative versions of "phase I," "phase II," and "phase III" were observed in our group [47] [G]. Similar phase structures arising from phase synchronization physics also show up in studies of dipolar systems [43], as well as in hot beam superradiance proposals [46], where new atoms continuously enter the cavity and synchronize via collective dissipation through the cavity field.

Despite the analogies between these systems and our setup, the underlying physics responsible for the predicted phases possesses key differences that should not be overlooked. First and foremost, the phases predicted in the systems outlined above are all driven-dissipative steady states, stabilized by the removal of entropy through the presence of an incoherent pump establishing population inversion. In contrast, the BCS dynamical phases explored in this chapter represent pure Hamiltonian dynamics of an excited state (not necessarily a steady state), and no entropy is ever removed from the system. As such, the post-quench dynamics and thus the phase diagram depend strongly on the initial state of the system before the quench. In particular, if we initialized our system with  $\langle \hat{S}^- \rangle = 0$ , say by optically pumping the atoms into the excited state, no quench parametrized by our three control parameters  $\chi N$ ,  $\delta_s$ , and  $E_W$  will ever cause the system to spontaneously develop phase coherence—hence, the entire phase diagram is phase I. But such a formation of phase coherence from nothing is exactly the sort of physics described by phase synchronization. As an example, the hot beam superradiance proposal [46] also optically pumps all atoms into the excited state, but in this case coherence spontaneously forms through

a self-seeding of superradiance. Subsequent atoms entering the cavity then synchronize with the rest of the ensemble despite possessing zero initial coherence. Further, experiments in our group have shown that superradiantly emitting atoms can forget their initial phase by synchronizing with an applied drive through injection locking [433]<sup>[G]</sup> or with a second ensemble of atoms possessing an initial phase difference that subsequently drops to zero [47]<sup>[G]</sup>. Such demonstrations show an independence of initial conditions that is only possible through entropy removal, and they reflect a fundamental difference between open quantum systems and the type of unitary dynamics studied in this chapter.

Beyond the difference in dynamical regimes, the control parameters in our system and those used in [41] serve different roles, making it difficult to interpret the connection between the two phase diagrams rigorously. In particular, the applied disorder  $E_{\rm W}$  in single-particle transition frequencies used in our experiment has quite different effects from the incoherent repump w in [41]. The former constitutes a  $T_2^*$  dephasing process with a Gaussian envelope in time, leaving the average spin excitation  $\langle \hat{S}^z \rangle$  unchanged. In contrast, the incoherent pump is a  $T_1$  type dephasing process, which is exponential in time, and it causes  $\langle \hat{S}^z \rangle$  to increase towards N/2 (all atoms in the excited state). These distinctions alter the system in ways that fundamentally affect the BCS dynamical phases studied here: our spin-exchange interactions can only gap protect against dephasing with a frequency scale smaller than the interaction rate  $\chi N$ , so the experiment would not work if we replaced  $E_{\rm W}$  with a white dephasing process (i.e., where fluctuations in the transition frequency exhibit a flat power spectrum) like an incoherent pump or spontaneous emission. Moreover, the pump plays a dual role in the driven-dissipative systems by changing both the phase coherence of the ensemble and the state populations. The population changes in particular appear to play a large role in predictions of chaotic dynamics near the phase II to phase III boundary in the driven-dissipative systems [42]. No such chaotic dynamics is predicted or observed in our experiment, an important qualitative difference in the phase diagrams. Due to these differences, one should be careful when drawing parallels between phase synchronization and the physics of many-body gap protection. To close, it might be of interest to consider regimes in which the two processes are simultaneously present and understand the interplay between the physics of Hamiltonian gap protection and the physics of synchronization via dissipation, both in two-level systems and in large multilevel systems

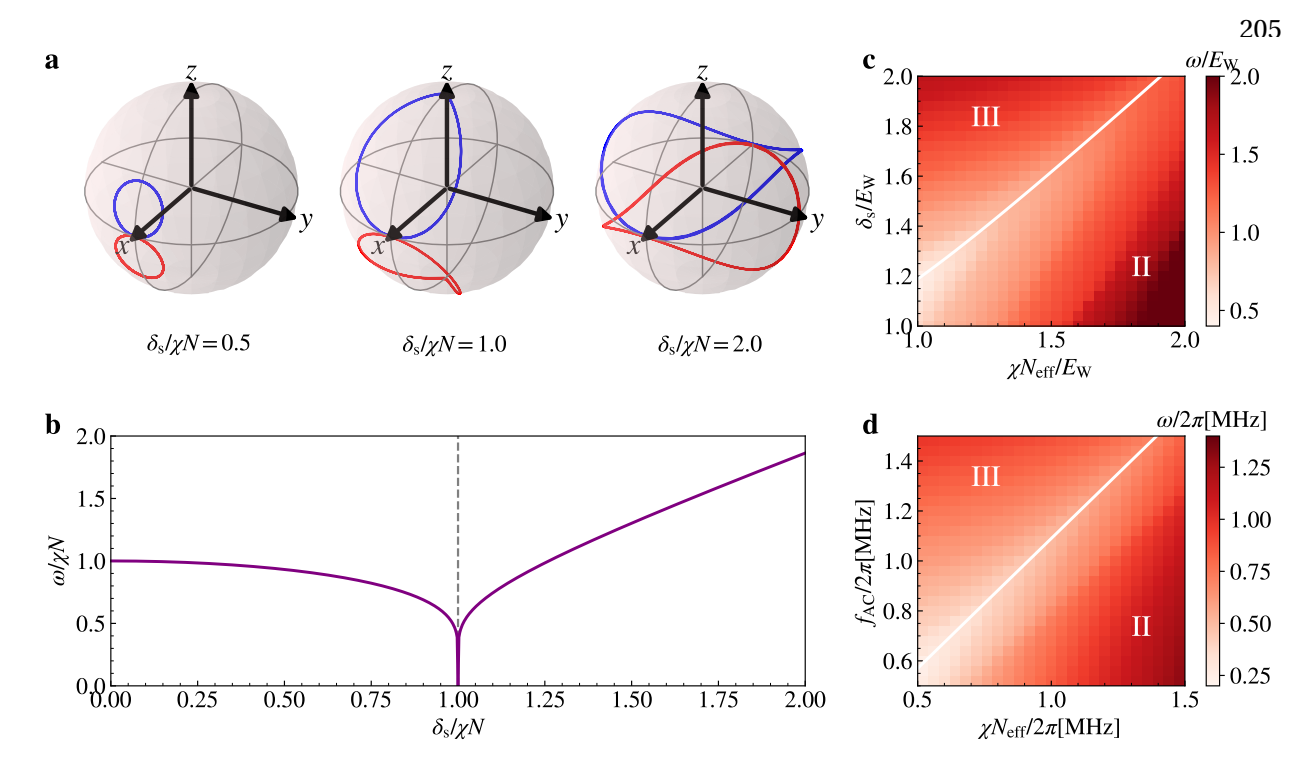


Figure 6.12: Frequency dip as a signature of the phase II to phase III transition. (a) Mean field trajectories of the two large spin model evolving under Eq. (6.11). From left to right, Bloch spheres display trajectories with  $\delta_s/(\chi N)=0.5,1$ , and 2 respectively. (b) Oscillation frequency of  $|\Delta_{BCS}|$  in the two-spin BCS model Eq. (6.11) as a function of  $\delta_s/\chi N$ . The frequency dip at  $\delta_s/\chi N=1$  marks the dynamical phase transition point. (c) Short-time frequency  $\omega$  of the dynamics under inhomogneous atom-light coupling (see Eq. (6.8)). The white line marks the phase II to phase III transition, the same boundary as shown in Fig. 6.10. (d) Short-time frequency  $\omega$  of the dynamics using experimental control parameters. The white line marks the phase II to phase III transition. The frequency dips match the dynamical critical points for both cases.

such as 87 Sr.

# 6.13 Additional information: understanding the phase II to phase III frequency dip

Earlier, we discussed a way to understand the phase II to phase III transition by visualizing the two atomic ensembles as two large spins. Here, we push on this analogy by briefly studying a model with two literal large spins, split by  $\delta_s$ :

$$\hat{H}/\hbar = \chi \hat{S}^{+} \hat{S}^{-} + \frac{\delta_{s}}{2} \hat{S}_{1}^{z} - \frac{\delta_{s}}{2} \hat{S}_{2}^{z}, \tag{6.11}$$

where  $\hat{S}^{\pm} = \hat{S}_1^{\pm} + \hat{S}_2^{\pm}$ . As shown in numerical simulations in Fig. 6.12, this simple model captures the observed dip in oscillation frequencies as  $\delta_s$  nears  $\chi N$  (panel (b)), and moreover this dip coincides with

the analytically predicted dynamical phase transition (panels (c)-(d)).

Given this analogy, we can build intuition about the mechanism behind this frequency dip using the two-spin model. Fig. 6.12(a) shows mean-field trajectories of the two spins on the collective Bloch sphere. Instantaneously, we can understand the trajectories as precession of the Bloch vectors about a fictitious magnetic field (as in Sec. 2.3.1), composed of a  $\hat{z}$ -component equal to  $\pm \delta_s/2$  and an  $\hat{x}$ -component equal to  $\pm \delta_s/2$  and an  $\pm \delta_s/2$  and an  $\pm \delta_s/2$  and an equal to  $\pm \delta_s/2$ . Above the phase transition, since  $\pm \delta_s/2$  are components of the magnetic fields dominate, causing the Bloch vector trajectories to travel around the poles and accrue an unbounded relative phase. The varying size of  $\pm \delta_s/2$  during the trajectory self-consistently turns the trajectories into the Pringle-shaped paths shown in the figure. Below the transition, the opposite regime holds:  $\pm \delta_s/2$  so the magnetic field points closer to the equator than the poles. As a result, the Bloch vector trajectories remain close to the equator and form snowman-like orbits. Here, unlike above the transition, the total  $\pm \delta_s/2$  stays large since the two spins do not accrue a large relative phase and instead stay tightly locked close to their initial condition point. This is the underlying mean-field dynamics behind the many-body gap protection induced by spin-exchange interactions.

The frequency dip at  $\delta_s = \chi N$  can be intuitively explained by a dynamical slowdown of the Bloch vector trajectories as they approach the poles of the Bloch sphere. At initial times, the fictitious magnetic field points somewhere between the equator and the poles, and the Bloch vectors are deflected off the equator as a result. As this dynamics progresses, and the distance from the poles decreases,  $\langle \hat{S}_i^- \rangle$  also decreases, and the magnetic field also moves towards pointing along the pole. Unlike above the transition, where the trajectories deflect off the equator into Pringle shapes but ultimately rotate around the Bloch sphere, at the transition the trajectories will exactly hit the poles, sending  $\langle \hat{S}_i^- \rangle$  to zero. Instantaneously, the dynamics still looks like Larmor precession around the fictitious magnetic field, with a minimum Rabi frequency equal to  $\delta_s/2$  at the pole. However, the radius of this orbit around the field axis also decreases, so the absolute distance traversed on the Bloch sphere per unit time slows down, leading to an increasing period time (and decreasing frequency) for the full oscillation. In this idealized model, the trajectory speed slows all the way to zero as the Bloch vectors approach the poles, leading to an oscillation frequency of zero. For our dirtier system, we only see a partial slowdown at the transition point.

Still, the essential physics is as described here.

# 6.14 Additional information: intensity distributions for Gaussian beams on Gaussian atomic clouds

#### 6.14.1 1D system, centered

Assume a cloud of atoms are Gaussian-distributed with standard deviation  $\sigma$  along the cavity axis (call this direction x). We will shine a Gaussian beam with waist w transversely at the cloud of atoms, such that the beam is centered on the atomic cloud. What distribution of intensities does the atomic ensemble experience?

The atom distribution and intensity vs. *x* are both given by:

$$P_x(x) = \frac{1}{\sqrt{2\pi\sigma^2}} e^{-\frac{x^2}{2\sigma^2}}$$

$$I(x) = I_0 e^{-\frac{2x^2}{w^2}}.$$
(6.12)

In order to get a distribution function  $P_I(I)$ , we might imagine making a differential comparison of the form  $P_I(I)dI = P_x(x)dx$ , implying  $P_I(I) = P_x(x)|\frac{dx}{dI}|$ . The main problem with this is that x(I) is not a well-defined function: in general there are two values of x which satisfy a given I. The solution is to define two branch functions

$$x_{\pm}(I) := \pm \frac{w}{\sqrt{2}} \sqrt{\ln\left(\frac{I_0}{I}\right)},\tag{6.13}$$

such that

$$P_{I}(I) = P_{X}(x_{+}(I)) \left| \frac{dx_{+}}{dI} \right| + P_{X}(x_{-}(I)) \left| \frac{dx_{-}}{dI} \right|$$

$$= \frac{2}{\sqrt{2\pi\sigma^{2}}} e^{-\frac{w^{2} \ln(I_{0}/I)}{4\sigma^{2}}} \times \frac{w}{2\sqrt{2}} \left( \ln\left(\frac{I_{0}}{I}\right) \right)^{-1/2} \frac{1}{I}$$

$$= \frac{1}{I_{0}\sqrt{\pi}} \left( \frac{w}{2\sigma} \right) \left( \frac{I}{I_{0}} \right)^{(\frac{w}{2\sigma})^{2} - 1} \left( \ln\left(\frac{I_{0}}{I}\right) \right)^{-1/2},$$
(6.14)

where we restrict  $I \in (0, I_0)$ .

#### 6.14.2 2D system, centered

Let us extend this model into two-dimensions, allowing for different-sized waists w and atomic extents  $\sigma$  in the two directions x and z. Our distributions will look like

$$P_{\vec{x}}(\vec{x}) = \frac{1}{2\pi\sigma_x \sigma_z} e^{-\frac{x^2}{2\sigma_x^2}} e^{-\frac{z^2}{2\sigma_z^2}}$$

$$I(\vec{x}) = I_0 e^{-\frac{2x^2}{w_x^2}} e^{-\frac{2z^2}{w_z^2}}.$$
(6.15)

Inverting the function I(x, z) like in the previous section seems out of reach now that it is a function of two variables. It turns out we can still progress if we can find a parametrization of  $\mathbb{R}^2$  in terms of I and some auxiliary parameter u. Then, we can apply the following prescription to solve for  $P_I(I)$ :

$$P_{I}(I)dIdu = P_{\vec{x}}(\vec{x})dxdz$$

$$P_{I}(I)dIdu = P_{\vec{x}}(\vec{x}(I,u))|J_{\vec{x}}(I,u)|dIdu$$

$$P_{I}(I) = \int_{u} P_{\vec{x}}(\vec{x}(I,u))|J_{\vec{x}}(I,u)|du,$$
(6.16)

where here I define the Jacobian  $J_{\vec{f}}(\vec{u})$  to be the matrix with (i,j)th element equal to  $\partial_{u_j} f_i$ .

In this particular system, we can define transformed polar coordinates to parametrize the space in terms of I and an "angle" u. Start by defining unitless coordinates  $\xi, \zeta = \frac{x}{w_x/2}, \frac{z}{w_z/2}$ . Then we can define a radius  $\rho^2 = \xi^2 + \zeta^2$ , such that  $\xi = \rho \cos(u)$ ,  $\zeta = \rho \sin(u)$  defines the variable u. In these variables, the intensity becomes

$$I(\rho) = I_0 e^{-\rho^2/2}. (6.17)$$

We can now rewrite x, z as functions of I, u:

$$x(I, u) = \frac{w_x}{2} \xi(I, u) = \frac{w_x}{2} \rho(I) \cos(u)$$

$$z(I, u) = \frac{w_z}{2} \zeta(I, u) = \frac{w_z}{2} \rho(I) \sin(u).$$
(6.18)

It follows that the Jacobian defined previously has the determinant

$$|J_{\vec{x}}(I,u)| = \left| \frac{\partial x}{\partial I} \frac{\partial z}{\partial u} - \frac{\partial x}{\partial u} \frac{\partial z}{\partial I} \right|$$

$$= \frac{w_x w_z}{4} \left| \rho(I) \rho'(I) \right|$$

$$= \frac{w_x w_z}{4} \left| \frac{d(\rho^2(I)/2)}{dI} \right|$$

$$= \frac{w_x w_z}{4} \left| \frac{d(\ln(I_0/I))}{dI} \right| = \frac{w_x w_z}{4} \frac{1}{I}.$$
(6.19)

Finally, we can solve for the probability distribution, defining unitless parameters  $\alpha_x \coloneqq \frac{w_x}{2\sigma_x}$ ,  $\alpha_z \coloneqq \frac{w_z}{2\sigma_z}$  for succinctness:

$$P_{I}(I) = \int_{u} \left( \frac{1}{2\pi\sigma_{x}\sigma_{z}} e^{-\frac{x^{2}}{2\sigma_{x}^{2}}} e^{-\frac{z^{2}}{2\sigma_{z}^{2}}} \right) \times \left( \frac{w_{x}w_{z}}{4} \frac{1}{I} \right) du$$

$$= \frac{\alpha_{x}\alpha_{z}}{2\pi I} \int_{0}^{2\pi} e^{-\frac{\rho^{2}}{2}(\alpha_{x}^{2}\cos^{2}u + \alpha_{z}^{2}\sin^{2}u)} du$$

$$= \frac{\alpha_{x}\alpha_{z}}{2\pi I_{0}} \int_{0}^{2\pi} \left( \frac{I}{I_{0}} \right)^{(\alpha_{x}^{2}\cos^{2}u + \alpha_{z}^{2}\sin^{2}u) - 1} du.$$
(6.20)

Using the integral formula for the Bessel  $\mathcal{I}$  -function:

$$\int_0^{2\pi} e^{x\cos\theta} d\theta = 2\pi I_0(x),\tag{6.21}$$

we can simplify the above to

$$P_{I}(I) = \frac{\alpha_{x}\alpha_{z}}{2\pi I} \int_{0}^{2\pi} e^{-\frac{\rho^{2}}{2} \left(\frac{\alpha_{x}^{2} + \alpha_{z}^{2}}{2} + \frac{\alpha_{x}^{2} - \alpha_{z}^{2}}{2} \cos 2u\right)} du$$

$$= \frac{\alpha_{x}\alpha_{z}}{2\pi I} e^{-\frac{\rho^{2}}{2} \left(\frac{\alpha_{x}^{2} + \alpha_{z}^{2}}{2}\right)} \int_{0}^{2\pi} e^{-\frac{\rho^{2}}{2} \left(\frac{\alpha_{x}^{2} - \alpha_{z}^{2}}{2} \cos v\right)} dv$$

$$= \frac{\alpha_{x}\alpha_{z}}{I_{0}} \left(\frac{I}{I_{0}}\right)^{\frac{\alpha_{x}^{2} + \alpha_{z}^{2}}{2} - 1} I_{0} \left(\frac{\alpha_{x}^{2} - \alpha_{z}^{2}}{2} \ln \left(\frac{I}{I_{0}}\right)\right). \tag{6.22}$$

We can confirm that this expression agrees with the one-dimensional case by taking  $w_z \to \infty$   $(\alpha_z \to \infty)$ . Since the Bessel I-functions satisfy  $I_m(z) \xrightarrow{z \to \infty} \frac{1}{\sqrt{2\pi z}} e^z$  and  $I_0$  is an even function, we obtain

$$P_{I}(I) \xrightarrow{\alpha_{z} \to \infty} \frac{\alpha_{x}}{I_{0}} \left(\frac{I}{I_{0}}\right)^{\alpha_{x}^{2}/2 - 1} \lim_{\alpha_{z} \to \infty} \left[\alpha_{z} \left(\frac{I}{I_{0}}\right)^{\alpha_{z}^{2}/2} I_{0} \left(\frac{\alpha_{x}^{2} - \alpha_{z}^{2}}{2} \ln\left(\frac{I}{I_{0}}\right)\right)\right]$$

$$= \frac{\alpha_{x}}{I_{0}} \left(\frac{I}{I_{0}}\right)^{\alpha_{x}^{2}/2 - 1} \lim_{\alpha_{z} \to \infty} \left[\alpha_{z} \frac{1}{\sqrt{\pi(\alpha_{z}^{2} - \alpha_{x}^{2})}} \left(\frac{I}{I_{0}}\right)^{\alpha_{z}^{2}/2} \left(\frac{I}{I_{0}}\right)^{(\alpha_{x}^{2} - \alpha_{z}^{2})/2} \left(\ln\left(\frac{I_{0}}{I}\right)\right)^{-1/2}\right]$$

$$= \frac{\alpha_{x}}{I_{0}\sqrt{\pi}} \left(\frac{I}{I_{0}}\right)^{\alpha_{x}^{2} - 1} \left(\ln\left(\frac{I_{0}}{I}\right)\right)^{-1/2} = P_{I}(I)\Big|_{1D}.$$
(6.23)

If instead we had  $\alpha_x = \alpha_z := \alpha$  (that is, the Gaussian beam has the same ellipticity as the atomic cloud, just scaled larger or smaller), then the expression simplifies to the particularly concise

$$P_I(I) = \frac{\alpha^2}{I_0} \left(\frac{I}{I_0}\right)^{\alpha^2 - 1}.$$
 (6.24)

#### 6.14.3 Displacing the Gaussian beam from center

Now, we will allow the beam to shine on the atoms with some displacement  $x_0$  from center along the cavity axis (we will still assume the beam is centered vertically for simplicity). In the one-dimensional system, we can essentially replace  $x_{\pm}(I)$  with

$$x_{\pm}(I) := x_0 \pm \frac{w}{\sqrt{2}} \sqrt{\ln\left(\frac{I_0}{I}\right)}.$$
 (6.25)

This relation returns mostly the same probability distribution  $P_I(I)$  with a couple modifications:

$$P_{I}(I) = P_{x}(x_{+}(I)) \left| \frac{dx_{+}}{dI} \right| + P_{x}(x_{-}(I)) \left| \frac{dx_{-}}{dI} \right|$$

$$= \frac{\alpha}{I_{0}\sqrt{\pi}} \left( \frac{I}{I_{0}} \right)^{\alpha^{2}-1} \left( \ln \left( \frac{I_{0}}{I} \right) \right)^{-1/2} \times \left[ e^{-x_{0}^{2}/(2\sigma^{2})} \cosh \left( \frac{wx_{0}}{\sigma^{2}\sqrt{2}} \sqrt{\ln \left( \frac{I_{0}}{I} \right)} \right) \right]$$
(6.26)

We can derive a similar expression in the 2D case. Defining  $\xi_0 \coloneqq \frac{x_0}{w_x/2}$ , we obtain:

$$P_I(I)\Big|_{2D} = \frac{\alpha_x \alpha_z}{2\pi I} e^{-\alpha_x^2 \xi_0^2 / 2} \int_0^{2\pi} e^{-\frac{\rho^2}{2} (\alpha_x^2 \cos^2 u + \alpha_z^2 \sin^2 u)} e^{\alpha_x^2 (\rho \cos u) \xi_0} du$$
 (6.27)

Unfortunately, I couldn't find a closed-form expression for this case in general. However, we can simplify the calculation somewhat by using the Jacobi-Anger expansion:

$$e^{iz\cos\theta} = \sum_{n=-\infty}^{\infty} i^n \mathcal{J}_n(z) e^{in\theta},$$
(6.28)

which in turn implies

$$e^{z\cos\theta} = \sum_{n=-\infty}^{\infty} I_n(z)e^{in\theta}.$$
 (6.29)

The above integral takes the form

$$\int_0^{2\pi} e^{A\cos 2u + B\cos u + C} du, \quad \text{where} \qquad A = -\frac{\rho^2}{2} \frac{\alpha_x^2 - \alpha_z^2}{2}, \quad B = \rho \xi_0 \alpha_x^2, \quad C = -\frac{\rho^2}{2} \frac{\alpha_x^2 + \alpha_z^2}{2}. \tag{6.30}$$

We plug in expansions for the two sinusoidal terms to obtain

$$e^{C} \sum_{m,n=-\infty}^{\infty} \left( I_{m}(A) I_{n}(B) \int_{0}^{2\pi} e^{2im\theta} e^{in\theta} du \right)$$

$$= 2\pi e^{C} \sum_{m=-\infty}^{\infty} I_{m}(A) I_{-2m}(B) = 2\pi e^{C} \sum_{m=-\infty}^{\infty} I_{m}(A) I_{2m}(B),$$
(6.31)

since  $I_{2m}$  are even functions. From this, we can obtain an alternate form for the 2D probability distribution:

$$P_{I}(I)\Big|_{2D} = \frac{\alpha_{x}\alpha_{z}}{I} e^{-\alpha_{x}^{2}\xi_{0}^{2}/2} e^{C} \sum_{m=-\infty}^{\infty} I_{m}(A) I_{2m}(B)$$

$$= \frac{\alpha_{x}\alpha_{z}}{I_{0}} \left(\frac{I}{I_{0}}\right)^{\frac{\alpha_{x}^{2}+\alpha_{z}^{2}}{2}-1} e^{-\alpha_{x}^{2}\xi_{0}^{2}/2} \sum_{m=-\infty}^{\infty} I_{m} \left(\frac{\alpha_{x}^{2}-\alpha_{z}^{2}}{2} \ln\left(\frac{I}{I_{0}}\right)\right) I_{2m} \left(\alpha_{x}^{2}\xi_{0}\sqrt{2\ln\left(\frac{I_{0}}{I}\right)}\right)$$

$$= \left[\frac{\alpha_{x}\alpha_{z}}{I_{0}} \left(\frac{I}{I_{0}}\right)^{\frac{\alpha_{x}^{2}+\alpha_{z}^{2}}{2}-1} e^{-\alpha_{0}^{2}I(2\sigma_{x}^{2})} \sum_{m=-\infty}^{\infty} I_{m} \left(\frac{\alpha_{x}^{2}-\alpha_{z}^{2}}{2} \ln\left(\frac{I}{I_{0}}\right)\right) I_{2m} \left(\frac{w_{x}x_{0}}{\sigma_{x}^{2}\sqrt{2}}\sqrt{\ln\left(\frac{I_{0}}{I}\right)}\right)\right].$$
(6.32)

We see that when  $x_0 \to 0$ , all terms in the sum except for m = 0 vanish, and we recover the original 2D distribution derived earlier. This sum is numerically easier to compute than a full integral, especially since in many cases only a few of the terms contribute to the sum.

#### Chapter 7

Time-resolved spectral gap spectroscopy in a quantum simulator of fermionic superfluidity inside an optical cavity

#### 7.1 Introduction

The simplified form of the BCS model studied in Ch. 6 assumes that fermions with opposite momenta  $\pm k$  can only ever exist in configurations of both occupied (a Cooper pair) or both not occupied (no Cooper pair). So-called "pair-broken terms" with only one of the two momentum states occupied are neglected, since their presence increases the energy of the system in the ideal reduced BCS Hamiltonian at zero temperature. Real systems, however, contain pair-breaking processes which modify the system behavior. Understanding this physics requires moving beyond the paradigm of the Anderson pseudospin mapping discussed previously and into a more complex description.

To that end, ultracold atomic systems have emerged as a promising platform for simulating complex theories of quantum many-body physics, using clean and tunable interactions of many forms [10–16] which could potentially enable a better understanding of the underlying mechanisms. An additional advantage lies in the complex internal structure of cold atoms, which have multiple ground and excited states and can lie beyond the paradigm of a traditional qubit. Such multilevel systems open up an even broader class of models and physical systems for study [15, 92, 198, 434–442].

An example that directly relevant to the BCS model is the development of ultracold Fermi gases using neutral atoms. Such experiments have enabled groundbreaking studies of the phenomenon of fermionic superfluidity, including a first realization of the BCS-BEC crossover [155, 399, 414, 415], and have provided insight into a broad range of many-body systems [396, 443]. To probe the superfluid pair-

ing gap, early experiments relied on a "radio-frequency (rf) spectroscopy" technique, which involved weakly driving a mixture of two spin states along an rf transition to a (nominally non-interacting) third state [147–149]. This additional degree of freedom allowed researchers to observe an energy shift related to breaking Cooper pairs [146]. While this technique has been used for many purposes [150], undesired effects, such as competing pair-breaking processes and unwanted interactions between the third state and the other two states, complicated efforts to analyze the pairing gap [151–153]. Additionally, the predicted shift, sometimes called the spectral gap  $\Delta_{SG}$ , [154], depends nontrivially on the chemical potentials of the component spin states and is not equivalent to the pairing gap  $\Delta_{BCS}$  [146, 155].

Inspired by this context, in the experiment described in this chapter [145]<sup>[G]</sup> we extend our study of the BCS model from Ch.6 by leveraging multiple internal levels of <sup>88</sup>Sr atoms. We start with implementing the so-called Anderson pseudospin mapping [143], mapping the presence and absence of a Cooper pair onto a long-lived electronic transition. The atoms, which are collectively coupled to a detuned optical cavity, experience an effective all-to-all interaction [95]<sup>[G]</sup> which emulates the attractive and collective interaction between electrons in different momentum states in a superconductor. With this setup, we previously studied the BCS Hamiltonian and observed dynamical phases in the pairing gap  $\Delta_{BCS}$  [126]<sup>[G]</sup>. By coupling to a third atomic state, we can mimic the setup of rf spectroscopy experiments and measure  $\Delta_{SG}$ .

At a high level, we construct an appropriate three-level system using an applied magnetic field to couple excited Zeeman states. By tuning the magnetic field strength, we explore this coupling both in a gapped regime and in a strong-coupling regime featuring large population transfer between states. Moreover, by varying the atomic inversion along the initial two-level system, we change both the number of particles participating in the pairing as well the pairing strength, allowing us to explore the distinction between  $\Delta_{SG}$  and  $\Delta_{BCS}$ . We accomplish all this through the use of two real-time probes, including a novel nondestructive, large dynamic range measurement of the cavity resonance frequency.

The experiment described in this chapter has worn many hats between its conception and eventual completion. At first, we thought it would be a "stepping stone" experiment on the road towards simulating BCS dynamical phases, since the experiment does not require modifying the single-particle energy distribution and thus was technically easier to perform. Later on, we discovered that the system was interesting in its own right, with connections to donor-acceptor models of light-harvesting complexes in photosynthetic organisms, systems whose underlying mechanisms are still poorly understood [444–446]. Finally, we settled on our current interpretation as an extension of the BCS model and an analogy to RF spectroscopy in ultracold Fermi gases.

# 7.2 Mapping RF spectroscopy onto a three-level ensemble

While the idea of modeling multilevel degenerate fermions with multilevel atoms coupled to a cavity seems intuitively reasonable, the precise mapping is a bit subtle. To tease out the details, we will first model the physical setup of the original RF spectroscopy experiments. Then, we will explore precisely how the two systems map onto each other.

The original degenerate Fermi gases in ultracold atomic platforms were performed using one of two isotopes:  $^{40}$ K [147, 149, 399] and  $^{6}$ Li [148, 415], the only two naturally-occuring fermionic isotopes that are also alkali atoms. Both have fine and hyperfine structure in the ground state, leading to a rich manifold of states to work with. To mimic the spin-1/2 nature of electrons, researchers in these experiments would prepare the atoms in a mixture of the two lowest energy states in the manifold. We will refer to these states as  $|1\rangle$  and  $|2\rangle$ , following the convention used in  $^{6}$ Li experiments. For more information on specific atomic properties, line data is available for  $^{6}$ Li [447] and  $^{40}$ K [448] in the style of Dan Steck's rubidium sheet.

Compared to electrons, which rely on Coulomb forces to generate strong interactions, neutral atoms tend to have lower scattering lengths (i.e., weaker interactions) by default. However, tuning a bias magnetic field close to special features called **Feshbach resonances** greatly enhance the scattering length [449]. Feshbach resonances occur at magnetic fields where the unbound atoms come onto resonance with a weakly-bound molecular state. These two configurations are generally weakly coupled

 $<sup>^{1}</sup>$  GLi experiments tend to number their ground states from 1 to 6 in order of increasing energy [447]. I suspect this is because the fine-structure splitting is quite small, such that at small fields the system is in a weak-field Zeeman limit, but at the large ( $\approx$  850 G) magnetic field necessary to reach the Feshbach resonance, the system is in the strong-field Zeeman limit. This means it would be insufficient to describe the states only as a hyperfine  $|m_F\rangle$  state or only as a fully-split  $|m_I,m_I\rangle$  state.

due to some details of the atomic physics, causing the system to oscillate between bound and unbound configurations (on resonance) or for the unbound state to be dressed by the weakly bound state (off resonance). By ramping through the resonance, you can adabiatically transfer the atoms into bound states; this is a standard technique used to form bialkali molecules such as KRb, NaK, and NaCs (followed by a STIRAP pulse to convert molecules from the excited Feshbach state into the ground state) [450, 451]. For these experiments, researchers tune close to a Feshbach resonance for the two spin states in the prepared mixture, which increases the s-wave scattering length in interactions between the two spin states. The scattering length obeys a universal reciprocal-like scaling about the Feshbach resonance, such that it is positive on one side of the resonance and negative on the other. Operating on the negative side of the resonance generates tunable, attractive interactions between atoms in  $|1\rangle$  and  $|2\rangle$  states, meeting the necessary condition to observe s-wave BCS physics.

The technique of RF spectroscopy aims to measure whether or not this strongly interacting spin mixture exhibits Cooper pairing. To do so, we can apply a radio-frequency (RF) drive between one of the two interacting states, such as  $|2\rangle$ , into a third state which we will call  $|3\rangle$ . Since Feshbach resonances are state-dependent, we will assume that the interaction rate between  $|3\rangle$  and the other states is negligible compared to the  $|1\rangle$  to  $|2\rangle$  interaction, making  $|3\rangle$  effectively noninteracting. Fig. 7.1(a) shows a cartoon providing basic intuition for the role of this drive: if the atoms have condensed into Cooper pairs with momentum and spin states of the form  $|k,1\rangle$  and  $|-k,2\rangle$ , then driving an atom into  $|k,3\rangle^2$  will destroy a Cooper pair. This carries an energy cost, as described in 6.2; therefore, the photon should require extra energy in order to drive the transition. The result is that a spectroscopic scan of the RF transition should reveal a frequency shift in the presence of Cooper pairs, relative to a noninteracting system. For the context of this work, we will call this frequency shift **the spectral gap**  $\Delta_{SG}$ .

We can connect this situation with an ensemble of three-level systems using a mapping similar to the Anderson pseudospin mapping discussed in Sec. 6.2. We will model the degenerate Fermi gas with

<sup>&</sup>lt;sup>2</sup> We will assume that the recoil momentum of an RF photon is negligible. For scale, an 80 MHz RF photon will impart a recoil velocity around 1-10 nm/s, depending on the mass of the atom.

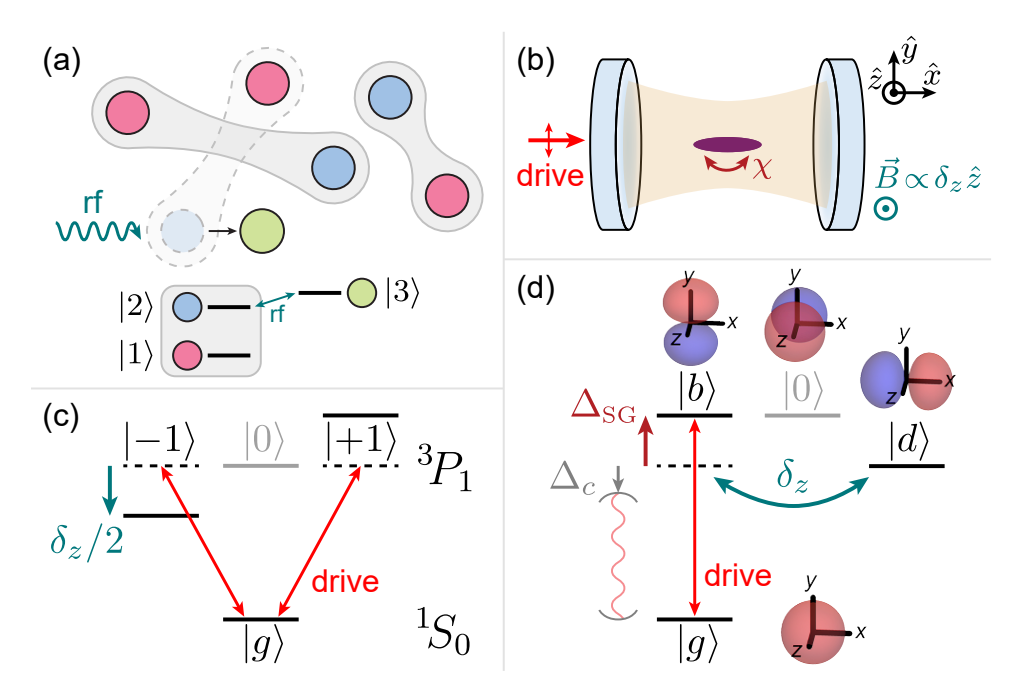


Figure 7.1: Simulating RF spectroscopy with an ensemble of three-level systems. (a) The technique of "rf spectroscopy" used in ultracold fermion experiments measures a frequency shift, associated with breaking a Cooper pair, along an auxiliary transition. (b) In our system, <sup>88</sup>Sr atoms experience an effective infinite-range spin-exchange interaction through detuned collective coupling to an optical cavity, oriented along  $\hat{x}$ . We apply a tunable magnetic field along  $\hat{z}$  and address the atoms with a  $\hat{y}$ -polarized laser drive. (c) We explore a three-level system consisting of  $|g\rangle = |{}^1S_0\rangle$  and  $|\pm 1\rangle = |{}^3P_1, m_j = \pm 1\rangle$ . We define  $\delta_z$  as the splitting between  $|\pm 1\rangle$  states. (d) The drive and cavity couple to the effective two-level system  $|g\rangle \leftrightarrow |b\rangle$ . In this basis,  $\delta_z$  couples  $|b\rangle$  to a third state  $|d\rangle$ , analogous to the level structure used in rf spectroscopy experiments. The cavity is detuned from the atomic transition by  $\Delta_c = \omega_{c0} - \omega_a$ ; this generates a collective shift  $\Delta_{SG}$  of  $|b\rangle$ , representing the spectral gap. Toy models of the atomic orbitals are shown to highlight the different polarizations required to address the excited states.

an RF drive using the following Hamiltonian:

$$\hat{H}/\hbar = \sum_{\mathbf{k},\sigma \in \{1,2,3\}} \frac{\varepsilon_{\mathbf{k}}}{2} \hat{c}_{\mathbf{k},\sigma}^{\dagger} \hat{c}_{\mathbf{k},\sigma} - \chi \sum_{\mathbf{k}\mathbf{k}'} \hat{c}_{\mathbf{k}',2}^{\dagger} \hat{c}_{-\mathbf{k}',1}^{\dagger} \hat{c}_{-\mathbf{k},1} \hat{c}_{\mathbf{k},2} + \frac{\delta_z}{2} \sum_{\mathbf{k}} (\hat{c}_{\mathbf{k},3}^{\dagger} \hat{c}_{\mathbf{k},2} + h.c.), \tag{7.1}$$

where  $\hat{c}_{k,\sigma}$  annihilates a fermion with momentum k and spin state  $\sigma$ ,  $\chi$  is the attractive s-wave BCS interaction,  $\varepsilon_k$  is the single-particle energy of a fermion with momentum k as in Ch. 6, assumed to be spin-independent, and  $\delta_z$  is the Rabi frequency of the RF drive connecting  $|2\rangle$  to  $|3\rangle$ . Here, we implicitly work in an interaction frame where the zero-momentum spin states all have zero single-particle energy. Additionally, we have fixed the "RF" drive to be a DC coupling in this frame, such that the drive resonantly couples  $|2\rangle$  and  $|3\rangle$  in a noninteracting system.

To study this Hamiltonian, we define basis of three states per momentum label k, instead of two as with the Anderson pseudospin mapping [143]. For reasons which will soon become apparent, we call them  $|g\rangle$ ,  $|b\rangle$ , and  $|d\rangle$  and define them as:

$$|g\rangle_{k} = |n_{-k,1} = 0, n_{k,2} = 0, n_{k,3} = 0\rangle$$

$$|b\rangle_{k} = |n_{-k,1} = 1, n_{k,2} = 1, n_{k,3} = 0\rangle$$

$$|d\rangle_{k} = |n_{-k,1} = 1, n_{k,2} = 0, n_{k,3} = 1\rangle.$$
(7.2)

If the system starts in the ground state of the undriven Hamiltonian ( $\delta_z=0$ ), then the initial-time wavefunction can be described using only  $|b\rangle$  and  $|g\rangle$  states, mapping onto  $|\uparrow_c\rangle$  and  $|\downarrow_c\rangle$  Anderson pseudospins. The RF drive then acts to couple the states  $|b\rangle$  and  $|d\rangle$ , and therefore the full dynamics is confined to this three-level basis. We can express the Hamiltonian in the reduced basis by introducing three-level operators  $\hat{S}_{\mu\nu,k}:=|\mu\rangle\langle\nu|_k$  with  $\mu,\nu\in\{b,d,g\}$ , in analogy to the pseudospin operators:

$$\hat{H}/\hbar = -\sum_{\mathbf{k}} \varepsilon_{\mathbf{k}} \hat{S}_{gg,\mathbf{k}} - \chi \sum_{\mathbf{k}\mathbf{k}'} \hat{S}_{bg,\mathbf{k}'} \hat{S}_{gb,\mathbf{k}} + \frac{\delta_z}{2} \sum_{\mathbf{k}} (\hat{S}_{db,\mathbf{k}} + \text{h.c.}), \tag{7.3}$$

where we have shifted the energy of the system by a constant offset in order to express the single-particle energy term using the ground state population  $\hat{S}_{gg,k}$  instead of the other state populations.

Note that, rather than mapping the three spin states of each fermion onto three states of an atom in our quantum simulator, we instead map three configurations of a *pair* of momentum states  $\pm k$  onto the three states of our atom. Two of these states correspond to the Anderson pseudospin states representing the presence and absence of a Cooper pair, and the third corresponds to a pair-broken configuration where one of the two states in the Cooper pair is occupied, and the other is empty since one of the fermions is occupying a noninteracting state instead. We will see that, like with the gap protection against dephasing observed in Ch. 6, transfer into this third state will be suppressed in the form of the spectral gap  $\Delta_{SG}$ .

#### 7.3 Experimental setup

To engineer the Hamiltonian in Eq. (7.3), we use a setup very similar to that of the BCS experiment from Ch. 6. We start by cooling and trapping  $N = 10^5 - 10^6$  88 Sr atoms into our high-finesse optical

cavity in the strong collective coupling regime. The cavity's unshifted resonance frequency  $\omega_{c0}$  is reddetuned from the bare  ${}^3P_1-{}^1S_0$  transition frequency  $\omega_a$  by  $\Delta_c/2\pi:=(\omega_{c0}-\omega_a)/2\pi=-51$  MHz. The relevant states include a single ground state  $|g\rangle:=|{}^1S_0\rangle$  and two long-lived  $(\gamma/2\pi=7.5 \text{ kHz})$  excited Zeeman states  $|\pm 1\rangle:=|{}^3P_1,m_j=\pm 1\rangle$ , with a quantization axis along  $\hat{z}$  using the coordinates in Fig. 7.1(b). A  $\hat{y}$ -polarized laser drive excites the "bright" superposition  $|b\rangle_k:=\frac{1}{\sqrt{2}}(|+1\rangle_k+|-1\rangle_k)$  for each atom k, which also couples to the  $\hat{y}$ -polarized cavity mode. The orthogonal "dark" state  $|d\rangle_k:=\frac{1}{\sqrt{2}}(|+1\rangle_k-|-1\rangle_k)$  has a spatial distribution aligned with the cavity axis  $(\hat{x})$ , as shown in Fig. 7.1(d), and thus does not radiate into the cavity. In this natural basis for our system, we define collective dipole operators  $\hat{f}^+=(\hat{f}^-)^{\dagger}:=\sum_{k=1}^N|b\rangle\langle g|_k$ , measuring dipole projections along  $\hat{y}$ , and the atomic inversion  $\hat{f}^z=\sum_{k=1}^N\hat{f}^z_k$  where  $\hat{f}^z_k:=\frac{1}{2}(|b\rangle\langle b|_k-|g\rangle\langle g|_k)$ . We also apply a tunable, uniform magnetic field  $\vec{B}\parallel\hat{z}$ , represented using the collective angular momentum operator  $\hat{L}^z:=\sum_{k=1}^N\frac{1}{2}(|+1\rangle\langle +1|_k-|-1\rangle\langle -1|_k)=\sum_{k=1}^N\frac{1}{2}(|b\rangle\langle d|_k+|d\rangle\langle b|_k)$  which describes linear Zeeman shifts.

Using the above definitions, up to atom-light coupling inhomogeneities neglected for the time being (see Sec. 7.7 for the model with inhomogeneous atom-light coupling included), we engineer an effective atomic Hamiltonian of the form:

$$\hat{H}_{a}/\hbar = -\chi \hat{J}^{+} \hat{J}^{-} + \delta_{z} \hat{L}^{z} + \sum_{k=1}^{N} \varepsilon_{k} |g\rangle\langle g|_{k}.$$

$$(7.4)$$

The first term describes an all-to-all cavity-mediated spin-exchange interaction with strength  $\chi=g^2/\Delta_c$ , where  $2g/2\pi=15.4$  kHz is the rms atom-cavity coupling as a single-photon Rabi frequency. Since this interaction is collective, it scales with atom number with characteristic strength  $\chi N$ .  $\delta_z$  is the tunable splitting between  $|\pm 1\rangle$  Zeeman states; in the bright/dark basis, it creates an effective torque that rotates the collective dipole moment and couples  $|b\rangle$  and  $|d\rangle$ . Finally,  $\varepsilon_k$  describes the differential light shift between the ground state  $|g\rangle$  and the excited states due to the intracavity trapping light at 813 nm for atom k. This shift varies between the atoms due to a finite motional distribution (the same as described in Sec. 6.9.2), which induces dephasing between the ground and excited states.

Based on the definitions for  $\hat{J}^-$  and  $\hat{L}^z$ , Eq. (7.4) is equivalent to Eq. (7.3) from the previous section (up to a sign difference for  $\varepsilon_k$ ) if we map momentum labels k for the ultracold fermion system onto

positional labels k of our strontium atoms. To reiterate, the spin-exchange term represents the BCS interaction between fermions, and the  $\varepsilon_k$  term describes the electrons' kinetic energy. Additionally, the (complex) BCS pairing gap  $\Delta_{BCS}$  corresponds to  $\chi\langle\hat{J}^-\rangle$ ; as discussed in Ch. 6, this quantity also sets the gap protection against single-particle dephasing in the case where  $\langle\hat{J}^z\rangle=0$ . We go beyond our previous results by mapping an atom in state  $|d\rangle$  onto a "broken" Cooper pair consisting of one fermion in  $|1\rangle$  and the other transferred to a third state  $|3\rangle$ . The Zeeman term coupling  $|b\rangle$  to  $|d\rangle$  then represents a drive which breaks up Cooper pairs. Unlike the drive in rf spectroscopy experiments, this coupling operates at DC; we tune the coupling strength, rather than an rf drive frequency, in order to probe features of the spectral gap  $\Delta_{SG}$ .

To study this model, we initialize the atoms with a collective drive angle  $\theta_0 = \pi/2$  (defined as a  $\pi/2$  pulse for maximally-coupled atoms) along the  $|g\rangle$  to  $|b\rangle$  transition using a < 250 ns laser drive pulse. At time t=0, we turn off the drive. As the atoms evolve under Eq. 7.4, they weakly emit  $\hat{y}$ -polarized light out of the far-detuned cavity at a rate  $\Gamma|\langle \hat{J}^- \rangle|^2$ , where  $\Gamma = |(\frac{\kappa}{\Delta_c})\chi| \approx \frac{|\chi|}{300}$  sets the scale for collective emission (as defined in Sec. 2.5). As outlined last chapter in Sec. 6.9.3, this allows us to measure  $\langle \hat{J}^- \rangle$  in real time by measuring this light as it leaks out of the cavity using a heterodyne detector (see Figs. 7.2(a)-(b)), with only a small fraction of atoms emitting light since  $\Gamma \ll |\chi|$ .

## 7.4 Time dynamics of the BCS gap subject to dark state coupling

We first explore the competition between spin-exchange interactions and excited state coupling in Fig. 7.2(b) by comparing the time dynamics of the BCS pairing gap  $|\Delta_{\rm BCS}| = |\chi\langle\hat{J}^-\rangle|$  for different coupling strengths  $\delta_z$ . Here, we scan  $\delta_z/2\pi$  from 0 MHz to 5 MHz between shots while holding a fixed characteristic interaction strength  $\chi N/2\pi = 1.0$  MHz. A background inhomogeneity set by  $\{\varepsilon_k\}$  with standard deviation  $\varepsilon/2\pi = 150$  kHz also remains fixed; in the absence of interactions, this sets a dephasing time of 1  $\mu$ s as shown by the gray trace. Consistent with results from the BCS dynamical phases experiment, we observe that sufficiently large interactions protect against dephasing at a scale set by  $\chi N$ , drastically enhancing the coherence time. The coupling induced by  $\delta_z$  rotates the collective dipole moment, inducing oscillations in  $|\langle \hat{J}^- \rangle|$ . For small  $\delta_z$ , weak oscillations open up at short times but damp after a few

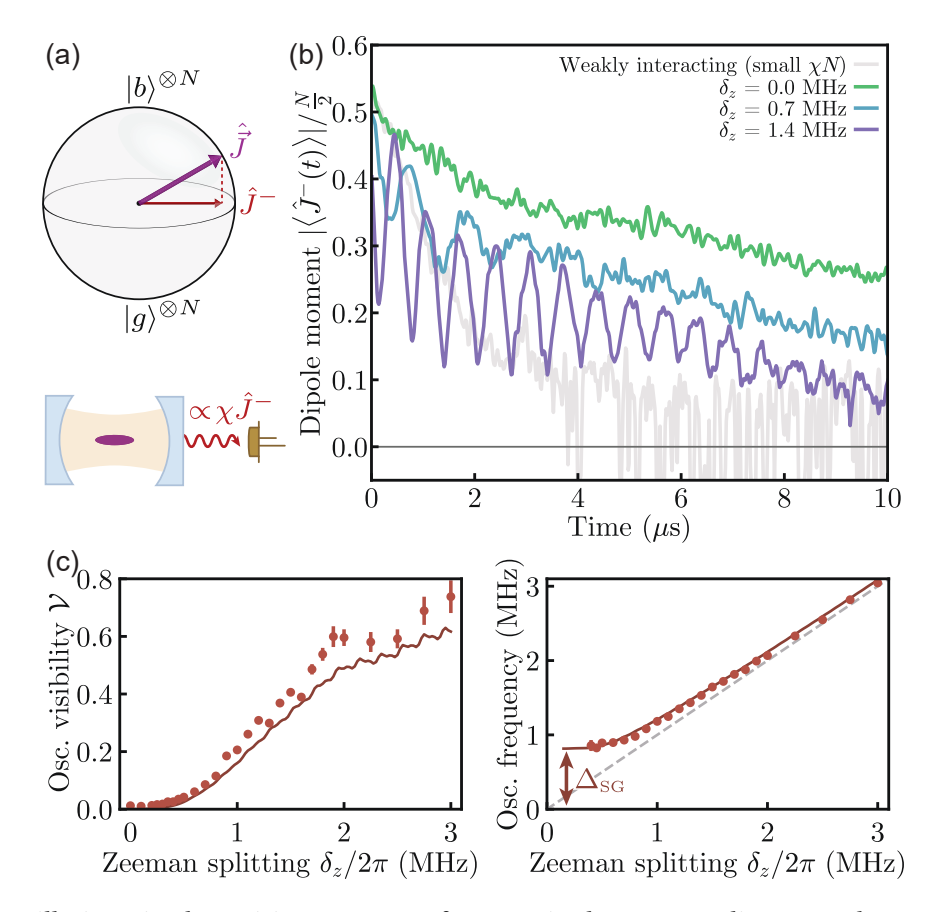


Figure 7.2: Oscillations in the pairing gap  $\Delta_{\rm BCS}$  from excited state coupling. (a) The atoms emit light weakly into the cavity at a rate proportional to  $\Delta_{\rm BCS} = \chi \langle \hat{J}^- \rangle$ , which we detect to infer dynamics. (b) Time traces of  $|\langle \hat{J}^- \rangle|$  with  $\chi N/2\pi = 1$  MHz. The Zeeman splitting  $\delta_z$  induces rotations in the collective dipole moment, which are suppressed for small  $\delta_z$ . The gray trace represents single-particle dynamics (with  $\delta_z/2\pi = 0$  MHz), using a smaller N to weaken the collective interactions. (c) The average oscillation visibility (left) and frequency (right) from  $t=0.5~\mu{\rm s}$  to  $t=5~\mu{\rm s}$  for different  $\delta_z$ . We also plot numerical simulations (solid curves) and the single-particle response  $\omega_{\rm osc} = \delta_z$  (gray dashed line). The dynamics resemble Rabi oscillation between excited states, with the Rabi frequency set by  $\delta_z$  and the detuning generated by collective interactions which we identify as the "spectral gap"  $\Delta_{\rm SG}$ . To measure  $\Delta_{\rm SG}$ , we extrapolate the measured  $\omega_{\rm osc}$  to  $\delta_z/2\pi \to 0$  MHz. All error bars in the paper represent  $\pm 1\sigma$  deviations over a bootstrap resampling on experimental shots ( $n_{\rm boot} = 100$ ).

microseconds. In contrast, large  $\delta_z$  traces feature large-amplitude oscillations with long lifetimes. The fact that  $|\langle \hat{J}^- \rangle|$  remains large in this limit at long times shows that the interactions continue to protect against dephasing from the single-particle inhomogeneity  $\{\varepsilon_k\}$ , even with a large  $\delta_z$ .

Fig. 7.2(c) further studies these two regimes by analyzing the oscillations in an interval from  $t=0.5~\mu s$  to  $t=5~\mu s$ . When  $\delta_z/2\pi \gtrsim 2$  MHz, the oscillation visibility (defined as  $\mathcal{V}=\frac{|\langle \hat{J}^- \rangle|_{\max}-|\langle \hat{J}^- \rangle|_{\min}}{|\langle \hat{J}^- \rangle|_{\max}+|\langle \hat{J}^- \rangle|_{\min}}$ ) is consistently large, and the oscillation frequency  $\omega_{\rm osc}$  approaches  $\delta_z$ . For small  $\delta_z$ , a different picture

emerges: the visibility is suppressed and approaches 0, and  $\omega_{\rm osc}$  plateaus to a constant frequency. The experimental data agrees with numerical simulations (solid curves) except for a small absolute scale factor in the oscillation visibility. This is likely related to additional dephasing mechanisms in our system (such as residual motional effects), which are unaccounted for in numerical simulations but would reduce the measured  $|\langle \hat{J}^- \rangle|$ , as discussed last chapter in Sec. 6.10.3. The oscillation frequency at small  $\delta_z$  can be directly connected to the spectral gap  $\Delta_{\rm SG}$  observed in degenerate Fermi gas experiments when coupling to a third state. This is because our measurement of oscillations induced by a quenched DC coupling provides information equivalent to mapping out an rf spectroscopic peak.

Before moving on, I want to briefly highlight the similarities and differences between this parameter scan (of a coupling  $\delta_z$  to a third state) and the phase II to phase III scan from Sec. 6.7 (scanning an energy splitting  $\delta_s$  between two subensembles). In both cases, introducing the frequency induces oscillations in  $\Delta_{BCS}$ . For sufficiently large frequencies of  $\delta_z$  or  $\delta_s$ , the induced oscillation frequency  $\omega_{osc}$ approaches the applied frequency. The oscillations are also longer-lived. In the limit of small frequency, the oscillations damp more quickly and have a frequency which is representative of a many-body gap  $(2\Delta_{BCS} \approx \chi N)$  for the BCS experiment, and  $\Delta_{SG}$  for the current experiment). However, the two situations have key differences as well. First, theoretical analysis of the three-level system does not predict a true dynamical phase between these two regimes, instead observing crossover behavior in the analytics and numerical simulations. From an implementation standpoint, the atomic ensemble is undergoing different processes: in the BCS phase II to phase III scan, the populations in the excited and ground state remain fixed, while the total phase coherence oscillates. However, in this experiment, the excited state coupling parametrized by  $\delta_z$  transfers atoms out of the bright excited state. We can already see data supporting the fact that these two experiments are different: in Fig. 7.2(c), we see that the oscillation frequency increases with  $\delta_z$  in a manner reminiscent of a quadrature sum. Notably, we do *not* see a dip in the oscillation frequency as reported in the BCS model.

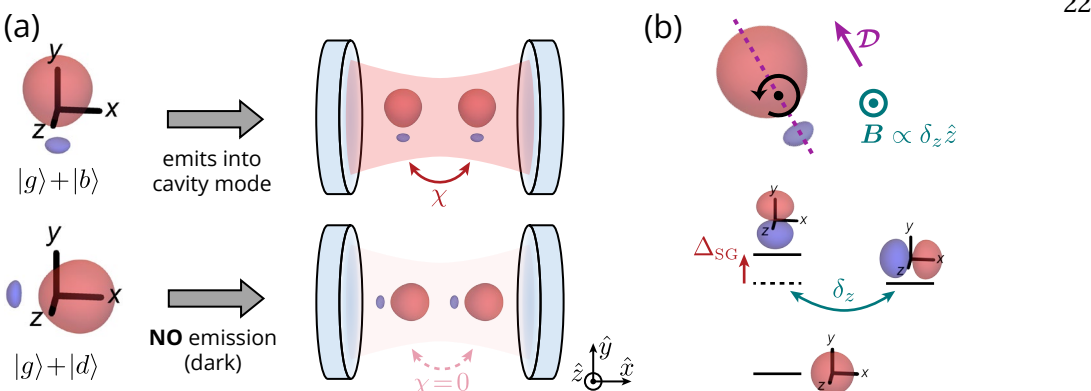


Figure 7.3: Rotating dipole interpretation of the spectral gap. (a) Atoms in a superposition of  $|g\rangle$  and  $|b\rangle$  exhibit an oscillating dipole moment along  $\hat{y}$ , which can emit into the  $\hat{y}$ -polarized cavity mode. This emission gives rise to the cavity-mediated interactions. In contrast, atoms in a superposition of  $|g\rangle$  and  $|d\rangle$  exhibit an oscillating dipole moment along  $\hat{x}$ , which is dark to the cavity due to dipole emission patterns. Therefore, this superposition does not experience gap protection. (b) When subject to a magnetic field, the oscillating dipole moment experiences an effective torque which causes it to rotate about the magnetic field axis. This manifests as a coupling between bright and dark states. However, the cavity-mediated interactions impose an energy cost to rotating between the two configurations, equivalent to the spectral gap  $\Delta_{\rm SG}$ .

# 7.5 Understanding the spectral gap

In this section, we study the spectral gap  $\Delta_{SG}$  from a couple of different perspectives. We also push on the differences between this experiment and the BCS experiment, contrasting  $\Delta_{SG}$  with the BCS gap  $\Delta_{BCS}$ .

#### 7.5.1 The spectral gap prevents the rotation of atomic orbitals

An intuitive picture of the oscillations can be gained by imagining the atoms as electric dipoles, as shown in Fig. 7.3. Atoms with coherence along the  $|g\rangle$  to  $|b\rangle$  transition exhibit a dipole moment proportional to  $|\langle \hat{J}^- \rangle|$  which oscillates along  $\hat{y}$  at optical frequencies. Applying a magnetic field along  $\hat{z}$  creates an effective torque on the dipoles, causing them to rotate in the xy-plane at a frequency set by the Zeeman splitting  $\delta_z$ . Therefore, the population in  $|b\rangle$  should periodically transfer between  $|b\rangle$  (aligned with  $\hat{y}$ ) and  $|d\rangle$  (aligned with  $\hat{x}$ ) while maintaining coherence with the ground state  $|g\rangle$ . This effectively causes the collective dipole moment  $|\langle \hat{J}^- \rangle|$  along  $\hat{y}$  to oscillate in time.

However, sufficiently strong spin-exchange interactions of the form  $\hat{J}^+\hat{J}^-$  disrupt this process. This term essentially shifts the excited state  $|b\rangle$  by a frequency  $\Delta_{SG}$  relative to  $|d\rangle$ , which does not radiate into the cavity. Quantitatively,  $\chi \hat{J}^+\hat{J}^- = \chi(\hat{J}^2 - (\hat{J}^z)^2 + \hat{J}^z)$  has eigenstates  $|J,J^z\rangle$  and eigenvalues  $E_{J,J^z} = \chi[J(J+1) - J^z(J^z-1)]$ . For fully collective states, i.e., where  $J = \frac{N_b + N_g}{2}$  and  $J^z = \frac{N_b - N_g}{2}$  with  $N_{b,g}$  denoting the populations in  $|b\rangle$  and  $|g\rangle$  respectively,  $E_{J,J^z} \approx (\chi N_g)N_b$  in the large-N limit. Therefore, transferring one atom from  $|b\rangle$  to  $|d\rangle$  imposes an energy penalty equal to  $\hbar\Delta_{SG} = \hbar\chi N_g$ . Note that  $\Delta_{SG}$  decreases with increasing atomic inversion, mirroring the chemical potential dependence in degenerate Fermi gases.

# 7.5.2 The spectral gap creates a detuning between coupled harmonic oscillators

For a more theoretically grounded understanding of the spectral gap, we can recast the system using a Schwinger boson formalism. At a high level, this formalism replaces each state  $(|g\rangle, |b\rangle, |d\rangle)$  with an abstract bosonic mode  $(\hat{a}_g, \hat{a}_b, \hat{a}_d)$  in which creating and annihilating excitations in these modes corresponds to collective (symmetrized) spin raising and lowering operators. For example, the operator  $\hat{J}^- = \sum_k |g\rangle\langle b|_k$  maps onto  $\hat{a}_g^\dagger \hat{a}_b$ . In the maximally symmetric manifold only,<sup>3</sup> the occupation  $\hat{N}_\mu = \hat{a}_\mu^\dagger \hat{a}_\mu$  of each mode  $\mu$  corresponds to the number of atoms in each state. Assuming that the system remains in the maximally symmetric manifold is a reasonable approximation (ignoring inhomogeneous atom-light coupling, as discussed later in Sec. 7.7), so long as the inhomogeneities set by  $\varepsilon_k$  are much smaller than  $\chi N$ . In this way, we can picture the atoms as representing excitations in harmonic oscillators defined by the Schwinger bosons.

Using this formalism, we rewrite the Hamiltonian as:

$$\hat{H} = \frac{\delta_z}{2} (\hat{a}_b^{\dagger} \hat{a}_d + \hat{a}_d^{\dagger} \hat{a}_b) - \chi \hat{a}_b^{\dagger} \hat{a}_g \hat{a}_g^{\dagger} \hat{a}_b, \tag{7.5}$$

where we explicitly neglect the inhomogeneity term since it is assumed to be unimportant for the dynamics. Using bosonic commutation relations, we can now rewrite the interaction term in terms of the number of atoms in the bright and ground state:  $\chi \hat{a}_b^{\dagger} \hat{a}_g \hat{a}_g^{\dagger} \hat{a}_b = \chi \hat{N}_b (\hat{N}_g + 1) \approx (\chi \hat{N}_g) \hat{N}_b$  in the large N

<sup>&</sup>lt;sup>3</sup> Schwinger bosons can be used to represent any state  $|J,m\rangle$  representing  $\frac{N}{2}$  spin-1/2 particles, for any angular momentum J. However, only in the maximally symmetric manifold  $(J=\frac{N}{2})$  does the number of Schwinger bosons correspond to the number of particles in spin-up or spin-down. This argument extends beyond two-level systems to the three-level systems discussed here.

limit. In other words, atoms in the bright state receive an energy shift equal to  $\chi N_g$  compared to atoms in the dark state.

We can further tease out the dynamics of the system by studying the of motion for the field operators  $\hat{a}_{\mu}$ . At the mean-field level, we can replace these operators with a normalized field amplitude:  $(\hat{a}_g, \hat{a}_b, \hat{a}_d) \rightarrow \sqrt{N}(\alpha_g, \alpha_b, \alpha_d)^T$ , where  $|\alpha_g|^2 + |\alpha_b|^2 + |\alpha_d|^2 = 1$ . The equations of motion then reduce to:

$$\dot{\alpha}_{g} = i\chi N(\alpha_{b}^{*}\alpha_{b})\alpha_{0},$$

$$\dot{\alpha}_{b} = -i\left(\frac{\delta_{z}}{2}\alpha_{d} - \chi N(\alpha_{g}^{*}\alpha_{g})\alpha_{b}\right),$$

$$\dot{\alpha}_{d} = -i\frac{\delta_{z}}{2}\alpha_{b}.$$
(7.6)

The first equation implies that the number of atoms in the ground state, given by  $N\alpha_g^*\alpha_g = N_g$ , remains constant. Therefore, we can simplify the equations for  $\alpha_b$  and  $\alpha_d$  as follows:

$$\dot{\alpha}_{b} = -i\left(\frac{\delta_{z}}{2}\alpha_{d} - \chi N_{g}\alpha_{b}\right),$$

$$\dot{\alpha}_{d} = -i\frac{\delta_{z}}{2}\alpha_{b},$$
(7.7)

which are linear and can be solved analytically. The general solution is then given by

$$\alpha_{g}(t) = \alpha_{g}(0) \exp\left[i\chi N \int_{0}^{t} \alpha_{b}^{*}(t')\alpha_{b}(t') dt'\right],$$

$$\alpha_{b}(t) = \left[\alpha_{b}(0) \cos\left(\frac{\omega t}{2}\right) + i\alpha_{b}(0) \frac{\chi N_{g}}{\omega} \sin\left(\frac{\omega t}{2}\right) - i\alpha_{d}(0) \frac{\delta_{z}}{\omega} \sin\left(\frac{\omega t}{2}\right)\right] \exp\left(i\frac{\chi N_{g}}{2}t\right),$$

$$\alpha_{d}(t) = \left[\alpha_{d}(0) \cos\left(\frac{\omega t}{2}\right) - i\alpha_{d}(0) \frac{\chi N_{g}}{\omega} \sin\left(\frac{\omega t}{2}\right) - i\alpha_{b}(0) \frac{\delta_{z}}{\omega} \sin\left(\frac{\omega t}{2}\right)\right] \exp\left(i\frac{\chi N_{g}}{2}t\right),$$

$$(7.8)$$

where

$$\omega = \sqrt{(\chi N_g)^2 + \delta_z^2}. (7.9)$$

The expressions for  $\alpha_b(t)$  and  $\alpha_d(t)$  describe dynamics that formally resemble Rabi oscillation between  $|b\rangle$  and  $|d\rangle$  with a Rabi frequency  $\delta_z$  and a (collective) detuning  $\chi N_g$ . This detuning represents the shift observed in rf spectroscopy experiments, so we identify the spectral gap as  $\Delta_{\rm SG} = \chi N_g$ .

#### 7.5.3 Comparing the spectral gap to the BCS gap

How do the spectral gap  $\Delta_{SG}$  and the BCS gap  $\Delta_{BCS}$  quantitatively differ? We have discussed the nature of  $\Delta_{SG}$  in the preceding sections. Intuition about  $\Delta_{BCS}$  can be gained by considering the mean-

field ground state, which under an Anderson pseudospin mapping is described by 4

$$\langle \hat{J}_k^- \rangle = \frac{1}{2} \frac{\Delta_{\text{BCS}}}{\sqrt{(\frac{\varepsilon_k}{2} - \mu)^2 + |\Delta_{\text{BCS}}|^2}}, \quad \langle \hat{J}_k^z \rangle = -\frac{1}{2} \frac{\frac{\varepsilon_k}{2} - \mu}{\sqrt{(\frac{\varepsilon_k}{2} - \mu)^2 + |\Delta_{\text{BCS}}|^2}}, \tag{7.10}$$

with self-consistent equations

$$\Delta_{\rm BCS} = \chi \sum_{k} \langle \hat{J}_{k}^{-} \rangle = \frac{1}{2} \sum_{k} \frac{\chi \Delta_{\rm BCS}}{\sqrt{(\frac{\varepsilon_{k}}{2} - \mu)^{2} + |\Delta_{\rm BCS}|^{2}}},\tag{7.11}$$

$$\langle \hat{J}^z \rangle = \sum_{k} \langle \hat{J}_k^z \rangle = -\frac{1}{2} \sum_{k} \frac{\frac{\varepsilon_k}{2} - \mu}{\sqrt{(\frac{\varepsilon_k}{2} - \mu)^2 + |\Delta_{\text{BCS}}|^2}}.$$
 (7.12)

In this work, we are mainly concerned with the regime  $\varepsilon_k \to 0$ . In this limit, one can obtain

$$\langle \hat{J}_k^- \rangle = \frac{1}{2} \frac{\Delta_{\text{BCS}}}{\sqrt{\mu^2 + |\Delta_{\text{BCS}}|^2}}, \quad \langle \hat{J}_k^z \rangle = \frac{1}{2} \frac{\mu}{\sqrt{\mu^2 + |\Delta_{\text{BCS}}|^2}}, \tag{7.13}$$

and the self-consistent equations become

$$\frac{\chi N}{2} = \sqrt{\mu^2 + |\Delta_{\text{BCS}}|^2}, \quad \mu = \chi \langle \hat{J}^z \rangle. \tag{7.14}$$

Therefore, we can express the pairing gap  $\Delta_{BCS}$  magnitude by

$$|\Delta_{\rm BCS}| = \chi \sqrt{\left(\frac{N}{2}\right)^2 - \langle \hat{J}^z \rangle^2}.$$
 (7.15)

In comparison, the spectral gap  $\Delta_{SG}$  can be expressed in the limit where  $\varepsilon_k \to 0$  by

$$\Delta_{SG} = \chi \langle \hat{N}_g \rangle = \chi \left( \frac{N}{2} - \langle \hat{J}^z \rangle \right) = \sqrt{|\Delta_{BCS}|^2 + \mu^2} - \mu. \tag{7.16}$$

Beyond the limit  $\varepsilon_k \to 0$ , the RF spectrum based on ideal BCS model shows an RF absorption threshold at  $\omega = \chi \langle \hat{N}_g \rangle$  (e.g., see Eq. (2.31) in [452], as well as [453]). The size of the mean-field collective detuning between  $|b\rangle$  and  $|d\rangle$  will therefore be smaller than  $\chi \langle \hat{N}_g \rangle$  outside of the fully collective regime. Likewise, when J < N/2,  $\Delta_{\rm BCS} = \chi \langle \hat{J}^- \rangle$  becomes smaller and is roughly equal to  $\chi \sqrt{J^2 - \langle \hat{J}^z \rangle^2}$ .

Our initial preparation scheme with tunable Rabi pulse area can be interpreted as preparing the mean-field ground state in the limit  $\varepsilon_k \to 0$  with fixed  $\langle \hat{J}^z \rangle$  (fixed number of Cooper pairs). It follows that we can measure  $|\Delta_{\rm BCS}|$  of this ground state looking at the measured value of  $|\Delta_{\rm BCS}(t)|$  in Fig. 7.2(b) at

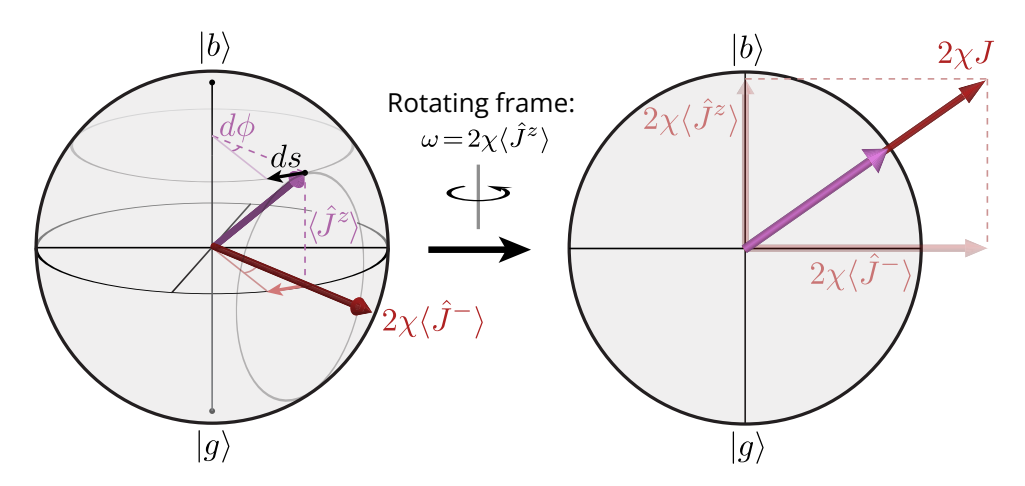


Figure 7.4: Visualizing spin-exchange gap protection with nonzero inversion. Left: Because of fardetuned atom-cavity coupling, the cavity field (red arrow) drives the atomic ensemble (purple arrow) with an instantaneous Rabi frequency equal to  $2\chi\langle\hat{J}^-\rangle$ . Over an infinitesimal time dt, this drives the Bloch vector a distance  $ds = \langle\hat{J}^z\rangle\big(2\chi\langle\hat{J}^-\rangle dt\big)$  in the azimuthal direction, corresponding to an angular displacement of  $d\phi = ds/\langle\hat{J}^-\rangle = \omega_{\rm disp}dt$ , where  $\omega_{\rm disp} = 2\chi\langle\hat{J}^z\rangle$ . If the drive were fixed in phase, then this dynamics would turn into rotation about the drive axis at longer times. However, because the cavity field adiabatically follows the Bloch vector phase, the drive vector also rotates with a frequency  $\omega_{\rm disp}$ , resulting in a global azimuthal rotation at longer times. Right: Moving into the rotating frame of this dynamics leads to a static Bloch vector and drive, with the addition of a fictitious  $\hat{z}$  field corresponding to the dispersive shift  $\omega_{\rm disp}$ . The total effective field then points parallel to the Bloch vector, with a total length equal to  $2\chi\sqrt{|\langle\hat{J}^-\rangle|^2+\langle\hat{J}^z\rangle^2}=2\chi J$ .

short times, immediately after initialization. In contrast,  $\Delta_{SG}$  represents the  $\delta_z \to 0$  limit of the oscillation frequency of the curves in Fig. 7.2(b), as shown in the right panel of Fig. 7.2(c).

Finally, in these expressions there is actually a third gap scaling, which when  $\epsilon_k \to 0$  looks like  $2\sqrt{\mu^2 + |\Delta_{\rm BCS}|^2} = \chi N$ . In our atomic physics implementation, this represents the gap protection strength against single-particle dephasing, which generically takes the form  $2\chi J$  away from the maximally symmetric manifold. This can be seen in a couple of ways: first, single-particle dephasing can be modeled as coupling different collective angular momentum manifolds without changing the atomic inversion, such that the state  $|J,J^z\rangle$  is coupled to  $|J-1,J^z\rangle$ . These two states have a collective detuning between them equal to  $\langle J,J^z|\chi \hat{J}^+\hat{J}^-|J,J^z\rangle - \langle J-1,J^z|\chi \hat{J}^+\hat{J}^-|J-1,J^z\rangle = 2\chi J$ . A more intuitive picture of the physics involves Bloch spheres, shown in Fig. 7.4. As described in Sec. 2.5, the spin-exchange interaction arises due

<sup>&</sup>lt;sup>4</sup> The factor of  $\frac{1}{2}$  in the single-particle energies comes from the normalization used in our spin implementation the BCS Hamiltonian. See Sec. 6.2 for more.

to a small intracavity field which adiabatically follows  $\langle \hat{J}^- \rangle$ . On the Bloch sphere, this looks like a fictitious magnetic field pointing along the equator, with a Rabi frequency of  $2\chi\langle \hat{J}^- \rangle$  and the same azimuthal angle as the Bloch vector. If the Bloch vector is along the equator, the fictitious field points exactly along the Bloch vector and creates the energy gap  $2\chi\langle \hat{J}^- \rangle$ . For a finite  $\langle \hat{J}^z \rangle$ , the Bloch vector will instantaneously begin to rotate about the field axis. However, the cavity field also rotates to follow the phase of the Bloch vector, leading to an effective rotation about the  $\hat{z}$ -axis with a frequency  $2\chi\langle \hat{J}^z \rangle$ . Moving into the rotating frame of this dynamics results in a  $\hat{z}$  component of the fictitious magnetic field, which now points exactly along the Bloch vector direction with length  $2\chi J$  (and setting this as the gap protection scale).

While in our previous work, we conflated the many-body gap  $2\chi J$  with  $\Delta_{BCS}$ , this is because we operated at the point  $\mu=0$  ( $\langle \hat{J}^z \rangle=0$ ) to reflect the conditions of typical superconducting platforms. Our platform in principle allows us to make a distinction between these two scales when  $\mu \neq 0$ , but to simplify the narrative we only consider  $\Delta_{BCS}$  and  $\Delta_{SG}$  as defined above (particularly since researchers in superconducting fields do not, to our knowledge, distinguish between  $\Delta_{BCS}$  and the gap described here).

## 7.6 Measuring the two gaps as a function of inversion

To explore the dependence of the two gaps on the atomic inversion  $\langle \hat{J}^z \rangle$ , we repeat the experiment from Sec. 7.4 with different initial drive angles  $\theta_0$  along the  $|g\rangle$  to  $|b\rangle$  transition. As Fig. 7.5(a) illustrates, increasing  $\theta_0$  decreases the initialized ground state population  $N_g^{\rm init}$ , which should reduce the splitting between the excited states and therefore  $\Delta_{\rm SG}$ . We see this trend in Fig. 7.5(b): when  $\theta_0=0.73\pi$ , the oscillation frequency resembles the expected single-particle response, whereas the  $\theta_0=0.25\pi$  data exhibits large frequency deviations which indicate a sizable spectral gap  $\Delta_{\rm SG}$ . We determine  $\Delta_{\rm SG}$  by fitting the data to the form  $\omega_{\rm osc}=\sqrt{\Delta_{\rm SG}^2+\delta_z^2}$ , the predicted response, over the domain  $\delta_z/2\pi \geq 0.6$  MHz where the oscillations are most prominent (dotted lines).

<sup>&</sup>lt;sup>5</sup> From this discussion, our hot take is that  $\Delta_{BCS}$  does not actually represent a many-body gap away from  $\langle \hat{J}^z \rangle = 0$ , despite the fact that we're calling it the BCS gap or pairing gap. Rather, the quantity  $2\chi J$  is the real frequency scale for many-body gap protection in our system. For the scope of this work, we didn't bother to push this take too far (we wanted to get published). But for example, we expect that away from the equator of the Bloch sphere, the frequency of Higgs oscillations (as discussed in Sec. 6.6) should be  $2\chi J$ , rather than  $2|\Delta_{BCS}|$ .

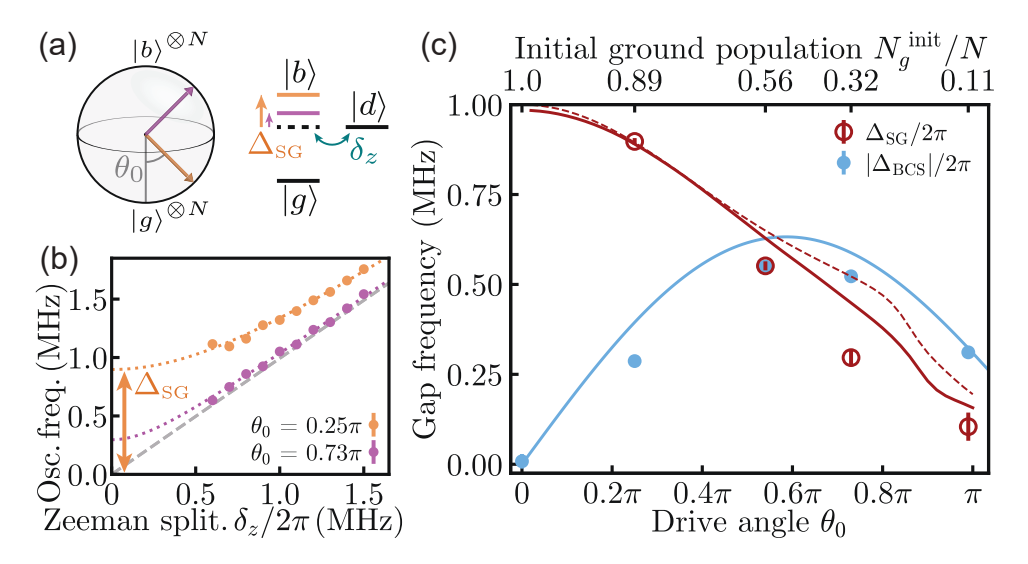


Figure 7.5: Probing the spectral gap  $\Delta_{\rm SG}$ . (a) As the drive angle  $\theta_0$  increases,  $N_g$  decreases, which should reduce the spectral gap  $\Delta_{\rm SG}$ . (b) We repeat the experiment in Fig. 7.2(c) for different drive angles  $\theta_0$ . For each  $\theta_0$ , we fit the results to the form  $\omega_{\rm osc} = \sqrt{\Delta_{\rm SG}^2 + \delta_z^2}$  (dotted lines) and extract  $\Delta_{\rm SG}$ . (c) Measured values of  $\Delta_{\rm SG}$  (as outlined in (b)) and  $|\Delta_{\rm BCS}|$  (at short times t=0  $\mu$ s to t=0.5  $\mu$ s) for different  $\theta_0$ , or equivalently the t=0 ground state population  $N_g^{\rm init}$  (circles). The two gaps overlap at  $\theta_0=0.54\pi$ . We compare against numerical simulations of the two gaps (solid curves) and  $\chi N_g^{\rm eff}$  (dashed curve), where  $N_g^{\rm eff}$  is the ground state population weighted by cavity coupling and averaged over the measured time interval t=0.5  $\mu$ s to t=5  $\mu$ s.

In Fig. 7.5(c), we observe that  $\Delta_{SG}$  and  $|\Delta_{BCS}|$  scale differently with the drive angle  $\theta_0$ :  $\Delta_{SG}$  monotonically decreases, and  $|\Delta_{BCS}|$  starts at 0 and peaks around  $\theta_0 \approx 0.6\pi$ . These qualitative behaviors are consistent with the expected relations  $\Delta_{SG} \propto N_g$  and  $\Delta_{BCS} \propto \langle \hat{J}^- \rangle$ . Numerical simulations calculated using a similar analysis (solid curves) agree qualitatively with experimental values but overestimate some points. We attribute this to the additional dephasing mechanism described earlier, which would weaken the interaction strength and therefore reduce the sizes of the gaps.

We also directly compare  $\Delta_{SG}$  with numerical simulations of  $\chi N_g$  for different  $\theta_0$  (dashed curve in Fig. 7.5(c)). Complications arise in this calculation from inhomogeneous atom-light coupling, since the effective  $N_g$  seen by the cavity varies in time (unlike in homogeneously coupled systems where it does not vary on timescales faster than the decay rate). To account for this, we weight atoms by cavity coupling and average the result over the measurement interval ( $t = 0.5 \ \mu s$  to  $t = 5 \ \mu s$ ) to obtain an effective shift  $\chi N_g^{\rm eff}$  (explained in further detail in the following section), represented by the black dashed curve in

Fig. 7.5(c). This curve qualitatively resembles the measured values of  $\Delta_{SG}$ , demonstrating the expected scaling.

# 7.7 Effects of inhomogeneous atom-light coupling on the spectral gap

The simple description of our setup, described by the Hamiltonian given in Eq. (7.4), assumes that all atoms couple equally strongly to the cavity mode. However, as we have just alluded to in the previous section, this is not actually the case: since our atoms are trapped in an 813 nm lattice which is incommensurate with our optical atomic transition wavelength of 689 nm, our atoms effectively experience a distribution of couplings  $g_k = g_c \eta_k$ , where  $g_c$  is the peak atom-cavity coupling, and  $\eta_k = \cos(\varphi_k)$  is uniformly distributed over  $\varphi \in [0, 2\pi)$  (this is the same setup as in Sec. 6.10.1). Despite these complications, we still expect to see spin-exchange interactions which generate a version of the BCS gap  $\Delta_{BCS}$  and the spectral gap  $\Delta_{SG}$ .

To model the expected behavior of this system, we define single-atom operators  $\hat{S}_{\mu\nu,j} := |\mu\rangle\langle\nu|_j$  on atom j with  $\mu,\nu\in\{b,d,g\}$  representing the three single-atom states. In terms of these operators, the full Hamiltonian is described by:

$$\hat{H}/\hbar = \frac{\delta_z}{2} \sum_j (\hat{S}_{bd,j} + \hat{S}_{db,j}) - \sum_j \varepsilon_j \hat{S}_{gg,j} + i g_c \sum_j \eta_j (\hat{S}_{bg,j} \hat{a} - \hat{S}_{gb,j} \hat{a}^{\dagger}) + \Delta_c \hat{a}^{\dagger} \hat{a} + \zeta \hat{a}^{\dagger} + \zeta^* \hat{a}.$$
 (7.17)

Here,  $\zeta$  represents any classical drive sent through the cavity, which encompasses both the initialization pulse and the QND cavity probe.

In addition to the Hamiltonian dynamics, we also consider the dissipation processes such as cavity loss with a rate  $\kappa$ , and spontaneous emission with a rate  $\gamma$ , so the dynamics of this system can be described by the following Lindblad master equation,

$$d_t \hat{\rho} = -\frac{i}{\hbar} [\hat{H}, \hat{\rho}] + \mathcal{L}[\hat{L}_{cav}](\hat{\rho}) + \sum_j \left( \mathcal{L}[\hat{L}_{b,j}](\hat{\rho}) + \mathcal{L}[\hat{L}_{d,j}](\hat{\rho}) \right), \tag{7.18}$$

where the jump operator for cavity loss is given by

$$\hat{L}_{\text{cav}} = \sqrt{\kappa} \,\hat{a},\tag{7.19}$$

and the single-particle jump operators for spontaneous emission out of the bright and dark states are given by

$$\hat{L}_{b,j} = \sqrt{\gamma} \hat{S}_{gb,j}, \quad \hat{L}_{d,j} = \sqrt{\gamma} \hat{S}_{gd,j}. \tag{7.20}$$

As described in Sec. 2.5, when  $\Delta_{ca}$  is the largest frequency scale in the system, then we can adiabatically eliminate the cavity and generate an effective Hamiltonian (and collective dissipation, corresponding to superradiance). For our driven, inhomogeneously coupled system, this effective Hamiltonian looks like

$$\hat{H}_{\text{eff}}/\hbar = \frac{\delta_z}{2} \sum_j (\hat{S}_{bd,j} + \hat{S}_{db,j}) - \sum_j \varepsilon_j \hat{S}_{gg,j} + \frac{i}{2} \sum_j \eta_j (\Omega \hat{S}_{bg,j} - \Omega^* \hat{S}_{gb,j}) - \chi \sum_{jk} \eta_j \eta_k \hat{S}_{bg,j} \hat{S}_{gb,k}, \tag{7.21}$$

where  $\Omega = -2g_c\zeta/(\Delta_c - i\kappa/2)$  is an effective Rabi frequency driving the atoms along the bright to ground transition.

We have previously described (see Sec. 6.10.1) how the BCS gap is modified under these conditions. What about the spectral gap? For a system with homogeneous atom-light coupling, an initial state in the maximally symmetric manifold (i.e.,  $J = \frac{N_b + N_g}{2}$ ) experiences a spectral gap equal to  $\Delta_{\rm SG} = \chi N_g$ . The presence of inhomogeneous coupling disrupts this picture. It is hard to analytically calculate the spectral gap  $\Delta_{\rm SG}$  in the case of inhomogeneous coupling. Instead, we rely on numerically simulating  $\Delta_{\rm SG}$  with the same analysis used on the experimental data. Additionally, we compare  $\Delta_{\rm SG}$  against what we believe is a reasonable analog for  $\chi N_g$  for an inhomogeneously coupled system. This analog replaces  $N_g$  with an estimate of the ground state population weighted by cavity coupling, which we will call  $N_g'$  (or, in an abuse of notation, just  $N_g$  outside of this section):

$$N_g' \coloneqq \frac{\sum_j \eta_j^2 N_{g,j}}{\frac{1}{N} \sum_j \eta_j^2},\tag{7.22}$$

normalized such that when all atoms are in the ground state,  $N'_g = N$ . The intuition for why this seems like a good choice comes from Sec. 7.8.1, where the weighted atomic inversion  $\hat{J}^{z\prime}$  turns out to be the correct observable to determine shifts in the cavity resonance frequency.

However, this quantity carries an additional complication: while the unweighted ground state atom number  $N_g$  is preserved under the spin-exchange interaction (the number of excitations does not

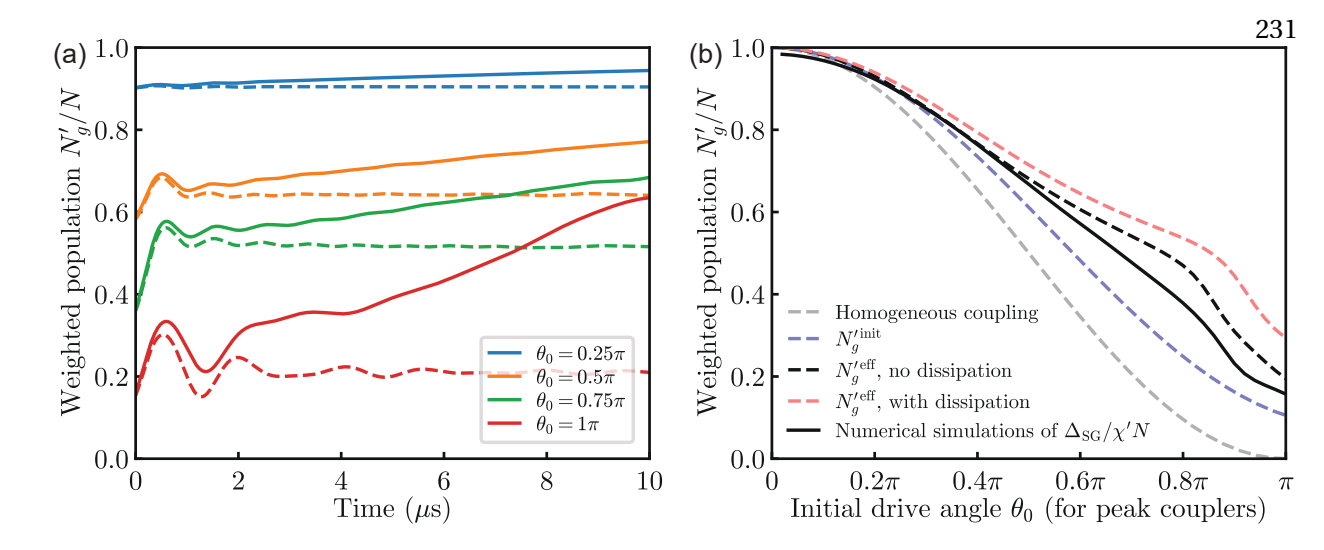


Figure 7.6: Analysis of the weighted ground state population  $N_g'$ . (a) Time dynamics after an initial Rabi pulse with drive angle  $\theta_0$  for peak couplers. Dashed lines are derived from simulations neglecting single-particle and collective dissipation, and solid lines represent a full numerical simulation of the experiment (including dissipation). (b) Comparison of various  $N_g'$  measurements vs.  $\theta_0$ . The gray dashed trace represents homogeneous coupling, with all other traces assuming uniformly inhomogeneous coupling. The blue dashed trace shows the expected initial-time population according to Eq. (7.23). The black and red traces represent  $N_g'$  averaged over the time interval  $t=0.5~\mu s$  to  $t=5~\mu s$  (the interval used to measure  $\Delta_{SG}$ ), using simulations neglecting and including dissipation, respectively. Finally, the black solid trace is  $\Delta_{SG}$  computed from numerical simulations with the same method used with the experimental data, normalized to 1 at  $\theta_0=0$ .

change),  $N'_g$  is not. This is because when atoms with different cavity coupling strengths exchange excitations, how the excitation is weighted also changes. This can be seen in Fig. 7.6(a), which shows numerical simulations of  $N'_g$  for several different drive angles  $\theta_0$  (defined as the angle experienced by atoms with maximum coupling). We see that  $N'_g$  oscillates for a few  $\mu$ s after initialization, sometimes drastically changing from the t=0 value. Interestingly, in simulations that neglect dissipation (dashed curves),  $N'_g$  appears to quickly approach a steady state, where the system attains a sort of detailed balance in the exchange between classes of atoms with different coupling strengths. With dissipation (solid curves),  $N'_g$  decays to N at long times.

Fig. 7.6(b) shows how various measurements of  $N_g'$  differ as a function of drive angle  $\theta_0$ . For homogeneous coupling (gray dashed line),  $N_g' = N\cos(\theta_0/2)^2$  is constant in the absence of dissipation. In the case of inhomogeneous coupling, we assume the atoms uniformly sample a coupling phase  $\varphi$ , resulting in a coupling strength  $\eta(\varphi) = \cos \varphi$ . In this case, the weighted ground state population at t = 0

 $(N_g^{'\text{init}}$ , blue dashed line) is given by:

$$N_g^{'\text{init}}(\theta_0) = N\left(\frac{1}{2} + \frac{J_1(\theta_0)}{\theta_0} - J_2(\theta_0)\right). \tag{7.23}$$

In the experiment, we estimate  $\Delta_{SG}$  by analyzing the oscillation frequency of  $\hat{J}^-$  within the measurement interval  $t \in [0.5 \ \mu s, 5 \ \mu s]$ . The black dashed line represents the average weighted ground state population in this time interval, which we call the effective ground state population  $N_g^{\text{reff}}$ , using numerical simulations without dissipation. By visual inspection of Fig. 7.6(a), this estimate should be fairly close to the long-time steady-state value fo  $N_g'$ . We also plot  $N_g^{\text{reff}}$  using simulations including dissipation (red dashed line). Finally, we compare all of these estimates against  $\Delta_{SG}$  calculated from numerical simulations and normalized to the same units.

One might be tempted to claim that  $\Delta_{SG}$  should increase in the presence of dissipation since  $N_g'$  increases over time. While this is true for collective dissipation, it is not necessarily true when single-particle spontaneous emission is the dominant loss process (as is the case in our experiment). This is because the relationship  $\Delta_{SG} = \chi N_g$  only holds for maximally symmetric states. In general, states with lower angular momentum will also have a smaller  $\Delta_{SG}$ . This can be seen for homogeneously coupled systems by considering a wavefunction of the form  $|\Psi_i\rangle = |J,J^z\rangle_{gb} \otimes |\psi\rangle_d$ , which is an eigenstate of the interaction term  $\chi \hat{J}^+\hat{J}^-$  with eigenvalue  $E_i = \chi(J(J+1)-J^z(J^z-1))$ . Transferring one atom symmetrically from  $|b\rangle$  to  $|d\rangle$  transforms the wavefunction to  $|\Psi_f\rangle = |J-\frac{1}{2},J^z-\frac{1}{2}\rangle_{gb} \otimes |\psi'\rangle_d$ , which can be seen using the Schwinger boson formalism introduced in Sec. 7.5.2. This is also an eigenstate of the interaction term with eigenvalue  $E_f$ , giving a total energy cost equal to

$$\Delta_{SG} = E_i - E_f = \chi \left( J(J+1) - J^z (J^z - 1) \right) - \chi \left( (J - \frac{1}{2})(J + \frac{1}{2}) - (J^z - \frac{1}{2})(J^z - \frac{3}{2}) \right)$$

$$= \chi \left( J - J^z + 1 \right) \le \chi \left( N_g + 1 \right), \tag{7.24}$$

with equality holding iff  $J = \frac{N_b + N_g}{2}$ . We conclude that as atoms dephase with fixed  $J^z$ ,  $\Delta_{\text{SG}}$  decreases.

The takeaway from this analysis is that the red dashed curve in Fig. 7.6(b) overestimates  $\Delta_{SG}$  because it does not take dephasing into account. This is verified by the fact that the computed value of  $\Delta_{SG}$  (black solid curve) lies below this curve. In Sec. 7.6, we compare  $\Delta_{SG}$  against the dissipation-free version

of  $N_g^{\prime \rm eff}$  (black dashed curve) for this reason. In fact, we see that this curve also overestimates  $\Delta_{\rm SG}$ . This is likely because the initial drive pulse does not place the system in a maximally symmetric state (atoms with different cavity couplings are initialized to a different position on the Bloch sphere).

# 7.8 Measuring the atomic inversion in real time

Earlier, we emphasized that one of the fundamental differences between the spectral gap  $\Delta_{SG}$  and the BCS gap  $\Delta_{BCS}$  is whether or not the gap-protected process involves population transfer between atomic states. We can explore this difference by directly probing the atomic inversion  $\hat{J}^z = \frac{N_b - N_g}{2}$  as a function of time after the quench. We accomplish this using a probe of the instantaneous cavity resonance frequency which we call the cavity probe. As we will describe in this section, the cavity probe utilizes the so-called "QND" Hamiltonian which takes the form [67]:

$$\hat{H}_{ac}/\hbar = (\Delta_c - 2\chi \hat{J}^z)\hat{a}^{\dagger}\hat{a}, \tag{7.25}$$

where  $\hat{a}$  is the annihilation operator for the  $\hat{y}$ -polarized cavity mode. In essence, this Hamiltonian causes a time-dependent shift in the cavity resonance frequency  $\omega_c(t)$  in response to a changing  $\langle \hat{J}^z \rangle$ , allowing us to infer the dynamics of  $\langle \hat{J}^z \rangle$  by measuring  $\omega_c(t)$ . The novel feature of this probe compared to related experiments is our pulsed cavity probe scheme, which allows us to detect rapid changes in  $\omega_c(t)$  with high dynamic range. The scheme, explained fully in the following sections, involves applying 100 ns laser pulses with center frequency  $\omega_{c0}$  every 5  $\mu$ s, similar to work performed in a resonant atom-cavity system [166].

#### 7.8.1 The QND Hamiltonian

Eq. (7.17) provides a full description of relevant features of the system. However, the effective Hamiltonian derived in Eq. (7.21) does not include the additional "QND" Hamiltonian term just introduced, which describes the key physics behind our nondestructive cavity probe. Where does the additional term come from?

The effective Hamiltonian derivation relies on an adiabatic elimination step that assumes all relevant dynamics occurs close to DC in the rotating frame of the pump laser, which is assumed to be resonant with the atomic transition. In this picture, because the cavity resonance frequency is sufficiently far-detuned, we conclude that the cavity field responds to the atoms "driving" the mode very quickly and thus can adiabatically eliminate the field. However, in the presence of an applied cavity probe laser close to resonance with the cavity (and not the atoms), the system can respond in two frequency bands, complicating this picture. In other words, the cavity field can now consist of photons both from atoms off-resonantly exciting the mode and from the resonant excitation of the mode by the laser.

To model this, we describe the pump field  $\zeta$  using two terms:  $\zeta = \zeta^{(a)} + \zeta^{(c)} e^{-i\Delta_c t}$ , near resonance with the atomic transition and cavity mode respectively. The two fields can vary in time, but we can cleanly separate the responses if we assume that  $|d_t\zeta^{(\sigma)}| \ll \Delta_c |\zeta^{(\sigma)}|$ , such that the Fourier transform of the field exhibits two well-separated regions centered at DC and  $\Delta_c$ . In experimental terms,  $\zeta^{(a)}$  represents the initial laser drive that excites the atoms.  $\zeta^{(c)}$  describes the cavity probe, which is described in detail in the next section. We can characterize the mean-field response of the system to these two separate drives by setting up the following ansatz:

$$\langle \hat{a} \rangle = a := a^{(a)} + a^{(c)} e^{-i\Delta_c t}$$

$$\langle \hat{S}_{gb,j} \rangle = S_{gb,j} := S_{gb,j}^{(a)} + S_{gb,j}^{(c)} e^{-i\Delta_c t}$$

$$\langle \hat{S}_{gb,j} \rangle = S_{gd,j} := S_{gd,j}^{(a)} + S_{gd,j}^{(c)} e^{-i\Delta_c t}$$

$$(7.26)$$

The other atomic observables ( $\hat{S}_{bd,j}$ ,  $\hat{S}_{bb,j}$ ,  $\hat{S}_{gg,j}$ , and  $\hat{S}_{dd,j}$ ) do not represent optical coherences and thus do not exhibit a response in the two (optical frequency) bands, which we will call the "atomic band" and the "cavity band." Fig. 7.7(a) demonstrates that we see well-separated atomic and cavity band responses on our heterodyne detector, justifying our treatment. In principle, the responses to the two bands can be coupled because the atomic degrees of freedom are highly nonlinear. However, if we assume any dynamics from the cavity band are sufficiently weak and that  $\Delta_c$  represents the largest dynamical frequency scale in the system, to leading order the responses are decoupled. Experimentally, this represents the limit taken by quantum nondemolition (QND) probes, which are designed to extract information with-

out significantly perturbing the atoms.

In the QND limit, the atomic band responses are well-described by the previous description in Sec. 7.7. We can calculate the mean-field cavity band responses by applying the Heisenberg equation of motion to Eq. (7.17) and separating out the frequency response at  $\Delta_c$ . This yields the following set of equations:

$$\frac{d}{dt}a^{(c)} = -\frac{\kappa}{2}a^{(c)} - g_c \sum_{j} \eta_{j} S_{gb,j}^{(c)} - i\zeta^{(c)}$$

$$\frac{d}{dt}S_{gb,j}^{(c)} = \left[i(\Delta_c - \epsilon_j) - \frac{\gamma}{2}\right] S_{gb,j}^{(c)} - i\frac{\delta_z}{2} S_{gd,j}^{(c)} - g_c \eta_{j} a^{(c)} (S_{bb,j} - S_{gg,j})$$

$$\frac{d}{dt}S_{gd,j}^{(c)} = \left[i(\Delta_c - \epsilon_j) - \frac{\gamma}{2}\right] S_{gd,j}^{(c)} - i\frac{\delta_z}{2} S_{gb,j}^{(c)} - g_c \eta_{j} a^{(c)} S_{bd,j}, \tag{7.27}$$

Note that, unlike with the atomic band, equations in the cavity band can have a macroscopic cavity mode population, and instead the atomic coherences adiabatically follow the cavity since they are off resonance by roughly  $\Delta_c$ . Therefore, we can set the time derivatives of the atomic coherences to 0. Solving the coupled equations to leading order in  $\Delta_c^{-1}$  yields:

$$S_{gb,j}^{(c)} = \frac{g_{c}\eta_{j}a^{(c)}}{\left[i(\Delta_{c} - \epsilon_{j}) - \frac{\gamma}{2}\right]^{2} + \frac{\delta_{z}^{2}}{4}} \left(i\frac{\delta_{z}}{2}S_{bd,j} + \left[i(\Delta_{c} - \epsilon_{j}) - \frac{\gamma}{2}\right](S_{bb,j} - S_{gg,j})\right)$$

$$= -i\frac{g_{c}}{\Delta_{c}}\eta_{j}a^{(c)}(S_{bb,j} - S_{gg,j}) + O(\Delta_{c}^{-2})$$

$$S_{gd,j}^{(c)} = \frac{1}{\left[i(\Delta_{c} - \epsilon_{j}) - \frac{\gamma}{2}\right]} \left(i\frac{\delta_{z}}{2}S_{gb,j}^{(c)} + g_{c}\eta_{j}a^{(c)}S_{bd,j}\right)$$

$$= -i\frac{g_{c}}{\Delta_{c}}\eta_{j}a^{(c)}S_{bd,j} + O(\Delta_{c}^{-2}).$$
(7.28)

We can then eliminate the atomic observables from the equation of motion for the classical field  $a^{(c)}$  to obtain:

$$\frac{\mathrm{d}}{\mathrm{d}t}a^{(c)} = -\frac{\kappa}{2}a^{(c)} + i\frac{g_c^2}{\Delta_c} \sum_j \eta_j^2 (S_{bb,j} - S_{gg,j})a^{(c)} - i\zeta^{(c)} 
= \left[ 2i\chi_0 \sum_j \eta_j^2 J_j^z - \frac{\kappa}{2} \right] a^{(c)} - i\zeta^{(c)},$$
(7.29)

where  $\chi_0 \approx g_c^2/\Delta_c$  is the spin-exchange interaction strength (for peak couplers) taken to the limit  $\Delta_c \gg \kappa/2$ , and  $J_j^z = \frac{1}{2}(S_{bb,j} - S_{gg,j})$  is the inversion for atom j along the bright-ground transition. We see that, at least at the mean-field level, the presence of atoms in the cavity acts as an effective frequency

shift. Experimental intuition comes from recognizing that the near-resonant atoms act as a gas with an inversion-dependent index of refraction, which changes the cavity resonance frequency.

Using the Reiter-Sørensen effective operator formalism [235] described in Sec. 2.5.2 for each  $m_J$  subspace separately, it is possible to promote this mean-field intuition into an effective QND Hamiltonian for the cavity field:

$$\hat{H}_{\text{QND}} = \left(\Delta_c - 2\chi_0 \sum_j \eta_j^2 \hat{J}_j^z\right) \hat{a}^{\dagger} \hat{a}. \tag{7.30}$$

We can follow definitions from the Supplemental Material of a previous work  $[95]^{[G]}$  and define an effective "weighted" inversion operator of the form

$$\hat{J}^{z\prime} := \frac{\sum_{j} \eta_{j}^{2} \hat{J}_{j}^{z}}{\frac{1}{N} \sum_{j} \eta_{j}^{2}},\tag{7.31}$$

defined such that  $\hat{J}^{z\prime}$  takes values between  $\pm N/2$ . Combined with an rms interaction strength  $\chi'=\chi_0(\frac{1}{N}\sum_j\eta_j^2)$ , Eq. (7.30) simplifies to  $\hat{H}_{\rm QND}=(\Delta_c-2\chi'\hat{J}^{z\prime})\hat{a}^\dagger\hat{a}$ , which is the form presented at the top of the section. In the experiment, the atoms exhibit couplings characterized by  $\eta_j=\cos(\varphi_j)$  with uniformly distributed phases  $\varphi_j\in[0,2\pi)$ . In this case, the weighted definitions evaluate to  $\hat{J}^{z\prime}=2\sum_j\eta_j^2\hat{J}_j^z$ ,  $\chi'=\chi_0/2$ . Note that both  $\chi$  and  $\hat{J}^z$  outside of this section always refer to the primed quantities defined here, which reflects weighting by cavity coupling.

## 7.8.2 The cavity probe setup

In order to measure the cavity resonance frequency  $\omega_c(t)$ , we apply a series of probe pulses at the cavity by sending RF pulses into a fiber phase modulator to periodically create an FM sideband nominally resonant with the cavity. To shape each RF pulse, we program an arbitrary waveform generator to produce an RF pulse of the form

$$V(t) = V_{\text{env}}(t)\cos(\tilde{\omega}t);$$
  $V_{\text{env}}(t) = V_0 e^{-\frac{t^2}{2\tau^2}};$   $\tau = 50 \text{ ns},$  (7.32)

where  $\tilde{\omega} = \omega_{c0} - \omega_l$  is the RF frequency necessary to generate a first-order sideband at the unshifted cavity resonance  $\omega_{c0}$ , given input light with frequency  $\omega_l$ . In our case,  $\tilde{\omega}/2\pi = -60$  MHz, which is large enough that  $V_{\rm env}(t)$  varies slowly compared to  $\tilde{\omega}$  ( $|\tilde{\omega}|\tau\gg 1$ ). The induced FM modulation therefore results in

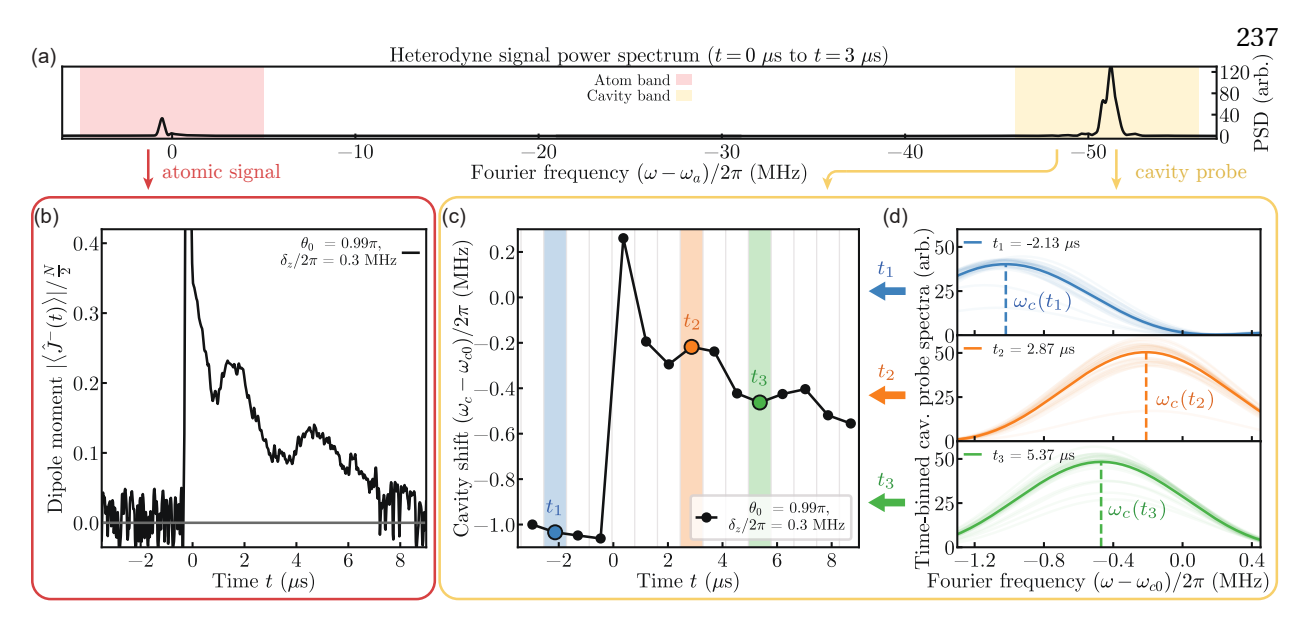


Figure 7.7: Simultaneously measuring  $\langle \hat{J}^- \rangle$  and  $\langle \hat{J}^z \rangle$ . (a) Power spectrum of the full signal measured in our heterodyne detector in a time bin from t = 0  $\mu$ s to t = 3  $\mu$ s. The atomic and cavity bands (shaded regions) are well-separated in Fourier space. (b) From the atomic band, we measure the collective dipole moment  $\langle \hat{J}^-(t) \rangle$  vs. time after the initialization drive pulse. Shown here is a trace with Rabi angle  $\theta_0 = 0.99\pi$  and Zeeman splitting  $\delta_z/2\pi = 0.3$  MHz. The inferred  $\langle \hat{J}^- \rangle$  becomes large in the roughly 200 ns during the initialization pulse, right before t = 0. We attribute this to detection of the initialization light on our detector and therefore disregard our measurements at that time. (c) From the cavity band, we measure the cavity frequency  $\omega_c$  over time (black points, with three example points highlighted in color). Rescaling by a factor of  $2\chi$  allows us to infer the effective atomic inversion  $\langle \hat{J}^z(t) \rangle = (\omega_c(t) - \omega_{c0})/2\chi$  along the  $|b\rangle$  to  $|g\rangle$  transition. We accomplish this measurement by dividing the raw heterodyne signal in this band into time bins (here,  $t_{bin} = 867$  ns for clarity, although for the main experimental result figures we use  $t_{\text{bin}} = 67$  ns for better time resolution). Three example bins are shaded to illustrate the process. (d) For each time bin, we calculate the power spectrum of the heterodyne signal. Here, we plot an averaged response (solid curves) over many instances of the experiment (faint curves) to extract a single estimate of the center frequency,  $\omega_c(t_{\rm bin})$  (dashed line). Our full analysis involves bootstrap resampling and aggregation over frequency estimates of individual runs to obtain a statistical uncertainty (not displayed).

resolved sidebands of light, which follow a Jacobi-Anger expansion:

$$E(t) = E_0 e^{i\omega_l t} \exp\left(i \frac{V_{\text{env}}(t)}{V_{\pi}} \pi \cos(\tilde{\omega} t)\right)$$

$$= E_0 \sum_{n=-\infty}^{\infty} i^n J_n \left(\frac{V_{\text{env}}(t)}{V_{\pi}} \pi\right) e^{i(\omega_l + n\tilde{\omega})t},$$
(7.33)

where  $J_n$  is the  $n^{\text{th}}$ -order cylindrical Bessel function, and  $V_\pi$  is the half-wave voltage of the fiber phase modulator. In our case,  $V_0/V_\pi \approx 0.23$ , meaning the modulator is driven close to the linear excitation regime (i.e.,  $J_1(\frac{V_{\text{env}}(t)}{V_\pi}\pi) \approx \frac{V_{\text{env}}(t)}{V_\pi}\frac{\pi}{2}$ ). As a result, we assume that the electric field of the first-order FM sideband roughly inherits the shape described by  $V_{\text{env}}(t)$ .

The Fourier spectrum of  $V_{\rm env}$  is also a Gaussian, with a standard deviation of  $\sigma=1/\tau\approx2\pi\times3.18$  MHz and a HWHM of  $\sigma\sqrt{2\ln2}\approx2\pi\times3.75$  MHz. This means that if  $\omega_c(t)-\omega_0=2\pi\times\pm3.75$  MHz at the time of the pulse, the injected electric field will be half as big as it would have been if the cavity were unshifted, resulting in a 50% reduction in signal-to-noise. In other words, the pulse ensures that the probe will have at least 50% of the maximum signal-to-noise over a 7.5 MHz band centered at  $\omega_{c0}$ . Over time, the light inside the cavity will leak out, with a 1/e time constant of  $2/\kappa\approx2.1$   $\mu$ s for the electric field. During this time, the cavity field will evolve according to Eq. (7.29) with  $\zeta^{(c)}=0$ , as long as changes in  $\hat{J}^{z\prime}$  occur much more slowly than  $\Delta_c$ , the scale separating the atomic and cavity bands. Therefore, as the light leaks out of the cavity, its frequency is modulated to match the dynamics of  $\hat{J}^{z\prime}$ . In other words, the frequency of the cavity photons adiabatically follows the cavity resonance frequency  $\omega_c(t)$ , since there are no other nearby eigenmodes to mix with. This is illustrated in Fig. 7.7(a): the cavity response (in the yellow cavity band) is well-split from the atomic transition frequency (in the red atomic band). Other cavity resonances such as different longitudinal modes are split by even larger detunings  $(\omega_{FSR}/2\pi=3.715\,{\rm GHz})$ .

We repeat the pulse described above every 5  $\mu$ s in order to keep the cavity populated with photons. In between pulses, we detect the cavity field in transmission by beating it against a local oscillator and measuring in heterodyne to infer a complex electric field amplitude as a function of time. We then time bin the trace into chunks of length  $t_{\text{bin}} = 67 \text{ ns}$  (15 bins per  $\mu$ s, compared with a 60 MS/s acquisition rate for the scope), similar to the binning shown in Fig. 7.7(c) which uses  $t_{\text{bin}} = 867 \text{ ns}$  for clarity. Within each time bin, we estimate  $\omega_c$  by calculating the peak Fourier response, as shown in Fig. 7.7(d). These fitted frequencies are then used to reconstruct the time-dependent behavior of  $\omega_c$  (Fig. 7.7(c)).

The precision of this probe relies heavily on signal-to-noise considerations. We operate at a power where the maximum intracavity photon number is roughly  $M_c \approx 30 \times 10^3$ . Due to imperfect quantum efficiency, we effectively collect about 40 photons per time bin per shot of the experiment, which does not allow for a high precision in frequency estimation. To improve this, we repeat the experiment 8 times within a single loading sequence of the experiment, over a time period of roughly 2 ms. In postprocessing, we average the complex electric field phasors from each of these experimental shots and then

estimate the frequency, which multiplies the effective photon number by 8. Then, we repeat this loading sequence for a total number of times  $n_{\rm seq}=100$ . Since we cannot ensure phase stability between loading sequences ( $t_{\rm seq}=3$  s), we could not directly average the complex phasors. Instead, we process each loading sequence separately to obtain  $n_{\rm seq}$  estimates of the cavity resonance frequency per time bin, which we then average down to increase precision by a factor of  $\sqrt{n_{\rm seq}}=10$ . We empirically find that the spread in frequency estimates is around 200 kHz at maximum intracavity power, giving us an estimated maximum frequency precision of  $\Delta\omega_c/2\pi=20$  kHz. The uncertainty region in later figures come not from this estimated precision but instead from performing a bootstrap resampling on the  $n_{\rm seq}$  frequency estimates per time bin ( $n_{\rm boot}=100$ ) and calculating the standard deviation over resampled estimates. Finally, since the signal-to-noise decreases exponentially between pulses, we repeat the experiment with the cavity probe pulses applied with a 2.5  $\mu$ s offset. In post-processing, we stitch together the two experiments to optimize the signal size in each time bin. We do not observe any distortion of the dynamics by applying the cavity probe pulses at different times.

In principle, we could improve the signal-to-noise of the probe by sending in more photons; however, if the probe becomes too strong it will start to affect the system dynamics (which we do not want). Eq. (7.30) can be interpreted as a shift of the atomic transition frequency by a characteristic amount  $\chi'\langle\hat{a}^{\dagger}\hat{a}\rangle=\chi'M_c$ , where  $M_c$  is the number of intracavity photons. We want this to be small compared with the frequencies of the Hamiltonian of interest, such as  $\chi'N\approx 2\pi\times 1$  MHz. For the estimated intracavity photon number  $M_c$ , we calculate a maximum frequency scale of  $\chi'M_c\approx (2\pi\times 35\text{ kHz})\ll \chi'N$ . The signal-to-noise could be further improved by increasing the quantum efficiency of our system, which is estimated to be around 0.02. Finally, although we don't believe it to be true in our system, laser frequency noise in the local oscillator could be a limiting factor if it is larger than the shot-noise-limited precision of the probe. Using a laser with narrower linewidth could then also benefit the probe.

## 7.8.3 Experimental results

Figs. 7.8(a)-(b) show a simplified cartoon which summarizes much of the previous section: the short pulse length induces Fourier broadening, allowing excitation of the cavity mode even if  $\omega_c(t)$  devi-

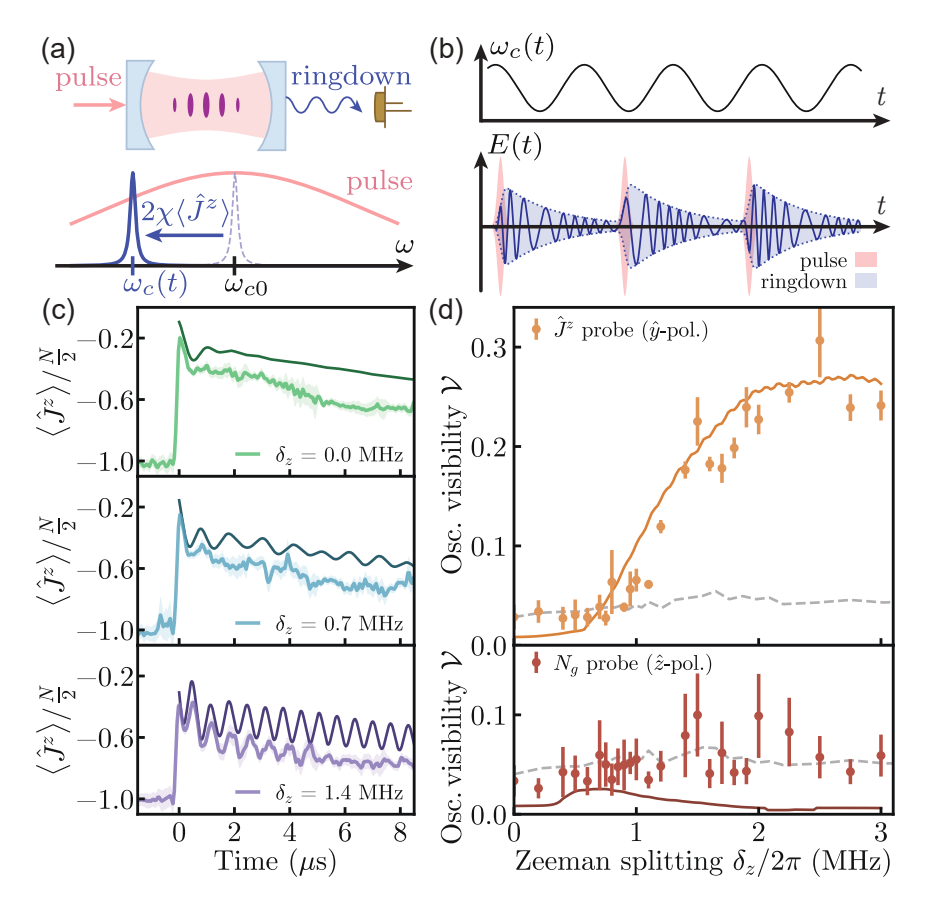


Figure 7.8: Directly measuring excited state population transfer with the cavity probe. (a) We probe the cavity resonance by sending light pulses at the cavity and detecting the transmitted light ("ringdown"). The pulses resonantly excite the cavity over a large range of  $\omega_c(t) = \omega_{c0} - 2\chi \langle \hat{J}^z \rangle$ . (b) The intracavity field adiabatically follows  $\omega_c(t)$ , which can be measured in ringdown to infer  $\langle \hat{J}^z \rangle$ . (c) Time traces of  $\langle \hat{J}^z \rangle$  (colored curves) with  $\pm 1\sigma$  bounds for different  $\delta_z$ , compared with numerical simulations (thinner dark curves).  $\langle \hat{J}^z \rangle$  is estimated in 50 ns time bins and then smoothed with a Gaussian filter ( $\tau_{\rm smooth} = 50$  ns). (d) Top:  $\langle \hat{J}^z \rangle$  oscillation visibility (circles) from t=0.5  $\mu s$  to t=5  $\mu s$ , relative to a baseline at  $\langle \hat{J}^z \rangle = -N/2$ , alongside numerical simulations (solid curve) and a noise floor (dashed line) inferred from data at  $\delta_z/2\pi = 0$  MHz. The noise floor is not flat because calculating visibility involves normalizing each data point separately. Bottom: a similar analysis for an orthogonal  $\hat{z}$ -polarized probe, which is sensitive to  $N_g$  instead of  $\langle \hat{J}^z \rangle$ . The noise floor is consistent with the top plot to aid in a visual comparison of the two probes.

ates by several MHz. This feature gives our probe a large dynamic range for  $\omega_c(t)$ . After each pulse, the cavity freely rings down, and the leakage "ringdown" light exhibits a frequency that adiabatically follows  $\omega_c(t)$  (Fig. 7.8(b)), which we measure to resolve fast changes in  $\omega_c(t)$ .

Fig. 7.8(c) shows time dynamics of  $\langle \hat{J}^z \rangle$  extracted from our probe. Before the sequence begins,  $\langle \hat{J}^z \rangle = -N/2$ . An initialization pulse at t=0 with drive angle  $\theta_0=0.5\pi$  rapidly increases  $\langle \hat{J}^z \rangle$ . Afterwards,

we observe oscillations in  $\langle \hat{J}^z \rangle$  in some datasets. For smaller  $\delta_z$ , these oscillations are hard to resolve above the probe noise floor, whereas larger  $\delta_z$  sets display more prominent oscillations. Assuming  $N_g$  does not change significantly, oscillations in  $\langle \hat{J}^z \rangle / \frac{N}{2} = (N_b - N_g)/N$  reflect transfer between  $|b\rangle$  and  $|d\rangle$ . We characterize this process by plotting the oscillation visibility for different  $\delta_z$  relative to a baseline at  $\langle \hat{J}^z \rangle = -N/2$  (orange points in Fig. 7.8(d)). Below  $\delta_z/2\pi = 1$  MHz, the lack of visibile oscillations above the noise floor indicates poor population transfer. Above this point, however, the visibility sharply rises and plateaus above 2 MHz, suggestive of large oscillations between  $|b\rangle$  and  $|d\rangle$ . The experimental data agrees well with numerical simulations (solid lines).

To confirm that the oscillations in  $\langle J^z \rangle$  arise from dynamics in  $N_b$  and not  $N_g$ , we also use a  $\hat{z}$ -polarized cavity probe (red points in Fig. 7.8(d)). In analogy with the  $\hat{y}$ -polarized probe, this probe measures oscillations of  $(N_0 - N_g)/N$ , where  $N_0$  is the population in  $|{}^3P_1, m_j = 0\rangle$ . Since we nominally do not excite this state, we assume  $N_0$  is small, such that this probe solely estimates changes in  $N_g$ . We do not measure an oscillation visibility significantly above the noise floor, so we conclude that the observed oscillations in  $\langle \hat{J}^z \rangle$  primarily represent population transfer between  $|b\rangle$  and  $|d\rangle$ .

# 7.9 Conclusion

In this work, we started with a pristine emulator of the BCS model with well-determined parameters and showed that we can add complexity in the form of controllable pair-breaking terms. Thanks to this added complexity, we were able to individually measure two distinct many-body gaps,  $\Delta_{BCS}$  and  $\Delta_{SG}$  and clarify the difference between them. These results are enabled by utilizing the relative advantages of cavity QED for studying superfluid systems: our system has direct access to multiple relevant observables, including the pairing gap  $\Delta_{BCS}$ . From a technical standpoint, the system exhibits tunable interactions without requiring a Feshbach resonance that induces significant two- and three-body losses, and our stronger interaction strength allows us to neglect the effects of vacuum loss.

In the future, we could consider further exploring the rich features of BCS superfluidity, such as higher interaction orders, using additional features in our system [144]. This experiment also shows the potential promise in leveraging multiple internal states for exploring more complex physics, such as cor-

related hopping processes between nuclear sublevels in  $^{87}$ Sr [440] or generation of multilevel entangled dark states [198, 441, 442].

## Chapter 8

#### Conclusion and outlook

In this thesis, I have presented a series of experiments engineering nonequilibrium quantum phases of matter using many ultracold strontium atoms coupled to a single mode of a high-finesse optical cavity. The central physics in these experiments is an all-to-all cavity mediated interaction between the atoms of the form  $\chi \hat{S}^+ \hat{S}^-$ , which despite its simiplicity is nonetheless responsible for basically all the interesting nonlinear and many-body phenomena highlighted in the preceding chapters. Moreover, the utility of this interaction is not limited to the experiments here. Concurrently with and following my works, the Thompson Lab has performed multiple related experiments applying these concepts to other models and systems. I would like to briefly walk through the various projects here, since I believe comparing and contrasting them helps to clarify certain subtleties. I will also tease some ideas we have been thinking about as next steps for the experiment.

### 8.1 Connections with other recent Thompson Lab experiments

### 8.1.1 Driven dissipative phases of the cooperative resonance fluorescence model

The dynamical phases in the Lipkin-Meshkov-Glick (LMG) model studied in Ch. 5 arose due to a competition between an applied drive the spin-exchange interactions, which are the dominant atom-cavity interaction when the cavity's detuning from the atomic transition  $\Delta_{ca}$  is much bigger than its linewidth  $\kappa$ . From an experimental perspective, it is easy to tune the system into a resonant regime instead ( $\Delta_{ca} = 0$ ), where now superradiance at a rate  $\Gamma N$  dominates over the spin-exchange interaction (see Ch. 2.5 for a definition of these quantities).

This new model, defined by an applied resonant drive competing with collective emission, is a classical quantum optics model known as cooperative resonance fluorescence (CRF) [454–456]. Unlike the LMG model, dissipation is crucial to the competition in the CRF model, and its resulting nonequilibrium phases are accordingly defined in terms of a steady state at long times, rather than the time-averaged Hamiltonian dynamics we explored previously. When the drive is sufficiently weak, the system is in a "superradiant phase" in which superradiance exactly cancels the drive, leading to a steady state with a finite atomic inversion but no light inside the cavity. Above a critical drive strength, superradiance cannot overcome the drive, and the system enters the "normal phase" which features rapid Rabi-like oscillation with an eventual maximally mixed steady state at inaccessibly long times. Qualitatively, the features of the superradiant and normal phases in the CRF model are quite similar to the ferromagnetic and paramagnetic phases in the LMG model, and both exhibit a second order phase transition. However, the underlying mechanisms for the two models are quite different, as are the natures of the order parameters (time-averaged compared to steady-state).

Although this model has been around for many decades and has received considerable theoretical interest, a clean experimental realization has proved elusive. A recent experiment observed qualitatively similar physics using a cloud of atoms in free space [457]. However, follow-up theoretical studies have revealed key differences between this experiment and a true CRF model, the former of which exhibits effective dipolar interactions which qualitatively and quantitatively modify the predictions [458–460]. In response to this controversy, my colleague Eric Yilun Song used our cavity QED experiment, which features true nonlocal interactions, to cleanly simulate the CRF model and observe its nonequilibrium phases along the  ${}^{1}S_{0} - {}^{3}P_{1}$  transition in  ${}^{88}Sr$  [80] [G]. Additionally, he explored a related regime in which both collective and spontaneous emission are relevant by running the experiment to timescales much longer than  $1/\gamma = 21~\mu s$ . He found that, in the presence of single-particle emission, the second order phase transition melts into a first order transition due the onset of bistability in the steady state solution. The position of the phase transition also shifts.

## 8.1.2 Cavity-mediated momentum exchange interactions

Throughout this thesis, I have referred to the cavity-mediated interactions between atoms as a "spin-exchange" interaction, despite the fact that the two-level system used in my experiments was really an electric dipole transition between atomic orbitals, rather than true spins. At the end of the day, what truly matters is that the cavity mode can mediate an exchange between states in a two-level system, regardless of what kind of two-level system you work with. My colleague Chengyi Luo on the rubidium matterwave interferometry experiment took this philosophy to heart and engineered an analogous exchange interaction between two momentum states, dubbing them "cavity-mediated momentum exchange interactions" [86] [G]. In this system, he was able to observe many of the same features as I did when simulating BCS dynamical phases (see Ch. 6), including a clean demonstration of Higgs oscillations with an oscillation frequency that scales with the interaction strength. <sup>1</sup>

On top of this, however, the fact that his interactions couple to momentum carried strange implications for the time evolution of the interferometer's atoms in position space. A superposition of momentum states looks like a standing wave in the atomic density, which acts as a Bragg grating for their input drive light. This actually forms the physical mechanism for the momentum exchange interactions, as light reflecting off that Bragg grating is equivalent to the self-generated intracavity field in my experiment. A residual momentum spread after velocity selection of less than  $0.1\hbar k$  gives the ensemble a finite extent which we refer to as a wave packet, but it also acts as a dephasing mechanism since different atoms have different kinetic energies, which leads to Doppler dephasing as discussed in Sec. 8.1.3. In position space, it turns out that this dephasing is exactly equivalent to the two wave packets separating and losing the interference responsible for their density grating. As a result, gap protecting against this dephasing must also prevent the wave packets from separating, effectively acting as a "spring" between the wave packets which causes them to oscillate but remain overlapped. Chengyi observed key signatures of this separation by applying the interaction for a short period of time during one half of a full Mach-Zehnder sequence and observing an imbalance in the echo time required to fully rephase the

<sup>&</sup>lt;sup>1</sup> Actually, his oscillations were much cleaner, since he did not suffer from the twin plagues of inhomogeneous atom-light coupling and residual motional dephasing that caused my Higgs-like excitation to quickly decay.

ensemble after recombining the wavepackets.

An additional fascinating consequence of cavity-mediated exchange interactions between untrapped atoms is that the ensemble will recoil collectively to photons in the Raman drive, rather than at a single-particle level. This concept is analogous to the Mössbauer effect in crystals, in which an individual lattice site absorbing a gamma ray causes the whole crystal to recoil rather than just the individual atom [461, 462]. To understand this claim, we'll consider the case of a single photon exciting a zero-temperature ensemble initially in the ground state. Without interactions, one of the atoms will absorb the photon and, at long times, separate from the rest of the ensemble with a recoil velocity  $v_{\rm rec}$ . However, the cavity mediated interactions cause this atom to exchange its excitation with every other atom in the ensemble, with each atom effectively possessing the excitation for a fraction 1/N of the time. On average, each atom will recoil with a reduced velocity  $v_{\rm rec}/N$ , preventing the ensemble from separating. Notably, this thought experiment does not require the exchange interactions be generated from a momentum-exchange process. In fact, it works just as well using internal levels on an optical transition (such as the experiment in Sec. 8.1.3), so long as the atoms are free to recoil from absorbing a photon.

# 8.1.3 Many-body gap protection against Doppler dephasing

Because we work with thermal atoms, the typical atom has a nonzero momentum in some random direction which causes it to move around as a function of time. If we attempt to address this atom with a laser to drive some optical transition, the phase relation between the laser and the atomic coherence then gets scrambled in the time it takes for an atom to move by one wavelength of the laser. This phenomenon is called **motional dephasing**. To formalize this, suppose the ensemble has an r.m.s. momentum  $mv_{\rm rms}$  along the direction of the laser, which has a wavevector k. Then the rate at which the atom accrues a phase shift relative to the laser due to motional dephasing is equal to  $d_t \varphi_{\rm rms} = kv_{\rm rms}$  (with a  $2\pi$  phase shift occuring in a time  $t_{2\pi} = \lambda/v_{\rm rms}$ , where  $\lambda$  is the wavelength of the laser). An equivalent picture is to note that the velocity distribution  $v_{\rm rms}$  leads to a distribution of Doppler shifts with an r.m.s. shift of  $\omega_{d,\rm rms} = kv_{\rm rms}$ , leading to **Doppler dephasing** (a synonym of motional dephasing).

A common solution to this problem is to pin the atoms in place with a sufficiently deep trap such

that the position of the atoms is defined to much better than one wavelength of the addressing light, which is equivalent to the Lamb-Dicke regime (see Ch. 3.5.2 for a more in-depth discussion). In this regime, even if the atoms are at a finite temperature, each individual atom does not undergo Doppler dephasing, allowing us to decouple internal and motional degrees of freedom.

Recently, my colleagues Zhijing Niu and Vera Schäfer on the strontium ring cavity experiment demonstrated an alternate way to suppress Doppler dephasing: by using cavity-mediated spin-exchange interactions [463]<sup>[G]</sup>. The key insight here was recognizing that, like any other mechanism for inhomogeneous broadening, Doppler dephasing can be suppressed by a sufficiently large many-body gap generated by a  $\chi \hat{S}^2$  term. To observe this physics, they loaded <sup>88</sup>Sr atoms into an optical dipole trap in their ring cavity, rather than the usual optical lattice. The dipole trap was to ensure that the atoms remain well-coupled to the cavity mode, even as they move freely along the cavity axis. Then, much like my experimental sequence when studying BCS dynamical phases in Ch. 6, they applied a  $\pi/2$  pulse along the  ${}^1S_0 - {}^3P_1$  transition using 689 nm light and measured an enhanced coherence time in their ensemble, consistent with a suppression of Doppler dephasing.

It's important to note that, despite the fact that both this experiment and the matterwave interferometry experiment (Sec. 8.1.2) both observed gap protection against Doppler dephasing, there are key differences in the way this dynamics manifested in position space. In particular, this experiment did not observe real-space oscillations of the atomic cloud analogous to the "bound" wave packets in the matterwave interferometer. Rather, the interaction forced the atoms to maintain phase coherence with the spin wave defined by the initial laser pulse, even as the atoms traversed several wavelengths of the light. Part of the reason for this is that the underlying mechanisms creating the cavity mediated exchange interactions are different. In the matterwave interferometer, exchange interactions arise from a density grating between the two momentum states which defines the relative phase between the drive and the generated intracavity field. In the ring cavity experiment, the interaction arises from an energy cost for atomic dipoles oscillating out of phase with the self-generated intracavity field, which in turn applies a corrective phase shift to the atoms. No density grating forms in this experiment due to the different internal states. Moreover, although the excited and ground states for each atom differ in momentum by one

recoil momentum  $\hbar k$ , this is much smaller than the r.m.s. momentum spread in the ensemble set by the finite temperature. As a result, while the momentum of each atom affects its spin state in the combined effects of a Doppler shift and the ensuing spin-exchange interaction dynamics, the changing spin state has negligible backaction on the momentum state. Accordingly, collective recoil effects like the thought experiment presented in Sec. 8.1.2 are difficult to observe on top of the large thermal background, even while the general principle remains true.

# 8.2 Future experiments

### 8.2.1 Photon-mediated correlated hopping on a synthetic ladder of states

The spin-exchange interactions I've discussed up until now have all effectively been along a two-level system: one atom lowers its state, and another raises its state. This is true even of the three-level system considered in Ch. 7, since the second excited state in that experiment was dark to the cavity. It's interesting to consider what happens when you expand the scope of cavity-mediated exchange interactions to a true multilevel system interacting with the cavity. In Monika Schleier-Smith's group at Stanford, researchers have explored exactly this kind of situation using the three-level F = 1 ground state manifold in <sup>87</sup>Rb, engineering a cavity-mediated interaction using a detuned two-photon process involving a Raman drive and the cavity mode [175, 377]. When they initialized their atoms in the  $|m_F = 0\rangle$  hyperfine sublevel and turned on interactions, they observed a pair production process where one atom raises its spin from  $|m_F = 0\rangle$  to  $|m_F = 1\rangle$ . Either jump on its own is a detuned process, analogous to emitting a photon into the cavity in our experiment, so in principle the number of atoms in  $|m_F = \pm 1\rangle$  should be perfectly correlated (hence, "pair creation"). This provides a mechanism for entanglement generation, which they have recently demonstrated and explored in the context of programmable graph state generation [92].

A few years ago, my colleague and close theory collaborator Anjun Chu, formerly a graduate student in Ana Maria Rey's group (along with Asier Piñeiro Orioli and Diego Barberena) published a proposal considering analogous physics in the ground  ${}^{1}S_{0}$  manifold of  ${}^{87}Sr$  [440] [G]. Due to the nuclear spin

of I=9/2, this state has not three but ten sublevels, allowing for even richer dynamics in principle. The proposal suggested initializing the atoms into the stretched  $m_F=\pm 9/2$  states and then applying circularly polarized drives detuned from the  ${}^1S_0-{}^3P_1$  transition. For the right combination of drive powers, drive frequencies, and cavity frequency, Anjun predicted that we could generate a correlated hopping process similar to that observed in the spin-1 system, but spread over all levels at once. The process involves one atom absorbing a circularly polarized photon and emitting with the opposite polarization into a detuned cavity mode, followed by another atom absorbing the cavity photon and emitting into the drive, with the two atoms thereby achieving hops of  $\Delta m=\pm 2$  respectively. At short times, atoms would hop out of  $m_F=\pm 9/2$  and into the  $m_F=\pm 5/2$  states in correlated pairs, and we may be able to measure the differential population of these states  $(N_{5/2}-N_{-5/2})$  with noise below the standard quantum limit. At longer times, these correlations should spread across all ten levels.

Around the time of writing this thesis, our lab has started attempting to engineer this physics. Admittedly, there are several challenges. Reading the populations of the different  $m_F$  states is challenging since they all couple to the same cavity mode. We are trying out methods to split the transitions out using a large magnetic field and measure ten different vacuum Rabi splittings by sweeping the cavity resonance, with some success. To observe the interaction, we must attain a four-photon resonance condition involving hops between different ground states. However, AC Stark shifts from our applied drives, which change depending on the populations of each states due to dispersive shifts of the cavity resonance, perturb this resonance significantly, requiring us to focus on stabilizing our experimental parameters. Additionally, the effects of Zeeman shifts and tensor shifts in the excited state  ${}^{3}P_{1}$  manifold are difficult to model. It is not obvious to what extent these will be an issue, and if we will have to cancel these shifts somehow. Finally, the ratio between our desired interactions and single-particle and collective dissipation scales as  $\sqrt{NC}$ , so we need this number to be large. However, Clebsch-Gordan coefficients, hyperfine branching ratios, and inhomogeneous atom-light coupling all reduce the effective size of this term, requiring us to work with a large atom number. The limited natural abundance of <sup>87</sup>Sr makes this a bit of a challenge, even with our newly replaced oven, so our cycle times are currently quite long in the 3-4 second range. Despite these challenges, I am confident that we can engineer the

interaction and see interesting physics.

#### **8.2.2** Simulating p + ip superconductors

When defining the BCS Hamiltonian in Ch. 6, we assumed that every pair of momentum labels k and k' interacted with equal strength, which maps well onto the ideal picture of an all-to-all spin-exchange interaction between Anderson pseudospins. To use language more typical for scattering theory, we modeled an s wave interaction, since electrons with momentum  $\pm k$  scatter into all possible outgoing momenta  $\pm k'$  equally. In reality, our system exhibits inhomogeneous atom-light coupling, since our trapping wavelength at 813 nm is incommensurate with our atomic transition wavelength of 689 nm (as discussed in several chapters, such as Ch. 6.10.1). If  $g_0$  represents the peak atom-cavity coupling for an atom at an antinode of the 689 nm light, then an atom at position  $z_i$  along the cavity axis will experience a coupling of  $g_i = g_0 \cos(\theta_i)$ , where  $\varphi_i = kz_i$  is the phase of the standing wave experienced by the atom. Despite this complication, we still observed the three desired dynamical phases with the help of numerical modeling.

It turns out that we may be able to utilize our inhomogeneous atom-light coupling to simulate dynamical phases of a superconductor with nonisotropic interactions between momentum states: specifically, a chiral p+ip superconductor, which can exhibit dynamical phases with nontrivial topological properties. This idea comes from a theory proposal originally designed for implementation in a Penning trap [144], but the similar all-to-all interactions between the two platforms makes it potentially feasible in a cavity QED system as well. The basic idea behind the mapping is to consider a two-dimensional momentum space, such that a 2D momentum k can be written espressed as a complex value  $k_x + ik_y$  with polar coordinates ( $r = k, \phi_k$ ). A p + ip interaction between two momenta k and k' then carries a non-isotropic dependence of the form  $kk'e^{i(\phi_k-\phi_{k'})}$ . To engineer this interaction, we can map an atom  $I = \{ij\}$  in our optical lattice with a coupling strength  $g_i$  and some semi-arbitrary phase  $\varphi_j$ , defined as the phase relative to a transverse spin wave (i.e., relative to some beam which does not have to physically exist), onto a momentum with polar coordinates ( $g_i, \varphi_j$ ). The magnitude of the cavity-mediated interaction between atoms I and I' scales like  $g_ig_{i'}$ . From the perspective of the transverse spin wave, this

coupling also carries a phase equal to  $e^{i(\varphi_j-\varphi_{j'})}$ , providing exactly the p+ip interaction form.

The prospects for simulating dynamical phases with nontrivial topology is intriguing, but there are unanswered questions about the implementation that we would need to explore. First, some of the suggested proposals for observing the desired physics have involved performing rapid  $\pi$  or  $2\pi$  pulses on the atomic state before letting the system evolve. However, in previous fast quenches of the optical transition, we have excited unwanted motional sidebands which rapidly cause dephasing in a manner which we still have not been able to perfectly model numerically Ch. 6.10.3. We could try to reduce the excitation of motional sidebands by working on methods to selectively load atoms into areas of peak coupling [464, 465], but it's not clear if we could do this without ruining the mapping between our ensemble and the 2D momentum space described previously. Additionally, directly observing the nontrivial topology of the dynamical phases probably requires performing a site-resolved measurement of the atomic state, which we currently do not have the capability to perform. There are potential indirect methods to read out a phase transition such as measuring a transition frequency, but it's not clear if the signal will be robust to experimental imperfections.

# **Bibliography**

- <sup>1</sup>X.-H. Liu, Z.-H. Li, J.-Z. Qi, and X. Zhang, "Galaxy-scale test of general relativity with strong gravitational lensing", Astrophys. J. **927**, 28 (2022).
- <sup>2</sup>P. Cladé, L. Morel, Z. Yao, and S. Guellati-Khélifa, "Determination of the fine-structure constant with a 81 parts-per-trillon accuracy", in 55th Rencontre Moriond Electroweak interactions and Unified Theories, Proceedings of the 55th Rencontre Moriond Electroweak interactions and Unified Theories (Mar. 2021).
- <sup>3</sup>B. P. Abbott et al. (LIGO Scientific Collaboration and Virgo Collaboration), "Observation of gravitational waves from a binary black hole merger", Phys. Rev. Lett. **116**, 061102 (2016).
- <sup>4</sup>ATLAS Collaboration, "Observation of a new particle in the search for the Standard Model Higgs boson with the ATLAS detector at the LHC", Phys. Lett. B **716**, 1–29 (2012).
- <sup>5</sup>P. W. Anderson, "More is different: broken symmetry and the nature of the hierarchical structure of science.", Science **177**, 393–396 (1972).
- <sup>6</sup>J. Bardeen, L. N. Cooper, and J. R. Schrieffer, "Theory of superconductivity", Phys. Rev. **108**, 1175–1204 (1957).
- <sup>7</sup>P. Anderson, **The theory of superconductivity in the high-** $T_c$  **cuprates**, Princeton series in physics (Princeton University Press, 1997).
- <sup>8</sup>D. P. Arovas, E. Berg, S. A. Kivelson, and S. Raghu, "The Hubbard model", Annu. Rev. Condens. Matter Phys. **13**, 239–274 (2022).

- <sup>9</sup>A. J. Daley, I. Bloch, C. Kokail, S. Flannigan, N. Pearson, M. Troyer, and P. Zoller, "Practical quantum advantage in quantum simulation", Nature **607**, 667–676 (2022).
- <sup>10</sup>R. Blatt and C. F. Roos, "Quantum simulations with trapped ions", Nat. Phys. **8**, 277–284 (2012).
- <sup>11</sup>C. Gross and I. Bloch, "Quantum simulations with ultracold atoms in optical lattices", Science **357**, 995–1001 (2017).
- <sup>12</sup>A. Browaeys and T. Lahaye, "Many-body physics with individually controlled Rydberg atoms", Nat. Phys. **16**, 132–142 (2020).
- <sup>13</sup>E. Altman, K. R. Brown, G. Carleo, L. D. Carr, E. Demler, C. Chin, B. DeMarco, S. E. Economou, M. A. Eriksson, K.-M. C. Fu, M. Greiner, K. R. A. Hazzard, R. G. Hulet, A. J. Kollár, B. L. Lev, M. D. Lukin, R. Ma, X. Mi, S. Misra, C. Monroe, K. Murch, Z. Nazario, K.-K. Ni, A. C. Potter, P. Roushan, M. Saffman, M. Schleier-Smith, I. Siddiqi, R. Simmonds, M. Singh, I. B. Spielman, K. Temme, D. S. Weiss, J. Vučković, V. Vuletić, J. Ye, and M. Zwierlein, "Quantum simulators: architectures and opportunities", PRX Quantum 2, 017003 (2021).
- <sup>14</sup>F. Mivehvar, F. Piazza, T. Donner, and H. Ritsch, "Cavity QED with quantum gases: new paradigms in many-body physics", Adv. Phys. **70**, 1–153 (2021).
- <sup>15</sup>L. Chomaz, I. Ferrier-Barbut, F. Ferlaino, B. Laburthe-Tolra, B. L. Lev, and T. Pfau, "Dipolar physics: a review of experiments with magnetic quantum gases", Rep. Prog. Phys. **86**, 026401 (2022).
- <sup>16</sup>N. Defenu, T. Donner, T. Macrì, G. Pagano, S. Ruffo, and A. Trombettoni, "Long-range interacting quantum systems", Rev. Mod. Phys. **95**, 035002 (2023).
- <sup>17</sup>C. W. Bauer, Z. Davoudi, A. B. Balantekin, T. Bhattacharya, M. Carena, W. A. de Jong, P. Draper, A. El-Khadra, N. Gemelke, M. Hanada, D. Kharzeev, H. Lamm, Y.-Y. Li, J. Liu, M. Lukin, Y. Meurice, C. Monroe, B. Nachman, G. Pagano, J. Preskill, E. Rinaldi, A. Roggero, D. I. Santiago, M. J. Savage, I. Siddiqi, G. Siopsis, D. Van Zanten, N. Wiebe, Y. Yamauchi, K. Yeter-Aydeniz, and S. Zorzetti, "Quantum simulation for high-energy physics", PRX Quantum 4, 027001 (2023).

- <sup>18</sup>T. Esslinger, "Fermi-Hubbard physics with atoms in an optical lattice", Ann. Rev. Condens. Matter Phys. **1**, 129–152 (2010).
- <sup>19</sup>J. Koepsell, D. Bourgund, P. Sompet, S. Hirthe, A. Bohrdt, Y. Wang, F. Grusdt, E. Demler, G. Salomon, C. Gross, and I. Bloch, "Microscopic evolution of doped Mott insulators from polaronic metal to Fermi liquid", Science **374**, 82–86 (2021).
- <sup>20</sup>B. M. Spar, E. Guardado-Sanchez, S. Chi, Z. Z. Yan, and W. S. Bakr, "Realization of a Fermi-Hubbard optical tweezer array", Phys. Rev. Lett. **128**, 223202 (2022).
- <sup>21</sup>X. Wang, E. Khatami, F. Fei, J. Wyrick, P. Namboodiri, R. Kashid, A. F. Rigosi, G. Bryant, and R. Silver, "Experimental realization of an extended Fermi-Hubbard model using a 2D lattice of dopant-based quantum dots", Nat. Commun. **13**, 6824 (2022).
- <sup>22</sup>M. Lebrat, M. Xu, L. H. Kendrick, A. Kale, Y. Gang, P. Seetharaman, I. Morera, E. Khatami, E. Demler, and M. Greiner, "Observation of Nagaoka polarons in a Fermi–Hubbard quantum simulator", Nature **629**, 317–322 (2024).
- <sup>23</sup>M. L. Prichard, B. M. Spar, I. Morera, E. Demler, Z. Z. Yan, and W. S. Bakr, "Directly imaging spin polarons in a kinetically frustrated Hubbard system", Nature **629**, 323–328 (2024).
- <sup>24</sup>C. S. Chiu, G. Ji, A. Bohrdt, M. Xu, M. Knap, E. Demler, F. Grusdt, M. Greiner, and D. Greif, "String patterns in the doped Hubbard model", Science **365**, 251–256 (2019).
- <sup>25</sup>J. Eisert, M. Friesdorf, and C. Gogolin, "Quantum many-body systems out of equilibrium", Nat. Phys.
   11, 124–130 (2015).
- <sup>26</sup>T. W. Clark, A. Dombi, F. I. B. Williams, Á. Kurkó, J. Fortágh, D. Nagy, A. Vukics, and P. Domokos, "Time-resolved observation of a dynamical phase transition with atoms in a cavity", Phys. Rev. A **105**, 063712 (2022).
- <sup>27</sup>B. P. Marsh, R. M. Kroeze, S. Ganguli, S. Gopalakrishnan, J. Keeling, and B. L. Lev, "Entanglement and replica symmetry breaking in a driven-dissipative quantum spin glass", Phys. Rev. X 14, 011026 (2024).

- <sup>28</sup>H. W. Chan, A. T. Black, and V. Vuletić, "Observation of collective-emission-induced cooling of atoms in an optical cavity", Phys. Rev. Lett. **90**, 063003 (2003).
- <sup>29</sup>A. T. Black, H. W. Chan, and V. Vuletić, "Observation of collective friction forces due to spatial selforganization of atoms: from Rayleigh to Bragg scattering", Phys. Rev. Lett. **91**, 203001 (2003).
- <sup>30</sup>A. T. Black, J. K. Thompson, and V. Vuletić, "Collective light forces on atoms in resonators", J. Phys. B: At. Mol. Opt. Phys. **38**, S605 (2005).
- <sup>31</sup>V. Vuletić, J. K. Thompson, A. T. Black, and J. Simon, "External-feedback laser cooling of molecular gases", Phys. Rev. A **75**, 051405 (2007).
- <sup>32</sup>K. Baumann, C. Guerlin, F. Brennecke, and T. Esslinger, "Dicke quantum phase transition with a superfluid gas in an optical cavity", Nature **464**, 1301–1306 (2010).
- <sup>33</sup>J. Klinder, H. Keßler, M. Wolke, L. Mathey, and A. Hemmerich, "Dynamical phase transition in the open Dicke model", Proc. Natl. Acad. Sci. U.S.A. **112**, 3290–3295 (2015).
- <sup>34</sup>M. Landini, N. Dogra, K. Kroeger, L. Hruby, T. Donner, and T. Esslinger, "Formation of a spin texture in a quantum gas coupled to a cavity", Phys. Rev. Lett. **120**, 223602 (2018).
- <sup>35</sup>R. M. Kroeze, Y. Guo, V. D. Vaidya, J. Keeling, and B. L. Lev, "Spinor self-ordering of a quantum gas in a cavity", Phys. Rev. Lett. **121**, 163601 (2018).
- <sup>36</sup>R. M. Kroeze, Y. Guo, and B. L. Lev, "Dynamical spin-orbit coupling of a quantum gas", Phys. Rev. Lett. **123**, 160404 (2019).
- <sup>37</sup>H. Keßler, P. Kongkhambut, C. Georges, L. Mathey, J. G. Cosme, and A. Hemmerich, "Observation of a dissipative time crystal", Phys. Rev. Lett. **127**, 043602 (2021).
- <sup>38</sup>D. Dreon, A. Baumgärtner, X. Li, S. Hertlein, T. Esslinger, and T. Donner, "Self-oscillating pump in a topological dissipative atom–cavity system", Nature **608**, 494–498 (2022).
- <sup>39</sup>J. Ho, Y.-H. Lu, T. Xiang, C. C. Rusconi, S. J. Masson, A. Asenjo-Garcia, Z. Yan, and D. M. Stamper-Kurn, "Optomechanical self-organization in a mesoscopic atom array", Nat. Phys. **21**, xx–xx (2025).

- <sup>40</sup>D. Rivero, C. Pessoa Jr, G. de França, R. C. Teixeira, S. Slama, and P. W. Courteille, "Quantum resonant optical bistability with a narrow atomic transition: bistability phase diagram in the bad cavity regime", New Journal of Physics **25**, 093053 (2023).
- <sup>41</sup>M. Xu, D. A. Tieri, E. C. Fine, J. K. Thompson, and M. J. Holland, "Synchronization of two ensembles of atoms", Phys. Rev. Lett. **113**, 154101 (2014).
- <sup>42</sup>A. Patra, B. L. Altshuler, and E. A. Yuzbashyan, "Chaotic synchronization between atomic clocks", Phys. Rev. A **100**, 023418 (2019).
- <sup>43</sup>B. Zhu, J. Schachenmayer, M. Xu, F. Herrera, J. G. Restrepo, M. J. Holland, and A. M. Rey, "Synchronization of interacting quantum dipoles", New J. Phys. **17**, 083063 (2015).
- <sup>44</sup>M. Xu, S. B. Jäger, S. Schütz, J. Cooper, G. Morigi, and M. J. Holland, "Supercooling of atoms in an optical resonator", Phys. Rev. Lett. **116**, 153002 (2016).
- <sup>45</sup>S. B. Jäger, M. J. Holland, and G. Morigi, "Superradiant optomechanical phases of cold atomic gases in optical resonators", Phys. Rev. A **101**, 023616 (2020).
- <sup>46</sup>S. B. Jäger, H. Liu, J. Cooper, T. L. Nicholson, and M. J. Holland, "Superradiant emission of a thermal atomic beam into an optical cavity", Phys. Rev. A **104**, 033711 (2021).
- <sup>47</sup>J. M. Weiner, K. C. Cox, J. G. Bohnet, and J. K. Thompson, "Phase synchronization inside a superradiant laser", Phys. Rev. A **95**, 033808 (2017).
- <sup>48</sup>R. Nandkishore and D. A. Huse, "Many-body localization and thermalization in quantum statistical mechanics", Annu. Rev. Condens. Matter Phys **6**, 15–38 (2015).
- <sup>49</sup>D. A. Abanin, E. Altman, I. Bloch, and M. Serbyn, "Colloquium: many-body localization, thermalization, and entanglement", Rev. Mod. Phys. **91**, 021001 (2019).
- <sup>50</sup>M. Gärttner, J. G. Bohnet, A. Safavi-Naini, M. L. Wall, J. J. Bollinger, and A. M. Rey, "Measuring out-of-time-order correlations and multiple quantum spectra in a trapped-ion quantum magnet", Nat. Phys. **13**, 781–786 (2017).

- <sup>51</sup>J. Li, R. Fan, H. Wang, B. Ye, B. Zeng, H. Zhai, X. Peng, and J. Du, "Measuring out-of-time-order correlators on a nuclear magnetic resonance quantum simulator", Phys. Rev. X **7**, 031011 (2017).
- <sup>52</sup>M. P. Zaletel, M. Lukin, C. Monroe, C. Nayak, F. Wilczek, and N. Y. Yao, "Colloquium: quantum and classical discrete time crystals", Rev. Mod. Phys. **95**, 031001 (2023).
- <sup>53</sup>C. J. Turner, A. A. Michailidis, D. A. Abanin, M. Serbyn, and Z. Papić, "Weak ergodicity breaking from quantum many-body scars", Nat. Phys. **14**, 745–749 (2018).
- <sup>54</sup>D. Bluvstein, A. Omran, H. Levine, A. Keesling, G. Semeghini, S. Ebadi, T. T. Wang, A. A. Michailidis, N. Maskara, W. W. Ho, S. Choi, M. Serbyn, M. Greiner, V. Vuletić, and M. D. Lukin, "Controlling quantum many-body dynamics in driven Rydberg atom arrays", Science 371, 1355–1359 (2021).
- <sup>55</sup>J. Marino, M. Eckstein, M. Foster, and A.-M. Rey, "Dynamical phase transitions in the collisionless pre-thermal states of isolated quantum systems: theory and experiments", Rep. Prog. Phys. **85**, 116001 (2022).
- <sup>56</sup>J. Bochmann, M. Mücke, C. Guhl, S. Ritter, G. Rempe, and D. L. Moehring, "Lossless state detection of single neutral atoms", Phys. Rev. Lett. **104**, 203601 (2010).
- <sup>57</sup>R. Gehr, J. Volz, G. Dubois, T. Steinmetz, Y. Colombe, B. L. Lev, R. Long, J. Estève, and J. Reichel, "Cavity-based single atom preparation and high-fidelity hyperfine state readout", Phys. Rev. Lett. **104**, 203602 (2010).
- <sup>58</sup>E. Deist, Y.-H. Lu, J. Ho, M. K. Pasha, J. Zeiher, Z. Yan, and D. M. Stamper-Kurn, "Mid-circuit cavity measurement in a neutral atom array", Phys. Rev. Lett. **129**, 203602 (2022).
- <sup>59</sup>B. Hu, J. Sinclair, E. Bytyqi, M. Chong, A. Rudelis, J. Ramette, Z. Vendeiro, and V. Vuletić, "Site-selective cavity readout and classical error correction of a 5-bit atomic register", Phys. Rev. Lett. **134**, 120801 (2025).
- <sup>60</sup>A. Kuzmich, N. P. Bigelow, and L. Mandel, "Atomic quantum non-demolition measurements and squeezing", EPL **42**, 481 (1998).

- <sup>61</sup>J. Appel, P. J. Windpassinger, D. Oblak, U. B. Hoff, N. Kjærgaard, and E. S. Polzik, "Mesoscopic atomic entanglement for precision measurements beyond the standard quantum limit", Proc. Natl. Acad. Sci. U.S.A. **106**, 10960–10965 (2009).
- <sup>62</sup>M. H. Schleier-Smith, I. D. Leroux, and V. Vuletić, "States of an ensemble of two-level atoms with reduced quantum uncertainty", Phys. Rev. Lett. **104**, 073604 (2010).
- <sup>63</sup>Z. Chen, J. G. Bohnet, S. R. Sankar, J. Dai, and J. K. Thompson, "Conditional spin squeezing of a large ensemble via the vacuum Rabi splitting", Phys. Rev. Lett. **106**, 133601 (2011).
- <sup>64</sup>J. G. Bohnet, K. C. Cox, M. A. Norcia, J. M. Weiner, Z. Chen, and J. K. Thompson, "Reduced spin measurement back-action for a phase sensitivity ten times beyond the standard quantum limit", Nat. Photonics **8**, 731–736 (2014).
- <sup>65</sup>K. C. Cox, G. P. Greve, B. Wu, and J. K. Thompson, "Spatially homogeneous entanglement for matterwave interferometry created with time-averaged measurements", Phys. Rev. A **94**, 061601 (2016).
- <sup>66</sup>M. Kitagawa and M. Ueda, "Squeezed spin states", Phys. Rev. A **47**, 5138–5143 (1993).
- <sup>67</sup>M. H. Schleier-Smith, I. D. Leroux, and V. Vuletić, "Squeezing the collective spin of a dilute atomic ensemble by cavity feedback", Phys. Rev. A **81**, 021804 (2010).
- <sup>68</sup>I. D. Leroux, M. H. Schleier-Smith, and V. Vuletić, "Implementation of cavity squeezing of a collective atomic spin", Phys. Rev. Lett. **104**, 073602 (2010).
- <sup>69</sup>O. Hosten, N. J. Engelsen, R. Krishnakumar, and M. A. Kasevich, "Measurement noise 100 times lower than the quantum-projection limit using entangled atoms", Nature **529**, 505–508 (2016).
- <sup>70</sup>K. C. Cox, G. P. Greve, J. M. Weiner, and J. K. Thompson, "Deterministic squeezed states with collective measurements and feedback", Phys. Rev. Lett. **116**, 093602 (2016).
- <sup>71</sup>G. P. Greve, C. Luo, B. Wu, and J. K. Thompson, "Entanglement-enhanced matter-wave interferometry in a high-finesse cavity", Nature **610**, 472–477 (2022).

- <sup>72</sup>E. Pedrozo-Peñafiel, S. Colombo, C. Shu, A. F. Adiyatullin, Z. Li, E. Mendez, B. Braverman, A. Kawasaki,
   D. Akamatsu, Y. Xiao, et al., "Entanglement on an optical atomic-clock transition", Nature 588, 414–418 (2020).
- <sup>73</sup>J. M. Robinson, M. Miklos, Y. M. Tso, C. J. Kennedy, T. Bothwell, D. Kedar, J. K. Thompson, and J. Ye, "Direct comparison of two spin-squeezed optical clock ensembles at the 10<sup>-17</sup> level", Nat. Phys. **20**, 208–213 (2024).
- <sup>74</sup>F. Brennecke, T. Donner, S. Ritter, T. Bourdel, M. Köhl, and T. Esslinger, "Cavity QED with a Bose–Einstein condensate", Nature **450**, 268–271 (2007).
- <sup>75</sup>F. Dimer, B. Estienne, A. S. Parkins, and H. J. Carmichael, "Proposed realization of the Dicke-model quantum phase transition in an optical cavity QED system", Phys. Rev. A **75**, 013804 (2007).
- <sup>76</sup>M. P. Baden, K. J. Arnold, A. L. Grimsmo, S. Parkins, and M. D. Barrett, "Realization of the Dicke model using cavity-assisted Raman transitions", Phys. Rev. Lett. **113**, 020408 (2014).
- <sup>77</sup>J. Klinder, H. Keßler, M. R. Bakhtiari, M. Thorwart, and A. Hemmerich, "Observation of a superradiant Mott insulator in the Dicke-Hubbard model", Phys. Rev. Lett. 115, 230403 (2015).
- <sup>78</sup>D. Nagy, G. Szirmai, and P. Domokos, "Self-organization of a Bose-Einstein condensate in an optical cavity", Eur. Phys. J. D **48**, 127–137 (2008).
- <sup>79</sup>P. Kongkhambut, J. Skulte, L. Mathey, J. G. Cosme, A. Hemmerich, and H. Keßler, "Observation of a continuous time crystal", Science **377**, 670–673 (2022).
- <sup>80</sup>E. Y. Song, D. Barberena, D. J. Young, E. Chaparro, A. Chu, S. Agarwal, Z. Niu, J. T. Young, A. M. Rey, and J. K. Thompson, "A dissipation-induced superradiant transition in a strontium cavity-QED system", Science Advances 11, eadu5799 (2025).
- <sup>81</sup>S. C. Schuster, P. Wolf, S. Ostermann, S. Slama, and C. Zimmermann, "Supersolid properties of a bose-einstein condensate in a ring resonator", Phys. Rev. Lett. **124**, 143602 (2020).

- <sup>82</sup>C. von Cube, S. Slama, D. Kruse, C. Zimmermann, P. W. Courteille, G. R. M. Robb, N. Piovella, Bonifacio, and R., "Self-synchronization and dissipation-induced threshold in collective atomic recoil lasing", Phys. Rev. Lett. **93**, 083601 (2004).
- <sup>83</sup>S. Slama, S. Bux, G. Krenz, C. Zimmermann, and P. W. Courteille, "Superradiant rayleigh scattering and collective atomic recoil lasing in a ring cavity", Phys. Rev. Lett. **98**, 053603 (2007).
- <sup>84</sup>S. Bux, H. Tomczyk, D. Schmidt, P. W. Courteille, N. Piovella, and C. Zimmermann, "Control of matterwave superradiance with a high-finesse ring cavity", Phys. Rev. A **87**, 023607 (2013).
- <sup>85</sup>E. J. Davis, A. Periwal, E. S. Cooper, G. Bentsen, S. J. Evered, K. Van Kirk, and M. H. Schleier-Smith, "Protecting spin coherence in a tunable Heisenberg model", Phys. Rev. Lett. **125**, 060402 (2020).
- <sup>86</sup>C. Luo, H. Zhang, A. Chu, C. Maruko, A. M. Rey, and J. K. Thompson, "Hamiltonian engineering of collective XYZ spin models in an optical cavity", Nat. Phys. **21**, 916–923 (2025).
- <sup>87</sup>S. Sachdev and J. Ye, "Gapless spin-fluid ground state in a random quantum Heisenberg magnet", Phys. Rev. Lett. **70**, 3339–3342 (1993).
- <sup>88</sup>G. Bentsen, T. Hashizume, A. S. Buyskikh, E. J. Davis, A. J. Daley, S. S. Gubser, and M. Schleier-Smith, "Treelike interactions and fast scrambling with cold atoms", Phys. Rev. Lett. **123**, 130601 (2019).
- <sup>89</sup>B. Swingle, G. Bentsen, M. Schleier-Smith, and P. Hayden, "Measuring the scrambling of quantum information", Phys. Rev. A **94**, 040302 (2016).
- <sup>90</sup>C. Luo, H. Zhang, C. Maruko, E. A. Bohr, A. Chu, A. M. Rey, and J. K. Thompson, **Realization of three** and four-body interactions between momentum states in a cavity through optical dressing, Provisionally accepted in Science, 2024, arXiv:2410.12132 [quant-ph].
- <sup>91</sup>L. W. Clark, N. Schine, C. Baum, N. Jia, and J. Simon, "Observation of Laughlin states made of light", Nature **582**, 41–45 (2020).
- <sup>92</sup>E. S. Cooper, P. Kunkel, A. Periwal, and M. Schleier-Smith, "Graph states of atomic ensembles engineered by photon-mediated entanglement", Nat. Phys. **20**, 770–775 (2024).

- <sup>93</sup>M. A. Norcia, J. R. K. Cline, J. A. Muniz, J. M. Robinson, R. B. Hutson, A. Goban, G. E. Marti, J. Ye, and J. K. Thompson, "Frequency measurements of superradiance from the strontium clock transition", Phys. Rev. X 8, 021036 (2018).
- <sup>94</sup>J. Hu, W. Chen, Z. Vendeiro, A. Urvoy, B. Braverman, and V. Vuleti ć, "Vacuum spin squeezing", Phys. Rev. A **96**, 050301 (2017).
- <sup>95</sup>M. A. Norcia, R. J. Lewis-Swan, J. R. Cline, B. Zhu, A. M. Rey, and J. K. Thompson, "Cavity-mediated collective spin-exchange interactions in a strontium superradiant laser", Science **361**, 259–262 (2018).
- <sup>96</sup>J. A. Muniz, D. J. Young, J. R. K. Cline, and J. K. Thompson, "Cavity-QED measurements of the <sup>87</sup>Sr millihertz optical clock transition and determination of its natural linewidth", Phys. Rev. Res. **3**, 023152 (2021).
- $^{97}$ S. B. Koller, J. Grotti, S. Vogt, A. Al-Masoudi, S. Dörscher, S. Häfner, U. Sterr, and C. Lisdat, "Transportable optical lattice clock with  $7 \times 10^{-17}$  uncertainty", Phys. Rev. Lett. **118**, 073601 (2017).
- <sup>98</sup>S. L. Campbell, R. B. Hutson, G. E. Marti, A. Goban, N. Darkwah Oppong, R. L. McNally, L. Sonderhouse, J. M. Robinson, W. Zhang, B. J. Bloom, and J. Ye, "A Fermi-degenerate three-dimensional optical lattice clock", Science **358**, 90–94 (2017).
- <sup>99</sup>R. Schwarz, S. Dörscher, A. Al-Masoudi, E. Benkler, T. Legero, U. Sterr, S. Weyers, J. Rahm, B. Lipphardt, and C. Lisdat, "Long term measurement of the <sup>87</sup>Sr clock frequency at the limit of primary Cs clocks", Phys. Rev. Res. **2**, 033242 (2020).
- <sup>100</sup>N. Ohmae, M. Takamoto, Y. Takahashi, M. Kokubun, K. Araki, A. Hinton, I. Ushijima, T. Muramatsu, T. Furumiya, Y. Sakai, N. Moriya, N. Kamiya, K. Fujii, R. Muramatsu, T. Shiimado, and H. Katori, "Transportable strontium optical lattice clocks operated outside laboratory at the level of 10<sup>-18</sup> uncertainty", Adv. Quantum Technol. 4, 2100015 (2021).
- $^{101}$ A. Aeppli, K. Kim, W. Warfield, M. S. Safronova, and J. Ye, "Clock with  $8 \times 10^{-19}$  systematic uncertainty", Phys. Rev. Lett. **133**, 023401 (2024).

- <sup>102</sup>M. Walhout, U. Sterr, A. Witte, and S. L. Rolston, "Lifetime of the metastable 6s' [1/2]<sub>0</sub> clock state in xenon", Opt. Lett. **20**, 1192–1194 (1995).
- $^{103}$ M. Yasuda and H. Katori, "Lifetime measurement of the  $^{3}P_{2}$  metastable state of strontium atoms", Phys. Rev. Lett. **92**, 153004 (2004).
- <sup>104</sup>S. Dörscher, R. Schwarz, A. Al-Masoudi, S. Falke, U. Sterr, and C. Lisdat, "Lattice-induced photon scattering in an optical lattice clock", Phys. Rev. A **97**, 063419 (2018).
- <sup>105</sup>S. Origlia, M. S. Pramod, S. Schiller, Y. Singh, K. Bongs, R. Schwarz, A. Al-Masoudi, S. Dörscher, S. Herbers, S. Häfner, U. Sterr, and C. Lisdat, "Towards an optical clock for space: compact, high-performance optical lattice clock based on bosonic atoms", Phys. Rev. A 98, 053443 (2018).
- <sup>106</sup>R. B. Hutson, A. Goban, G. E. Marti, L. Sonderhouse, C. Sanner, and J. Ye, "Engineering quantum states of matter for atomic clocks in shallow optical lattices", Phys. Rev. Lett. **123**, 123401 (2019).
- <sup>107</sup>M. M. Boyd, T. Zelevinsky, A. D. Ludlow, S. Blatt, T. Zanon-Willette, S. M. Foreman, and J. Ye, "Nuclear spin effects in optical lattice clocks", Phys. Rev. A **76**, 022510 (2007).
- <sup>108</sup>J. A. Muniz, D. Barberena, R. J. Lewis-Swan, D. J. Young, J. R. Cline, A. M. Rey, and J. K. Thompson, "Exploring dynamical phase transitions with cold atoms in an optical cavity", Nature **580**, 602–607 (2020).
- <sup>109</sup>H. Lipkin, N. Meshkov, and A. Glick, "Validity of many-body approximation methods for a solvable model: (I). exact solutions and perturbation theory", Nucl. Phys. **62**, 188–198 (1965).
- <sup>110</sup>P. Ribeiro, J. Vidal, and R. Mosseri, "Thermodynamical limit of the Lipkin-Meshkov-Glick model", Phys. Rev. Lett. **99**, 050402 (2007).
- <sup>111</sup>A. Smerzi, S. Fantoni, S. Giovanazzi, and S. R. Shenoy, "Quantum coherent atomic tunneling between two trapped Bose-Einstein condensates", Phys. Rev. Lett. **79**, 4950–4953 (1997).
- <sup>112</sup>M. Albiez, R. Gati, J. Fölling, S. Hunsmann, M. Cristiani, and M. K. Oberthaler, "Direct observation of tunneling and nonlinear self-trapping in a single bosonic Josephson junction", Phys. Rev. Lett. 95, 010402 (2005).

- <sup>113</sup>A. Reinhard, J.-F. Riou, L. A. Zundel, D. S. Weiss, S. Li, A. M. Rey, and R. Hipolito, "Self-trapping in an array of coupled 1D Bose gases", Phys. Rev. Lett. **110**, 033001 (2013).
- <sup>114</sup>M. Abbarchi, A. Amo, V. Sala, D. Solnyshkov, H. Flayac, L. Ferrier, I. Sagnes, E. Galopin, A. Lemaître, G. Malpuech, et al., "Macroscopic quantum self-trapping and Josephson oscillations of exciton polaritons", Nat. Phys. 9, 275–279 (2013).
- <sup>115</sup>M. Eckstein, M. Kollar, and P. Werner, "Thermalization after an interaction quench in the Hubbard model", Phys. Rev. Lett. **103**, 056403 (2009).
- <sup>116</sup>M. Schiró and M. Fabrizio, "Time-dependent mean field theory for quench dynamics in correlated electron systems", Phys. Rev. Lett. **105**, 076401 (2010).
- <sup>117</sup>B. Sciolla and G. Biroli, "Quantum quenches and off-equilibrium dynamical transition in the infinite-dimensional Bose-Hubbard model", Phys. Rev. Lett. **105**, 220401 (2010).
- <sup>118</sup>A. Gambassi and P. Calabrese, "Quantum quenches as classical critical films", EPL **95**, 66007 (2011).
- <sup>119</sup>P. Smacchia, M. Knap, E. Demler, and A. Silva, "Exploring dynamical phase transitions and prethermalization with quantum noise of excitations", Phys. Rev. B **91**, 205136 (2015).
- <sup>120</sup>J. Zhang, G. Pagano, P. W. Hess, A. Kyprianidis, P. Becker, H. Kaplan, A. V. Gorshkov, Z.-X. Gong, and C. Monroe, "Observation of a many-body dynamical phase transition with a 53-qubit quantum simulator", Nature **551**, 601–604 (2017).
- <sup>121</sup>S. Smale, P. He, B. A. Olsen, K. G. Jackson, H. Sharum, S. Trotzky, J. Marino, A. M. Rey, and J. H. Thywissen, "Observation of a transition between dynamical phases in a quantum degenerate Fermi gas", Sci. Adv. 5, eaax1568 (2019).
- <sup>122</sup>H.-X. Yang, T. Tian, Y.-B. Yang, L.-Y. Qiu, H.-Y. Liang, A.-J. Chu, C. B. Da ğ, Y. Xu, Y. Liu, and L.-M. Duan, "Observation of dynamical quantum phase transitions in a spinor condensate", Phys. Rev. A 100, 013622 (2019).

- <sup>123</sup>T. Tian, H.-X. Yang, L.-Y. Qiu, H.-Y. Liang, Y.-B. Yang, Y. Xu, and L.-M. Duan, "Observation of dynamical quantum phase transitions with correspondence in an excited state phase diagram", Phys. Rev. Lett. **124**, 043001 (2020).
- <sup>124</sup>A. Chu, J. Will, J. Arlt, C. Klempt, and A. M. Rey, "Simulation of *XXZ* spin models using sideband transitions in trapped bosonic gases", Phys. Rev. Lett. **125**, 240504 (2020).
- <sup>125</sup>A. Aeppli, A. Chu, T. Bothwell, C. J. Kennedy, D. Kedar, P. He, A. M. Rey, and J. Ye, "Hamiltonian engineering of spin-orbit-coupled fermions in a Wannier-Stark optical lattice clock", Sci. Adv. 8, eadc9242 (2022).
- <sup>126</sup>D. J. Young, A. Chu, E. Y. Song, D. Barberena, D. Wellnitz, Z. Niu, V. Schäfer, R. J. Lewis-Swan, A. M. Rey, and J. K. Thompson, "Observing dynamical phases of BCS superconductors in a cavity QED simulator", Nature **625**, 679–684 (2024).
- <sup>127</sup>R. A. Barankov, L. S. Levitov, and B. Z. Spivak, "Collective Rabi oscillations and solitons in a time-dependent BCS pairing problem", Phys. Rev. Lett. **93**, 160401 (2004).
- <sup>128</sup>E. A. Yuzbashyan, B. L. Altshuler, V. B. Kuznetsov, and V. Z. Enolskii, "Solution for the dynamics of the BCS and central spin problems", J. Phys. A: Math. Gen. **38**, 7831–7849 (2005).
- <sup>129</sup>E. A. Yuzbashyan, O. Tsyplyatyev, and B. L. Altshuler, "Relaxation and persistent oscillations of the order parameter in fermionic condensates", Phys. Rev. Lett. **96**, 097005 (2006).
- <sup>130</sup>R. A. Barankov and L. S. Levitov, "Synchronization in the BCS pairing dynamics as a critical phenomenon", Phys. Rev. Lett. **96**, 230403 (2006).
- <sup>131</sup>E. A. Yuzbashyan and M. Dzero, "Dynamical vanishing of the order parameter in a fermionic condensate", Phys. Rev. Lett. **96**, 230404 (2006).
- <sup>132</sup>V. Gurarie and L. Radzihovsky, "Resonantly paired fermionic superfluids", Ann. Phys. (N. Y.) **322**, January Special Issue 2007, 2–119 (2007).
- <sup>133</sup>E. A. Yuzbashyan, "Normal and anomalous solitons in the theory of dynamical Cooper pairing", Phys. Rev. B **78**, 184507 (2008).

- <sup>134</sup>V. Gurarie, "Nonequilibrium dynamics of weakly and strongly paired superconductors", Phys. Rev. Lett. **103**, 075301 (2009).
- $^{135}$ M. S. Foster, M. Dzero, V. Gurarie, and E. A. Yuzbashyan, "Quantum quench in a p+ip superfluid: winding numbers and topological states far from equilibrium", Phys. Rev. B **88**, 104511 (2013).
- <sup>136</sup>M. S. Foster, V. Gurarie, M. Dzero, and E. A. Yuzbashyan, "Quench-induced Floquet topological *p*-wave superfluids", Phys. Rev. Lett. **113**, 076403 (2014).
- <sup>137</sup>E. A. Yuzbashyan, M. Dzero, V. Gurarie, and M. S. Foster, "Quantum quench phase diagrams of an *s*-wave BCS-BEC condensate", Phys. Rev. A **91**, 033628 (2015).
- <sup>138</sup>B. Mansart, J. Lorenzana, A. Mann, A. Odeh, M. Scarongella, M. Chergui, and F. Carbone, "Coupling of a high-energy excitation to superconducting quasiparticles in a cuprate from coherent charge fluctuation spectroscopy", Proc. Natl. Acad. Sci. U.S.A. 110, 4539–4544 (2013).
- $^{139}$ R. Matsunaga, Y. I. Hamada, K. Makise, Y. Uzawa, H. Terai, Z. Wang, and R. Shimano, "Higgs amplitude mode in the BCS superconductors  $Nb_{1-x}Ti_xN$  induced by terahertz pulse excitation", Phys. Rev. Lett. **111**, 057002 (2013).
- <sup>140</sup>R. Matsunaga, N. Tsuji, H. Fujita, A. Sugioka, K. Makise, Y. Uzawa, H. Terai, Z. Wang, H. Aoki, and R. Shimano, "Light-induced collective pseudospin precession resonating with Higgs mode in a superconductor", Science 345, 1145–1149 (2014).
- <sup>141</sup>A. Behrle, T. Harrison, J. Kombe, K. Gao, M. Link, J.-S. Bernier, C. Kollath, and M. Köhl, "Higgs mode in a strongly interacting fermionic superfluid", Nat. Phys. 14, 781–785 (2018).
- <sup>142</sup>P. Dyke, S. Musolino, H. Kurkjian, D. J. M. Ahmed-Braun, A. Pennings, I. Herrera, S. Hoinka, S. J. J. M. F. Kokkelmans, V. E. Colussi, and C. J. Vale, "Higgs oscillations in a unitary Fermi superfluid", Phys. Rev. Lett. 132, 223402 (2024).
- <sup>143</sup>P. W. Anderson, "Random-phase approximation in the theory of superconductivity", Phys. Rev. **112**, 1900–1916 (1958).

- $^{144}$ A. Shankar, E. A. Yuzbashyan, V. Gurarie, P. Zoller, J. J. Bollinger, and A. M. Rey, "Simulating dynamical phases of chiral p+ip superconductors with a trapped ion magnet", PRX Quantum **3**, 040324 (2022).
- <sup>145</sup>D. J. Young, E. Y. Song, A. Chu, D. Barberena, Z. Niu, V. M. Schäfer, R. J. Lewis-Swan, A. M. Rey, and J. K. Thompson, "Time-resolved spectral gap spectroscopy in a quantum simulator of fermionic superfluidity inside an optical cavity", Phys. Rev. Lett. 134, 183404 (2025).
- <sup>146</sup>P. Törmä and P. Zoller, "Laser probing of atomic Cooper pairs", Phys. Rev. Lett. **85**, 487–490 (2000).
- <sup>147</sup>C. A. Regal and D. S. Jin, "Measurement of positive and negative scattering lengths in a Fermi gas of atoms", Phys. Rev. Lett. **90**, 230404 (2003).
- <sup>148</sup>S. Gupta, Z. Hadzibabic, M. W. Zwierlein, C. A. Stan, K. Dieckmann, C. H. Schunck, E. G. M. Van Kempen, B. J. Verhaar, and W. Ketterle, "Radio-frequency spectroscopy of ultracold fermions", Science 300, 1723–1726 (2003).
- <sup>149</sup>M. Greiner, C. A. Regal, and D. S. Jin, "Probing the excitation spectrum of a Fermi gas in the BCS-BEC crossover regime", Phys. Rev. Lett. **94**, 070403 (2005).
- <sup>150</sup>C. J. Vale and M. Zwierlein, "Spectroscopic probes of quantum gases", Nat. Phys. **17**, 1305–1315 (2021).
- <sup>151</sup>Y. He, Q. Chen, and K. Levin, "Radio-frequency spectroscopy and the pairing gap in trapped Fermi gases", Phys. Rev. A **72**, 011602(R) (2005).
- <sup>152</sup>M. Punk and W. Zwerger, "Theory of rf-spectroscopy of strongly interacting fermions", Phys. Rev. Lett. 99, 170404 (2007).
- 153 S. Giorgini, L. P. Pitaevskii, and S. Stringari, "Theory of ultracold atomic Fermi gases", Rev. Mod. Phys.80, 1215–1274 (2008).
- <sup>154</sup>Y. Shin, C. H. Schunck, A. Schirotzek, and W. Ketterle, "Tomographic rf spectroscopy of a trapped Fermi gas at unitarity", Phys. Rev. Lett. **99**, 090403 (2007).
- <sup>155</sup>M. Randeria and E. Taylor, "Crossover from Bardeen-Cooper-Schrieffer to Bose-Einstein condensation and the unitary Fermi gas", Annu. Rev. Condens. Matter Phys. **5**, 209–232 (2014).
- <sup>156</sup>R. H. Dicke, "Coherence in spontaneous radiation processes", Phys. Rev. **93**, 99–110 (1954).

- <sup>157</sup>N. Skribanowitz, I. P. Herman, J. C. MacGillivray, and M. S. Feld, "Observation of Dicke superradiance in optically pumped HF gas", Phys. Rev. Lett. **30**, 309–312 (1973).
- <sup>158</sup>M. Gross, C. Fabre, P. Pillet, and S. Haroche, "Observation of near-infrared Dicke superradiance on cascading transitions in atomic sodium", Phys. Rev. Lett. **36**, 1035–1038 (1976).
- <sup>159</sup>H. M. Goldenberg, D. Kleppner, and N. F. Ramsey, "Atomic hydrogen maser", Phys. Rev. Lett. **5**, 361–362 (1960).
- <sup>160</sup>D. Kleppner, H. M. Goldenberg, and N. F. Ramsey, "Theory of the hydrogen maser", Phys. Rev. **126**, 603–615 (1962).
- <sup>161</sup>M. Gross, P. Goy, C. Fabre, S. Haroche, and J. M. Raimond, "Maser oscillation and microwave superradiance in small systems of Rydberg atoms", Phys. Rev. Lett. **43**, 343–346 (1979).
- <sup>162</sup>Y. Kaluzny, P. Goy, M. Gross, J. M. Raimond, and S. Haroche, "Observation of self-induced Rabi oscillations in two-level atoms excited inside a resonant cavity: the ringing regime of superradiance", Phys. Rev. Lett. 51, 1175–1178 (1983).
- <sup>163</sup>D. Meschede, H. Walther, and G. Müller, "One-atom maser", Phys. Rev. Lett. **54**, 551–554 (1985).
- <sup>164</sup>D. J. Heinzen and M. S. Feld, "Vacuum radiative level shift and spontaneous-emission linewidth of an atom in an optical resonator", Phys. Rev. Lett. **59**, 2623–2626 (1987).
- <sup>165</sup>M. G. Raizen, R. J. Thompson, R. J. Brecha, H. J. Kimble, and H. J. Carmichael, "Normal-mode splitting and linewidth averaging for two-state atoms in an optical cavity", Phys. Rev. Lett. **63**, 240–243 (1989).
- <sup>166</sup>Y. Zhu, D. J. Gauthier, S. E. Morin, Q. Wu, H. J. Carmichael, and T. W. Mossberg, "Vacuum Rabi splitting as a feature of linear-dispersion theory: analysis and experimental observations", Phys. Rev. Lett. **64**, 2499–2502 (1990).
- <sup>167</sup>R. J. Thompson, G. Rempe, and H. J. Kimble, "Observation of normal-mode splitting for an atom in an optical cavity", Phys. Rev. Lett. **68**, 1132–1135 (1992).
- <sup>168</sup>G. Nogues, A. Rauschenbeutel, S. Osnaghi, M. Brune, J.-M. Raimond, and S. Haroche, "Seeing a single photon without destroying it", Nature **400**, 239–242 (1999).

- <sup>169</sup>J. Ye, D. W. Vernooy, and H. J. Kimble, "Trapping of single atoms in cavity QED", Phys. Rev. Lett. **83**, 4987–4990 (1999).
- <sup>170</sup>J. A. Sauer, K. M. Fortier, M. S. Chang, C. D. Hamley, and M. S. Chapman, "Cavity QED with optically transported atoms", Phys. Rev. A **69**, 051804 (2004).
- <sup>171</sup>A. K. Tuchman, R. Long, G. Vrijsen, J. Boudet, J. Lee, and M. A. Kasevich, "Normal-mode splitting with large collective cooperativity", Phys. Rev. A **74**, 053821 (2006).
- <sup>172</sup>B. Braverman, A. Kawasaki, E. Pedrozo-Peñafiel, S. Colombo, C. Shu, Z. Li, E. Mendez, M. Yamoah, L. Salvi, D. Akamatsu, Y. Xiao, and V. Vuletić, "Near-unitary spin squeezing in <sup>171</sup>Yb", Phys. Rev. Lett. **122**, 223203 (2019).
- <sup>173</sup>S. Colombo, E. Pedrozo-Peñafiel, A. F. Adiyatullin, Z. Li, E. Mendez, C. Shu, and V. Vuletić, "Time-reversal-based quantum metrology with many-body entangled states", Nat. Phys. **18**, 925–930 (2022).
- <sup>174</sup>A. Kumar, A. Suleymanzade, M. Stone, L. Taneja, A. Anferov, D. I. Schuster, and J. Simon, "Quantum-enabled millimetre wave to optical transduction using neutral atoms", Nature **615**, 614–619 (2023).
- <sup>175</sup>A. Periwal, E. S. Cooper, P. Kunkel, J. F. Wienand, E. J. Davis, and M. Schleier-Smith, "Programmable interactions and emergent geometry in an array of atom clouds", Nature **600**, 630–635 (2021).
- <sup>176</sup>C. W. Gardiner and M. J. Collett, "Input and output in damped quantum systems: quantum stochastic differential equations and the master equation", Phys. Rev. A **31**, 3761–3774 (1985).
- <sup>177</sup>D. F. Walls and G. J. Milburn, **Quantum optics**, 2nd ed. (Springer-Verlag Berlin Heidelberg, 2008).
- <sup>178</sup>D. A. Steck, **Quantum and atom optics**, revision 0.16.2 (2024).
- <sup>179</sup>O. Svelto, **Principles of lasers**, edited by D. C. Hanna, 5th ed. (Springer US, 2010).
- <sup>180</sup>H. Tanji-Suzuki, I. D. Leroux, M. H. Schleier-Smith, M. Cetina, A. T. Grier, J. Simon, and V. Vuletić, "Chapter 4 - interaction between atomic ensembles and optical resonators: classical description", in Adv. At. Mol. Opt. Phys. Vol. 60, edited by E. Arimondo, P. Berman, and C. Lin, Adv. At. Mol. Opt. Phys. (Academic Press, 2011), pp. 201–237.
- <sup>181</sup>J. D. Jackson, **Classical electrodynamics**, 3rd ed. (Wiley, 1999).

- <sup>182</sup>Z. Chen, J. G. Bohnet, J. M. Weiner, K. C. Cox, and J. K. Thompson, "Cavity-aided nondemolition measurements for atom counting and spin squeezing", Phys. Rev. A **89**, 043837 (2014).
- <sup>183</sup>R. W. Drever, J. L. Hall, F. V. Kowalski, J. Hough, G. Ford, A. Munley, and H. Ward, "Laser phase and frequency stabilization using an optical resonator", Appl. Phys. B **31**, 97–105 (1983).
- <sup>184</sup>E. D. Black, "An introduction to Pound-Drever-Hall laser frequency stabilization", Am. J. Phys. **69**, 79–87 (2001).
- <sup>185</sup>I. I. Rabi, "On the process of space quantization", Phys. Rev. 49, 324–328 (1936).
- <sup>186</sup>I. I. Rabi, "Space quantization in a gyrating magnetic field", Phys. Rev. **51**, 652–654 (1937).
- <sup>187</sup>E. Jaynes and F. Cummings, "Comparison of quantum and semiclassical radiation theories with application to the beam maser", Proc. IEEE **51**, 89–109 (1963).
- <sup>188</sup>J. J. Hopfield, "Theory of the contribution of excitons to the complex dielectric constant of crystals", Phys. Rev. **112**, 1555–1567 (1958).
- <sup>189</sup>R. Houdré, C. Weisbuch, R. P. Stanley, U. Oesterle, P. Pellandini, and M. Ilegems, "Measurement of cavity-polariton dispersion curve from angle-resolved photoluminescence experiments", Phys. Rev. Lett. 73, 2043–2046 (1994).
- <sup>190</sup>J. J. Sanchez-Mondragon, N. B. Narozhny, and J. H. Eberly, "Theory of spontaneous-emission line shape in an ideal cavity", Phys. Rev. Lett. **51**, 550–553 (1983).
- <sup>191</sup>G. S. Agarwal, "Vacuum-field Rabi splittings in microwave absorption by Rydberg atoms in a cavity", Phys. Rev. Lett. **53**, 1732–1734 (1984).
- <sup>192</sup>K. Hepp and E. H. Lieb, "On the superradiant phase transition for molecules in a quantized radiation field: the Dicke maser model", Ann. Phys. (N. Y.) **76**, 360–404 (1973).
- $^{193}$ M. Tavis and F. W. Cummings, "Exact solution for an N-molecule—radiation-field Hamiltonian", Phys. Rev. **170**, 379–384 (1968).
- <sup>194</sup>A. S. Sørensen and K. Mølmer, "Entangling atoms in bad cavities", Phys. Rev. A **66**, 022314 (2002).

- <sup>195</sup>L. Salvi, N. Poli, V. Vuleti ć, and G. M. Tino, "Squeezing on momentum states for atom interferometry", Phys. Rev. Lett. **120**, 033601 (2018).
- <sup>196</sup>R. J. Lewis-Swan, M. A. Norcia, J. R. K. Cline, J. K. Thompson, and A. M. Rey, "Robust spin squeezing via photon-mediated interactions on an optical clock transition", Phys. Rev. Lett. **121**, 070403 (2018).
- <sup>197</sup>D. Barberena, A. Chu, J. K. Thompson, and A. M. Rey, "Trade-offs between unitary and measurement induced spin squeezing in cavity QED", Phys. Rev. Res. **6**, L032037 (2024).
- <sup>198</sup>B. Sundar, D. Barberena, A. P. Orioli, A. Chu, J. K. Thompson, A. M. Rey, and R. J. Lewis-Swan, "Bosonic pair production and squeezing for optical phase measurements in long-lived dipoles coupled to a cavity", Phys. Rev. Lett. **130**, 113202 (2023).
- <sup>199</sup>J. Borregaard, E. Davis, G. S. Bentsen, M. H. Schleier-Smith, and A. S. Sørensen, "One-and two-axis squeezing of atomic ensembles in optical cavities", New J. Phys. **19**, 093021 (2017).
- <sup>200</sup>D. Meiser, J. Ye, and M. Holland, "Spin squeezing in optical lattice clocks via lattice-based QND measurements", New J. Phys. **10**, 073014 (2008).
- <sup>201</sup>B. M. Peden, D. Meiser, M. L. Chiofalo, and M. J. Holland, "Nondestructive cavity QED probe of Bloch oscillations in a gas of ultracold atoms", Phys. Rev. A **80**, 043803 (2009).
- <sup>202</sup>A. Shankar, G. P. Greve, B. Wu, J. K. Thompson, and M. Holland, "Continuous real-time tracking of a quantum phase below the standard quantum limit", Phys. Rev. Lett. **122**, 233602 (2019).
- <sup>203</sup>Z. Chen, "Breaking quantum limits with collective cavity-QED: generation of spin squeezed states via quantum non-demolition measurements", PhD thesis (University of Colorado, Boulder, 440 UCB, Boulder, Colorado, May 2013).
- <sup>204</sup>M. O. Scully and M. S. Zubairy, **Quantum optics** (Cambridge University Press, Cambridge, 1997).
- <sup>205</sup>F. Bloch, "Nuclear induction", Phys. Rev. **70**, 460–474 (1946).
- <sup>206</sup>L. Allen and J. H. Eberly, **Optical resonance and two-level atoms** (John Wiley and Sons, Inc., New York, Jan. 1975).
- <sup>207</sup>D. Manzano, "A short introduction to the Lindblad master equation", AIP Adv. **10**, 025106 (2020).

- <sup>208</sup>J. Dalibard, Y. Castin, and K. Mølmer, "Wave-function approach to dissipative processes in quantum optics", Phys. Rev. Lett. **68**, 580–583 (1992).
- <sup>209</sup>M. Nomura, N. Kumagai, S. Iwamoto, Y. Ota, and Y. Arakawa, "Laser oscillation in a strongly coupled single-quantum-dot–nanocavity system", Nat. Phys. **6**, 279–283 (2010).
- <sup>210</sup>C. Gies, F. Gericke, P. Gartner, S. Holzinger, C. Hopfmann, T. Heindel, J. Wolters, C. Schneider, M. Florian, F. Jahnke, S. Höfling, M. Kamp, and S. Reitzenstein, "Strong light-matter coupling in the presence of lasing", Phys. Rev. A 96, 023806 (2017).
- <sup>211</sup>D. A. Tieri, M. Xu, D. Meiser, J. Cooper, and M. J. Holland, **Theory of the crossover from lasing to steady state superradiance**, 2017, arXiv:1702.04830 [quant-ph].
- <sup>212</sup>K. Debnath, Y. Zhang, and K. Mølmer, "Lasing in the superradiant crossover regime", Phys. Rev. A **98**, 063837 (2018).
- <sup>213</sup>J. Chen, "Active optical clock", Sci. Bull. **54**, 348–352 (2009).
- <sup>214</sup>D. Meiser, J. Ye, D. R. Carlson, and M. J. Holland, "Prospects for a millihertz-linewidth laser", Phys. Rev. Lett. **102**, 163601 (2009).
- <sup>215</sup>G. A. Kazakov and T. Schumm, "Active optical frequency standard using sequential coupling of atomic ensembles", Phys. Rev. A **87**, 013821 (2013).
- <sup>216</sup>M. Xu and M. J. Holland, "Conditional ramsey spectroscopy with synchronized atoms", Phys. Rev. Lett. **114**, 103601 (2015).
- <sup>217</sup>H. Liu, S. B. Jäger, X. Yu, S. Touzard, A. Shankar, M. J. Holland, and T. L. Nicholson, "Rugged mHz-linewidth superradiant laser driven by a hot atomic beam", Phys. Rev. Lett. **125**, 253602 (2020).
- <sup>218</sup>Y. Zhang, C. Shan, and K. Mølmer, "Active frequency measurement on superradiant strontium clock transitions", Phys. Rev. Lett. **128**, 013604 (2022).
- <sup>219</sup>M. Tang, S. A. Schäffer, and J. H. Müller, "Prospects of a superradiant laser based on a thermal or guided beam of <sup>88</sup>Sr", Phys. Rev. A **106**, 063704 (2022).

- <sup>220</sup>S. Dubey, G. A. Kazakov, B. Heizenreder, S. Zhou, S. Bennetts, S. A. Schäffer, A. Sitaram, and F. Schreck (MoSaiQC Collaboration), "Modeling of a continuous superradiant laser on the sub-mHz  $^1S_0 \rightarrow {}^3P_0$  transition in neutral strontium-88", Phys. Rev. Res. 7, 013292 (2025).
- <sup>221</sup>J. G. Bohnet, Z. Chen, J. M. Weiner, D. Meiser, M. J. Holland, and J. K. Thompson, "A steady-state superradiant laser with less than one intracavity photon", Nature **484**, 78–81 (2012).
- <sup>222</sup>M. A. Norcia and J. K. Thompson, "Cold-strontium laser in the superradiant crossover regime", Phys. Rev. X **6**, 011025 (2016).
- <sup>223</sup>M. A. Norcia, M. N. Winchester, J. R. Cline, and J. K. Thompson, "Superradiance on the millihertz linewidth strontium clock transition", Sci. Adv. **2**, e1601231 (2016).
- <sup>224</sup>J. R. K. Cline, V. M. Schäfer, Z. Niu, D. J. Young, T. H. Yoon, and J. K. Thompson, "Continuous collective strong coupling of strontium atoms to a high finesse ring cavity", Phys. Rev. Lett. **134**, 013403 (2025).
- <sup>225</sup>V. M. Schäfer, Z. Niu, J. R. Cline, D. J. Young, E. Y. Song, H. Ritsch, and J. K. Thompson, "Continuous recoil-driven lasing and cavity frequency pinning with laser-cooled atoms", Nat. Phys. **21**, 902–908 (2025).
- <sup>226</sup>T. Laske, H. Winter, and A. Hemmerich, "Pulse delay time statistics in a superradiant laser with calcium atoms", Phys. Rev. Lett. **123**, 103601 (2019).
- <sup>227</sup>D. Pan, B. Arora, Y.-m. Yu, B. K. Sahoo, and J. Chen, "Optical-lattice-based Cs active clock with a continual superradiant lasing signal", Phys. Rev. A **102**, 041101 (2020).
- <sup>228</sup>S. L. Kristensen, E. Bohr, J. Robinson-Tait, T. Zelevinsky, J. W. Thomsen, and J. H. Müller, "Subnatural linewidth superradiant lasing with cold <sup>88</sup>Sr atoms", Phys. Rev. Lett. **130**, 223402 (2023).
- <sup>229</sup>F. Famà, S. Zhou, B. Heizenreder, M. Tang, S. Bennetts, S. B. Jäger, S. A. Schäffer, and F. Schreck, "Continuous cavity QED with an atomic beam", Phys. Rev. A **110**, 063721 (2024).
- <sup>230</sup>R. Takeuchi, H. Chiba, S. Okaba, M. Takamoto, S. Tsuji, and H. Katori, "Continuous outcoupling of ultracold strontium atoms combining three different traps", Appl. Phys. Express **16**, 042003 (2023).

- <sup>231</sup>M. A. Norcia, "New tools for precision measurement and quantum science with narrow linewidth optical transitions", PhD thesis (University of Colorado, 440 UCB, Boulder, Colorado, 2017).
- <sup>232</sup>H. J. Kimble, "Strong interactions of single atoms and photons in cavity QED", Phys. Scr. **1998**, 127 (1998).
- <sup>233</sup>P. Horak, B. G. Klappauf, A. Haase, R. Folman, J. Schmiedmayer, P. Domokos, and E. A. Hinds, "Possibility of single-atom detection on a chip", Phys. Rev. A **67**, 043806 (2003).
- <sup>234</sup>E. M. Purcell, "Spontaneous emission probabilities at radio frequencies", in Proc. Am. Phys. Soc. Vol. 69 (June 1946), pp. 674–674.
- <sup>235</sup>F. Reiter and A. S. Sørensen, "Effective operator formalism for open quantum systems", Phys. Rev. A **85**, 032111 (2012).
- <sup>236</sup>M. Schwartz, **Quantum field theory and the standard model** (Cambridge University Press, 2013).
- <sup>237</sup>C. Luo, "Twisting, binding, and probing matter waves in a rubidium cavity QED system", PhD thesis (University of Colorado, Boulder, 440 UCB, Boulder, Colorado, May 2024).
- <sup>238</sup>J. T. Young, E. Chaparro, A. Piñeiro Orioli, J. K. Thompson, and A. M. Rey, "Engineering one axis twisting via a dissipative Berry phase using strong symmetries", Phys. Rev. Lett. **134**, 040801 (2025).
- <sup>239</sup>J. D. Wilson, S. B. Jäger, J. T. Reilly, A. Shankar, M. L. Chiofalo, and M. J. Holland, "Beyond one-axis twisting: simultaneous spin-momentum squeezing", Phys. Rev. A **106**, 043711 (2022).
- <sup>240</sup>H. Zhang, A. Chu, C. Luo, J. K. Thompson, and A. M. Rey, "Control and amplification of Bloch oscillations via photon-mediated interactions", Phys. Rev. Res. **5**, L032039 (2023).
- <sup>241</sup>J. D. Wilson, J. T. Reilly, H. Zhang, C. Luo, A. Chu, J. K. Thompson, A. M. Rey, and M. J. Holland, "Entangled matter waves for quantum enhanced sensing", Phys. Rev. A **110**, L041301 (2024).
- <sup>242</sup>M. A. Norcia and J. K. Thompson, "Strong coupling on a forbidden transition in strontium and non-destructive atom counting", Phys. Rev. A **93**, 023804 (2016).

- <sup>243</sup>M. N. Winchester, M. A. Norcia, J. R. K. Cline, and J. K. Thompson, "Magnetically induced optical transparency on a forbidden transition in strontium for cavity-enhanced spectroscopy", Phys. Rev. Lett. **118**, 263601 (2017).
- <sup>244</sup>S. Stellmer, "Degenerate quantum gases of strontium", PhD thesis (Jan. 2013).
- <sup>245</sup>S. Bennetts, "1000 times closer to a continuous atom laser: steady-state strontium with unity phase-space density", PhD thesis (Netherlands, 2019).
- $^{246}S.\ Pucher, S.\ L.\ Kristensen, and\ R.\ M.\ Kroeze, \\ ^{88}\textbf{Sr}\ \textbf{reference\,data}, 2025, arXiv: 2507.10487\ [physics.atom-ph].$
- <sup>247</sup>S. Stellmer and F. Schreck, "Reservoir spectroscopy of 5s5p  $^3P_2$ –5snd  $^3D_{1,2,3}$  transitions in strontium", Phys. Rev. A **90**, 022512 (2014).
- <sup>248</sup>J. C. Hill, W. Huie, P. Lunia, J. D. Whalen, S. K. Kanungo, Y. Lu, and T. C. Killian, "Photoassociative spectroscopy of <sup>87</sup>Sr", Phys. Rev. A **103**, 023111 (2021).
- <sup>249</sup>J. Samland, S. Bennetts, C.-C. Chen, R. G. Escudero, F. Schreck, and B. Pasquiou, "Optical pumping of 5s4d  $^1D_2$  strontium atoms for laser cooling and imaging", Phys. Rev. Res. **6**, 013319 (2024).
- <sup>250</sup>A. Cooper, J. P. Covey, I. S. Madjarov, S. G. Porsev, M. S. Safronova, and M. Endres, "Alkaline-earth atoms in optical tweezers", Phys. Rev. X **8**, 041055 (2018).
- <sup>251</sup> "The radiative lifetime of the  $^1D_2$  state of Ca and Sr: a core-valence treatment", J. Phys. B: At. Mol. Opt. Phys. **18**, 1523 (1985).
- <sup>252</sup>T. Ido, T. H. Loftus, M. M. Boyd, A. D. Ludlow, K. W. Holman, and J. Ye, "Precision spectroscopy and density-dependent frequency shifts in ultracold Sr", Phys. Rev. Lett. **94**, 153001 (2005).
- $^{253}$ J. Trautmann, D. Yankelev, V. Klüsener, A. J. Park, I. Bloch, and S. Blatt, " $^{1}$ S $_{0}$   $^{3}$ P $_{2}$  magnetic quadrupole transition in neutral strontium", Phys. Rev. Res. **5**, 013219 (2023).
- <sup>254</sup>G. Breit and L. A. Wills, "Hyperfine structure in intermediate coupling", Phys. Rev. **44**, 470–490 (1933).
- $^{255}$ B. Lu, X. Lu, J. Li, and H. Chang, "Reconciliation of theoretical lifetimes of the 5s5p  $^3P_2^o$  metastable state for  $^{88}$ Sr with measurement: the role of the blackbody-radiation-induced decay", Chin. Phys. Lett. **39**, 073201 (2022).

- <sup>256</sup>A. V. Taichenachev, V. I. Yudin, C. W. Oates, C. W. Hoyt, Z. W. Barber, and L. Hollberg, "Magnetic field-induced spectroscopy of forbidden optical transitions with application to lattice-based optical atomic clocks", Phys. Rev. Lett. 96, 083001 (2006).
- <sup>257</sup>A. W. Young, W. J. Eckner, W. R. Milner, D. Kedar, M. A. Norcia, E. Oelker, N. Schine, J. Ye, and A. M. Kaufman, "Half-minute-scale atomic coherence and high relative stability in a tweezer clock", Nature **588**, 408–413 (2020).
- <sup>258</sup>G. García and J. Campos, "Transition probabilities for triplet levels of Sr(I)", J. Quant. Spectrosc. Radiat. Transfer **39**, 477–483 (1988).
- <sup>259</sup>J. E. Sansonetti and G. Nave, "Wavelengths, transition probabilities, and energy levels for the spectrum of neutral strontium (SrI)", J. Phys. Chem. Ref. Data **39**, 033103 (2010).
- <sup>260</sup>I. Courtillot, A. Quessada-Vial, A. Brusch, D. Kolker, G. D. Rovera, and P. Lemonde, "Accurate spectroscopy of Sr atoms", Eur. Phys. J. D **33**, 161–171 (2005).
- <sup>261</sup>K. Hashiguchi, T. Akatsuka, N. Ohmae, M. Takamoto, and H. Katori, "Frequency measurement on the  $5s5p^3P_2 5s4d^3D_3$  transition of <sup>88</sup>Sr atoms using the photon-momentum-transfer technique", Phys. Rev. A **100**, 042513 (2019).
- <sup>262</sup>M. S. Safronova, S. G. Porsev, U. I. Safronova, M. G. Kozlov, and C. W. Clark, "Blackbody-radiation shift in the Sr optical atomic clock", Phys. Rev. A 87, 012509 (2013).
- <sup>263</sup>T. Akatsuka, K. Hashiguchi, T. Takahashi, N. Ohmae, M. Takamoto, and H. Katori, "Three-stage laser cooling of Sr atoms using the  $5s5p^3P_2$  metastable state below Doppler temperatures", Phys. Rev. A **103**, 023331 (2021).
- <sup>264</sup>P. Mickelson, Y. M. de Escobar, P. Anzel, B. DeSalvo, S. Nagel, A. Traverso, M. Yan, and T. Killian, "Repumping and spectroscopy of laser-cooled Sr atoms using the (5s5p)  $^3P_2$ –(5s4d)  $^3D_2$  transition", J. Phys. B: At. Mol. Opt. Phys. **42**, 235001 (2009).

- <sup>265</sup>P. Thekkeppatt, Digvijay, A. Urech, F. Schreck, and K. van Druten, Measurement of the g factor of ground-state <sup>87</sup>Sr at the parts-per-million level using co-trapped ultracold atoms, 2025, arXiv:2504.
  11242 [physics.atom-ph].
- <sup>266</sup>B.-q. Lu, Y. Wang, Y. Guo, Q. Xu, M. Yin, J. Li, and H. Chang, "Experimental determination of the landé g-factors for 5s2 <sup>1</sup>S and 5s5p <sup>3</sup>P states of the <sup>87</sup>Sr atom", Chin. Phys. Lett. **35**, 043203 (2018).
- <sup>267</sup>M. Boyd, "High precision spectroscopy of strontium in an optical lattice: towards a new standard for frequency and time", PhD thesis (440 UCB, Boulder, Colorado, Oct. 2007).
- <sup>268</sup>N. Stone and V. (International Atomic Energy Agency International Nuclear Data Committee, "Table of nuclear magnetic dipole and electric quadrupole moments", (2014).
- <sup>269</sup>J. H. A. Park, "Towards quantum simulations with strontium in cavity-enhanced optical lattices", PhD thesis (Dec. 2021).
- <sup>270</sup>B. Saxberg, B. Plotkin-Swing, and S. Gupta, "Active stabilization of a diode laser injection lock", Rev. Sci. Instrum. **87**, 063109 (2016).
- <sup>271</sup>M. A. Norcia and J. K. Thompson, "Simple laser stabilization to the strontium <sup>88</sup>Sr transition at 707 nm", Rev. Sci. Instrum. **87**, 023110 (2016).
- <sup>272</sup>Y. Shimada, Y. Chida, N. Ohtsubo, T. Aoki, M. Takeuchi, T. Kuga, and Y. Torii, "A simplified 461-nm laser system using blue laser diodes and a hollow cathode lamp for laser cooling of Sr", Rev. Sci. Instrum.
  84, 063101 (2013).
- <sup>273</sup>G. Camy, C. Bordé, and M. Ducloy, "Heterodyne saturation spectroscopy through frequency modulation of the saturating beam", Opt. Commun. **41**, 325–330 (1982).
- <sup>274</sup>F. Bertinetto, P. Cordiale, G. Galzerano, and E. Bava, "Frequency stabilization of DBR diode laser against Cs absorption lines at 852 nm using the modulation transfer method", IEEE Trans. Instrum. Meas. **50**, 490–492 (2001).
- <sup>275</sup>H.-R. Noh, S. E. Park, L. Z. Li, J.-D. Park, and C.-H. Cho, "Modulation transfer spectroscopy for <sup>87</sup>Rb atoms: theory and experiment", Opt. Express **19**, 23444–23452 (2011).

- <sup>276</sup>F. Zi, X. Wu, W. Zhong, R. H. Parker, C. Yu, S. Budker, X. Lu, and H. Müller, "Laser frequency stabilization by combining modulation transfer and frequency modulation spectroscopy", Appl. Opt. **56**, 2649–2652 (2017).
- <sup>277</sup>M. Ducloy and D. Bloch, "Theory of degenerate four-wave mixing in resonant Doppler-broadened media. II. Doppler-free heterodyne spectroscopy via collinear four-wave mixing in two- and three-level systems", J. Phys. (Paris) **43**, 57–65 (1982).
- <sup>278</sup>D. J. Wineland and W. M. Itano, "Laser cooling of atoms", Phys. Rev. A **20**, 1521–1540 (1979).
- <sup>279</sup>P. D. Lett, R. N. Watts, C. I. Westbrook, W. D. Phillips, P. L. Gould, and H. J. Metcalf, "Observation of atoms laser cooled below the Doppler limit", Phys. Rev. Lett. **61**, 169–172 (1988).
- <sup>280</sup>J. Dalibard and C. Cohen-Tannoudji, "Laser cooling below the Doppler limit by polarization gradients: simple theoretical models", J. Opt. Soc. Am. B **6**, 2023–2045 (1989).
- <sup>281</sup>M. Weidemüller, T. Esslinger, M. A. Ol'shanii, A. Hemmerich, and T. W. Hänsch, "A novel scheme for efficient cooling below the photon recoil limit", EPL **27**, 109 (1994).
- <sup>282</sup>D. Boiron, C. Triché, D. R. Meacher, P. Verkerk, and G. Grynberg, "Three-dimensional cooling of cesium atoms in four-beam gray optical molasses", Phys. Rev. A **52**, R3425–R3428 (1995).
- <sup>283</sup>P. M. Duarte, R. A. Hart, J. M. Hitchcock, T. A. Corcovilos, T.-L. Yang, A. Reed, and R. G. Hulet, "Alloptical production of a lithium quantum gas using narrow-line laser cooling", Phys. Rev. A **84**, 061406 (2011).
- <sup>284</sup>D. C. McKay, D. Jervis, D. J. Fine, J. W. Simpson-Porco, G. J. A. Edge, and J. H. Thywissen, "Low-temperature high-density magneto-optical trapping of potassium using the open  $4S \rightarrow 5P$  transition at 405 nm", Phys. Rev. A **84**, 063420 (2011).
- <sup>285</sup>D. Rio Fernandes, F. Sievers, N. Kretzschmar, S. Wu, C. Salomon, and F. Chevy, "Sub-Doppler laser cooling of fermionic 40K atoms in three-dimensional gray optical molasses", EPL **100**, 63001 (2012).
- <sup>286</sup>A. T. Grier, I. Ferrier-Barbut, B. S. Rem, M. Delehaye, L. Khaykovich, F. Chevy, and C. Salomon, " $\Lambda$ -enhanced sub-Doppler cooling of lithium atoms in  $D_1$  gray molasses", Phys. Rev. A **87**, 063411 (2013).

- <sup>287</sup>F. Schreck and K. v. Druten, "Laser cooling for quantum gases", Nat. Phys. 17, 1296–1304 (2021).
- <sup>288</sup>Y. Castin, H. Wallis, and J. Dalibard, "Limit of Doppler cooling", J. Opt. Soc. Am. B 6, 2046–2057 (1989).
- <sup>289</sup>H. Katori, T. Ido, Y. Isoya, and M. Kuwata-Gonokami, "Magneto-optical trapping and cooling of strontium atoms down to the photon recoil temperature", Phys. Rev. Lett. **82**, 1116–1119 (1999).
- <sup>290</sup>K. Vogel, T. Dinneen, A. Gallagher, and J. Hall, "Narrow-line Doppler cooling of strontium to the recoil limit", IEEE Trans. Instrum. Meas. **48**, 618–621 (1999).
- <sup>291</sup>T. Kuwamoto, K. Honda, Y. Takahashi, and T. Yabuzaki, "Magneto-optical trapping of Yb atoms using an intercombination transition", Phys. Rev. A **60**, R745(R) (1999).
- <sup>292</sup>M. A. Norcia, J. R. K. Cline, J. P. Bartolotta, M. J. Holland, and J. K. Thompson, "Narrow-line laser cooling by adiabatic transfer", New J. Phys. **20**, 023021 (2018).
- <sup>293</sup>J. A. Muniz, M. A. Norcia, J. R. K. Cline, and J. K. Thompson, **A robust narrow-line magneto-optical trap using adiabatic transfer**, 2018, arXiv:1806.00838 [physics.atom-ph].
- <sup>294</sup>J. P. Bartolotta, M. A. Norcia, J. R. K. Cline, J. K. Thompson, and M. J. Holland, "Laser cooling by sawtooth-wave adiabatic passage", Phys. Rev. A **98**, 023404 (2018).
- <sup>295</sup>J. P. Bartolotta and M. J. Holland, "Sawtooth-wave adiabatic passage in a magneto-optical trap", Phys. Rev. A **101**, 053434 (2020).
- <sup>296</sup>J. P. Bartolotta, J. T. Reilly, and M. J. Holland, "Speeding up particle slowing using shortcuts to adiabaticity", Phys. Rev. A **102**, 043107 (2020).
- <sup>297</sup>J. P. Bartolotta, S. B. Jäger, J. T. Reilly, M. A. Norcia, J. K. Thompson, G. Smith, and M. J. Holland, "Entropy transfer from a quantum particle to a classical coherent light field", Phys. Rev. Res. 4, 013218 (2022).
- <sup>298</sup>R. González Escudero, C.-C. Chen, S. Bennetts, B. Pasquiou, and F. Schreck, "Steady-state magneto-optical trap of fermionic strontium on a narrow-line transition", Phys. Rev. Res. **3**, 033159 (2021).
- $^{299}$ K. Kim, A. Aeppli, T. Bothwell, and J. Ye, "Evaluation of lattice light shift at low  $10^{-19}$  uncertainty for a shallow lattice Sr optical clock", Phys. Rev. Lett. **130**, 113203 (2023).

- <sup>300</sup>J. Sakurai and J. Napolitano, **Modern quantum mechanics**, 2nd ed. (Cambridge University Press, 2017).
- <sup>301</sup>M. Martin, "Quantum metrology and many-body physics: pushing the frontier of the optical lattice clock", PhD thesis (440 UCB, Boulder, Colorado, Apr. 2013).
- <sup>302</sup>C. Shi, J.-L. Robyr, U. Eismann, M. Zawada, L. Lorini, R. Le Targat, and J. Lodewyck, "Polarizabilities of the <sup>87</sup>Sr clock transition", Phys. Rev. A **92**, 012516 (2015).
- $^{303}$ G. Kestler, K. Ton, D. Filin, M. S. Safronova, and J. T. Barreiro, "Magic wavelengths of the Sr  $(5s^2 \ ^1S_0 5s5p \ ^3P_1)$  intercombination transition near the  $5s5p \ ^3P_1 5p^2 \ ^3P_2$  transition", Phys. Rev. A **105**, 012821 (2022).
- <sup>304</sup>G. Rempe, R. J. Thompson, H. J. Kimble, and R. Lalezari, "Measurement of ultralow losses in an optical interferometer", Opt. Lett. **17**, 363–365 (1992).
- <sup>305</sup>N. Jin, C. A. McLemore, D. Mason, J. P. Hendrie, Y. Luo, M. L. Kelleher, P. Kharel, F. Quinlan, S. A. Diddams, and P. T. Rakich, "Micro-fabricated mirrors with finesse exceeding one million", Optica **9**, 965–970 (2022).
- <sup>306</sup>L. Pinard, B. Sassolas, R. Flaminio, D. Forest, A. Lacoudre, C. Michel, J. L. Montorio, and N. Morgado, "Toward a new generation of low-loss mirrors for the advanced gravitational waves interferometers", Opt. Lett. 36, 1407–1409 (2011).
- <sup>307</sup>L. Pinard, C. Michel, B. Sassolas, L. Balzarini, J. Degallaix, V. Dolique, R. Flaminio, D. Forest, M. Granata, B. Lagrange, N. Straniero, J. Teillon, and G. Cagnoli, "Mirrors used in the LIGO interferometers for first detection of gravitational waves", Appl. Opt. 56, C11–C15 (2017).
- <sup>308</sup>X. Baillard, A. Gauguet, S. Bize, P. Lemonde, P. Laurent, A. Clairon, and P. Rosenbusch, "Interference-filter-stabilized external-cavity diode lasers", Opt. Commun. **266**, 609–613 (2006).
- <sup>309</sup>D. J. Thompson and R. E. Scholten, "Narrow linewidth tunable external cavity diode laser using wide bandwidth filter", Rev. Sci. Instrum. **83**, 023107 (2012).

- <sup>310</sup>L. Ricci, M. Weidemüller, T. Esslinger, A. Hemmerich, C. Zimmermann, V. Vuletić, W. König, and T. Hänsch, "A compact grating-stabilized diode laser system for atomic physics", Opt. Commun. 117, 541–549 (1995).
- <sup>311</sup>A. S. Arnold, J. S. Wilson, and M. G. Boshier, "A simple extended-cavity diode laser", Rev. Sci. Instrum. **69**, 1236–1239 (1998).
- <sup>312</sup>C. J. Hawthorn, K. P. Weber, and R. E. Scholten, "Littrow configuration tunable external cavity diode laser with fixed direction output beam", Rev. Sci. Instrum. **72**, 4477–4479 (2001).
- <sup>313</sup>F. Riehle, **Frequency standards: basics and applications** (Wiley, 2006).
- <sup>314</sup>G. D. Domenico, S. Schilt, and P. Thomann, "Simple approach to the relation between laser frequency noise and laser line shape", Appl. Opt. **49**, 4801–4807 (2010).
- <sup>315</sup>M. L. Day, P. J. Low, B. White, R. Islam, and C. Senko, "Limits on atomic qubit control from laser noise", npj Quantum Inf. **8**, 72 (2022).
- <sup>316</sup>I. Ushijima, M. Takamoto, M. Das, T. Ohkubo, and H. Katori, "Cryogenic optical lattice clocks", Nat. Photonics **9**, 185–189 (2015).
- <sup>317</sup>A. D. Ludlow, M. M. Boyd, J. Ye, E. Peik, and P. O. Schmidt, "Optical atomic clocks", Rev. Mod. Phys. **87**, 637–701 (2015).
- T. Takano, M. Takamoto, I. Ushijima, N. Ohmae, T. Akatsuka, A. Yamaguchi, Y. Kuroishi, H. Munekane,
   B. Miyahara, and H. Katori, "Geopotential measurements with synchronously linked optical lattice clocks", Nat. Photonics 10, 662–666 (2016).
- <sup>319</sup>M. Schioppo, R. C. Brown, W. F. McGrew, N. Hinkley, R. J. Fasano, K. Beloy, T. Yoon, G. Milani, D. Nicolodi, J. Sherman, et al., "Ultrastable optical clock with two cold-atom ensembles", Nat. Photonics 11, 48–52 (2017).
- <sup>320</sup>J. Grotti, S. Koller, S. Vogt, S. Häfner, U. Sterr, C. Lisdat, H. Denker, C. Voigt, L. Timmen, A. Rolland, et al., "Geodesy and metrology with a transportable optical clock", Nat. Phys. **14**, 437–441 (2018).

- <sup>321</sup>S. M. Brewer, J.-S. Chen, A. M. Hankin, E. R. Clements, C. W. Chou, D. J. Wineland, D. B. Hume, and D. R. Leibrandt, "<sup>27</sup>Al<sup>+</sup> quantum-logic clock with a systematic uncertainty below 10<sup>-18</sup>", Phys. Rev. Lett. **123**, 033201 (2019).
- $^{322}$ E. Oelker, R. Hutson, C. Kennedy, L. Sonderhouse, T. Bothwell, A. Goban, D. Kedar, C. Sanner, J. Robinson, G. Marti, et al., "Demonstration of  $4.8 \times 10^{-17}$  stability at 1 s for two independent optical clocks", Nat. Photonics **13**, 714–719 (2019).
- 323 L. Hu, N. Poli, L. Salvi, and G. M. Tino, "Atom interferometry with the Sr optical clock transition", Phys. Rev. Lett. **119**, 263601 (2017).
- $^{324}$ R. P. del Aguila, T. Mazzoni, L. Hu, L. Salvi, G. M. Tino, and N. Poli, "Bragg gravity-gradiometer using the  $^{1}S_{0}$ - $^{3}P_{1}$  intercombination transition of  $^{88}$ Sr", New J. Phys. **20**, 043002 (2018).
- <sup>325</sup>A. Arvanitaki, P. W. Graham, J. M. Hogan, S. Rajendran, and K. Van Tilburg, "Search for light scalar dark matter with atomic gravitational wave detectors", Phys. Rev. D **97**, 075020 (2018).
- <sup>326</sup>M. S. Safronova, D. Budker, D. DeMille, D. F. J. Kimball, A. Derevianko, and C. W. Clark, "Search for new physics with atoms and molecules", Rev. Mod. Phys. **90**, 025008 (2018).
- <sup>327</sup>P. Wcisło, P. Ablewski, K. Beloy, S. Bilicki, M. Bober, R. Brown, R. Fasano, R. Ciuryło, H. Hachisu, T. Ido,
  J. Lodewyck, A. Ludlow, W. McGrew, P. Morzyński, D. Nicolodi, M. Schioppo, M. Sekido, R. L. Targat,
  P. Wolf, X. Zhang, B. Zjawin, and M. Zawada, "New bounds on dark matter coupling from a global network of optical atomic clocks", Sci. Adv. 4, eaau4869 (2018).
- <sup>328</sup>G. M. Tino, A. Bassi, G. Bianco, K. Bongs, P. Bouyer, L. Cacciapuoti, S. Capozziello, X. Chen, M. L. Chiofalo, A. Derevianko, et al., "SAGE: a proposal for a space atomic gravity explorer", Eur. Phys. J. D **73**, 1–20 (2019).
- <sup>329</sup>C. J. Kennedy, E. Oelker, J. M. Robinson, T. Bothwell, D. Kedar, W. R. Milner, G. E. Marti, A. Derevianko, and J. Ye, "Precision metrology meets cosmology: improved constraints on ultralight dark matter from atom-cavity frequency comparisons", Phys. Rev. Lett. **125**, 201302 (2020).

- <sup>330</sup>M. Abe, P. Adamson, M. Borcean, D. Bortoletto, K. Bridges, S. P. Carman, S. Chattopadhyay, J. Coleman, N. M. Curfman, K. DeRose, et al., "Matter-wave atomic gradiometer interferometric sensor (magis-100)", Quantum Sci. Technol. 6, 044003 (2021).
- <sup>331</sup>S. Kolkowitz, S. Bromley, T. Bothwell, M. Wall, G. Marti, A. Koller, X. Zhang, A. Rey, and J. Ye, "Spinorbit-coupled fermions in an optical lattice clock", Nature **542**, 66–70 (2017).
- <sup>332</sup>S. Bromley, S. Kolkowitz, T. Bothwell, D. Kedar, A. Safavi-Naini, M. Wall, C. Salomon, A. Rey, and J. Ye, "Dynamics of interacting fermions under spin–orbit coupling in an optical lattice clock", Nat. Phys. **14**, 399–404 (2018).
- <sup>333</sup>R. Senaratne, S. V. Rajagopal, T. Shimasaki, P. E. Dotti, K. M. Fujiwara, K. Singh, Z. A. Geiger, and D. M. Weld, "Quantum simulation of ultrafast dynamics using trapped ultracold atoms", Nat. Commun. **9**, 2065 (2018).
- <sup>334</sup>A. Goban, R. Hutson, G. Marti, S. Campbell, M. Perlin, P. Julienne, J. D'Incao, A. Rey, and J. Ye, "Emergence of multi-body interactions in a fermionic lattice clock", Nature **563**, 369–373 (2018).
- <sup>335</sup>M. Walhout, A. Witte, and S. L. Rolston, "Precision measurement of the metastable 6s [3/2]<sub>2</sub> lifetime in xenon", Phys. Rev. Lett. **72**, 2843–2846 (1994).
- $^{336}$ P. A. Barton, C. J. S. Donald, D. M. Lucas, D. A. Stevens, A. M. Steane, and D. N. Stacey, "Measurement of the lifetime of the  $3d^2D_{5/2}$  state in  $^{40}$ Ca<sup>+</sup>", Phys. Rev. A **62**, 032503 (2000).
- <sup>337</sup>T. Becker, J. v. Zanthier, A. Y. Nevsky, C. Schwedes, M. N. Skvortsov, H. Walther, and E. Peik, "High-resolution spectroscopy of a single In<sup>+</sup> ion: progress towards an optical frequency standard", Phys. Rev. A **63**, 051802 (2001).
- $^{338}$ P. Staanum, I. S. Jensen, R. G. Martinussen, D. Voigt, and M. Drewsen, "Lifetime measurement of the metastable  $3d^2D_{5/2}$  state in the  $^{40}$ Ca<sup>+</sup> ion using the shelving technique on a few-ion string", Phys. Rev. A **69**, 032503 (2004).

- <sup>339</sup>A. Kreuter, C. Becher, G. P. T. Lancaster, A. B. Mundt, C. Russo, H. Häffner, C. Roos, J. Eschner, F. Schmidt-Kaler, and R. Blatt, "Spontaneous emission lifetime of a single trapped Ca<sup>+</sup> ion in a high finesse cavity", Phys. Rev. Lett. **92**, 203002 (2004).
- <sup>340</sup>T. Rosenband, P. O. Schmidt, D. B. Hume, W. M. Itano, T. M. Fortier, J. E. Stalnaker, K. Kim, S. A. Diddams, J. C. J. Koelemeij, J. C. Bergquist, and D. J. Wineland, "Observation of the  ${}^1S_0 \rightarrow {}^3P_0$  clock transition in  ${}^{27}\text{Al}^+$ ", Phys. Rev. Lett. **98**, 220801 (2007).
- $^{341}$ B. B. Jensen, H. Ming, P. G. Westergaard, K. Gunnarsson, M. H. Madsen, A. Brusch, J. Hald, and J. W. Thomsen, "Experimental determination of the  $^{24}$ Mg I  $(3s3p)^3P_2$  lifetime", Phys. Rev. Lett. **107**, 113001 (2011).
- <sup>342</sup>R. X. Schüssler, H. Bekker, M. Braß, H. Cakir, J. Crespo López-Urrutia, M. Door, P. Filianin, Z. Harman, M. W. Haverkort, W. J. Huang, et al., "Detection of metastable electronic states by Penning trap mass spectrometry", Nature 581, 42–46 (2020).
- $^{343}$ S. G. Porsev and A. Derevianko, "Hyperfine quenching of the metastable  $^{3}P_{0,2}$  states in divalent atoms", Phys. Rev. A **69**, 042506 (2004).
- <sup>344</sup>R. Santra, K. V. Christ, and C. H. Greene, "Properties of metastable alkaline-earth-metal atoms calculated using an accurate effective core potential", Phys. Rev. A **69**, 042510 (2004).
- $^{345}$ X.-T. Lu, F. Guo, Y.-Y. Liu, J.-J. Xia, G.-D. Zhao, Y.-X. Chen, Y.-B. Wang, B.-Q. Lu, and H. Chang, "Determining the lifetime of the  $5s5p^3P_0^0$  metastable state in  $^{87}$ Sr from the electric dipole matrix element", Phys. Rev. Appl. **21**, 024042 (2024).
- <sup>346</sup>M. A. Norcia, A. W. Young, W. J. Eckner, E. Oelker, J. Ye, and A. M. Kaufman, "Seconds-scale coherence on an optical clock transition in a tweezer array", Science **366**, 93–97 (2019).
- <sup>347</sup>I. S. Madjarov, A. Cooper, A. L. Shaw, J. P. Covey, V. Schkolnik, T. H. Yoon, J. R. Williams, and M. Endres, "An atomic-array optical clock with single-atom readout", Phys. Rev. X **9**, 041052 (2019).

- $^{348}$ D. G. Matei, T. Legero, S. Häfner, C. Grebing, R. Weyrich, W. Zhang, L. Sonderhouse, J. M. Robinson, J. Ye, F. Riehle, and U. Sterr, "1.5  $\,\mu$ m lasers with sub-10 mHz linewidth", Phys. Rev. Lett. **118**, 263202 (2017).
- <sup>349</sup>W. Zhang, J. M. Robinson, L. Sonderhouse, E. Oelker, C. Benko, J. L. Hall, T. Legero, D. G. Matei, F. Riehle, U. Sterr, and J. Ye, "Ultrastable silicon cavity in a continuously operating closed-cycle cryostat at 4 K", Phys. Rev. Lett. **119**, 243601 (2017).
- <sup>350</sup>J. M. Robinson, E. Oelker, W. R. Milner, W. Zhang, T. Legero, D. G. Matei, F. Riehle, U. Sterr, and J. Ye, "Crystalline optical cavity at 4 K with thermal-noise-limited instability and ultralow drift", Optica 6, 240–243 (2019).
- <sup>351</sup>M. J. Martin, D. Meiser, J. W. Thomsen, J. Ye, and M. J. Holland, "Extreme nonlinear response of ultranarrow optical transitions in cavity QED for laser stabilization", Phys. Rev. A **84**, 063813 (2011).
- <sup>352</sup>B. T. R. Christensen, M. R. Henriksen, S. A. Schäffer, P. G. Westergaard, D. Tieri, J. Ye, M. J. Holland, and J. W. Thomsen, "Nonlinear spectroscopy of Sr atoms in an optical cavity for laser stabilization", Phys. Rev. A 92, 053820 (2015).
- <sup>353</sup>D. Barberena, R. J. Lewis-Swan, A. M. Rey, and J. K. Thompson, "Ultra narrow linewidth frequency reference via measurement and feedback", en, C. R. Phys. **24**, 55–68 (2023).
- <sup>354</sup>J. Lodewyck, P. G. Westergaard, and P. Lemonde, "Nondestructive measurement of the transition probability in a Sr optical lattice clock", Phys. Rev. A **79**, 061401 (2009).
- <sup>355</sup>J.-B. Béguin, E. M. Bookjans, S. L. Christensen, H. L. Sørensen, J. H. Müller, E. S. Polzik, and J. Appel, "Generation and detection of a sub-Poissonian atom number distribution in a one-dimensional optical lattice", Phys. Rev. Lett. **113**, 263603 (2014).
- <sup>356</sup>G. Vallet, E. Bookjans, U. Eismann, S. Bilicki, R. Le Targat, and J. Lodewyck, "A noise-immune cavity-assisted non-destructive detection for an optical lattice clock in the quantum regime", New J. Phys. **19**, 083002 (2017).

- <sup>357</sup>R. Hobson, W. Bowden, A. Vianello, I. R. Hill, and P. Gill, "Cavity-enhanced non-destructive detection of atoms for an optical lattice clock", Opt. Express **27**, 37099–37110 (2019).
- <sup>358</sup>W. Bowden, A. Vianello, I. R. Hill, M. Schioppo, and R. Hobson, "Improving the *Q* factor of an optical atomic clock using quantum nondemolition measurement", Phys. Rev. X **10**, 041052 (2020).
- <sup>359</sup>S. A. Schäffer, B. T. R. Christensen, M. R. Henriksen, and J. W. Thomsen, "Dynamics of bad-cavity-enhanced interaction with cold Sr atoms for laser stabilization", Phys. Rev. A **96**, 013847 (2017).
- <sup>360</sup>E. A. Bohr, S. L. Kristensen, C. Hotter, S. A. Schäffer, J. Robinson-Tait, J. W. Thomsen, T. Zelevinsky, H. Ritsch, and J. H. Müller, "Collectively enhanced Ramsey readout by cavity sub-to superradiant transition", Nat. Commun. **15**, 1084 (2024).
- <sup>361</sup>S. A. Schäffer, M. Tang, M. R. Henriksen, A. A. Jørgensen, B. T. R. Christensen, and J. W. Thomsen, "Lasing on a narrow transition in a cold thermal strontium ensemble", Phys. Rev. A **101**, 013819 (2020).
- <sup>362</sup>J. Ye, H. J. Kimble, and H. Katori, "Quantum state engineering and precision metrology using state-insensitive light traps", Science **320**, 1734–1738 (2008).
- <sup>363</sup>S. Blatt, J. W. Thomsen, G. K. Campbell, A. D. Ludlow, M. D. Swallows, M. J. Martin, M. M. Boyd, and J. Ye, "Rabi spectroscopy and excitation inhomogeneity in a one-dimensional optical lattice clock", Phys. Rev. A 80, 052703 (2009).
- <sup>364</sup>A. Yariv, **Optical electronics**, Electrical engineering (Saunders College Pub., 1991).
- <sup>365</sup>T. L. Nicholson, S. Campbell, R. Hutson, G. E. Marti, B. Bloom, R. L. McNally, W. Zhang, M. Barrett, M. S. Safronova, G. Strouse, et al., "Systematic evaluation of an atomic clock at 2× 10- 18 total uncertainty", Nat. Commun. **6**, 6896 (2015).
- <sup>366</sup>V. B. Braginsky and F. Y. Khalili, "Quantum nondemolition measurements: the route from toys to tools", Rev. Mod. Phys. **68**, 1–11 (1996).
- $^{367}$ R. Drozdowski, M. Ignaciuk, J. Kwela, and J. Heldt, "Radiative lifetimes of the lowest  $^{3}P_{1}$  metastable states of Ca and Sr", Z. Phys. A **41**, 125–131 (1997).

- <sup>368</sup>T. Zelevinsky, M. M. Boyd, A. D. Ludlow, T. Ido, J. Ye, R. Ciuryło, P. Naidon, and P. S. Julienne, "Narrow line photoassociation in an optical lattice", Phys. Rev. Lett. **96**, 203201 (2006).
- <sup>369</sup>E. Peik and C. Tamm, "Nuclear laser spectroscopy of the 3.5 eV transition in Th-229", EPL **61**, 181 (2003).
- <sup>370</sup>L. Von Der Wense, B. Seiferle, M. Laatiaoui, J. B. Neumayr, H.-J. Maier, H.-F. Wirth, C. Mokry, J. Runke, K. Eberhardt, C. E. Düllmann, et al., "Direct detection of the <sup>229</sup>Th nuclear clock transition", Nature 533, 47–51 (2016).
- 371B. Seiferle, L. von der Wense, P. V. Bilous, I. Amersdorffer, C. Lemell, F. Libisch, S. Stellmer, T. Schumm,
   C. E. Düllmann, A. Pálffy, et al., "Energy of the <sup>229</sup>Th nuclear clock transition", Nature **573**, 243–246 (2019).
- <sup>372</sup>C. Zhang, T. Ooi, J. S. Higgins, J. F. Doyle, L. von der Wense, K. Beeks, A. Leitner, G. A. Kazakov, P. Li, P. G. Thirolf, et al., "Frequency ratio of the <sup>229</sup>mTh nuclear isomeric transition and the <sup>87</sup>Sr atomic clock", Nature 633, 63–70 (2024).
- $^{373}$ V. A. Dzuba, A. Derevianko, and V. V. Flambaum, "High-precision atomic clocks with highly charged ions: nuclear-spin-zero  $f^{12}$ -shell ions", Phys. Rev. A **86**, 054501 (2012).
- <sup>374</sup>M. G. Kozlov, M. S. Safronova, J. R. Crespo López-Urrutia, and P. O. Schmidt, "Highly charged ions: optical clocks and applications in fundamental physics", Rev. Mod. Phys. **90**, 045005 (2018).
- <sup>375</sup>M. A. Cazalilla and A. M. Rey, "Ultracold Fermi gases with emergent SU(N) symmetry", Rep. Prog. Phys. **77**, 124401 (2014).
- <sup>376</sup>A. J. Daley, "Quantum computing and quantum simulation with group-II atoms", Quantum Inf. Process. **10**, 865–884 (2011).
- <sup>377</sup>E. J. Davis, G. Bentsen, L. Homeier, T. Li, and M. H. Schleier-Smith, "Photon-mediated spin-exchange dynamics of spin-1 atoms", Phys. Rev. Lett. **122**, 010405 (2019).
- <sup>378</sup>V. D. Vaidya, Y. Guo, R. M. Kroeze, K. E. Ballantine, A. J. Kollár, J. Keeling, and B. L. Lev, "Tunable-range, photon-mediated atomic interactions in multimode cavity OED", Phys. Rev. X **8**, 011002 (2018).

- <sup>379</sup>H. Ritsch, P. Domokos, F. Brennecke, and T. Esslinger, "Cold atoms in cavity-generated dynamical optical potentials", Rev. Mod. Phys. **85**, 553–601 (2013).
- <sup>380</sup>A. Lamacraft and J. Moore, "Chapter 7 potential insights into nonequilibrium behavior from atomic physics", in **Ultracold bosonic and fermionic gases**, Vol. 5, edited by K. Levin, A. L. Fetter, and D. M. Stamper-Kurn, Contemporary Concepts of Condensed Matter Science (Elsevier, 2012), pp. 177–202.
- <sup>381</sup>M. Heyl, A. Polkovnikov, and S. Kehrein, "Dynamical quantum phase transitions in the transverse-field Ising model", Phys. Rev. Lett. **110**, 135704 (2013).
- <sup>382</sup>B. Žunkovič, M. Heyl, M. Knap, and A. Silva, "Dynamical quantum phase transitions in spin chains with long-range interactions: merging different concepts of nonequilibrium criticality", Phys. Rev. Lett. **120**, 130601 (2018).
- <sup>383</sup>P. Jurcevic, H. Shen, P. Hauke, C. Maier, T. Brydges, C. Hempel, B. P. Lanyon, M. Heyl, R. Blatt, and C. F. Roos, "Direct observation of dynamical quantum phase transitions in an interacting many-body system", Phys. Rev. Lett. **119**, 080501 (2017).
- <sup>384</sup>J. Zhang, P. W. Hess, A. Kyprianidis, P. Becker, A. Lee, J. Smith, G. Pagano, I.-D. Potirniche, A. C. Potter, A. Vishwanath, N. Y. Yao, and C. Monroe, "Observation of a discrete time crystal", Nature 543, 217–220 (2017).
- <sup>385</sup>S. Choi, J. Choi, R. Landig, G. Kucsko, H. Zhou, J. Isoya, F. Jelezko, S. Onoda, H. Sumiya, V. Khemani, C. von Keyserlingk, N. Y. Yao, E. Demler, and M. D. Lukin, "Observation of discrete time-crystalline order in a disordered dipolar many-body system", Nature 543, 221–225 (2017).
- <sup>386</sup>N. Fläschner, D. Vogel, M. Tarnowski, B. S. Rem, D. S. Lühmann, M. Heyl, J. C. Budich, L. Mathey, K. Sengstock, and C. Weitenberg, "Observation of dynamical vortices after quenches in a system with topology", Nat. Phys. **14**, 265–268 (2018).
- <sup>387</sup>M. Prüfer, P. Kunkel, H. Strobel, S. Lannig, D. Linnemann, C.-M. Schmied, J. Berges, T. Gasenzer, and M. K. Oberthaler, "Observation of universal dynamics in a spinor Bose gas far from equilibrium", Nature 563, 217–220 (2018).

- <sup>388</sup>S. Erne, R. Bücker, T. Gasenzer, J. Berges, and J. Schmiedmayer, "Universal dynamics in an isolated one-dimensional Bose gas far from equilibrium", Nature **563**, 225–229 (2018).
- $^{389}$ S. Backhaus, S. Pereverzev, R. W. Simmonds, A. Loshak, J. C. Davis, and R. E. Packard, "Discovery of a metastable  $\pi$ -state in a superfluid  $^{3}$ He weak link", Nature **392**, 687–690 (1998).
- <sup>390</sup>J. Marino and S. Diehl, "Quantum dynamical field theory for nonequilibrium phase transitions in driven open systems", Phys. Rev. B **94**, 085150 (2016).
- <sup>391</sup>F. Mivehvar, F. Piazza, and H. Ritsch, "Disorder-driven density and spin self-ordering of a Bose-Einstein condensate in a cavity", Phys. Rev. Lett. **119**, 063602 (2017).
- <sup>392</sup>D. Barberena, R. J. Lewis-Swan, J. K. Thompson, and A. M. Rey, "Driven-dissipative quantum dynamics in ultra-long-lived dipoles in an optical cavity", Phys. Rev. A **99**, 053411 (2019).
- <sup>393</sup>A. Lerose, B. Žunkovič, J. Marino, A. Gambassi, and A. Silva, "Impact of nonequilibrium fluctuations on prethermal dynamical phase transitions in long-range interacting spin chains", Phys. Rev. B **99**, 045128 (2019).
- <sup>394</sup>B. Juliá-Díaz, D. Dagnino, M. Lewenstein, J. Martorell, and A. Polls, "Macroscopic self-trapping in Bose-Einstein condensates: analysis of a dynamical quantum phase transition", Phys. Rev. A **81**, 023615 (2010).
- <sup>395</sup>B. Swingle, "Unscrambling the physics of out-of-time-order correlators", Nat. Phys. 14, 988–990 (2018).
- <sup>396</sup>N. Chamel, "Superfluidity and superconductivity in neutron stars", J. Astrophys. Astron. **38**, 43 (2017).
- <sup>397</sup>A. Sedrakian and J. W. Clark, "Superfluidity in nuclear systems and neutron stars", Eur. Phys. J. A **55**, 1–56 (2019).
- $^{398}$ J. G. Bednorz and K. A. Müller, "Possible high  $T_c$  superconductivity in the Ba-La-Cu-O system", Z. Phys. B **64**, 189–193 (1986).
- <sup>399</sup>B. DeMarco and D. S. Jin, "Onset of Fermi degeneracy in a trapped atomic gas", Science **285**, 1703–1706 (1999).

- <sup>400</sup>A. F. Volkov and S. M. Kogan, "Collisionless relaxation of the energy gap in superconductors", Zh. Eksperim. i Teor. Fiz. **38**, [Russian original Zh. Eksp. Teor. Fiz. **65**, 2038 (1973)], 1018 (1974).
- <sup>401</sup>H. P. O. Collado, N. Defenu, and J. Lorenzana, "Engineering Higgs dynamics by spectral singularities", Phys. Rev. Res. **5**, 023011 (2023).
- <sup>402</sup>X. Zhou, W.-S. Lee, M. Imada, N. Trivedi, P. Phillips, H.-Y. Kee, P. Törmä, and M. Eremets, "High-temperature superconductivity", Nat. Rev. Phys. **3**, 462–465 (2021).
- <sup>403</sup>E. Shuryak, "Strongly coupled quark-gluon plasma in heavy ion collisions", Rev. Mod. Phys. **89**, 035001 (2017).
- <sup>404</sup>D. Harlow, "Jerusalem lectures on black holes and quantum information", Rev. Mod. Phys. **88**, 015002 (2016).
- <sup>405</sup>R. J. Lewis-Swan, D. Barberena, J. R. K. Cline, D. J. Young, J. K. Thompson, and A. M. Rey, "Cavity-QED quantum simulator of dynamical phases of a Bardeen-Cooper-Schrieffer superconductor", Phys. Rev. Lett. 126, 173601 (2021).
- <sup>406</sup>S. P. Kelly, J. K. Thompson, A. M. Rey, and J. Marino, "Resonant light enhances phase coherence in a cavity QED simulator of fermionic superfluidity", Phys. Rev. Res. **4**, L042032 (2022).
- <sup>407</sup>J. C. Allred, R. N. Lyman, T. W. Kornack, and M. V. Romalis, "High-sensitivity atomic magnetometer unaffected by spin-exchange relaxation", Phys. Rev. Lett. **89**, 130801 (2002).
- <sup>408</sup>A. Kleine, C. Kollath, I. P. McCulloch, T. Giamarchi, and U. Schollwoeck, "Excitations in two-component Bose gases", New J. Phys. **10**, 045025 (2008).
- <sup>409</sup>C. Deutsch, F. Ramirez-Martinez, C. Lacroûte, F. Reinhard, T. Schneider, J. N. Fuchs, F. Piéchon, F. Laloë, J. Reichel, and P. Rosenbusch, "Spin self-rephasing and very long coherence times in a trapped atomic ensemble", Phys. Rev. Lett. **105**, 020401 (2010).
- <sup>410</sup>P. Fulde and R. A. Ferrell, "Superconductivity in a strong spin-exchange field", Phys. Rev. **135**, A550–A563 (1964).

- <sup>411</sup>A. I. Larkin and Y. N. Ovchinnikov, "Nonuniform state of superconductors", Zh. Eksperim. i Teor. Fiz. **Vol: 47** (1964).
- <sup>412</sup>R. Richardson and N. Sherman, "Exact eigenstates of the pairing-force Hamiltonian", Nucl. Phys. **52**, 221–238 (1964).
- <sup>413</sup>M. Gaudin, "Diagonalization of a class of spin Hamiltonians", J. Phys. (Paris) **37**, 1087–1098 (1976).
- <sup>414</sup>C. A. Regal, M. Greiner, and D. S. Jin, "Observation of resonance condensation of fermionic atom pairs", Phys. Rev. Lett. **92**, 040403 (2004).
- <sup>415</sup>M. W. Zwierlein, C. A. Stan, C. H. Schunck, S. M. F. Raupach, A. J. Kerman, and W. Ketterle, "Condensation of pairs of fermionic atoms near a Feshbach resonance", Phys. Rev. Lett. **92**, 120403 (2004).
- <sup>416</sup>A. V. Andreev, V. Gurarie, and L. Radzihovsky, "Nonequilibrium dynamics and thermodynamics of a degenerate Fermi gas across a Feshbach resonance", Phys. Rev. Lett. **93**, 130402 (2004).
- <sup>417</sup>M. Baghdad, P.-A. Bourdel, S. Schwartz, F. Ferri, J. Reichel, and R. Long, "Spectral engineering of cavity-protected polaritons in an atomic ensemble", Nat. Phys. **19**, 1104–1109 (2023).
- <sup>418</sup>N. Sauerwein, F. Orsi, P. Uhrich, S. Bandyopadhyay, F. Mattiotti, T. Cantat-Moltrecht, G. Pupillo, P. Hauke, and J.-P. Brantut, "Engineering random spin models with atoms in a high-finesse cavity", Nat. Phys. **19**, 1128–1134 (2023).
- <sup>419</sup>A. M. Rey, L. Jiang, M. Fleischhauer, E. Demler, and M. D. Lukin, "Many-body protected entanglement generation in interacting spin systems", Phys. Rev. A **77**, 052305 (2008).
- <sup>420</sup>J. M. Weiner, K. C. Cox, J. G. Bohnet, Z. Chen, and J. K. Thompson, "Superradiant Raman laser magnetometer", Appl. Phys. Lett. **101**, 261107 (2012).
- <sup>421</sup>J. G. Bohnet, Z. Chen, J. M. Weiner, K. C. Cox, and J. K. Thompson, "Active and passive sensing of collective atomic coherence in a superradiant laser", Phys. Rev. A **88**, 013826 (2013).
- <sup>422</sup>G. R. Stewart, "Unconventional superconductivity", Adv. Phys. **66**, 75–196 (2017).
- <sup>423</sup>M. Sato and Y. Ando, "Topological superconductors: a review", Rep. Prog. Phys. **80**, 076501 (2017).

- <sup>424</sup>T. Schäfer and D. Teaney, "Nearly perfect fluidity: from cold atomic gases to hot quark gluon plasmas", Rep. Prog. Phys. **72**, 126001 (2009).
- <sup>425</sup>Y. Pehlivan, A. Balantekin, T. Kajino, and T. Yoshida, "Invariants of collective neutrino oscillations", Phys. Rev. D **84**, 065008 (2011).
- $^{426}$ A. M. Black-Schaffer, "Edge properties and Majorana fermions in the proposed chiral d-wave superconducting state of doped graphene", Phys. Rev. Lett. **109**, 197001 (2012).
- <sup>427</sup>R. Nandkishore, L. S. Levitov, and A. V. Chubukov, "Chiral superconductivity from repulsive interactions in doped graphene", Nat. Phys. **8**, 158–163 (2012).
- <sup>428</sup>M. L. Kiesel, C. Platt, W. Hanke, D. A. Abanin, and R. Thomale, "Competing many-body instabilities and unconventional superconductivity in graphene", Phys. Rev. B **86**, 020507 (2012).
- $^{429}$ M. L. Kiesel, C. Platt, W. Hanke, and R. Thomale, "Model evidence of an anisotropic chiral d+id-wave pairing state for the water-intercalated Na $_x$ CoO $_2 \cdot y$ H $_2$ O superconductor", Phys. Rev. Lett. **111**, 097001 (2013).
- <sup>430</sup>M. H. Fischer, T. Neupert, C. Platt, A. P. Schnyder, W. Hanke, J. Goryo, R. Thomale, and M. Sigrist, "Chiral *d*-wave superconductivity in SrPtAs", Phys. Rev. B **89**, 020509 (2014).
- <sup>431</sup>R. Laughlin, "Magnetic induction of  $d_{x^2-y^2}+id_{xy}$  order in high- $T_c$  superconductors", Phys. Rev. Lett. **80**, 5188 (1998).
- <sup>432</sup>A. V. Balatsky, I. Vekhter, and J.-X. Zhu, "Impurity-induced states in conventional and unconventional superconductors", Rev. Mod. Phys. **78**, 373–433 (2006).
- <sup>433</sup>K. C. Cox, J. M. Weiner, and J. K. Thompson, "Phase diagram for injection locking a superradiant laser", Phys. Rev. A **90**, 053845 (2014).
- <sup>434</sup>D. M. Stamper-Kurn and M. Ueda, "Spinor Bose gases: symmetries, magnetism, and quantum dynamics", Rev. Mod. Phys. **85**, 1191–1244 (2013).

- $^{435}$ X. Zhang, M. Bishof, S. L. Bromley, C. V. Kraus, M. S. Safronova, P. Zoller, A. M. Rey, and J. Ye, "Spectroscopic observation of SU(N)-symmetric interactions in Sr orbital magnetism", Science **345**, 1467–1473 (2014).
- <sup>436</sup>M. Hebenstreit, B. Kraus, L. Ostermann, and H. Ritsch, "Subradiance via entanglement in atoms with several independent decay channels", Phys. Rev. Lett. **118**, 143602 (2017).
- <sup>437</sup>A. Asenjo-Garcia, H. Kimble, and D. E. Chang, "Optical waveguiding by atomic entanglement in multilevel atom arrays", Proc. Natl. Acad. Sci. U.S.A. **116**, 25503–25511 (2019).
- <sup>438</sup>A. Piñeiro Orioli and A. M. Rey, "Dark states of multilevel fermionic atoms in doubly filled optical lattices", Phys. Rev. Lett. **123**, 223601 (2019).
- <sup>439</sup>D. Hemmer, E. Montaño, B. Q. Baragiola, L. M. Norris, E. Shojaee, I. H. Deutsch, and P. S. Jessen, "Squeezing the angular momentum of an ensemble of complex multilevel atoms", Phys. Rev. A **104**, 023710 (2021).
- <sup>440</sup>A. Chu, A. P. Orioli, D. Barberena, J. K. Thompson, and A. M. Rey, "Photon-mediated correlated hopping in a synthetic ladder", Phys. Rev. Res. **5**, L022034 (2023).
- <sup>441</sup>A. Piñeiro Orioli, J. K. Thompson, and A. M. Rey, "Emergent dark states from superradiant dynamics in multilevel atoms in a cavity", Phys. Rev. X **12**, 011054 (2022).
- <sup>442</sup>B. Sundar, D. Barberena, A. M. Rey, and A. P. Orioli, "Squeezing multilevel atoms in dark states via cavity superradiance", Phys. Rev. Lett. **132**, 033601 (2024).
- <sup>443</sup>Q. Chen, Z. Wang, R. Boyack, S. Yang, and K. Levin, "When superconductivity crosses over: from BCS to BEC", Rev. Mod. Phys. **96**, 025002 (2024).
- <sup>444</sup>H. Dong, D.-Z. Xu, J.-F. Huang, and C.-P. Sun, "Coherent excitation transfer *via* the dark-state channel in a bionic system", Light Sci. Appl. 1, e2 (2012).
- <sup>445</sup>A. Potočnik, A. Bargerbos, F. A. Y. N. Schröder, S. A. Khan, M. C. Collodo, S. Gasparinetti, Y. Salathé, C. Creatore, C. Eichler, H. E. Türeci, A. W. Chin, and A. Wallraff, "Studying light-harvesting models with superconducting circuits", Nat. Comm. 9, 904 (2018).

- <sup>446</sup>D. J. Gorman, B. Hemmerling, E. Megidish, S. A. Moeller, P. Schindler, M. Sarovar, and H. Haeffner,
  "Engineering vibrationally assisted energy transfer in a trapped-ion quantum simulator", Phys. Rev. X
  8, 011038 (2018).
- <sup>447</sup>M. E. Gehm, "Preparation of an optically-trapped degenerate Fermi gas of <sup>6</sup>Li: finding the route to degeneracy", PhD thesis (Duke University, Feb. 2003).
- <sup>448</sup>T. G. Tiecke, "Feshbach resonances in ultracold mixtures of the fermionic quantum gases <sup>6</sup>Li and <sup>40</sup>K",
  PhD thesis (University of Amsterdam, Dec. 2009).
- <sup>449</sup>C. Chin, R. Grimm, P. Julienne, and E. Tiesinga, "Feshbach resonances in ultracold gases", Rev. Mod. Phys. **82**, 1225–1286 (2010).
- <sup>450</sup>T. Köhler, K. Góral, and P. S. Julienne, "Production of cold molecules via magnetically tunable Feshbach resonances", Rev. Mod. Phys. **78**, 1311–1361 (2006).
- <sup>451</sup>T. Langen, G. Valtolina, D. Wang, and J. Ye, "Quantum state manipulation and cooling of ultracold molecules", Nat. Phys. **20**, 702–712 (2024).
- <sup>452</sup>R. Haussmann, M. Punk, and W. Zwerger, "Spectral functions and rf response of ultracold fermionic atoms", Phys. Rev. A **80**, 063612 (2009).
- 453 M. Inguscio, W. Ketterle, and C. Salomon, Ultra-cold Fermi gases: proceedings of the international school of physics "Enrico Fermi", course CLXIV, [held in] Varenna on Lake Como, Villa Monastero, 20-30 June 2006, Proceedings of the International School of Physics "Enrico Fermi" (IOS Press, 2007).
- <sup>454</sup>I. R. Senitzky, "Interaction between a nonlinear oscillator and a radiation field", Phys. Rev. A **6**, 1175–1196 (1972).
- <sup>455</sup>P. Drummond and H. Carmichael, "Volterra cycles and the cooperative fluorescence critical point", Opt. Commun. **27**, 160–164 (1978).
- <sup>456</sup>H. Carmichael, "Analytical and numerical results for the steady state in cooperative resonance fluorescence", J. Phys. B: Atom. Mol. Phys. **13**, 3551 (1980).

- <sup>457</sup>G. Ferioli, A. Glicenstein, I. Ferrier-Barbut, and A. Browaeys, "A non-equilibrium superradiant phase transition in free space", Nat. Phys. **19**, 1345–1349 (2023).
- <sup>458</sup>S. Agarwal, E. Chaparro, D. Barberena, A. P. Orioli, G. Ferioli, S. Pancaldi, I. Ferrier-Barbut, A. Browaeys, and A. Rey, "Directional superradiance in a driven ultracold atomic gas in free space", PRX Quantum **5**, 040335 (2024).
- <sup>459</sup>J. Ruostekoski, "Superradiant phase transition in a large interacting driven atomic ensemble in free space", Opt. Quantum **3**, 15–21 (2025).
- <sup>460</sup>D. Goncalves, L. Bombieri, G. Ferioli, S. Pancaldi, I. Ferrier-Barbut, A. Browaeys, E. Shahmoon, and D. Chang, "Driven-dissipative phase separation in free-space atomic ensembles", PRX Quantum 6, 020303 (2025).
- $^{461}$ R. L. Mössbauer, "Kernresonanzabsorption von  $\gamma$ -Strahlung in Ir191", Z. Naturforsch. A **14**, 211–216 (1959).
- <sup>462</sup>R. V. Pound and G. A. Rebka, "Apparent weight of photons", Phys. Rev. Lett. **4**, 337–341 (1960).
- <sup>463</sup>Z. Niu, V. M. Schäfer, H. Zhang, C. Wagner, N. R. Taylor, D. J. Young, E. Y. Song, A. Chu, A. M. Rey, and J. K. Thompson, "Many-body gap protection against motional dephasing of an optical clock transition", Phys. Rev. Lett. **134**, 113403 (2025).
- <sup>464</sup>B. Wu, G. P. Greve, C. Luo, and J. K. Thompson, **Site-dependent selection of atoms for homogeneous atom-cavity coupling**, 2021, arXiv:2104.01201 [quant-ph].
- <sup>465</sup>C. Shu, S. Colombo, Z. Li, A. Adiyatullin, E. Mendez, E. Pedrozo-Peñafiel, and V. Vuletić, "Increased atom-cavity coupling through cooling-induced atomic reorganization", Phys. Rev. Res. **6**, L032049 (2024).